I. Mutltiscaling: Size and Time

WHAT IS THERE TO GAIN BY MULTISCALING FROM THE VERY SMALL TO THE VERY LARGE?

G. C. Sih
School of Mechanical and Power Engineering, East China University of Science and Technology, Shanghai 200237, China
Department of Mechanical Engineering and Mechanics, Lehigh University, Bethlehem, PA 18015, USA
*Email: gcs@ecust.edu.cn and gcs8866@yahoo.com

Abstract

Manipulation of atoms and molecules for the enhancement of the macroscopic behavior of materials is no longer uncommon to the researchers in material science. The concept of use specific materials has also attracted the manufacturers in aeronautics where composites are readily used. This entails a spectrum of scale for the microstructure to the bulk properties of the material going from the nano to the macro. From the structure and material integrity view point, if the abnormal conditions can be detected at the lower scale, this may lead to early detection of malfunction at the higher scale to provide early warning. Such a benefit, however, can be achieved only if effective models can be developed by multiscaling and covering a sufficiently wide scale range of several orders of magnitude in lineal dimension. This is not within the capability of the theoretic non-linear continuum approach.

The general scheme of multiscaling in material science application has been addressed. It involved the division of the non-equilibrium process into several smaller equilibrium segments such that conventional methodologies can be applied. Characteristic length parameters, say at the macro, micro and dislocation level, were introduced to account for change in the degree of inhomogeneity when scale range is shifted. Specific application to engineering problems, however, further requires effective physical models of the defect configuration whose morphology changes with the size scale. Even the theoretical and physical differences of a macrocrack and microcrack has not been explored up to now. Their only distinction is that one is microscopic and the other is macroscopic in length. This in principle is not acceptable, the details of which will be pointed out in light of developing multiscale damage models. Unlike previous models, the microcrack surfaces will no longer be assumed as traction free. That is the microcrack will have a stress singularity other then $1/r^{0.5}$ because of the influence of the material microstructure that can exert a variety of constraints on the microcrack surface. Such an allowance can lead to a microcrack tip singularity of the order of $1/r^{0.75}$ depending on the particular mixed boundary conditions on the microcrack. This is in contrast to the $1/r^{0.5}$ macrocrack stress singularity for the traction free condition and to the 1/r singularity of the dislocational stresses of the edge- or screw-type. For a fault line or crack in the microscopic range, the singularity representation scheme suggests the order

$1/r^{\lambda}$ where $0.5<\lambda<1.0$. A cluster of such single fault lines can then be considered to generate macro-defects. In this way, a multiscale damage model can be developed where the change in system inhomogeneity can be accounted for in addition to non-equilibrium by adapting the segmentation approach.

1. Introduction

The parallel advancement of fundamental science and applied technology cannot be more evident than the field of nanoelectronics which has set the pace for other disciplines. This includes chemistry, physics, biology, material science and mechanics. The trend has been the micromanipulation of atoms and/or molecules for controlling the behavior of macroscopic material properties or of cells in vivo. Material science alone has benefited from the concept of use specificity. The application has ranged from the studies of bio-tissues to jumbo-jet aircraft structural component materials. The realization that micromanipulation can be made more effective by relating the results at the nano-scale to that of the micro-scale has prompted the development of multiscale models rather than relying on speculative and empirical approaches. No theories at the present can be extended to cover the space/time scale where quantum mechanics terminates and continuum mechanics begins. While the former has been custom made for subatomic particles the latter has been developed for large bodies where the bulk material properties can be used. However, there are a host of physical events that are left unconnected in between the quantum and the continuum. One of these segments in electronics has now been identified as meso-electronics [1]. The same applies to the mechanics of deformable bodies where the unfamiliar domain is being referred to as Mesomechanics [2-4]. Similar regions have yet to be found for other fields. What this means is that the available theories are unable to keep pace with the space/time range required by the physical events that are being discovered. The reconciliation of quantum mechanics with general relativity is still pending on the outcome of quantum gravity theory. Multiscaling as considered here pertains to connecting results from the different space/time segments. The aim is to understand macroscopic consequences of microscopic structure. Such an objective is not new. It has been attempted by non-linear continuum mechanics theoretic approach in the past with limited success. Ii should have been known that those theories advocating the vanishing rate change of volume with surface expressed by $\Delta V/\Delta A \rightarrow 0$ are disqualified for application to problems with non-equilibrium phenomena which are inherent characteristics of interface and/or inter-phase. The Navier-Stokes equation is invalid near the wall where the bulk properties of the fluid are inadequate for describing the near surface fluid behavior. It should also have been known that classical continuum mechanics disconnects the surface from the volume. The condition $\Delta V/\Delta A \rightarrow 0$ would be regarded as a fatal blow to the holy grail for those who delve in developing the string theory. One of the basic premises is that “surface” laws where quantum particles interacting like quarks and gluons are equivalent to “volume” (or interior) laws that are a form of string theory including the force of gravity. The detrimental consequence of disconnecting surface from the volume cannot be over emphasized. It would deprive the equivalency of the particle description on the surface to that of the gravity dependent object in the volume, the pillar of the holographic theory [5].

Interaction of surface and volume should be of no surprise to everyday engineers and scientists who in fact make use of such relationships without question. Volume integrals in finite element

analysis are converted to boundary integrals as a matter of foregone conclusion. The divergence theorem testifies to such an operation. The Green's theorem is used in text books time and over again to show the equivalence of surface and boundary integrals for satisfying certain boundary conditions. Reduction in dimensionality is not a strange notion in engineering application. The energy used in a surface layer weighed against that expended in a unit volume has been known to determine the size of a grain in the Gibb's theory of crystal nucleation. If a three dimensional volume integral can be reduced to a two-dimensional surface integral and if a two-dimensional surface integral can be reduced to a one-dimensional contour integral, then there is no reason why the deduction cannot work for the reduction of a three-dimensional space to one dimension. This is precisely what happens in an isoenergy density space where a three-dimension physical space transforms into one-dimension [6]. That is a tensorial quantity becomes a scalar. If indeed, the string theory is able to resolve the duality separating the particles and fields, then multiscaling can cover the full range from the subatomic to the continuum. Until then, there prevails the mesoscopic zone that will take the transition for granted. Even in the absence of the fundamental issue of particle and field, mutliscaling is not a trivial undertaking.

This is because size reduction encourages non-equilibrium where the microscopic character of the material properties can no longer be averaged as the bulk and approximated by equilibrium conditions where time and non-homogeneity are smeared out. And yet this is precisely the region where nano-technology applies. This work represents the initial effort made to model defects and imperfections at the macro-, micro- and atomic scale by application of the continuum theories stopping short at quantum mechanics, the equivalent of which in continuum mechanics would the theory of non-equlibrium mechanics [6,7]. That is when spatial and temporal effects are intrinsically interwoven and the solutions are no longer unique by definition. Keep in mind that there is no proof for uniqueness when the medium is completely non-homogeneous. Refer to the work in [7,8] for physical examples of bi-phase media. In an open thermo-dynamic system, the system and its surrounding would be regarded as bi-phase. To circumvent the use of non-equilibrium theories, the scale range from macroscopic to atomic will be segmented into three stages, i,e., macro-, micro- and smaller-scale if needed. Meso-zones can be introduced to soften the jumps at the connections. Segmen-tation is made to allow the use of equilibrium mechanics within each segments. This is accomplished by appli-cation of the singularity representation method of material damage. The approach was originally used at the macroscopic scale, later extended to include damage at the microscopic scale [9,10]. In this way, physical parameters at the different scales can be stretched several order of magnitude (say 8 or more in lineal dimension). The range of ordi- nary linear or non-linear theories posse- sses at most one order of magnitude in lineal dimension. With the advent of the scale multiplier concept [11], closed form solutions can also be obtained for localized regions where dominant energy transfer takes place. The methodology, however, were developed for a micro-crack that satisfies the same free-free traction conditions as those for a macro-crack. Such an assumption was necessary because of the lack of a more realistic solution for the microcrack. This shortcoming was examined only recently [12] in connection with associating physical characteristic lengths to the strong and weak singularities to multiscale modelling.

This work continues the discussion and explores the possibility of including a more realistic microcrack before concerning imperfections at the quantum scale where the discrete and continuum disparities remain to be reconciled. Also keep in mind that multiscaling would be stymied if the distinction between the local and bulk properties of the materials is not made. This gigantic step has been skipped in solid state physics and material science texts by equating the results obtained from the inter-atomic force potential directly to the classical thermodynamic relations for bulk compression. Tabulated bulk modulus for the different chemical elements are reported without realizing that an empirical scale shifting factor was used. The bulk or Young's modulus E is a macroscopic quantity while the strength calculated from the inter-atomic force potential is microscopic. The approximate agreement of the end result with the uniaxial tensile data for metals is made possible by the empirical factor E/10 or E/15 that accounted for scale shifting. Such a defacto procedure cannot be justified in the development of multiscale models.

Proposed therefore is to implement the non-equilibrium process by equilibrium segments limited in range such that conventional methodologies can be applied. Characteristic length parameters, say at the macro, micro and dislocation level, can then be introduced for the respective volume energy densities. The total energy or force criterion being scale invariant can be applied to connect the divided segments. Because there is still no general agreement with reference to the unification of the four fundamental forces, multiscaling cannot be expected to do any better.

2. Scale shifting scheme based on singularity representation

The scheme for relating the results in small regions to those in large regions will be accomplished in segments by application of the volume energy density function dW/dV to be written as $\dot{W}$. Recall that the form dW/dV = S/r has been used frequently in connection with the strain energy density criterion [14,15] where the energy density factor S depends only on the polar angle θ for homogeneous systems. When system inhomogeneity prevails, the function S will also depend on r, the distance from the point of singularity. For the sake of familiarity the 1/r form will be preserved with the emphasis that

$$S = S(\theta) \text{ homogeneous} \quad \text{and} \quad S = S(r,\theta) \text{ non-homogeneous} \qquad (1)$$

The dependency of S on r arises from system inhomogeneity which deprives the uniquenss of solution in the theory of elasticity.

Segmentation in scaling.
Change of system homogeneity is made possible by introducing characteristic length parameters ℓ_j for each segment j within which the subsystem is homogeneous. A time dependent scale shifting criterion can thus be stated [16]:

The time rate of the energy density factor is assumed to remain unchanged between two successive scale range.

Stated mathematically are the expressions [16]

$$m_j \dot{S}_j = \dot{S}_{j+1} \quad \text{or} \quad m_j \ell_j \dot{W}_j = \ell_{j+1} \dot{W}_{j+1} \qquad (2)$$

where use has been made of the relation S = r $\dot{W}$ with r being replaced by ℓ. The factor m_j is unity for all segments j = 1,2, etc. if the curve for $\dot{W}$ versus distance r is a perfect hyperbola. This corresponds to a perfectly homogeneous system. The deviation from a hyperbola is expressed by the factor m_j for segments j = 1,2, etc. It is not difficult to see that $\dot{S}$ is the area

under the time rate of $\dot{W}$ or $\dot{W}$ versus distance r curve as shown in Fig. 1. Application of Eq. (2) to two successive sizes, say

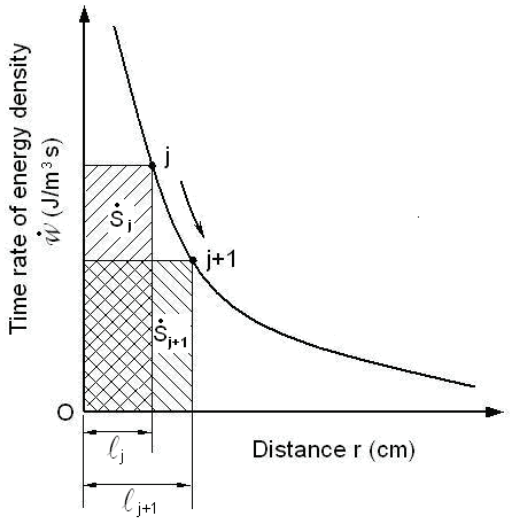

Figure 1: *Time rate of energy density* $\dot{W}$ *versus distance r: scale shifting scheme.*

nano to micro and micro to macro can then be written as

$$m_{nano\to micro}\dot{S}_{nano} = \dot{S}_{micro} \quad \text{and}$$
$$m_{micro\to macro}\dot{S}_{micro} = \dot{S}_{macro} \qquad (3)$$

To repeat, the shaded areas $\dot{S}_j$ and $\dot{S}_{j+1}$ for segment from j to j+1 would be equal if the curve is a true hyperbola. Assuming that j and j+1 correspond, respectively to nano and micro, then $m_{nano\to micro} = 1$. The factor $m_{nano\to micro}$ serves as a measure of the change in homogeneity when size scale is switched from nano to micro. This change for each segments can be determined by using the singularity representation approach that will be discussed later. That is by finding the $\dot{W}$ versus r curve. The use of Eq. (2) or (3) follows the same thought process as that used in applying the strain energy density criterion [14,15].

System inhomogeneity associated with segment characteristic length.

Singularities are known to represent the character of a system in the limit when the denominator of the quotient out competes the nominator in the time- and/or the space-related variable. Stresses being defined as the quotient of the increment of force to the area become unbounded at a re-entrant corner or crack when the increment of the area tends to be vanishingly small. The degree of severity of this unbounded limit is determined by the order of the stress singularity. They have been discussed [13] in relation to a class of singularities with order weaker and stronger than the classical branch cut in complex variable.

By relating the stress singularity order with the eigenvalue λ in the form $\sigma \approx 1/r^{\lambda}$ with r being the distance to the singularity point, it is possible to assign a characteristic length ℓ to each stress singularity order range based on the physical defect types that have observed experimentally. Their relations can be found in [16] and summarized in Table 1. A graphical display of the information in Table 1 can be found in Fig.2. Determination of the parameter m in Eq. (3) can be best illustrated in Fig. 3 which shows how each successive steps are carried out by following the dW/dV or $\dot{W}$ curve. This is also expressed by the expressions in Eqs. (4):

$$m_{disl\to subg}\ell_{disl.}\dot{W}_{disl} = \ell_{subg}\dot{W}_{subg}$$
$$m_{subg\to micro}\ell_{subg}\dot{W}_{subg} = \ell_{micro}\dot{W}_{micro}$$
$$m_{micro\to macro}\ell_{micro}\dot{W}_{micro} = \ell_{macro}\dot{W}_{.macro.} \qquad (4)$$

Defect type	Order of singularity λ	Characteristic length ℓ (cm)
Dislocation	0.90-0.95	$10^{-6.5}$
Subgrain defect	0.80-0.85	10^{-5}
Microcrack	0.55-0.75	$10^{-3.5}$
Macrocrack	0.50	10^{-2}

Table 1: Order of stress singularity associated with characteristic length [16].

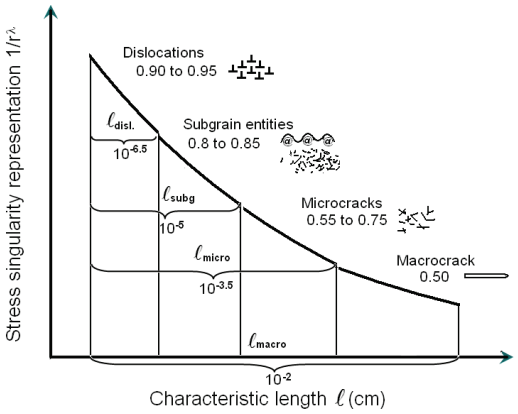

Figure 2: *Characteristic length related to order of stress singularities.*

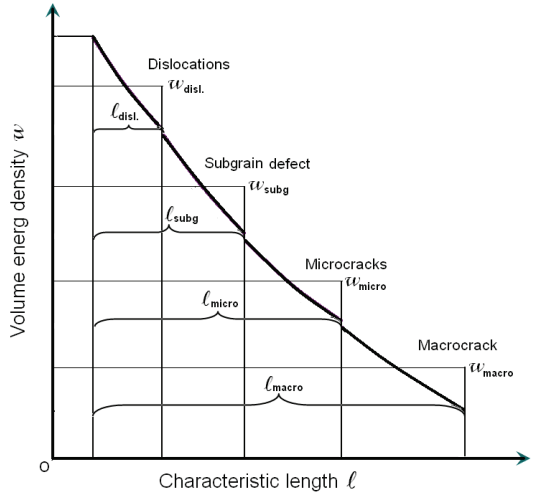

Figure 3: *Classification of volume energy density with characteristic length.*

There remains the determination of the volume energy density functions W_{disl}, W_{subg}, W_{micro} and W_{macro} so that the factors m_j in Eqs. (2) or those in Eqs. (4) can be found. The various segments can then be linked to bridge the results from the small scale to the large scale. For the sake of illustration, discussion will be made only for W_{micro} and W_{macro}. Moreover, time rate effects will be neglected as they would add complexities that are secondary to the development of mutliscale models.

3. Multiscale model with microscopic fault line or microcrack

Consider a macro-stress field with uniform load σ_∞ applied in the x_2 direction as shown in Fig. 4. The medium contains a microcrack of length 2a with a tip section d, the geometry of which depends on the local morphology of the material microstructure. A notch with mixed boundary conditions and variable angle 2β can be used to model the situation. This is particularly essential for modeling the microcrack tip entranched in the microstructure entities. Without loss in generality, the free-fixed boundary condition is used as depicted in Fig. 5 where $\beta^* = \pi - \beta$. Tractions of varying magnitude σ_o can be present on the surfaces of the microcrack. They determine the tightness of the microcrack surfaces. In what follows, uniform σ_o will be taken for simplicity although varying σ_o will likely to be the rule rather than the exception.

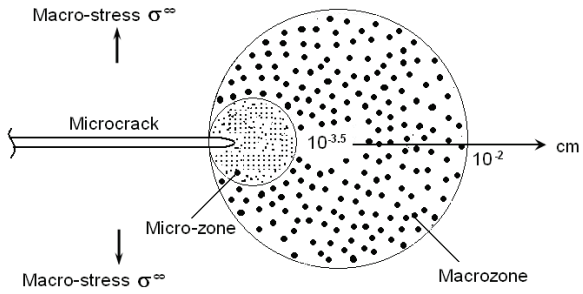

Figure 4: *A microcrack engulfed by a uniform macro-stress field.*

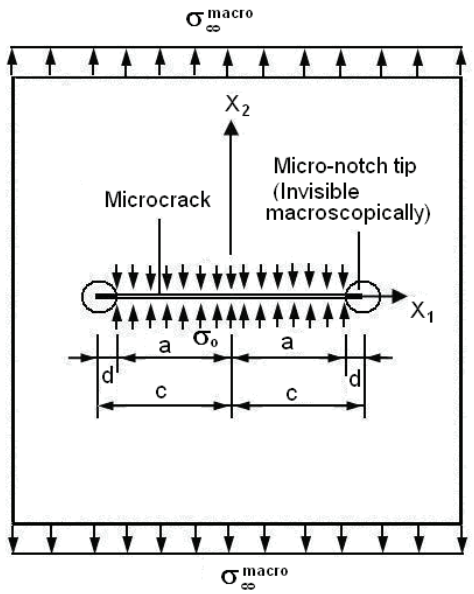

Figure 5: *Surface traction on microcrack with a notch tip.*

Macro-intensification caused by microcracking.

This work will take the opportunity to emphasis not only the need to model microcracks with the effect of microstructure but also the additional feature that a microcrack can cause local macro-intensification. This is illustrated in Fig. 6.Note that there two near field stress zones, one at the microscopic scale and one at the macroscopic scale. The subscript "mimacro" will be adopted to indicate that the macro-intensification $K_I^{mimacro}$ is caused by a microcrack. It should be distinguished from K_I^{macro} representing the stress intensity factor that is caused by the presence of an actual macrocrack. There is no macrocrack in this model but there is a macro-stress intensification around a microcrack with a mixed boundary condition tip where the notch angle 2β can vary or be zero for a crack. Since the applied load in Fig. 4 induces macroscopic symmetry, the macro-displacements contain only $K_I^{mimacro}$ as follows:

$$4\mu_{macro}\sqrt{2\pi}u_r^{mimacro}=\sqrt{r}\{K_I^{mimacro}[(5-8\nu_{macro})\cos\frac{\theta}{2}-\cos\frac{3\theta}{2}]+\cdots$$
$$4\mu_{macro}\sqrt{2\pi}u_\theta^{mimacro}=\sqrt{r}\{K_I^{mimacro}[-(7-8\nu_{macro})\sin\frac{\theta}{2}+\sin\frac{3\theta}{2}]+\cdots \quad (5)$$

where ν_{macro} and μ_{macro} are the macroscopic material constants. Terms of order higher than $r^{1/2}$ with r being macroscopic have been neglected. The corresponding polar

$$\sigma_r^{mimacro}=\sqrt{\frac{2}{\pi r}}[K_I^{mimacro}(3-\cos\theta)\cos\frac{\theta}{2}]+\cdots$$
$$\sigma_\theta^{mimacro}=\sqrt{\frac{2}{\pi r}}[K_I^{mimacro}(1+\cos\theta)\cos\frac{\theta}{2}]+\cdots$$
$$\sigma_{r\theta}^{mimacro}=\sqrt{\frac{2}{\pi r}}[K_I^{mimacro}\sin\theta\cos\frac{\theta}{2}]+\cdots \quad (6)$$

components of the macro-stress field are singular and of the order $r^{-1/2}$ as indicated in Eqs. (6). Fig. 6 shows the relative size of the dual scale near stress field two zones. One is more intensified with the densely spaced dots, the other being less intensified.

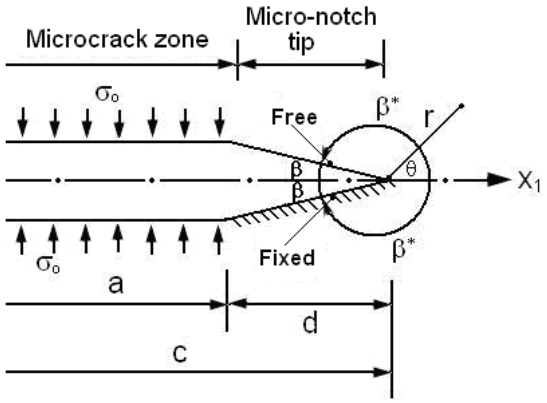

Figure 6: *Dual scale stress intensification zones around a microcrack.*

Without going into details, $K_I^{mimacro}$ can be obtained by a procedure similar to that used for the dual scale model [9] except that the physical interpretation is different since the present model consists of only a microcrack. The result is

$$K_I^{mimacro}=(1-\frac{2\sigma_o}{\pi\sigma_\infty}\sin^{-1}\frac{a}{c})\sigma_\infty\sqrt{\pi c} \quad (7)$$

Note that σ_∞ is the applied macro-stress in Fig. 4 while the ratio σ_o/σ_∞ adjust the tightness of the contacting microcrack surfaces. Higher σ_o/σ_∞ corresponds to microcrack surfaces that are compressed together more severely while. σ_o/σ_∞ 0 is the case of no crack surface constraint where the macro-intensification would be the largest. This effect is exhibited in Fig. 7 for a = 10mm and σ_∞ = 10 MPa as the ratio d/a is varied in increment of 0.01 from 0.0 to 0.1. The intensification increases slightly with the size of the microcrack tip segment d on which part of the surface is free and part is fixed. This corresponds to β = 0 in Fig. 5. Macro-intensification disappears or

$K_I^{mimacro} = 0$ for d = 0 and $\sigma_o/\sigma_\infty = 1$,i.e., when the medium is under uniform stress but not damaged.

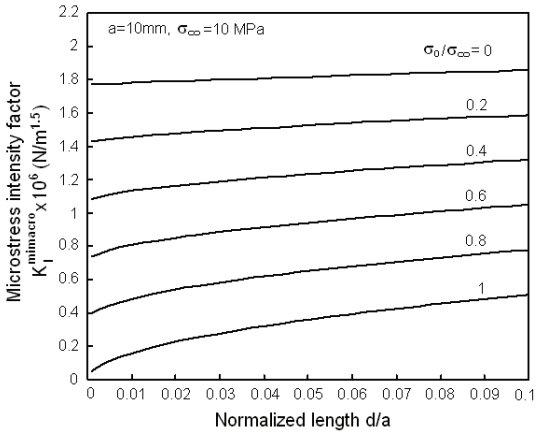

Figure 7: *Variations of macro-intensification with the ratio d/a for different* σ_o/σ_∞

Microcrack tip stress intensity factor.
If the distance r is reduced to the microscopic scale in Fig. 5 with β = 0, then the effect of the microcrack tip will be felt. The order of the micro-stress singularity will depend on the Poisson's ratio. This behavior has been discussed in detailed [13] and will not be repeated here. Of interest is the case of strong singularity where λ > 0.5. Such a possibility can prevail in the limit as $\nu_{micro} \to 0.5$. The governing eigen equation from [13] reduces to

$$1 - \sin^2(2\pi\lambda) = 0 \qquad (8)$$

which yields λ = 0.75 for the order of the micro-stress singularity. The micro-displacements near the tip are given by

$$2\mu_{micro}u_r^{micro} = \frac{K_{I/II}^{micro}}{\sqrt{2\pi}} r_{micro}^{0.25} \frac{5}{4}[-\cos(\tfrac{5}{4}\theta)+\cos(\tfrac{3}{4}\theta)+\sin(\tfrac{5}{4}\theta)+\sin(\tfrac{3}{4}\theta)]+\cdots$$
$$2\mu_{micro}u_\theta^{micro} = \frac{K_{I/II}^{micro}}{\sqrt{2\pi}} r_{micro}^{0.25} \frac{5}{4}[\sin(\tfrac{5}{4}\theta)-\frac{5}{3}\sin(\tfrac{3}{4}\theta)+\cos(\tfrac{5}{4}\theta)+\frac{5}{3}\cos(\tfrac{3}{4}\theta)]+\cdots \qquad (9)$$

The corresponding microcrack tip stresses are

$$\sigma_r^{micro} = \frac{K_{I/II}^{micro}}{r_{micro}^{0.75}\sqrt{2\pi}} \frac{5}{16}[-\cos(\tfrac{5}{4}\theta)+\frac{11}{3}\cos(\tfrac{3}{4}\theta)+\sin(\tfrac{5}{4}\theta)+\frac{11}{3}\sin(\tfrac{3}{4}\theta)]+\cdots$$
$$\sigma_\theta^{micro} = \frac{K_{I/II}^{micro}}{r_{micro}^{0.75}\sqrt{2\pi}} \frac{5}{16}[\cos(\tfrac{5}{4}\theta)+\frac{5}{3}\cos(\tfrac{3}{4}\theta)-\sin(\tfrac{5}{4}\theta)+\frac{5}{3}\sin(\tfrac{3}{4}\theta)]+\cdots$$
$$\sigma_{r\theta}^{micro} = \frac{K_{I/II}^{micro}}{r_{micro}^{0.75}\sqrt{2\pi}} \frac{5}{16}[\sin(\tfrac{5}{4}\theta)+\sin(\tfrac{3}{4}\theta)+\cos(\tfrac{5}{4}\theta)-\cos(\tfrac{5}{4}\theta)]+\cdots \qquad (10)$$

The evaluation of the micro-stress intensity factor $K_{I/II}^{micro}$ can be found in [17] and will not be dealt with here since it would be beyond the scope of this work. The subscript I/II signifies microscopic anti-symmetry is permitted even though the loading is symmetric at the macroscopic scale. In this special case of $\nu_{micro} \to 0.5$, the skew-symmetric portion of the micro-stress field vanishes. Except for the macro-stress σ_∞ , Poisson's ratio ν_{macro} and shear modulus μ_{macro}, all of the other quantities in Eq. (11) are microscopic.

$$K_{I/II}^{micro} = \frac{6\sqrt{\pi}(1-\nu_{macro})\mu_{micro}\sigma_\infty\sqrt{c^2-a^2}}{5d^{0.25}\mu_{macro}}\left(1-\frac{2\sigma_o}{\pi\sigma_\infty}\sin^{-1}\frac{a}{c}\right) \qquad (11)$$

Numerical values of Eq. (11) are obtained for a = 10 mm, σ_∞ = 10 MPa and ν_{macro}= 0.3 although the condition of microscopic $\nu_{micro} \to 0.5$ was used to find Eq. (11).

Fig. 8 gives a plot of $K_{I/II}^{micro}$ versus d/a for E_{micro}/E_{macro} = 4 as σ_o/σ_∞ = 0.0, 0.2, ---, 1.0. Although the general trend of the curves are similar to that in Fig. 7 but the micro-stress intensity factor is more sensitive to d/a and the curves rise faster for small d/a as they should. A similar plot of $K_{I/II}^{micro}$ versus d/a can be found in Fig. 9 for σ_o/σ_∞ = 0.5 but for three values of E_{micro}/E_{macro}=3, 4 and 5. It is seen that the microcrack tip stress becomes more intensified as the micro-modulus is increased relative to the macro-modulus. This effect increases with increasing d/a.

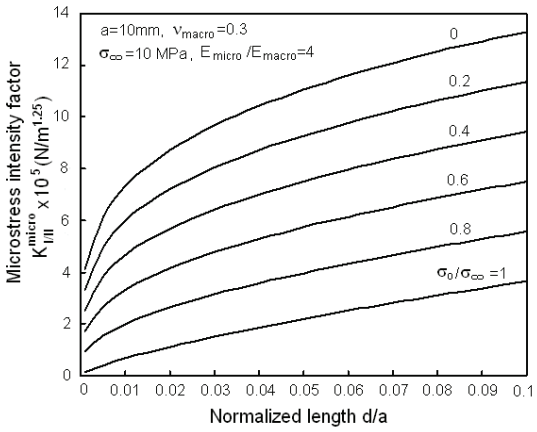

Figure 8: *Micro-stress intensity factor versus ratio d/a for different σ_o/σ_∞ with E_{micro}/E_{macro} = 4.*

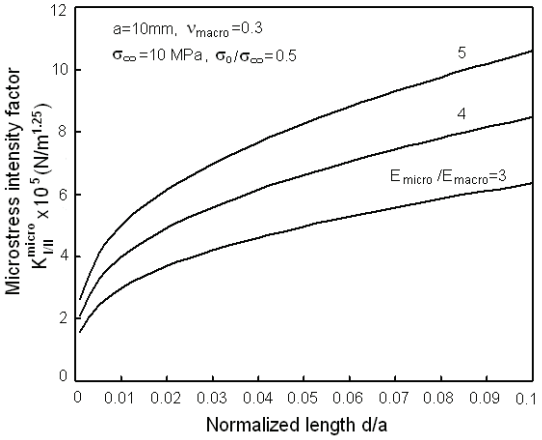

Figure 9: *Micro-stress intensity factor versus ratio d/a for different E_{micro}/E_{macro} with σ_o/σ_∞ = 0.5.*

Macro/micro intensification of volume energy density.

Once the stresses are known from Eqs. (6) and (10), the corresponding volume energy densities can also be found in the macro-size zone as

$$W^{mimacro}=\frac{(1+\nu_{macro})(1-2\nu_{macro})(\sigma_\infty)^2}{2E_{macro}}\left(1-\frac{2\sigma_o}{\pi\sigma_\infty}\sin^{-1}\frac{a}{c}\right)^2\frac{c}{r_{macro}} \quad (12)$$

and the micro-size zone as

$$W^{micro}=\frac{(1-2\nu_{micro})(1-\nu_{macro})^2}{4\mu_{micro}}\left(\frac{\mu_{micro}}{\mu_{macro}}\sigma_\infty\right)^2\left(1-\frac{2\sigma_o}{\pi\sigma_\infty}\sin^{-1}\frac{a}{c}\right)^2\frac{(c}{d^0} \quad (13)$$

Eqs. (12) and (13) correspond to $\theta = 0$, i.e., along the x_1 axis.More specifically, the notation $W^{mimacro}$ and W^{micro} stand, respectively, for $(dW/dV)^{mimacro}$ and $(dW/dV)^{micro}$. The macro-dW/dV has the $1/r_{macro}$ singularity and the micro-dW/dV has the $1/ r_{micro}^{1.5}$ singularity. There is a discontinuity which occurs at $r = 10^{-3}$ cm. This is illustrated in Figs. 10 and 11 for plots of $W^{mimacro}$ and W^{micro} versus the radial distance r along the x_1 axis in Fig. 4. The numerical values chosen for the various parameters are a = 10mm, d/a= 0.01, $\nu_{macro} = 0.3$, $\nu_{micro} \approx 0.5$, E_{macro}= 200 GPa and σ_∞ = 10 MPa. In Fig. 10, the moduli ratio is fixed at $E_{micro}/ E_{macro} = 4$ while σ_o/σ_∞ = 0.0, 0.2, ---, 1.0. Both the micro- and macro-volume energy density increase with decreasing constraint to the microcrack surface. The top curves for $\sigma_o/\sigma_\infty = 0$ correspond to no constraint. The discontinuities in dW/dV may be reduced by introducing a meso zone such that the transition from micro to macro can be less sudden. By having $\sigma_o/\sigma_\infty = 0.5$, the ratio E_{micro}/ E_{macro} can take values of 3, 4 and 5. These results are displayed graphically in Fig. 11. the same discontinuity is observed at $r = 10^{-3}$ cm but the curves are spaced much closer than those in Fig. 10.That is $W^{mimacro}$ and W^{micro} are less sensitive to variations in E_{micro}/ E_{macro}. It should be said in passing that the micro and macro material constants need not be the same. They are distinguished as

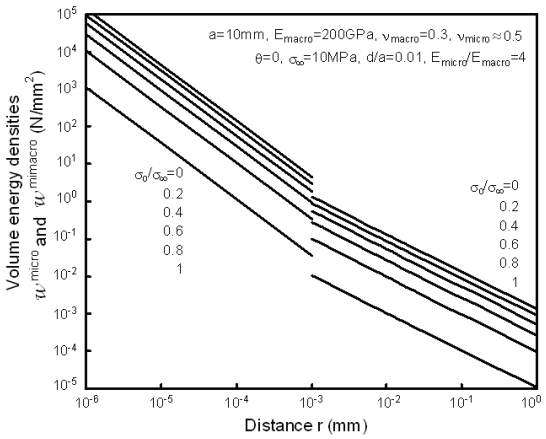

Figure 10: *Variations of micro- and macro-volume energy density with distance for E_{micro}/ E_{macro} = 4 and different σ_o/σ_∞.*

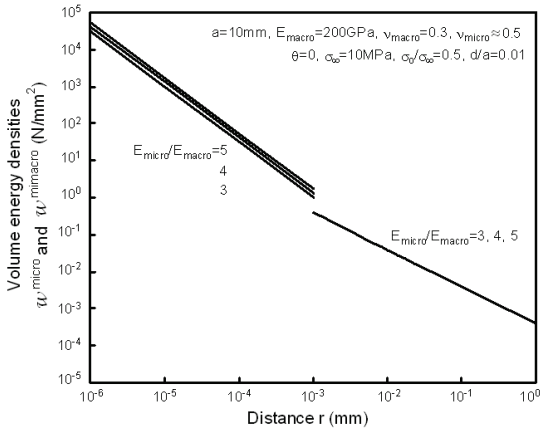

Figure 11: *Variations of micro- and macro-volume energy density with distance for* σ_o/σ_∞ *= 0.5 and different* E_{micro}/E_{macro}.

$$\mu_{macro} = \frac{E_{macro}}{2(1+\nu_{macro})}, \qquad \mu_{micro} = \frac{E_{micro}}{2(1+\nu_{micro})} \tag{14}$$

For ν_{macro}=0.3, ν_{micro}=0.48, Eqs. (14) yield.

$$\frac{\mu_{micro}}{\mu_{macro}} = 0.87\frac{E_{micro}}{E_{macro}} \tag{15}$$

Computer results have generally acknowledged that E_{micro}/E_{macro}=3, 4, 5. Hence, the application of Eqs. (14) and (15) suggest that

$$\frac{\nu_{micro}}{\nu_{macro}} = 0.87\frac{E_{micro}}{E_{macro}} = 2.60, 3.67, 4.33 \tag{16}$$

These results appear to be consistent with known findings although there are no precise validation from experiments.

4. Concluding remarks and future research

The benefit to be gained by quantifying the results at the lower scale to that at the macroscopic scale can be best recognized in brain-simulation research. Electrodes may be implanted in animals or humans [18] to correct disorders such as epilepsy, Parkinson's decease and blindness. Detection of disorder of cells and relate it to macroscopic behavior would involve the abridgement of scale range of several orders of magnitude. The same basic idea applies to materials that might have degraded prematurely in an aggressive environment and the detrimental effects may not show up at the macroscopic scale until much later in time such that irreversibility has been set. This may well be the scenario found in low alloy steels for LWR where nanometer size defects have been identified by tests as potential source of inter-granular stress corrosion cracking. Even smaller size defects or imperfections might have occurred but their detection may have to wait for further refinement of electron microscope resolution. The development of multi-scale damage models becomes an absolute necessity.

The difficulty associated with multiscaling is the enormous range of size scale extending from the nano to the macro, not to mention the time scale as well. This problem is not unique in material science, it occurs in life science as well. Such a challenge was not realized until the advent of nanotechnology [19] and the recognition that there is a gold mine to be benefited by going small. Upon closer examination, the process of multiscaling is stymied at the very stage when attempting to relate micro and macro damage effects, even for the simple configuration of a line defect or crack. Previously taken for granted was that a microcrack differed from a macrocrack only in size. Such a simplistic view is no longer accepted in this work where the very existence of a microcrack must consider the effect of material microstructure and hence the change in system inhomogeneity when compared to that for a macrocrack. In other words, irregularities of a microcrack cannot be neglected from the fact that microcracking deviates from symmetry, a physical

fact that has to be inherent in model. Although this feature is not demonstrated in general from this work, it is reflected from the example of $\nu_{micro} \rightarrow 0.5$ where the order of the microcrack tip singularity $\lambda \rightarrow 0.75$. In can be shown that only in this case that the minimum of $(dW/dV)_{micro}$ [14,15] coincided with the x_1 axis in Fig. 4. This means that the microcrack would grow straight ahead. For ν_{micro} other than 0.5, the direction of $(dW/dV)_{micro}$ would deviate from $\theta = 0$. According to the strain energy density criterion, the microcrack would grow off to the side of the original path. The off axis direction will depend on the boundary conditions specified on the microcrack that are dictated by the material microstructure. Such details can be demonstrated and will be disussed in future work.

Part of the success of being able to exhibit the influence of the microstructure details can be attributed to the obtainment of closed form solution for the microcrack stress intensity factor and that of macro-intensification caused by the microcrack. Keep in mind that the order of the microcrack tip stress singularity is no longer $1/\sqrt{r}$. The order would depend on the sharpness or bluntness of the microcrack tip. These geometric details and the micro/macro material constants are expressed in closed form in a manner similar to the classical stress intensity factors that have been used so successfully for designing macro-structural components. Not withstanding the progress made in multiscaling, the factors $K_I^{mimacro}$ and $K_{I/II}^{micro}$ have clear the way for the further development of a macrocack model to include micro-damage. The idea of multiscaling to consider the physical damage at the different size scale without addressing non-linearity of the stress-strain response by keeping the scale range sufficiently small. This circumvent the questionable use of the non-linear portion of the stress-strain data, two third of which falls into the non-equilibrium region.

References

[1] Roukes M, Plenty of rooms, indeed, Scientific American September (2001) 92-100.

[2] Panin VE, Overview on mesomechanics of plastic deformation and fracture of solids, J. of Theoretical and Applied Fracture Mechanics, 30(1) (1998) 1-11.

[3] Makarov PV, Character of localized deformation and fracture of solids at mesolevel, in G. C. Sih (Ed.), Mesomechanics 2000, Role of Mechanics for Development of Science and Technology, Vol. 1, Tsingua University Press, 2000, 143-152.

[4] Sih GC, Liu B, Mesofracture mechanics: a necessary link, in: G. C. Sih and V. E. Panin (Eds.), Prospects of mesomechanics in the 21st century, Special issue of Theoretical and Applied Fracture Mechanics, 37 (2002) 371-395.

[5] MaldacenaJ, The illusion of gravity, Scientific American (2005) 56-63.

[6] Sih GC, Thermomechanics of solids: nonequilibrium and irreversibility, J. of Theoretical and Applied Fracture Mechanics, 9(3) (1988) 175-198.

[7] Sih GC, Some basic problems in nonequilibrium thermomechanics, eds. S. Sienietyez and P. Salamon, Taylor and Francis, New York, 1992, 218-247.

[8] Sih GC, Implication of scaling hierarchy associated with nonequilibrium: field and particulate, in: G. C. Sih and V. E. Panin, (eds.), Prospects of meso-mechanics in the 21st century, Special issue of J. of Theoretical and Applied Fracture Mechanics, 37 (2002) 335-369.

[9] Sih GC, Tang XS, Dual scaling damage model associated with weak singularity for macroscopic crack possessing a micro/mesoscopic notch tip, J. of Theoretical and Applied Fracture Mechanics, 42(1) (2004) 1-24.

[10] Sih GC, Tang XS, Simultaneity of multiscaling for macro-meso-micro damage model represented by strong singularities, J. of Theoretical and Applied Fracture Mechanics, 42(3) (2004) 199-225.

[11] Sih GC, Tang XS, Triple scale segmentation of non-equilibrium system simulated by macro-micro-atomic line model with mesoscopic transitions, J. of Theoretical and Applied Fracture Mechanics, 44(2) (2005) 116-145.

[12] Sih GC, Segmented multiscale approach by microscoping and telescoping in material science, in: G. C. Sih (Ed.), Multiscaling in Molecular and Continuum Mechanics: Interaction of Time and Size from Macro to Nano, Springer (2006) 259-289.

[13] Tang XS, Sih GC, Weak and strong singularities reflecting multiscale damage:Micro-boundary conditions for free-free, fixed-fixed and free-fixed constraints, J. of Theoretical and Applied Fracture Mechanics, 43(1) (2005) 5-62.

[14] Sih GC, Introduction to a series on Mechanics of Fracture, in: G. C. Sih (ed.) Methods of Analysis and Solutions to Crack Problems", Noordhoff International Publishing, Leyden (1972) 9-12.

[15] Sih GC, Mechanics of fracture initiation and propagation, Kluwer Academic Publishers,The Netherlands, 1991.

[16] Sih GC, Survive with time o'clock of nature,in: G. C. Sih and L. Nobile (eds.), Restoration, Recycling and Rejuvenation technology for engineering and architecture application, Aracne Editrice S.r.l. (2004) 3-22.

[17] Sih GC, Tang XS, Asymptotic micro-stress field dependency on mixed boundary conditions dictated by micro-structural asymmetry; Mode I macro-stress loading, J. of Theoretical and Applied Fracture Mechanics, 46(1) (2006) in press.

[18] Horgan J, The forgotten era of brainchips, Scientific American, October (2005), 66-73.

[19] Feynman RP, There's plenty of room at the bottom. Engineering and Science, California Institute of Technology, February (1960).

MULTISCALE EQUILIBRIUM MECHANICS APPROACH IN ENGINEERING: COUPLED ATOMIC-MICRO-MACRO DAMAGE MODEL

G. C. Sih* and H. F. Ren
School of Mechanical and Power Engineering, East China University of Science and Technology, Shanghai 200237, China
*Email: gcs@ecust.edu.cn and gcs8866@yahoo.com

Abstract

Multiscaling involves the discussion of physical events that extends over a wide range of size and time. With reference to material science, the system is concerned with inhomogeneity of the material microstructure, especially when the size is reduced while mechanics is associated with the non-equilibrium aspect of the behavior. Both non-homogeneity and non-equilibrium are in fact synonymous in some ways. The former may imply that the material properties can change from location to location. The latter may infer that the temporal behavior of a system changes from one instance to the next. The available theories and models, however, are not equipped to describe mutltiscale phenomena. They are valid only within a narrow range of size and time. The objective of this communication is to offer an alternate approach that makes use of classical mechanics but only in narrow segments for approximating the full range of the non-homogneous and non-equilibrium process.

Morphology change of the material substructure is one of the main cause of non-homogeneity. It has been referred to as damage since the process involves the dissipation of energy. This may entail the nucleation of defects and imperfections in the crystal lattice or the creation of cracks and interfaces in the polycrystals. Assessment of damage evolution has been addressed in terms of a variety of parameters. The energy per unit volume or the energy density function denoted by dW/dV will be chosen in conjunction with the use of a characteristic length. The distinction $(dW/dV)^{disl,}$ $(dW/dV)^{micro}$ and $(dW/dV)^{macro}$ will be made since dW/dV is scale dependent. Characteristic lengths ℓ_{disl}, ℓ_{micro} and ℓ_{macro} at the respective scales can be defined to express the degree of local inhomogeneity. They also convert dW/dV to the total energy that is needed for obtaining the scale invariant criterion Depicted is a triple scale segmentation model where a macrocrack, microcrack and edge dislocations are assumed to prevail along a line segment. Meso zones are introduced at the scale crossing regions to smooth out the transitions. A coefficient for adjusting the degree of inhomogeneity between two consecutive segments of the volume energy density curve is introduced. Computed are the $(dW/dV)^{disl,}$ $(dW/dV)^{micro}$ and $(dW/dV)^{macro}$ values from which the coefficients of local inhomogeneity can be found. In the ideal case of a homogeneous system, this coefficient is unity and the volume energy density versus distance relation is a perfect hyperbola. It can be seen from the analytical expressions of dW/dV that the material properties at the each scale, the restraining stress and applied loading as a combination contribute to the change of system

inhomogeneity. Under normal circumstances, effects of the local details are not significant. This, however, cannot be taken as a general conclusion, especially when time effects are taken into account. The exceptions are usually significant. Based on the frame work for treating the spatial aspect of multiscaling, the time effects can be supplemented as a future addition.

Keywords: Multiscaling, inhomogeneous, non-equilibrium, segmentation, size and time scale, volume energy density, characteristic length, scale shifting criterion, macro/micro/dislocation.

1. Introduction

A process is said to be in non-equilibrium when the local properties of the system can not be represented as a whole. The local behavior changes continuously with time giving rise to non-homogeneity [1,2]. Uniqueness of solution can no longer be expected since fluctuations of the environment will perturb the system boundary and affect the surface conditions that in turn would affect the behaviour in the volume. The uncertainty aspect of nature is well reflected in quantum mechanics via the uncertainty principle. Uniqueness theorem is an idealization for closed thermodynamic systems that should not be expected to hold in general. Solutions, however, can be bounded for a given set of prescribed condition. This has been discussed [1] in relation to the isoenergy density theory.

The essence of multiscaling is to address the varying system inhomogeneity from the very small to the very large. The particular concern of material science is to learn how a solid would degrade by defects and imperfections at the atomic scale and would eventually affect the integrity of a specimen at the macroscopic scale. Among the disciplines that have received wide attention concerning size scale are fracture mechanics, non-linear continuum mechanics and dislocation theories. Leaving out the field of fluid mechanics, each of the other disciplines lacked coordination and progressed individually. By in large, they all shied away from discussing system inhomogeneity and/or non-equilibrium. The attitude of the scientific community changed drastically in mid 1900s when nanotechnology pointed out the need and advantage to go small. The pretentiousness to work on size effects without admitting the change of fundamental laws of physics [3,4] can no longer be justified. Empirical and/or technological approaches based on instrumentation may be appealing at the outlook but they are no substitute for converting the data to physical interpretation. Monitored signals from the local material and/or structure response serve little or no purpose if they are not identified with the malfunction of the system from the sub-critical to the termination state. Multiscaling can assist in extending the range of prediction.

Previous works [5-9] have attempted to lay the ground work for developing a multiscale material damage model although there remains much fine details that must be investigated. One of them is a more realistic model of the microcrack [10] in contrast to that of the macrocrack. The importance of this difference has only been recognized during the development of multiscale models. It is not so much of the size of the cracks but rather the conditions under which the material microstructure will dictate the growth characteristics of the crack. This may include the zig-zag path of the microcrack and the tightness of the adjoining crack surfaces. Classification by the crack length and/or opening alone may not always be relevant unless the other factors are also included. Because of space limitation, this work will focus only on the general approach of multiscaling. One of the details reserved for future

consideration is the obtainment of closed form solutions for microcracks that would reflect the influence of material microstructure. The $1/\sqrt{r}$ singularity will no longer be assumed for the microcrack. The present model involving a macrocrack, microcrack and edge dislocations will entail the following salient features:

- Singularity representation used to characterize the combined effect of load, geometry and material at each scale.
- Scale segmentation allowing the use of equilibrium mechanics.
- Restraining stress zones introduced to smooth scale change transitions.
- Criterion using volume energy density and characteristic lengthy.
- Coefficient of system inhomogeneity.

In contrast to the traditional thought of continuum mechanics where material behaviour is classified by constitutive relations, stress and strain relation for each scale segment is assumed to be linear and considered homogeneous and isotropic such that only two constants are used. This is equivalent to modelling a nonlinear curve by linear segments. The use of linear elasticity theory for characterizing atomic lattice structure is not new. Nonlinearity can be viewed as the reflection of effects at a lower scale and can be avoided by restricting the size of scale range of investigation. Connection of the results of the different segments is made possible by invoking the scale invariant criterion based on force or total energy.

2. Singularity representation by segments

Although the choice of breaking up the non-equilibrium process by small segments of equilibrium processes is arbitrary, available knowledge will be used as much as possible such that much of the existing results can be pieced together in the chain of event. Cases in point are the $1/\sqrt{r}$ singularity for the crack and 1/r singularity for the classical edge or screw dislocation. This is illustrated in Fig. 1 with λ denoting the order of the stress singularity, i.e., $\sigma \sim 1/r^{\lambda}$. Except for the base of reference $\lambda = 0.5$

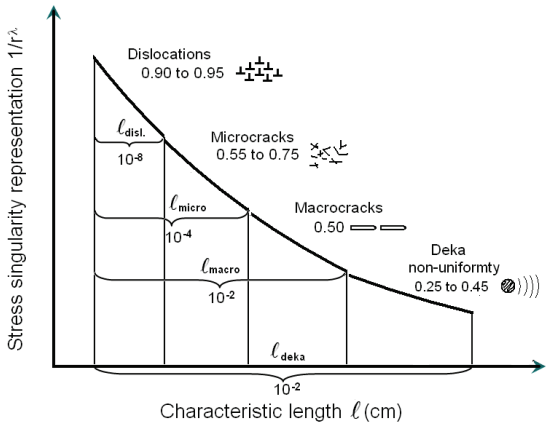

Figure 1: *Classification of stress singularities with characteristic lengths.*

for macrocracks, a range of λ is suggested for the other defects. The corresponding characteristic lengths denoted by ℓ_{disl}, ℓ_{micro} and ℓ_{macro} are assigned with the average values 10^{-7}, 10^{-5} and 10^{-3} cm, respectively. This selection of choice was made in [11] on the basis of physical argument. A possible extension in the direction of weaker singularity for λ = 0.45 to 0.25 is referred to as deka with $\ell_{\text{deka}} = 10^{1.5}$ cm, the size of a structural member. This would be the direction of connecting the model to the larger size scale. Fig. 2 illustrates how the macro-scale is extended to the deka-scale based on the singularity approach for a macrocrack. Ahead of the macroscopic zone of stress intensification, there is also a larger zone possessing a weaker singularity of the order of 0.25 to 0.45 as suggested in Fig. 1. The influence of this zone extends via the component members into the structure.

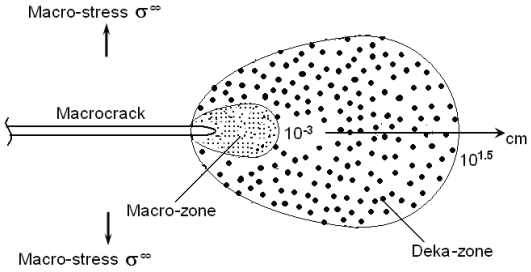

Figure 2: *Deka-zone of stress intensification.*

Base reference of the macrocrack.
Let the macrocrack be the base reference. The asymptotic macro-stress field referred to a rectangular system with axes x_1 and x_2 as shown in Fig. 3.for symmetric loading is given by

$$\sigma_{11}^{macro}=\frac{K_I^{macro}}{\sqrt{2\pi r_{macro}}}\cos\frac{\theta}{2}\left(1-\sin\frac{\theta}{2}\sin\frac{3\theta}{2}\right)+\cdots$$
$$\sigma_{22}^{macro}=\frac{K_I^{macro}}{\sqrt{2\pi r_{macro}}}\cos\frac{\theta}{2}\left(1+\sin\frac{\theta}{2}\sin\frac{3\theta}{2}\right)+\cdots$$
$$\sigma_{12}^{macro}=\frac{K_I^{macro}}{\sqrt{2\pi r_{macro}}}\sin\frac{\theta}{2}\cos\frac{\theta}{2}\cos\frac{3\theta}{2}+\cdots \qquad (1)$$

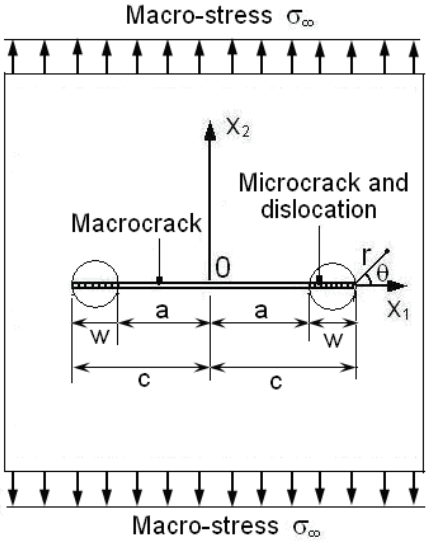

Figure 3: *Macro/micro/dislocation subjected to uniform stress field.*

In Eqs. (1), the macro-stress intensity factor takes the form

$$K_I^{macro}=\Lambda_{macro}\sigma_1\sqrt{\pi c} \qquad (2)$$

in which σ_1 is the restraining macro-stress on the segment d. It is the resistance of the material to do further damage at the macroscopic scale. Note further that

$$\Lambda_{macro}=\frac{2}{\pi}\left(\frac{\pi}{2}\frac{\sigma_\infty}{\sigma_1}-\Lambda_1-\frac{\sigma_2}{\sigma_1}\Lambda_2\right) \qquad (3)$$

while the functions Λ_1 and Λ_2 stand for

$$\Lambda_1=\sin^{-1}\frac{a+d}{c}-\sin^{-1}\frac{a}{c},$$
$$\Lambda_2=\sin^{-1}\frac{f+h}{c}-\sin^{-1}\frac{f}{c} \qquad (4)$$

Fig. 3 gives an enlarge view of the restraining zone together with the dimensions of line segments of the damage model:

$$f=a+d+g \quad ,$$
$$c=a+d+g+h+r_b=f+h+r_b \qquad (5)$$

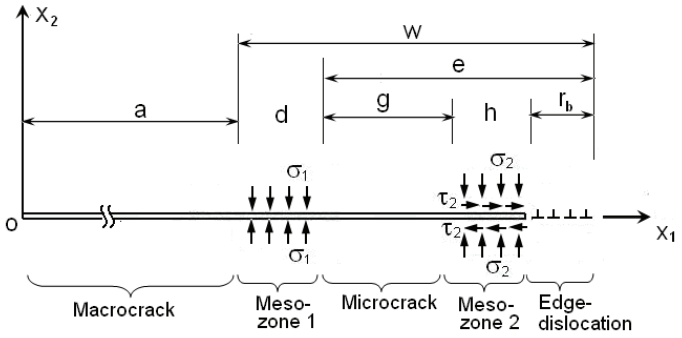

Figure 4: *Enlarged view of the triple scale damage model.*

Microcrack stress fields: symmetric and skew-symmetric.
Assuming that qualitative behavior of the microcrack tip stresses is the same as that for the macrocrack, then the symmetric and skew-symmetric angular distributions can be written as

$$\sigma_{11}^{micro}=\frac{K_I^{micro}}{\sqrt{2\pi r_{micro}}}\cos\frac{\theta}{2}\left(1-\sin\frac{\theta}{2}\sin\frac{3\theta}{2}\right)-\frac{K_{II}^{micro}}{\sqrt{2\pi r_{micro}}}\sin\frac{\theta}{2}(2+\cos\frac{\theta}{2}\cos\frac{3\theta}{2})+\cdots$$
$$\sigma_{22}^{micro}=\frac{K_I^{micro}}{\sqrt{2\pi r_{micro}}}\cos\frac{\theta}{2}\left(1+\sin\frac{\theta}{2}\sin\frac{3\theta}{2}\right)+\frac{K_{II}^{micro}}{\sqrt{2\pi r_{micro}}}\sin\frac{\theta}{2}\cos\frac{\theta}{2}\cos\frac{3\theta}{2}+\cdots$$
$$\sigma_{12}^{micro}=\frac{K_I^{micro}}{\sqrt{2\pi r_{micro}}}\sin\frac{\theta}{2}\cos\frac{\theta}{2}\cos\frac{3\theta}{2}+\frac{K_{II}^{micro}}{\sqrt{2\pi r_{micro}}}\cos\frac{\theta}{2}(1-\sin\frac{\theta}{2}\sin\frac{3\theta}{2})+\cdots \quad (6)$$

Note that the micro-stress field need not be symmetric as the applied load because anti-symmetry at a lower scale can be allowed where $K_I^{micro}\neq 0$ and $K_{II}^{micro}\neq 0$ can occur simultaneously. A more refined definition of the microcrack can be found in [10] where the local stress field will no longer satisfy the conditions of free tractions as in Eqs. (6). The microcrack surfaces may be in contact following the configuration of the material microstructure. Moreover, the boundary conditions at the tip is likely to be mixed with the prescription of displacement and traction. For the simplified version referred to in Eqs. (6), the micro-stress intensity factor K_I^{micro} can be expressed as

$$K_I^{micro}=\Lambda_{micro}\sigma_2\sqrt{\pi e} \quad (7)$$

According to the notation in Fig. 4, $e=g+h+r_b$. In Eq. (7), Λ_{micro} is another positive scale parameter that can be taken as

$$\Lambda_{micro}=(1-\sqrt{\frac{h}{g}}) \quad (8)$$

which serves as a good approximation [5]. The skew-symmetric micro-stress intensity factor K_{II}^{micro} is given by

$$K_{II}^{micro}=\frac{2}{\pi}\Lambda_2\tau_2\sqrt{\pi c} \quad (9)$$

in which Λ_2 corresponds to the second of Eqs. (4). Both σ_2 and τ_2 are, respectively, the restraining normal and shear stress along meso zone 2 in Fig. 4.

Edge dislocation stress field.

The singular stress field for an edge dislocation is well known [12]. It is of the form

$$\sigma_{11}^{disl}=-\frac{K_{II}^{disl}}{(1-\nu_{disl})\sqrt{2\pi}}\frac{\sin\theta(2+\cos2\theta)}{r_{disl}}+\cdots$$
$$\sigma_{22}^{disl}=\frac{K_{II}^{disl}}{(1-\nu_{disl})\sqrt{2\pi}}\frac{\sin\theta\cos2\theta}{r_{disl}}+\cdots$$
$$\sigma_{12}^{disl}=\frac{K_{II}^{disl}}{(1-\nu_{disl})\sqrt{2\pi}}\frac{\cos\theta\cos2\theta}{r_{disl}}+\cdots \quad (10)$$

Eqs. (10) is skew-symmetric in θ with reference to the x_1 axis. The corresponding dislocation-stress intensity factor can be defined as

$$K_{II}^{disl}=\frac{E_{disl}nb}{2(1+\nu_{disl})\sqrt{2\pi}}=\frac{\mu_{disl}nb}{\sqrt{2\pi}} \quad (11)$$

in which E_{disl} is the elastic modulus, ν_{disl} the Poisson's ratio, b the length of the Burger's vector, n the number of edge dislocations in the segment r_b and μ_{disl} the shear modulus. The theory of elasticity considers no size effect and it can be used at the atomic as well as the macroscopic scale. For a homogeneous and isotropic system, two constants are sufficient for describing the material behaviour.

Interaction of macro/micro/dislocation effects.

The interactive effects of the macrocrack, microcrack and dislocation are obtained by using the concept of scale multipliers [5-7] so as to satisfy the stress compatibility condition. Connection of the local stress intensity between the

macro- and micro-scale can be satisfied by substituting Eqs. (2) and (7) into

$$K_I^{micro} = \alpha_1 K_I^{macro} \tag{12}$$

For finding α_1 as

$$\alpha_1 = \frac{\Lambda_{micro}}{\Lambda_{macro}} \frac{\sigma_2}{\sigma_1} \sqrt{\frac{e}{c}} \tag{13}$$

which is positive and dimensionless. In a similar manner, Eqs. (9) and (11) may be inserted into

$$K_{II}^{disl} = \alpha_2 \sqrt{h} K_{II}^{micro} \tag{14}$$

to yield

$$\alpha_2 = \frac{E_{disl} nb}{4(1+\nu_{disl})\Lambda_2 \tau_2 \sqrt{2hc}} \tag{15}$$

Interaction between the microcrack and dislocations is thus established. It is seen that only the skew-symmetric portion of the microcrack stress field has an effect on the edge dislocation while the symmetric portion of the microcrack stress field makes connection to the macrocrack stress field.

3. Scale invariant and shifting

Volume energy density and characteristic length.

In order to make use of the concept of scale shifting, it is necessary to compute for the volume energy densities at the different scales. For plane strain at the macroscopic scale, it can be shown that

$$\left(\frac{dW}{dV}\right)^{macro} = \frac{1+\nu_{macro}}{2E_{macro}}[(\sigma_{11}^{macro})^2 + (\sigma_{22}^{macro})^2 - \nu_{macro}(\sigma_{11}^{macro} + \sigma_{22}^{macro})^2 + 2(\sigma_{12}^{macro})^2] \tag{16}$$

Making use of Eqs. (1), it is found that

$$\left(\frac{dW}{dV}\right)^{macro} = \frac{(1+\nu_{macro})(1-2\nu_{macro})(\Lambda_{macro}\sigma_1)^2 c}{2E_{macro} r_{macro}} \tag{17}$$

In the same way, the micro-volume energy density takes the form

$$\left(\frac{dW}{dV}\right)^{micro} = \frac{1+\nu_{micro}}{2E_{micro}}[(\sigma_{11}^{micro})^2 + (\sigma_{22}^{micro})^2 - \nu_{micro}(\sigma_{11}^{micro} + \sigma_{22}^{micro})^2 + 2(\sigma_{12}^{micro})^2] \tag{18}$$

Making use of Eqs. (6) to (9), there results

$$\left(\frac{dW}{dV}\right)^{micro} = \frac{(1+\nu_{micro})c}{2E_{micro} r_{micro}} \times [(1-2\nu_{micro})(\Lambda_{micro}\sigma_2)^2 \frac{e}{c} + \frac{4}{\pi^2}(\Lambda_2 \tau_2)^2] \tag{19}$$

Finally, the dislocation-volume energy density is given by

$$\left(\frac{dW}{dV}\right)^{disl} = \frac{1+\nu_{disl}}{2E_{disl}} \times \left[(\sigma_{11}^{disl})^2 + (\sigma_{22}^{disl})^2 - \nu_{disl}(\sigma_{11}^{disl} + \sigma_{22}^{disl})^2 + 2(\sigma_{12}^{disl})^2\right] \tag{20}$$

Eqs. (10) and (11) lead to

$$\left(\frac{dW}{dV}\right)^{disl} = \frac{E_{disl}(nb)^2}{16\pi^2(1+\nu_{disl})(1-\nu_{disl})^2} \frac{1}{r_{disl}^2} \tag{21}$$

The edge dislocation number n can be determined from the displacement compatibility condition. This detail can be found elsewhere [8,9]. Eqs. (17), (19) and (21) can now be computed numerically to complete three segments of the volume energy density curve in Fig. 5. The fourth segment involves the deka scale that can also be computed.

Scale shifting criterion.

It is now more pertinent to connect the four line segmentations shown in Fig. 5. In general, a plot of dW/dV versus r may be used to exhibit the behavior of system homogeneity. For the line crack solution used in fracture mechanics, it is known that dW/dV versus r follows a perfect hyperbola if the system is homogeneous. That is the rectangular area S = r x dW/dV

is the same at each point of the hyperbolic curve. Reference can be made to [13] for many crack problems where the S-criterion were used to determine subcritical and/or the onset of macrocrack propagation. The extension to a multiscale system of defects is depicted in Fig. 6. Let $\overline{W} = dW/dV$. The values of $\overline{W}_{disl}$, $\overline{W}_{micro}$ and $\overline{W}_{macro}$ are computed, respectively from Eqs. (21), (19) and (17) by assigning numerical values to the material, length and load parameters shown in Figs. 3 and 4. They are a = 10 mm, g = 1 mm, E_{micro} = 200 GPa, $E_{micro}/E_{macro} = E_{disl}/E_{micro} = 5$, $\nu_{disl} = \nu_{micro} = \nu_{macro} = 0.3$, σ_∞ = 20 MPa and τ_2 = 20 GPa. The five normalized quantities σ_1/σ_∞, σ_2/σ_1, d/a, h/g and r_b/h are varied about the respective values of 2, 4, 0.05, 0.2 and 0.2 to obtain the dotted curve as an average. It is not a hyperbola. That is the system is not homogeneous. The deviation from a hyperbola can be quantified via the characteristic lengths ℓ_{disl}, ℓ_{micro}, ℓ_{macro} and ℓ_{deka} by the two consecutive relations

$$m_{disl\to micro}\ \ell_{disl}\ \overline{W}_{disl} = \ell_{micro}\ \overline{W}_{micro},\quad m_{microsl\to macro}\ \ell_{micro}\ \overline{W}_{micro} = \ell_{macro}\ \overline{W}_{macro} \tag{22}$$

In Eqs. (22), $m_{disl\to micro}$ and $m_{microsl\to macro}$ stand for the coefficients of inhomogeneity when crossing the scale range from dislocation to microcrack and from microcrack to macrocrack, respectively. Keep in mind that $\ell_{meso}\,\overline{W}_{meso}$ may have to used in between disl /micro and/or micro/macro if the segmented gap needs to be refined. In this case, any two consecutive points on the curve in Fig. 6 may be related as

$$m_j S_j = S_{j+1} \text{ or } m_j \ell_j W_j = \ell_{j+1} W_{j+1} \tag{23}$$

The criterion in Eq. (23) may be generalized to consider time rate effects. With the notation that dot represents time rate Eq. (23) can also be expressed as

$$m_j \dot{S}_j = \dot{S}_{j+1} \text{ or } m_j \ell_j \dot{W}_j = \ell_{j+1} \dot{W}_{j+1} \tag{24}$$

A statement equivalent to Eq. (24) is that

the time rate of the energy density factor is assumed to remain unchanged between two successive scale ranges.

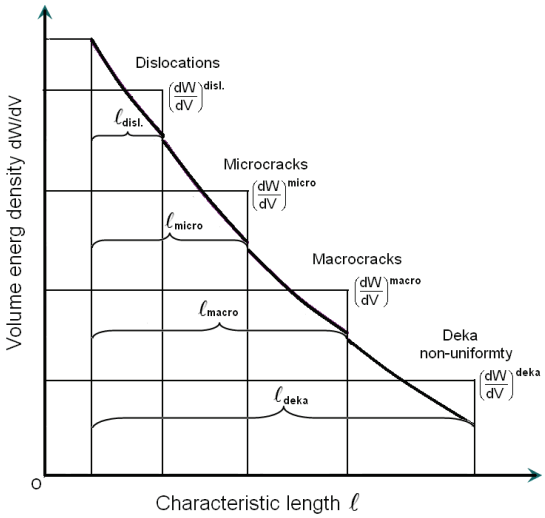

Figure 5: *Volume energy densities as a function of the characteristic lengths.*

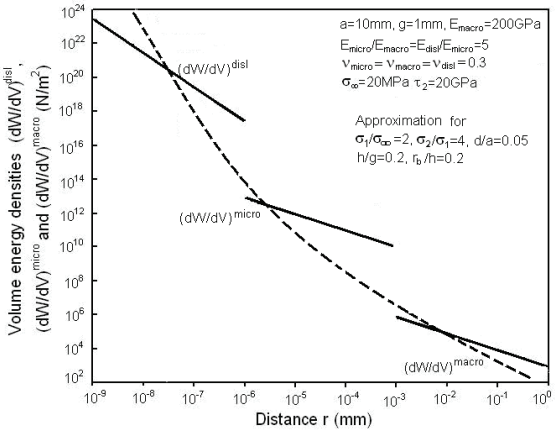

Figure 6: *Macro/micro/dislocation volume energy densities versus distance.*

4. Concluding remarks and future considerations

Several possible improvements of the line damage multiscale model have been pointed out. The anticipation is that the

extension of the size range beyond the macrocrack size to the structural component range may be accomplished by applying the weak singularities [6]. They involve singularity orders lower than the $1/\sqrt{r}$ which has been regarded as the base reference. Regularity of the crack tip displacement field must still be invoked. This possibility is encouraged by the obtainment of closed form solutions for a microcrack [10] with a variable angle wedge shaped notch head that can model different orders of stress singularities representing the variance in the material microstructure. The analytical solution can be used to advantage in the development of physical models for examining the sensitivity of the geometric and material parameters at the different scale levels. The field of fatigue is particularly in need of such an approach where data interpretation becomes cumbersome when using numerical models. Effective mutliscale physical damage models can assist the signal recognition of sensor data that are now widely used in the health monitoring of civil engineering and high energy storage structures. The correlation between signal data and potential malfunction of any physical systems is not always straightforward.

References

[1] G. C. Sih, Thermomechanics of solids: nonequilibrium and irreversibility, J. of Theoretical and Applied Fracture Mechanics, 9(3) (1988) 175-198.

[2] G. C. Sih, Some basic problems in nonequilibrium thermomechanics, in: S. Sienietyez and P. Salamon, (eds.), Flow, Diffusion and Rate Processes, Taylor and Francis, New York, (1992) 218-247.

[3] M. Roukes, Plenty of rooms, indeed, Scientific American September (2001) 92-100.

[4] R. P. Feynman, There's plenty of room at the bottom. Engineering and Science, California Institute of Technology, February (1960).

[5] G. C. Sih and X. S. Tang, Dual scaling damage model associated with weak singularity for macroscopic crack possessing a micro/mesoscopic notch tip, J. of Theoretical and Applied Fracture Mechanics, 42(1) (2004) 1-24.

[6] X. S. Tang and G. C. Sih, Weak and strong singularities reflecting multiscale damage: micro-boundary conditions for free-free, fixed-fixed and free-fixed constraints, J. of Theoretical and Applied Fracture Mechanics, 43(1) (2005) 1-58.

[7] G. C. Sih and X. S. Tang, Scaling of volume energy density function, J. of Theoretical and Applied Fracture Mechanics, 43(2) (2005)1-21.

[8] G. C. Sih and X. S. Tang, Screw dislocations generated from crack tip of self-consistent and self-equilibrated systems of residual stresses: atomic, meso and micro, J. of Theoretical and Applied Fracture Mechanics, 43(3)(2005) in press.

[9] X. S. Tang and G. C. Sih, Edge dislocations generated from a micro-crack under initial residual stress with varying amplitudes, J. of Theoretical and Applied Fracture Mechanics, 44(3)(2005) in press.

[10]G. C. Sih and X. S.Tang, Asymptotic micro-stress field dependency on mixed boundary conditions dictated by micro-structural asymmetry; Mode I macro-stress loading, J. of Theoretical and Applied Fracture Mechanics, 46(1) (2006) in press.

[11]G. C. Sih, Segmented multiscale approach by microscoping and telescoping in material science, in: G. C. Sih (Ed.), Multiscaling in Molecular and Continuum Mechanics: Interaction of Time and Size from Macro to Nano,

Springer (2006) 259-289.

[12]J. Friedel, Dislocations, Addison Wsley Publishing Co., Inc. London (1967).

[13]G. C. Sih, Mechanics of Fracture Initiation and Propagation, Kluwer Academic Publishers, Boston, (1991).

TIME AND SIZE DEPENDENCIES OF FLOW AND FAILURE BEHAVIOUR OF METALLIC MATERIALS: AN EXPERIMENTAL STUDY

Norman Herzig, Lothar W. Meyer, Thorsten Halle
Chemnitz University of Technology, Materials and Impact Engineering, 09107 Chemnitz, Germany

Abstract

The increased miniaturisation of parts and processes leads to increased interest on size effects. These effects may appear as a not directly predictable change of component or process behaviour, even if scaling is done in correct similarity relations.

In this study size dependencies on flow stress and failure behaviour of an unalloyed 1045 steel, a titanium alloy Ti-6-22-22S and an aluminium alloy Al7075 T6 under compressive loading and over a wide range of strain rates are discussed. Based on experimental and numerical results the influence of friction at scaled deformation processes is described and provides a possible explanation for measured size effects at low dynamic deformation processes. At high strain rates, the explanation for the measured behaviour requires the consideration of thermo dynamical aspects including the transition of an isothermal to an adiabatic process.

Keywords: size effects, flow stress, failure, strain rate

1. Introduction

The increased complexity of products and processes leads to an increased miniaturisation of components to be manufactured. Actually, the influence of size appearing at scaled manufacturing processes is not explained and has to be clarified especially where plastic shape changing of metals takes a central part. In material characterisation size effects under various loading types and conditions are widely discussed (e.g. [1]-[6]). Nevertheless, less is known about size dependencies at high strain rates.

Within this study size and time dependencies of flow stress, strengthening and failure behaviour of an unalloyed 1045 steel, a titanium alloy Ti-6-22-22S and an aluminium alloy Al7075 T6 under compressive loading is presented. Under quasistatic and low dynamic loading conditions the measured effects are explained by increased friction with reducing size. At high strain rates thermodynamic aspects are considered. By applying a simple thermodynamic approach the measured size dependent material behaviour is explained.

2. Materials

For the experimental investigations of size dependencies three types of metals were used. The body-centred cubic unalloyed steel 1045 in a normalised condition was used for the determination of size and time dependent flow stress behaviour under compressive loading and different loading rates.
Additionally, a titanium alloy (Ti-6-22-22S) and an aluminium alloy (Al7075 T6) were applied for studying size effects on failure behaviour under compressive loading. The final bimodal microstructure of the titanium alloy contains globular α -phase between the lamellar arrangement of

α - and β -phase. The aluminium alloy was used in a solution heat treated and artificially aged state (peak aged).

3. Experimental setup

Within this work the material behaviour under compressive loading with special emphasis on size and time dependencies was investigated. Cylindrical compression specimens were scaled in a range of 1 and 9 mm in diameter and 0.5 to 1.5 in aspect ration (height to diameter), respectively.
Experimental work was carried out by use of both common available universal testing machines and special designed testing devices. Under quasistatic and low dynamic loading rates up to 10^1 s^{-1} mechanical and servo hydraulic testing machines were used. Force was measured by calibrated and adjusted load cells. The deformation was measured by strain gauges and incremental gauges, respectively.

At high strain rates the design of drop weight towers and the Split Hopkinson Pressure Bar were used. The drop weight towers (Fig. 1) consist of a frame and a guided mass (120 and 600 kg). A detailed description of the test procedure is given e.g. in [7]. The displacement is measured either by incremental gauges and strain gauges or by electro optical extensometer. The force is calculated from the elastic deformation of the punch by means of calibrated strain gauges and Hooke's law.

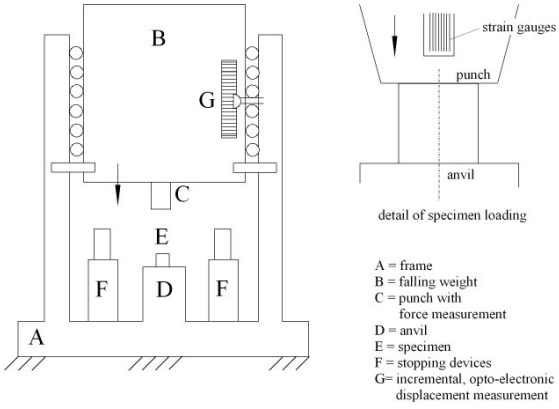

Figure 1: *Drop weight tower [7].*

Compression tests at strain rates $>10^3$ s^{-1} were realised by split Hopkinson pressure bars (Fig. 2). The determination of stress-strain-response of the materials is based on the principles of one-dimensional elastic-wave propagation within the pressure bars [8].

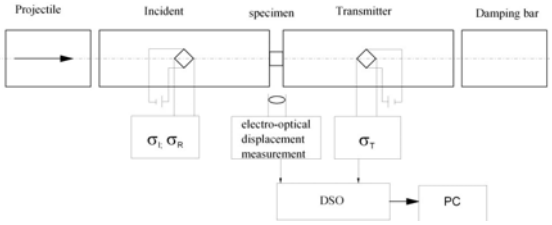

Figure 2: *Split Hopkinson Pressure Bar.*

Hence, with the experimental setup described above investigations within a range of strain rates of 10^{-4} to 10^4 were realised.

4. Experimental results and discussion

4.1. Flow stress behaviour

Fig. 3 illustrates the size and time dependent flow stress and strengthening behaviour of 1045 steel. With increasing strain rate from 10^{-3} to 200 s^{-1} an increase of the flow stress in the order of 250 MPa was measured. This is due to the thermally activated flow stress behaviour of 1045 steel. However, it can be evaluated that flow stress of smaller specimens is significantly higher than the larger ones. The difference in flow stress is increased with increasing strain rate from 50 MPa under quasistatic loading to 100 MPa under high strain rates. However, if the strain rate is kept constant a similar strengthening behaviour of the different specimen geometries is observed.

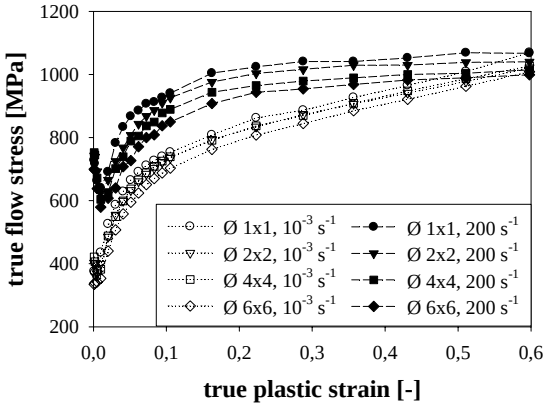

Figure 3: *Specimen size and time dependent flow and strengthening behaviour of 1045 steel.*

To explain the measured behaviour the influence of friction was investigated. Due to a disproportionate increase of the ratio surface area to volume with reducing size, a size dependent frictional behaviour was expected. Recently, numerical and experimental investigations on the development of friction coefficient as a function of size [9] have shown, that friction coefficient μ is increased with reducing size. Hence, under quasistatic loading conditions friction corrected flow curves were calculated, which were nearly identical between the different specimen sizes and the assumption of friction affected flow stress behaviour was confirmed.
Additionally, at high strain rates the temperature development during the deformation process was considered. Numerical simulations (Fig. 4) have shown, that no temperature increase under quasistatic and low dynamic loading is to be expected.

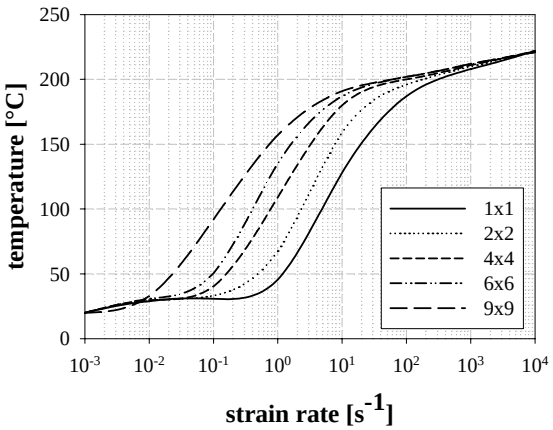

Figure 4: *Size and time dependent temperature development for 1045 steel after 50 % plastic strain (calculated by DEFORM™-2D).*

The deformation process is nearly isothermal. At high strain rates, the temperature increase of the different specimen sizes is similar. With a further increase of strain rate no significant difference in the temperature increase of different specimen sizes can be found. The process is nearly adiabatic. Within the transition area a specimen size dependent temperature development was found. Hence, this may influence the flow stress behaviour within this range of high strain rates and lead to an increase of the differences in flow stresses of small and large specimens compared to quasistatic loading (Fig. 3).

Scaling of the aspect ratio (height to diameter) between 0.5 and 1.5 shows a similar yield behaviour up to 0.2 plastic strain under quasistatic loading conditions (Fig. 5). With increasing strain a higher flow stress for specimens with a smaller aspect ratio is measured. At high strain rates differences of flow stresses of different specimen geometries occur at approximately 0.1 plastic strain.

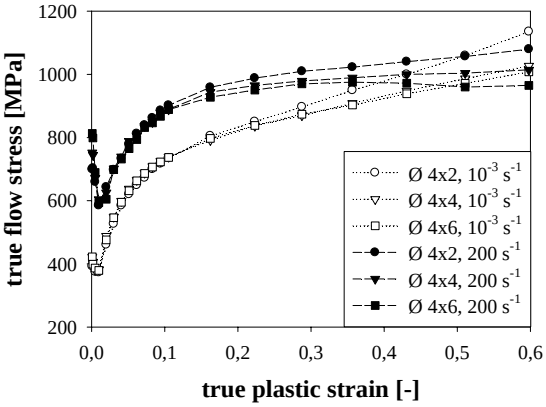

Figure 5: *Influence of aspect ratio on flow stress of 1045 steel under quasistatic and dynamic compressive loading.*

An intersection of the flow curves of quasistatic and dynamic compression tests between 0.4 and 0.6 plastic strain (Fig. 3 and 5) occurs due to the adiabatic heating of the specimen at high strain rates and the thermal softening, respectively.

4.2. Failure behaviour

To investigate the influence of specimen size on failure, a titanium alloy and an aluminium alloy were used. The titanium alloy even failed under quasistatic loading conditions. At high strain rates both materials tend to fail due to adiabatic shear banding.
Cylindrical compression tests within a range of strain rates from 10^{-3} to 10^{4} s^{-1} lead to a decrease of compressive deformability with increasing strain rate. Furthermore, for both materials a size dependent failure behaviour was observed, where the larger specimens tend to fail earlier than smaller (Fig. 5).

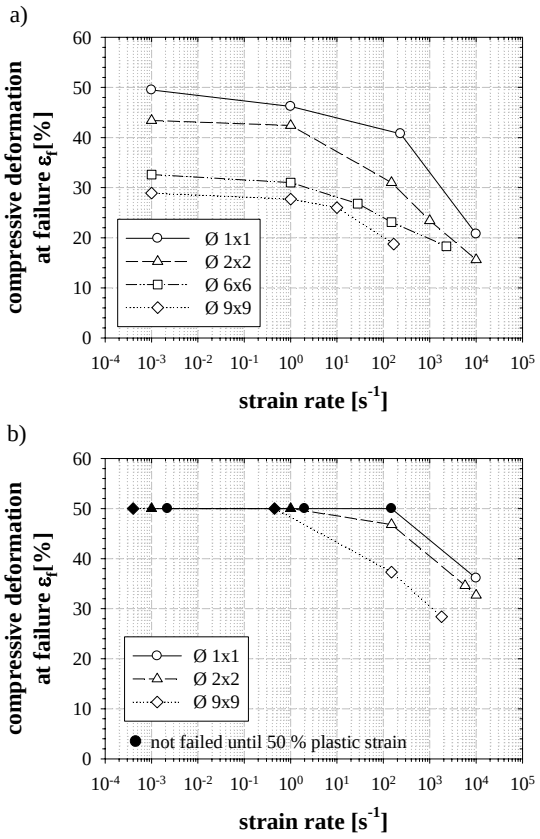

Figure 5: *Size and time dependent compressive deformability of (a) Ti-6-22-22S and (b) Al7075 T6.*

However, the measured failure strain depends on both a geometrical and a process variable. Using a simple approach to describe failure strain ε_f as a function of strain rate and diameter (Eq. 1), where d^* is the normalised characteristic length and $\dot{\varepsilon}$ the strain rate, Fig. 6 can be drawn.

$$\ln(\varepsilon_f) = a + b \cdot \ln(d^*) + \sqrt{\dot{\varepsilon}^*} \qquad (1)$$

Fig. 6 illustrates, that the geometry of the specimen is the major influencing variable under quasistatic and low dynamic loading conditions up to 10^2 s^{-1}. At high strain rates, the influence of size seems to be reduced and the strain rate mainly affects the macroscopically measured plastic deformability until fracture.

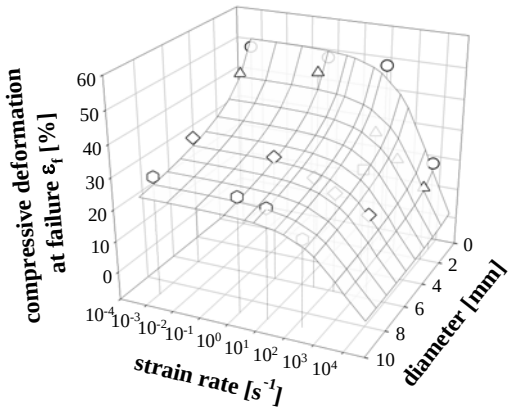

Figure 6: *Compressive deformability of Ti-6-22-22S as a function of strain rate and length according to Eq. (1).*

To investigate the failure process itself stopped cylindrical compression tests followed by microstructure investigations were realised by use of Ti-6-22-22S. Under quasistatic loading the larger specimens tend to fail earlier than the smaller ones, although the crack initiation is similar. However, differences were found in bulging of the specimens which indicates different friction conditions (Fig. 7).

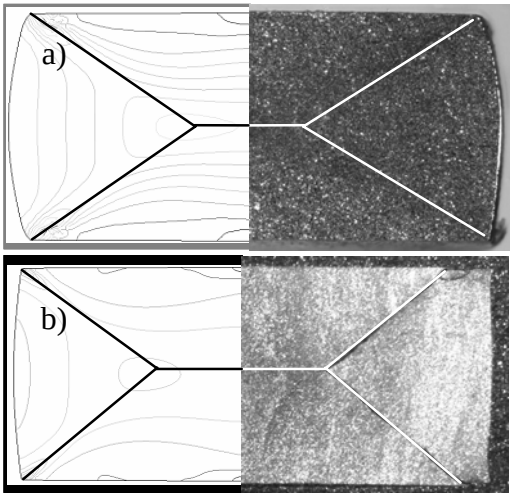

Figure 7: *Ti-6-22-22S, $\dot{\varepsilon}$ = 10^{-3} s^{-1}, after 40 % plastic strain: a) Ø2x2 and b) Ø6x6.*

Applying an approach of size dependent friction coefficients described in section 4.1 and [9], in FEM calculations an alteration of the distribution of equivalent plastic strain was found. However, assuming a crack development in regions of highest plastic strain ("forging cross") the different crack geometry can be explained.

At high strain rates, a size dependent failure behaviour was found, too. Friction effects may also play an important role. Additionally, thermodynamic aspects including temperature development and heat conduction have to be considered.

Zehnder et al. [10] used the Fourier number F_0 (Eq 2) to estimate the time span over which a deformation process is adiabatic. In Eq. 2 the time t is substituted by strain ε and strain rate $\dot{\varepsilon}$.

$$F_0 = \frac{\alpha \cdot t}{l^2} = \frac{\alpha \cdot \varepsilon}{\dot{\varepsilon} \cdot l^2} \qquad (2)$$

α is the thermal diffusivity and l a characteristic length. Using Eq. 2, Fig. 8 can be drawn. If F_0 is larger than 10 the process is isothermal. If F_0 is smaller than 0.1 the process is essentially adiabatic.

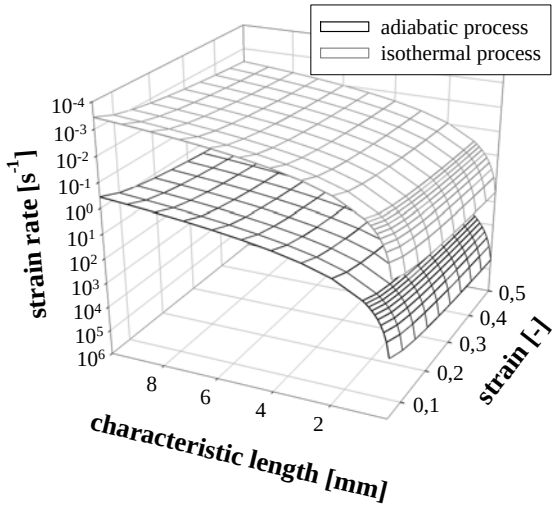

Figure 8: *Size dependent transition of isothermal to adiabatic process conditions for Ti-6-22-22S according to Eq. (2).*

It can be evaluated that the transition from an isothermal to an adiabatic process is much more influenced by specimen geometry than by the extend of deformation. Furthermore, it can be seen that for large specimens (>4 mm) the transition is nearly independent on size. However, for smallest geometries the transition area is displaced to high strain rates. This means, a decrease of specimen size in order to obtain higher strain rates needs attention between 10^{-2} to 10^{2} s^{-1}. This will lead to a not determinable increase of flow stress due to less temperature development during the deformation process. The influence of thermal softening on flow stress behaviour would be underestimated. Fig. 4 and 9 confirm this statement.

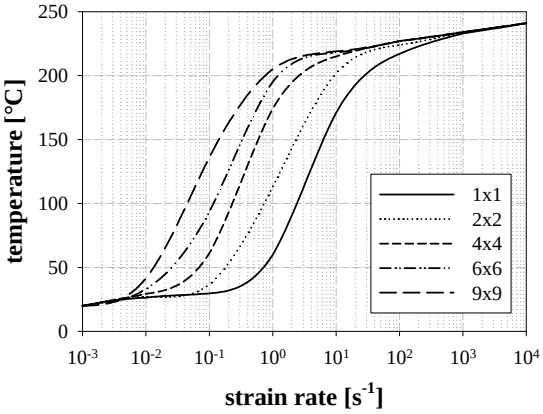

Figure 9: *Size and time dependent temperature development for Ti-6-22-22S after 30 % plastic strain (calculated by DEFORM^{TM}-2D).*

In Fig. 9 the size and time dependent temperature development within a compression specimen of Ti-6-22-22S can be evaluated. According to Fig. 4 at quasistatic and low dynamic loading conditions no significant temperature increase is observed. This is due to heat conduction processes during the deformation process and the isothermal process character, respectively. At high strain rates the process is nearly adiabatic and heat conduction can be neglected. In the transition area a significant temperature increase from room temperature to approximately 220 °C is found. However, the transition area is displaced to higher strain rates with decreasing size. This may be explained by different thermodynamic state according to Eq. 2. The question now arises: What happens, when the thermodynamic state is kept constant ?

Table 1 shows the influence of size on thermodynamic state represented by Fourier number F_0 and strain rate respectively. All values are normalised to a reference size of 6 mm in diameter and height.

	$\dot{\varepsilon}$ = const.	F_0 = const.
Ø 1 mm	$36 \cdot F_0$	$36 \cdot \dot{\varepsilon}_{Ø6}$
Ø 2 mm	$9 \cdot F_0$	$9 \cdot \dot{\varepsilon}_{Ø6}$
Ø 4 mm	$2.25 \cdot F_0$	$2.25 \cdot \dot{\varepsilon}_{Ø6}$
Ø 6 mm	F_0	$\dot{\varepsilon}_{Ø6}$
Ø 9 mm	$0.44 \cdot F_0$	$0.44 \cdot \dot{\varepsilon}_{Ø6}$

Table 1: *Influence of size on F_0 and $\dot{\varepsilon}$ related to a reference size of Ø6x6.*

Table 1 illustrates, that e.g. a nine times larger strain rate is required between Ø2x2 and Ø6x6 specimens to keep F_0 constant. Keeping the thermodynamic state related to Ø6x6 specimens constant by adjusting the strain rate a size and time dependent temperature development shown in Fig. 10 is observed. Assuming α to be in the order of $7.3 \cdot 10^{-6}$ m²/s and a plastic strain of 0.3, Fig. 10 can be drawn.

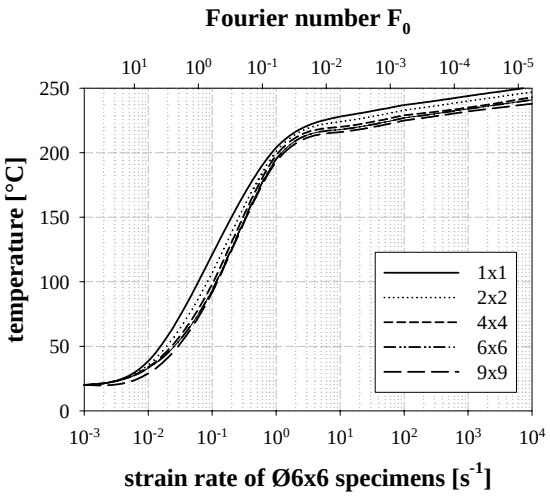

Figure 10: *Size and time dependent temperature development for Ti-6-22-22S after 30 % plastic strain (calculated by DEFORM^{TM}-2D). The thermodynamic state is kept constant relating to Ø6x6 specimens and Table 1.*

It can be evaluated that keeping the thermodynamic state represented by Fourier number F_0 constant, a nearly size independent temperature evolution profile as a function of strain rate is calculated. The differences of temperature between small and large specimens can be explained by the increased flow stresses with increasing strain rate. Small specimens have to be tested at higher strain rates which lead to increased flow stresses due to thermal activated deformation processes. According to Eq. 3 a larger temperature increase ΔT due to plastic deformation is expected.

$$\Delta T = \frac{\eta}{\rho \cdot C} \cdot \int \sigma \, d\varepsilon_p \tag{3}$$

η is the partition of plastic work converted to heat and assumed to be constant at 0.9, ρ and C are the density and heat capacity, respectively.

If the temperature is related to the initial flow stress, the influence of thermal activation is suppressed and Fig. 11 can be drawn.

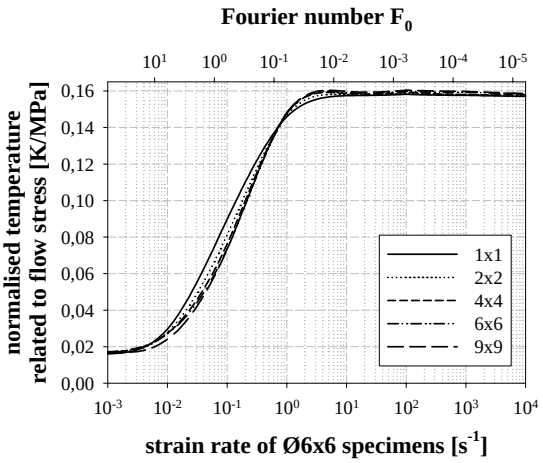

Figure 11: *Normalised temperature development related to initial flow stress for Ti-6-22-22S after 30 % plastic strain (calculated by DEFORM^{TM}-2D).*

However, applying the basic assumption described above, stopped cylindrical compression tests were realised by use of Ø6x6 and Ø2x2 specimens. The Fourier number was kept constant at $2.193 \cdot 10^{-3}$ which requires a strain rate of 250 s^{-1} for the small and 28 s^{-1} for the large specimens. The results are shown in Fig. 12.

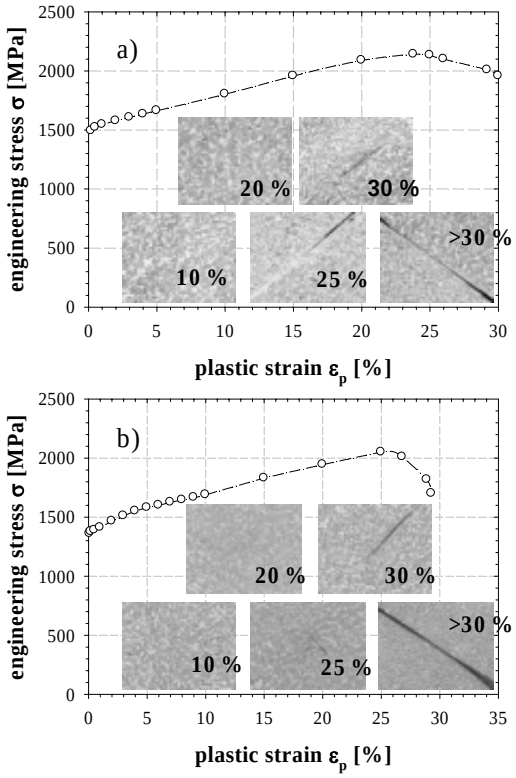

Figure 12: *Failure characteristics: Ti-6-22-22S: a) Ø2x2, $\dot{\varepsilon} = 250\ s^{-1}$ and b) Ø6x6, $\dot{\varepsilon} = 28\ s^{-1}$.*

From Fig. 12 similar failure characteristics both for initiation at approximately 25 % as well as for compressive deformability at 30 % plastic strain can be evaluated, whereby the flow stress differs between the two geometries due to the thermal activated flow stress behaviour in the order of 100 MPa. Nevertheless, if the thermodynamic state is kept constant, no size dependent failure is observed.

However, testing Ø6x6 specimens at 250 s^{-1} requires a strain rate of 2250 s^{-1} for the Ø2x2 specimens to keep F_0 constant. Experiments have shown, that an approach in the direction of high strain rates $>10^3\ s^{-1}$ do not fulfil the assumptions made above. The effect may be explained by the transition to adiabatic process conditions, which means, according to Fig 9 no size dependent temperature development was found. Furthermore, experimental work at strain rates $>10^4\ s^{-1}$ shows, that the plastic deformability of Ti-6-22-22S obtained with Ø2x2 specimens seems to be increasing at highest strain rates. This effect is finally not explained and part of future efforts.

5. Conclusions

From our work the following conclusions can be drawn:

- The measured flow stress of 1045 steel is size and time dependent. The flow stress of smaller specimens is higher than the larger ones. The effect is increased with increasing strain rate.
- Scaling the aspect ratio (height to diameter) leads to increased flow stresses with smaller aspect ratios at high strains (>15 %).
- Under quasistatic and low dynamic loading conditions friction effects may explain the measured flow stress behaviour. Additionally, at high strain rates temperature development provides an explanation for the measured behaviour.
- For an aluminium alloy (Al7075 T6) and a titanium alloy (Ti-6-22-22S) a size and time dependent failure behaviour was measured. Both materials tend to fail due to adiabatic shear banding under high strain rates.
- At quasistatic loading conditions and intermediate strain rates the different failure characteristics may be explained by changed frictional conditions at different sizes.
- At high strain rates, the failure characteristic is strongly dependent on thermodynamic state, including length dependencies. A specimen size and time dependent temperature development was predicted by FEM calculations.
- Anyhow, assumptions made at low and intermediate strain rates are not directly applicable to describe the material behaviour at highest strain rates.

6. Acknowledgement

This work is part of the DFG priority programme “Process Scaling”. The authors like to thank the DFG for its financial support.

References

[1] Armstrong, R.W. (1961), *J. Mechanics and Physics of Solid*, **9**, pp. 196-199.

[2] Gunasekera, J.S., Havranek, J., Littlejohn, M.H. (1982), *Trans. ASME*, **104**, pp. 274-279.

[3] Gorham, D.A. (1991), *Appl. Physics*, **24**, pp. 1489-1492.

[4] Geiger, M., Meßner, A., Engel, U. (1997), *Production Engineering*, **IV/1**, pp.55-58.

[5] Fleck, N.A., Muller, G.M., Ashby, M.F., Hutchinson, J.W. (1994), *Acta Materialia et Metallurgica*, **42**, pp. 475-487.

[6] Stölken, J.S., Evans, A.G. (1998), *Acta Materialia et Metallurgica*, **46**, pp. 5109-5115.

[7] Meyer, L.W., Krüger, L. (2000) In: ASM Handbook, Volume 8, Mechanical Testing and Evaluation, pp. 452-454, Kuhn, H. And Medlin, D. (Eds.), ASM International, Materials Park, Ohio.

[8] Gray, G.T. (2000), In: ASM Handbook, Volume 8, Mechanical Testing and Evaluation, pp. 462-476, Kuhn, H. and Medlin, D. (Eds.), ASM International, Materials Park, Ohio.

[9] Meyer, L.W., Herzig, N. (2005): In: Process Scaling, pp. 147-156, Vollertsen, F. and Hollmann, F. (Eds.), BIAS Verlag, Bremen.

[10] Zehnder, A.T., Babinsky, E., Palmer, T. (1998), *Experimental Mechanics* **38**, pp.295-302.

A MULTISCALE APPROACH TO CRACK GROWTH

R. Jones
DSTO Centre for Structural Mechanics, Department of Mechanical Engineering, Monash University, P.O. Box 31, Monash University, Victoria, 3800, Australia

C. Wallbrink
CRC Integrated Engineering Asset Management, Department of Mechanical Engineering, Monash University, P.O. Box 31, Monash University, Victoria, 3800, Australia.

S. Pitt
Air Vehicles Division, Defence Science and Technology Organisation, 506 Lorimer Street, Fishermans Bend 3207, Australia

L. Molent
Air Vehicles Division, Defence Science and Technology Organisation, 506 Lorimer Street, Fishermans Bend 3207, Australia

Abstract (bold, leave 1 line blank after)

This investigation first discusses the link between the Frost-Dugale crack growth law, incomplete self similarity, the two parameter crack growth law, and fractal fatigue concepts. We then illustrate its applicability to predict crack growth from 30 microns to the macro scale. This methodology is then used to predict crack growth in the F/A-18 specimen test program.

Keywords: Crack growth, Multi-scale, Frost-Dugdale, Fractals; Non self similar.

1. Introduction

The science of fatigue crack growth traditionally revolved around the relationship between the stress intensity factor range, ΔK and the crack growth rate, *da/dN*. The first paper making this correlation was published in 1961 by Paris, Gomez and Anderson [1], who adopted the K-value from the analysis of the stress field around the tip of a crack as proposed by Irwin in 1957 [2]. The results of the constant-amplitude crack growth tests by Paris were expressed in terms of *da/dN* (where *N* is the number of fatigue cycles, *a* is the crack depth or length at time N) as a function of ΔK on a double log scale. Plotting the data in this fashion reveals a region of growth where a linear relation between *log(da/dN)* and *log(ΔK)* appears to exist. This led to the well-known Paris equation:

$$da/dN = C\Delta K^m \quad (1)$$

where *C* and m are experimentally obtained constants.

This law has continued to be modified to account for a variety of real life observations including, stress ratio R and

crack closure effects [3, 4], and dependency on the peak stress intensity factor (K_{max}) [5, 6], etc. However, in recent years a number of earlier modifications have been questioned [5, 6].

In the mid 1970' Pearson [7] showed that fatigue crack growth laws determined for macroscopic cracks could not be used to predict the growth of small sub-millimetre cracks and that the constants in the crack growth law were a function of the size of the crack. He also revealed that this inconsistency was not due to crack-tip plasticity effects.

In this paper we will present an explicit expression for this crack length dependency and reveal how it is related to incomplete self-similarity, the two parameter crack growth model [5, 6], and to fractal fatigue concepts.

At this stage it is important to note that the Paris equation was not the first law proposed to describe crack growth. The first law (according to Frost et al [[8]]) can be attributed to an early Australian Defence Science and Technology Organisation (DSTO) researcher, A. K. Head [[9]]. Subsequently Frost and Dugdale [8], using Head's observation of self-similar crack growth, expanded Head's law and reported that crack growth under constant amplitude loading could be described via a simple log linear relationship, viz:

$$Ln(a) = \lambda N + Ln(a_o) \quad \text{or} \quad a = a_o e^{\lambda N} \quad (2)$$

which gives as the crack growth rate equation:

$$da/dN = \lambda a \quad (3)$$

where λ, which we will define as the "growth acceleration rate" constant, is a parameter that is geometry and load dependent, N is the "fatigue life", and a_0 is the initial crack-like flaw size (depth of the crack at the start of loading). When the far field stress and crack geometry remain relatively constant then:

$$\lambda = f(\sigma) \quad (4)$$

For constant amplitude loading [8, 10] found that λ could be expressed as:

$$\lambda = \phi(\Delta\sigma)^3 \quad (5)$$

where ϕ is only a function of the loading and geometry of the structure.

A near linear relationship between ln(a) and N has also been reported for physically short cracks by a large number of researchers including Harkegard, Denk, and Stark [11], Nisitani et al [[12]], Kawagoishi et al [[13]], Caton et al [[14]], Murakamia and Miller [[15]], Polak and Zezulka [[16]], Tomkins [[17], etc, see Figure 1 and 2. Indeed, Polak and Zezulka found that this approximation held for sub micron cracks.

With respect to MEMS technology it is now known that, although bulk silicon does not exhibit a significant susceptibility to cyclic fatigue, micron-scale structures made from silicon films are vulnerable to fatigue in ambient air environments. Of particular interest is the fact that the crack growth histories presented by Ritchie et. al. [[18] and Mulhstein et al [19] also appear to conform to the Frost & Dugdale law, see Figure .

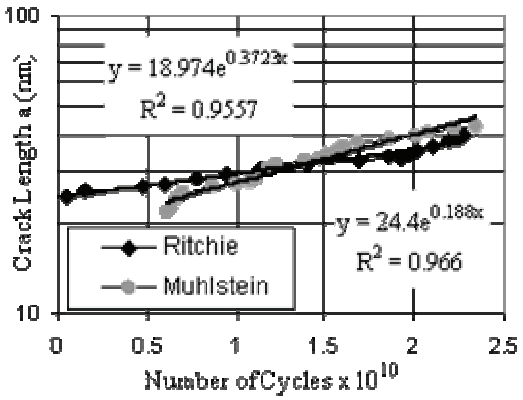

Figure 1: Crack growth at the nano-scale in 2 μm-thick polysilicon, adapted from [[18]

Molent, Sun and Green in their compendium of F/A-18 fatigue crack growth data [[20], which examined more than 300 different cracks in a various full scale fatigue tests and the associated coupon test programs, also found that a near log linear relationship holds for crack growth from a starting length of less than 100 microns to lengths of 5 mm's or more. A more general and comprehensive review of the applicability of the Frost-Dugdale

law to represent crack growth is given in Barter et al [[21], and by Molent et al [[22] who reviewed crack growth in the fuselage lap joints in commercial transport aircraft.

2. Relationship to the two parameter crack growth model

It is now known that fracture surfaces can be considered as an invasive fractal set, see Mandelbrot et al, 1984 [23]. Indeed, Mandelbrot et al has shown that:

"When a piece of metal is fractured either by tensile or impact loading the facture surface that is formed is rough and irregular. Its shape is affected by the metal's microstructure (such as grains, inclusions, and precipitates where characteristic length is large relative to the atomic scale), as well as by 'macrostructural' influences (such as the size, the shape of the specimen, and the notch from which the fracture begins). However, repeated observation at various magnifications also reveal a variety of additional structures that fall between 'micro' and 'macro' and have not yet been described satisfactorily in a systematic manner. The experiments reported here reveal the existence of broad and clearly distinct zone of intermediate scales in which the fracture is modelled very well by a fractal surface."

This concept, i.e. of a fracture surface as a fractal, has been further developed by Carpinteri and Spagnoli [24] and Spagnoli [25] who used renormalisation techniques to develop a growth law for an invasive *lacunar* fractal, viz.

$$da/dN = C_1(a)\,(\Delta K)^{p} = C_1\, a^{\phi}\,(\Delta K)^{p} \qquad (6)$$

This law is formally identical to the classical Paris law except that the coefficient C_1 depends on *a* whereas in the Paris law it is assumed to be a material constant (ϕ and p are constants). Spagnoli [[25] also revealed that such a crack growth law also corresponds to incomplete self-similarity, or self-similarity of the second kind.

These findings together with the realisation that "in the threshold regime, there is something missing either in the model…", see [[26], led to the conjecture [21, 22] that in the low ΔK region, i.e. Region I, the crack growth rate can be expressed in the form:

$$da/dN = C\,(a/a^*)^{(1-m^*/2)}\,(\Delta K_{eff})^{m} \qquad (7)$$

where C, a*, and m* are constants, and ΔK_{eff} is an "effective stress intensity factor" range. It is clear that this relationship follows the form proposed in [24], and therefore has a fundamental basis. Furthermore, for small cracks we can write

$$K = \beta\,\Delta\sigma\sqrt{\pi a} \qquad (8)$$

so that da/dN becomes proportional to a.

Noroozi, Glinka and Lambert [[27] modelled the crack as a notch with a small but finite tip radius $\rho^* > 0$, see Figure 1, which as per the Neuber micro-support concept [[28] remains open during crack growth. They then used the Smith-Watson-Topper (SWT) fatigue damage parameter to determine failure of the ligament immediately in front of the notch, to obtain a crack growth law of the form first proposed by Dinda and Kujawski [[29], viz:

$$da/dn = C\,(\Delta K_{tot}^{(1-p)}(K_{max,tot})^{p})^{\gamma} \qquad (9)$$

Here ΔK^{+} corresponds to the tensile part of the load cycle, i.e. the tensile part of the stress intensity range. After rearranging the expression for C given in [[27] we find that C can be expressed in the form

$$C = \rho^{1-\gamma/2}\,\underline{C} \qquad (10)$$

where $\underline{C}$ is independent of ρ^*.

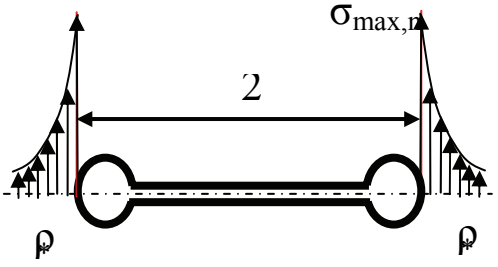

Figure 2 Crack with a finite tip radius, from [[27]

Noroozi, Glinka and Lambert [[27] revealed that

$$\rho = (\psi_{y,1})^2(\Delta K_{th}/\Delta\tilde{\sigma}^a_{th})^2/2\pi \qquad (11)$$

where $\Delta\tilde{\sigma}^a_{th}$ is the actual threshold stress range over the first elementary block in front of the crack tip, $\psi_{y,1}$ is a constant, and ΔK_{th} is the threshold stress intensity range.

The formulae presented in Section 2.3.1 of the Nasgro users manual [[30] can now be used to relate the threshold stress intensity range to the crack length, viz:

$$\Delta K_{th} = \varpi\sqrt{(a/(a+a_0))} \qquad (12)$$

where ϖ is a function of the R ratio, constraint state and prior load history.

$$\Delta K_{th} = \varpi\sqrt{(a/a_0)} \qquad (13)$$

so that ρ becomes proportional to a/a_0, viz:

$$\rho = (a/a_0)\,(\varpi/\Delta\tilde{\sigma}^a_{th})^2\,\psi_{y,1}^2/2\pi\,\alpha(a/a_0) \qquad (14)$$

and the crack growth Equation (9) can both be written in the generalized form:

$$da/dn = (a/a_0)^{1-\gamma/2}\,C'\,(\Delta K_{tot}{}^p(K_{max,tot})^{(1-p)})^{\gamma} = (a)^{1-\gamma/2}\,\tilde{C}\,(\Delta K_{tot}{}^p(K_{max,tot})^{(1-p)})^{\gamma} \qquad (15)$$

where the parameter C' is independent of a and ρ^* and $\tilde{C} = C'/a_0^{1+\gamma/2}$.

It is clear that this expression coincides with that presented in [21, 22].

It is interesting to note that this relationship between the generalised Frost & Dugdale law and the two parameter crack growth law mirrors the findings of Wnuk [[31]] who concluded that:

"For any given fractal dimension D (or roughness exponent H) a fractal crack may be reduced to an equivalent smooth crack equipped with a finite root radius dependent on D (or H). Once this transformation is accomplished, the laws of linear elastic fracture mechanics apply. Since the root radius of the equivalent crack is finite, the crack may be further reduced to a notch visualized as an elongated elliptical void. Therefore, the laws of the LEFM and those of Neuber's notch mechanics coincide, and they can be used interchangeably."

Expressions similar to Equation (9) have also been proposed by Donald and Paris [[32]] and Sadananda and Vasudevan [[33]]. who postulated the existence of two thresholds, i.e. the maximum threshold stress intensity factor $K_{\max,th}$ and the threshold stress intensity range ΔK_{th}, and that both should simultaneously be exceeded to make the fatigue crack grow.

One problem associated with current crack growth codes such as AFGROW, FASTRAN, NASGRO, and CRACKS 2000 is that they are unable to predict crack growth from small defects. In this paper we will show the generalised Frost-Dugdale law, as given in Equation (7), enables accurate predictions of the crack growth history from less than 100 microns to several mm's.

3. Crack Growth in 7050-T7451

Two test programs were undertaken to study the fatigue behaviour of 7050-T7451 aluminium alloy. In each case the test coupons were intended to represent the "mould line flange" on the F/A-18 FS488 wing attachment carry-through bulkhead, and were machined from a 6.35 mm thick 7050-T7451 aluminium alloy plate. The dimensions of the coupon test specimens used in the first test investigation are shown in Figure 3, and the material properties for 7050-T7451 are given in Table 1. These specimens were tested under the SPEC1 spectra, i.e. obtained from the operational strain data from a RAAF fleet aircraft, see [[33]] for more details. Tests were performed at two reference stresses, viz: 57.5 ksi (396.5MPa) and 47 ksi (324.1MPa).

The generalised Frost-Dugdale crack growth law presented in Equ. (7) was used to predict fatigue life on a cycle by cycle approach. C , m and a* are the material fatigue crack growth parameters

The constants C = 3.36 and m =1.78 10^{-10} were directly obtained from the "average" crack growth data, as presented by Sharp et al [16], and a transition value ΔK_{eff} of 11 MPa√m together with a K_c of 35.4 MPa√m, as quoted in [35], was used. Below the transition value we used the Frost-Dugdale law as shown in equations (1) and (2), whilst above this value we

used the standard FASTRAN algorithm. The transition value should always lie in the low end of the "Paris" region where Frost, Pook, and Denton [35] established that the Frost-Dugdale law and the Paris law are equally valid in describing crack growth.

A finite element model of the specimen was developed. The analysis allowed for two different crack configurations, viz: semi-elliptical surface flaws and corner flaws. This was necessitated by the nature of the cracks that developed during testing. To illustrate this Figure 4 presents micrographs of the fracture surfaces of two indicative specimens KD1R13 and KD1P24. Specimen KD1R13 contained a corner crack, and as such was typical of the majority of the cracks. Two of the specimens contained cracks that initiated as semi-elliptical cracks and later grew to become a corner crack, e.g.. specimen KD1P24 in Figure 4 For these cases the analysis considered them as semi-elliptical and halted when the surface crack tip reached the boundary.

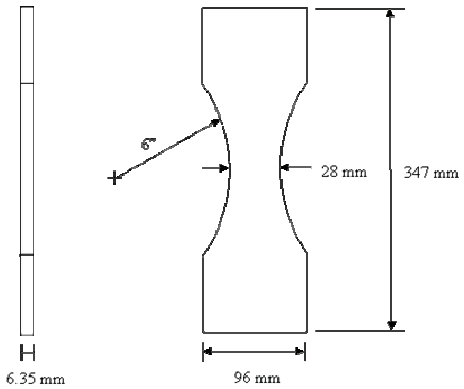

Figure 3: Specimen Geometry

Table 1: Material Parameters

Property	Coupon
Thickness	6 inches
Radius	6.35 mm
Cross-sectional area	177.8 mm^2
Stress concentration factor K_t	1.055
Elastic Modulus	71,000MPa
Poisson's ratio	0.33
Fracture Toughness	35.6 $MPa.m^{½}$
C crack growth parameter	$1.78x10^{-10}$
γ crack growth parameter	3.36

For each configuration we computed the stress intensity factors at both the deepest point and the surface points.

The results of this analysis for a SPEC 1 load spectra with a peak stress of 396.5 MPa are shown in Figure 5 for seven specimens that failed due to either corner cracks, in five cases, or from semi-elliptical initial cracks, two cases, and in Figure 6 for six crack cases that were tested under a SPEC 1 load spectra with a peak stress of 321.4 MPa.

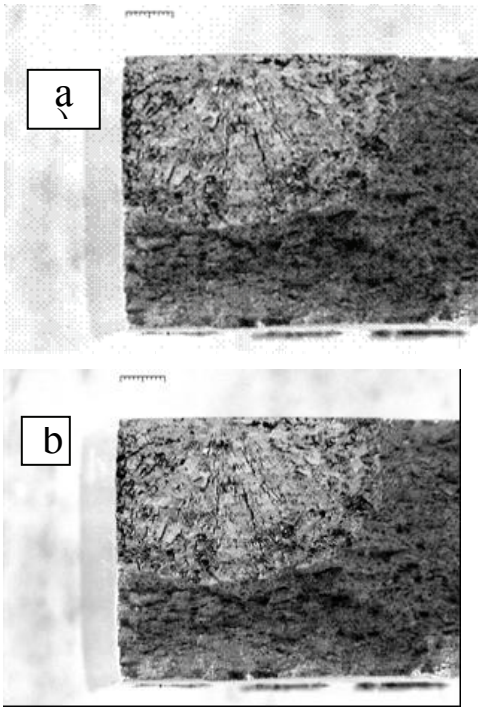

Figure 4: Macrograph of the fracture surfaces of coupons a) KD1R13 and b) KD1P24

In the second test program a slightly different test specimen geometry was used. These coupons were surface etched using the chemicals to produce surface pitting, which, on examination, had pitting similar to the pitting in the F/A-18 FT488/1 bulkhead. The etch solution was 50% (volume) Nitric Acid (HNO3, 70%) and 1% volume percent Hydrofluoric acid (HF, 70% Technical grade), remainder tap water, with an etching time of 5 minutes. In this test program the test spectrum, miniFALSTAF was modified to aid in its recognition during quantitative fractography by moving the flights with the most severe loads closer together.

The resultant predictions are shown below in Figure 6 for 3 different crack sizes together with a prediction made using FASTRAN. The FASTRAN prediction started at a comparably large flaw, i.e. a 0.019 mm quadrant flaw. For the 0.008 mm initial flaw associated with specimen KY48 FASTRAN yielded an essentially infinite life.

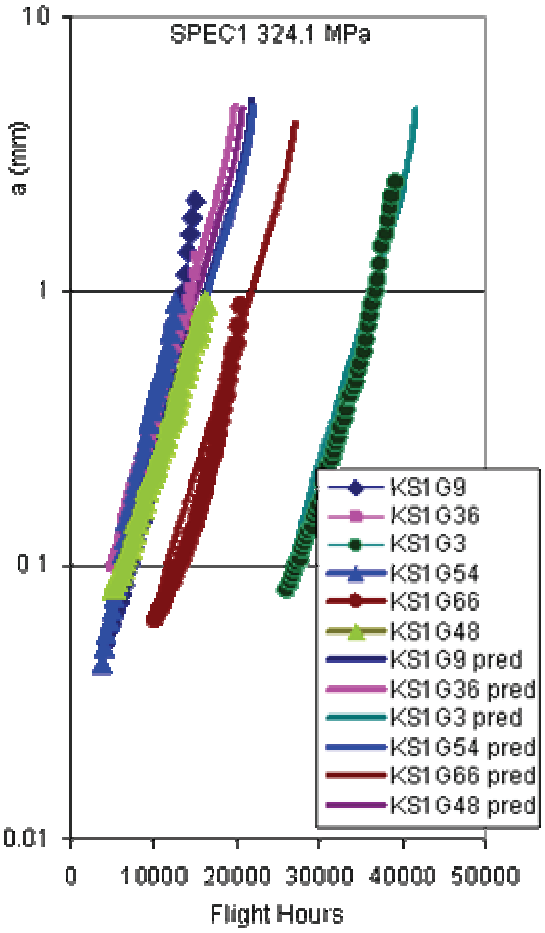

Figure 4: Fatigue life predictions for the SPEC1 test coupons with a reference stress of 396.5 MPa

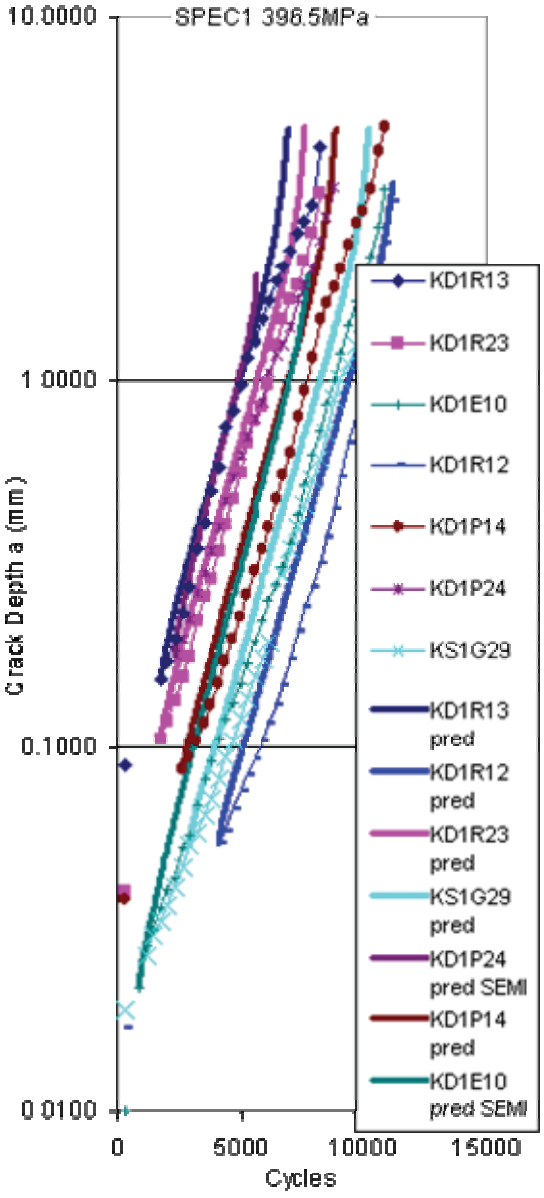

Figure 5. Crack growth predictions for SPEC1 load spectra at 324.1 MPa

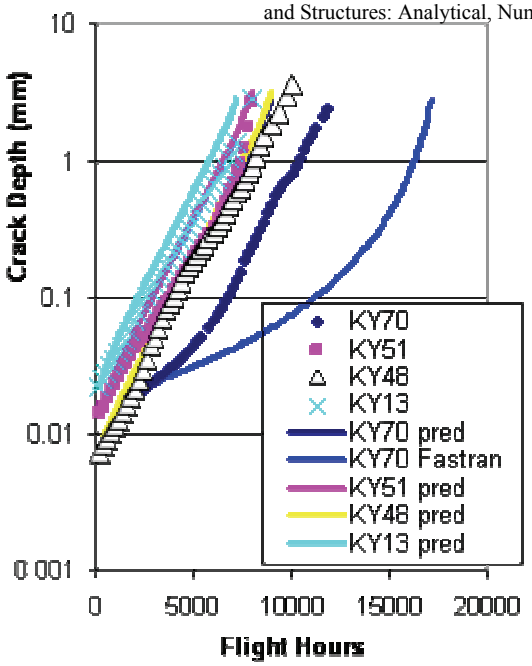

Figure 6. Crack growth predictions for mini-Falstaff load spectra at 390 MPa

4. Conclusion

This paper has shown how the generalised Frost-Dugale growth law presented in [21], which may also be viewed as a fractal/non-self similar based growth law, can be used to successfully predict crack growth in coupon tests under realistic spectrum loading.

References

[1] Paris, P. C, Gomez MP, and Anderson W. P., (1961), "A rational analytic theory of fatigue", The Trend in Engineering; 13:9-14.

[2] Irwin, G. R., (1957), "Analysis of stresses and strains near the end of a crack traversing a plate", *Trans ASME J Appl. Mech*., 24:361-4.

[3] Schijve, J., "Fatigue of structures and materials in the 20th century and the state of the art", *International Journal of Fatigue,* 2003; 25: 679-702.

[4] Elber, W., (1971) The significance of fatigue crack closure. Damage Tolerance of Aircraft Structures, ASTM STP-486, pp. 230-242.

[5] Kujawski D., (2003), "ΔK_{eff} parameter under re-examination", *International Journal of Fatigue,* 25:793-800.

[6] Sadananda, K, Vasudevan, A. K., (1993), "Analysis of fatigue crack closure and threshold", Fracture Mechanics, edited by F. Erdogan, ASTM, STP, p484-501.

[7] Pearson S., "Initiation of fatigue cracks in commercial aluminium alloys and the subsequent propagation of very short cracks", *Engineering Fracture Mechanics*, 1975. Vol. 7, pp. 235-247.

[8] Frost N. E., Marsh K. J. and Pook L. P. Metal Fatigue, Clarendon Press, Oxford, 1974.

[9] Head A K. "The growth of fatigue cracks", *Phil. Mag.*, 1953; 44 (7): 925-938.

[10] Frost N. E. and Dugdale D. S., "The propagation of fatigue cracks in test specimens", *Journal Mechanics and Physics of Solids*, 1958; 6: 92-110.

[11] Harkegard G., Denk J., and Stark K., "Growth of naturally initiated fatigue cracks in ferritic gas turbine rotor steels", *International Journal of Fatigue*, (2005), pp 1–12.

[12] Nisitani, H, Goto M. and Kawagoishi, N., "A small-crack growth law and its related phenomena", *Engineering Fracture Mechanics*, Vol. 41, No. 4, pp. 499-513, 1992.

[13] Kawagoishi, N. Chen Q. and Nisitani H., "Significance of the small crack growth law and its practical application", *Metallurgical and Materials Transactions A*, Volume 31A, pp 2005-2013, 2000.

[14] Caton M. J., Jones J. W., Boileau J. M., and Allison J. E., "The effect of solidification rate on the growth of small fatigue cracks in a cast 319-type aluminum alloy", *Metallurgical and Materials Transactions A*, Volume 30A, pp 3055-3068, 1999.

[15] Murakamia Y and Miller K. J., (2005), What is fatigue damage? A view point from the observation of low cycle fatigue process, *International Journal of Fatigue*, pp 1–15.

[16] Polak J. and Zezulka P., (2005), Short crack growth and fatigue life in austenitic-ferritic duplex stainless steel, *Fatigue Fract Engng Mater Struct*, **28**, 923–935, 2005.

[17] Tomkins, B. (1968) Fatigue crack propagation—an analysis, " *Phil. Magazine* ", **18**, 1041–1066.

[18] Ritchie R. O, Kruzic JJ, Muhlstein C. L, Nalla R. K.. Stach, E., (2004),

A. Characteristic dimensions and the micro-mechanisms of fracture and fatigue in 'nano' and 'bio' materials, *International Journal of Fracture*, 128, pp 1-15.

[19] Muhlstein C. L., Howe R. T. and Ritchie RO., (2004), Fatigue of polycrystalline silicon for microelectromechanical system applications: crack growth and stability under resonant loading conditions, *Mech. Mater*., 36, 13–33.

[20] L. Molent, Q. Sun and A. J. Green, (2005), The F/A-18 Fatigue Crack Growth Data Compendium, DSTO-TR-1677, Platform Sciences Laboratory, Melbourne, Australia.

[21] Barter S., Molent L., Goldsmith N., and Jones R., 2005, An experimental evaluation of fatigue crack growth, Journal of Engineering Failure Analysis, Vol 12, 1, pp 99-128.

[22] Molent L, Jones R and Pitt S., (In press), Understanding crack growth in fusealge lap joints, Theo and Applied Fract Mech.

[23] Mandelbrot, B. B., Passoja, D. E., Paullay, AJ., Fractal character of fracture surfaces of metals, *Nature*, 308, 721– 722, 1984.

[24] Carpinteri An. and Spagnoli An., (2004), A fractal analysis of size effect on fatigue crack growth, *Int. J. Fatigue*, 26, 125–133.

[25] An., Spagnoli, "Self-similarity and fractals in the Paris range of fatigue crack growth", *Mechanics of Materials*, 37, 519–529, 2005.

[26] Newman J. C. Jr, Brot A., Matias C, (2004), Crack-growth calculations in 7075-T7351 aluminum alloy under various load spectra using an improved crack-closure model, *Engineering Fracture Mechanics*, 71 2347–2363, 2004.

[27] Noroozi A.H., Glinka G., Lambert S., (2005), A two parameter driving force for fatigue crack growth analysis, *International Journal of Fatigue*, 27 1277–1296.

[28] Neuber H.,(1985), Kerbspannugslehre, Springer Verlag, Berlin.

[29] Dinda S, Kujawski D, (2004), Correlation and prediction of fatigue crack growth for different R-ratios using K_{max} and ΔK^{+} parameters, *Engineering Fracture Mechanics*, 71, 1779–1790..

[30] Fatigue Crack Growth Computer Program "Nasgro" Version 3.0: Reference Manual, JSC-22267b, March 2002.

[31] Wnuk M. P. and Yavari A., (2005), correspondence principle for fractal and classical cracks", Engineering Fracture Mechanics 72,2744–2757.

[32] Donald K, Paris P. C., (1999), An evaluation of ΔK_{eff} estimation procedure on 6061-T6 and 2024-T3 aluminium alloys, *International Journal of Fatigue*, Vol. 21, pp. S47-S57.

[33] Vasudevan AK, Sadananda K, Louat N., (1994), A review of crack closure, fatigue crack threshold and related phenomena, Material Science and Engineering, Vol. A188, pp. 1-22.

[34] Pell, RA, Molent L and Green AJ., (2004), The fractographical comparison of F/A-18 aluminium alloy 7050-T7451 bulkhead representative coupons tested under two fatigue load spectra at several stress levels. DSTO-TR-1547, Melbourne, Australia.

[35] P. K. Sharp, R. Byrnes and G. Clark, (, 1998), Examination of 7050 Fatigue Crack Growth Data and its Effect on Life Prediction, DSTO-TN-0729.

[36] N. E. Frost, L. Pook, and K. Denton, , (1971), A fracture mechanics analysis of fatigue crack growth data for various materials, *Engineering Fracture Mechanics*, 3, pp 109-126.

II. Micromechanics and Heterogeneity

EXPERIMENTAL STUDY AND MICROMECHANICAL MODELLING OF NON LINEAR BEHAVIOR OF PARTICLE-REINFORCED ELASTOMER

Vanessa BOUCHART
Mathias BRIEU, Djimédo KONDO, Moussa NAIT ABDELAZIZ
Laboratoire de Mécanique de Lille, UMR CNRS 8107
Université de Lille1, France

Abstract

The present study deals with an experimental characterization and a micromechanical modelling of the behaviour of a hyperelastic composite with random microstructure. The studied material is an elastomeric matrix reinforced by rigid spherical particles. In the perspective of a multiscale modelling, we first carried out uniaxial and equibiaxial tension tests on the elastomeric matrix. Then, the composite material with different volume fractions of the particle is tested under uniaxial tensile loading. The modelling of the macroscopic hyperelastic behaviour of this class of non linear composites is performed by using the second order method introduced by [(8)] in the framework of their variationnal homogenization technique. Detailled analysis of the numerical implementation of the method is given. Finally, the predictive capabilities of the modelling approach are evaluated by comparison of the numerical results with the experimental data.

Keywords: reinforced elastomer; micro mechanic; homogenization.

1 Introduction

Thanks to their remarkable properties of flexibility, deformability and resistance to the high deformation levels, the elastomers are often considered for various industrial applications. In order to compensate the largely deformable character of these materials which, paradoxically, constitutes the main reason of their use, particles reinforcement are usually added to the matrix. However, the study of hyperelastic behaviour of reinforced elastomers still raises many questions which are related to their heterogeneous character; for instance, the real impact of the reinforcement of this class of materials is still poorly understood. So, the objectives of the present study are to provide experimental data allowing to characterize the composite and its constituents and to applied a homogenization approach for the modelling of the reinforced material. A confrontation of the predictions of the model with experiments allows to evaluate the relevance of the approach.

2 Experimental characterization and identification of the mechanical behavior

The studied material is an Ethylene Propylene Diene Monomer (E.P.D.M.) matrix having a hyperelastic behaviour and reinforced by isostatic Polypropylene particles (P.P.). In this section, we first recall some basic results on the mechanical behavior of hyperelastic materials. Then, we summarize the experimental investigation and the identification of the mechanical behavior of the elastomeric matrix. The particles are assumed rigid with respect to the matrix.

2.1 The matrix strain-energy density

The hyperelastic behaviour of elastomers is classically defined in the form:

$$\mathbf{T} = \frac{\partial \mathrm{W}(\underline{\mathrm{X}},\ \mathbf{F})}{\partial \mathbf{F}} \qquad (1)$$

where T denotes the first Piola-Kirchhoff stress,W the strain-energy density at a ma-

terial point M_0 having coordinates $\underline{X}$ in the reference configuration Ω_0. $\mathbf{F}$ represents the deformation gradient at M_0.
The studied materials being assumed isotropic in their reference configuration and having to satisfy the principle of material indifference, W can be expressed in terms of the invariants of the right Cauchy-Green deformation tensor $\mathbf{C} = \mathbf{F}^t\mathbf{F}$ (cf. for instance Ogden [(6)]):

$$W(\underline{X},\ \mathbf{F}) = W(\underline{X},\ I_1,\ I_2,\ I_3)$$

$\mathbf{F}^t$ denotes the transpose of tensor $\mathbf{F}$.
For this study, we adopt an appropriate energy density, initially proposed by Lambert-Diani and Rey [(5)]:

$$W = \int_3^{I_1} e^{\left(\alpha_0+\alpha_1(I_1-3)+\alpha_2(I_1-3)^2\right)} dI_1 + \int_3^{I_2} \beta_1 I_2{}^{\beta_2} dI_2 \qquad (2)$$

α_0, α_1, α_2, β_1 et β_2 are parameters which have to be identified for the considered elastomeric matrix.

2.2 Experimental characterization and identification of the mechanical behavior of the matrix

For the purpose of the identification of all these parameters, we perform an uniaxial tensile test and an equi-biaxial tensile test on the elastomeric matrix.

Experimental protocol:
The tensile tests were carried out on standardized samples of type 2 [(2)], subjected to cyclic loadings with imposed maximum deformation. These tests, controlled in displacement, were carried out on a conventional machine (INSTRON 4302) equipped with a load cell of low capacity (1kN). The device which has been used for the equi-biaxial tensile tests was designed at the laboratory of Mechanics of Lille [(1)]; it is adaptable to the uniaxial tensile testing machine in finite deformation. The deformation rate chosen for the whole study is $10^{-4}/s$, which makes it possible to ensure the quasi-static character of the tests. Note also that the tests were carried out several times in order to guarantee a good reproducibility. The average responses of the matrix, obtained by means of these tests are given on figure 1.

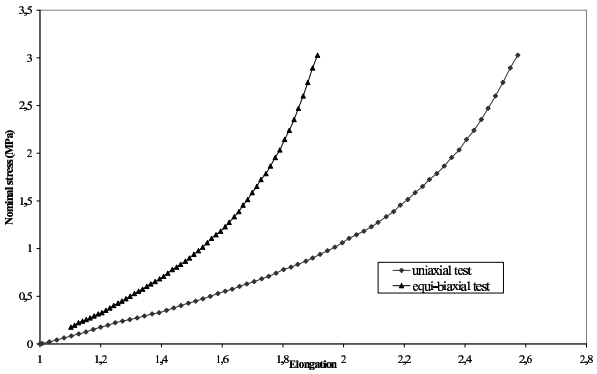

Figure 1: Mechanical response corresponding to the uniaxial and equi-biaxial tensile test of the matrix

Identification of the strain energy density:
The determination of the parameters of the energy density is done from from experimental stress-strain curve data of the matrix by using the software Excell . These parameters are determined with the solvor which minimizes the relative error in stress. For the n nominal-stress/nominal-strain data pairs, the relative error measure E is minimized, with:

$$E = \sum_{i=1}^{n} \left(1 - \frac{T_i^{(th)}}{T_i^{(exp)}}\right)^2 \qquad (3)$$

$T_i^{(exp)}$ is a stress value from the test data, and $T_i^{(th)}$ comes from the nominal stress expression calculated by means of the strain-energy density adopted.
From the tests carried out, the following values were obtained:

$$\alpha_0 = -1.8439;\ \alpha_1 = 0.14139;\ \alpha_2 = 0.0098;$$

$$\beta_1 = 0.0082;\ \beta_2 = 0.5674$$

3 Homogenization of particle-reinforced elastomer

We now come to the nonlinear homogenization modelling of the composite with random microstructure, justified by its heterogeneous character and the hyperelastic behavior. This micromechanical modelling is primarily based on the second order theory introduced by P. Ponte

Castañeda [(7)] and thereafter extend to the hyperelastic behaviour (cf.[(8)]). A description of this method is made in the subsection 3.1; its implementation is the subject of the subsection 3.2.

3.1 Second order Method applied to elastomer reinforced with rigid particles

The composite is subjected to a homogeneous strain conditions at the boundary of the representative elementary volume: $\bar{\mathbf{F}} = \langle \mathbf{F} \rangle$. The second order homogenization procedure [(7)], whose variational interpretation was proposed by Ponte Castañeda and Willis [(9)], makes it possible to obtain estimates of the energy density of the hyperelastic composite from the behavior of its constituents (matrix and particles). On the basis of available observation on the studied material, we make an assumption of rigid particles embedded in the hyperelastic matrix whose energy density is denoted $\mathrm{W}^{(1)}$. Moreover, we assume that these particles, whose volume fraction $c^{(2)} = c$, are spherical and dispersed in a random manner, so that the composite remains statistically isotropic in the non deformed configuration. The adherence between particles and matrix is supposed to be perfect, even if the processesing of material do not totally guarantees this one.
The assumption of rigid particles led, through the identity ($\bar{\mathbf{F}}^{(2)} = \mathbf{I}$), to :

$$\bar{\mathbf{F}}^{(1)} = \frac{1}{1-c}\left(\bar{\mathbf{F}} - c\mathbf{I}\right) \tag{4}$$

which, in the context of the second order method, gives:

$$\widetilde{\mathrm{W}}\left(\bar{\mathbf{F}}\right) = (1-c)\mathrm{W}^{(1)}\left(\bar{\mathbf{F}}^{(1)}\right)$$

$$+\frac{1}{2}\left(\bar{\mathbf{F}}-\mathbf{I}\right) : \left[\widetilde{\mathbb{L}} - \frac{1}{1-c}\mathbb{L}\right] : \left(\bar{\mathbf{F}}-\mathbf{I}\right) \tag{5}$$

$\mathbb{L} = \mathbb{L}_t^{(1)} = \frac{\partial \mathbf{T}^{(1)}}{\partial \bar{\mathbf{F}}}\left(\bar{\mathbf{F}}^{(1)}\right) = \frac{\partial^2 \mathrm{W}^{(1)}}{\partial \mathbf{F}\partial \mathbf{F}}\left(\bar{\mathbf{F}}^{(1)}\right)$ represents the tangent moduli tensor of the matrix (into the linear thermoelastic composite of comparison involved in the homogenization procedure [(7)]). $\widetilde{\mathbb{L}}$ is the overall tangent moduli tensor corresponding to the linear comparison composite (two-phase) made up of rigid inclusions with volume fraction c, distributed in a matrix of modulus tensor $\mathbb{L}$ and having the same microstructure as the elastic nonlinear composite in its undeformed configuration. It follows that, the overall mechanical behaviour is determined by computing the macroscopic first Piola-Kirchoff stress tensor by derivation of the overall energy density with respect to $\bar{\mathbf{F}}$ (see Hill [(4)]):

$$\begin{aligned}\widetilde{\mathbf{T}}\left(\bar{\mathbf{F}}\right) &= \mathbf{T}^{(1)}(\bar{\mathbf{F}}^{(1)}) \\ &+\frac{1}{2}\left(\bar{\mathbf{F}}-\mathbf{I}\right) : \left[\widetilde{\mathbb{L}} - \frac{1}{1-c}\mathbb{L}\right] \\ &+\frac{1}{2}\left[\widetilde{\mathbb{L}} - \frac{1}{1-c}\mathbb{L}\right] : \left(\bar{\mathbf{F}}-\mathbf{I}\right) \\ &+\frac{1}{2}\left(\bar{\mathbf{F}}-\mathbf{I}\right) : \frac{\partial}{\partial \bar{\mathbf{F}}}\left[\widetilde{\mathbb{L}} - \frac{1}{1-c}\mathbb{L}\right] : \left(\bar{\mathbf{F}}-\mathbf{I}\right)\end{aligned} \tag{6}$$

The use of (6) requires the determination of the local deformation $\bar{\mathbf{F}}^{(1)}$ in the matrix and the homogenization scheme. Considering rigid particle, it was shown from the deformation average rule that $\bar{\mathbf{F}}^{(1)}$ is given by (4).

3.2 Numerical implementation

The estimate of the effective tangent modulus tensor $\widetilde{\mathbb{L}}$ of the linear comparison composite requires the consideration of a linear homogenization scheme. For the implementation of the second order method in this study, two well known schemes were considered: Reuss model and Hashin-Shtrikman estimate (HS). It is pointed out that the strain-energy density of the hyperelastic matrix, $\mathrm{W}^{(1)}$, was selected in the form (2) with the parameters identified in section 2.2.
The very simple REUSS estimate, corresponding to an assumption of uniform stress in the linear comparison composite, leads to $\widetilde{\mathbb{L}} = \frac{1}{1-c}\mathbb{L}$, from where it follows that:

$$\begin{aligned}\widetilde{\mathbf{T}}\left(\bar{\mathbf{F}}\right) = \mathbf{T}^{(1)}(\bar{\mathbf{F}}^{(1)}) = \mathbf{T}^{(1)}\left[\frac{1}{1-c}\left(\bar{\mathbf{F}}-c\mathbf{I}\right)\right] \\ \text{with} \quad \mathbf{T}^{(1)}(\bar{\mathbf{F}}^{(1)}) = \frac{\partial \mathrm{w}^{(1)}}{\partial \mathbf{F}}(\bar{\mathbf{F}}^{(1)})\end{aligned} \tag{7}$$

Note that the Reuss-based model corresponds to the one already introduced by [(3)] The more sophisticated Hashin-Shtrikhman estimate, takes a priori into account the interactions between the different constituants (phases) in the composite

for a spherical spatial distribution of the phases. It leads to:

$$\widetilde{\mathbb{L}} = \mathbb{L} + \frac{c}{1-c}\mathbb{P}^{-1} \tag{8}$$

Due to the anisotropic character of the tangent modulus, even in the case of an isotropic behavior, tensor $\mathbb{P}$ can be evaluated by the following expression: $\mathbb{P} = \mathbb{P}^{(1)} = \frac{1}{4\pi}\int_{|\xi|=1}\mathbf{H}^{(1)}(\xi)dS$, with $\mathbf{K}^{(1)}{}_{ik} = \mathbf{L}^{(1)}{}_{ijkl}\xi_j\xi_l$, $\mathbf{N}^{(1)} = \mathbf{K}^{(1)^{-1}}$, $\mathbf{H}^{(1)}{}_{ijkl}(\xi) = \mathbf{N}^{(1)}{}_{ik}\xi_j\xi_l$.
It must be therefore emphasized that the Hashin-Shtrikman estimate requires the calculation due to the anisotropy of the tangent tensor $\mathbb{L}$, there is no analytical expressions for $\mathbb{P}$ in the general case. So, we have performed numerical integration on the sphere unit $|\xi| = 1$. Two numerical methods of integration, namely Newton-Cotes and Gaussian integration technique, were implemented, compared and validated both in various cases. The introduction of (8) in (6) led to the macroscopic stress-strain relation:

$$\begin{aligned}\widetilde{\mathbf{T}}\left(\bar{\mathbf{F}}\right) &= \mathbf{T}^{(1)}(\bar{\mathbf{F}}^{(1)}) \\ &+\frac{1}{2}\frac{c}{1-c}\left(\bar{\mathbf{F}}-\mathbf{I}\right):\left[\mathbb{P}^{-1}-\mathbb{L}\right] \\ &+\frac{1}{2}\frac{c}{1-c}\left[\mathbb{P}^{-1}-\mathbb{L}\right]:\left(\bar{\mathbf{F}}-\mathbf{I}\right) \\ &+\frac{1}{2}\frac{c}{1-c}\left(\bar{\mathbf{F}}-\mathbf{I}\right):\frac{\partial}{\partial\bar{\mathbf{F}}}\left[\mathbb{P}^{-1}-\mathbb{L}\right]:\left(\bar{\mathbf{F}}-\mathbf{I}\right)\end{aligned} \tag{9}$$

A last key point which have to be adressed is the requirement of a mathematical derivation which enters in (9). For this purpose, a numerical derivation has been performed. In order to have ggod accuracy at this step, a Ridders-Richardson method (cf Numerical Recipes, Press et al. [(10)]) was implemented. This method is based on an algorithm in which a control and optimization of the computations errors are performed at each step of the derivation procedure.

4 Application to a compressible uniaxial tensile loading

The macroscopic deformation gradient associated to a compressible uniaxial traction is written in the form:

$$\bar{\mathbf{F}} = \mathrm{Diag}\left(\lambda(t), \alpha(t), \alpha(t)\right)$$

λ (increasing from 1.0). The fact that the uniaxial tensile sollicitation applied on the composite is controlled in deformation implies, for a given λ, to determine the value of α in order to fulfill the uniaxial tensile loading:

$$\bar{\mathbf{T}} = \mathrm{Diag}\left(T_{11}(t), 0, 0\right)$$

In practice, since the matrix and the composite are assumed compressible, the above conditions can be obtained only by an iterative procedure. For this, we have considered an algorithm based on a dichotomy procedure which, after convergence, yiels the suitable value of α for a given λ. Application of the hole method to the considered reinforced rubber yields numerical results for the two estimates which have been described before. The Reuss and Hashin-Shtrikman estimates are compared to the experimental results on figures 2, 3 and 4 respectively for 5%, 10% and 35% of reinforcement volume fractions. In order to underline the effect of these reinforcements, we also report the response of the elastomeric matrix on the same figures. From the obtained results, the following observations can be made:

- For weak volume fraction of the rigid particles (5% and 10%), we note a rather good agreement between the predictions of the Reuss estimate and the experimental data, whereas the results based on the Hashin-Shtrikman model gives an underestimate of the macroscopic deformation. Due to the simplicity of the Reuss model, this numerical prediction is quite surprising; however, this can be explained by the two strong assumptions (rigid particles, perfect adherence between matrix and particles) which are made at the present step of the modelling.

- For the relatively high volume fraction of 35%, it is seen that the Hashin-Shtrikman estimate show better agreement with the experimental data. It is believed that this agreement illustrates the capability of the Hashin-Shtrikman scheme to take into account the notable effect of the interacting reinforcements.

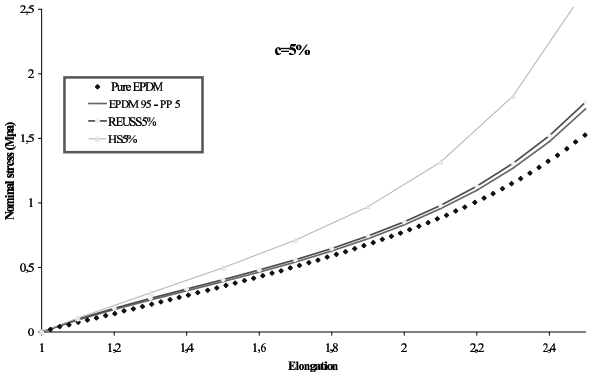

Figure 2: Predictions of Hashin-Shtrikman and Reuss models for the composite with a volume fraction of 5%

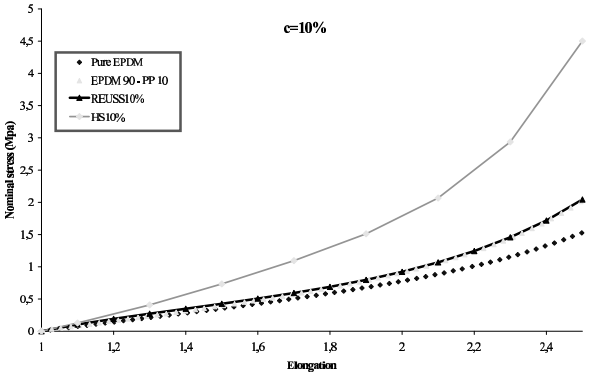

Figure 3: Predictions of Hashin-Shtrikman and Reuss models for the composite with a volume fraction of 10%

5 **Conclusions**

The study presented in this paper concerns the experimental characterization and the multiscale modelling of the mechanical behaviour of reinforced elastomers. Uniaxial and equi-biaxial tensile tests were first performed on the elastomeric matrix material and on the different reinforced materials. The tests carried out on the matrix allows to calibrate the parameters of the strain-energy density considered for the study. The particles used for reinforcements are assumed rigid. For the nonlinear multiscale modelling, a second order method is numerically implemented using a Reuss and a Hashin-Shtrikman estimates for the linear comparison composite. It is shown that the model based on the Hashin-Shtrikman estimate gives results in agreement with the experimental data for high volume fraction of particles, while the Reuss model seems to agree with the available data for the low volume fractions. Although interesting, these results needs to be improved, at least by the consideration of deformable particles and by incorporation of the fluctuations of fields in the second order method (cf [(8)]).

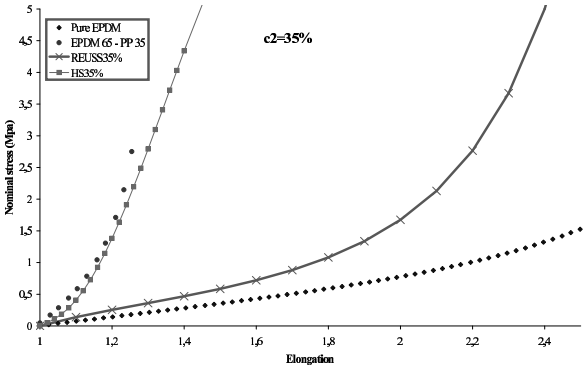

Figure 4: Predictions of Hashin-Shtrikman and Reuss models for the composite with a volume fraction of 35%

REFERENCES

[1] Brieu, M., Diani J., (2005), Bi-axial torsion machine in large deformation for the characterization of the behavior of rubber-like materials, *submitted to Rubber Chemistry Technology*

[2] Brown, R.P. (1984), *Physical testing of Polymer*, 3rd Edition, Chapman and Hall

[3] Govindjee S., Simo J. (1991), A micromechanically based continuum damage model for carbon black-filled rubbers incorporating Mullin's effect, *J. Mech. Phys. Solids*, **39**, pp. 87-112

[4] Hill, R., (1972), Convexity conditions and existence theorems in non linear elasticity, *Arch. Rat. Mech. Anal.*, **63**, pp. 337-403

[5] Lambert-Diani J., Rey C. (1999), New phenomenological behavior laws for rubbers and thermoplastics elastomers, *Eur. J. Mech., A, Solids*, **18**, pp. 1027-1043

[6] Ogden, R.W., (1984), *Non linear elastic deformations*

Dover Publications Inc, New York

[7] Ponte Castaneda, P., (1996), Exact second order estimates for the effective mechanical properties of non linear composite materials, *J. Mech. Phys. Solids*, **44**, pp. 827-862

[8] Ponte Castaneda, P., Tiberio E. (2000), A second order homogenization method in finite elasticity and applications to black-filled elastomers, *J. Mech. Phys. Solids*, **48**, pp. 1389-1411

[9] Ponte Castaneda, P., Willis J. (1999), Variationnal second order estimates for non linear composites, *Proc. R. Soc. London*, A, **455**, pp. 1799-1811

[10] Press, W.H., Teukolsky S.A., Vetterling W.T., Flannery B.P. (1992), *Numerical Recipes in Fortran, The art of scientific computing*, 2nd Edition, Cambridge University Press

NUMERICAL COMPUTATION OF MECHANICAL BEHAVIOUR OF HETEROGENEOUS MATERIALS USING A MICROSTRUCTURE BASED MESOMODEL

S. Ataya, M. Korthäuer, E. El-Magd
Department of Materials Science, Aachen University,
Augustinerbach 4, 52062-Aachen, Germany

Abstract

The shear behaviour of W/Cu composites (W/Cu-80/20, 70/30 and 60/40 wt.%) was experimentally investigated using axisymmetrical hat-shaped specimens with different shear zone width. To show the deformation and failure at the shear zone the microstructure was imaged after different degree of deformation.

The relevant deformation zone the shear specimen was used as a 2D-mesomodel for the numerical computation. A micrograph of the microstructure was scanned digitally to define the composite components. The brightness of the composite components (Cu and W) was used to distinguish between them. The material law of the composite components (Cu and W) was determined from the flow curves that are determined in compression tests.

The development of deformation and damage at the shear zone were followed up by step loading and with the FE-simulation as well. The FE-simulation on the real microstructure with different shear zone width values confirmed the experimentally measured size effects of shear specimens.

Keywords

FE-Simulation, mesomodel, W/Cu particle composites, size effects, shear deformation

1. Introduction

The computation of the mechanical behaviour of heterogeneous materials from the knowledge of the behaviour of their components using the FE-technique gains in the present time greater interest. In this respect, an idealized representative volume element (RVE) is used. Computation of the deformation and fracture behaviour of the heterogeneous material using a mesomodel based on the real microstructure of the material will be more definite. There are many efforts [1 , 2] for examining the deformation the composites behaviour using the microstructure as a base of the FE-mesh using the SEM based grating method by in-situe recorded image during loading.

Size effects play a decisive role in manufacturing and deformation processes due to either physical or structural properties [3,4]. The deformation behaviour of a metallic matrix reinforced with hard particles depends on volume fraction, size, shape, and distribution of the reinforcements [5,6,7]. The effects of the volume fraction in the W/Cu composites on the mechanical properties were studied in [8,9]. Cleveringa et al [5] have numerically investigated the effect of the particles´ morphology on the deformation behaviour of particle composite materials. It has been concluded that when the reinforcements block all the slip planes of the matrix the composite shows a high strain hardening and there is a significant size effect. On the other hand when veins of unreinforced matrix material or clustering of the reinforcement exist [7] the matrix will easily be deformed in these zones,

therefore, the overall flow stress of the composite decreases and there is no size effect. Obvious scaling effects in the W/Cu composites were found at testing cylindrical specimens under compression loading especially at lower temperatures and at higher contents of the hard phase (W) [9, 10]. The dominance of shear deformation in the state of stress during machining of metallic materials [11] makes it reasonable to investigate the scaling effect under shear loading.

Besides studying the size effects under shear loading, the major goal of this paper is to simulate numerically the deformation behaviour of the composite material (tungsten/copper) from a microstructure based 2D-mesomodel.

2. Test materials and experimental work

W/Cu composites in different weight percentages (W/Cu-80/20, 70/30 and 60/40) were tested under shear loading. These composites were studied with two different mean particle size of the tungsten particles (D_P) namely 10 µm and 30µm. Figure 1 shows the structure of the composite material W/Cu-80/20 and W/Cu-60/40.

Shear test was conducted on hat-shaped shear specimens [12] as in Figure 2a. The shear zone width (S) was varied to be 0.1, 0.2, or 0.3 mm. Shear test was conducted at a temperature range between 20°C and 800°C and strain rates of 0.01, 1.0 and 100 s^{-1}.

Step-loading and metallographic examination were carried out to follow the development of the deformation and the damage due to shear loading. To conduct such test, hat-shaped shear specimens composed of two metallographically prepared longitudinal separated halves were prepared, Figure 2c. The microstructure of the relevant shear zone is shown in Figure 2b was documented. The micrograph of the shear zone before loading was used for the mesh generation of 2D mesomodel. The tow halves were supported tightly in a holder to avoid the relative displacement between the two halves. Three steps of loading were done before reaching the complete fracture. After each loading step the shear zone of the specimen's halves were photographed.

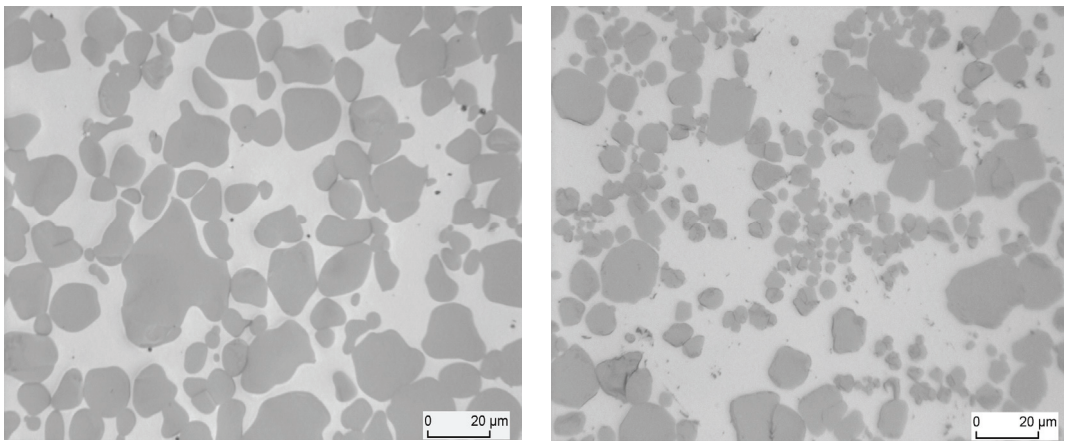

(a) W/Cu-80/20 (wt.%) *(b) W/Cu-60/40 (wt.%)*

Figure 1: Examples for microstructure of the W/Cu composite materials.

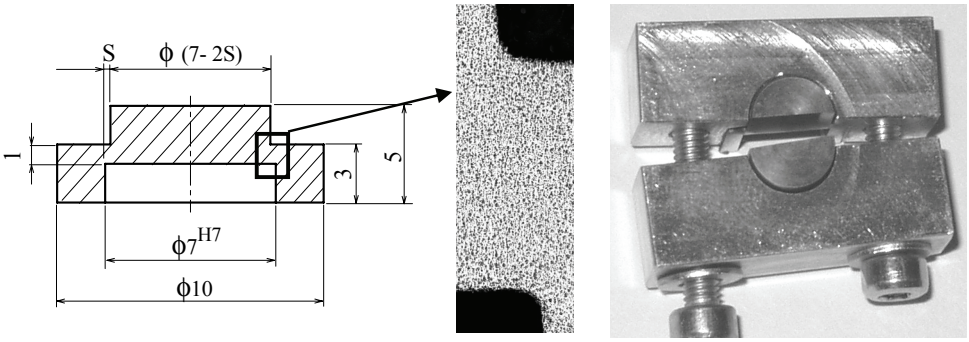

(a) (b) (c)

Figure 2: (a) Hat-shaped cylindrical shear specimen, (b) the relevant shear zone and (c) the two-half specimen for step loading.

3. Deformation behaviour under shear loading

The shear stress and the shear strain up to fracture of the shear specimens with narrow shear zone (S=0.1mm, Figure 3-a) was higher than the wider shear zone (S=0.3mm, Figure 3-b) due to the increased strain concentration in the narrower shear zone. This tendency occurs regardless the strain rate and the test temperature. Figure 4 shows the size effect on the shear stress for the different W/Cu composites. Due to the high volume fraction of tungsten in W/Cu-80/20 an increased obstruction of the deformation, consequently, a higher size effect than in the other tested composites was obtained (Figure 4-a).

The variation of tungsten particle sizes (D_P) from 30 μm to 10 μm increases the stress levels, with the same effects of the deformed size (Figure 4). W/Cu composites have shown strain rate sensitivity on loading at relatively higher strain rates (100 s^{-1}).

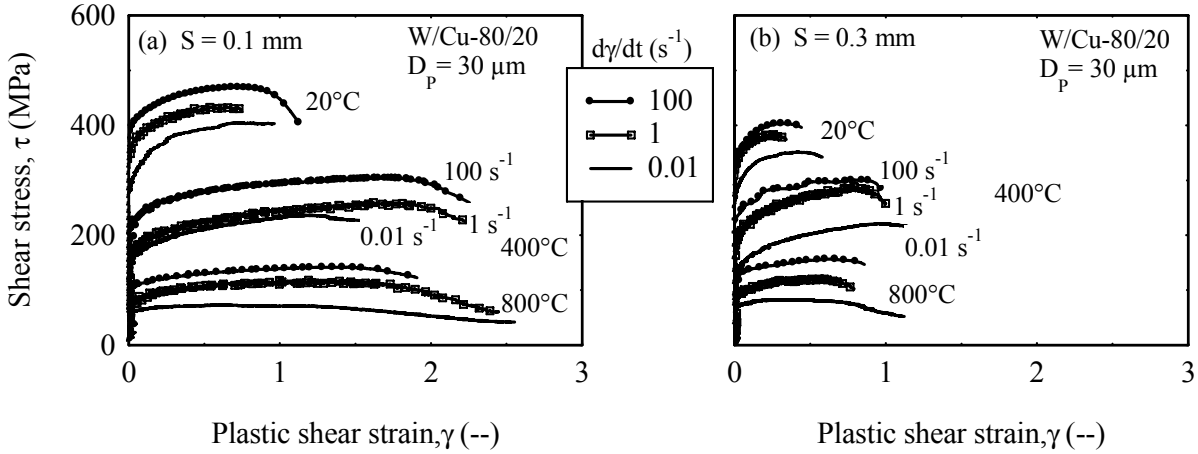

Figure 3: Effect of the shear zone width (S) on the shear stress-shear strain curves of W/Cu-80/20 with particle size of 30μm under strain rates of 0.01s^{-1}, 1s^{-1} and 100s^{-1} and at temperatures of 20°C, 400°C and 800°C.

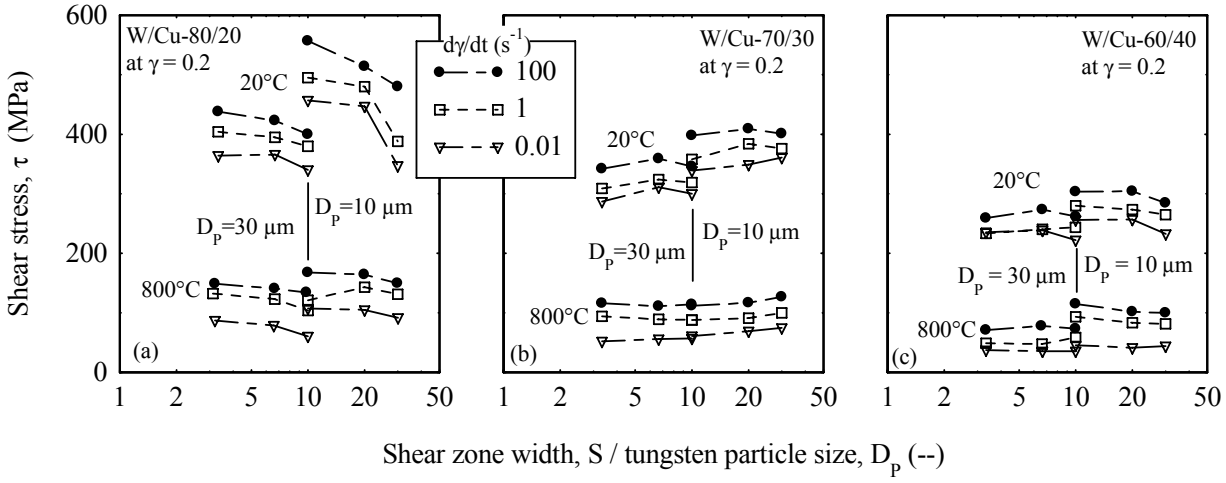

Figure 4: Size effects (S=0.1, 0.2 and 0.3 mm and D_P= 10 and 30μm) under shear deformation of W/Cu composites at 20°C and 800°C under strain rates of $0.01s^{-1}$, $1s^{-1}$ and $100s^{-1}$.

Since the wider shear zone (S=0.3mm, Figure 5-b) resulted in a diffused deformation that was mostly expended in the deformation of copper so that the fracture takes place mainly through the softer component (Cu) with unmarkable deformation of tungsten particles. In contrary, high shear localization was occurred in the smaller shear zone (S=0.1mm, Figure 5-a). The stresses were high enough to deform the hard tungsten particles and the fracture grows through copper and tungsten as well [10]. This can explain the effect of the smaller shear zone widths on increasing the stress level of the shear stress-shear strain curves in Figure 3.

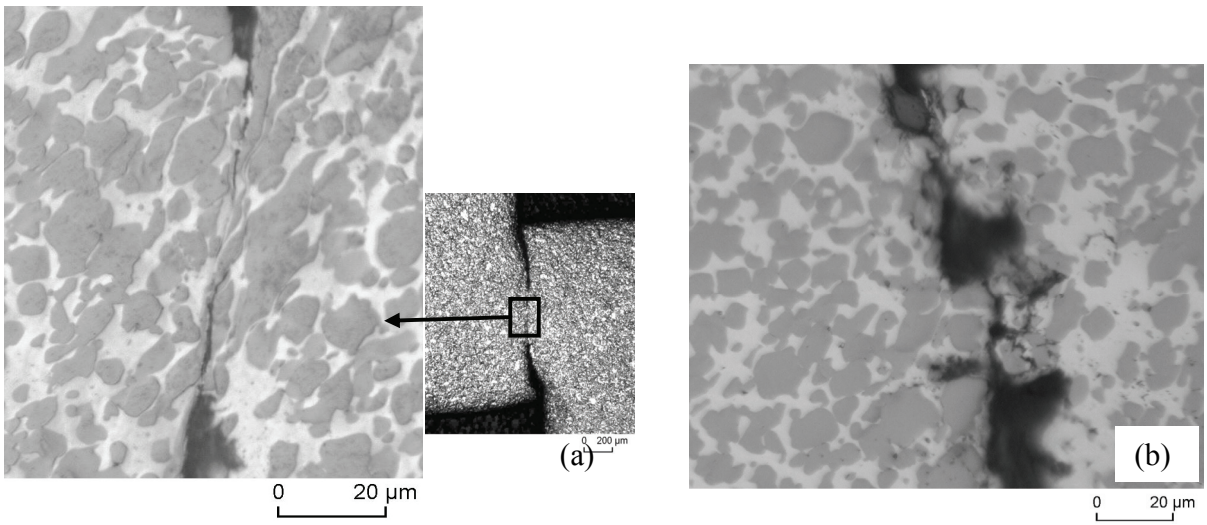

Figure 5: Effect of the shear zone width (S) on the fracture of W/Cu-80/20 at 20°C.
(a) S = 0.1 mm, $d\gamma/dt = 0.01\,s^{-1}$ and D_P=10μm (b) S = 0.3 mm, $d\gamma/dt = 0.01\,s^{-1}$ .and D_P=10μm

4. Step loading and FE-simulations

FE-simulation based on the real microstructure was carried out to determine the deformation and fracture behaviour of composite W/Cu under shear loading. The microstructure of the relevant shear zone of one half of the shear specimen prepared for step loading was used as a mesomodel for FE-Simulation. Figure 6-a includes a micrograph of the relevant region of the shear specimen of the composite W/Cu-60/40 with a particle size of 30µm and shear zone width of 0.1 mm. A fine mesh with one material element based on the microstructure before loading was produced. Figure 6.b shows to what extent the generated mesh can represent the microstructure components.

The mechanical properties of the composite components (W and Cu) were fed to the FE-Code "ABAQUS" separately. The elastic properties were in the values as in Table (1).

	SE-Copper	Tungsten
E-modulus, GPa	110	400
Poisson's ration, ν	0.35	0.28

Table 1. Elastic properties of Cu and W [13]

The plastic properties were calculated from the flow curves determined in quasi-static compression test on the tungsten and SE-Cupper. The flow curves were described by a modified Mecking-Kocks model [14]:
The flow stress in MPa is given by

For tungsten:
$$\sigma = 500 + 426\ \varepsilon + 715\left[1 - exp\left(-1076\ \varepsilon\right)\right]$$

For copper:
$$\sigma = 190 + 162\ \varepsilon + 97\left[1 - exp\left(-140\ \varepsilon\right)\right]$$

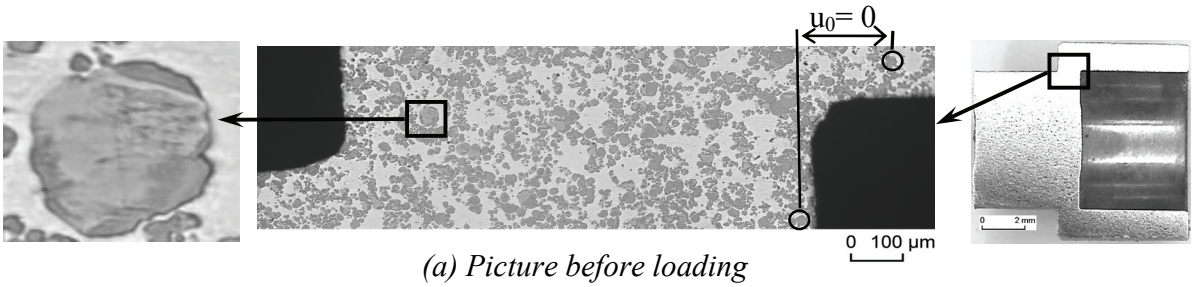

(a) Picture before loading

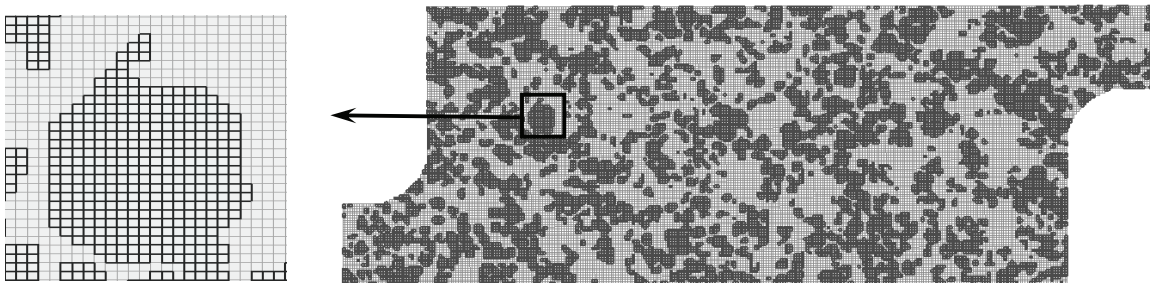

(b) Fine mesh, 35710 elements (one element = 3 x 3 pixels)

Figure 6: Transformation of the microstructure picture of the relevant shear region of a hat-shaped of W/Cu-60/40 before loading (displacement of two reference particles u_0=0) into 2D-idealization. Dark = tungsten, bright = copper.

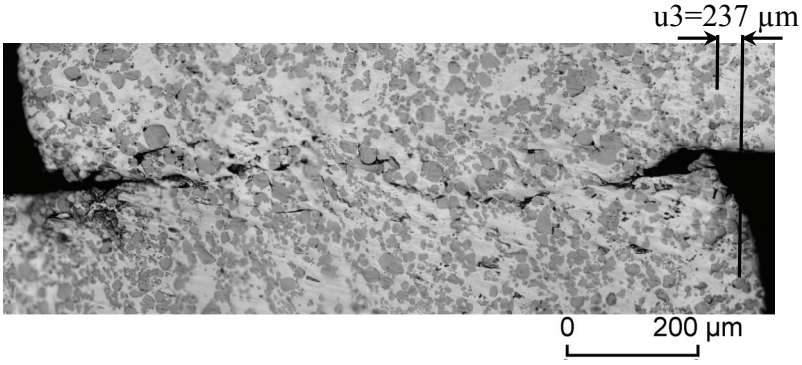

(a) The microstructure after the third step of loading (W/Cu-60/40, 30µm).

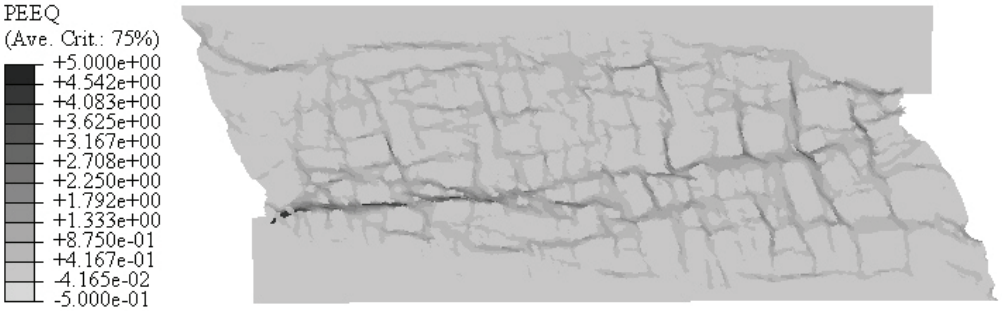

(b) The equivalent strain distribution after displacement of 0.25 mm.

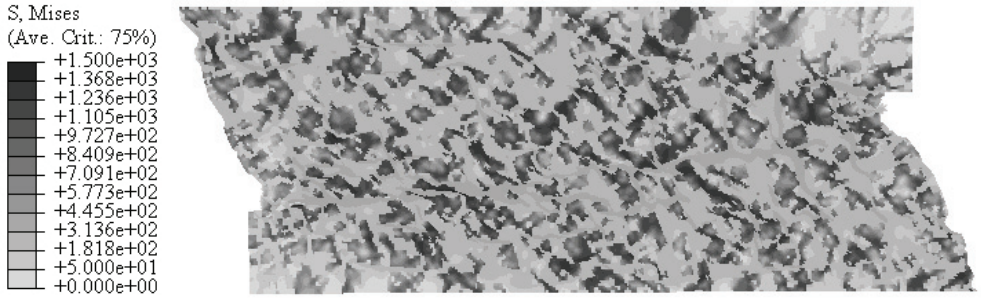

(c) The equivalent stress distribution after displacement of 0.25 mm.

Figure 7: Distribution of the equivalent stress and strain compared with the microstructure after the third stage of step loading.

The concentrated deformation in the shear zone of the specimens with small shear zone widths allows choosing the sides of the model as rigid boundary condition. One side was held constant and the other was moved for a distance of 0.25 mm which is slightly higher than the permanent plastic deformation (u3 =237 µm) measured from the relative displacement of nearly not affected positions on the sides of the shear zone (Figure 6-a and Figure 7-a). The distribution of the equivalent strain obtained from the FE-simulation shows a relatively similar deformation pattern to the microstructure after the last step of loading (Figure 7-a and b).

As shown in Figure 7-a, the cracks grow through the copper matrix. A deformation limit was

applied as failure criterion for copper. The elements of copper which reach the limit (ε = 3) will be considered as failed elements. This leads to the decrease of the stress level beyond the peak in the FE-results in analogy to the experimental results (Figure 8a).

The numerical calculations of this 2D-mesomodel were carried out first with plane strain condition and second with the plane stress condition, as shown in *Figure 8*. The experimental shear stress-shear strain curves lies between the two solutions. The mean value of the two solutions is comparable with experimental one.

The FE-simulation was also carried out for shear zone width of S = 0.3 mm of the composite W/Cu-60/40 starting from the microstructure of an unloaded specimen. The results are shown in Figure 8-b.

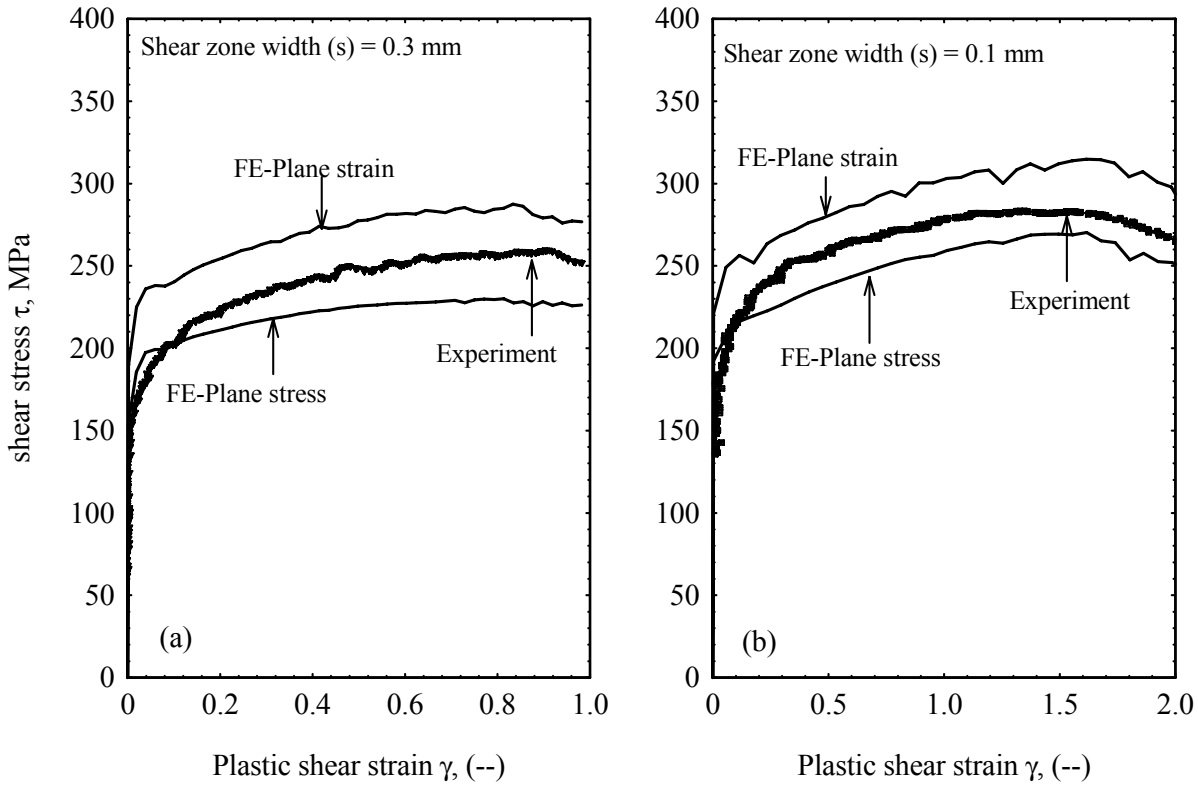

Figure 8: FE-simulation results compared with the experimental shear stress-shear strain curves of W/Cu-60/40 with shear zone width (S) of 0.1 and 0.3 mm at the quasi-static strain rate at room temperature.

5. Conclusions

1. The size effects on the deformation of W/Cu under shear loading were obvious at higher content of the reinforcement (W).
2. The strong W-particles were deformed particularly in the case of thin shear zone (S = 0.1).
3. The composites studied show a strain rate sensitivity by loading at strain rates up to 100 s^{-1}.
4. The FE computation of the 2D mesomodel obtained from the micrograph simulated the pattern of the shear zone.

5. The FE-simulation delivered comparable deformation behaviour either for the stress distribution pattern or the stress strain curves with the experiment; however, the experimental curves were between plane strain and plan stress solutions.

References

[1] E. Soppa, S. Schmauder, G. Fischer, J. Brollo, U. Weber, (2003), *Computational Materials Science*, **28**, issue 3-4, (2003), pp. 574-58.
[2] Y.L. Liu and G. Fissher, (1997), *Scripta Materialia*, **36**, No. 10, pp. 1187-1194.
[3] F. Vollertsen, (2003), in Process Scaling, F. Vollertsen, F. Hollmann (Eds.), BIAS Verlag, Bremen, **24**, pp.1-9.
[4] O. Kienzle, (1952), *Zeitschrift VDI*, **94**, No. 11/12, pp. 299-305
[5] H.H. Cleveringa, E. van der Giessen, Needleman, (1997), *Acta Mat.* **45 A**., No. 8, pp. 3163-3179
[6] A. Borbely, H. Biermann, (2000), *Adv. Eng. Mater.*, **2**, No. 6, pp. 366-369
[7] T.C. Tszeng, (1998), *Composites*, **29B**. pp. 299-308
[8] S. Schmauder, U. Weber, I. Hofinger and A. Neubrand, (1999), *Technische Mechanik*, 19, No. 4, pp. 313-320
[9] E. El-Magd, M. Korthäuer and S. Ataya, (2003), in Prosess Scalin F.Vollertsen and F. Hollmann (Edt.), Bias Verlag, Bremen, Vol. 24 pp. 57-64.
[10] E. El-Magd, M. Korthäuer, S. Ataya, (2005), in: G.S. Sih and T. Vu-Khanh (Eds.) proceeding of the 7Th Inter. Conf. on Mesomechanics, Montreal, pp. 183-192
[11] U. Hofmann, E. El-Magd, (2005), *Mater. Sci. & Eng.*, **395A**, pp. 129-140.
[12] K-H. Hartmann, H-D. KUNZE and L.W. MEYER, (1981), in M.A. Meyers and L.E. Murr (Eds.), Shock Waves and High Strain Rate Phenomena in Metals, M.A. Plenum Press, New York, pp. 325-337.
[13] Metals Handbook, Properties and Selection, Nonferrous Alloys and Special-Purpose Materials, ASM International, Metals Park, Ohio, vol. 2, 10th Ed., (1990).
[14] E. El-Magd, (2004), *Modeling and Simulation for Material Selection and Mechanical Design,* Totten, G. E., Xie, L., and Funatani, K. (Eds.) Marcel Dekker, Inc., New York, pp. 195-300.

SIZE EFFECT IN FORMATION OF ADIABATIC SHEAR BANDS

M. Nabil Bassim
Department of Mechanical Engineering, University of Manitoba, Winnipeg, Manitoba, Canada R3T 5V6

Abstract

Adiabatic Shear Bands (ASB) have been observed during high stain rate deformation (in excess of 10^{3-1}) of metallic materials.

There are manifestations of occurrence of plastic deformation and stain softening due to rise in temperature in the material. In this study, the process of development of ABS is modeled by a finite element method which predicts the characteristic size of the ASB. The model was verified by experimental techniques involving the use of a direct impact Split Hopkinson Pressure Bar and torsional SHB. Several steels were tested to investigate the occurrence and characteristic of the produced ASB in these materials.

Keywords: High stain rates, adiabatic shear bands finite element modeling.

1. Introduction

At very high stain rates, metallic materials may experience adiabatic conditions where part of the retained heat generated during impact causes stain softening. During deformation under adiabatic conditions, both work hardening and stain softening take place simultaneously causing the occurrence of adiabatic shear bands (ASBs) [1, 2]. These appear as narrow bands with localized stains in the 100s percent. Strain rates in excess of 10^{3-1} are required to produce ASBs. Also, ASBs can be the source for initiation of microcracks leading to the fracture of the material.

In the present study, modeling of the formation of ASB in a typical steel is performed using finite element methods. This is followed by an experimental study to verify the occurrence of ASBs in steels and to study their characteristic features.

2. Present Study

Modeling

In this part, we used a rate depending constitutive equation approach based on ANSYS [3]. The constitutive equations have been given previously by Feng and Bassim [4].

Fig 1 shows the dimensions of the sample used in a torsional SHB. The cross section A-A is cut in the middle of the specimen and a torque M is applied at both the top and bottom sides. A shear band is usually found in the middle part of the specimen.

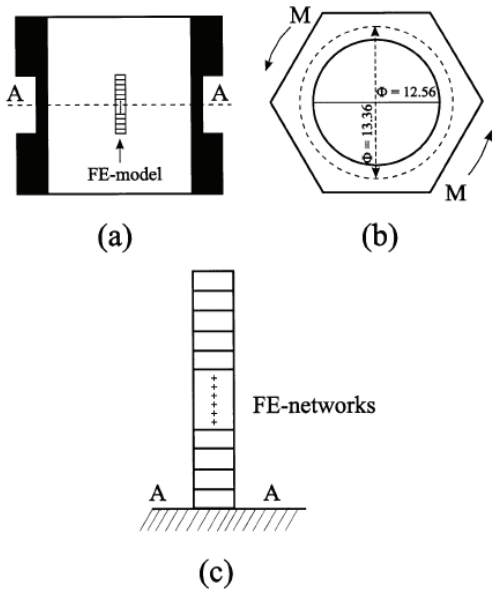

Figure 1: Representation of a torsional specimen for finite element modeling

The modeling was started at time t=0. After the first step of deformation, there was some strain hardening. The temperature rise was calculated at every node to account for the thermal softening.

Input data pertinent to a typical heat heatable (AISI 4340) were used for the modeling [5], A typical F-E analysis is shown in Fig 2 which also shows, for comparison, experimental date obtained for this steel.

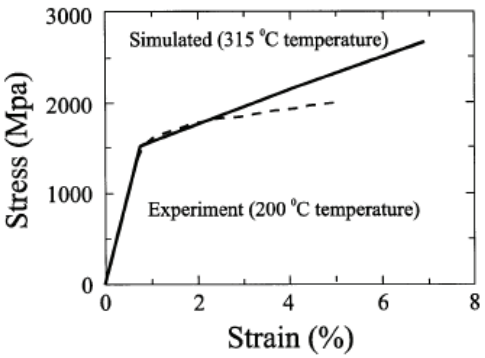

Figure 2: Simulated (by F-E) and measured properties for 4340 steel tested at high strain rates

The formation of ASB at high stain rate was simulated by F-E method and shown in fig. 3. it can be observed that the localized shear deformation increases resulting in increased width of the ASB as the onset of fracture approaches.

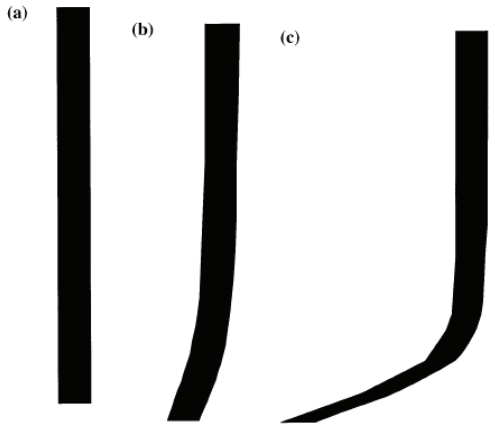

Figure 3: Evolution of the ASB from the beginning (a) to fracture (c)

Experimental Techniques

An experimental study to verify the occurrence and width of ASB in steels and other materials was conducted. Two Split Hopkinson Bar systems were used. One is a direct impact bar shown in fig.4, while fig 5 shows a torsional bar and fig 6 shows the hexagonal specimen used for torsional testing. These systems were described earlier in detail in [6,7].

The steels tested included 4340 steel and other rail steels with a carbon content ranging from 0.73% to 0.79% and various alloying elements (Mo, V, G, Al). Some tests were performed using direct impact while the tests on 4340 steel used the torsional bar.

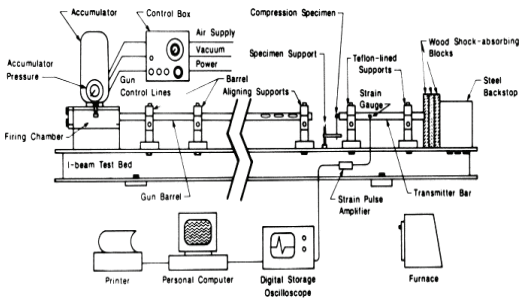

Figure 4: Direct impact split Hopkinson Bar

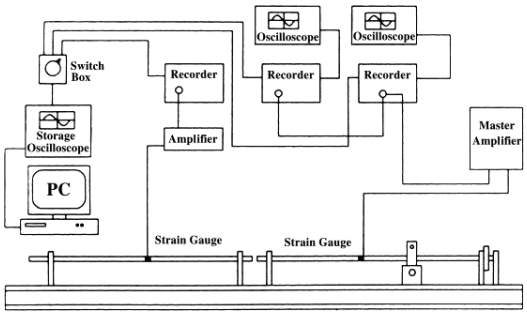

Figure 5: Torsional Split Hopkinson Bar

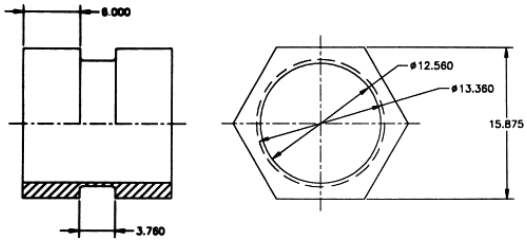

Figure 6: Hexagonal specimen used in torsional bar

Experimental Results

Distinct occurrence of ASBs was observed in both testing approaches. Fig 7 shows such an ASB which also contains a microcrack within the ASB. Fig 8 a and b show occurrence of ASB in 4340 steel with (a) corresponding to a heat heated specimen and in fig. 8b, multiple layers of ASB are observed.
Fig 9 shows initiation of cracks within the ASB of 4343 which is treated to high strength.

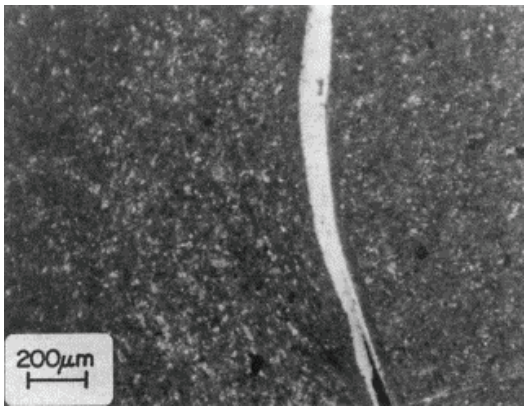

Figure 7: ASB containing a crack

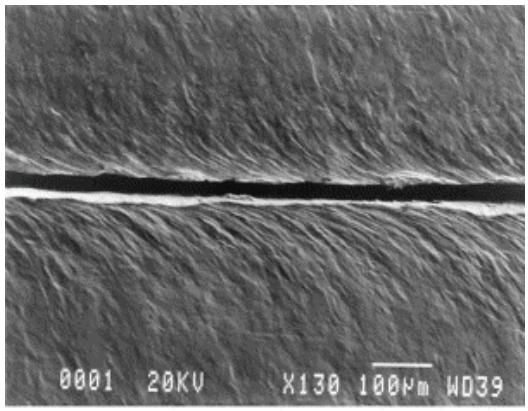

(a)

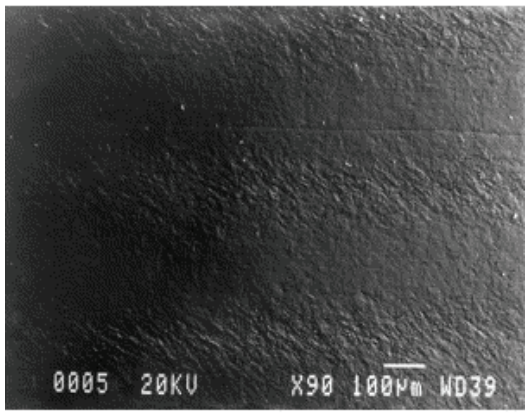

(b)

Figure 8: Single and multiple ASB during torsional test

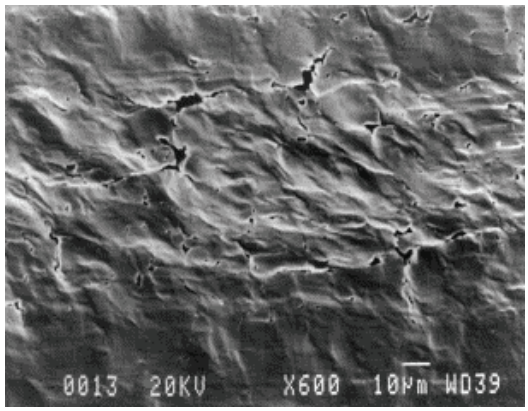

Figure 9: SEM of crack within an ASB

3. Conclusions

A finite element study investigated the process of evolution and extension of ASB in metallic materials leading to crack initiation within the ASB. It was found that the ASB can initiate at

localized material defects and extend in width till cracking is initiated. Experimental investigation of the occurrence of ASB in steels validates the model and shows that ASB are a primary source of crack initiation at high stain rates.

References

[1] Lemaire, J.C, Beckofer, W. A (1972), Mettal Trans **3**, pp. 477
[2] El-Magd, E. (1994), J. Physique C **8**, pp. 149
[3] Swanson Analysis System, Inc, ANSYS 5.3
[4] Feng, H and Bassin, M.N (1999) Materials Sci. Eng, **A266**, pp. 255
[5] ASM Metals Handbook (1978), 9th Edition, **Vol 1**, pp. 145
[6] Cepus E., Liu C.D. and Bassim M.N. (1994) Journal de Physique IV. **4**, pp. 533
[7] Panic N, M.sc Thesis (1997) University of Manitoba, Canada.

A MICROMECHANICS-BASED DAMAGE MODEL FOR COMPOSITE LAMINATES

P.P. Camanho
DEMEGI, Faculdade de Engenharia, Universidade do Porto, Rua Dr. Roberto Frias, 4200-465 Porto
Portugal

J.A. Mayugo, P Maimí
AMADE, University of Girona, Campus Montilivi, 17071Girona, Spain

Abstract

A new damage model based on a micromechanical analysis of cracked laminates subjected to multiaxial loads is proposed. The model predicts the onset and accumulation of transverse matrix cracks in laminates uniformly stressed, the effect of matrix cracks on the stiffness of the laminate, as well as the ultimate failure of the laminate. The model also accounts for the effect of the ply thickness on the ply strength. Predictions relating the elastic properties of different laminates under multiaxial loads are presented.

Keywords: Micromechanics, Fracture Mechanics, Damage Mechanics

1. Introduction

The aerospace industry is committed to improve the performance of aircraft whilst reducing emissions and weight. Such a goal can be achieved by the use of composite materials, which have excellent properties for aerospace applications, such as low density, and fatigue and corrosion resistance.

The design procedure used for advanced composite structures relies on a 'building-block' approach, where a large number of experimental tests are performed throughout the product development process. The use of improved analytical or numerical models in the prediction of the mechanical behavior of composite structures can significantly reduce the cost of such structures. Such models should predict the onset of material degradation, usually in the form of transverse matrix cracks, the effect of the non-critical damage mechanisms on the stiffness of the laminate, and ultimate structural failure.

Strength-based failure criteria are commonly used to predict failure in composite materials [1]-[4]. Failure criteria predict the onset of the several damage mechanisms occurring in composites and, depending on the laminate, geometry and loading conditions, may also predict structural collapse.

Multidirectional composite laminates accumulate damage before structural collapse. Under this circumstance, failure criteria are not sufficient to predict ultimate failure. Final failure occurs by a process of damage accumulation and the ultimate failure load is higher than that predicted by any strength-based failure criteria. Furthermore, stress-based failure criteria cannot represent size effects that occur in quasi-brittle materials [5].

Methods based on Continuum Damage Mechanics have been proposed to predict the material response, from the onset of damage up to final structural collapse [6]-[8]. Although the existing models can

accurately predict the evolution of damage, some of the existing models rely on empirical parameters, such as critical values of thermodynamic forces that need to be measured at laminate level.

Alternative methods based on the combination of elastic analysis of cracked plies and finite Fracture Mechanics provide the basis for an accurate representation of the response of composite materials [9], [10]. Typically, micromechanical models represent the initiation and evolution of transverse matrix cracks under either in-plane shear or transverse tension, and generalizations for the more usual case of multiaxial loading are required.

The objective of this work is to define a new damage model based on micromechanical models of transverse matrix cracks. The onset and evolution of transverse matrix cracks under multiaxial loading is predicted using a micromechanical model. Based on the proposed micromechanical model a new constitutive model is derived. The model proposed is able to predict the onset and propagation of matrix transverse cracks under multiaxial loading as well as final failure of laminates uniformly stressed.

2. Micromechanical Model

The continuum damage model proposed is based on two major components: stress based failure criterion and micromechanical models of transverse matrix cracks in multidirectional laminates. The failure criterion defines the onset of transverse matrix cracking, i.e. the activation of the damage variables. Micromechanical models of transverse matrix cracks are required to define the evolution of the damage variables.

Using the assumption of generalized plane strain, Tan and Nuismer [9], [10] developed a model able to relate the density of transverse matrix cracks in a central 90º ply to the homogenized elastic properties of that ply. The model developed by Tan and Nuismer was used for the prediction of the evolution of transverse matrix cracks under either in-plane shear or transverse tensile stresses.

The laminates under investigation are symmetric and balanced with a $(\pm\theta/90_n)_s$ layup containing a periodic distribution of transverse matrix cracks, as shown in Figure 1. The micromechanics analysis of a balanced symmetrical laminate requires the division of the laminate in two sub-laminates: the 90º layers in the middle layer (sublaminate 1), and the outer plies (sublaminate 2).

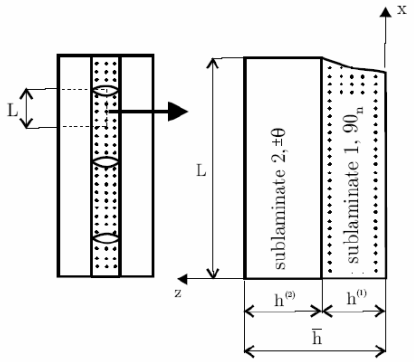

Figure 1: *Representative volume element.*

Stiffness tensor of cracked sublaminate

Considering Figure 1, the stiffness tensor of a balanced and symmetric laminate, relating the through-the-thickness averaged stress and strain tensors, is established as a function of the density of transverse matrix cracks (L) in the sublaminate 1:

$$\bar{\mathbf{A}}(L) = \begin{bmatrix} \bar{A}(L)_{11} & \bar{A}(L)_{12} & 0 \\ \bar{A}(L)_{21} & \bar{A}(L)_{22} & 0 \\ 0 & 0 & \bar{A}(L)_{66} \end{bmatrix} \qquad (1)$$

The components of the laminate stiffness tensor are obtained according to the micromechanical model developed by Tan and Nuismer [10]. Assuming that the degradation due to the transverse matrix cracks only occur in sublaminate 1, the damaged stiffness tensor of laminate 1 can be obtained using lamination theory as:

$$\bar{A}_{ij}^{(1)}(L) = \frac{1}{h^{(1)}}\left(\bar{h}\bar{A}_{ij}(L) - h^{(2)}Q_{ij}^{(2)}\right) \qquad (2)$$

Having defined damaged stiffness tensor of laminate 1 it is possible to calculate the transversal modulus, the Poisson ratio, and

the shear modulus of sublaminate 1 as a function of the density of transverse matrix cracks.

$$\bar{E}_2^{(1)}(L) = \bar{E}_x^{(1)}(L) = \bar{A}_{11}^{(1)}(L) - \frac{\left[\bar{A}_{12}^{(1)}(L)\right]^2}{\bar{A}_{22}^{(1)}(L)}$$

$$\bar{\upsilon}_{21}^{(1)}(L) = \bar{\upsilon}_{xy}^{(1)}(L) = \frac{\bar{A}_{12}^{(1)}(L)}{\bar{A}_{22}^{(1)}(L)} \quad (3)$$

$$\bar{G}_{12}^{(1)}(L) = \bar{G}_{xy}^{(1)}(L) = \bar{A}_{66}^{(1)}(L)$$

The plane stress compliance tensor of the damaged sublaminate 1 only contains two components that depend on the density of transverse matrix cracks. The tensor $\mathbf{H}^{(1)}$ is established as a function of the density of transverse matrix cracks, L, as:

$$\mathbf{H}^{(1)} = \begin{bmatrix} \frac{1}{E_1} & -\frac{\upsilon_{21}}{E_2} & 0 \\ -\frac{\upsilon_{12}}{E_1} & H_{22}^{(1)}(L) & 0 \\ 0 & 0 & H_{66}^{(1)}(L) \end{bmatrix} \quad (4)$$

with:

$$H_{22}^{(1)}(L) = \frac{1}{\bar{E}_2^{(1)}(L)} = \frac{\bar{A}_{22}^{(1)}(L)}{\bar{A}_{11}^{(1)}(L)\bar{A}_{22}^{(1)}(L) - \left[\bar{A}_{12}^{(1)}(L)\right]^2}$$

$$H_{66}^{(1)}(L) = \frac{1}{\bar{G}_{12}^{(1)}(L)} = \frac{1}{\bar{A}_{66}^{(1)}(L)} \quad (5)$$

The relation between the homogenized elastic properties of a cracked ply 90º in a $(\pm 25^{\circ}/90_3)_s$ laminate and $\beta = 1/(2L)$ is shown in Figure 2.

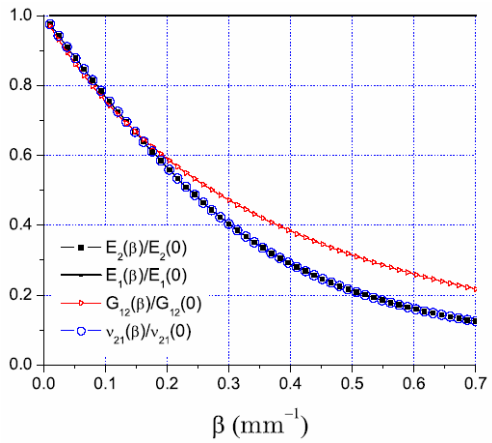

Figure 2: *Elastic properties of sublaminate 1 as a function of the density of matrix cracks.*

Onset of transverse matrix cracking

In general, the sublaminate 1 represented in Figure 1 is subjected to transverse tensile stresses and in-plane shear stresses. Under multiaxial loading it is necessary to use a failure criterion to predict the onset of matrix cracking. The criterion used is the LaRC04 [2], [3] failure criterion, established in terms of the components of the stress tensor and in-situ strengths:

$$(1-g)\frac{\sigma_{22}}{Y_T} + g\left(\frac{\sigma_{22}}{Y_T}\right)^2 + \left(\frac{\sigma_{12}}{S_L}\right)^2 - 1 \le 0 \quad (6)$$

with $g = G_{Ic}/G_{IIc}$. The parameters G_{Ic} and G_{IIc} are respectively the mode I and mode II components of the fracture toughness associated with matrix transverse cracking. The in-situ strengths, Y_T and S_L, are calculated using the closed-form equations previously developed by the authors [11].

Evolution of transverse matrix cracks

In order to predict laminate failure under general loading it is necessary to know how the density of transverse matrix cracks evolve in a ply subjected to both in-plane shear and transverse tensile stresses.

To define damage evolution laws it is necessary to relate the applied stress or strain state to the density of transverse matrix cracks. This relation is obtained from a Fracture Mechanics analysis of cracked plies combined with the definition of the damaged constitutive tensor.

It is assumed that the relation between the tensile and shear strains is constant throughout the loading history and defined by the multiaxial strain ratio κ:

$$\kappa = \frac{\gamma_{xy}}{\varepsilon_{xx}} \quad (7)$$

The strain energy stored in a laminate unit cell of length 2L, just prior to fracture, U_{2L}, can be established as a function of the strain tensor and of the crack density as:

$$U_{2L} = 2\overline{h}Lb\left[E_x(L)\varepsilon_{xx}^2 + A_{66}(L)\gamma_{xy}^2\right] \quad (8)$$

After the creation of additional matrix cracks the strain energy stored in the original unit cell of length 2L is:

$$U_L = 2\overline{h}Lb\left[E_x\left(\frac{L}{2}\right)\varepsilon_{xx}^2 + A_{66}\left(\frac{L}{2}\right)\gamma_{xy}^2\right] \quad (9)$$

The energy required to generate a new matrix crack in sublaminate 1 equals the loss of strain energy of the laminate. Therefore the difference between equation (11) and equation (10) is equal to the energy released by the sublaminate 1:

$$\Delta U = 2h^{(1)}bG_c = 2h^{(1)}bG_I + 2h^{(1)}bG_{II} \quad (10)$$

where G_c is the mixed-mode fracture toughness of sublaminate 1 under tensile (mode I) and shear (mode II) loading.

Equation (10) is established as a function of the mixed-mode fracture toughness, G_c, that needs to be defined. The criterion proposed by Hahn [12] for the prediction of transverse matrix cracking under transverse tensile and in-plane shear loads is used:

$$(1-g)\sqrt{\frac{G_I}{G_{Ic}}} + g\frac{G_I}{G_{Ic}} + \frac{G_{II}}{G_{IIc}} = 1 \quad (11)$$

Figure 3 show the relation between the crack density in a $(\pm 25^o/90_3)_s$ laminate and the applied strain for different multiaxial strain ratios.

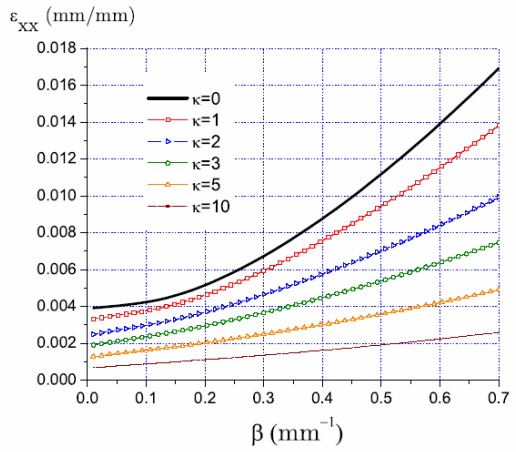

Figure 3: *Relation between applied strain and density of matrix cracks.*

The effects of multiaxial strain states on the crack density are clearly shown in Figure 3: the density of transverse matrix cracks increases with the multiaxial strain ratio for a fixed value of ε_{xx}.

3. Damage model

Constitutive model

A damage model able to represent the onset and accumulation of a periodic distribution of transverse matrix cracks should yield a compliance tensor similar to the one obtained from the micromechanical model, equation. To accomplish this, the Gibbs free energy per unit volume is defined as:

$$\Psi_G = \frac{1}{2}\sigma : \mathbf{H} : \sigma + \Delta T\alpha : \sigma + \Delta M\beta : \sigma \quad (12)$$

The constitutive model is obtained from the derivative of the Gibbs free energy with respect to the stress tensor:

$$\varepsilon = \frac{\partial \Psi_G}{\partial \sigma} = \mathbf{H} : \sigma + \Delta T\alpha + \Delta M\beta \quad (13)$$

The compliance tensor **H** is defined as:

$$\mathbf{H} = \frac{\partial^2 \Psi_G}{\partial \sigma^2} = \begin{bmatrix} \frac{1}{E_1} & -\frac{\upsilon_{21}}{E_2} & 0 \\ -\frac{\upsilon_{12}}{E_1} & \frac{1}{(1-d_2)E_2} & 0 \\ 0 & 0 & \frac{1}{(1-d_6)G_{12}} \end{bmatrix} \quad (14)$$

The compliance matrix is established in terms of the damage variables is similar to the compliance tensor derived in the micromechanical model. The damage variables d_2 and d_6 are related to the crack density β as:

$$d_{2+} = 1 - \frac{1}{E_2 H_{22}(\beta)}$$
$$d_6 = 1 - \frac{1}{G_{12} H_{66}(\beta)} \quad (15)$$

Damage activation functions

Transverse matrix cracks are predicted using two scalar functions, F_k (k=2+, 2-),

established in terms of the effective stress tensor, $\tilde{\sigma}^t$, and of the damage threshold value, r^t:

$$F_k\left[\phi_k\left(\tilde{\sigma}^t, r^t\right)\right] \leq 0 \qquad F_k := \phi_k\left(\tilde{\sigma}^t\right) - r^t \tag{16}$$

The functions used to predict transverse matrix cracking are based on the LaRC04 failure criteria previously proposed by the authors [2], [3]. The damage activation function used to predict matrix cracking under transverse tension and in-plane shear is:

$$\phi_{2+}\left(\tilde{\sigma}^t\right) = \sqrt{(1-g)\frac{\tilde{\sigma}_{22}^t}{Y_T} + g\left(\frac{\tilde{\sigma}_{22}^t}{Y_T}\right)^2 + \left(\frac{\tilde{\sigma}_{12}^t}{S_L}\right)^2} \tag{17}$$

The damage activation function used to predict matrix cracking under moderate values of transverse compression and in-plane shear is defined as:

$$\phi_{2-}\left(\tilde{\sigma}^t\right) \underset{\alpha=0^o}{=} \frac{1}{S_L}\left\langle\left|\tilde{\sigma}_{12}^t\right| + \eta^L \tilde{\sigma}_{22}^t\right\rangle \tag{18}$$

The damage activation functions used predict the onset of transverse matrix cracks lying in ply thickness direction, as shown in Figure 1. Transverse matrix cracks lying in the direction of the ply thickness occur under transverse tension and in-plane shear, or under moderate values of transverse compression and in-plane shear. For high values of transverse compression, the matrix crack does not lie along the direction of the ply thickness as shown in Figure 4.

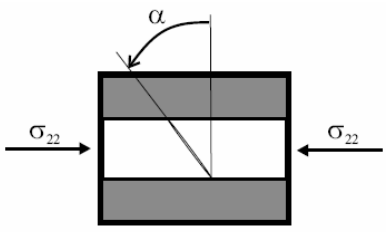

Figure 4: *Matrix crack in a created by high in-plane compressive transverse stress.*

High values of transverse compression and a fracture angle α different from zero favour the occurrence of a delamination between the plies. This damage mechanism is usually catastrophic in uniformly stressed composites. Laminate catastrophic failure is assumed to occur when matrix cracking under high values of transverse compression or fibre fracture are predicted using the LaRC04 failure criteria [2], [3].

Damage evolution functions

The density of transverse matrix cracks is a state variable. Therefore, it is necessary to define an evolution law subjected to thermodynamic restrictions.

The first condition to be satisfied is the requirement of positive dissipation. To satisfy the condition of positive dissipation, the evolution of the state variable β must be defined by a monotonic increasing function:

$$\dot{\beta} \geq 0 \tag{19}$$

The evolution of the elastic domain must satisfy the following inequalities:

$$F_k(\tilde{\sigma}^t, \beta^t) \leq 0 \tag{20}$$

$$\dot{\beta} F_k(\tilde{\sigma}^t, \beta^t) = 0 \tag{21}$$

Using Eqs. (19)-(21), the damage evolution law is established as:

$$\dot{F}_k = \frac{\partial F_k}{\partial \tilde{\sigma}} : \left(\mathbf{C}^o : \frac{\partial \varepsilon}{\partial \beta} - \frac{\partial r}{\partial \beta}\right)\dot{\beta} = 0 \tag{22}$$

Eq. (22) can be integrated using a numerical method, such as the return-mapping algorithm, in order to calculate the density of transverse matrix cracks β.

4. Examples

The damage model developed can be used in combination with classical lamination theory using stand-alone codes. Alternatively, the damage model can be implemented in numerical models, such as the Finite Element Method.

The damage model proposed is used in the prediction of the response of glass-epoxy laminates. A ply thickness of 0.144mm and temperature between stress free and working temperatures of -100ºC are used. The coefficients of thermal expansion in the longitudinal and transverse directions are $\alpha_{11}=7.43\text{x}10^{-6}$ /ºC and $\alpha_{22}=22.4\text{x}10^{-6}$ /ºC respectively. The remaining material properties used are shown in Tables 1 and 2.

E_1 (GPa)	E_2 (GPa)	G_{12} (GPa)	G_{23} (GPa)	υ_{12}	υ_{23}
44.7	12.8	5.8	4.5	0.30	0.42

Table 1: Glass-epoxy elastic properties.

Y_T^{ud} (MPa)	S_L^{ud} (MPa)	G_{Ic} (N/mm^{-1})	G_{IIc} (N/mm^{-1})
40.0	73.0	0.20	0.40

Table 2: Glass-epoxy strengths and fracture toughness.

Figure 5 compares the predicted response of two laminates for different values of the multiaxial strain ratio.

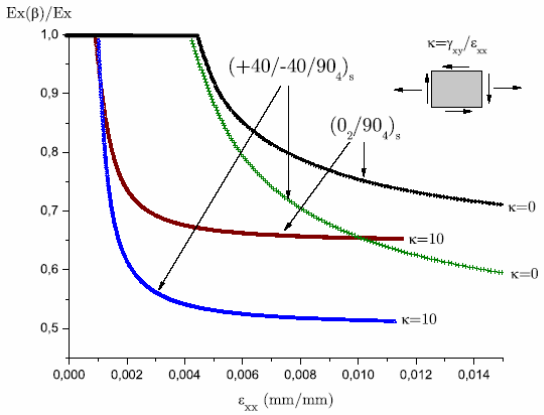

Figure 5: *Relation between laminate modulus and applied strain.*

Figure 5 shows that the rate of degradation of the elastic properties of the laminate is higher when the axial stiffness of the outer sublaminate decreases. The effect of multiaxial loading is also clear in Figure 6: as expected, the application of shear strains leads to a reduction of the extension corresponding to the onset of transverse matrix cracks and to a higher rate of degradation of the elastic properties of the laminate.

5. Conclusions

A new, micromechanics-based, continuum damage model able to simulate the onset and propagation of transverse matrix cracks and final laminate failure is proposed. The model is applicable in laminates, under multiaxial loading and uniform stresses or small stress gradients.

The model uses ply properties and does not require any tests performed at laminate level to identify damage onset and evolution functions. The onset of damage is predicted using failure criteria and damage evolution laws are established from the micromechanical analysis of cracked plies.

The model can be effectively used in Finite Element analysis because the resulting constitutive model does not result in strain-softening. The onset and accumulation of transverse matrix cracks are represented as a distributed damage mechanism; the onset of localization, triggered by either fibre fracture or matrix cracking with $\alpha \neq 0º$ results in structural collapse.

The predictions show that the rate of degradation of the laminate elastic properties increases when decreasing the stiffness of the outer sublaminate.

Acknowledgements

The financial support of the Portuguese Foundation for Science and Technology (FCT) under the project PDCTE-EME-50354-2003 is acknowledged by the first author.

References

[1] Hinton, M. J., Kaddour, A. S., Soden, P. D., (2002), *Composites Science and Technology*, **62**, pp. 1725-1797.

[2] Dávila, C. G, Camanho, P. P., (2003), *NASA-TM-2003-212663*, National Aeronautics and Space Administration.

[3] Pinho, S. T.; Dávila, C. G.; Camanho, P. P., Iannucci, L., Robinson, P., (2005), *NASA-TM-2005-213530*, National Aeronautics and Space Administration.

[4] Liu, K. S, Tsai, S. W., (1998), *Composites Science and Technology*, **58**, pp. 1023-1032.

[5] Bazant, Z. P., (2000), *International Journal of Solids and Structures*, **37**, pp. 69-80.

[6] Williams, K. V., Vaziri, R., Poursartip, A., (2003) *International Journal of Solids and Structures*, **40**, pp. 2267-2300.

[7] Allen, D. H., Harris, C. E., Groves, S. E., (1987), *International Journal of Solids and Structures*, **23**, pp. 1301-1318.

[8] Allen, D. H., Harris, C. E., Groves, S. E., (1987), *International Journal of Solids and Structures*, **23**, pp. 1319-1338.

[9] Nuismer, R. J., Tan, S. C., (1988), *Journal of Composite Materials*, **22**, pp. 306-321.

[10] Tan, S. C., Nuismer, R. J., (1989), *Journal of Composite Materials*, **23**, pp. 1029-1047.

[11] Camanho, P. P., Dávila, C. G., Pinho, S. T., Iannucci, L., Robinson, P., (2006) Composites-Part A, **37**, pp. 164-176.

[12] Hahn, H. T., (1983), *Composites Technology Review*, **5**, pp. 26-29.

DIGIMAT: A NUMERICAL TOOL TO MODEL 3D HETEROGENOUS MATERIALS

Hugues Digonnet
Faculdade de Engenharia da Universidade do Porto (FEUP)
Rua Dr. Roberto Frias, s/n 4200-465 Porto PORTUGAL

Thierry Coupez
Centre de Mise en Forme des Matériaux (CEMEF)
1, rue Claude Daunesse BP207 06904 Sophia Antipolis Cedex FRANCE

Roland Logé
Centre de Mise en Forme des Matériaux (CEMEF)
1, rue Claude Daunesse BP207 06904 Sophia Antipolis Cedex FRANCE

José César de Sá
Faculdade de Engenharia da Universidade do Porto (FEUP)
Rua Dr. Roberto Frias, s/n 4200-465 Porto PORTUGAL

Abstract

This paper presents the first developments performed during the DIGIMAT project. This European United-States collaboration project aims to help understanding the recrystallisation of metal alloys after deformation. In this project, experimental and numerical simulations are performed at several scales. At the end of the project, we must be able to simulate the microstructure evolution during the deforming phase but also during the recrystallisation one. At the moment we are interested in simulating directly the evolution of a microstructure composed by several hundreds of grains (up until one thousand). Thus, we present in this paper some strategies to reduce the CPU time needed to perform such a simulation. Two strategies are used: the first one concerns adapted anisotropic meshing, which reduces the size of the computational mesh (when compared to isotropic remeshing); the other one is parallel computing (including parallel remeshing) that reduces the CPU time by using several processors at the same time. Results shown concern the metric calculation used to adapt the mesh around grains' interfaces. Furthermore, some parallel performances are presented using a "simple" prototype of the application, tested on a thousand grains microstructure using twenty processors.

Keywords: microstructure, level set, finite element, large deformation, remeshing, parallel computation.

1. Introduction

This work is a part of the DIGIMAT project. The objective of this project is to better understand metallic alloys recrystallisation after large deformation. In fact, the engineering properties of the metallic alloys can be optimized through thermal/mechanical processes.

Recrystallisation phenomena will occur inevitably during processing and may have a major impact on the final in-use properties of the material.
The DIGIMAT project started in December 2005, and its aim is to provide numerical tools that are able to simulate such phenomena.
In this project we use the Digital Material Framework [1-3] to represent the microstructure of an alloy with several hundreds of grains. We also use parallel computing that, with current CPU, allows us to simulate in a reasonable time, the evolution of this microstructure during and after large deformation, for a representative volume element (RVE). Two main steps are considered:
• the first one determines the deformation of the structure and the evolution of the thermal and internal energy for each grain. For that, we need a suitable mesh that allows us to compute the microstructure evolution as well as the energy stored in each grain during the process;
• the second one is a consequence of the first one; the energy stored leads to recrystallisation where grain size changes, some grains disappear and other new grains appear. In this case, we need to follow the microstructure topology changes.
The first objective is to develop numerical tools that allow us, from a given microstructure, to build a suitable representative mesh. The following step is to connect these tools in an overall program that compute large deformations using both a Lagrangian formulation (with remeshing), but also an interface-tracking Eulerian formulation during the recrystallisation step.

2. Grain representation

We need to follow the deformation and the re-crystallization of a large amount of heterogeneous grains. By large amount of grains, we mean several hundreds of grains. Representing such a number of grains is not easy, and there are two main possibilities:
• The first one (front tracking) is to mesh independently each grain. But then we need to deal with contact detection of a large amount of deformable bodies, with is not feasible in our case. It may also be impossible to introduce inter-grains behaviour laws.
• the second one (front capturing), uses only one mesh for all the material, representing each grain in this mesh through a descriptor field that allows us to know in which grain we are, for each point.
If we consider the second solution, the choice for the descriptor field is an open discussion. As we need a descriptor per grain, we will look carefully to the memory usage need to store all the fields. Here also, we have many choices, such as:
• the VOF (volume of fluid) method, where the descriptor field is a scalar representing the percentage of filling of each grain filled for each element of the mesh;
• the Level-Set approach [4], where we have a scalar nodal field that represents the distance between the node and the boundary of each grain.

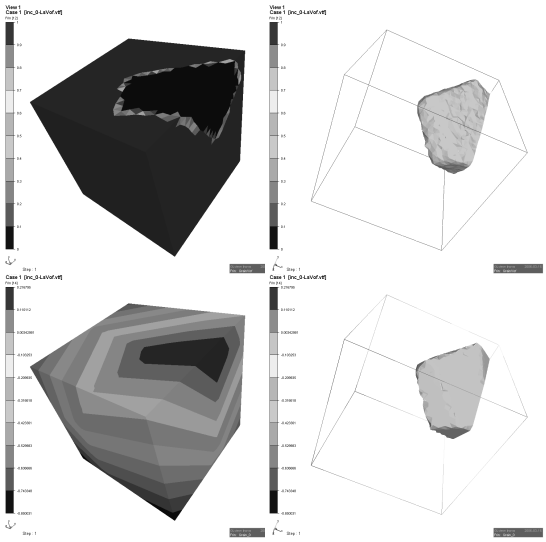

Figure 1: *two ways to represent a grain domain into a mesh: up, the VOF method, down, the Level-Set approach.*

The advantage of the VOF technique is its stability when combined with a Discontinuous Galerkin formulation in an Eulerian strategy, and is used for most advection problems (such as re-crystallisation). On the other hand, its low level of interpolation makes the grain representation less accurate than with a Level-Set function. The inconvenient of the Level-Set approach is that it can be unstable (strategies exist to stabilise it), but give a better precision on the same mesh. Finally, if we look at the memory requirements for both cases the Level-Set method is less expensive, as the number of

elements is larger than the number of nodes (two times more elements than nodes in 2D and nearly 6 times in 3D). This last point justifies our use of a level-set to represent the grains.

3. MTC: an anisotropic mesher

If we want 1000 grains in a 1mm-sided cube, we need 10 grains in each direction, which implies a mesh size of 0.01mm, if we suppose that 10 elements define the grain. This represents, at least, a 1 million-node mesh. If we want to be more accurate in the definition of the grains, we need several layers of elements near their boundary. As we deal with very large meshes, we need to optimise the sizes, and consider anisotropic meshing. Anisotropy allows us to refine differently in each direction (in particular, perpendicular to the grains interfaces). In this way, we increase the number of elements only where it is needed.

To illustrate this point, we take an initial mesh of a 1mm-sided cube with an homogenous mesh size of 0.05 mm (8000 nodes). We decrease the mesh size by a factor two in the band [0.4;0.6] mm in the x-direction. We compare three cases: homogeneous, isotropic and anisotropic refinement. In the first case, the mesh size is divided by two (to 0.025 mm) and the mesh grows to 64000 nodes (eight times the number of nodes on the initial mesh). In the second case, the mesh size stays at 0.05 mm and only in the central band this mesh size is divided by two to 0.025. In that case, the number of nodes grows to 19200 nodes (6400 nodes + 12800 nodes) only, but is still 2.5 times the initial mesh. In the last case, there is a different mesh size in each direction so the mesh size stays at 0.05 mm in the y and z directions, and is divided by two in the x direction and inside the central band. The number of nodes goes to 9600 nodes that is 1.2 times the initial mesh, but only half size of the isotropic adapted mesh.

Mesh	Structured	Unstructured
Initial	8000	15169
Uniform	64000	111689
Isotropic	19200	33107
Anisotropic	9600	18457

Table 1: *Number of nodes for the adapted mesh for 3 different cases: homogeneous, isotropic and anisotropic refinement (for structured and unstructured meshes).*

In this simple case, we see that when we refine around a grain interface by a factor of two, we multiply by eight the size of the mesh using a uniform refinement, but only by 1.2 using an anisotropic technique.

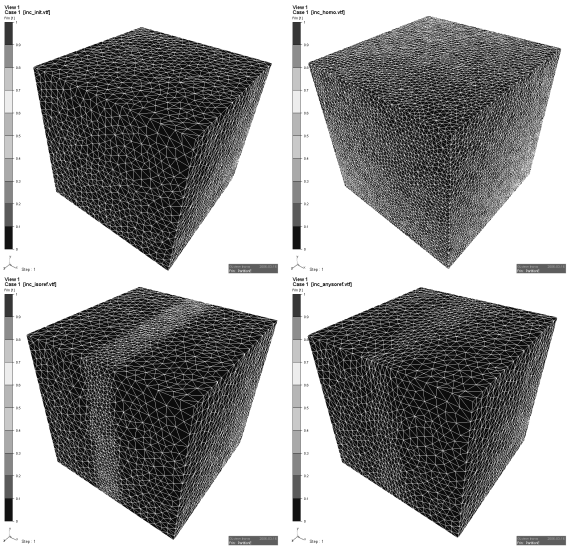

Figure 2: *initial and unstructured adapted meshes obtained after homogeneous, isotropic and anisotropic refinement in a centred layer (with a mesh size along x divided by two).*

To represent our digital material and still be able to simulate the deformation, we are going to use an anisotropic mesh. Each grain is supposed to be homogeneous, and we provide an isotropic metric field inside a grain, and an anisotropic one at the grain boundary, where heterogeneities occur.

Definition: A metric is a symmetric positive tensor that represents a local base that modifies the way on how to compute a distance, such that

$$< x, x >_M = {}^t x M x \qquad (1)$$

If M is the identity tensor, we are in the general Euclidian space. Let us consider the following given metric (in 2D).

$$M = \begin{pmatrix} 4 & 0 \\ 0 & 1 \end{pmatrix} \qquad (2)$$

The length of the vector (1 0) in this metric is 2, but the size of the vector (0 1) is only 1. With such a metric field, we can deform the space to make it denser in some directions. The last decomposition of the metric is its rotation to modify the space in other directions than the canonical ones.

$$M = RD^tR \tag{3}$$

For meshing a domain using these metrics, we use the MTC mesher-remesher developed by Coupez at the Cemef [5-7]. MTC is a topological mesher that improves a mesh topology by regarding the quality of the elements. The quality of an element is defined through a shape factor that gives to equilateral triangles the highest quality, and the worst to a triangle which degenerate into a segment. This quality is normalised to an interval [0;1], and the shape factor is given by

$$c(e) = c_0 \frac{|e|}{l(e)^d} \tag{4}$$

where c_0 is a normalised coefficient, $|e|$ the volume of the element, $l(e)$ the average length of the element edges and d the space dimension. This shape factor is then modified to take into account the mesh size or the metric we want to use: the volume and the length are defined using equation (Eq 1.)
The MTC mesher improves the topology of the elements by improving the quality (shape factor) of the elements that define this topology.

4. Link between metrics and grains

We have now to define the metric field that gives the reduced mesh size at the grain boundaries. As presented in the previous section, the metric is a tensor with eigenvalues that are linked with the mesh size, and with eigenvectors that define the direction in which this mesh size is applied.
Let us consider a simple case with only two grains (thus, one interface). We need a metric field that gives several element layers around this interface. The direction in which the mesh size must be reduced is clearly perpendicular to the iso-surface (Level-Set) that represents an ensemble of equidistant points to the interface (see Fig 3.).

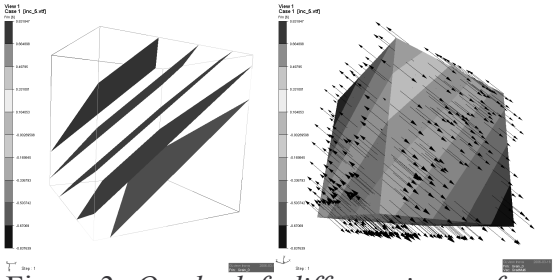

Figure 3: *On the left different iso-surfaces of the Level-Set field, on the right the gradient of the Level-Set, which is perpendicular to each iso-surface.*

The direction of mesh refinement being defined, we need to specify the mesh size in that direction, as well as the zone where the mesh size will be changed. For that, we introduce a characteristic length l_0 which will be used to characterize when we are positioned inside a grain or near to the grains interface.

$$\begin{cases} |d(x)| < l_0 & \text{near interface} \\ |d(x)| > l_0 & \text{far from the interface} \end{cases} \tag{5}$$

If we are positioned far from the interface, the mesh size will stay at the default value, and near the interface, it will be reduced perpendicularly to this interface. Here, we could also take advantage of the Level-Set field that is homogenous to a distance. We can therefore make the mesh size h as a function of the Level-Set value.

$$h = f(ls(x)) \tag{6}$$

For example we will use the following function defined as:

$$\begin{cases} |ls(x)| > l_0 \quad \Rightarrow \quad h = h_d \\ |ls(x)| < l_0 \quad \Rightarrow \\ h = \dfrac{h_d(m-1)}{ml_0}|ls(x)| + \dfrac{h_d}{m} \end{cases} \tag{7}$$

If x is on the interface the mesh size is minimal and is equal to the default mesh size divided by the parameter m. This mesh size increases with the "distance" (Level-Set) to the default value h_d at the distance l_0.

The next figure (Fig 4) represents different meshes obtained using the same Level-Set, but different values of l_0 and m.

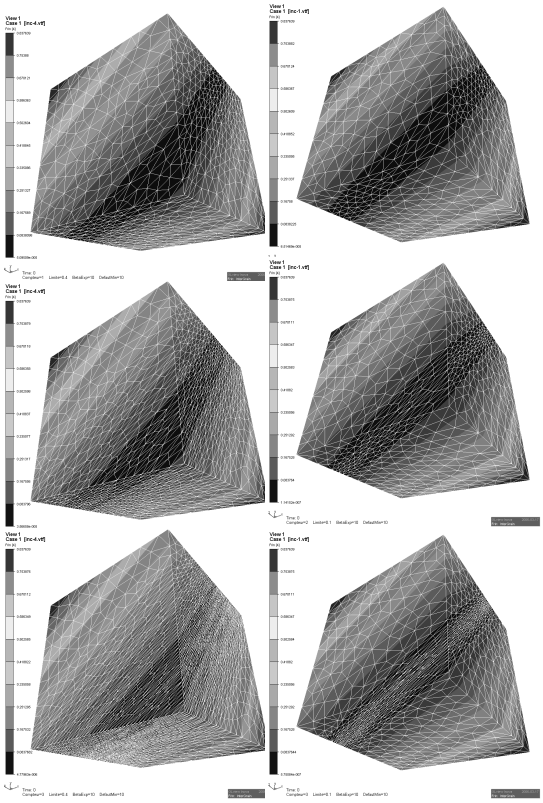

Figure 4: *adapted meshes of the unit cube near the Level-Set Zero. On the left the limit region l_0 is set to 0.4 and to 0.1 on the right. From up to down the adapted mesh size is 4, 8 and 16 times lower than the default value of 0.1.*

In the case study several grains and interfaces exist. The idea is then to repeat what we have done for each grain, giving us a family of normals and distances. As we are only interested on those that are close to the interface (the others don't modify the mesh size), we can reduce the number of couples of normal-distance to the only ones for which the distance is lower than the defined criteria l_0. At this stage, if we only have one normal, we are in the previous case. If not, there are two possible situations:

• all the normals are collinear, and we keep only one that represents the direction of refinement;

• the normals are not collinear, and we are positioned at an intersection of different grains; then we need to refine the mesh size in several directions.

In the second case, we construct a vector base induced by theses normals, and we refine across this vectors using the different mesh sizes given by the value of the Level-Set associated to the vector.
At the end, we obtain from 0 to d normals: with 0 normal we have isotropic mesh with the default mesh size; with d normals we have isotropic refinement.

Given these normals, we reduce the mesh size only in the direction of the normals, and we keep the default mesh size in the other directions. The next figure (Fig 5) illustrates the metrics and the meshes built when there is more than two grains.

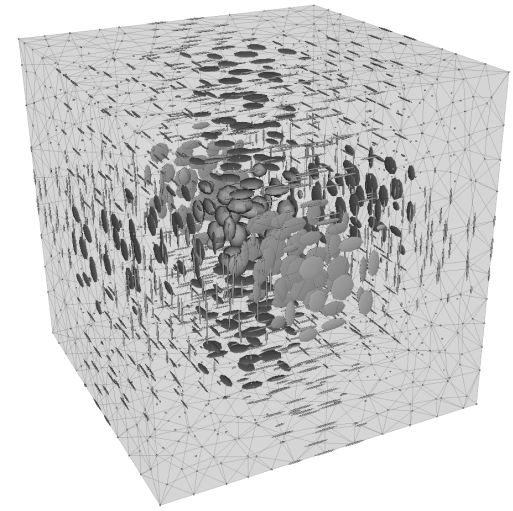

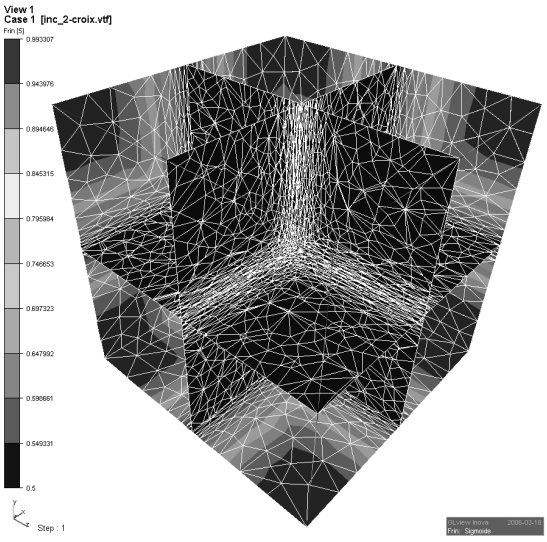

Figure 5: *Test case with 8 grains constituted by eight small cubes. Here we have all the cases from zero to three directions where the mesh size is reduced.*

On the figure (Fig 5.), the top image gives a graphic representation of the metrics tensor on the mesh: the eigenvectors of the metric tensor are represented by ellipsoids. A small sphere represents an isotropic default mesh size (0 normal), a big sphere an isotropic imposed mesh size (3 normals), and the ellipsoids a mesh size imposed in 1 or 2 directions.

We need now to use a random generation of grains. Actually, in the previous case, the directions of refinement where only the canonical ones, thus the metric matrix remained diagonal. The next figure (Fig 6) presents the adapted mesh obtained for eight grains randomly build.

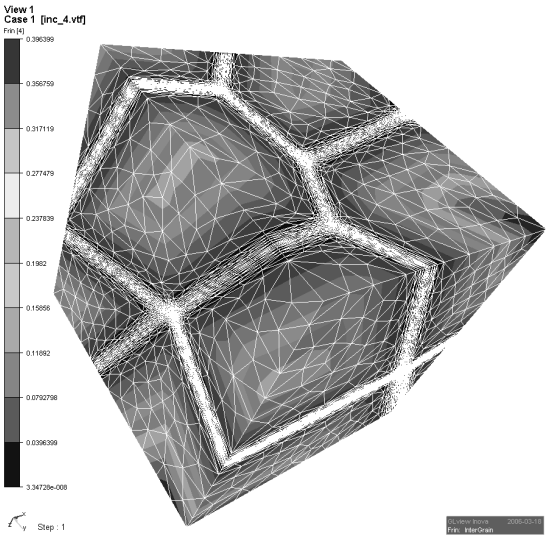

Figure 6: *Adapted mesh around 8 randomly generated grains.*

5. Large deformations

The work described in the previous section allows us to have a good representation of the microstructure through an adapted anisotropic mesh. A finite element computation is then performed to simulate the deformation of this RVE and to calculate the energy stored in the grains during this process. During this step, large deformations (and, in the future, also the use of crystalline constitutive laws) may locally introduce strong mesh deformations and so anisotropic remeshing procedures need to be used.

We present in the next figure (Fig 7.) the deformation, of the REV with 6 grains using incompressible Stokes equation with heterogeneous consistence in each grain.

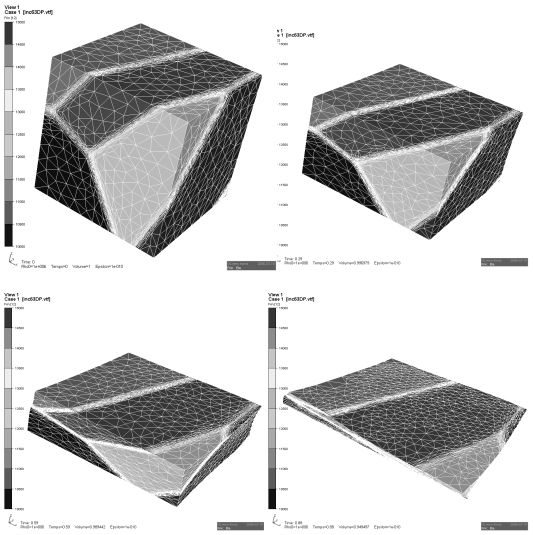

Figure 7: *Simulation of the deformation of a six grains representative volume with anisotropic remeshing.*

This case is similar to classical metal forming process simulation, but we need here enough elements in the mesh to be able to simulate correctly a large number of heterogeneous grains (several hundreds of grains). This constraint pushes us to parallel computation. If parallel calculation solves CPU time and memory problems, dealing with fully parallel remeshing is not so straight forward [6].

The deformation of the grains leads to energy storage in each grain. This energy as well as thermal treatment will be the engine of the recrystallisation (second step still in development).

4. Recrystallisation

This section is not yet developed but a large part of the assumptions made previously depend on it. We will here just explain how we intend to proceed.

The level-set type framework [8] is developed to describe the kinetics of grain boundary motion at the crystal or polycrystal levels, due to thermal recovery and grain growth processes. A novel aspect of this work is that the level-set method will be coupled with the local energetic quantities calculated in the modelling of the RVE deformation. Consequently the level set approach is implemented within the same finite element model as for the RVE deformation stage. When modelling

recovery processes, the goal will be to predict the evolution of the sub-grain structure, which may lead to the formation of the recrystallisation nuclei.

The evolution of a Level-Set drawn mostly by convection equations has already be used in other contexts: Navier-Stokes equations coupled to moving interface determination for example [9].

5. Parallel computation

In this section, we present computations performed on FEUP's cluster of PC named NxPy. This cluster is constituted by 32 bi-processors Intel Xeon 64bits at 3.0 Ghz linked by a Dual Gigabit Ethernet network and with 2GB of memory per CPU.

The first test is the compression of a cube with 50 grains, on a mesh containing around 100 000 nodes. We have chosen this test case to be able to run it from 1 processor to 8 processors to evaluate the parallel performance of the application.

The next figure (Fig 8.) shows the partition of the domain into several sub-domains, each is affected to a processor. In this way, the work done by each processor is proportional to the size of the sub-domain, the communications being proportional to the interface between sub domains.

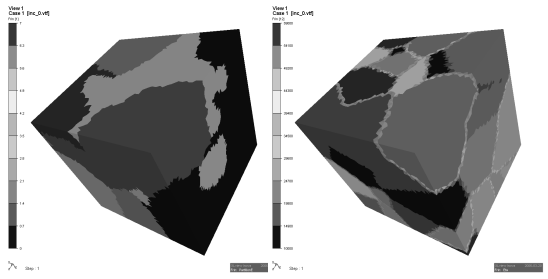

Figure 8: *on the left: the partition of the 100000 nodes mesh in 8 sub-domains, on the right a view of the 50 grains.*

We remark that the parallel partition is totally independent of the grains position, so the number of processor used is only linked to the time spent to make the simulation and do not depend on the number of grains.

Time (s)	1 processor		2 processors	
Outputs	520	1	530	0.98
Assemble	1172	1	610	1.92
Resolution	8930	1	4996	1.79
Metric	1589	1	795	2.00
Remeshing	7944	1	5341	1.49
Sum	20155	1	12272	1.64
Wall-clock	20722	1	12586	1.65
Neglected	567	1	314	1.81

Time (s)	4 processors		8 processors	
Outputs	527	0.99	525	0.99
Assemble	327	3.58	185	6.34
Resolution	2098	4.26	896	9.97
Metric	405	3.92	208	7.64
Remeshing	2944	2.70	1334	5.96
Sum	6301	3.20	3421	6.06
Wall-clock	6468	3.20	3520	5.89
Neglected	167	3.40	99	5.72

Table 2: *Time spent (in seconds) and speed-up of the different parts of the code. The code has been run from 1 to 8 processors.*

The time for outputting the results is almost the same time independently of the number of processors used. This is due to de fact that the output files are written by only one processor to keep our classical sequential post-processor. When we look at the resolution of the mechanical problem, we see that the time spent is divided by the number of processors used (even a bit more: cache effect) which represents a very good parallelisation of the assembly and resolution of the linear systems involved. The calculation of the metric field is also well parallelised with a Speed-Up of 7.64 over 8 processors. In what concerns the remeshing phase the Speed-Up is around 6 over 8 processors but this could be explained by the fact that in sequential we have only one remeshing step, even though in parallel we need to use several steps of remeshing-repartitioning to obtain a good mesh, as explained in [6]. The overall speed-up is close to 6, which is a good result, taking into account the partitioning phase and the results files.

This is worth noting that the time spent in the resolution of the mechanical problem is minimal: in fact, only the incompressible Stokes equations were solved. When a real crystal law will be

used, this time will increase, leading to a ratio, between the mechanical resolution over remeshing, largely in favour of the mechanical resolution, which has been previously efficiently parallelised.

A second test has been run to illustrate what sort of simulation we intend to perform later. The number of grains chosen here is one thousand, and we use a mesh containing around 1 million nodes. But even if the time spent is important - 10 hours (some improvements related to a large number of grains can still to be done) – we remark that we are able to run such case. The only inconvenient is that the sequential post-processor used was unable to visualise the results.

6. Conclusion and Perspectives

In this paper, we have presented some numerical techniques that allowed us to simulate the evolution of a microstructure in a 3D representative volume. The anisotropic meshing strategy reduced the size of the mesh for a given inter-grain precision. Another important way to reduce the CPU time is achieved by using parallel computation: we are able to reduce the simulation time by a factor of 6 over 8 processors. The use of parallel computers like PC clusters makes also possible to run bigger test cases giving access to more memory and reasonable simulation times.
The Level-Set representation for grain boundaries can be easily coupled with boundary evolution in an eulerian context. This will be important in the future to enable the recrystalisation phase after deformation.

Parallel works will be done in this project, including Monte Carlo simulations to deeper understanding recrystallisation phenomena. Furthermore, initial microstructure states will be based on both calculations (dynamics dislocation) and experiments. Sub-grain boundary energies and motions will be obtained from calculations at the atomistic and dislocation levels, and also from experiments conducted on a hot stage within a SEM chamber. The objective will be to define criteria for locating recrystallisation nuclei in the deformed microstructure, with the right crystallographic orientation.

References

[1] Dawson, P. (2000), Computational crystal plasticity, *Int. J. Solids Structures*, **37**, pp 115-130.

[2] Dawson, P., Miller, M., Han T.S. and Bernier J. (2005), An Accelerated Methodology for the Evaluation of Critical Properties in Polyphase Alloys*, Met. Mater. Transactions A*., **36A**, pp 1627-1641.

[3] Forest, S., Cailletaud, G., Jeulin, D., Feyel, F., Galliet, I., Mounoury, V., and Quilici, S. (2002), Introduction au calcul de microstructures, *Mécanique & Industries,* **3**, pp 439-456

[4] Adalsteinsson, D. and Sethian, J.A., (1995) A fast level set method for propating interfaces, *Journal of Computational Physics*, **118**, pp. 269-277

[5] Coupez, T., (2000), Génération et Adaptation de maillage par optimisation locale, *la Revue Européenne des éléments finis*, **9(4)**, pp. 403-423.

[6] Coupez, T., Digonnet, H. and Ducloux, R. (2000), Parallel meshing and remeshing by repartitioning, *Appl. Math. Modeling,* **25**, pp 153-175.

[7] Basermann, A., Clinckemaillie, J., Coupez, T., Fingberg, J., Digonnet, H., Ducloux, R., Gratien, J.-M., Hartmann, U., Lonsdale, G., Maerten, B., Roose, D. and Walshaw C. (2000) Dynamic load balancing of finite element applications with the drama library, *Applied Mathematical Modelling*, **25(2)**, pp. 83-98.

[8] Osher, S. and Sethian J.A. (1988), Fronts propagating with curvature-dependent speed: algorithms based on Hamilton-Jacobi formulations, *J. Comp. Phys*., **79**, pp 12-49

[9] Basset, O., Digonnet, H., Coupez, T. and Guillard, H. (2005) In: Coupled Problems 2005: Multi-phase flow calculation with interface tracking coupled solution, Papadrakakis, M., Oñate, E. and Schrefler, B. (Eds) CIMNE, Barcelona.

RELATIONSHIP BETWEEN APPARENT DENSITY AND MECHANICAL BEHAVIOUR OF FDM PARTS

Yvan Petit[1,2,3], Karine Dupuis[1,3], Jean-Sébastien Mérette[1,2]

[1]École de technologie supérieure, 1100, rue Notre-Dame Ouest, Montréal (Canada) H3C 1K3

[2] Hôpital du Sacré-Cœur de Montréal, 5400, boul. Gouin Ouest, Montréal (Canada) H4J 1C5

[3] Hôpital Sainte-Justine de Montréal, 3175, Chemin de la Côte-Ste-Catherine, Montréal, H3T 1C5

Abstract

The purpose of this study is to investigate on the use of quantitative computed tomography (QCT) to estimate trabecular bone mechanical properties. The specific objective is to study how the mesostructure of parts built with a known material affects the ability to predict the mechanical behaviour with QCT.

An experiment has been proposed into which 60 compression specimens were built with a predefined mesostructure. They were tested mechanically to determine their mechanical properties, CT scanned and measured experimentally to establish relationships predicting their mechanical behaviour from the image properties. Finally, finite element analyses were performed in order to verify how a FEM with personalized mechanical properties obtained using the proposed method could predict adequately the mechanical behaviour of an object.

Results of this study suggest that QCT allows predicting the density and the mechanical properties of ABS parts but it is not sufficient without an appropriate knowledge of their mesostructure. This may represent a limitation in predicting the mechanical properties of trabecular bone from CT images.

Keywords: Fused deposition modelling, Rapid prototyping, Quantitative computed tomography, Mesostructure, Mechanical behaviour.

1. Introduction

Computed tomography (CT) is a powerful imaging tool used for several medical applications. In particular, this imaging method allows defining comprehensive 3D geometric models of bony structures. Quantitative computed tomography (QCT) is also a long-standing method for assessing the trabecular bone density of vertebral bodies [2] based on quantitative analyses of the linear attenuation coefficients (CT numbers) measured by the CT scanner. To do this, a calibration object is placed in the scan field and is used to convert the CT numbers into bone mineral density units. Correlations have also been proposed between CT number, density and mechanical properties of vertebrae [3;4;6] to build biomechanical simulation models using finite element methods. However, the relationship between the mechanical properties of bone and the apparent density estimated from CT images is not yet understood since several parameters such as the effect of the trabecular structure is still unclear. Actually, results of previous studies [5;7] suggest an unpredictable adequacy of such models with respect to experimental data.

As a result, there is still a need to better understand the effect of the bone mesostructure on the relationship between CT number, density and mechanical properties of bone.

The specific objective of this work is to study the effect of the mesostructure on the relationship between the apparent density and the mechanical behaviour of parts built with a material of known mechanical properties.

2. Material and Methods

Cylindrical ABS compression specimens were fabricated by fused deposition modelling (FDM) in order to study the effect of apparent density and mesostructure on their mechanical behaviour. FDM is a free-form fabrication process which deposit molten filaments of thermoplastic in a criss-cross pattern to build a part layer by layer. This process results in ABS parts with anisotropic properties depending of the build parameters.

Specimens Fabrication. Three build parameters were varied in this study to simulate the effect apparent density and the mesostructure in ABS parts (Figure 1): air gap, layer orientation and raster orientation. The layer thickness is another important build parameter. It has been kept constant (0,18 mm) for all specimens in this study. The air gap (figure 1a) consists of the spacing between the filaments of FDM material. Five values of air gap were used (0mm, 0,13mm, 0,54mm, 1,2mm and 1,95 mm) in order to obtain parts with apparent density between 300 mg/cm^3 and 1000 mg/cm^3. The layer orientation (figure 1b) was defined either as transverse or longitudinal. Finally, the raster orientation (figure 1c) refers to the direction of the filaments relative to the loading of the part for two consecutive layers. Three raster orientations were used: 0°&90°, 45°&-45° and 30°&-60°.

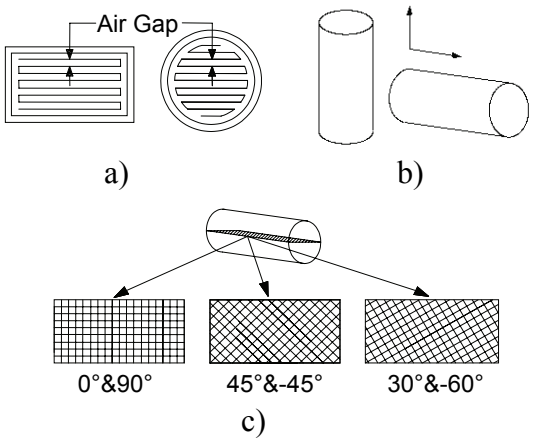

Figure 1 ***Build parameters*****: a) air gap, b) layer orientation, c) raster orientation**

A total of 60 ABS compression specimens were fabricated using a Prodigy Plus (Stratasys Inc., Eden Pairie, MN) FDM machine according to a plan of experiment varying the 3 build parameters mentioned above: 30 specimens in 0°&90° raster orientation (5 air gap values x 2 layer orientations x 3 replications), 15 specimens in 30°&-60° raster orientation (5 air gap values x 3 replications) and 15 specimens in 45°&-45° (5 air gap values x 3 replications). In this experiment, the layer orientation was varied only for specimens with a 0°&90° raster orientation. All other specimens were built longitudinally.

Specimens Apparent Density. The apparent density of specimens was calculated as the ratio between their overall measure of weight (w) and volume. Four measurements of the diameter and two measurements of the length evenly distributed along the specimens were made using a calliper. The average value of height (h_{avg}) and diameter (d_{avg}) were then used to estimate the apparent density of the objects using equation 1.

$$\rho_{app} = \frac{\pi d_{avg}^2 h_{avg}}{4 * w} \qquad \textbf{(1)}$$

Specimens Imaging and Analysis. All specimens were imaged (figure 2) using a PQ5000 (Picker International Inc., Highland Heights, OH) CT scanner. The scanner parameters were set to 120 kV, 30 mA, 140 mm field of view and 1 mm slice thickness and slice spacing. The specimens were placed into a custom made jig to stabilize it horizontally and longitudinal with respect to the moving table. A small recipient containing water was also placed in the field of view.

All images were analysed using a commercially available semi-automated segmentation and 3D reconstruction software (SliceOmatic, Tomovision Inc,

Montreal, CANADA) in order to identify regions of interest (ROI) on the compression specimens. ROI were defined as cylindrical areas avoiding the outer contour of the parts. They were then used to compute the average CT numbers of every compression specimens and to convert them into Houndsfield units (HU) using equation 2 [6], for which CT(air) = -1000 and CT(water) = 0.

$$HU = 1000 * \frac{(CT - CT_{water})}{(CT_{water} - CT_{air})} \qquad \textbf{(2)}$$

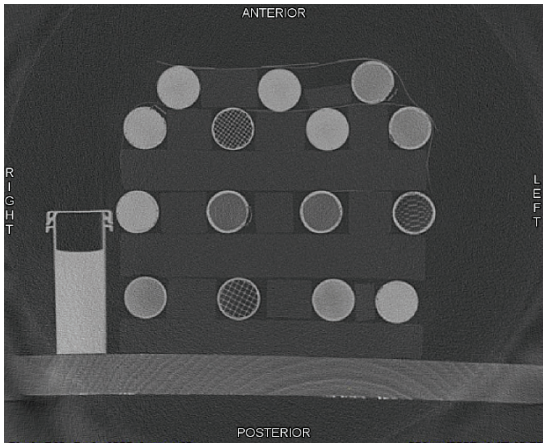

Figure 2 CT image of compression specimens

Mechanical Testing of Specimens. Uniaxial compression tests were performed on the cylinder specimens using an MTS 810 machine (MTS Corp., Eden Prairie, MN) to evaluate their elastic modulus. The tests and data analysis were performed according to the ASTM D695-96 [1] standard test method for compression properties of plastics.

Finite Element Analysis. Nine additional compression specimens were built with different density than the ones used to establish the relationships, the 0°&90° raster orientation and the 2 layer orientations (6 longitudinal, 3 transverse). A personalized FEM was built using the QCT data to predict their mechanical properties from the relationship corresponding to their build orientation. Finite element analyses were performed on the specimens (figure 3). Finally, compression tests were performed and compared with the stiffness (N/mm) predicted using the slope of the FEM force-displacement curves.

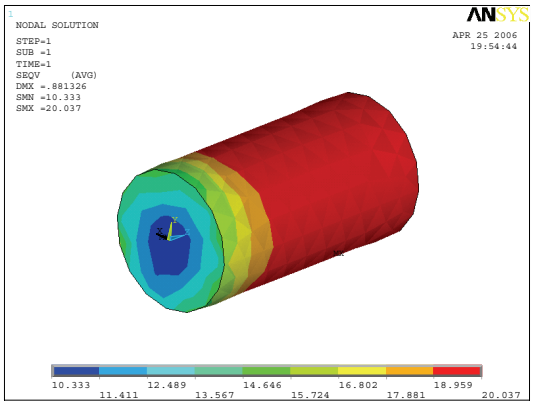

Figure 3 Typical FEM analysis of a specimen

3. Results

The results were first analysed as a mixed design of experiment (DOE) using a statistical analysis software (Statistica, StatSoft Inc., Tulsa, OK) in order to estimate the effect of build parameters on the properties of compression specimens built by FDM. Figures 4, 5 and 6 present pareto charts of the absolute effects of build parameters on the elastic modulus, the apparent density and the standardized attenuation coefficient, respectively.

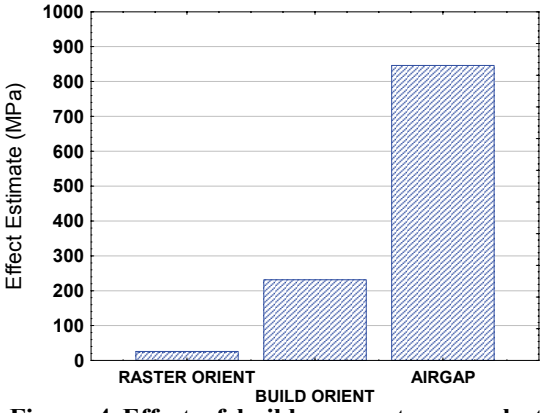

Figure 4 Effect of build parameters on elastic modulus

The air gap is clearly the build parameter affecting the most all properties. It did affect the apparent density of 0,54 g/cm^3, the image properties of 631 HU and the elastic modulus of 845 MPa for this particular experiment. Although all parameters were found to have a significant effect ($p < 0{,}005$), the layer orientation has a very small influence on all properties. Moreover, the raster orientation has a very small effect on the CT image properties and the apparent density but is affecting more importantly the elastic modulus (~200 MPa).

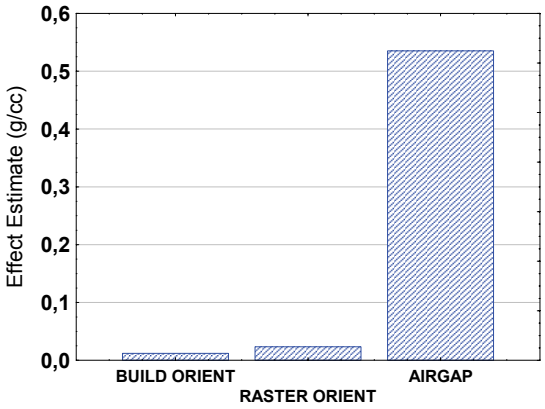

Figure 5 Effect of build parameters on apparent density

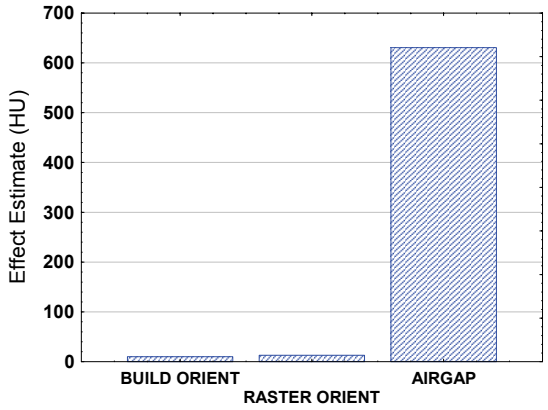

Figure 6 Effect of build parameters on standardized attenuation coefficients

The relationships between image intensity (HU), apparent density, and elastic modulus were also studied. Linear and quadratic regressions were calculated to identify the most relevant for predicting elastic moduli from CT images.

Table 1 presents the relationships obtained between the image intensities and the apparent density for: 1) 30°&-60° of raster angle; 2) 45°&-45° of raster angles; 3) 0°&90° of raster angles and longitudinal build layers; 4) 0°&90° of raster angles and transverse build layers; and 5) all confounded. Linear relationships were found between the apparent density and the image intensities. These results suggest that one relationship (#5) would be sufficient to predict the apparent density regardless of the build parameters used.

Table 1 Relationships between image intensity and apparent density

	Relationships	R^2
1	ρ=0,0008CT + 1,0578	0,9995
2	ρ=0,0008CT + 1,0564	0,9995
3	ρ=0,0008CT + 1,0479	0,9991
4	ρ=0,0009CT + 1,0634	0,9993
5	ρ=0,0008CT + 1,0567	0,995

On the other hand, the relationships between the apparent density and elastic modulus were found to be quadratic. Table 2 presents the relationships obtained for: 1) 30°&-60° of raster angle; 2) 45°&-45° of raster angles; 0°&90° of raster angles and longitudinal build layers; 4) 0°&90° raster angles and transverse build layers; and 5) all raster angles confounded and longitudinal layers; 6) 0°&90° raster angle and layer orientation confounded; and 7) all build parameters confounded. These results suggest that the predicted elastic modulus is dependent on the build parameters. Thus, one relationship could not predict adequately the elastic modulus without knowledge of the mesostructure.

Table 2 Relationships between apparent density and elastic modulus

	Relationships	R^2
1	$E=4345\rho^2 - 4079\rho + 1324$	0,9835
2	$E=4293\rho^2 - 4068\rho + 1320$	0,9897
3	$E=1960\rho^2 - 938\rho + 499$	0,9946
4	$E=1629\rho^2 - 643\rho + 233$	0,9991
5	$E=3552\rho^2 - 3042\rho + 1046$	0,967
6	$E=1367\rho^2 - 235\rho + 210$	0,908
7	$E=2645\rho^2 - 1854\rho + 662$	0,9308

Figure 7 presents the results of the FEM analysis using personalized mechanical properties from QCT. It shows the comparison between experimental stiffness and FEM estimation using: 1- the relationship for longitudinal layers (Table 1, relation 3) for the 9 specimens, 2- the relationship for transverse layers (table 1, relation 4) for all specimens and 3- the relationship corresponding to the layer orientation of each specimen.

This latter result indicates a better agreement between FEM and experimental measurements when the mesostructure of the part (layer orientation) is taken into account (r^2=0.979) than for the 2 other cases (r^2=0.839).

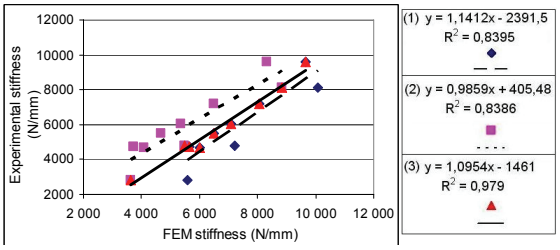

Figure 7 Relationships between measured and FEM predicted stiffness

4. Discussion and Conclusion

The specific objective of this study was to study the effect of the mesostructure on the relationship between the apparent density and the mechanical behaviour of parts built with a material of known mechanical properties. The long term goal of this is to verify if QCT could be appropriate to predict the mechanical properties of trabecular bone.

An experiment has been proposed into which compression specimens were built with a predefined mesostructure, tested mechanically, CT scanned and measured experimentally to establish relationships predicting their mechanical behaviour from images properties. Finally, finite element analyses were performed in order to verify how a FEM with personalized mechanical properties obtained using the proposed method could predict adequately the mechanical behaviour of an object.

The first results of this study suggest that CT images could predict adequately the apparent density of ABS objects regardless to their mesostructure using equation 3.

$$\rho = 0{,}0008CT + 1{,}0567 \qquad \textbf{(3)}$$

However, the relationships obtained to predict the elastic modulus from the apparent density of an object seem to be strongly dependent of the mesostructure. This finding was confirmed by the analysis of the effects of FDM build parameters. It showed that the air gap strongly affects the CT image, the apparent density as well as the elastic modulus of parts. It also suggests that the layer orientation affects the elastic modulus of parts built by FDM. This suggests that the relationship used to predict the mechanical behaviour of an object should be carefully chosen by taking into account the mesostructure of the object.

This result was also confirmed by FEM analyses showing that the agreement between the predicted behaviour and experimental measurements was better when the layer orientation was taken into account.

These findings could explain in part the disagreement found in the literature [5;7] on the efficiency of QCT to predict the mechanical properties of the trabecular bone. Actually, the trabecular bone is a mixture of a CaP type minerals, collagen, cellular marrow and fatty marrow. Moreover, the mineral content forms a complex architecture, the trabeculae, spatially arranged to resist to the external loads applied to the bone, similar to composite materials. Overall, the CT image intensity (HU) represents a weighted average of these constituents.

These observations could mean that QCT, as it is currently used, allows predicting the density and the mechanical properties of ABS parts but is not sufficient without an appropriate knowledge of their mesostructure. This may represent a limitation in predicting the mechanical properties of trabecular bone from CT images. However, more experiments are currently underway to confirm the preliminary conclusions drawn from this study. Other improvements to QCT are presently under investigation, such as: calibration objects with controlled mesostructure and close to bone properties material, multiscale image analysis, quantitative microCT, etc.

Nevertheless, QCT is a powerful clinical tool that allows extending the knowledge and understanding on the mechanical behaviour of bone as related to bone fractures. The use of such non invasive tools in clinical practice could improve the preoperative assessment, the surgical planning and the healing of complex bone fractures.

Acknowledgements
This study was funded by the Canadian Institute of Health Research (CIHR). The authors are also thankful to Catherine Jobin for the mechanical testing of specimens.

References

[1] ASTM. (1996). ASTM D695-96, Test Method for Compressive Properties of Plastics. *ASTM*.

[2] Cann, C. E., Genant, H. K. (1980). Precise measurement of vertebral mineral content using computed tomography. *J Comput Assist Tomogr, 4*(4), 493-500.

[3] Hobatho, M. C., Rho, J. Y., Ashman, R. B. (1997). Mechanical properties and predictive relationships of the lumbar spine. *Research into spinal deformities, 1*, 181-184.

[4] Kopperdahl, D. L., Morgan, E. F., Keaveny, T. M. (2002). Quantitative computed tomography estimates of the mechanical properties of human vertebral trabecular bone. *J Orthop Res, 20*(4), 801-805.

[5] Liebschner, M. A., Kopperdahl, D. L., Rosenberg, W. S., Keaveny, T. M. (2003). Finite element modeling of the human thoracolumbar spine. *Spine, 28*(6), 559-565.

[6] Rho, J. Y., Hobatho, M. C., Ashman, R. B. (1995). Relations of mechanical properties to density and CT numbers in human bone. *Med Eng Phys, 17*(5), 347-355.

[7] Silva, M. J., Keaveny, T. M., Hayes, W. C. (1998). Computed tomography-based finite element analysis predicts failure loads and fracture patterns for vertebral sections. *J Orthop Res, 16*(3), 300-308.

SHEAR FRACTURE MESOMECHANICS: NEW MODELLING STRATEGIES AND CRITERIA

Edward Stanislaw Dzidowski
Wroclaw University of Technology, Faculty of Mechanical Engineering, Faculty Division of Deformable Body Mechanics, Smoluchowskiego 25, Wroclaw, Poland

Abstract

The conventional ductile (also shear) fracture mechanism models – based on the nucleation and development of voids around inclusions and separations – have many limitations such as their inability to explain the damage and fracture mechanism for pure metals and single-phase metal alloys. A more serious limitation is their inability to generate shear fracture control criteria.

The lack of shear fracture control criteria makes it difficult to optimise mechanical material working processes and prevent any damage preceded by large local plastic strains. The problem is compounded by the lack of suitable solutions within the classical theory of continuous medium and within fracture mechanics. There are few indications that the problem can not be solved within existing damage mechanics.

Hence the paper's main goal is to present a strategy of the mesoscopic-macroscopic modelling of the damage and shear fracture mechanism. The strategy is based on the properties of a mesostructure which forms in the final isothermal stage in the evolution of dislocation structures.

Keywords: Physical mesomechanics, shear fracture, modelling, control strategies, criteria.

1. Introduction

Mesomechanics is a newly created scientific discipline [1,2]. The establishment of this discipline provided a stimulus for innovative research and has made possible effective management of the previously existing interdisciplinary researches.

The main aim of this paper is to show the benefits stemming from the application of mesomechanics to the analysis of the development of strains and fracture in processes based on shear.

The earlier methods of such analysis were based mainly on the slip line field theory and the theory of transition zones. Both theories have serious limitations.

According to the slip line field theory, the plastic sinking of the cutting tool in the sheared material first causes gradual widening and then narrowing of the plastic strain area [3]. Characteristically, this area finally assumes the shape and dimensions a line (a plane) with zero thickness. The line defines the location of slip velocity discontinuity and it is identified with the presumed trajectory of fracture. It is thought that the only way in which the shape of the fracture trajectory can be changed is by eliminating the rotation (bending) of the sheared material, which is

usually done by pressing the sheared material against the cutting tool. With this the possibilities of the method are exhausted. The fact that shear strain determined by this method approaches infinity poses an additional problem. The problem has been partially solved by the development of the theory of transitional zones [4].

The introduction of the theory of transitional zones made the values and distribution of strain in the final stage of shearing real. This means that instead of a line (a surface) with zero thickness, an area having the shape of a biconvex lens is considered.

The beginning of the formation of this area is identified with conditions corresponding to the action of an absolute stress concentrator. But it is not known when and why such a significant change in the stress concentration conditions occurs. Moreover, it is assumed that once the lens is formed, it does not change its shape but only diminishes as the displacement of the cutting tool increases.

The inconsistency between the model of the brittle fracture mechanism and that of the ductile fracture mechanism is another problem, which will be illustrated by maps of the mechanisms of: fracture (figs 1 and 2), deformation (fig. 3) and dislocation structures development (fig. 4).

2. Maps of mechanisms

Maps of fracture mechanisms

Typical views on fracture mechanisms are presented on maps of fracture mechanisms (figs 1 and 2).

As the figures show, the brittle fracture mechanisms (fig. 1a, b) and the ductile fracture ones are explained quite differently even though both require preceding plastic deformation. The brittle fracture mechanism is explained by the effects of a flat pile-up of dislocations (fig. 1a,b), whereas the ductile fracture mechanism (fig. 2a) is explained by the nucleation and development of voids around inclusions and separations. This means that two different theories of fracture are applied here: the theory of dislocations in the case of brittle fracture and a modified theory of the porous body in the case of ductile fracture [5,6].

Problem. Due to the lack of cohesion between the above theories the causes of the transition from ductility to brittleness (fig. 1d) cannot be clearly explained. Moreover, the above model of the ductile fracture mechanism does not explain the fracture of pure metals or the fracture of monophase metal alloys. Neither does this model generate any criteria for the control the trajectory of shear fracture.

Since it is not possible to control the trajectory of shear fracture, several technical problems, connected with, e.g., the precision of die shearing and similar technological processes, arise. Neither is the problem of shear fracture trajectory control solved by the theory of adiabatic shear bands (fig. 3).

Maps of deformation mechanisms

Figure 3 shows the location of the areas in which adiabatic shear bands occur depending on the kind of material, the rate of its deformation, the temperature and the magnitude of the strains (not shown on the map) – grey area on fig. 3.

According to fig. 3, adiabatic shear bands (ASB) occur during cold deformation. The presence of adiabatic shear bands is equated with thermal softening which takes place in the region of the dislocation mechanism of deformation (blackened area on fig. 3).

Adiabatic shear bands appear only after critical strain γ_{crit} and critical strain rate γ^*_{crit} are exceeded. Moreover, their appearance largely depends on temperature.

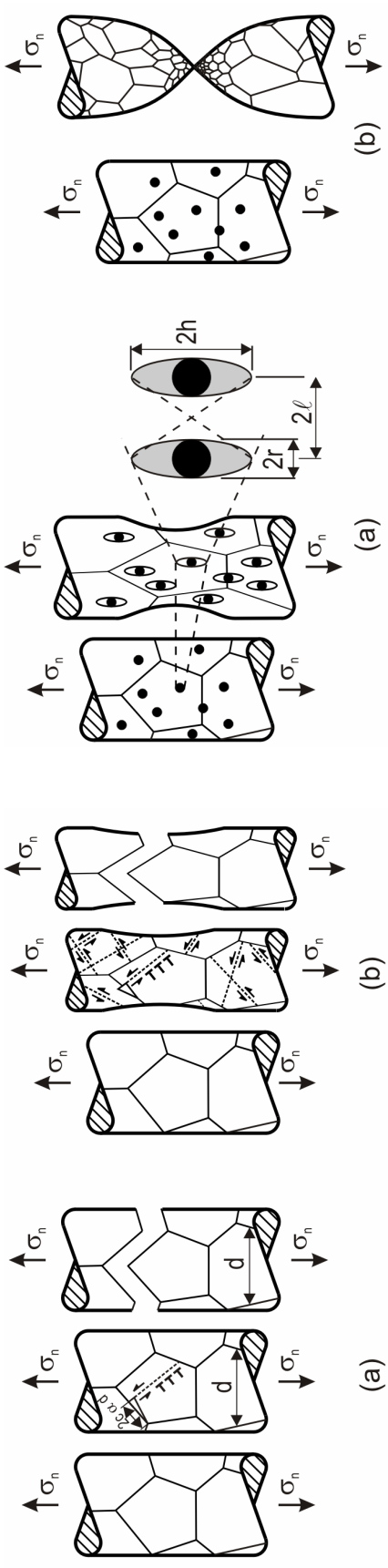

Fig 1. Mechanisms of brittle fracture: a – type 2, b – type 3, c – type 1, d – definition of the three type of brittle fracture. Based on [5].

Fig. 2. Mechanisms of non-brittle fracture: a – ductile, b – rupture, c – intergranular creep fracture. Based on [6,7].

In some cases, the temperature is very low, e.g. for aluminium it is about -200°C.

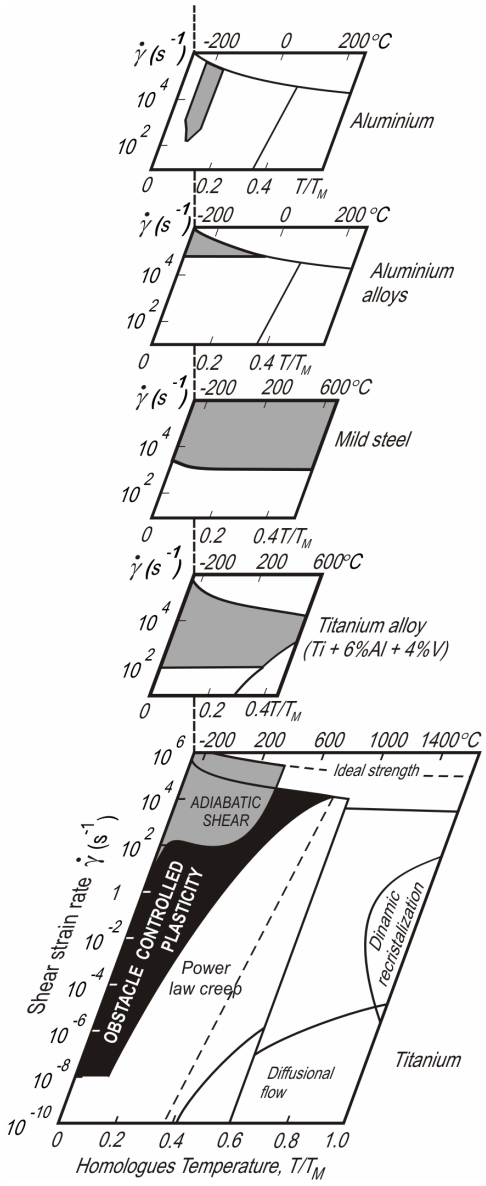

Fig. 3. Strain rate/homologous temperature deformation maps. Base on [9,10]

Problem. The theory of adiabatic shear bands does not explain the mechanism of shear fracture which occurs at strain rates lower than the critical ones ($\gamma^* < \gamma^*_{crit}$).

Therefore one can conclude that the shear fracture problem still is not fully correlated with the dislocation mechanism of plastic deformation, although the research on the evolution of dislocation structures seems to be quite advanced (fig. 4).

Maps of dislocation structures

Figure 4 shows a map of the evolution of dislocation structures depending on temperature and the magnitude of strain. Characteristic strain values divide the map into three main areas separated from each other by thick lines.

The upper limit of the first area marks the strain measured at the end of the yield threshold (ε_p). The upper limit of the second area is marked by uniform strains (ε_r). The boundaries of the third area are marked by failure strains (ε_f).

Against the background of the three areas the boundaries of subareas, corresponding to the successive stages in the evolution of the dislocation structures, can be distinguished. No complete coincidence of the boundaries of the subareas and those of the three main areas is observed. But this poses no problem for the approach adopted below.

The present author proposes to focus on the subarea with strongly disoriented cellular structure (the shaded subarea in fig. 4). In the author's opinion this subarea is closely linked to the shear fracture mechanism.

Problem. The above subarea of strongly disoriented cellular structure is not contiguous with the failure strain (ε_f) curve. In other words, there is still no clear connection between the evolution of dislocation structures and ductile fracture, and particularly shear fracture.
This is due to, among other things, the fact that a cellular structure belongs to low-energy structures, and as such does not explain the causes of the fracture.

Thesis. The author proposes the following thesis:
The causes of shear fracture lie in the formation of high-energy dislocation structures which the boundaries of subgrains forming within isothermal mesoscopic shear bands can constitute.

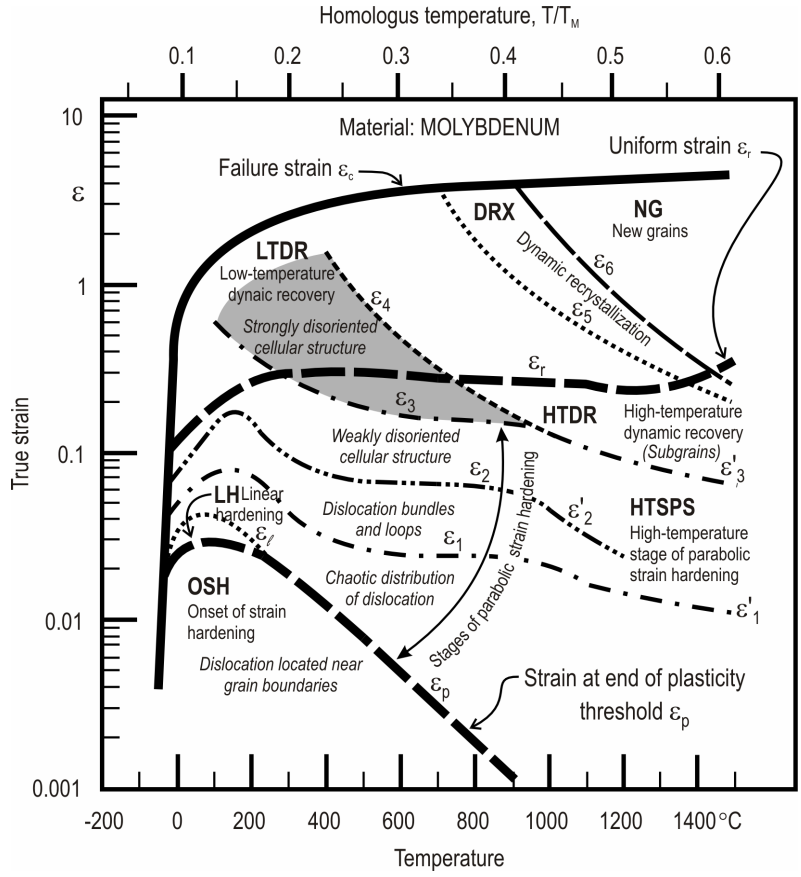

Fig. 4. Map of dislocation structure evolution. Based on [11].

3. Mesoscopic-macroscopic concept and model of shear fracture

The mesoscopic-macroscopic concept of the shearing process, proposed by the author of this paper, is illustrated in figs 5 and 6. According to this concept, the onset (fig. 5b) and then the development of strain localization in mesoscopic shear bands (fig. 6a) are of key importance. Here a case of strain localization in quasi-isothermal, mesoscopic shear bands (SB) is considered. The development of shear bands manifests itself in the appearance of a lenticular strain localization zone (fig. 5b).

The beginning of strain localization in the mesoscopic shear bands puts an end to the displacements of the free surface:
$U_s = U_{s,max}$ (fig. 5a, b).

The moment when shear bands appear and the free surface displacements are inhibited can be easily predicted. It is enough to know the relationship between limiting strain U_l and strain-hardening coefficient n [12,13]. Strain (displacement) U_l is limiting from the strain localization point of view. The development and properties of the dislocation structure within shear bands (fig. 5 h, i, j) determine the susceptibility of the material to fracturing along the shear bands. The macroscopic course of fracture depends on the shape of the boundaries of the strain localization zone (fig. 5b, 6b) and the magnitude of the displacements of the material along the defective grain boundaries (fig. 6a).

The original grain boundaries become defective as a result of the interaction between them and the shear bands (fig. 6a, boundary GB_2). This means that the course and effects of the shearing process depend here only on the synergy between the strain localization mechanism and the

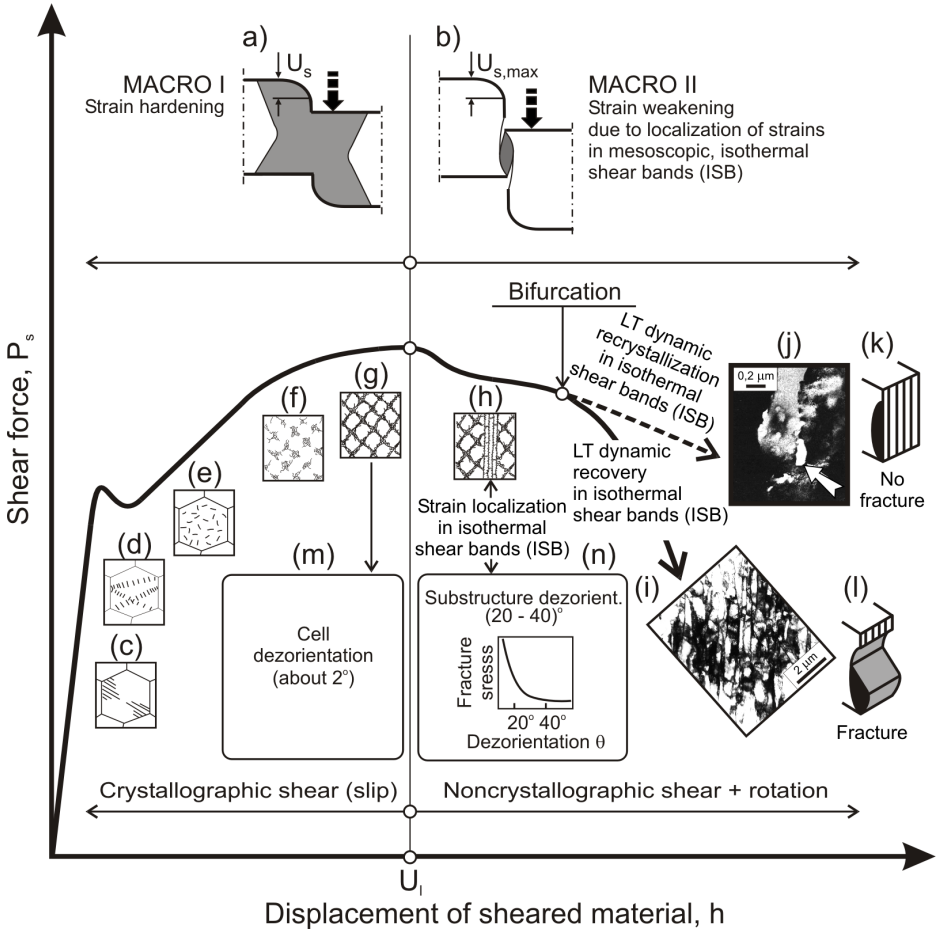

Fig. 5. Mesoscopic-macroscopic concept of shearing. According to E.S. Dzidowski. Description in text.

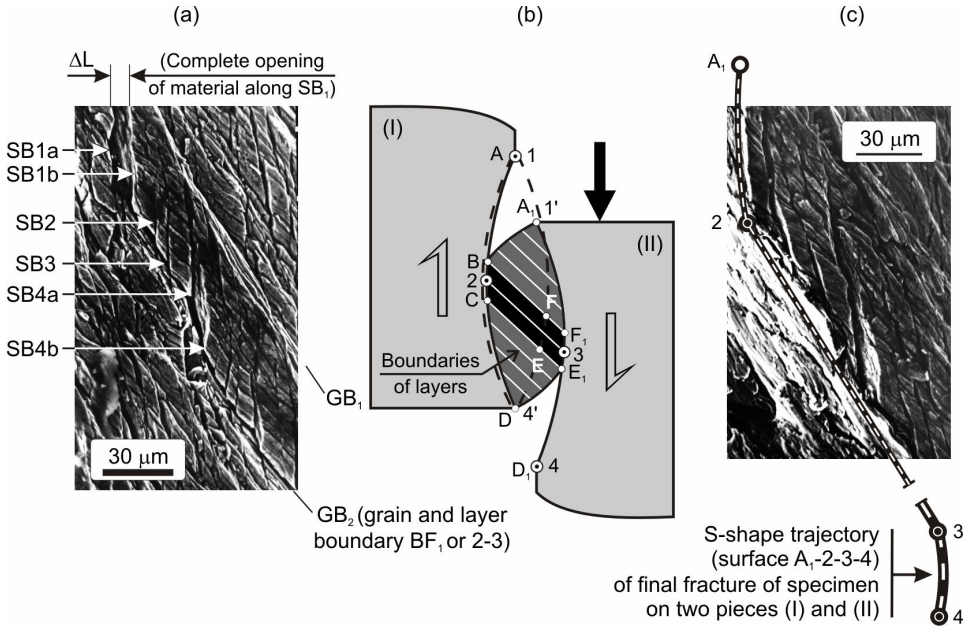

Fig. 6. Model of shear fracture mechanism (b) and scanning electron microscopy results which validate it (a,c). According to E.S. Dzidowski. Description in text.

mechanism of fracture along mesoscopic shear bands.

As fig. 6 shows, the fracture of the sheared material consists in its separation along mesoscopic shear bands SB (fig. 6a, separation ΔL)). Initially the fracture propagates along the shear bands (fig. 6b, trajectories A-B and E_1-D_1) and it consists in the loss of cohesion between the particular layers of the material. As the fracture reaches points 2 and 3, the fracture mechanism changes. From now on the fracture propagates only along the defective grain boundaries (fig. 6b, line 2-3 and fig. 6a, boundary GB_2).

Hence the final shape of fracture surface A-2-3-4' and that of surface A_1-2-3-4 depend on the shape and width of the lenticular strain localization zone and on the magnitude of the displacements along the defective grain boundaries (fig. 6 a, b).

This means that the fracture initially propagates along the boundaries and then across the strain localization zone formed by the shear bands (fig. 6b,c). Characteristically, the strain localization zone shrinks from top and bottom and eventually widens as a result of intercrystalline displacements of the material. Immediately before the total separation of the sheared material into two parts, the zone assumes a shape similar to parallelogram BCE_1F_1 (fig. 6b, blackened area).

The above shear fracture mechanism model relates fracture not only to the properties (misorientation) of the material's substructure within shear bands, but also to transverse (acting transversely to the direction in which shear bands (SBs) develop) tensile stresses. Such stresses may arise naturally or be artificially generated as in shear with tension. One should note here that the effective value of artificially generated tensile stresses amounts to about 0.25 of the yield point value ($\sigma_{0.2}$) [12].

Conventional shearing (fig. 6) is an example of the natural generation of transverse tensile stresses. The stresses arise because of interaction between SBs and the original grain boundaries (see fig. 6a, GB_2). The development of shear bands results in strong flattening and rotation of the grains and in the formation of characteristic laminar lenticular strain localization zones (SLZ). This may be accompanied by the formation of wedge-shaped discontinuities along the original grain boundaries (see fig. 6a, GB_2). The tendency to form such discontinuities depends to a large degree on the condition of the original grain boundaries. One of the factors conducive to the lamination of the original grain boundaries may be adsorption of foreign atoms.

The defective grain boundaries become some kind of inclined planes whereby the sheared portions of material move and separate along the SBs (fig. 6a, shear bands SB1-SB4 and the next ones). The separation is the most complete near the boundaries of SLZs, i.e. at the places where displacement (non-dilatational strain) gradients are the steepest (see fig. 6 a and b).

To sum up, the shape of slip fracture trajectories depends here on: the way in which shear bands develop, the properties of the shear bands, the condition of the original GBs and the shape of the SLZ formed by the mesoscopic SBs.
This means that by properly changing the properties and direction of development of shear bands and the way in which transverse tensile stresses are generated one can change the shape of the shear fracture trajectories or totally eliminate the fracture.

4. Conclusion

The mesoscopic-macroscopic concept of investigating and modelling the mechanism of shear fracture along

isothermal mesoscopic shear bands generates criteria which allow one to:

1. control of the trajectory of fracture,
2. accelerate and slow down the development of shear fracture,
3. prevent the development of shear fracture.

The main such criteria are:

1. The material's strain hardening ability which determines the onset of strain localization in isothermal shear bands.
2. Stacking fault energy which determines:

a) the course of the evolution of dislocation structures and their properties and so:
b) the susceptibility to cracking along isothermal shear band and its dynamics.

Exemplary applications of the presented concept can be found in [12-17].

References

[1] Panin V.E. (1988), *Physical Mesomechanics* 1, pp. 5.

[2] Panin V.E. (1998), Ed., *Physical mesomechanics of heterogeneous media and computer-aid design of materials.* CISP.

[3] Timoshchenko V.A. (1979), *Elementy teorii i tekhnologii razdelitel'nykh protsessov*. Shtiintsa, Kishinev.

[4] Belyaev V.I. (1985), *Inzhenernaya teoriya plastichnosti*. Nauka i Tekhnika, Minsk.

[5] Gurson A.L. (1984), *J. Eng. Mater. and Technology*, 99, pp.2.

[6] Needleman and Tvergard V. (1984) *J. Mech. Phys. Solids*, 32, pp. 461.

[7] Gandhi C., Ashby M. F. (1979), *Acta Metallurgica* **Vol. 27**, pp. 1565.

[8] Ashby M.F. Gandhi C., Taplin D.M.R. (1979), *Acta Metallurgica* **Vol. 27**, pp. 699.

[9] Sarget P. M., Ashby M. F. (1983) Cambridge Univ. Engng. Dept. Report No. CUEDCMATSTR.98.

[10] Bai Y., Dodd B. (1992), *Adiabatic shear localization. Occurrence, theories and applications*, Pergamon Press, Oxford.

[11] Firstov S.A., Pechkovski E.P. (2002), *Voprosy Materialobedeniya* No 1(**29**), St. Petersburg. pp. 70.

[12] Dzidowski E.S. (1990), *Mechanism of Shear Fracture in the Aspect of Controlled Decohesion of Metals* (in Polish), Scientific Papers of the Technical University of Wroclaw, Monographs No. 11, Wroclaw.

[13] Dzidowski E.S. (1993), *Materials Science and Engineering*, **A168**, pp. 11.

[14] Dzidowski E.S. (2001), In: Proceedings of the 4th international ESAFORM Conference on Material Forming (**Vol. I**), Liege, Belgium, pp. 241.

[15] Dzidowski E.S., Chruscielski G. (2003), In: Proceedings of the 6th ESAFORM Conference on Material Forming, Salerno, Italy, pp. 523.

[16] Dzidowski E.S. (2004), In: Proceedings of the 7th International ESAFORM Conference on Material Forming, Trondheim, Norway, pp. 745.

[17] Dzidowski E.S. (2004), *Physical Mesomechanics*, **Vol. 7**, No.3, pp. 75.

MODELLING CRACK INITIATION IN STRUCTURES USING A TWO-SCALE MICROMECHANICS-BASED CDM APPROACH

De Jesus, Abílio M.P., Ribeiro, Alfredo S.
University of Trás-os-Montes and Alto Douro, Engineering Department, Quinta de Prados, 5001-801 Vila Real, Portugal

Fernandes, António A.
Faculty of Engineering, University of Porto
Rua Dr. Roberto Frias, 4200-465 Porto, Portugal

Abstract

This paper applies a Continuum Damage Mechanics (CDM) model in lifetime assessment of a full size pressure vessel. The CDM model adopted in the analysis is a ductile damage model, which can be extended to model fatigue damage, since can be argued that fatigue loading develops plasticity, at least at the mesoscale level of a weak inclusion. A hypothesis of local coupling between damage and elastoplastic behaviour is assumed. The damage model was identified, based on experimental data, in order to model both ductile and fatigue damages. The CDM model was applied in the assessment of a fully size pressure vessel which was tested until failure, under variable internal pressure. The failure occurred at a nozzle-to-vessel intersection. The application of the damage model to that location suggested that the vessel failed due to excessive plastic deformation and not due to fatigue as was initially expected with the test.

KEYWORDS: Fatigue, Crack initiation, CDM, Plasticity.

1. Introduction

The problem of propagation of macroscopic cracks up to failure has been intensively studied through fracture mechanics concepts. The crack initiation, which requires the knowledge of what happens before a mesocrack breaks the representative volume element (RVE), cannot be modelled by classical fracture mechanics that deals with pre-existing meso or macro cracks.

A tool for modelling the evolution of the progressive deterioration of materials up to mesocrack initiation is the Continuum Damage Mechanics (CDM). A continuous damage variable is introduced as an internal variable of tensorial nature, but it reduces to a scalar, D, if damage is isotropic, which is the base hypothesis considered in this study.

For most applications, and especially in fatigue, the damage is highly localized in such a way that the damaged material occupies a small volume in comparison to the macroscale of the structural component or even the mesoscale of the RVE. This means that the effect of the damage on the stress/strain behaviour only occurs in very small damaged regions. The coupling between damage and strains may be neglected everywhere in the structure, except in the RVE, where damage develops, leading to the principle of locally coupled analysis, which is considered in this paper.

This paper applies a ductile CDM model, originally proposed by Lemaitre *et al* [1-3], to the modelling of the lifetime of a

full size pressure vessel, which was tested by the authors. The paper also describes the ductile damage model and its identification using experimental data obtained for the tested pressure vessel material – the P355NL1 steel [4].

2. The ductile CDM Model

A ductile CDM model is proposed to model both plastic and fatigue failures. In this section the base assumptions of this model are discussed, the respective constitutive equations are summarized and some numerical implementation issues are discussed.

Base assumptions

For many practical situations, plastic damage and mainly fatigue damage can be considered highly localized, only affecting locally the stress-strain behaviour. The damage localization is due to stress concentrations and also due to some weakness in strength at the microscale. Then, a locally coupled analysis is applied into two stages: i) a global elastoplastic finite element analysis (FEA) of the structure to derive the strains history; ii) a local analysis at the critical points, considering an elastoplastic damageable constitutive behaviour.

Lemaitre *et al* [1-3] suggested a micromechanics-based model for the RVE at mesoscale which is applied in this paper. The RVE is made of a matrix containing a micro-element or inclusion weakened by its lower plasticity threshold; all other material characteristics are the same for both inclusion and matrix. In the present study it is assumed an elastoplastic behaviour for the matrix with a yield stress, σ_y, ultimate tensile strength, σ_u, and a fatigue limit, σ_{fl} ($\sigma_{fl} < \sigma_y$). The inclusion is considered to follow an elastic-perfectly plastic behaviour coupled with damage. Its weakness is due to a plasticity threshold lower than σ_y and equal to σ_{fl} if not known by another consideration: $\sigma_s^{\mu} \geq \sigma_y^{\mu} = \sigma_{fl}$. Below the fatigue limit no damage should occur. The fatigue limit of the inclusion is supposed to be reduced in the same proportion:

$$\sigma_{fl}^{\mu} = \sigma_{fl}(\sigma_{fl} / \sigma_y) \tag{1}$$

A law of localization is adopted based on the Lin-Taylor's hypothesis [5], which states that the state of strain at microscale is considered equal to the state of strain calculated, independently, at macroscale. Then, there is no boundary value problem to be solved. Only a set of coupled constitutive equations must be solved for a given history of mesostrains at the critical point(s). The criterion of microcrack initiation is also the criterion for brittle crack instability at mesoscale [1].

Constitutive equations

The constitutive equations for the weak inclusion are described. The superscript μ is omitted hereafter for sake of simplicity. It is assumed an elastic-perfectly plastic behaviour coupled with isotropic damage. Let's assume valid the decomposition of the strain tensor into elastic and plastic components:

$$\varepsilon_{ij} = \varepsilon_{ij}^{E} + \varepsilon_{ij}^{P} \tag{2}$$

The strain tensor ε_{ij} is evaluated through a global elastoplastic analysis, without damage, for the whole structure. Its complete history is known in advance to the integration of the constitutive equations for the weak inclusion.

The elasticity law coupled with damage can be expressed as follows:

$$\sigma_{ij} = E(1-D)\left[\frac{\varepsilon_{ij}^{E}}{1+\nu} + \frac{\nu\varepsilon_{kk}^{E}\delta_{ij}}{(1+\nu)(1-2\nu)}\right] \tag{3}$$

or, inversely, as:

$$\varepsilon_{ij}^{E} = \left[\frac{1+\nu}{E}\tilde{\sigma}_{ij} - \frac{\nu}{E}\tilde{\sigma}_{kk}\delta_{ij}\right] \tag{4}$$

where δ_{ij} is the delta Kronecker operator and $\tilde{\sigma}_{ij}$ is the effective stress tensor defined as follows:

$$\tilde{\sigma}_{ij} = \sigma_{ij} /(1-D) \quad (5)$$

A plastic yield function is established as follows:

$$f = \frac{\sigma_{eq}}{1-D} - \sigma_s = 0 \Leftrightarrow f = \tilde{\sigma}_{eq} - \sigma_s = 0 \quad (6)$$

where σ_{eq} is the equivalent stress defined using the deviatoric stress tensor, S_{ij}, as follows:

$$\sigma_{eq} = \left(\tfrac{3}{2} S_{ij} S_{ij}\right)^{1/2}; S_{ij} = \sigma_{ij} + \tfrac{1}{3}\sigma_{kk} \quad (7)$$

In the framework of associate plasticity, the plastic strain tensor rate can be expressed as follows:

$$\dot{\varepsilon}_{ij}^P = \frac{\partial f}{\partial \sigma_{ij}} \dot{\lambda} = \frac{3}{2}\frac{S_{ij}}{\sigma_{eq}}\frac{\dot{\lambda}}{1-D} \text{ if } f = \dot{f} = 0 \quad (8)$$

where $\dot{\lambda}$ is the plastic multiplier. Taking into account the definition of the accumulated plastic deformation $\dot{p} = (\tfrac{2}{3}\dot{\varepsilon}_{ij}^P \dot{\varepsilon}_{ij}^P)^{1/2}$, the plastic strain rate can be expressed as:

$$\dot{\varepsilon}_{ij}^P = \frac{3}{2}\frac{S_{ij}}{\sigma_{eq}}\dot{p} = \frac{3}{2}\frac{\tilde{S}_{ij}}{\sigma_s}\dot{p} = N_{ij}\dot{p} \quad (9)$$

where N_{ij} is a normal to the yield function, with a magnitude of $\tfrac{3}{2}$.

The kinematic damage law can be stated as follows:

$$\dot{D} = \frac{Y}{S}\dot{p} \text{ if } p > p_D \quad (10)$$

where p_D is the damage threshold corresponding to microcrack nucleation; S is a damage strength constant and Y is the strain energy release rate, defined as:

$$Y = \sigma_{eq}^2 R_v \Big/ \left[2E\left(1-D\right)^2\right] \quad (11)$$

In the previous equation, R_v is the triaxility function, defined as:

$$R_v = \tfrac{2}{3}\left(1+\nu\right) + 3\left(1-2\nu\right)\left(\frac{\sigma_H}{\sigma_{eq}}\right)^2; \quad (12)$$
$$\sigma_H = \tfrac{1}{3}\sigma_{kk}$$

Assuming an elastic-perfectly plastic behaviour, the triaxility function can be expressed using information directly from the strain tensor:

$$R_v = \tfrac{2}{3}\left(1+\nu\right) + 3\left(1-2\nu\right)\left(\frac{E\varepsilon_H}{\left(1-2\nu\right)\sigma_s}\right)^2 \quad (13)$$

The accumulated plastic strain associated with the damage threshold, p_D, can be associated with the corresponding axial plastic strain, ε_D^P, based on energetic considerations [1]:

$$p_D = \varepsilon_D^P \frac{\sigma_u - \sigma_{fl}}{\sigma_s - \sigma_{fl}^2 / k} \quad (14)$$

The conditions of failure of the RVE are reached for a critical value of damage, D_c. This critical damage can be related with the corresponding uniaxial damage, using energetic arguments [1]:

$$D_c = D_{1c}\frac{\sigma_u^2}{\sigma_s{}^2 R_v} \quad (15)$$

Numerical Integration

The numerical integration of the constitutive equations was performed using an incremental strain driven algorithm since the strain tensor is known

in advance for any time. The aim of the integration procedure is to evaluate the stress tensor, the plastic strain tensor, damage, and other material model variables, for the time t_{n+1}, knowing the corresponding values for the time t_n. The integration algorithm is applied into two stages: an elastic trial followed by an eventual plastic correction. The elastic trial leads, for the time t_{n+1}:

$$\varepsilon_{ij}^{P}\Big|_{n+1} = \varepsilon_{ij}^{P}\Big|_{n} \tag{16}$$

$$p_{n+1} = p_n \tag{17}$$

$$D_{n+1} = D_n \tag{18}$$

$$\tilde{\sigma}_{ij}\Big|_{n+1} = \lambda\, \varepsilon_{kk}\Big|_{n+1}\, \delta_{ij} + 2\mu\left(\varepsilon_{ij}\Big|_{n+1} - \varepsilon_{ij}^{P}\Big|_{n}\right) \tag{19}$$

$$\sigma_{ij}\Big|_{n+1} = \tilde{\sigma}_{ij}\Big|_{n+1}\left(1 - D_n\right) \tag{20}$$

If the effective stress, given by Eq. (19), leads to a yield function value, defined by Eq. (6), $f \le 0$, then Eqs. (16) to (20) define the final state for time t_{n+1}. Inversely, if $f > 0$ then a plastic correction is required. The consideration of a perfect plastic material model allows the explicit derivation of the plastic correction. Eqs. (9) and (10) can be stated in the incremental form using the Backward-Euler fully implicit scheme:

$$\varepsilon_{ij}^{P}\Big|_{n+1} - \varepsilon_{ij}^{P}\Big|_{n} = N_{ij}\Big|_{n+1}\left(p_{n+1} - p_n\right) \tag{21}$$

$$D_{n+1} - D_n = \frac{Y_{n+1}}{S}\left(p_{n+1} - p_n\right) \tag{22}$$

In the final of the increment the yield function should be verified:

$$f_{n+1} = \tilde{\sigma}_{eq}\Big|_{n+1} - \sigma_s = 0 \tag{23}$$

with the effective stress tensor given by:

$$\tilde{\sigma}_{ij}\Big|_{n+1} = \lambda\, \varepsilon_{kk}\Big|_{n+1}\, \delta_{ij} + 2\mu\left(\varepsilon_{ij} - \varepsilon_{ij}^{P}\right)\Big|_{n+1} \tag{24}$$

The previous equation can be rewritten using the result of Eq. (21):

$$\begin{aligned}\tilde{\sigma}_{ij}\Big|_{n+1} &= \lambda\, \varepsilon_{kk}\Big|_{n+1}\, \delta_{ij} + \\ &+2\mu\left[\varepsilon_{ij}\Big|_{n+1} - \varepsilon_{ij}^{P}\Big|_{n} - N_{ij}\Big|_{n+1}\left(p_{n+1} - p_n\right)\right]\end{aligned} \tag{25}$$

Eqs. (23) and (25) form a non-linear system of equations in the unknowns $\tilde{\sigma}_{ij}\Big|_{n+1}$ and p_{n+1}:

$$\begin{cases} f_{n+1} = \tilde{\sigma}_{eq}\Big|_{n+1} - \sigma_s = 0 \\ h_{ij}\Big|_{n+1} = \tilde{\sigma}_{ij}\Big|_{n+1} - \lambda\, \varepsilon_{kk}\Big|_{n+1}\, \delta_{ij} + \\ \qquad - 2\mu\left(\varepsilon_{ij}\Big|_{n+1} - \varepsilon_{ij}^{P}\Big|_{n}\right) + \\ \qquad + 2\mu\, N_{ij}\Big|_{n+1}\left(p_{n+1} - p_n\right) = 0 \end{cases} \tag{26}$$

They can be linearized and solved simultaneously, using the Newton method:

$$\begin{cases} f + \dfrac{\partial f}{\partial \tilde{\sigma}_{ij}} C_{ij}^{\tilde{\sigma}} = 0 \\ h_{ij} + \dfrac{\partial h_{ij}}{\partial \tilde{\sigma}_{kl}} C_{kl}^{\tilde{\sigma}} + \dfrac{\partial h_{ij}}{\partial p} C_p = 0 \end{cases}, t = t_{n+1} \tag{27}$$

The coefficients $C_{ij}^{\tilde{\sigma}}$ and C_p are defined for iteration l as follows:

$$\begin{cases} C_{ij}^{\tilde{\sigma}} = \left(\tilde{\sigma}_{ij}\right)_{l+1} - \left(\tilde{\sigma}_{ij}\right)_{l} \\ C_p = \left(p\right)_{l+1} - \left(p\right)_{l} \end{cases}, \; t = t_{n+1} \tag{28}$$

The iteration $l = 0$ corresponds to the elastic prediction. The coefficients $C_{ij}^{\tilde{\sigma}}$ and C_p can be evaluated explicitly for $t = t_{n+1}$:

$$\begin{cases} C_p = \dfrac{f - N_{ij} h_{ij}}{3\mu} \\ C_{ij}^{\tilde{\sigma}} = -\dfrac{2}{3}\left(f - N_{kl} h_{kl}\right) N_{ij} - \\ \dfrac{1}{1 + \dfrac{3\mu}{\tilde{\sigma}_{eq}} \Delta p}\left[h_{ij} + \dfrac{2\mu}{\tilde{\sigma}_{eq}} \Delta p \left(N_{kl} h_{kl}\right) N_{ij}\right] \end{cases} \tag{29}$$

After the evaluation of the $\tilde{\sigma}_{ij}\big|_{n+1}$ and p_{n+1}, one can evaluate the $\varepsilon_{ij}^{P}\big|_{n+1}$, D_{n+1} and $\sigma_{ij}\big|_{n+1}$ using Eqs. (21), (22) and (5), respectively.

This ductile damage model is implemented in the DAMAGE 90 code [1,3]. This code admits the strain tensor history, $\varepsilon_{ij}(t)$, at the critical point as input. Also, the constants of the plasticity and damage model are required. The outputs of the code are the damage, the accumulated plastic strain and the stress tensor.

3. Model Identification

The constants of the model can be identified to model distinct damage behaviours. Two alternative sets of constants are proposed to model the plastic damage and the low/medium cycle fatigue damage. While plastic damage is associated with monotonic loading, fatigue damage is associated with cyclic loading. The constants to be evaluated can be grouped into four distinct sets: elastic constants (E, ν); general strength constants (σ_u, σ_y, σ_{lf}); plastic constants (σ_s) and damage constants (ε_D^P, D_{lc}, S). The elastic and general strength constants were determined using standard tests for the P355NL1 steel [4]. The ductile damage model should model the complete uniaxial tensile test. This test is used to identify damage constants. The critical damage, D_{lc}, can be evaluated through a relation between the ultimate tensile strength, σ_u, and the fracture strength, σ_r [1]:

$$D_{lc} = 1 - \frac{\sigma_r}{\sigma_u} \tag{30}$$

The damage threshold, ε_D^P, can be assumed equal to the uniaxial ultimate tensile strain, ε_u:

$$\varepsilon_D^P = \varepsilon_u \tag{31}$$

The damage strength coefficient S is evaluated through a trial and error process in order to guarantee the following conditions:

$$\begin{aligned} &\varepsilon \le \varepsilon_u, \sigma \le \sigma_u \Rightarrow D = 0 \\ &D = D_{lc} \Rightarrow \varepsilon = \varepsilon_r, \sigma = \sigma_r \end{aligned} \tag{32}$$

Table 1 summarizes the constants under option 1. The plastic behaviour of the material is simulated using a perfectly plastic model, being the strain hardening simulated through several plastic thresholds, σ_s. These plastic thresholds are listed in Table 2. Fig. 1 illustrates the simulation of the uniaxial tensile test. Alternatively to the constants of Option 1, the ductile damage model can be identified to model a theoretical uniaxial tensile test: after reaching the maximum, the strength decreases progressively until zero. The condition of null strength means unit damage. The model constants are presented in Table 1 for Option 2.

Parameters	Option 1	Option 2
E [MPa]	205200	
ν	0.275	
σ_u [MPa]	568	
σ_y [MPa]	362	
σ_{lf} [MPa]	284	
D_{lc}	0.19	1.00
ε_D^P	0.15	
S [MPa]	0.600	0.118

Table 1: Properties for the ductile model.

ε [%]	0.0	0.1	0.2	1.5	4.0	6.5	10
σ_s [MPa]	284	324	362	440	500	540	568

Table 2: Plastic thresholds.

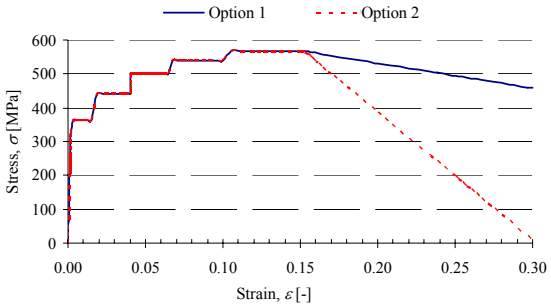

Figure 1: *Simulation of the uniaxial tensile test.*

The ductile damage constants are now identified in order to model the low/medium cycle fatigue ($\sim 10^2 < N_f <\sim 10^5$ cycles). The constants of the model are estimated indirectly in order to minimize the deviations between the response of the model and the experimental data. The experimental data used to identify the constants of the model are results from fatigue tests of smooth specimens, performed under total strain control with fully-reversed straining [4]. Two sets of constants were proposed. Table 3 summarizes the constants of the fatigue damage model. Fig. 2 presents predictions of strain-life data using the proposed CDM model. Both sets of constants (Options 1 and 2) give very reasonable predictions. Although both options led to similar fatigue life predictions, they are based on distinct damage thresholds. The Option 1 considers the same damage threshold of the plastic damage model. This damage threshold is, for low/medium cycle fatigue regimes, achieved for the very first cycles. Hence, a linear relation between damage and the accumulated plastic strain, and consequently the number of cycles, is observed from the beginning as is illustrated by Fig. 3a. This damage evolution is not according to the actual fatigue damage evolution curves of the material as illustrated by Fig. 3b. Fig. 3b compares the damage evolution curves simulated with the Option 2 set of constants and the experimental results from reference [4]. It is clear that the fatigue damage evolves non-linearly which is reasonably captured by the model with the set of constants from Option 2.

Parameters	Option 1	Option 2
E [MPa]	205200	
ν	0.275	
σ_u [MPa]	568	
σ_y [MPa]	362	310
σ_{lf} [MPa]	284	
D_{1c}	1.00	
ε_D^P	0.15	13
S [MPa]	26.0	2.5

Table 3: Properties for the fatigue damage model.

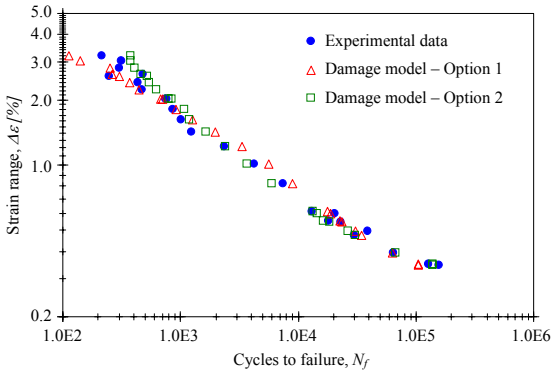

Figure 2: *Strain-life data prediction.*

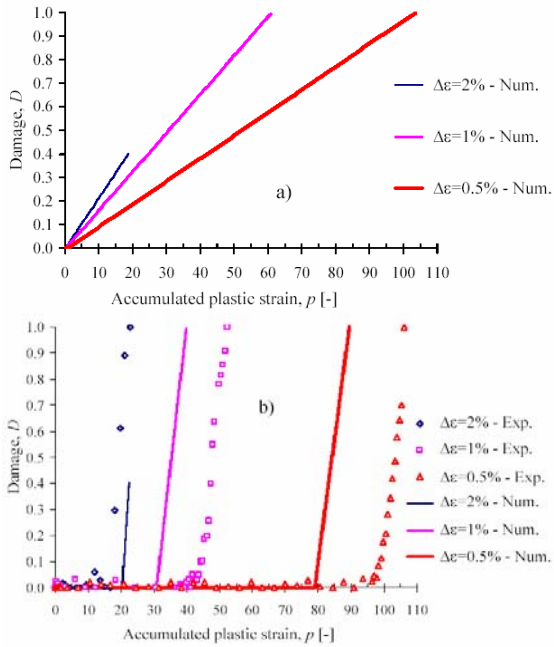

Figure 3: *Damage evolution for Option 1 (a) and Option 2 (b).*

Fig. 4 illustrates the application of the fatigue damage model in the prediction of the damage accumulation for a two-block loading. It can be concluded that the Option 1 of the model yields a non-linear damage accumulation; the Option 2 of the damage model simulates almost linear damage accumulation. The predictions are compared with the experimental data derived in reference [4] for the P355NL1 steel. The non-linear predictions achieved with the Option 1 model are very satisfactory in terms of damage accumulation.

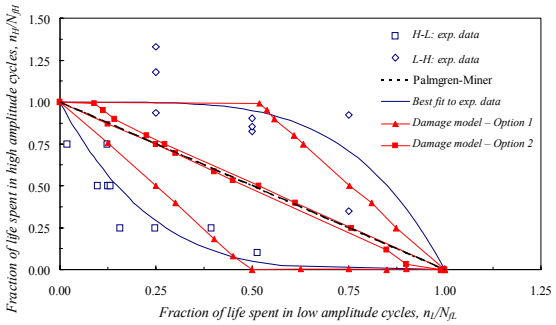

Figure 4: *Simulation of damage accumulation under two-block loading.*

4. Damage Analysis of a Pressure Vessel

The described CDM model is now applied in the lifetime assessment of a full size pressure vessel. The pressure vessel was tested under fluctuating internal pressure. Details about the experimental test of the vessel can be found in reference [4]. The vessel failed at 12 455 full pressure cycles ranging from 0 to 35 bars, due to a crack initiated at the crotch corner of the nozzle-to-vessel intersection. Figs. 5 and 6 illustrate the geometry, boundary conditions and FEM mesh used in a global elastoplastic analysis of the vessel.

The global elastoplastic analsis was performed using the Chaboche model with superposition of 3 non-linear kinematic hardening variables (c_1=180GPa, γ_1=1200, c_2=20.4GPa, γ_2=120, c_3=0.48GPa, γ_3=12). A radius of the yield function equal to 200 MPa was assumed. The simulation was carried out over 20 pressure cycles. The strain history was recorded at the crotch corner, where damage localization is expected.

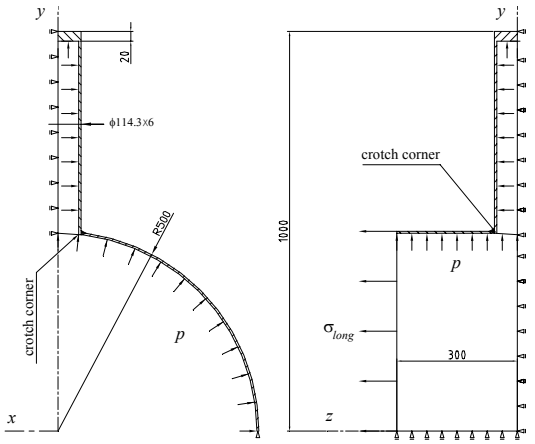

Figure 5: *Pressure vessel.*

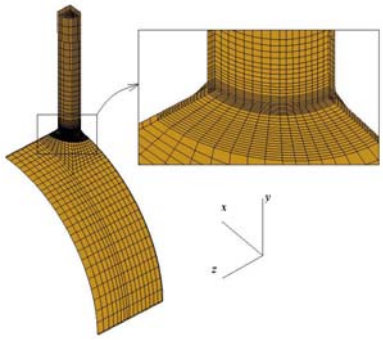

Figure 6: *Finite element mesh of the nozzle-to-vessel intersection.*

An asymptotic progressive cyclic mean strain is observed and confirmed in the experimental tests [4], which is superimposed to the respective cyclic strains. The transient behaviour can be expressed through the following equations for the increments of the three cyclic mean direct strain components at the crotch corner:

$$\delta\varepsilon_{xx,med} / \delta N = 0.0744 N^{-0.7399}$$
$$\delta\varepsilon_{yy,med} / \delta N = -0.0466 N^{-0.7453} \quad (\%) \quad (33)$$
$$\delta\varepsilon_{zz,med} / \delta N = -0.0453 N^{-0.8664}$$

It is assumed that a stabilized behaviour is achieved as soon as the strain increments between to successive cycles are lower than a critical value:

$$\xi = \frac{\left(\delta\varepsilon_{ij,med}/\delta N\right)_N - \left(\delta\varepsilon_{ij,med}/\delta N\right)_{N-1}}{\left(\delta\varepsilon_{ij,med}/\delta N\right)_N} \leq \xi_c \quad (34)$$

If N_c corresponds to the minimum number of cycles for which $\xi \leq \xi_c$, then the strain increments, for $N \geq N_c$, can be assumed constant:

$$\left(\delta\varepsilon_{ij,med}/\delta N\right)_N = \left(\delta\varepsilon_{ij,med}/\delta N\right)_{N_c} \quad (35)$$

Eqs. (33) to (35) allow the simulation of the cyclic mean strain. The alternate behaviour is characterized by the following strain ranges:

$$\begin{aligned} \Delta\varepsilon_{xx} &= 0.386\,\% \\ \Delta\varepsilon_{yy} &= 0.130\,\% \\ \Delta\varepsilon_{zz} &= 0.123\,\% \end{aligned} \quad (36)$$

Both ductile and fatigue damage models are used to simulate the lifetime of the nozzle-to-vessel behaviour. The history of strains at the crotch corner is processed using the DAMAGE90 software [3]. The ductile damage model, identified to predict the low/medium cycle fatigue, predicts fatigue lives of 67 320 cycles and 66 990 cycles, for Options 1 and 2, respectively. These lives are about four times the observed experimental life (12 455 cycles). This prediction suggests that the observed failure is not a fatigue type failure. The ductile damage model, identified to model the plastic failure was applied to process the cyclic mean strains at the crotch corner. The predictions depend on the ξ_c values. The following values were obtained with the Option 2: $\xi_c = 3.87\% \Rightarrow N = 2582\ cycles$; $\xi_c = 1\% \Rightarrow N = 4141\ cycles$; $\xi_c = 0.5\% \Rightarrow N = 7485\ cycles$. These values are the same order of magnitude of the observed experimental life, which confirms a plastic failure of the vessel.

The proposed CDM model predicts the crack initiation which represents the failure of the RVE. In general, a propagation period is expected. This propagation period was verified to be reduced for the tested vessel due to the high applied pressures. Neglecting the propagation period, it is expected that the CDM model give conservative predictions.

5. Conclusions

This paper describes a CDM model which is formally a ductile damage model. The model was identified to model both plastic and low/medium cycle fatigue damages. Locally elastoplastic coupled with damage behaviour is assumed. The CDM model was applied in the lifetime assessment of a full size pressure vessel. The model predictions clarify that the vessel failure was of plastic type rather than fatigue, in contradiction with expected by the vessel testing.

References

[1] Lemaitre, J. (1996), *A course on Damage Mechanics*, 2nd Edition, Springer-Verlag, New York.

[2] Lemaitre, J., Sermage, J.P., Desmorat, R. (1999), *A two scale damage concept applied to fatigue* , International Journal of Fracture, **97**, pp. 67-81.

[3] Lemaitre, J., Doghri, I. (1994), *Damage 90: a post processor for crack initiation*, Comput. Methods Appl. Mech. Engrg, **115**, pp. 197-232.

[4] Jesus, A.M.P. (2004), *Validation of procedures for fatigue assessment of pressure vessels*, PhD thesis, UTAD, Vila Real (in Portuguese).

[5] Taylor, G.I. (1938), *Plastic strains in metals*, J. Inst. Met., pp. 62-307.

III. Polymers and Composites

ENERGY METHODS FOR PREDICTING DAMAGE IN A VARIETY OF LAYERED SYSTEMS

L N McCartney
Materials Centre, National Physical Laboratory,
Teddington, Middlesex, TW11 0LW, UK

Abstract

Energy methods are used to consider damage formation in both laminated composites and other smaller scaled multi-layered systems. For laminates, the damage mode is the formation of arrays of ply cracks that progressively form during loading. Crack damage also forms in other multi-layered systems (e.g. small scale metal-ceramic super-lattices). For other multi-layered systems, such as silicon germanium systems encountered in the electronics sector, dislocation formation can be the preferred damage mode and is also considered using energy methods.

Keywords: Energy, Laminates, First ply cracking, Super-lattices, Dislocations.

1. Introduction

Multi-layered multi-material systems are used for many engineering applications in various forms, where the assembly of a three-dimensional components from materials having a two-dimensional structure is used to enhance properties in one or more directions. Applications areas are wide ranging in the sectors involved, and in the length scales encountered. For example, at the macroscopic level, some laminated composite structures involve many layers of unidirectional composite material at various orientations, having total thicknesses in the 0.1-0.5 mm range, bonded together to form composite laminates. At the microscopic level metal-ceramic super-lattices, used as hard-wearing coatings applied to cutting tools, involve alternating layers of different essentially epitaxial materials where individual layer thicknesses are in the range 10-100 nm. Also at this length scale, epitaxial semi-conductor materials are in widespread use, which are often functionally graded to obtain desired electronic properties. Such material systems are a very special class of layered composite material.

At the macroscopic level, the integrity of an engineering structure is determined by its geometry, which is often complex 3D structure, and the loading, which is often not known accurately and is complex involving triaxial stress states that arise from combined in-plane and out-of-plane loading modes. Structural failure of composite laminates can depend on the nature of localised damage modes such as, delaminations, ply cracks, fibre and fibre/matrix interface failure. The integrity of structure whose dimensions are measured in metres might be determined by localised damage modes that involve much smaller dimensions such as millimetres in the case of ply cracking, and such as micrometres in the case of fibre failures. The prediction of the integrity of a composite structure thus requires a fully integrated multi-scale modelling approach traversing many length scales, connecting macroscopic structural features to microstructural features such as ply lay-up,

fibre architectures and the very localised behaviour of clusters of molecules and atoms when considering fibre/matrix interfacial effects.

For layered composite materials of any type, mechanical and thermal loading can lead to the initiation and growth of damage followed by component failure. Recent progress will be summarised on the application of stress transfer models developed for ply cracking in composite laminates, in conjunction with energy methods, to predict progressive damage formation in several different areas of layered composite systems having practical importance, where the structure is defined at two distinct length scales.

The requirement for the modelling of composite structure to bridge many length scales needs to be accompanied by the application of appropriate physical principles at each length scale involved. The key principles involved are the balance (or conservation) of mass, momentum (both linear and angular) and energy. At the same time the laws of thermodynamics must also be obeyed. Such principles must also be applied when modelling damage mechanisms. However, failure theories for composite systems are usually based on stress-based criteria that are empirical in nature, as evidenced by many of the models presented in the International Failure Prediction Exercise [1-3] where a final analysis of results and conclusions has recently been published. Such methods are applied to predict the failure of individual plies in laminates, and combined with ply discount schemes to model progressive damage growth and eventual failure of the laminates. Evidence has been presented [4] that stress-based failure criteria are not able to predict ply thickness and ply lay-up effects, issues that were not in fact addressed in the recent Failure Prediction Exercise [1-3]. It has been shown [4] that energy methods are required to explain these effects. It will be shown in this paper that as length scales reduce, energy methods indicate that damage formation becomes more difficult to analyse, as observed in nature, and it must be emphasised that stress-based methods cannot explain this behaviour. For very small length scales, often encountered in the electronics sector, dislocation, rather than crack formation, can be the damage mode that occurs. It will be shown that energy methods are capable of predicting dislocation formation in epitaxial layered systems.

2. Ply cracking in laminates

The first type of composite to be considered is the conventional laminate where the problem is to make use of physically-based prediction methods for the degradation of properties due to damage, and for laminate strength in multiaxial loading conditions, in contrast to the empirical failure criteria normally used by engineers. The damage in composites appears as fully developed cracks in the individual plies of laminates. Recently developed homogenisation methods, can be combined with energetic methods [5, 6], and with a fibre failure criterion based on strain, to predict the failure of many types of composite laminate. The simulation method recently developed models progressive ply cracking in any ply of a symmetric laminate using an homogenisation method [6], and has led to a very useful technique of predicting laminate failure. In particular it has been shown how ply thickness and ply ordering affects laminate strength, including a discussion of experimental data for CFRP [7]. Energy methods indicate that as the ply thickness is reduced, the first ply failure stress increases, a phenomenon observed in practice that cannot be explained using conventional stress-based approaches. It is emphasised that most of the recommended methods for predicting laminate failure resulting from the International Failure Prediction Exercise for Composites [1-3] are not capable of accounting for such

effects as they are derived from stress-based rather than energy-based failure criteria. This should be a matter of concern for composite engineers who are building ever-larger structures where manufacturing cost considerations may tempt them to use thicker plies. In passing it is emphasised that methods exist (see for example [5]) for predicting the required undamaged ply properties from fibre and matrix properties, and when these are combined with the damage prediction methods outlined above, they offer a rigorous bridging of mechanics method from the fibre and matrix level through to laminates and on to structures where the methodology is designed for application. A commercially available PC software system known as PREDICT [8] is now available to enable users to carry out some of the required calculations.

3. Predicting first ply failure

As already mentioned, when a composite laminate is loaded, catastrophic failure is usually preceded by a number of different interacting failure mechanisms such as ply cracking, delamination, fibre fracture, and fibre/matrix interface failure. Ply cracking is often the first damage mode to occur, and if it occurs in a structure where gas or liquid is contained, perhaps under pressure, a leakage failure mode becomes a possibility that must be avoided. Also, if the structure is subjected to fatigue loading, damage growth from ply cracks in the form of delaminations can lead to the degradation of the structure and catastrophic failure at some time in the future. Clearly the avoidance of ply cracking is a prudent approach when designing some types of laminated composite structure. The requirement is to design a structure that avoids first ply failure for all expected operating conditions.

The prediction of first ply failure has traditionally involved the application of a stress-based failure criterion in each of the plies of a laminate. The effective (or global) stresses that are sufficient to satisfy the ply failure criterion in a particular ply defines the first ply failure stress that can be used in design. Sometimes plies that have failed are discounted by reducing their Young's and shear moduli to zero so that the local effective properties of the laminate are degraded using classical laminate theory (i.e. the ply discount method). This procedure may be continued progressively until all plies in the laminate have failed. While this approach is used frequently, it suffers from the significant problem that the predicted failure stress of the laminate does not depend in any way upon the thickness of the plies. It is useful to consider a specific example. Consider the two quasi-isotropic laminates $[0_2,90_2,45_2,\text{-}45_2]_s$ and $[0,90,45,\text{-}45]_{2s}$. They both have the same number of lamina at various angles and classical laminate theory predicts that the same stress field will arise in each of the plies having the same angle (assuming the region considered is free of edge effects). The application of a stress-based first ply failure criterion then leads to the conclusion that both laminates would generate ply failures at the same stress. This type of behaviour is not observed in practice [7]. Also the application of conventional failure criteria to the laminate as a whole would lead to the conclusion that both laminates have the same strength which is another situation that does not occur in practice [7]. Clearly first ply failure is governed by other physical principles, and some of these will now be described.

Energy-based approach to ply failure

In the following analysis, the symbols E_A, E_T and μ_A will be used to denote the axial and transverse Young's moduli of a laminate, and the axial shear modulus for a damaged state, while ν_A, ν_a and ν_t denote the corresponding major and minor axial Poisson's ratios and the transverse Poisson's ratio, respectively. The symbols α_A and α_T will be used to denote the axial and in-plane transverse thermal expansion

coefficients of a damaged laminate. The same notation is used for laminar properties except that the symbol is written in italics to denote that the property refers to a single lamina. A superscript 'o' denotes that the elastic constant refers to that for an undamaged laminate.

An effective applied stress s, accounting for in-plane biaxial and through-thickness loading, is defined by (see [5, and cited papers] for details of its derivation)

$$s = k'\sigma_t + \sigma + k\sigma_T \ , \qquad (1)$$

where σ_t is the through-thickness stress, σ is the effective axial stress and where σ_T is the effective in-plane transverse stress that are applied to the laminate. The parameters k' and k, which are laminate constants that depend on the effective elastic constants of the laminate (when undamaged) and on the elastic constants of the individual plies, are given by (see [5] for details)

$$k = \frac{E_A^o}{E_T^o}\,\frac{B - \nu_A^o E_T^o / E_A^o}{1 - \nu_A^o B}\ , \qquad k' = \frac{E_A^o A - \nu_a^o - \nu_t^o (E_A^o / E_T^o) B}{1 - \nu_A^o B}\ . \qquad (2)$$

where A and B are defined by the elastic properties of individual plies (in italics)

$$A = \nu_t / E_T + \nu_a \nu_A / E_A \ , \ B = \nu_A \qquad (3)$$

When laminates are balanced (so that for any ply orientation angle θ the number of $+\theta$ plies is equal to the number of $-\theta$ plies), it can be shown using the results given in [5] that the criterion for ply cracking in a specific ply can be expressed in terms of just two loading parameters: i) an effective stress defined by s, and ii) the in-plane shear stress to be denoted by τ.
The criterion for first ply cracking is energy based and may be derived from results given in [5] so that

$$\left(\frac{1}{E_A} - \frac{1}{E_A^o}\right)\left[s + k_1 \Delta T\right]^2 + \left(\frac{1}{\mu_A} - \frac{1}{\mu_A^o}\right)\tau^2 - 2\Gamma > 0\ , \qquad (4)$$

where ΔT is the difference between the current temperature of the laminate and its stress-free temperature, and where k_1 is another laminate constant defined by

$$k_1 = \frac{E_A^o\left[\alpha_A^o + B\alpha_T^o - C\right]}{1 - \nu_A^o B}\ . \qquad (5)$$

The parameter C is defined by the thermo-elastic properties of individual plies (in italics)

$$C = \alpha_T + \nu_A \alpha_A\ . \qquad (6)$$

In (4), the term $k_1 \Delta T$ has the property that when $s = -k_1 \Delta T$ and $\tau = 0$ the axial stress in the 90^o plies of an undamaged laminate is zero. It is also the stress at which the ply cracks in the 90^o plies of a damaged laminate (for which there is no in-plane shear strain) are *just* closed. It is emphasised that the term $k_1 \Delta T$ appearing in (4) takes full account of the effects of thermal residual stresses in the laminate. The criterion (4) is quadratic in the effective stress s, the shear stress τ and the temperature difference ΔT. The relation (4) is in fact an approximation as very small shear coupling terms and a shear expansion coefficient have been assumed to be zero. For balanced undamaged laminates they are precisely zero, but when the laminate has a distribution of ply cracks they have small values due to the fact that if a θ-ply has cracks then there are no cracks in the corresponding $-\theta$ ply leading to an asymmetry that generates small non-zero shear coupling and shear thermal expansion terms. This effect is most easily observed by using the software system

known as PREDICT, which is a specific application module of the commercial product developed by NPL that is known as CoDA [8].

When using (4) to undertake energy balance calculations determining the conditions for first ply failure, the laminate and stress field are rotated so that the ply in which ply crack formation is being considered has a 90^o orientation. Ply cracking damage in the 90^o plies of a length 2L of laminate is defined by $\{L_1, L_2, \ldots L_n\}$ where n is the number of cracks in length 2L of the 90^o plies and where L_I, I = 1...n denote the distances between neighbouring cracked planes. For this case the energy absorption per unit volume for length 2L of laminate appearing in (4) is given by

$$\Gamma = \frac{h^{(90)}}{hL} \sum_{j=1}^{M} \delta_j \gamma_j^{(90)} \quad , \qquad (7)$$

where $2h^{(90)}$ is the total thickness of all 90^o plies in the laminate having total thickness 2h, and where M is the number of potential cracking sites in 90^o plies which are ordered in a regular way, e.g. from top to bottom in the plies which are taken in order from the centre of the laminate to the outside, symmetry about the mid-plane of the laminate being assumed. The quantity $2\gamma_j^{(90)}$ is the fracture energy for the j^{th} potential cracking site of the 90^o plies. The parameters δ_j describe the crack pattern in the laminate such that $\delta_j = 1$ if the j^{th} site of the 90^o ply is cracked and $\delta_j = 0$ otherwise. An examination of the L.H.S. of the energy-based first ply cracking criterion (4) reveals that, even though it involves four distinct loading modes characterised by the parameters σ_t, σ, σ_T and τ, it is in fact a quadratic function of only two independent parameters for a given temperature, namely the effective stress s and the applied shear stress τ. A 'two-dimensional' first ply failure envelope can be constructed that captures the effects of through-thickness loading, in-plane biaxial and shear loading on the formation of the first ply cracks. This is a new approach and needs to be applied to all orientations of the plies in one half of the laminate.

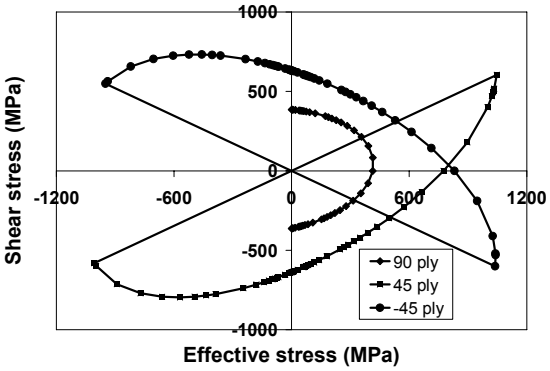

Figure 1: *First ply failure envelopes for a CFRP quasi-isotropic laminate for the case when $\Delta T = -90^o C$.*

Fig.1 shows the first ply failure envelopes for the 90^o and the $\pm 45^o$ plies of a CFRP quasi-isotropic $[45/-45/0/90]_s$ laminate having thermal residual stresses ($\Delta T = -90^o C$). The envelope for the 0^o ply involves very large stresses and is not shown. The fracture energy for ply cracking is assumed to be 150 J/m^2. There are mixed-mode loading issues that also need to be considered. Each point is obtained from a single run of PREDICT [8]. The appropriate fracture energy can be determined from a single test for a simple loading case, e.g. uniaxial tension.

The envelopes suggest that during loading ply cracking always occurs first of all in the 90^o ply. It is worth noting that the 90^o ply is located next to the mid-plane so that the total thickness of the 90^o ply is double that of any $\pm 45^o$ and 0^o plies. The envelopes are not closed, but terminate at points of ply crack closure. The lines drawn joining the closure points pass through the origin as shown in Fig.1.

Fig.2 shows first ply failure envelopes for a GRP $[-55/55]_s$ angle-ply laminate having thermal residual stresses such that $\Delta T = -90^o C$. The envelopes again are

not closed, but terminate at points of ply crack closure as shown in Fig.2. The lines joining the closure points again pass through the origin. Again the fracture energy for ply cracking is assumed to be 150 J/m^2, and each point is obtained from a single run of PREDICT [8].

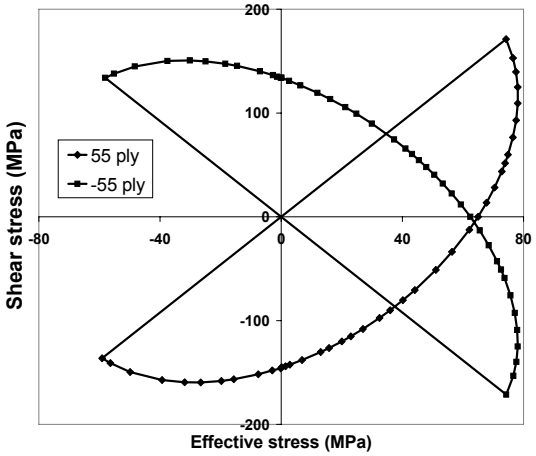

Figure 2: *First ply failure envelopes for a GRP [55/–55]$_s$ laminate for the case when ΔT = –90^{o}C.*

4. Cracking in small scale multi-layers

The first type of multi-layer having thin layers is a laminated composite where the ply thicknesses are reduced in size. Figure 3 shows the first ply cracking stress as a function of ply thickness predicted (using PREDICT [8]) for typical GRP and CFRP cross-ply laminates subject to uniaxial loading and a temperature difference ΔT = -85^{o}C. The total thickness of the laminate is always 4 mm so that as the ply thickness is reduced the number of plies progressively increases.

It is seen from Fig.3 that as the ply thickness reduces the first ply cracking stress increases (dramatically for the case of CFRP). Failure theories based on stress-based criteria would not predict this effect that has been observed in experiments (e.g. [7]).

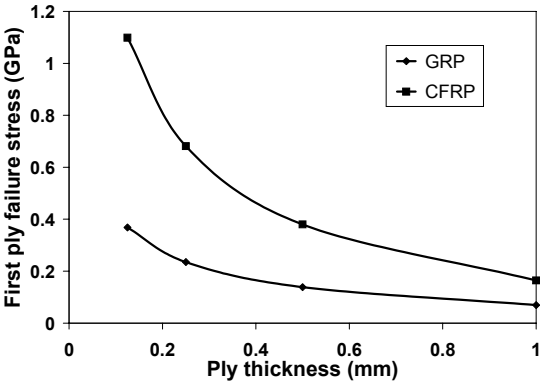

Figure 3: *Effect of ply thickness on first ply cracking stress for CFRP and GRP laminates.*

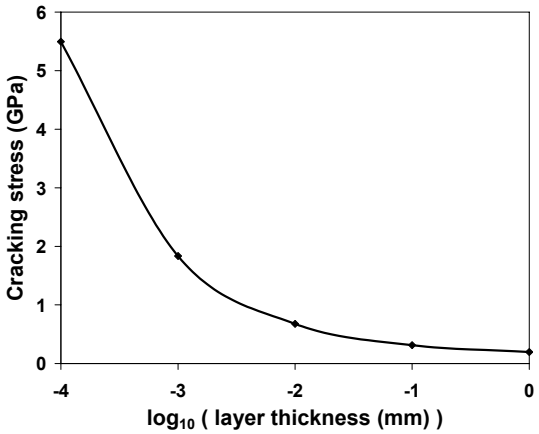

Figure 4: *Dependence of cracking stress on the thickness of the layers.*

The second type of composite involves nanoscale metal-ceramic super-lattices [9] where alternating very thin layers of steel and titanium nitride are bonded together to form a material system that exhibits improved properties when compared to the bulk properties of the weakest constituent (titanium nitride). The problem is to try to explain observed improvements in performance using physical principles. Fig.4 shows the cracking stress for the titanium nitride layers when 16 multi-layers having the same thickness are uniaxially loaded when ΔT = -500^{o}C. It is seen that as the layer thickness decreases, the cracking stress increases to the extent that through-thickness cracking damage is virtually impossible. Other types of damage occur,

such as dislocation formation, and the modelling of this type of damage will now be discussed.

5. Dislocation formation in multi-layers

A method [10] will now be described for predicting defect formation in multi-layer materials using energy-based rather than stress-based criteria for the case where the layers exhibit an epitaxial structure having a lattice mismatch. Defects will be considered in the form of arrays of edge dislocations in individual layers of the system. Continuum methods [10] are used to develop solutions, extending the use of stress-transfer methods that were originally developed for ply cracks in composite laminates. Dislocations are modelled as cracks having modified boundary conditions where a prescribed displacement profile is imposed in place of the usual stress-free condition. By modifying the displacement discontinuity profile of the dislocation in the core region, it is possible to remove the troublesome 1/r stress singularity that is encountered when using the classical model of an edge dislocation, which is much stronger than the $1/r^{1/2}$ singularity that is associated with cracks. The dislocation model can be used to examine the onset of yielding, for multiaxial stress states, of epitaxial metals in constrained conditions, and its dependence on layer thickness. The dislocation model can also be used to model defect formation in epitaxial semi-conductor systems where the practical problem is to enable desirable electronic properties while minimising defect formation that degrades electronic performance. The validity of the model has been demonstrated [10] by comparing in Fig.5 predictions of dislocation densities with an exact analytic solution [11] that is possible only for the very special case of a system of two layers where the only difference between the layer properties is their lattice parameter.

A key issue for dislocation formation is the prediction of the critical thickness below which it is energetically impossible for any dislocations to form. This concept is illustrated, for a silicon-germanium system, where the normalised energy (calculated using the methods described in [10]) is plotted in Fig. 6 as a function of the ratio b/p where the dislocation separation is p and where b is the Burgers vector for the dislocations. For thicknesses lower than the critical thickness of 11.211 nm, where the energy curve minimum occurs when b/p = 0, the energy curve does not exhibit a local minimum and the existence of an equilibrium distribution of dislocations is then impossible. For thicknesses greater than the critical value, the local minimum that occurs defines the normalised equilibrium dislocation density b/p.

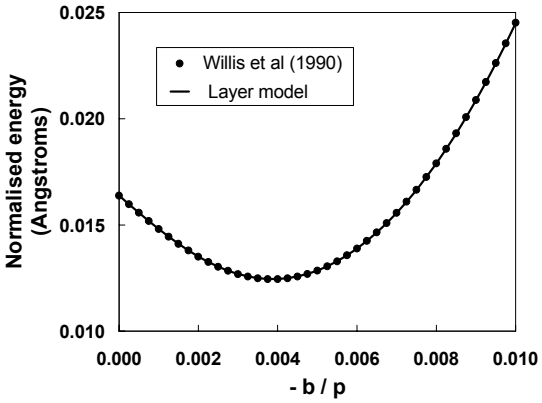

Figure 5: *Comparison of predictions with an exact analytical solution.*

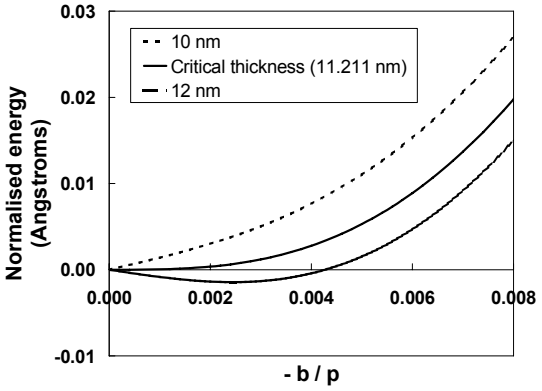

Figure 6: *Energy plots showing how to*

identify the critical thickness for dislocation formation.

The dislocation analysis [10] has been applied to capped dislocations and the resulting critical thicknesses as a function of germanium content are shown in Fig.7 and compared with the uncapped solution and predictions of the approximate analytical solution given by the Matthews and Blakeslee model (see [10]).

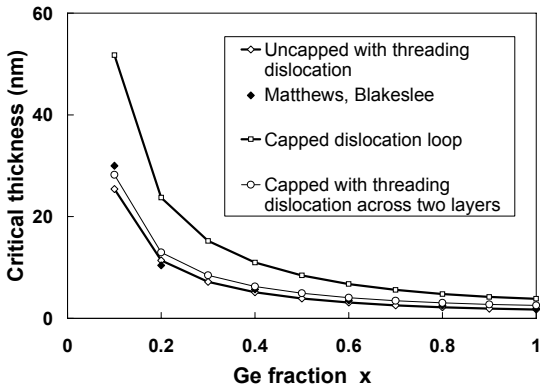

Figure 7: *Plots showing the dependence of the critical thickness for dislocation formation on germanium content.*

It is seen that as the germanium content increases the critical thickness decreases implying the easier it becomes for dislocations to form.

5. Conclusions

The results of this paper have shown that energy methods are able to explain various damage phenomena that occur in multi-layer systems at various length scales. When applied to laminated composites, the energy approach can explain experimentally observed ply thickness and ply layup effects, including the increasing difficulty of forming ply cracks when the layers are thin. A similar effect is shown to occur when the layer thickness of metal-ceramic super-lattices is reduced. Energy methods are also shown to explain the occurrence of critical layer thicknesses for dislocation formation in semi-conductor materials.

Acknowledgement

The results presented in this paper were derived in projects supported by the DTI Materials Measurement Programme and the NPL Strategic Research Programme.

References

[1] Part A of International Exercise on Failure Prediction in Composites, (1998), a series of papers in special issue of *Comp. Sci. Tech.*, **58** (7).
[2] Part B of International Exercise on Failure Prediction in Composites, (2002), a series of papers in special issue of *Comp. Sci. Tech.*, **62** (12 and 13).
[3] Part C of International Exercise on Failure Prediction in Composites, (2004), a series of papers in special issue of *Comp. Sci. Tech.*, **64** (3 and 4).
[4] L N McCartney, (2004, April) Proc. Advanced Polymer Composites for Structural Applications in Construction Conference, Guildford.
[5] L N McCartney, (2003), *Proc. Instn. Mech. Engrs.*, **217**, Part L: J. Materials: Design & Applications, 163-199.
[6] L N McCartney, (2005), *Engng. Fract. Mech.*, **72**, 909-930.
[7] P Johnson and F-K Chang, (2001), *J. Comp. Mater.*, **35,** 2009-2035, and **35**, 2037-2073.
[8] Software system 'PREDICT' which is a specific module of CoDA. (see www.npl.co.uk/npl/cmmt/cog/coda.html)
[9] Special issue of *Scripta Materialia*, **50** (6), March 2004.
[10] L N McCartney, (2005), *Phil. Mag.*, **85**, 1575-1610.
[11] J R Willis, S C Jain and R Bullough, (1990), *Phil. Mag.*, **62**, 115-129.

EFFECTS OF PHYSICAL AGEING ON YIELDING KINETICS OF POLYPROPYLENE

M. El Majdoubi, T. Vu-Khanh*, E. David
Université du Québec - École de technologie supérieure
Department of Mechanical Engineering
1100 Notre-Dame Street West
Montreal, Quebec, Canada, H3C 1K3
(*corresponding author : toan.vu-khanh@etsmtl.ca)

Abstract

This work aims to investigate the influence of ageing, at room temperature, and for different ageing times, on the yielding kinetics of polypropylene, having different morphologies, induced by different cooling rates during molding. Compressive tests were performed over various loading rates to analyze the effect of ageing on the yielding kinetics. Ree-Eyring's model was used to analyze the effect of ageing on the yielding behavior. Ageing only slightly affects the yielding stress, but it causes a significant variation in the pre-exponential factor values. The results suggest that plastic deformation implies more cooperative segmental motions for higher crystalline content, which result in higher values of the pre-exponential factor containing the entropy term. The parameters related to the β-process did not undergo any significant change during ageing, suggesting that ageing at room temperature does not affect localized molecular motions.

Dielectric spectroscopy was conducted in the frequency domain using a broadband dielectric spectrometer for the lowest and highest crystalline morphologies in both aged and unaged states. The results showed significant changes in the dissipation factors of the primary relaxations with ageing time, for both low and high crystallinity samples. On the other hand, no change in the secondary relaxation was observed in either case. DSC measurements did not show any effect of ageing at room temperature the degree of crystallinity as well as the melting temperature of polypropylene.

Keywords: Polypropylene, Ageing, Crystallity, Yielding, Plasticity, Microstructure, Molecular Relaxation.

1. Introduction

Polypropylene (PP) is one of the most widely used polymers. Despite the use of antioxidants, ageing can pose significant problems in practical applications of these materials. Ageing is defined as the occurrence of a gradual change of state and properties that affects the mechanical performance and shortens the useful live of polymers. There are two types of ageing; physical ageing, and chemical ageing. In chemical ageing, changes of the material structure are irreversible such as ruptures of chemical bonds and oxidation; whereas physical ageing is reversible. It is an evolution of the polymer structure towards a more stable thermodynamic state, after cooling from its liquid state. During cooling, molecular rearrangements, due to the drop in temperature, decrease to such a point that they are much slower than the imposed rate of cooling. The material is thus frozen in an unstable thermodynamic state and tends to reach a more stable conformation with time. The evolution of the material towards its thermodynamic equilibrium is

called physical ageing. For polypropylene, at the ambient temperature, chemical ageing does not take place. The rupture of chemical bonds by oxidation has been found to occur only within a depth between 8 to 10 nm [1, 2]

Several reported studies on polypropylene have showed important changes of its mechanical and physical properties after ageing at ambient temperature. Gezovich and Geil [3] reported an increase in the yield stress with ageing of a polypropylene film, without any change of its crystallinity or of its crystalline structure. Schael [4] explained the effect of ageing by the reduction of the free volumes distributed in the bulk material, resulting a reduction in the mobility of the chain segments. Kapur and Rogers [5] noted an increase in the tensile modulus, the dynamic shearing modulus, and the tensile yield stress after physical ageing. However the yield strain and the relaxation rate decrease with ageing. To interpret these results, the authors suggested that the mechanisms of ageing could imply molecular rearrangements comparable with those of the secondary crystallization process, with a reduction of the mobility of the chain segments in the intercrystalline areas. Agarwal and Schultz [6] explained the increase in the density during to ageing, by a volume reduction in the noncrystalline regions. Due to this reduction, the amorphous regions are partially confined in more restricted regions, resulting in a reduction of the mobility of the polymer. To explain the effect of physical ageing on mechanical properties of semicrystalline polymers such as polypropylene, Hutchinson and Kriesten [7] associated the reduction in the relaxation rate of polypropylene after ageing at ambient temperature, to the rearrangement of the amorphous mesophase between the crystallites and the inter-lamella amorphous phase.

This work aims to investigate the influence of ageing at room temperature, on the mechanical performance of polypropylene with different morphologies, induced by different cooling rates during molding. Ree-Eyring's model was used to analyze the kinetics of the yielding. DSC measurements were also performed in order to determine the effect of ageing at room temperature the degree of crystallinity as well as the melting temperature of polypropylene. Dielectric spectroscopy measurements were conducted in the frequency domain using a broadband dielectric spectrometer for both aged and unaged states.

2. Experimental

The isotactic polypropylene (PP) was supplied by Dow Chemical, Inspire H308-02Z. The PP pellets were compression molded into plaques (22.5cm x 225.5 x 3.5mm) at 205°C, under a pressure of 4.3 MPa. The plaques were cooled down at various cooling rates using either running water or immersion in water baths at various temperatures. Four cooling rates were attained: 1°C/min, 10°C/min, 50°C/min, and quenching in cold water (>100°C/min). Compressive tests were performed on an Instron Automated Material Testing System, Model 4206, at various crosshead speeds over various temperatures to analyze the effect of ageing on the yielding kinetics. Dielectric spectroscopy measurements were conducted in the frequency domain using a broadband dielectric spectrometer from Novocontrol on a 20 mm-diameter circular disk with the parallel surfaces coated with evaporated electrodes. Since the leakage currents flowing on the sample edges were found to be negligible, guarded electrodes were not used. Differential-scanning-calorimeter measurements were carried out on a Perkin-Elmer DSC-7 calorimeter. The heat of fusion was measured at a constant heating rate (20°C/mn), using samples with a mass between 6 and 10 mg.

3. Results and discussions

To investigate yielding behavior, compression tests were carried out at the various temperatures, ranging from -60°C to 40°C, and various loading rates, ranging from 0.0003 to 0.3 s-1 (corresponding to crosshead speeds between 0.2 and 200 mm/min). Ree-Eyring viscosity theory [8] was used to analyze the yielding kinetics. The yield stress is frequently derived from the following equation:

$$\frac{\sigma_y}{T} = \frac{R}{V^*}\left(\frac{\Delta H}{RT} + 2.303\log\left(\frac{2\dot{\varepsilon}}{\dot{\varepsilon}_o}\right)\right) \quad (1)$$

where ΔH is the activation energy of the yielding process, T is the absolute temperature, $\dot{\varepsilon}$ is the strain rate (proportional to the cross-head speed), V^* is called the activation volume, $\dot{\varepsilon}_o$ is the pre-exponential factor and R is the universal gas constant. In fact, over a very large range of temperatures and loading rates, the yielding kinetics of polymers has been shown to be controlled by two molecular motion processes acting in parallel [9, 10]. Equation (1) has been modified from the theory of Ree-Eyring and expressed by:

$$\frac{|\sigma_c|}{T} = \frac{|\sigma_{c_\alpha}|}{T} + \frac{|\sigma_{c_\beta}|}{T}$$
$$= \frac{R}{V^*_{t_\alpha}}\left[\frac{\Delta H_\alpha}{RT} + 2.303\log\left(\frac{2\dot{\varepsilon}}{\dot{\varepsilon}_{o\alpha}}\right)\right] + \frac{R}{V^*_{t_\beta}}\sinh^{-1}\left[\frac{\dot{\varepsilon}}{\dot{\varepsilon}_{o\beta}}\exp\left(\frac{\Delta H_\beta}{RT}\right)\right] \quad (2)$$

where $V^*_{t_\alpha}$, $V^*_{t_\beta}$, $V^*_{c_\alpha}$, $V^*_{c_\beta}$, ΔH_α, ΔH_β, $\dot{\varepsilon}_{o\alpha}$ and $\dot{\varepsilon}_{o\beta}$ have the same meanings as in Equation (1) but are related to the primary (α) and the secondary (β) relaxation processes.

Figure 1 shows the semi-logarithmic plots of σ_y/T against loading rate, for the samples with lowest and highest crystalline levels (42 % and 66 %). The plots exhibit two distinct areas with two different slopes. In area I, corresponding to high temperatures and low loading rates, the primary molecular relaxation dominates. Whereas in area II, corresponding to lower temperatures and the higher loading rates, the secondary molecular relaxation also contributes to the yielding kinetics, resulting in a different activation energy. Table 1 shows the values of the parameters $V_\alpha^*, \Delta H_\alpha, \dot{\varepsilon}_{o\alpha}, V_\beta^*, \Delta H_\beta, \dot{\varepsilon}_{o\beta}$, in Eq. [2] determined by best fitting the data shown in Fig. 1 with this equation. It can be observed that only $\dot{\varepsilon}_{o\alpha}$ and ΔH_α, corresponding respectively to the jump frequency (or entropy) and the energy barrier of the polymer segments during plastic deformation, change with the crystalline level.

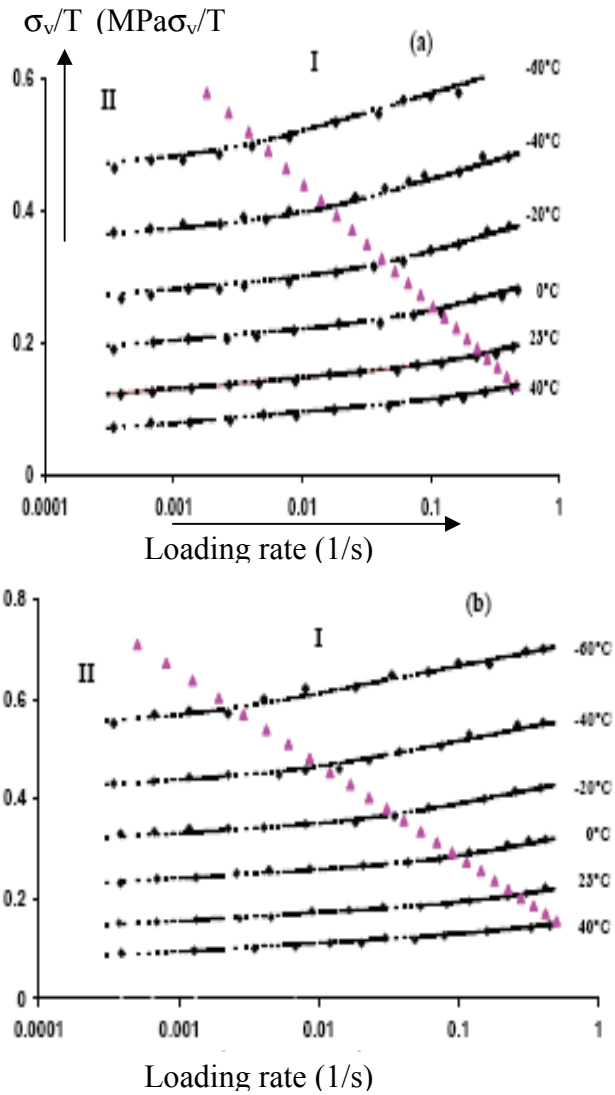

Figure 1: *σ_y/T versus loading rate; (a) 42%, (b) 66%*

The Ree-Eyring model assumes that, in moving from one equilibrium position to another, a molecule (or a segment of a macromolecule for polymers) must pass over an energy barrier. In the absence of stress, the segments of the polymer jump over the barrier very infrequently and they do so in random directions. The rate of jump between two equilibrium positions is expressed by an Arrhenius-type equation as:

$$jump\ rate = \dot{\varepsilon}_o \exp\left[-\left(\frac{\Delta H}{RT}\right)\right]$$

(3)

where $\dot{\varepsilon}_o$ ~ Forward jump rate ~ Backward jump rate at equilibrium.

Cris.	42%	50%	66%
ΔH_α (kJ/mol)	313	329	366
$\dot{\varepsilon}_{o\alpha}$ (s^{-1})	6.0 x10^{44}	3.0 x10^{47}	4.0 x10^{52}
V_α^* (m^3/mol)	2.336 x10^{-3}	2.337 x10^{-3}	2.349 x10^{-3}
ΔH_β (kJ/mol)	25.5	27.1	29.7
$\dot{\varepsilon}_{o_\beta}$ (s^{-1})	2 x10^4	5 x10^4	11 x10^4
V_β^* (m^3/mol)	9.215 x10^{-4}	9.396 x10^{-4}	9.998 x10^{-4}

Table 1: *Ree-Eyring parameters of α and β relaxations controlling yielding for different crystalline contents*.

It has also been proposed [11] that the parameter $\dot{\varepsilon}_{o\alpha}$ contains an entropy term, ΔS, that varies with physical ageing. In the above equations, the activation energy ΔH corresponds to the height of a potential energy barrier over which a molecular segment has to pass when it makes a single step of displacement, whereas the activation entropy ΔS is a measure of the number of segments jumping over the barrier ΔH. According to [11], the parameter $\dot{\varepsilon}_{o\alpha}$ can be expressed by:

$$\dot{\varepsilon}_{o\alpha} = \frac{J_o}{2} = \frac{1}{2}\nu \exp\left(\frac{\Delta S}{R}\right) \qquad (4)$$

where ν, frequency factor, may be taken to be equal to the Debye frequency, as a first approximation. The increases in both parameters with higher crystalline content suggest that plastic flow is mostly controlled by the crystallized polymer.

Varying the ageing time at room temperature up to about eight months does not reveal any effect on the Ree-Eyring parameters controlling the primary (α) and the secondary (β) relaxations for all crystalline levels. The results confirm again that yielding energy dissipates mostly in the crystallized polymer. In fact, at room temperature, the bulk amorphous polymer is not frozen in an unstable thermodynamic state because its T_g is about 0°C. However, it has been demonstrated that the amorphous material in contact with the crystalline lamellas is partially blocked and cannot move freely. This explains a peak sometime observed in PP around the upper glass transition temperature between 40-100°C. It has also been suggested that physical ageing can take place at temperatures below this region, in the amorphous-crystalline interfacial polymer [7]. It is thus interesting to note that compressions tests also suggest that ageing at room temperature seems to alter slightly the number of jumping segments involved in plastic flow of PP. The entropy corresponding to the primary (α) relaxation of yielding seems to slightly decrease with ageing time as shown in Table 2. This may be due to physical ageing of PP at room temperature.

t_a (days)	$\dot{\varepsilon}_\alpha$ (s^{-1})	ΔS_α (J/mol.K)
2	6.1 x 10^{44}	618
15	9.3 x 10^{43}	603
60	3.85 x 10^{43}	596
240	2.21 x 10^{43}	590

Table 2: *Effect of ageing time at room temperature on jump frequency factors of primary relaxation in 42% crystalline sample*.

To verify in more detail this effect, compressions tests were also performed at higher temperatures. The results indeed revealed another relaxation process as shown in Fig. 2. Above about 60°C, the plots of σ_y/T *vs Log* $\dot{\varepsilon}$ show another change in slope. This can be explained by the particularly broad glass transition region in PP as discussed above. In this semicrystalline material, T_g can take place

over a broad range of temperatures, with a lower limit around 0°C, corresponding to T_g of the bulk amorphous material, and an upper limit between 40-100°C, corresponding to the amorphous phase that is partly entangled with the crystalline lamellas. The first term in Eq. (2) of the α process can thus be divided into two relaxations α_1 and α_2 with increasing temperature in a similar way:

$$\frac{\sigma_\alpha}{T} = \frac{\sigma_{\alpha 1}}{T} + \frac{\sigma_{\alpha 2}}{T} \qquad (5)$$

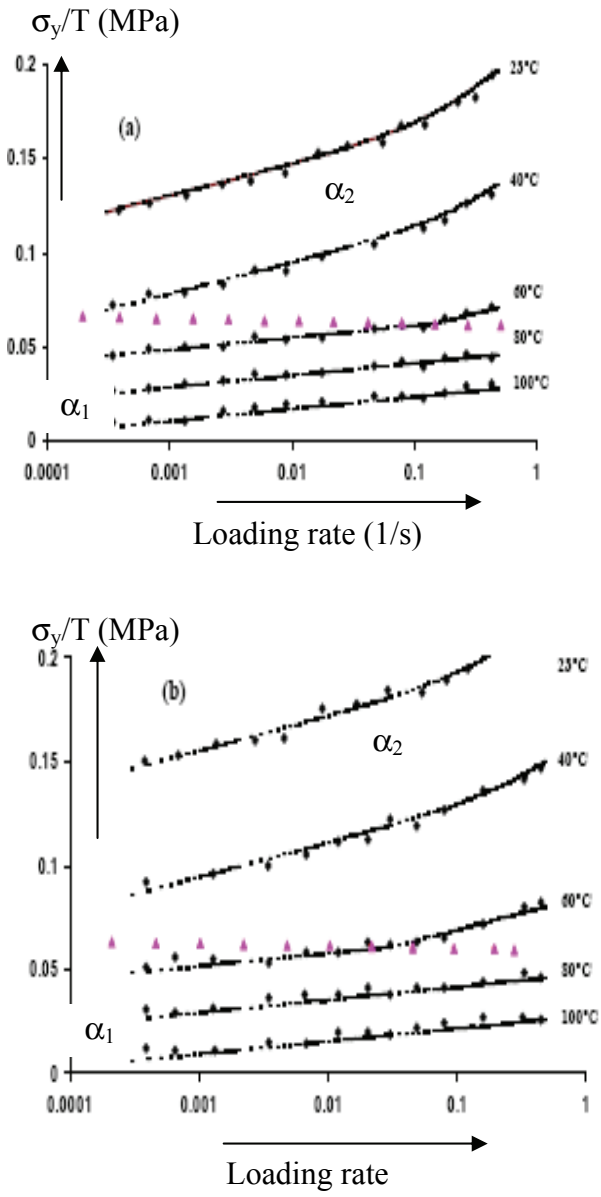

Figure 2: *σ_y/T versus loading rate for 42% (a) and 66% crystalline sample.*

The experimental results of compression test at high temperatures suggest that ageing does not affect the jump frequency factor of α_1 but only that of α_2 as shown in Table 3. The results confirm that physical ageing takes place in the amorphous regions next to the crystalline lamellas, due to an unstable conformation state, induced by crystallization during cooling.

t_a (days)	$\dot{\varepsilon}_{o\alpha 2}$ (s^{-1}) 42 %	$\dot{\varepsilon}_{o\alpha 2}$ (s^{-1}) 66 %
2	4.63×10^{44}	2.84×10^{52}
15	8.3×10^{43}	7.14×10^{51}
60	2.35×10^{43}	3.20×10^{51}
240	4.06×10^{42}	2.95×10^{50}

Table 3: Effect of ageing time at room temperature on jump frequency factors of primary relaxation α_2.

To verify the above assumptions, dielectric spectroscopy was used to analyze the aged and unaged samples. Dielectric spectroscopy has proven to be very useful for studying the conformation, the structure and the dynamics of relaxation processes of polymeric systems. Since the reorientation of the molecular dipoles within the polymeric chain results in a dielectric activity that can be measured, the dielectric spectroscopy allows to characterized the various relaxation processes, from localized motions (<< 1 nm) to segmental motions (1 – 2 nm) and chain motions. The dielectric processes in the case of wholly amorphous polymers have been well studied and are well documented [12]. Most amorphous polymers exhibit a principal, or α-process, and a secondary, or β-process, located at higher frequency (or lower temperature). While the α-relaxation is related to the glass transition of the system, the β-relaxation is generally consider to originate from localized fluctuations but the actual molecular mechanisms is not yet fully understood [12]. For semi-crystalline polymers such as PP, the relaxation processes, especially the glass transition process, are strongly perturbed by the

presence of the crystal phase. Furthermore, dielectric relaxation processes can also occur directly in the crystals for several semi-crystalline polymers such as PE or PP.

The dielectric dissipation factor at 23°C for unaged PP samples, as a function of frequency in the range of 10^{-2} to 10^{3} Hz, is illustrated in Figure 3 for the least and the most crystalline samples in an unaged state.

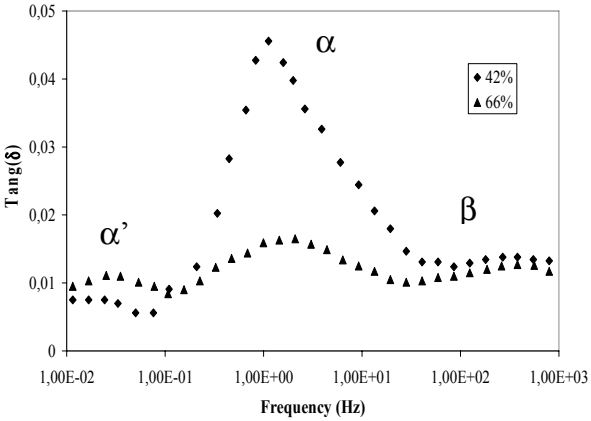

Figure 3: *Dielectric dissipation factor versus frequency for high- and low-crystalline contents*.

The results display three distinct peaks over the above frequency range. Since the crystalline relaxation process, possibly involving screw-type motion of the chains [13], it lies at the lowest frequency, and can be labelled α'. On the other hand, the sub-glassy β-process, related to the localized chain segment motion, occurs at high frequency. Between these two extremes, a third relaxation peak α can be seen for both crystalline levels. The observed higher α' peak of the 66% crystalline sample confirms that this relaxation takes place in the crystalline region. Conversely, the α peak would correspond the dielectric activity in the amorphous polymer, confirmed by the higher α peak of the 42% crystalline sample.

The effects of physical ageing at room temperature for three months on the dielectric response of PP are shown in Figures 4 and 5 for the 42% and 66% crystalline samples respectively.

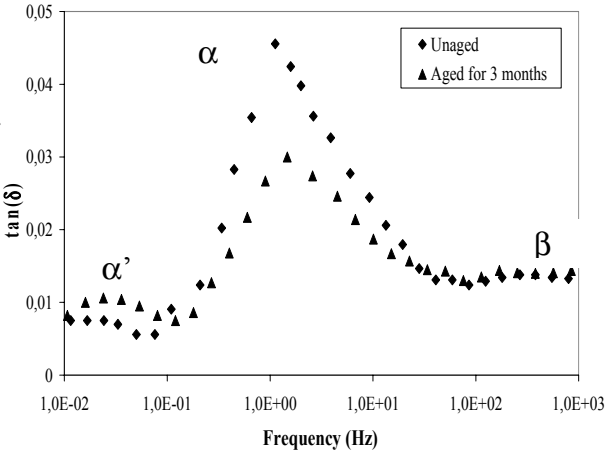

Figure 4: *Effect of ageing on dielectric dissipation factor for 42% crystalline sample*.

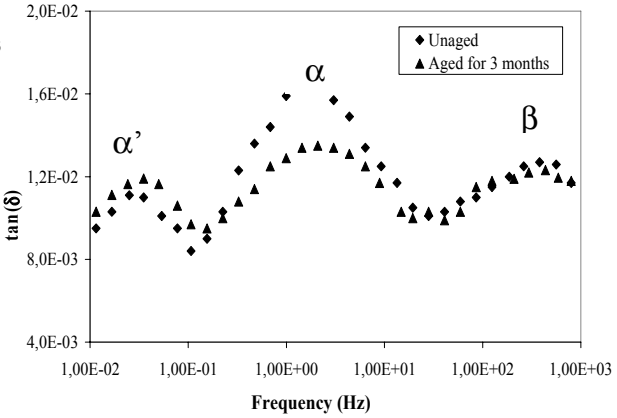

Figure 5: *Effect of ageing on dielectric dissipation factor for 66% crystalline sample*.

The results indicate that ageing does not affect the side motions of the secondary or β-process located at higher frequency. This is consistent with the lack of influence of physical ageing on the secondary relaxation of the yielding process observed above. The primary relaxations, α' and α, undergo two opposite effects of ageing at room temperature. The peak α' is increased whereas the peak α is reduced by physical ageing. These variation confirm again that α' is related to the dielectric activity in the crystalline polymer and α corresponds to

that of the amorphous region. Physical ageing strongly reduces the dielectric dissipation factor of the amorphous region but increases the dissipation of the crystalline material, suggesting a reduction in the mobility of the amorphous polymer.

For most amorphous thermoplastics, the reduction in the mobility of molecular segments usually results in an increase in yield stress. However, this effect is not observed in the case of PP. Figures 6 and 7 show respectively the effects of ageing time at room temperature on the yield stress, measured under various test temperatures.

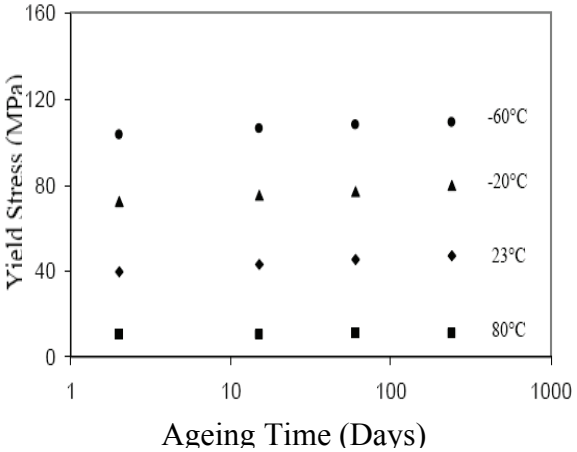

Figure 6: *Effect of ageing time at room temperature on yield stress (42% crystalline sample)*

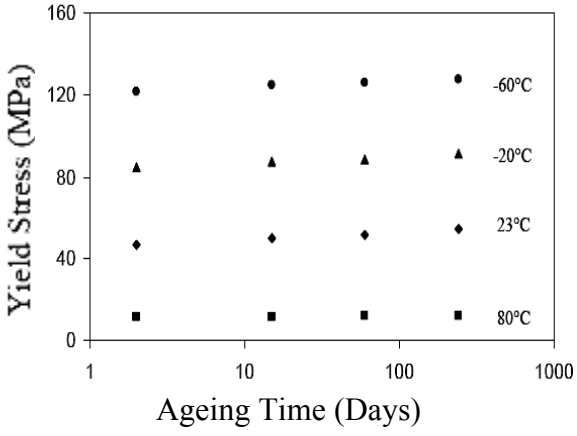

Figure 7: *Effect of ageing time at room temperature on yield stress (66% crystalline sample)*

It can be seen that physical ageing does not alter the yield stress of PP, regardless of the crystalline content. The results further confirm the dominant role of the crystalline region in the mechanism of yielding discussed above. The results of compression tests at various loading rates and temperatures do not show a significant effect of physical ageing at room temperature on the Ree-Eyring parameters governing yielding kinetics. This can be explained by the fact that yielding energy is mostly dissipated by the crystalline PP. The change in molecular mobility in the amorphous region is not sufficient to alter the yielding behavior of the polymer. In fact a closer look at the data in Figures 6 and 7 could reveal a small increase in the yield stress measured at very low test temperatures. In the region well below the glass transition temperature, the amorphous polymer becomes rigid enough to slightly contribute to plastic deformation.

Acknowledgment

The authors would like to thank the National Sciences and Engineering Research Council of Canada for the financial support of this work.

Conclusion

Varying the ageing time at room temperature up to about eight months does not have a significant effect on primary (α) and secondary (β) relaxation parameters, controlling the yielding kinetics of PP. Energy dissipated in plastic deformation mostly takes place in the crystallized polymer. At room temperature, above Tg (~0°C), the bulk amorphous polymer is not frozen in an unstable thermodynamic state. However the amorphous material partly entangled with the crystalline lamellas is partially blocked and cannot move freely, resulting in a relaxation around the upper glass transition temperature around 40-100°C. Compression tests at high temperatures also revealed another relaxation process above about 60°C. The α process can be divided into two relaxations α_1 and α_2 with increasing temperature. Ageing does

not affect the jump frequency factor of α_1 but only that of α_2. Physical ageing takes place in the amorphous regions next to the crystalline lamellas, due to an unstable conformation state, induced by crystallization during cooling.

Measurements of dielectric dissipation at 23°C in the range of frequencies from 10^{-2} to 10^3 Hz display three distinct relaxation peaks. The peak at lowest frequency corresponds to the relaxation process of the crystalline polymer (α'). The sub-glassy β-process, related to the localized chain segment motion, occurs at high frequency. Between these two extreme, a third relaxation peak α, observed for all crystalline levels, corresponds to the dielectric activity in the amorphous region. Ageing does not affect the side motions of the secondary or β-process located at higher frequency. However, the primary relaxations, α' and α, undergo two opposite effects. The α' peak is increased whereas the α is reduced by physical ageing. These variation confirm again that α' is related to the dielectric activity in the crystalline region and α corresponds to that of the amorphous region. Physical ageing strongly reduces the dielectric dissipation factor of the amorphous region but increases the dissipation factor of the crystalline material, suggesting a reduction in the mobility of the amorphous polymer. Energy of plastic deformation is mainly dissipated by the crystalline region. The reduction in molecular mobility of the amorphous region, due to physical ageing, is not sufficient to alter the yielding behavior of PP.

References

[1] Rjeb A., Letarte S., Elidrissi M. C., Adnot A., Roy D., Clare Y., Kaloustian J. (2000), Polypropylene natural ageing studied by X-ray photoelectron spectroscopy, *Journal of Electron Spectroscopy and Related Phenomena1*, **07**, pp. 221–230

[2] Massey S., Roy D., Adnot A. (2003), Study of natural ageing of polypropylene by X-ray photoelectron spectroscopy, *Nuclear Instruments and Methods in Physics Research*, **B 208**, pp 236-241

[3] Gezovich D. M., Geil P. H. (1968), Morphology of quenched polypropylene, *Polym. Eng. Sci*., **8**, pp. 202-209.

[4] Schael G. W. (1966), A study of the morphology and physical properties of polypropylene films, *J. Appl. Polym. Sci*, **10,** pp. 901-915.

[5] Sudhur Kapur, Rogers C. E. (1972), Ageing of quenched polypropylene, J. *Polym. Sci. A-2,* **10**, pp 2107-2124.

[6] Agarwal M. K., Schultz J. M. (1981), The physical ageing of isotactic polypropylene, *Polym. Eng. Sci*., **21**, pp. 776-781

[7] Hutchinson J. M, Kriesten U. (1994), Physical ageing and enthalpy relaxation in polypropylene, *J. of Non-Crystalline Solid,s* **172-7**, pp. 592-596.

[8] Ree, T.; Eyring, H. (1958) in *Rheology,* vol. II, Eirich, F. R., Ed., New York, Academic Press, chapter III.

[9] Bauwens-Crowet, C.; Bauwens, J. C. ; Homes, G. (1972), The temperature dependence of yield of polycarbonate in uniaxial compression and tensile tests, *Journal of Materials Science*, vol. 7, pp. 176-183.

[10] BAUWENS-CROWET, C. (1973) The compression yield behaviour of polymethyl methacrylate over a wide range of temperatures and strain-rates, Journal of Materials Science, vol. 8, pp. 968-979.

[11] Bauwens, J. C. (1986) in *Failure of Plastics*, BROSTOW, W.; CORNELIUSSEN, R. D., Eds., Munich, Hanser, chapter XII.

[12] Schönhals A. (1997), "Dielectric Properties of Amorphous Polymers", in *Dielectric Spectroscopy of Polymeric Materials*, J.P. Runt, J.J. Fitzgerald (Ed's), American Chemical Society, Washington, DC.

[13] Boyd R.H. (1985), "Relaxation processes in crystalline polymers: molecular interpretation – a review", *Polymer*, **26**, pp. 1123-1133.

PHOTOAGEING AND FRACTURE BEHAVIOUR OF A POLYPROPYLENE FILM

F. Benkhenafou
Département de physique B.P. n° 119, Université A.B., Tlemcen 13000 Algérie

M. Naït-Abdelaziz
Laboratoire de Mécanique de Lille, B^{d} P. Langevin, Villeneuve d'Ascq 59655 France

F. Zaïri
Laboratoire de Mécanique de Lille, B^{d} P. Langevin, Villeneuve d'Ascq 59655 France

M. Chikh-Bled
Département de physique B.P. n° 119, Université A.B., Tlemcen 13000 Algérie

J. Verdu
Laboratoire d'ingénierie des Matériaux, 151 B^{d} de l'hôpital, Paris 75013 France

Abstract

The effect of photoageing on the behaviour of isotactic polypropylene films was studied on samples of weight average molar mass M_w=270Kgmol^{-1}. The chemical modifications (molar mass, carbonyl and hydroperoxide indexes) of the material were analysed. The influence of photoageing on the fracture toughness was examined by using the EWF and the J-integral methods.

Keywords: EWF, J-integral, elastic-plastic fracture, finite element method, photooxidation, polypropylene film.

1. Introduction

Polymer films have many major applications in the industry. Their physical and mechanical properties are then important from an industrial point of view. Over the past four decades, considerable progress has been achieved in the understanding of the fracture of polymers at a molecular level. However, the understanding of the macroscopic fracture mechanics in ductile polymers has still to be developed. More precisely, an accurate evaluation of the fracture toughness of polymer films requires to improve the methodologies.

The global approach of the fracture mechanics is now commonly used for the characterisation of the materials fracture. In this energy approach, it is considered that the fracture phenomenon is initiated from a pre-existing crack. However, this approach does not require the knowledge of the stress and strain fields around the crack tip. Due to significant deviations from linear elastic fracture mechanics (LEFM) under large-scale crack tip plasticity, essential work of fracture and J-integral methods are commonly considered as quite good approaches to

quantify fracture toughness in this configuration. However, in particular for polymer films, there is still a great effort to do because of the complex behaviour of such materials and their sensitivity to many factors (such as strain rate, temperature, ageing...).

It is well known that polymers are sensitive to environmental parameters and in particular to ultraviolet (UV) radiation which affects their intrinsic mechanical properties. The loss of mechanical integrity reflects modifications of the macromolecular skeleton such as polymer chain scission and cross linking. General features of the mechanism of photodegradation in polymers has been intensively investigated and they are fairly well understood [1-6] for most of common polymers. However, various aspects of the involved mechanisms remain unelucidated. Furthermore, the understanding of the link between the photodegradation process and the macroscopic mechanical behaviour is not really established.

In this work, the photoageing behaviour of a semi-crystalline polypropylene film is examined from a physico-chemical and mechanical properties point of view. The chemical modification (molar mass, carbonyl and hydroperoxide indexes) of the polymer is analysed and correlated to ultimate tensile response. The essential work of fracture and the J-integral methods are used to estimate fracture toughness of the film. Therefore, this paper investigates the techniques to calibrate the fracture mechanics parameters.

2. Background on photoageing

The effect of photoageing on the behaviour of semi-crystalline polymers has been the subject of many investigations [1-6]. This type of chemical ageing is the main component of climatic ageing, i.e. ageing resulting from direct exposure to solar radiations. Photodegradation governed by diffusion of O_2 in the polymer irreversibly modifies the structure and the behaviour of this material. Polypropylene contains impurities which make it especially sensitive to the presence of UV rays. Natural polypropylene without stabilizers and pigments is very sensitive to this kind of degradation.

The primary act of any photooxidation process is the absorption of a photon by the molecule. After absorption, the latter is in an excited electronic state. The potential energy of the excited molecule (400KJ/mol) is much higher when compared with that obtained by increasing the temperature (<100KJ/mol); this explains how certain non-existent processes in thermo-degradation become possible in photodegradation. The energy of the firstly excited molecule can be transferred to another molecule. The photooxidation can be described by the following chemical reactions:

$$\mathrm{Polymer(POOH)} + h\nu \rightarrow P^*$$

$$P^* + O_2 \rightarrow PO_2^*$$

$$PO_2^* + PH \rightarrow POOH + P^*$$

$$\left.\begin{array}{l} P^* + P^* \\ P^* + PO_2^* \\ PO_2^* + PO_2^* \end{array}\right\} \text{ inactive products}$$

The reactions of oxidation in the macromolecule chain of polypropylene start by the decomposition of hydroxides. This reaction self-accelerates by following a closed loop [4] (see Fig. 1).

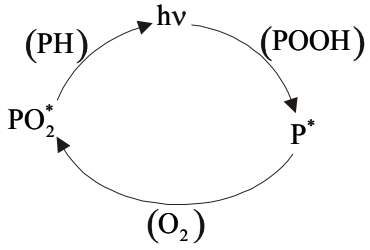

Fig. 1. Diagram of photoageing.

The photooxidation, by the formation of free radicals, leads to molecule scissions. Consequently, it has a large

influence on the physical and mechanical properties of polypropylene. In oxygen diffusion-controlled processes, as photooxidation, the crystallinity of polypropylene increases with rate of oxidation. The scission of the macromolecules involves the formation of smaller molecules which allow easier crystallization. Many researchers observed the decrease of molar mass caused by the scission of chains during the photodegradation of the polypropylene [1].
The decrease of glass transition temperature (T_g) and melting temperature with increase of exposure time was also observed [5]. This kind of ageing generally leads to an embrittlement of polymer materials. It causes a dramatic effect on the mechanical properties and fracture behaviour.
The study of ageing is complicated by the heterogeneous distribution of the chain scissions. Ageing by photooxidation is a surface phenomenon and it locally propagates.

3. Materials and exposure

Extruded films of 100µm thickness were made from a polypropylene (PP) homopolymer (3050MN1 from ATOFINA) stabilized by a mixture of Irganox 1010 and Irgafos 168 (0.5% by weight). The number and weight average molar masses, determined by size exclusion chromatography (SEC), were M_n = 55Kgmol^{-1} and M_w = 270Kgmol^{-1} respectively.
The crystallinity rate, determined by differential scanning calorimetry (DSC), was 65%. The PP was selected because it can be considered as a model material according to its sensitivity to photoageing.
The PP films were exposed in reactors equipped with a fluorescent lamp ($300<\lambda<450$nm; λ_{max}=365nm) at 70°C in air with free edges or in wooden frames 10x20cm^2 (Fig. 2). These boundary conditions avoid edge effect, so that the film is considered infinite at the scale of heterogeneous oxidation phenomena.

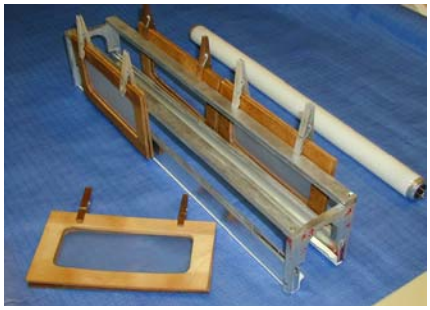

Fig. 2. Set-up for the photoageing of films.

After ageing, tension samples of 25mm length and 4mm width, were cut out from the films using a MTS H2 stamp. Tensile tests were performed on an Instron 4502 under a nominal strain rate of 50mm/min. Load is measured by using a load cell of 1KN full range with a relative error of 0.5 %. As shown in Fig. 3, the yield stress remains quite constant and is not dependent on the exposure time. One can conclude that yield stress is not a convenient mean to describe the polymer lifetime.

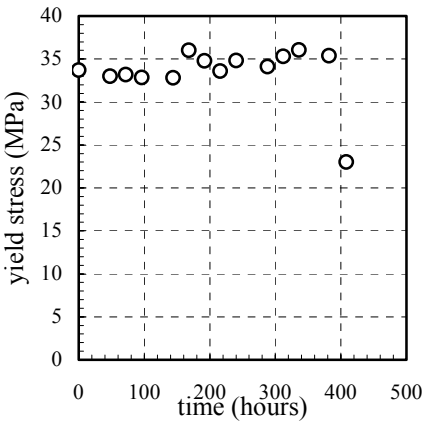

Fig. 3. Evolution of yield stress during exposure.

According to the literature, the ultimate stress can not be considered as a representative parameter to describe the lifetime of polymers [6]. On the other hand, the ultimate strain is generally considered as a suitable indicator of photoageing. As shown in Fig. 4a, the ultimate strain remains almost constant

at a value of about 830% during the initial period of exposure and decreases abruptly after 305±10h to reach a value close to the initial yield strain. An induction time may thus be defined as the time elapsed from the beginning of exposure to this ductile-brittle transition.

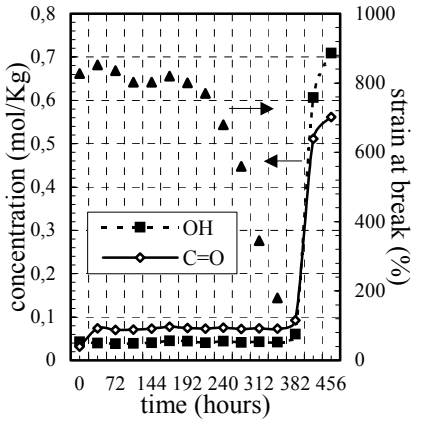

(a)

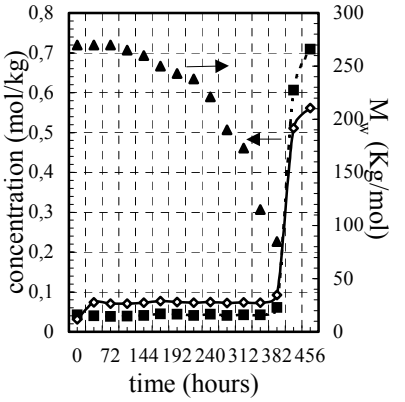

(b)

Fig. 4. Evolution of (a) strain at break, (b) average molar mass weight during exposure and kinetic curves of C=O at 1720cm^{-1} and OH groups at 3400cm^{-1}.

In order to record spectra (carbonyl and hydroperoxide indexes), fourier transform infrared spectroscopy (FTIR) Bruker IFS 28 equipped with a computerized XY translational mapping system was used by steps of 20μm. The absorbances of OH (3400cm^{-1}) and C=O (1720cm^{-1}) bands were converted into concentrations using the Beer-Lambert law with molar absorptivity values of 70lmol^{-1}cm^{-1} (OH) and 300lmol^{-1}cm^{-1} (C=O) respectively. Note that in the literature, the hydroperoxide (OH) and the carbonyl (C=O) bands are considered as the most suitable indicators for photoageing in polypropylene. The kinetic curves of carbonyl and hydroperoxide build-up, which have been also included in Fig. 4, display an induction time t_{iCO} of approximately 370±10h. In Fig. 4b the decrease of weight average molar mass M_w after an ageing time of 190h indicates that the chain scission process begins during the classical induction period t_{iCO} of 380h. We can conclude that embrittlement occurs at a very low conversion of the oxidation process.

Does the sudden change of ductile to brittle behaviour result from the existence of a critical structural state? At the end of ductile-brittle transition (300h), the value of critical molar mass for embrittlement is very close to 190Kgmol^{-1}. The fact that embrittlement occurs at very low conversion could then be linked to some peculiar character of the tie chain: in semi-crystalline polymers tie molecules interconnecting lamellar play a crucial role in process of yielding [7]. The following causal chain may be thus assumed: Oxidation in the amorphous phase ⇒ chain scission ⇒ rupture of ties chains ⇒ loss of plasticity/ductility potential.

In order to investigate the ductile fracture behaviour of the PP film, it is very important to find appropriate experimental methodology. The fracture mechanics may be a suitable alternative to the traditional tensile tests achieved above. In this work, the fracture behaviour of the film was studied by two different approaches under mode I loading: the J-integral and the essential work of fracture (EWF) theory.

4. EWF method

The LEFM as a matter of fact does not take into account the energy dissipated

during the blunting and the stable crack propagation precedes the fracture of highly ductile polymer films. So, Hashemi and O'Brien [8] and Chan and Williams [9] have adopted an aproach for characterizing polymers films based upon Broberg's suggestion [10]: the essential work of fracture (EWF) method.

In the EWF approach, the zone around the crack tip is divided into two regions: the inner fracture process zone (IFPZ) related to the actual fracture and the outer plastic deformation zone (OPDZ) related to shear yielding as shown in Fig. 5 for a double edge notch in tension (DENT) specimen.

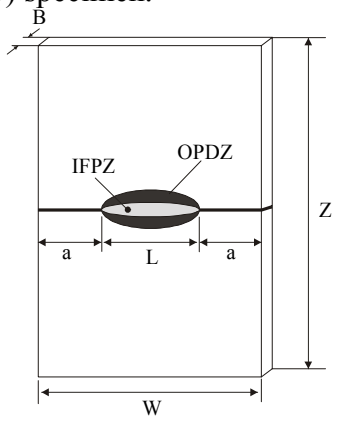

Fig. 5. DENT specimen geometry showing the OPDZ and IFPZ zones.

The method consists of dividing the total energy for fracture W_f into two components: the specific essential work of fracture w_e and the specific non-essential work of fracture βw_p as illustrated in Fig. 6. To obtain these two components, the total work of fracture W_f, recorded during the mechanical test and containing all the energy dissipated during the test, can be expressed by [11]:

$$W_f = W_e + W_p \quad (1)$$

Assuming that W_e is proportional to the uncracked ligament area while W_p is linked to the volume of the plastic zone, it comes:

$$W_f = \int P du = w_e LB + \beta w_p L^2 B \quad (2)$$

where P is the load, u is the displacement, B is the sample thickness, β is the shape factor of the plastic zone and $L = W - 2a$ is the uncracked ligament length (W being the sample width and $2a$ the initial total crack length). So that one has, per unit cross section:

$$w_f = \frac{W_f}{LB} = w_e + \beta w_p L \quad (3)$$

As schematically shown in Fig. 6, the work of fracture is plotted versus ligament length. Assuming a linear evolution, w_e is the ordinate at the origin and βw_p is the slope of the straight line. The component accounting for the essential work of fracture w_e and the plastic deformation term βw_p are expected to be independent on specimen geometry since the fracture process is in pure plane stress configuration.

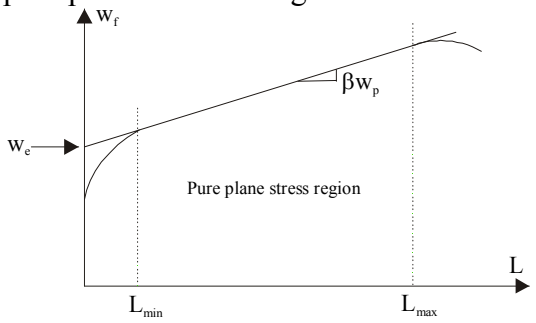

Fig. 6. Determination of EWF parameters.

The films of polypropylene consist in sheets of 100μm thin; rectangular samples of 25mm width and 90mm length were cut out from the sheets (clamped zones length equal to 55mm, i.e. Z=35mm). DENT samples (Fig. 5) were precracked using a razor blade with ligament lengths L ranging from 6 to 16mm [12].

Samples were tested in uniaxial tension using the Instron 4502 setup under a constant crosshead speed of 5mm/min and at room temperature. The specimens were tested up to complete failure and the load-displacement curve for each specimen was recorded using a data acquisition computer. Load-displacement curves examples are

shown in Fig. 7 for various values of a/W ratio. These curves display a maximum which corresponds to the blunting due to complete ligament yielding (zone I in Fig. 7). Beyond this maximum, a slow decrease of the load corresponding to zone II, indicates slow stable crack growth in the yielded ligament, perpendiculary to the load direction.

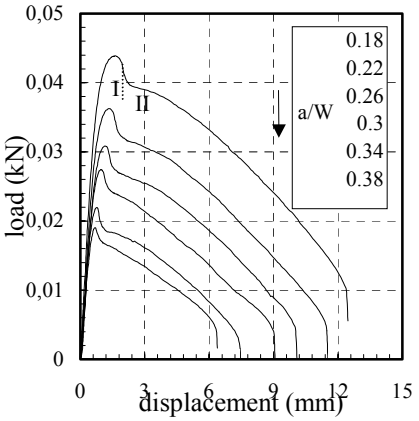

Fig. 7. Typical load-displacement curves as a function of a/W ratio.

The influence of photoageing on the specific essential work and non-essential work of fracture is given in Fig. 8.

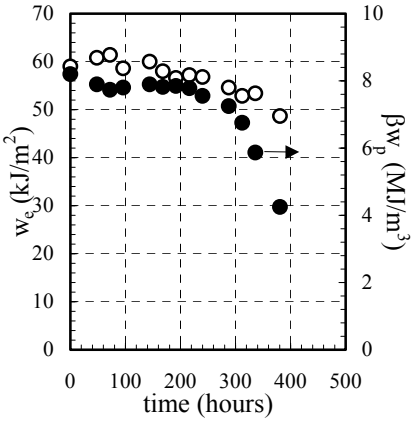

Fig. 8. Effect of ageing on the EWF parameters.

The EWF parameters show two zones of varying photoageing dependence. In the first zone (0≤time≤240h), they are more or less independent of photoageing, having an average value of 58.7kJ/m^2 for w_e and 7.8MJ/m^3 for βw_p. In the second zone (time>240h), w_e and βw_p decrease with the time of exposure and then with fragility. The decrease of βw_p is more emphasized and the dependence of this parameter with photoageing implies that both the shape of the plastic zone β and the work dissipated in the plastic deformation zone w_p depend on photoageing.

5. J-integral method

The fracture toughness of the material is now examined with an alternative tool: the J-integral. This concept was firstly proposed by Cherepanov [13] and Rice [14] for the ductile fracture characterization of metallic alloys and extended to the evaluation of polymers fracture toughness [15]. The J-integral is a path independent contour integral given, for a two dimensional crack, by:

$$J = \int_{\Gamma} \left(W^* dy - T \frac{\partial u}{\partial x} ds \right) \tag{4}$$

where (x, y) are coordinates normal to the crack front, W^* is the strain energy density, T and u are stress and displacement acting on a contour Γ and ds is a small element on Γ. The crack initiation can be evaluated from a critical value J_c of J.

The J-integral, under elasticity assumption, is the potential energy decrease per unit area required to create new surfaces. Under monotonic loading, this energy concept has been extended to non-linear and irreversible behaviour but the energy includes the dissipative terms (involved by plastic deformation for instance). The energy parameter J is expressed as:

$$J = -\frac{1}{B} \left. \frac{\partial U}{\partial a} \right|_u \tag{5}$$

where U is the expended energy of the body which can be obtained by the area under the load-displacement curve, u is

the displacement, a is the crack length and B is the thickness of the specimen.
The parameter J can be also seen as a multiplicative form of a geometrical η-factor and the energy per unit area:

$$J = \eta \frac{U}{BL} \tag{6}$$

where L is the uncracked ligament.
Considering an elastic-plastic material, the parameter J is generally decomposed into an elastic J_{el} (related to the stress intensity factor) and a plastic part J_{pl} (related to the dissipated energy) expressed as [16]:

$$J = J_{el} + J_{pl} = \eta_{el} \frac{U_{el}}{BL} + \eta_{pl} \frac{U_{pl}}{BL} \tag{7}$$

where U_{el} and U_{pl} are the elastic and plastic parts of the area under the load-displacement curves, η_{el} and η_{pl} are the elastic and plastic calibration factors which are functions of the a/W ratio.
The aim of the following sections is particularly focused on the identification of the calibration factors, directly derived from the load-displacement records or by using a finite element analysis.

5.1. Experimental calibration of η

The elastic calibration factor η_{el} is related to the compliance C of the specimen [17] in the following way:

$$\eta_{el} = \frac{L}{C}\frac{dC}{da} \tag{8}$$

C is determined from the initial slope of the load-displacement curve and is only function of the a/W ratio.
From experimental data, the elastic calibration factor η_{el} can be then expressed with a polynomial function:

$$\eta_{el} = 4.58(a/W)^2 - 5.26(a/W) + 1.53 \tag{9}$$

An analytical formula of the stress intensity factor K_1 is given in [18] for a DENT plate:

$$K_1 = \frac{P\sqrt{\pi a/(2W)}}{B\sqrt{W}\sqrt{1-a/W}} f(a/W) \tag{10}$$

with:

$$f(a/W) = \{1.122 - 0.561(a/W) - 0.205(a/W)^2 + 0.471(a/W)^3 + 0.19(a/W)^4\}$$

The analytical expression of the elastic calibration factor η_{el} can be then obtained from:

$$\eta_{el} = \frac{K_1^2}{E}\frac{BL}{U_{el}} = 2\frac{K_1^2}{E}\frac{BL}{P^2 C} \tag{11}$$

where E is the Young's modulus.
Fig. 9 gives the evolution of η_{el}-factor versus the a/W ratio. A quite good agreement is obtained between the experimental and analytical solutions. However, some slight divergence can be pointed out for a/W ratio smaller than 0.25.

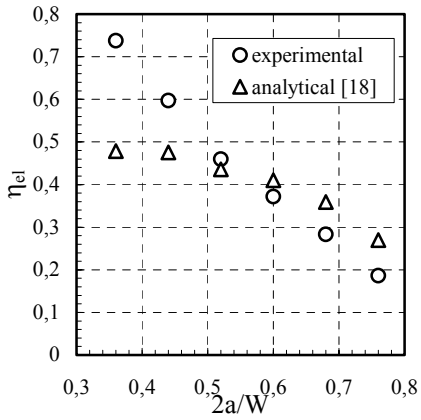

Fig. 9. η_{el}-factor as a function of a/W ratio.

The plastic calibration factor η_{pl} is experimentally determined from a methodology based on the load separation criterion. According to that, the load can be written as the following separable form [19]:

$$P(a, u_{pl}) = G(a/W) H(u_{pl}/W) \tag{12}$$

where $G(a/W)$ is the crack geometry function depending only on crack length to width ratio (a/W) and $H(u_{pl}/W)$ is the deformation function depending only on the normalized plastic displacement (u_{pl}/W). So, η_{pl} exists only if the load can be expressed in a multiplicative form of the two functions [20].

The separation parameter S_{ij} is defined as the ratio of the applied load to a specimen with a crack length a_i, with the applied load to another specimen with crack length a_j:

$$S_{ij} = \left.\frac{P(a_i, u_{pl})}{P(a_j, u_{pl})}\right|_{u_{pl}=u-CP} \quad (13)$$

The suffixe u_{pl} denotes that the ratio is taken at constant plastic displacement. S_{ij} is expected to have a constant value over the range of the load separation validity zone:

$$S_{ij} = \frac{G(a_i/W)}{G(a_j/W)} = \text{constant} \quad (14)$$

The separation parameter S_{ij} was evaluated at different values of the plastic displacement by using the a/W =0.22 record as the reference. Fig. 10 shows the separation parameter variation with the plastic displacement for different a/W ratios.

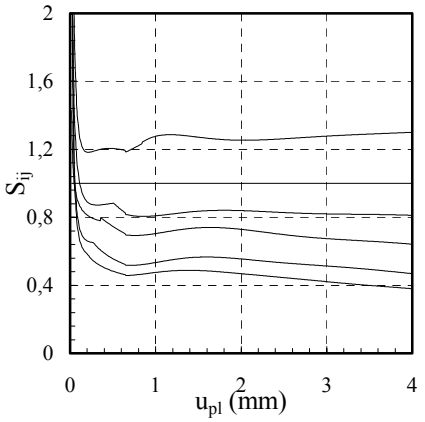

Fig. 10. Separation parameter S_{ij} as a function of the plastic displacement u_{pl}.

In Fig. 10, the limits of the load separation validity is pointed out. Indeed, the separation factor is quite constant, and it only depends on the crack length, for plastic displacement values greater than 0.2 and smaller than 4. In this range the load can be separated into the two multiplicative functions and outside this range η_{pl} does not exist.

The plastic factor η_{pl} can be expressed as [19]:

$$\eta_{pl} = \frac{dG(L/W)/d(L/W)}{G(L/W)}\frac{L}{W} \quad (15)$$

The geometry function $G(L/W)$ can be easy given by the following power law:

$$G(L/W) = c(L/W)^{\eta_{pl}} \quad (16)$$

with c a constant.

In order to determine the η_{pl} parameter, the data of the load-displacement record must be used. By taking logarithms to both sides of the equation, the η_{pl} parameter is obtained from a less square method.

In Fig. 11, S_{ij} is plotted versus L/W for the plastic displacement interval defined earlier where no major influence of plastic displacement was pointed out. The data are fitted by the power law function (16) giving a η_{pl} value very close to 1 as shown in Tab. 1.

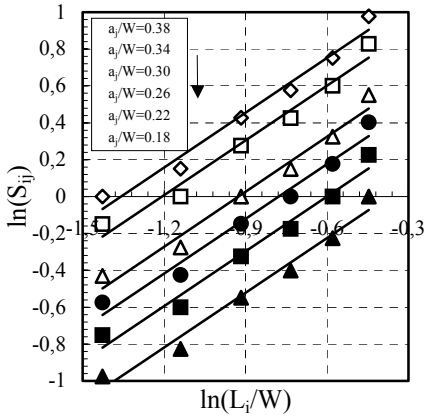

Fig. 11. Separation parameter S_{ij} as a function of the uncracked ligament ratio L/W.

a_i/W	0.38	0.34	0.3	0.26	0.22	0.18
η_{pl}	0.9916	0.9899	0.9946	0.9911	0.9905	0.9901

Tab. 1. Values of η_{pl}-parameter.

5.2. Numerical calibration of η

In order to avoid to separate U into its elastic and plastic parts, we examine an alternative technique to determine the calibration factor η via a finite element approach.

5.2.1. Constitutive model

In order to achieve finite element simulations, the constitutive law of the material is required. The material behaviour is described using a phenomenological elastic-viscoplastic law [21] containing an internal variable. It must be noted that the viscoplastic model is suitable only for isotropic behaviour since the induced anisotropy is not described by this model.

The total strain rate is decomposed into an elastic and a plastic part as follows:

$$\dot{\varepsilon}_{ij} = \dot{\varepsilon}_{ij}^{el} + \dot{\varepsilon}_{ij}^{pl} \tag{17}$$

The elastic strain rate obeys to the following law:

$$\dot{\varepsilon}_{ij}^{el} = C_{ijkl}^{-1}\dot{\sigma}_{kl} \tag{18}$$

where C_{ijkl} is the fourth-order isotropic elastic modulus tensor.

The plastic strain rate is given by:

$$\dot{\varepsilon}_{ij}^{pl} = \frac{3}{2}\dot{p}\frac{\sigma'_{ij}}{\sigma_{eq}} \tag{19}$$

where σ'_{ij} is the stress deviator, σ_{eq} is the equivalent stress and $\dot{p}$ is the equivalent plastic strain rate depending on internal variable according to:

$$\dot{p} = \left\langle \frac{\sigma_{eq} - k - R}{K} \right\rangle^{n} \tag{20}$$

with $\langle x \rangle = x$ if $x > 0$ and $\langle x \rangle = 0$ otherwise.

In (20), the exponent n and K are viscosity parameters, k is the initial yield stress and R is the isotropic hardening defined by the following evolution equation:

$$\dot{R} = b(Q - R)\dot{p} \tag{21}$$

b and Q are hardening variables.

In order to determine the material parameters involved in the elastic-viscoplastic model, experimental uniaxial tension tests on unnotched specimens have been achieved under various strain rates for the unaged material. The experimental set-up is mainly constituted by an Instron machine and a Video-Traction© device. The unnotched specimen used has a specific geometry as shown in the schematic representation of the Fig. 12. The specimen presents a fairly large radius of curvature which ensure both the strain localization and the minimization of stress triaxiality in the center.

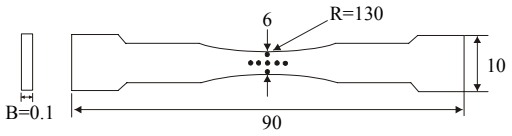

Fig. 12. Specimen geometry used for Video-Traction© tensile tests (dimensions in mm).

The following of the gravity centers of seven round black markers (Fig. 12) is achieved by the Video-Traction© device [22], which allows to determine their relative displacement in real time. Hence, according to the position of the markers, the two principal strains (axial and transversal strains) were measured in the region where the plastic necking occurs.

The method allows to keep the true strain rate under control during the test, even when the heterogeneous deformation occurs, by regulating the cross-head velocity (Fig. 13).

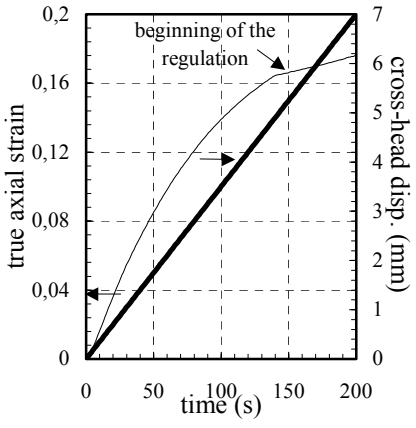

Fig. 13. True axial strain and cross-head displacement as functions of time.

The yield stress, determined from the Considere's criterion on the true stress-strain curves, allows to determine k, n and K. The hardening parameters b

and Q were calibrated on the tensile curves. Tensile modulus E was calculated using the initial slope of the stress-strain curve and Poisson'ratio ν was determined using the ratio between the transversal strain and the axial strain. The values of the parameters are listed in Tab. 2.

E	ν	k	K	n	b	Q
MPa	-	MPa	MPa	-	-	MPa
550	0.47	10	33.8	3.3	50	10

Tab. 2. Material parameters.

Fig. 14 presents a comparison between the experimental data and the theoretical model. A relatively good agreement is pointed out. However, some sligth divergence is highlighted for large strains.

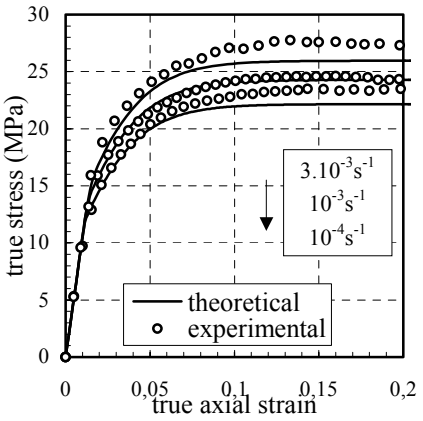

Fig. 14. Theoretical and experimental stress-strain curves.

5.2.2. FE model of DENT specimens

In this section the η-factor is estimated using a finite element (FE) analysis. The commercial FE program Marc© was used to carry out the numerical simulations. DENT specimens were discretised, with different crack lengths, using triangular elements with six nodes in the vicinity of the crack tip and quadrilateral elements with eight nodes far from the crack. Due to symmetries, only a quarter of the geometry is modelled. The boundary conditions are given in terms of assigned displacements as shown in Fig. 15. The displacement velocity is applied to the node set at the top of the mesh, by gradually incrementing the applied displacement.

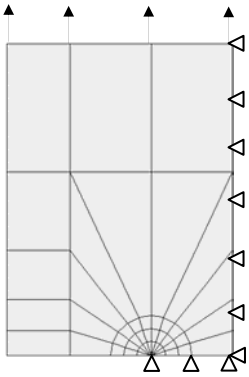

Fig. 15. Mesh of the DENT specimen.

The numerical load-displacement curves are compared with those experimentally obtained for different a/W ratio in Fig. 16. Although a scatter is depicted between simulated and experimental values, the validity of the numerical modelling is clearly pointed out.

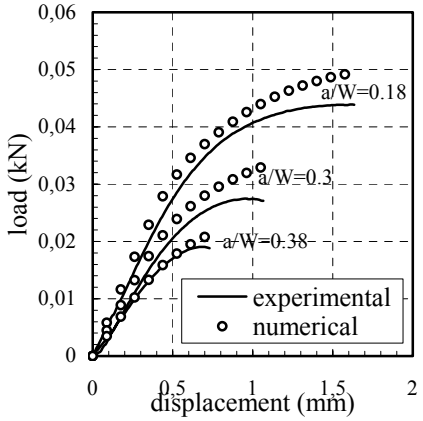

Fig. 16. Numerical and experimental load-displacement curves.

The numerical J-integral was computed using the Lorenzi method and the independence property of this quantity on the integration contour was checked by comparing the calculations made for various integration contours sufficiently far from the crack tip. Fig. 17 shows an illustrative example (a/W=0.3) of the path independence of the J-integral where the ratio $J_{FE}(\text{conti})$ of a contour

i over $J_{FE}(\text{cont j})$ of a contour j is plotted versus displacement. This result shows without any ambiguity the relevance of the adopted meshing.

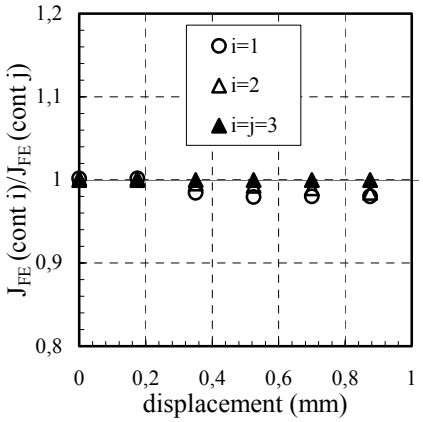

Fig. 17. Effect of contour integration on the J-integral values.

The value of η for each ligament length was calculated from [23]:

$$\eta_{FE} = J_{FE}\frac{BL}{U_{FE}} \tag{22}$$

The evolution of η_{FE}, determined from FE calculation, versus a/W ratio is plotted in Fig. 18. The dependence of η_{FE} on the crack length is clearly pointed out.

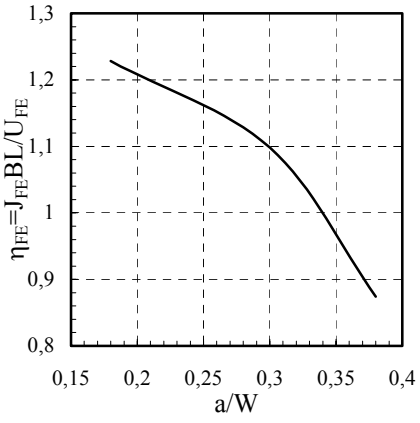

Fig. 18. η-factor determined by finite element modelling as a function of a/W ratio.

Since the η-factor is now known, the parameter J can be experimentally evaluated. Fig. 19 presents a comparison between the two methodologies for the η-factors identification through the evolution of the ratio $(J_{el}+J_{pl})/J(\eta_{FE})$ for different a/W ratio. An important divergence between the two solutions is highlighted at small displacements and it decreases when the displacement increases. The ratio is crack length dependent. When considering a/W <0.34, the J value given by the purely experimental methodology is always smaller than that given by the FE approach.

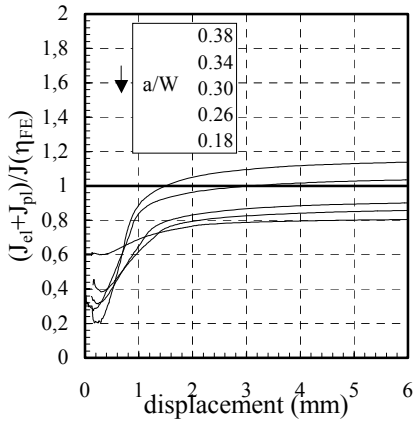

Fig. 19. Comparison between the two methods of η-factors calibration.

The J-integral was determined by using both the load-displacement curves obtained for aged samples and the factor of calibration determined by FE (the η-factor was assumed to be ageing-independent). The effect of photoageing on the J-integral is given in Fig. 20.

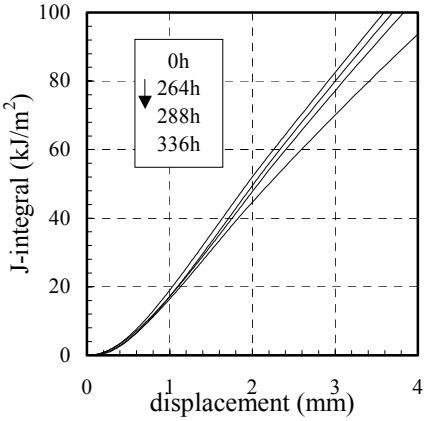

Fig. 20. Effect of ageing on the J-integral.

With increasing time of ageing the J-integral decreases. Assuming that the

onset of the crack growth starts at a critical displacement corresponding to the beginning of the necking stage (see Fig. 7), the critical value of J (J_c) decreases slightly with the photoageing.

6. Conclusion

Polypropylene films were subjected to photoageing and its effect on physico-chemical and mechanical properties was investigated.
Chemical modifications of the polymer were established as functions of ageing. The modifications induced by the photoageing are well reflected in the changes of the molar mass, the carbonyl and hydroperoxide indexes.
The effect of ageing on the tensile and fracture toughness behaviour of the polymer was investigated. The ultimate strain can be considered as a good indicator of ageing. The η-factors, introduced in the J-integral expression, were experimentally and numerically estimated in the DENT configuration specimens. The EWF parameters were determined in the same configuration. Results indicated that the specific essential work of fracture w_e and the critical value of J (J_c) are not very sensitive to time of exposure while the plastic deformation term βw_p varies with this factor. It seems then that both w_e and J_c can not be considered as adequate variables being able to reflect the structural changes of this material caused by photoageing. The changes of the plastic deformation term can be correlated with the photoageing and give useful informations on the alteration due to ageing.

References

[1] Turton, T.J., White, J.R., (2001), *Polym. Degrad. Stab.*, **74**, pp. 559.
[2] Philippart, J.L., Sinturel, C., Arnaud, R., Gardette, J.L., (1999), *Polym. Degrad. Stab.*, **64**, pp. 213.
[3] Allen, N.S., Edge, M., Corrales, T., Catalina, F., (1998), *Polym. Degrad. Stab.*, **61**, pp. 139.
[4] Achimsky, L., Audouin, L., Verdu, J., (1997), *Polym. Degrad. Stab.*, **57**, pp. 231.
[5] Gijsman, P., Dozeman, A., (1996), *Polym. Degrad. Stab.*, **53**, pp. 45.
[6] Pabiot, J., Verdu, J., (1981), *Polym. Eng. Sci.*, **21**, pp. 32.
[7] Peterlin, A., (1971), *J. Mater. Sci.*, **6**, pp. 490.
[8] Hashemi, S., O'Brien, D., (1993), *J. Mater. Sci.*, **28**, pp. 3977.
[9] Chan, W.Y.F., Williams, J.G., (1994), *Polym.*, **35**, pp. 1666.
[10] Broberg, K.B., (1968), *Int. J. Fract.*, **4**, pp. 11.
[11] Mai, Y.W., Cotterell, B., (1986), *Int. J. Fract.*, **32**, pp. 105.
[12] ESIS test protocol for essential work of fracture (version 5), 1997.
[13] Cherepanov, G.P., (1967), *J. Appl. Math. Mech.*, **31**, pp. 503.
[14] Rice, J.R., (1968), *J. Appl. Mech.*, **35**, pp. 379.
[15] Chan, M.K.V., Williams, J.G., (1983), *Int. J. Fract.*, **23**, pp. 145.
[16] Sumpter, J.D., Turner, C.E. (1976) In: Cracks and Fracture ASTM STP 601, ASTM Philadelphia, PA, pp. 3-18.
[17] Paris, P.C., Ernst, H.A., Turner, C.E. (1978) In: Nuclear Regulatory Commission.
[18] Anderson, T.L. (1995), *Fracture Mechanics - Fundamentals and Applications*, CRC Press, Boca Raton.
[19] Sharobeam, M.H., Landes, J.D., (1991), *Int. J. Fract.*, **47**, pp. 81.
[20] Ernst, H.A., Paris, P.C. (1980) In: Nuclear Regulatory Commission.
[21] Chaboche, J.L., (1997), *Int. J. Solids Struct.*, **34**, pp. 2239.
[22] G'Sell, C., Bai, S.L., Hiver, J.M., (2004), *Polym.*, **45**, pp. 5785.
[23] Aït-Hocine, N., Naït-Abdelaziz, M., (2003), *Int. J. Fract.*, **124**, pp. 79.

PREDICTION OF LONGITUDINAL TENSILE STRENGTH OF POLYMER MATRIX COMPOSITES

A. B. de Morais
University of Aveiro, Department of Mechanical Engineering,
Campus Santiago, 3810-193 Aveiro, Portugal

Abstract

A micromechanical model was developed for the prediction of the longitudinal tensile strength of polymer matrix composites. The model considers successive fibre breaks within an infinitely wide L_i-long representative volume element (RVE), L_i being the so-called ineffective length. An elastic-plastic stress transfer model is used to define L_i and fibre strength is described by a Weibull distribution. The composite strength is obtained by solving numerically an equation for the maximum RVE stress. A simplified closed-form solution derived proved to be in very good agreement with the base formulation. Although there is still significant uncertainty over model input data, predictions agreed well with experimental strengths of carbon fibre composites.

Keywords: Polymer-matrix composites, longitudinal tensile strength, ineffective length, Weibull distribution.

1. Introduction

Laminated polymer matrix composites are increasingly used in structural applications. This is mainly due to the outstanding fibre dominated ply longitudinal modulus and tensile strength. It is well known that, in contrast with matrix cracking, fibre fracture usually causes overall laminate failure. It is also known that modern structural design methodologies aim at taking full advantage of material properties. Therefore, accurate prediction of the ply longitudinal tensile strength, σ_{ut1}, is an important contribution to avoid large safety factors. However, longitudinal failure is a complicated process [1-6].

Let us consider a unidirectional composite subjected to a rising tensile load. Owing to the statistical distribution of fibre strength, various fibre breaks occur at different locations. Broken fibres cannot support any load at the fractured section. However, shear stresses in the surrounding matrix gradually transfer stress to broken fibres. These fibres can actually recover the stress acting on unbroken fibres at some length L_i, known as "ineffective length". Early strength prediction models have viewed the composite as a chain of L_i-bundles [1-6]. However, oversimplifying assumptions have been made to maintain analytical tractability. In order to overcome these limitations, Monte Carlo simulations have recently become widespread [7-14]. The models may contain hundreds of fibre elements, but computational cost limits model dimensions and thus makes further size scaling essential to predict σ_{ut1}. Moreover, model predictions overestimate significantly experimental σ_{ut1} values.

This paper presents a simplified model that compares favourably with experimental data for several carbon fibre composites.

2. Model description

The aim of the present model is to predict the longitudinal tensile strength of an infinite composite. In these circumstances, the composite can be seen as an infinite stack of L_i-long infinitely wide regions. Obviously, any of such regions can be considered the representative volume element (RVE). Therefore, the analysis yields the longitudinal tensile strength without requiring any further size scaling. Moreover, one fibre only undergoes a single break, thus greatly simplifying the analysis [14]. Failure occurs when the number of fibre breaks prevents further load increases.

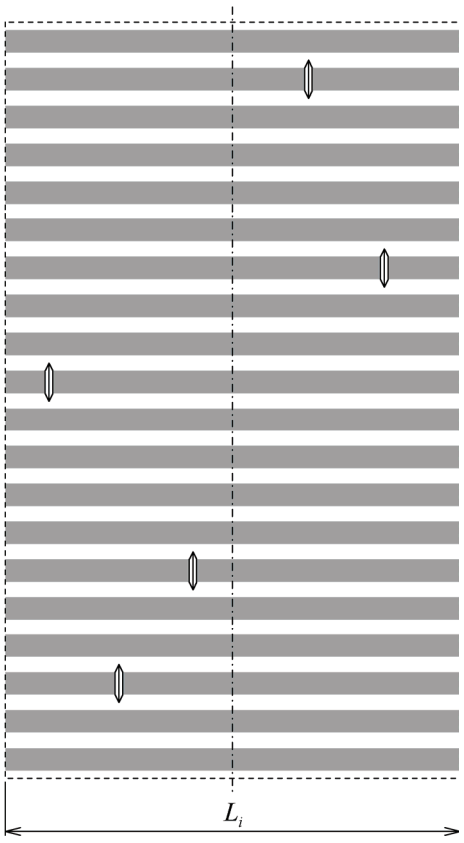

Figure 1: Fibre breaks in the RVE.

Early work by Hedgepeth [15,16] indicated that fibres adjacent to a broken one would be subjected to significant stress concentration effects. Most Monte Carlo simulations based models have included such effects and therefore predict the formation of broken fibre clusters. Furthermore, one of the clusters becomes unstable and triggers final failure [7-14]. Clusters of fibre breaks have been reported in model composites containing a very limited number of fibres [17]. They could also occur in contacting fibres of real composites, although they have not been observed in bundle tests [14]. In particular, the formation of one large cluster of fibre breaks leading to final failure seems unlikely and clearly lacks experimental support [14]. Moreover, three-dimensional finite element analyses showed very modest highly localised stress concentration in fibres adjacent to a broken fibre [18-20]. Therefore, it is assumed that fibre breaks are uniformly distributed in the RVE. This implies that the average axial distance of the breaks to the RVE mid-plane is $L_i/4$. The average stress supported by broken fibres in any transverse plane is thus the stress at $L_i/4$ from the fibre break. The RVE average fibre stress can then be expressed as

$$\sigma_{fa} = \sigma_{fl}\left[1 - P(\sigma_{fl})\right] + P(\sigma_{fl})\sigma_{fb}(L_i/4) \quad (1)$$

where σ_{fl} and σ_{fb} are the stresses on the unbroken and broken fibres, respectively, and P is the cumulative probability of fibre failure. The two-parameter Weibull distribution is known to provide a good fit to experimental fibre strength data [21-23]. Thus, at gauge length L_i,

$$P(\sigma_{fl}) = 1 - \exp\left[-L_i\left(\frac{\sigma_{fl}}{\sigma_{fi}}\right)^{\rho}\right] \quad (2)$$

where σ_{fi} is a characteristic strength and ρ the Weibull modulus. Since it is not possible to perform tensile tests at such small gauge lengths, the distribution of fibre strength must be scaled down from

experimental data for some larger gauge length L_0,

$$\sigma_{fi} = \sigma_{f0}\left(\frac{L_0}{L_i}\right)^{1/\rho} \quad (3)$$

This scaling seems to be reasonably accurate [21-23], although it tends to overestimate strength at small gauge lengths [23]. However, this can be explained by premature near the grips failure [22]. Eq. (2) is thus re-written as

$$P(\sigma_{fl}) = 1 - \exp\left[-\frac{L_i^2}{L_0}\left(\frac{\sigma_{fl}}{\sigma_{f0}}\right)^{\rho}\right] \quad (4)$$

It is now necessary to determine L_i, which is strongly influenced by interface and matrix shear strengths. In general, interface debonding takes place when the interface is weaker than the matrix, while localised matrix cracking and yielding occur otherwise [19]. Recent experimental studies [24-26] suggest that matrix yielding is the main stress transfer mechanism in modern composite systems with treated and sized fibres. Accordingly, perfect interface bonding is assumed and L_i is calculated from the stress transfer model presented in [19]. This model is based on the analysis of a concentric cylinder cell formed by the broken fibre and the surrounding matrix layer (Fig. 2). The outer diameter of the matrix layer is tangent to the nearest neighbour fibres of the hexagonal packing arrangement, which is the most representative for the usual range of fibre contents. The thickness of the matrix layer is

$$t_m = d_f\left(\sqrt{\frac{\pi\sqrt{3}}{6V_f}} - 1\right) \quad (5)$$

where d_f is the fibre diameter and V_f the fibre volume fraction. The matrix is assumed elastic-perfectly plastic with shear yield stress τ_{pm}. Neglecting normal stresses, stress transfer along the matrix yielding zone ($0 \le z \le z_p$) is [19]

$$\sigma_{fb} = \frac{4\tau_{pm}}{d_f} z \quad (6)$$

In the subsequent elastic zone ($z \ge z_p$) [19],

$$\sigma_{fb} = \sigma_{fl} - \frac{4\tau_{pm}}{\beta d_f} e^{\beta(z_p - z)} \quad (7)$$

where

$$\beta = \sqrt{\frac{4G_m}{d_f t_m E_f}} \quad (8)$$

and G_m and E_f are the matrix shear modulus and the fibre longitudinal modulus, respectively. Stress continuity at z_p leads to

$$z_p = \frac{d_f \sigma_{fl}}{4\tau_{pm}} - \frac{1}{\beta} \quad (9)$$

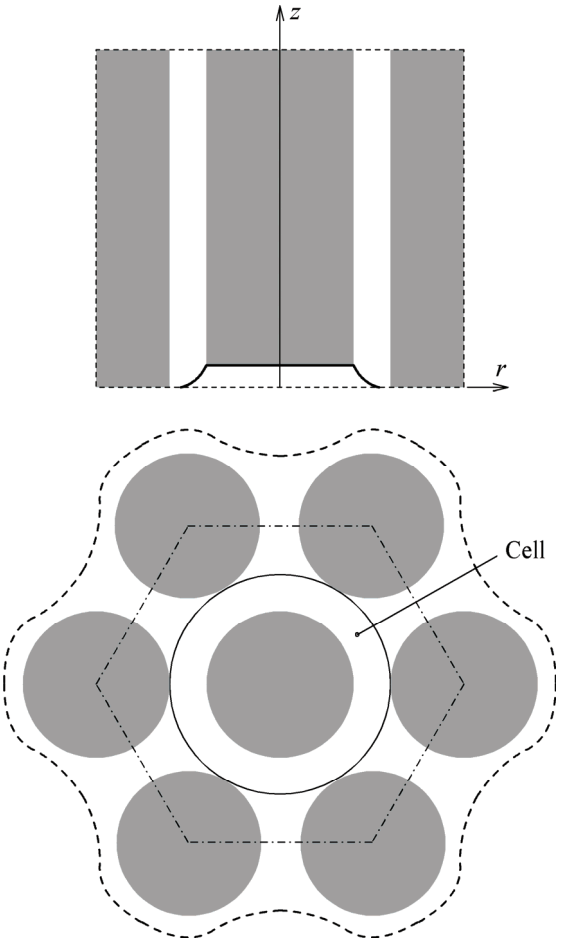

Figure 2: Scheme of the stress transfer model.

On the other hand, at $z = L_i$ the broken fibre recovers a high fraction α of the remote stress σ_{fl}, e.g. α = 95 %. Eqs. (7) and (9) allow us to write

$$L_i = \frac{d_f \sigma_{fl}}{4\tau_{pm}} - \frac{1}{\beta}\left\{1+\ln\left[\frac{(1-\alpha)\beta d_f \sigma_{fl}}{4\tau_{pm}}\right]\right\} \quad (10)$$

Finally, we can determine the maximum fibre stress in the RVE from

$$\frac{d\sigma_{fa}}{d\sigma_{fl}} = 0 \quad (11)$$

After substitution of (4), (6) and (10), Eq. (11) can be expressed as

$$F_l(\sigma_{fl}) + F_b(\sigma_{fl}) = 0 \quad (12)$$

where

$$F_l(\sigma_{fl}) = \left[1 - \frac{\rho L_i^2}{L_0}\left(\frac{\sigma_{fl}}{\sigma_{f0}}\right)^{\rho} - \frac{2L_i \sigma_{fl}^{\rho+1} L'_i}{L_0 \sigma_{f0}^{\rho}}\right] H \quad (13)$$

and

$$F_b(\sigma_{fl}) = \frac{\tau_{pm} L'_i}{d_f} - \frac{\tau_{pm}}{d_f}\left[\frac{dL_i}{d\sigma_{fl}} - \frac{\rho L_i^3 \sigma_{fl}^{\rho-1}}{L_0 \sigma_{f0}^{\rho}} - \frac{2L_i^2 L'_i}{L_0}\left(\frac{\sigma_{fl}}{\sigma_{f0}}\right)^{\rho}\right] H \quad (14)$$

are the contributions of unbroken and broken fibres, respectively, and

$$L'_i = \frac{dL_i}{d\sigma_{fl}} \quad (15)$$

$$H = \exp\left[-\frac{L_i^2}{L_0}\left(\frac{\sigma_{fl}}{\sigma_{f0}}\right)^{\rho}\right] \quad (16)$$

Eq. (12) can be solved by a simple numerical procedure e.g. Newton's method. The result is then inserted in (1) and the tensile strength calculated from the rule-of-mixtures

$$\sigma_{ut1} \approx V_f \sigma_{fa} \quad (17)$$

If we neglect:

- the contribution of broken fibres to the RVE stress;
- the stress transfer along the matrix elastic zone, and thus assume that

$$L_i \approx \frac{d_f \sigma_{fl}}{4\tau_{pm}} \quad (18)$$

we obtain the closed-form equation

$$\sigma_{ut1} = V_f \left[\frac{16\tau_{pm}^2 L_0 \sigma_{f0}^{\rho}}{(\rho+2) d_f^2}\right]^{\frac{1}{\rho+2}} e^{-1/(\rho+2)} \quad (19)$$

which is quite convenient if validated by the base model.

3. Results and discussion

The developed model is applied below to carbon fibre composites. The first objective was to evaluate the accuracy of the closed-form Eq. (19) in the usual range of material properties.

Epoxy resins have tensile moduli between 3.5 and 4.3 GPa and Poisson ratios from 0.35 to 0.42. Therefore, one can expect shear moduli G_m from 1.2 to 1.6 GPa, which a narrow interval. On the other hand, tensile strengths σ_{pm} vary from 60 to 100 MPa, but shear strength data is scarce and somewhat controversial. The von Mises type relation $\tau_{pm} = 0.577\sigma_{pm}$ has often been employed, but there substantial evidence that polymers actually undergo local tensile failure under shear loadings [27-31]. Accordingly, it is assumed here that $\tau_{pm} \approx \sigma_{pm}$.

As mentioned above, measuring parameters of the statistical fibre strength distributions is difficult at small gauge-lengths. Nevertheless, recent single fibre tensile tests on wide variety of carbon fibres showed Weibull moduli ρ = 4 to 6 [21]. For the most common carbon fibres (T300, T800 and AS4), $\rho \approx 5$ [13,32,33], the value that is used here.

Comparison between Eq. (19) and the base formulation was first made in 4 cases, which correspond to the combinations of 2 fibres (WF and SF) and 2 matrices (WM and SM). The fibres used were:

- WF with d_f = 7 μm, E_f = 230 GPa and σ_{f0} = 3500 MPa for L_0 = 15 mm;
- SF having d_f = 5 μm, E_f = 300 GPa and σ_{f0} = 7000 MPa for L_0 = 15 mm;

properties that bound those of well known Toray's T300 and T800 fibres. The softer WM matrix had G_m = 1.2 GPa and τ_{pm} = 40 MPa, while G_m = 1.6 GPa and τ_{pm} = 100 MPa were assumed for the stronger WM.

Fig. 3 shows that Eq. (19) is in very good agreement with the base model for all cases considered. Therefore, it was used for comparison with experimental data.

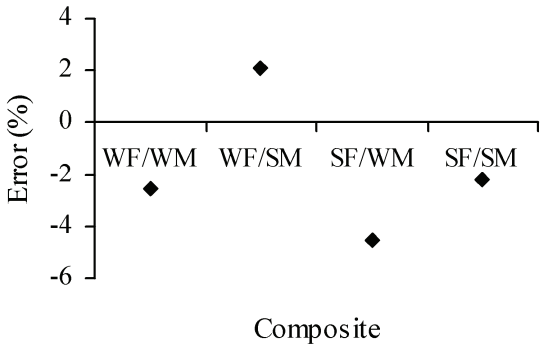

Figure 3: Errors (%) of Eq. (19) in the 4 cases considered (see text for details).

The present model is now applied to Hexcel AS4 and Toray T300 carbon fibre composites, since there is considerable experimental data in the literature and material supplier datasheets (Tables 1 and 2). Data sources are Cytec, Hexcel, Matweb, Qinetic and Soficar. The fibre volume fraction V_f was estimated from the composite-to-fibre moduli ratio, E_1/E_f.

At this stage, the main difficulty in model evaluation is the lack of reliable data for the fibre characteristic strength σ_{f0}. Nevertheless, it is possible to evaluate the model by the following procedure:

- use experimental σ_{ut1} values and Eq. (19) to back-calculate σ_{f0} for some pre-defined L_0; similar values should be obtained for the composites with the same fibres;
- apply Eq. (19) with the average σ_{f0} values obtained previously.

Composite design.	Matrix	V_f	σ_{pm} [MPa]	σ_{ut1} [MPa]
A1	828m	0.59	90	1890
A2	828m	0.64	90	2044
A3	934	0.54	83	1586
A4	934	0.60	83	1792
A5	997	0.57	90	1930
A6	997	0.63	90	2206
A7	8551.7	0.63	97	2170
A8	APC2	0.58	100	2060
A9	APC2	0.66	100	2297

Table 1: Experimental data of AS4 fibre composites used for model evaluation.

Composite design.	Matrix	V_f	σ_{pm} [MPa]	σ_{ut1} [MPa]
T1	3601	0.59	60	1575
T2	3631	0.59	90	1740
T3	934	0.60	83	1790
T4	914	0.60	48	1432
T5	924	0.60	65	1698
T6	3631	0.57	90	1760

Table 2: Experimental data of T300 fibre composites used for model evaluation.

Results presented in Fig. 4 for L_0 = 10 mm confirm that consistent σ_{f0} values could be back-calculated. The largest error was −11.7 % for an AS4 composite. As expected, calculated σ_{f0} values were higher than those of single fibre tests [32,33]. This is due to the high stress transfer effects that lead to premature near the grips failure.

Finally, Figs. 5 and 6 show that model predictions agree quite well with the experimental data of Tables 1 and 2.

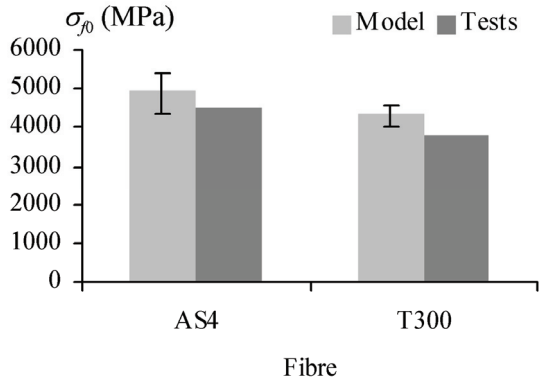

Figure 4: Calculated (see text) and measured [32,33] characteristic fibre strengths.

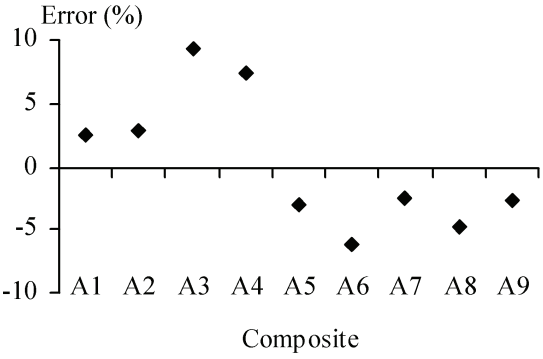

Figure 5: Errors (%) of Eq. (19) predictions relative to experimental data of AS4 composites (Table 1).

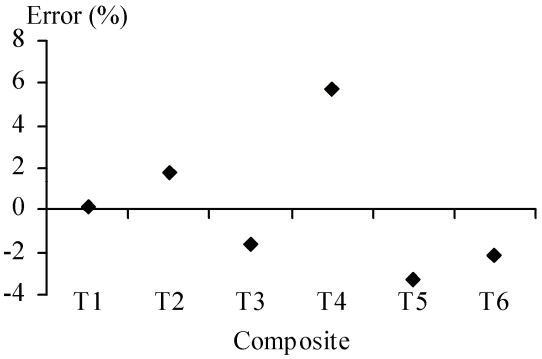

Figure 6: Errors (%) of Eq. (19) predictions relative to experimental data of T300 composites (Table 2).

4. Conclusions

A micromechanical model was presented in this paper for predicting the longitudinal tensile strength of polymer matrix composites. The model considered an infinitely wide L_i-long representative volume element (RVE), L_i being the so-called ineffective length. Its value was calculated from an elastic-plastic stress transfer model previously developed by the author. Fibre strength was assumed to follow a Weibull distribution and therefore, under increasing load, various fibres breaks take place in the RVE. Tensile strength can be obtained by solving numerically an equation for the maximum RVE stress. An additional closed-form solution was obtained by neglecting the contribution of broken fibres and the elastic stress transfer length. A preliminary parametric study showed that the closed-form solution gave very good approximations to the base formulation.

The present model allowed back-calculation of consistent fibre characteristic strengths from experimental data of AS4 and T300 carbon fibre composites. Moreover, strength predictions agreed quite well with experimental values.

References

1. Rosen, B.W., (1964), *AIAA J*, **2**, pp. 1982-1991.
2. Zweben, C., Rosen, B.W., (1970), *J Mech Phys Solids*, **18**, pp. 180-206.
3. Harlow, D.G., Phoenix, S.L., (1978), *J Compos Mater*, **12**, pp. 195-214.
4. Batdorf, S.B., (1982), *J Reinf Plastics Compos*, **1**, pp. 153-164.
5. Phoenix, S.L., Smith, R.L., (1983), *Int J Solids Struct*, **19**, pp. 479-496.
6. Harlow, D.G., Phoenix, S.L., (1991), *J Mech Phys Solids*, **39**, pp. 173-200.
7. Curtin, W.A., Takeda, N., (1998), *J Compos Mater*, **32**, pp. 2042-2059.

8. Curtin, W.A., Takeda, N., (1998), *J Compos Mater*, **32**, pp. 2060-2081.
9. Mahesh, S., Beyerlein, I.J., Phoenix S.L., (1999), *Physica*, **D133**, pp. 371-389.
10. Landis, C.M., Beyerlein, I.J., McMeeking, R.M., (2000), *J Mech Phys Solids*, **48**, pp. 621-648.
11. Okabe, T., Takeda, N., Kamoshida, Y., Shimizu, M., Curtin, W.A., (2001), *Compos Sci Technol*, **61**, pp. 1773-1787.
12. Okabe, T., Takeda, N., (2002), *Composites Part A*, **33**, pp. 1327-1335.
13. Okabe, T., Takeda, N., (2002), *Compos Sci Technol*, **62**, pp. 2053-2064.
14. Mahesh, S., Phoenix, S.L., Beyerlein, I.J., (2002), *Int J Fract*, **115**, pp. 41-85.
15. Hedgepeth, J.M., (1961), NASA-TND-882.
16. Hedgepeth, J.M., Van Dyke, P., (1967), *J Compos Mater*, **1**, pp. 294-309.
17. Aroush, D.R.-B., Maire, E., Gauthier, C., Youssef, S., Cloetens, P., Wagner, H.D., *Compos Sci Technol*, in Press.
18. Nedele, M.R., Wisnom, M.R., (1994), *Compos Sci Technol*, **51**, pp. 517-524.
19. de Morais, A.B., (2001), *Compos Sci Technol*, **61**, pp. 1571-1580.
20. van den Heuvel, P.W.J., Goutianos, S., Young, R.J., Peijs, T., (2004), *Compos Sci Technol*, **64**, pp. 645-656.
21. Tagawa, T., Miyata, T., (1997), *Mater Sci Engng*, **A238**, pp. 336-342.
22. Pickering, K.L., Bader, M.G., Kimber, A.C., (1998), *Composites Part A*, **29A**, pp. 435-441.
23. Pickering, K.L., Murray, T.L., (1999), *Composites Part A*, **30A**, pp. 1017-1021.
24. Deng, S., Ye, L., Mai, Y.W., Liu, H.Y., (1998), *Composites Part A*, **29A**, pp. 423-434.
25. van den Heuvel, P.W.J., Wubbolts, M.K., Young, R.J., Peijs, T., (1998), *Composites Part A*, **29A**, pp. 1121-1135.
26. van den Heuvel, P.W.J., Peijs, T., Young, R.J., (2000), *Composites Part A*, **31A**, pp. 161-171.
27. Chai, H., (1988), *Int J Fract*, **37**, pp. 137-159.
28. Chai, H., (1993), *Int J Fract*, **60**, pp. 311-326.
29. O'Brien, T.K., (1998), In: ASTM STP 1330, pp. 3-18.
30. Liu, K., Piggott, M.R., (1998), *Polym Engng Sci*, **38**, pp. 60-68.
31. Liu, K., Piggott, M.R., (1998), *Polym Engng Sci*, **38**, pp. 69-78.
32. Fukuda, H., Miyazawa, T., (1994), *Adv Compos Mater*, **4**, pp. 101-110.
33. Beyerlein, I.J., Phoenix, S.L., (1996), *Compos Sci Technol*, **56**, pp. 75-92.

A CRACKING MODEL FOR COMPOSITES UNDER ATTACK FROM STRESS AND ENVIRONMENT

Hideki Sekine
Aeronautics and Space Engineering, Tohoku University
Aoba-yama 01, Aoba-ku, Sendai 980-8579, Japan

Peter W R Beaumont
Department of Engineering, University of Cambridge
Trumpington Street, Cambridge CB2 1PZ, UK

Abstract

A micro-mechanical theory of macroscopic stress-corrosion cracking in a unidirectional glass fibre-epoxy composite is proposed. It is based on the premise that under tensile loading, the time-dependent failure of the composite is controlled by the initiation and propagation of a crack from a pre-existing surface flaw in a glass fibre. A physical model is constructed, based on a model of a thermally-activated chemical reaction, using the law of Arrhenius. Emphasis is placed on the significance of the size of the initial (inherent) flaw and the possibility of matrix crack bridging in the crack wake. There exists a threshold value of the crack tip stress intensity factor below which cracking does not occur. For the limiting case, a simple power law to the power of two gives the relationship between crack velocity and stress intensity factor. This assumes the glass fibre is free of inherent flaws and matrix crack bridging is negligible.

Key words: stress corrosion-cracking; composites, micro-mechanical modelling; failure prediction

1. The Path of Physical Modelling

There is a path, which takes us in an alternative direction to conventional mechanical (or empirical) design, where we come upon well-known laws or principles of physics and chemistry. From them, are derived the laws of the micro-mechanics of cracking, which can be applied to predictive (intelligent) design.

A physical model, unlike an empirical law (e.g., Hooke's Law), has powers of prediction that originate from those established rules of physical behaviour. But even if we take this route, a complete physical treatment of problems of fracture isn't always possible. Consider, for example, a model of a thermally activated chemical reaction, based on the law of Arrhenius, which has its basis in statistical mechanics. Sometimes the activation energy, which enters that law, can be predicted from molecular models, but the value of the pre-exponential in the equation more often than not eludes current modelling methods; it must be inserted empirically.

Interesting material behaviour, (which is frequently dynamic, meaning material properties that are time-dependent),

originates (usually) from a kinetic process, diffusion or the rate of a chemical reaction, and often contains an empirical component. An excellent example is the stress corrosion cracking of glass fibre-epoxy composites (1), which is the subject of this paper.

2. Understanding Mechanisms

To understand the consequences of damage accumulation in composite material systems requires the design process at each size level of structure to include the dominant (meaning most influential) crack growth mechanism(s). Making links or connections between a material's fracture resistance and the environment and applied stress relies critically on understanding the differences between the structural changes taking place over the entire range of size with time. Predicting material behaviour demands an intricate knowledge of these mechanisms (of which more is said in another paper of this Meeting by Beaumont and Beaumont).

Choice of designer's box of tools

The materials engineer relies upon a box of tools, which contain *micro-mechanical models*, (sometimes known as mechanism or physical models). We use these tools to create a picture, a representation or model of the real thing. (The model can be compared to a 2-dimensional ordnance survey map or a 3-dimensional physical relief map of geographical landscape). Whilst a topographical map clearly misrepresents elevations and misleads with distances, it elegantly displays the connectivity with sufficient precision and usefulness. Although the model is an idealization or massive simplification, nevertheless it captures the essential characteristics and features of what truly exists or happens. The model needs to be sufficiently uncomplicated or else there is a danger it will lose sight of physical reality. It requires simplicity and with it comes elegance. Physical modelling can be thought of as an art form.

3. Picture of Stress Corrosion Cracking

The synergistic effect of a stress and chemical attack (e.g., from an acid) weakens glass fibre-epoxy laminates. It begins when an atomistic defect on the surface of a glass fibre under load grows into a micron-size flaw. Failure of the fibre progresses as a crack initiates, extending slowly with time, finally snapping completely as the result of unstable (fast) crack propagation. Under increasing load, the crack progresses through the composite, fracturing neighbouring fibres and the matrix in between. Growth of a macroscopic crack thereafter is by the simultaneous fracture of fibre and matrix that can be seen using an optical microscope. Observation by scanning electron microscopy of a fractured glass fibre shows its surface characterised by a smooth or "mirror" region, (which indicates the initial slow cracking regime), interfacing with a "hackle" region or rough surface created by the fast fracture process (Fig. 1).

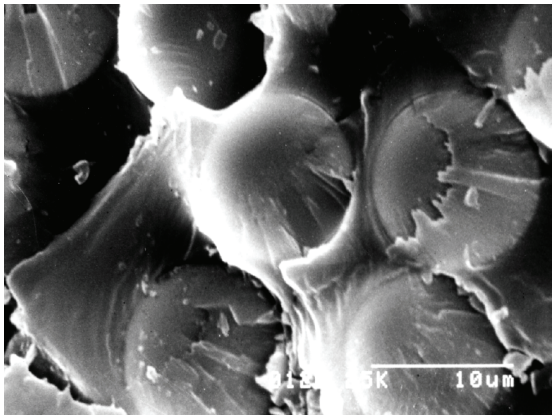

Fig. 1 SEM of the fracture surfaces of glass fibres

For a slowly propagating stress corrosion crack, there is little or no de-cohesion of fibre-matrix interface or the pulling out of broken fibres. This means the fracture planes of fibre and matrix are

coincidental. In conditions of increasing crack velocity, however, there is an increasing amount of fibre-matrix de-bonding. Fibres that fracture at weak points below the plane of matrix crack are extracted during matrix crack opening. Ductile matrix bridges between fibres may form in the crack wake when tougher polymers are used. Matrix bridging, as well as fibre bridging in the crack wake shield the crack tip damage zone from the intensification of local tensile stress. Crack tip shielding by bridging mechanisms is discussed below.

4. Micro-mechanical Model: Applying the Law of Arrhenius

A micro-mechanical model is set up as follows. In bulk glass, the crack propagation rate, *da/dt,* due to stress-corrosion cracking can be given by:

$$\frac{da}{dt} = \nu \exp -\left(\frac{\Delta Q - \alpha K_I}{RT}\right) \qquad [1]$$

In the Arrhenius equation, ΔQ is the activation energy of the chemically activated process, K_I is the crack tip stress intensity factor, R is the gas constant, T is absolute temperature, and ν and α are empirical constants. Application of the micro-mechanical model requires knowledge of the activation energy, which enters the Arrhenius law.

In our model of the growth of a crack in a single glass fibre (Fig. 2), the shape of the crack front is represented as a circular arc of radius r, equal to the radius of fibre r_f (1). The average crack propagation rate can be written thus (from equation [1]):

$$\left(\frac{1}{2r_f\theta}\right)\left(\frac{dY}{dt}\right) = \nu \exp -\left(\frac{\Delta Q - \alpha K_I}{RT}\right) \qquad [2]$$

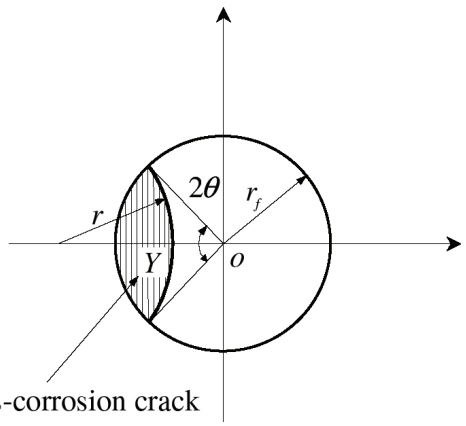

Fig. 2 Shape of stress corrosion crack in a glass fibre (Y is the crack surface area)

Y is the area of the stress corrosion crack in the fibre, θ is half the angle made by two fibre radii on the edges of the stress corrosion crack, and t is time. In equation [2], the stress intensity factor K_I, should be interpreted as the average value of K_I along the entire front of the stress corrosion crack tip. Since the stress intensity factor for the crack opening mode (designated by the subscript I) is constant, more or less, along the larger central portion of the circular crack front, K_I can be represented, approximately, by the stress intensity factor at the maximum depth of crack:

$$K_I = F(\theta)\sigma_f\left(\sqrt{2\pi r_f}\right) \qquad [3]$$

σ_f is the tensile stress acting on the fibre and the geometrical function $F(\theta)$ is:

$$F(\theta) = \sqrt{1-\cos\theta}\left\{1.12 - 3.4(1-\cos\theta) + 13.87(1-\cos\theta)^2\right\}$$

Crack propagation rate and time to failure

The model consists of aligned continuous glass fibres distributed, for convenience, in a doubly periodic square array.

In a geometrical sense, the spacing, D, between neighbouring rows of fibres is simply (Fig. 3):

$$D = c\sqrt{\frac{\pi}{V_f}}\, r_f \qquad [4]$$

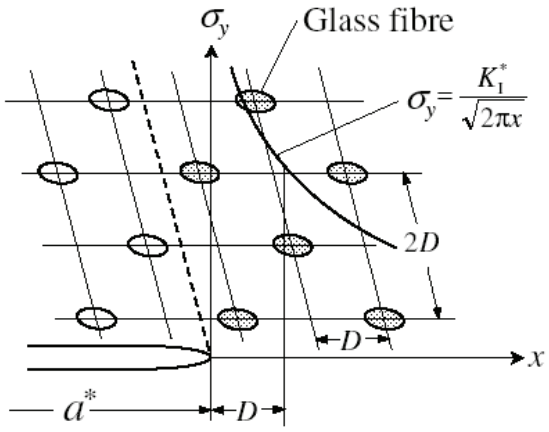

Fig. 3 Doubly periodic array of fibres (face-centred hexagonal array)

V_f is the fibre volume fraction and c is a geometrical constant equal to unity for a square fibre array of fibre, (0.7 for a face-centred square array, and 0.9 for a face-centred hexagonal array).

According to the laws of linear elastic fracture mechanics of an orthotropic elastic solid, the local tensile stress at the tip of a crack is given by (Fig. 3):

$$\sigma_y = \frac{K_I^*}{\sqrt{2\pi x}} \qquad [5]$$

K_I^* is the apparent crack tip stress intensity factor for a mode *I* crack and x is the rectilinear coordinate axis whose origin is located at the crack tip. We can write for the average local tensile stress over a small distance *D* in front of the crack tip:

$$\tilde{\sigma}_y = \frac{1}{D}\int_0^D \frac{K_I^*}{\sqrt{2\pi x}}\,dx = K_I^*\sqrt{\frac{2}{\pi D}} \qquad [6]$$

We propose this average local tensile stress is shared between fibre and matrix according to a law of mixtures. Hence, this average tensile stress $\tilde{\sigma}_y$ close to the crack front is given by:

$$\tilde{\sigma}_y = \left\{ V_f + \frac{\left(1-V_f\right)E_m}{E_f} \right\} \sigma_f \qquad [7]$$

The Young's moduli of fibre and matrix are denoted E_f , E_m, respectively, and the local stress in front of the crack tip carried by the fibre is σ_f.

Hence, the relationship between this tensile stress carried by the fibre and the crack tip stress intensity factor is given by:

$$\sigma_f = \beta K_I^* \qquad [8]$$

where $\beta = \frac{E_f}{V_f E_f + \left(1-V_f\right)E_m}\sqrt{\frac{2}{\pi D}}$.

If the matrix is made of a ductile polymer, bridges or ligaments of the polymer may stretch between crack surfaces in the wake (Fig. 4).

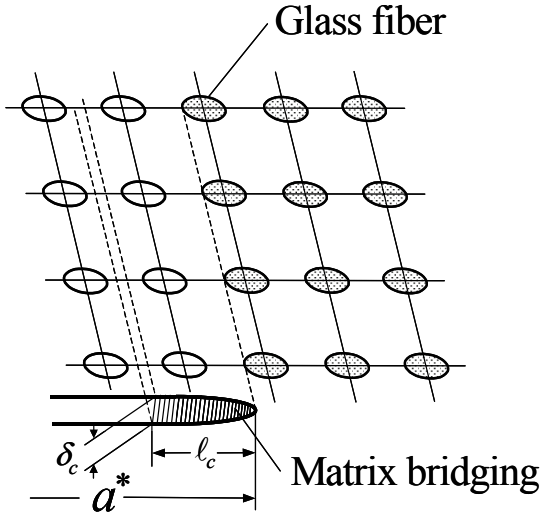

Fig. 4 Matrix bridge model with fibres in a square array. (δ_c is the critical crack opening and l_c is the critical bridge length)

A bridged crack has a reduced apparent crack tip stress intensity factor:

$$K_I^* = K_{Ia}^* + K_{Ib}^* \qquad [9]$$

The first term is due to the remote applied stress and the second term is due to crack bridging given by (1):

$$K_{Ib}^{*} = -4\left(1-V_f\right)\sigma_c\sqrt{\frac{\ell_c}{2\pi}} \qquad [10]$$

In this bridged zone, we have assumed that the polymeric fibrils or ligaments stretched between the matrix crack surfaces behave according to a cohesive force model. On these ligaments, there is a constant cohesive stress $\sigma = \sigma_c$ for $0 \le \delta \le \delta_c$, where δ is the crack opening displacement and δ_c is the opening at the edge of the fully developed bridging zone of length ℓ_c (for steady-state cracking), as shown in Fig. 4. For a short bridged zone compared to the crack length, the relationship between δ_c and ℓ_c is:

$$\delta_c = 4\phi K_I^{*}\sqrt{\frac{\ell_c}{2\pi}} \qquad [11]$$

For the plane problem of a rectilinear anisotropic elastic solid

$$\phi = \sqrt{b_{22}\left\{2\left(b_{11}b_{22}\right)^{1/2} + 2b_{12} + b_{66}\right\}}.$$

These elastic constants can be expressed in terms of the constituent moduli of the composite laminate:

$$b_{11} = \frac{1}{E_T};\ b_{12} = -\frac{\nu_{LT}}{E_L};$$
$$b_{22} = \frac{1}{E_L};\ b_{66} = \frac{1}{G_{LT}} \quad \text{(in plane stress).}$$

E_L and E_T are the Young's moduli of the laminate in the longitudinal and transverse directions, respectively; υ_{LT} is the Poisson's ratio for transverse strain; and G_{LT} is the shear modulus.

Combining equations (9 and 10) and eliminating ℓ_c (equation 11), we get:

$$K_I^{*} = \frac{K_{Ia}^{*} + \sqrt{K_{Ia}^{*\,2} - 4\left(1-V_f\right)\sigma_c\delta_c/\phi}}{2} \qquad [12]$$

where $K_{Ia}^{*} \ge 2\sqrt{\left(1-V_f\right)\sigma_c\delta_c/\phi}$.

Meanwhile, from a consideration of the geometry of the stress corrosion crack in a single fibre (1), the crack growth rate is given by:

$$\frac{dY}{dt} = 4r_f^{\,2}\sin^2\theta\frac{d\theta}{dt} \qquad [13]$$

Re-call that Y is the area of the stress corrosion crack in a glass fibre (Fig. 1). Substituting equation [13] into equation [2] and combining equations [3, 5], we obtain:

$$dt = \frac{2r_f}{\upsilon k}\frac{\sin^2\theta}{\theta}\exp\left(-\frac{\alpha\beta F(\theta)\sqrt{2\pi r}}{RT}KI^{*}\right)d\theta \qquad [14]$$

where $k = \exp\left(-\frac{\Delta Q}{RT}\right)$.

Now the time required for the slow crack growth stage of failure, t_F, of a single glass fibre is obtained by integrating equation [14]:

$$\int_{\theta_0}^{\theta_f}\frac{\sin^2\theta}{\theta}\exp\left(-\frac{\alpha\beta F(\theta)\sqrt{2\pi r_f}}{RT}KI^{*}\right)d\theta \qquad [15]$$

(Re-call that θ_0 is half the angle made by two fibre radii on the edges of the pre-existing (inherent) surface flaw, and θ_F is the critical value at unstable (fast) fracture of the glass fibre).

Unstable fracture takes place when K_I^* attains the value of fracture toughness K_{IC} of glass. By combining equations [3 and 5], we obtain the critical angle θ_F at fast fracture:

$$\theta_F = F^{-1}\left(\frac{K_{IC}}{\beta K_I^* \sqrt{2\pi r_f}}\right) \qquad [16]$$

F^{-1} is the inverse function of $F(\theta)$ given previously.

The brittle fracture (final) stage (of the glass fibre) is much shorter than time t_F given by equation [15]. It follows, therefore, that the macroscopic crack propagation rate, da^*/dt, in the composite is approximately given by:

$$\frac{da^*}{dt} = \frac{D}{t_F} \qquad [17]$$

Re-call that D is the distance between neighbouring fibres in a doubly periodic square array of fibre (equation [4]).

By introducing the following quantities:

$$\xi = \left(\frac{\nu k D}{2r_f}\right) \text{ and } \mu = \frac{\alpha\beta\sqrt{2\pi r_f}}{RT} \qquad [18]$$

and by combining eqns [15] and [17]:

$$\frac{da^*}{dt} = \frac{\varsigma}{I} \qquad [19]$$

where

$$I = \int_{\theta_0}^{\theta_f} \frac{\sin^2\theta}{\theta} \exp\left\{-\mu K_I^* F(\theta)\right\} d\theta \qquad [20]$$

Now consider the integrand of the integral. Choose sensible values for the following: α = 0.11 - 0.216 $m^{5/2}$ /mol; V_f = 0.40~0.57; V = 0.5 for a cross-ply laminate (where V is that fraction of plies of the laminate in which glass fibre is perpendicular to the macroscopic crack, equal to 1.0 for a unidirectional laminate); R = 8.31 J/(mol.K) and T = 298 K. This gives a value of μ estimated to be within the range μ = 97 ~ 295 (MPa $\sqrt{m}$)$^{-1}$.

Generally speaking, the range of experimentally observed values of stress intensity factor K_I at the crack tip is between 2 and 15MPa $\sqrt{m}$. It follows that the integrand tends to zero, except for very small values of θ.

Since the angle θ_0 is small and much smaller than θ_F, it follows that (1):

$$I \approx \frac{4}{1.6\mu K_I^*}\left(\frac{1}{1.6\mu K_I^*} + \frac{\theta_0}{2}\right)\exp\left(-0.8\mu\theta_0 K_I^*\right) \qquad [21]$$

Typical values for the Young's moduli of fibre and matrix and fibre volume fraction are: 72 GPa, 4 GPa, and 0.5, respectively. An apparent value of K_I^* was fixed at 5MPa $m^{1/2}$. For the fracture toughness of glass, we used 0.73 MPa $m^{1/2}$; and for SiO_2 glass, a fracture energy γ_c = 3.7 J/m^2. Based on these values, we obtain for the angle θ_F (using equation [16]) 4.3^o (or 7.5 x 10^{-2} rad).

Hence, by combing equations [19 and 21], the macroscopic crack propagation rate, da^*/dt, as a function of K_I^* can be written in the form:

$$\frac{da^*}{dt} = 1.25\xi\mu^2 K_I^{*2}\left(\frac{1}{2+1.6\mu\theta_0 K_I^*}\right)\exp\left(0.8\mu\theta_0 K_I^*\right) \qquad [22]$$

This equation indicates that the macroscopic crack propagation rate is independent of fibre radius, r, and fracture toughness of glass fibre.

Figure 5 shows a logarithmic plot of macroscopic crack propagation rate,

da^*/dt, versus the crack tip stress intensity factor, K_I^*, for selected values of θ_0 and δ_c. (equation [22]).

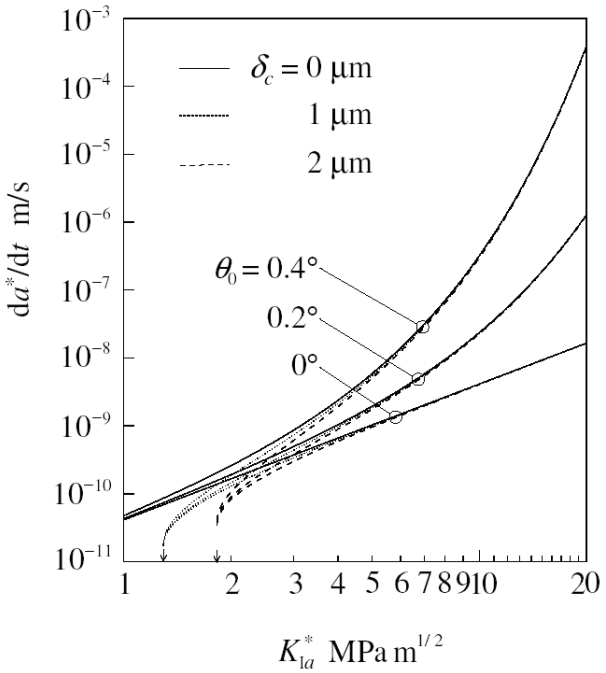

Fig. 5 Macroscopic crack propagation rate vs apparent crack tip stress intensity factor

Figure 6 shows a experimental values of macroscopic crack propagation rate versus the crack tip stress intensity factor K_{Ia}^*.

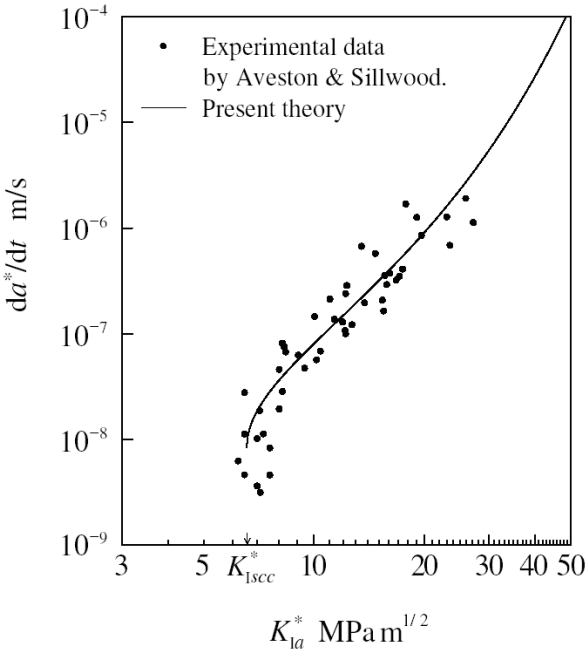

Fig. 6 Crack growth rate data vs apparent crack tip stress intensity factor

Values of ξ and μ are set at 5x10^{-15} m/s and 115 (MPa m$^{1/2}$)$^{-1}$, respectively. The figure indicates a linear log (da^*/dt) - log K_I^* relationship over an order of magnitude range of da^*/dt. In particular, the figure shows that the larger the inherent flaw size, the faster the crack growth rate. Furthermore, matrix crack bridging effects, which become noticeable at lower values of K_I^*, shift the threshold value of K_I^* to higher values. The lowest threshold value of K_I^* indicated by the arrow (Fig. 5) is given by:

$$K_{Iscc}^* = 2\sqrt{\frac{(1-V_f)\sigma_c\delta_c}{\varphi}} \qquad [23]$$

Verification by experiment

There is experimental data in the literature for a unidirectional laminate of E-glass fibre (50% by vol.) in an orthophthalic polyester resin matrix. Crack propagation experiments were carried out in 1Normal sulphuric acid at room temperature. The data shown in Fig. 6 is that of Aveston and Sillwood, and the reference is given in (1). Comparison between experiment and theory can be made by setting values of ξ = 8.5 x 10^{-14} m/s, μ = 118 (MPa $\sqrt{m}$)$^{-1}$, θ_0 = 0.076^o, $\sigma_c\delta_c$ =1.85 kPa.m, and ϕ = 8.6 x 10^{-2} (GPa)$^{-1}$. The solid line shows the prediction of macroscopic crack propagation rate, which is in good agreement with experimental measurement. This gives confidence in the physical soundness of the model.

In the special case of θ_0 = 0^o and δ_c = 0, the relationship between da^*/dt and K_{Ia}^* (from equations 12, 22), reduces to:

$$\frac{da^*}{dt} 0.625\xi\mu^2 K_{Ia}^{*2} \qquad [24]$$

This is a straightforward Paris law to the power of two.

5. Failure Maps

In a cross-ply $(0/90)_n$ composite, resistance to crack propagation is determined essentially by the fracture toughness of the load bearing (0^o) plies. The physical model is based on the initial phase of stable cracking of fibres followed by fast fracture of the individual (0^o) ply. Macroscopic laminate fracture, then, is brought about by a sequence of failed (0^o) plies. As a first approximation, this ignores any cracking resistance of the transverse (90^o) ply. The total time to failure, t_F, of the cross-ply laminate is given by:

$$t_F = \frac{1}{\xi\mu}\sum_{i=1}^{n}\int_{a_i}^{a_F}\left(\frac{1.6}{\mu K_{Ii}^{*2}}+\frac{1.26\theta_o}{K_{Ii}^{*}}\right)\exp\left(-0.8\mu\theta_o K_{Ii}^{*}\right)da^{*} \qquad [25]$$

where

$$K_{Ii}^{*}=\frac{K_{Iai}^{*}+\sqrt{K_{Iai}^{*2}-4(1-V_f)\sigma_c\delta_c/\phi}}{2}$$

(for $a^{*}\geq l_c$) [26a]

$$K_{Ii}^{*}=K_{Iai}^{*}-1.12(1-V_f)\sigma_c\sqrt{\pi a^{*}}$$

(for $a^{*}\leq l_c$) [26b]

a_i, is the size of stable inherent flaw or initial crack depth at the surface of the $(n+1^{-i})^{th}$ (0^o) ply; and a_F is the critical length of unstable crack in the $(n+1^{-i})^{th}$ (0^o) ply. In computing the failure map, the depth of the pre-existing macroscopic surface crack in the (0^o) ply is assumed to be $a_i = a_o (i = 1, 2, 3, 4, 5)$. Typically, the apparent fracture toughness, K_Q, of a cross-ply glass fibre-epoxy laminate is 35 MPa $m^{1/2}$. Fig. 7 displays the predicted times to failure of a cross-ply $(0^o/90^o)_5$ glass fibre-epoxy laminate with working (applied) tensile stress for various values of a_i and θ_o. Matrix bridging by stretched polymer fibrils or ligaments increases life-time. We understand from the second map (Fig. 8) that pre-existing flaw size in the surface (0^o) ply influences the time to failure.

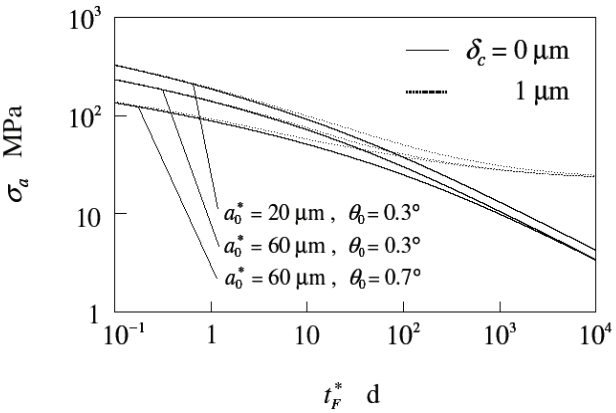

Fig. 7 Time to Failure Predictions

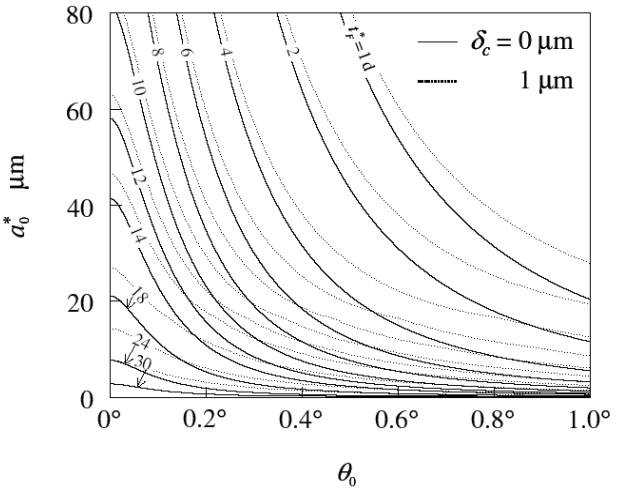

Fig. 8 Time to Failure Predictions

6. Final Remarks

Successful modelling of physical processes can be achieved by following a set of steps: identify the physical mechanisms; construct the model (using previously modelled problems); test the model (by comparing with data) and tune the model (lumping together empirical parameters). In other words, determine the dominant mechanisms; simplify it (them); and exploit the modelling successes of others in materials science and engineering. But even now the job is still incomplete; the last word is *iterate.*

Reference

(1) Sekine H and Beaumont PWR "*Composites Science and Technology*, **58**, (10) (1998)1659-1665.

MODELLING OF SCALING EFFECTS ON DEFORMATION BEHAVIOUR OF W/CU COMPOSITES

M. Korthäuer, S. Ataya, E. El-Magd
Department of Material Science, Aachen University
Augustinerbach 4, 52062-Aachen, Germany

Abstract

Copper (Cu) reinforced with tungsten particles (W) has a high potential for applications in the field of electronics where high strength combined with electrical conductivity is required. The effects of different scaling parameters (tungsten volume fraction, the tungsten particle size and the volume of the deformation zone) have great effect on the forces needed in the machining process of the tungsten/copper (W/Cu) particle composites.
W/Cu composites with different fractions of the tungsten content (W/Cu-80/20, 70/30, and 60/40 wt.%) were examined under compression tests. The influence of the tungsten particle size was also studied. Therefore, each volume fraction was varied to be 10 and 30µm. Different sizes of the compression specimens were tested to get a wider scope of the scaling effects. The diameter (D_S) of the specimens was varied with 1, 2, 4, 6, 8 mm, while the specimen height (H_S) was kept equal to the diameter ($D_o = H_o$). The experiments were carried out at a wide range of temperature between 20 °C and 800°C.

An investigation of the influence of the strain rate on the scaling effects was also carried out. Therefore compression tests were done at strain rates from quasi-static ($0.001s^{-1}$) up to high strain rates ($5500\ s^{-1}$). Compression tests at strain rates from $0.001\ s^{-1}$ to $100\ s^{-1}$ were conducted on a servohydraulic Universal Testing Machine while the experiments in the dynamic strain rate range were done using a Split-Hopkins pressure bar.

A clear dependence of the flow stress on the deformed specimen‘s volume, on the tungsten volume fraction and the tungsten particle size volume has been observed. Metallographic investigation has shown an obvious effect of the specimens' size on the failure behaviour under compression loading. Basic informations which explain the influence of the scaling parameters on the flow behaviour of the investigated composite materials were also revealed from the metallographic investigation of the deformed specimens under quasi-static and dynamic strain rates.

In this paper the quasi-static as well as the dynamic flow curves were modelled for the different investigated W/Cu composites to show the scaling effect on the flow stress. A material model based on Swift hardening law was applied. A further parameter was added as multiplier to this material law to take into consideration the effect of the deformed volume, tungsten particle size and the volume fraction of the composite component. The effect of the temperature on these different parameters was also described.

Keywords: Particle composites, W/Cu, tungsten, copper, size effects, dynamic material behaviour, modelling

1. Introduction

Size effects play a decisive role in manufacturing and deformation processes. These effects are divided into physical effects and structural effects [1]. The physical effects are the absolute volume size effects, the surface to volume size effects SVS [2] and the forces related size effects (e.g. Van-der-Waals-force, surface tension and gravitation). In this respect Kienzle [3] found out that the geometry of the deformed zone has a great influence on the value of the required specific force in the machining processes. The structural effects that could be taken into consideration are the grain size to deformed part thickness and the surface structure resulting from the history of the work piece [1].
The deformation behaviour of a metallic matrix reinforced with hard particles depends on volume fraction, size, shape, and distribution of the reinforcements [4-6]. Cleveringa et al [4] have numerically investigated the effect of the particles´ morphology on the deformation behaviour of the particle composite materials. It has been concluded that when the reinforcements block all the slip planes of the matrix, the composite has a high strain hardening and there is a significant size effect. On the other hand when veins of unreinforced matrix or clustering of the reinforcement exist [6] the matrix will be easily deformed in these zones, the overall flow stress of the composite decreases and there is no size effect.

2. Test materials and experimental work

W/Cu composites in different weight percentages (W/Cu-80/20, 70/30 and 60/40 wt%) were tested under compression loading in a wide range of strain rate and temperature. These composites were studied in two different tungsten particle sizes of D_P = 10 µm and 30 µm. Compression tests were carried out using cylindrical specimens with ratio of diameter (D_S) to height (H_S) as 1. The diameter D_S was varied with the values 1 mm, 2 mm, 4 mm, 6 mm and 8 mm. The tests were conducted with strain rates between 0.001 s^{-1} and 5500 s^{-1}. The mechanical tests up to a strain rate of 100 s^{-1} were conducted on a servo-hydraulic universal testing machine, while the higher strain rates experiments were done on a Split-Hopkinson-bar [7]. The tested specimens were metallographically investigated to show the deformation and fracture behaviour of the tested materials.

3. Experimental results

Influence of strain rate and temperature

At first all six different W/Cu composites were investigated at different specimen sizes and temperatures in a range of strain rate between 0.001 s^{-1} and 5500 s^{-1}. In Figure 1 the strain rate sensitivity of W/Cu-80/20 is shown at three different specimen sizes with 2x2, 4x4 and 6x6 mm. A clear transition can be observed from the isothermal towards the adiabatic material behaviour at high strain rates, where the test time is too short for the transfer of heat generated by the deformation work. The investigation with different strain rates was also performed at different temperatures between room temperature and 800°C. Figure 1 represents as example the experimental results at room temperature (a) and 400°C (b). Especially at higher temperatures a distinct increase of the level of flow stress between the quasi-static and dynamic strain rates is visible.

Influence of the specimen size

Under quasi-static und fast strain rates the different composite materials showed a definitive scaling effect due to different specimen sizes. This scaling effect leads to a decrease of the flow stress with rising specimen size and concentrates on a higher tungsten fraction.
Figure 2 shows that this scaling effect is visible under quasi-static and dynamic loading according to different specimen sizes. The figure shows exemplary the flow curves of three investigated materials with a particle size of 10 µm at five different specimen sizes (1x1, 2x2, 4x4, 6x6 and 8x8 mm) at a strain rate of $\dot{\varepsilon}=10\,s^{-1}$ (a). In Figure 2b three different specimen sizes (2x2, 4x4 and 6x6 mm) at a strain rate of $\dot{\varepsilon}=3500\,s^{-1}$ are represented. For all tested materials the stress level increases with decreasing specimen size. This effect is getting lower with the increase of the copper content in the W/Cu composites such as in the material W/Cu-60/40. The size effect also

decreases at higher temperatures resulting in lower flow stress of copper [8].

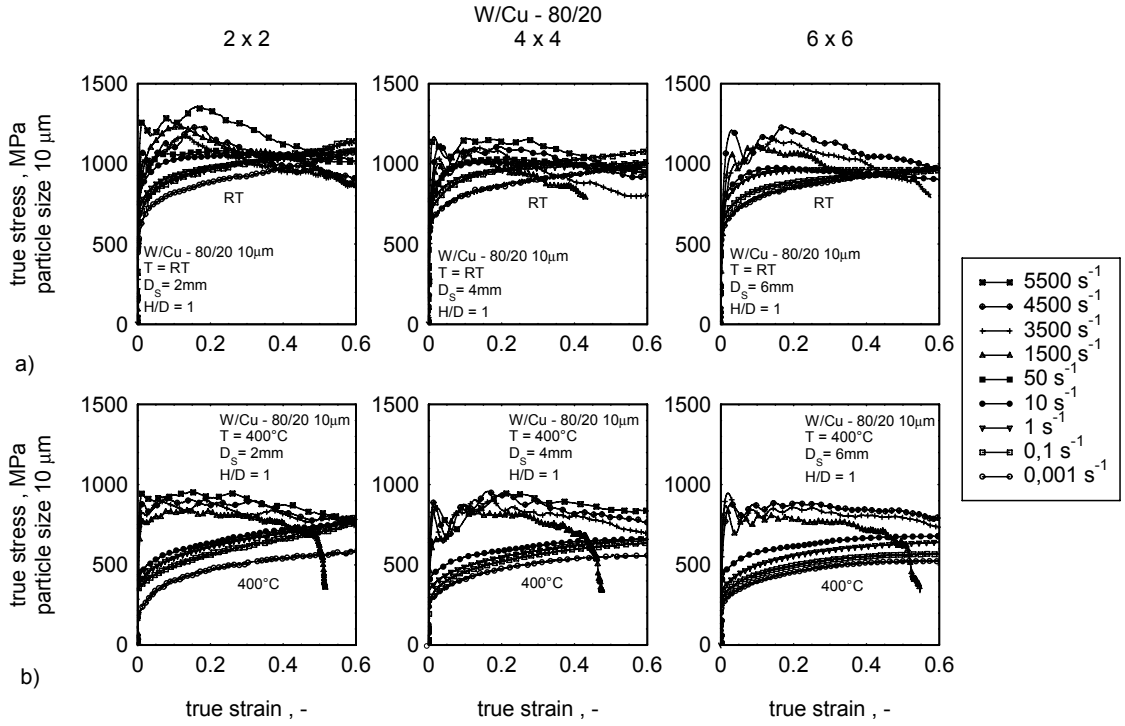

Figure 1: *Flow curves of W/Cu-80/20 with a particle size of D_P=10 µm at three different specimen sizes (2x2, 4x4 and 6x6 mm) and different strain rates at room temperature and 400°C*

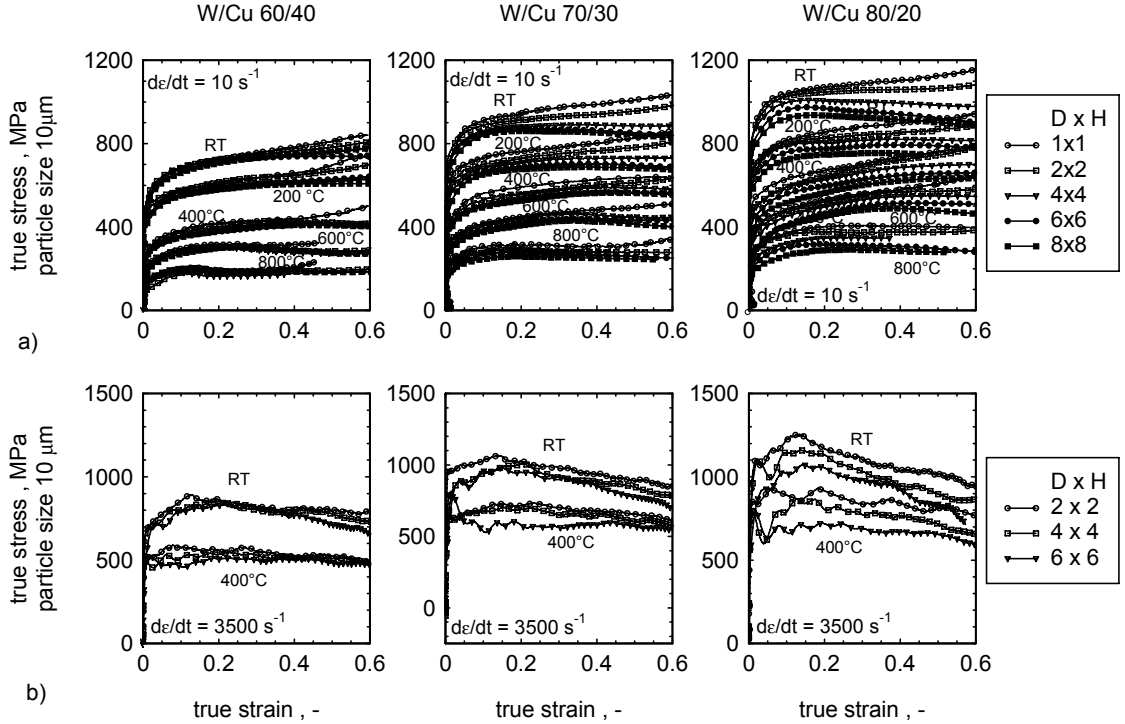

Figure 2: *Influence of the specimen size of W/Cu-60/40, 70/30 and 80/20 with a particle size of D_P=10 µm at a strain rate of $\dot{\varepsilon}=10\,s^{-1}$ and $\dot{\varepsilon}=3500\,s^{-1}$ at different temperatures*

Deformation and fracture behaviour of W/Cu composites under dynamic strain rates

In metal/metal composites the contribution of the composite components in the deformation process has a significant role in the overall deformation behaviour of the

composites. Figure 3 shows the deformation degree of the tungsten particles in compression specimens deformed up to a reduction of height of 70%. Two specimen sizes were used in this investigation (2 mm and 6 mm) with stopped Hopkinson-bar-tests at different degrees of deformation. A specific area in the longitudinal section in the middle of the specimen of the deformed specimens is documented in Figure 3. A higher deformation of the tungsten particles has been observed in the small specimen compared with the bigger specimen of the composite W/Cu-80/20 (Figure 3a). In the case of the composite W/Cu-60/40 (Figure 3b) the higher copper content has absorbed the whole amount of deformation with minimal sharing of the tungsten particles in the deformation process in both tested specimen sizes (2 mm and 6 mm). This can also explain the relatively lower size effect of the composites having a lower content of tungsten.

Furthermore, the dense packing of the tungsten particles in the composites containing high tungsten contents raises the chance of homogeneity of the particle distribution. On the other hand the probability of occurring particle free zones or veins in the composite materials with low particle content such as in W/Cu-60/40 is higher. These zones allow an easier way of deformation through the matrix resulting in inhomogeneous deformation of the specimen [4]. This is an additional cause of the lower scaling dependence of the composite materials with lower content of tungsten W/Cu-60/40 as in Figure 3b).

Also the fracture behaviour depends on the volume fraction of tungsten and copper. The metallographic pictures in Figure 4 exemplifies the deformation and fracture behaviour of W/Cu-80/20 with a particle size of 30 µm at two different specimen sizes with 2x2 and 6x6 mm. The failure of the composites starts at the boundaries of the specimens with a very high localised deformation also through the hard tungsten particles. In contrary to this material behaviour the fracture takes place in W/Cu-60/40 through the soft component with only minimal deformation of the hard component.

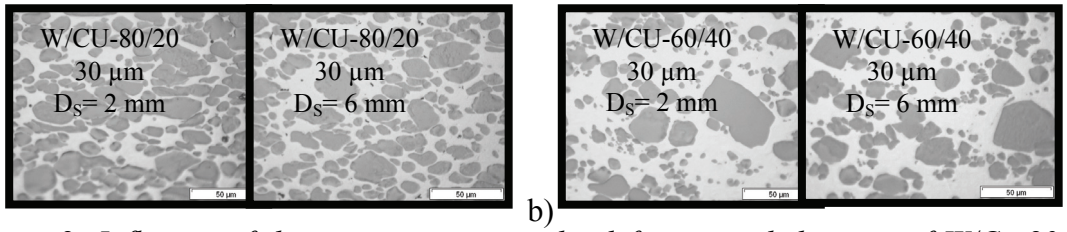

Figure 3: *Influence of the specimen size on the deformation behaviour of W/Cu-80/20 and 60/40 at two different specimen sizes with 2x2 and 6x6 mm after 70% deformation*

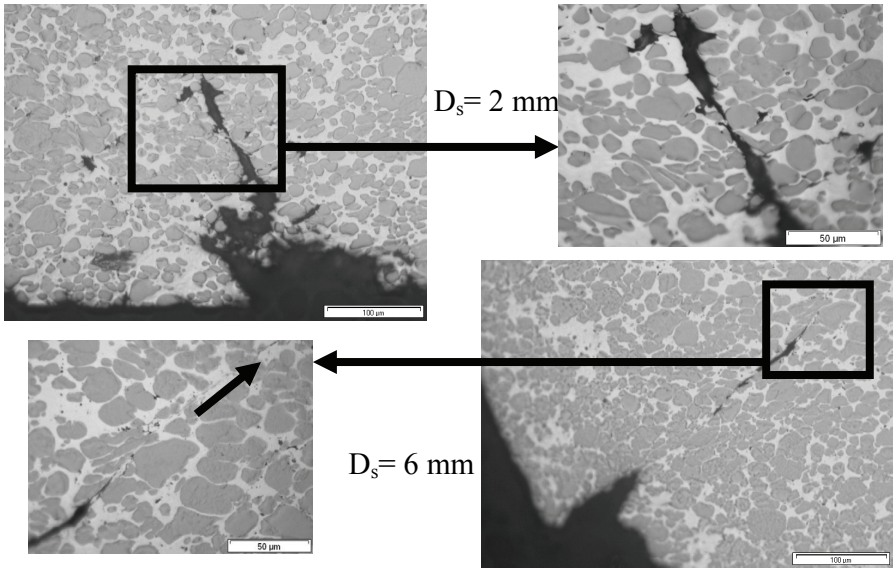

Figure 4: *Fracture behaviour of W/Cu-80/20 30 µm at two different specimen sizes with 2x2 and 6x6 mm after 70% deformation*

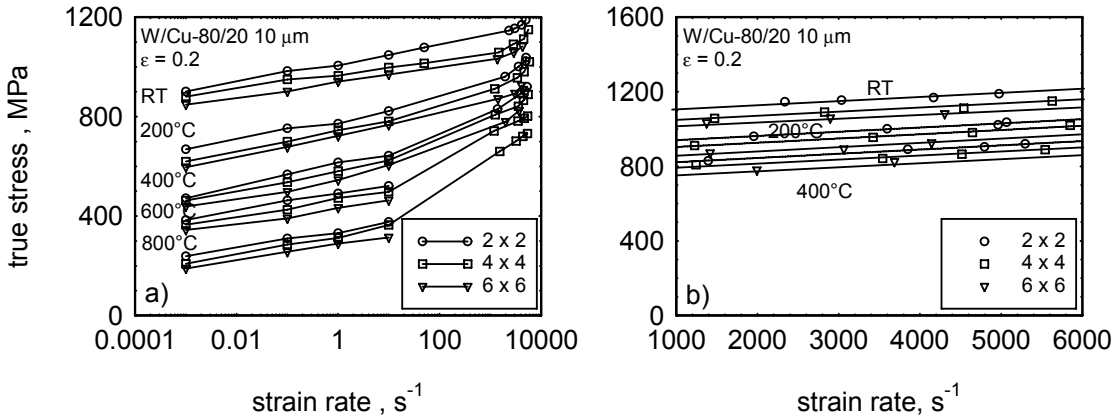

Figure 5: *Material behaviour 80/20 in a wide range of strain rate (left) and in the dynamic range of strain rate (1000 s^{-1} to 6000 s^{-1}, right) at different temperatures and specimen sizes*

Material behaviour over a wide range of strain rate and temperature

Figure 5a shows on the left the material behaviour in a wide range from strain rate (0.001 s^{-1} up to 5500 s^{-1}) and temperature (RT-800°C) according to the different specimen sizes. The true stress is plotted over strain rate at a plastic strain of 0.2. Especially for W/Cu-80/20 there is a distinctive scaling effect with different specimen sizes from quasi-static up to dynamic strain rates. On the right the true stress over the dynamic range of strain rate is represented. The stress follows the strain rate by a linear relation. This is typical for an adiabatic damping controlled gliding mechanism at very high strain rates [9]. The slope $\partial\sigma/\partial\dot{\varepsilon}$ remains approximately constant for all three specimen geometries. However, the flow stress level decreases with rising specimen size.

4. Modelling of the material behaviour

Description of the quasi-static flow curves

For the numerical simulation of different machining or deformation processes of such materials, adequate material laws are needed. The experimentally determined flow curves of all composite materials were described (Figure 8). The material law from Swift [10] was found to be suitable for getting the nearest fitting of the experimental results,

$$\sigma = K(T, D_S)(B + \varepsilon)^{n(T)} \qquad (1)$$

where B = 0.001, K and n are material parameters, which could be described as a function of the temperature (T) in the following equations [11].The lowest and highest K-value (for D_S=8 and D_S=1) were taken as reference values and described as a function of the absolute test temperature.

$$K_1(T) = a_1 \cdot \exp\left(-\frac{T-293}{1356}\right) - b_1 \qquad (2)$$

$$K_8(T) = a_8 \cdot \exp\left(-\frac{T-293}{1356}\right) - b_8 \qquad (3)$$

The parameter K can be described for all other specimen geometries (2mm, 4mm and 6mm) by

$$K(T, D_S) = K_8 + (K_1 - K_8)\left(1 - D_S/8\right) \qquad (4)$$

The parameter n is constant for all specimen geometries and was described as a function of the absolute test temperature.

$$n(T) = c - d \cdot \exp\left(-\frac{T-293}{1356}\right) \qquad (5)$$

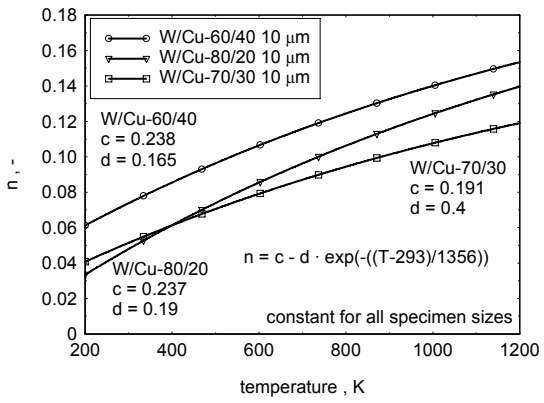

Figure 6: *the parameter n as a function of temperature*

Figure 6 shows the relation n(T) for the W/Cu composites 60/40, 70/30 and 80/20 with 10 µm particle size. The parameters c and d for the description of n are material dependent and were also given in Figure 6. The parameter K is represented in Figure 7 as a function of the temperature and the specimen size. A clear increase of K to smaller specimen sizes is visible. This effect intensifies with a higher fraction of tungsten particles. With this parameter functions the flow curves were calculated and compared with the experimental ones (Figure 8).

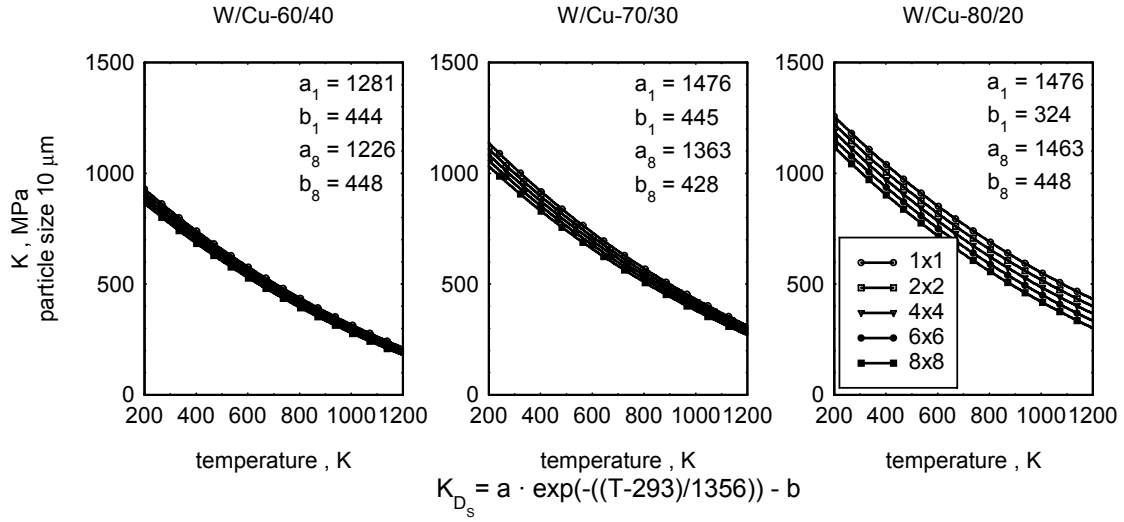

Figure 7: *The parameter K as a function of specimen size and temperature for W/Cu-60/40, 70/30 and 80/20 with a particle size of 10 µm*

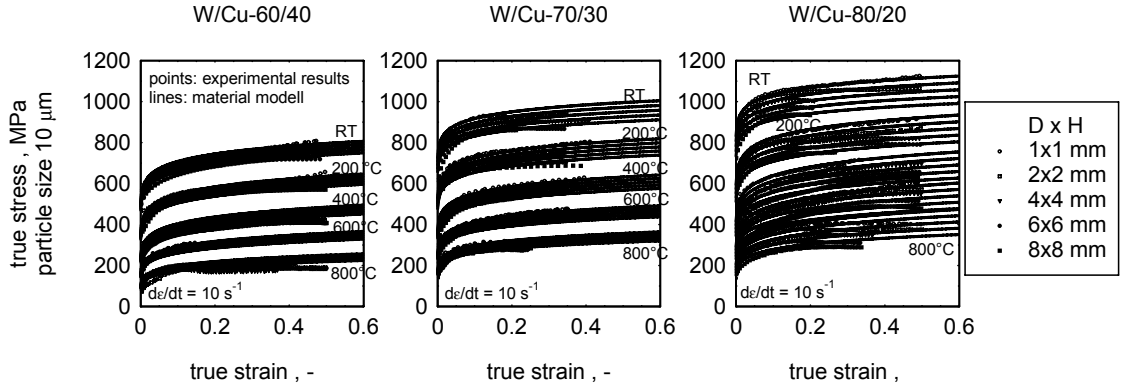

Figure 8: *Description of the material behaviour of W/Cu-60/40, 70/30 and 80/20 according to different specimen sizes and temperatures*

Description of the dynamic flow curves

For the numerical simulation under dynamic strain rates of W/Cu materials the flow stress follows.

$$\sigma = f(\varepsilon, \dot{\varepsilon}, T, D_S) \qquad (6)$$

The material law consists of the swift hardening function [12] with an additional linear viscous damping term. This law was used for describing of the experimental results of all investigated specimen sizes and W/Cu weight fractions. The strain hardening exponent n shows a unique temperature dependency for all materials and specimen sizes, where as the parameter K is temperature and specimen size dependant.

$$\sigma = \left(K(T, D_S) \cdot (B + \varepsilon)^{n(T)} + \eta \cdot \dot{\varepsilon} \right) \qquad (7)$$

B is assumed to be constant with a value of 0.001. The exponent n can be described by a linear function of the temperature (Figure 9):

$$n(T) = -0.0000511 \cdot T + 0.159 \qquad (8)$$

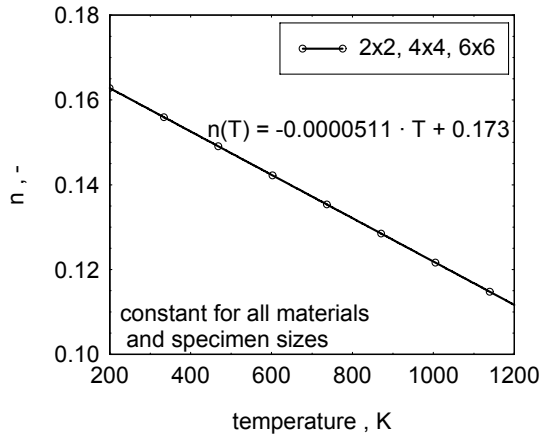

Figure 9: *the parameter n as a function of temperature*

Also the parameter K can be described with a linear temperature function for all materials and specimen sizes in the investigated range of temperature. The distribution of K is shown in Figure 10.

$$K(T, D_S) = m_1 \cdot T + (m_2 \cdot D_S + b_1) \qquad (9)$$

Under dynamic loading conditions, the deformation process is no longer isothermal, as there is no time for heat transfer. The process has to be considered as adiabatic. It can be assumed that 90% of the deformation work is transformed into heat:

$$\rho \cdot c_p \cdot \Delta T = \kappa \cdot \sigma(\varepsilon, \dot{\varepsilon}, T, D_S) \cdot \Delta\varepsilon \qquad (10)$$

ρ is the density of the material, c_p its specific heat capacity, $\kappa = 0.9$ the thermal efficiency and σ the value of flow stress which is already influenced by the temperature increase. With eq. 3 the temperature increase on the adiabatic flow curves can be inculded in the material description. All experimentally determined flow curves of the composite materials W/Cu-60/40, 70/30 and 80/20 were described with that material model.
Figure 11 shows a comparison between experimental and computation results for the dynamic flow curves of W/Cu-60/40, 70/30 and 80/20 at all three used specimen sizes with 2x2, 4x4 and 6x6 mm and a particle size of 10 µm. The description for low strain rates the parameter K (Figure 10) is described as a function of specimen size and temperature with a linear decrease to higher temperatures.

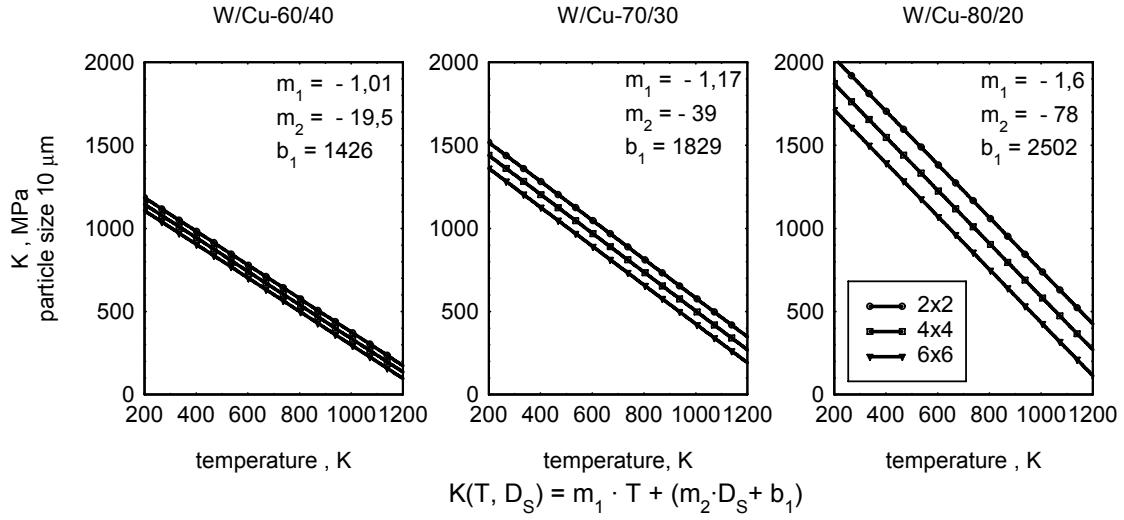

Figure 10: *The parameter K as a function of specimen size and temperature for W/Cu-60/40, 70/30 and 80/20 with a particle size of 10 µm*

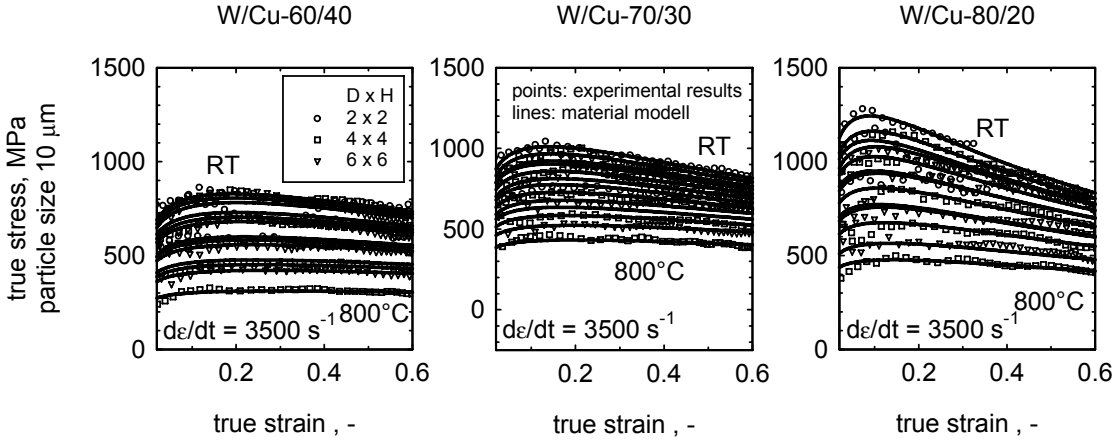

Figure 11: *Description of the dynamic material behaviour of W/Cu-60/40, 70/30 and 80/20 according to different specimen sizes and temperatures*

5. Summary

W/Cu composites have an obvious scaling effect on the flow behaviour against the volume fraction of tungsten and copper, the tungsten particle size, the used specimen size, strain rate and temperature. Especially at W/Cu-80/20, a composite with a very high tungsten fraction, a clear scaling effect at different specimen sizes is visible, which raises to higher strain rates. The deformation and fracture behaviour were investigated with stopped split-hopkinson-bar tests. The quasi-static and dynamic material baheviour of the composites were modelled in dependence to the temperature and the specimen size.

References

[1] Vollertsen, F. (2003), *Process Scaling*, **24**, pp. 1-9, Vollertsen, F. and Hollmann, F. (Eds.) BIAS Verlag, Bremen

[2] Geiger, M., Vollertsen, F., Kals, R. (1996), *CIRP Anneals*, **45**, No.1, pp. 277-282

[3] Kienzle, O. (1952), *Zeitschrift VDI*, **94**, No. 11/12, pp. 299-305

[4] Cleveringa, H.H.; van der Giessen, E.; Needleman, A. (1997), *Acta Mat.* **45**, No.8, pp. 3163-3179

[5] Borbely, A. , Biermann,H. (2000), *Adv. Eng. Mater.*, **2**, No. 6, pp. 366-369

[6] Tszeng,T.C. (1998), *Composites*, **29B**, pp. 299-308

[7] El-Magd, E., Treppmann, C.: In: Proceeding of Third International Conference on Metal Cutting and High Speed Machining, Metz, 2,2001, 25-28

[8] Poole, W.J.; Embury, J.D.; Macewen, S. ; Kocks, U.F.: Large strain deformation of a copper tungsten composite system, I. Strain distributions, Philosophical Magazine, 69A, No.4, 1994, 667-687

[9]El-Magd, E.; Treppmann C. and Korthäuer, M.: Constitutive modelling of CK45N, AlZnMgCu1.5 and Ti-6Al-4V in a wide range of strain rate and temperature, J. Phys. IV France, 110, 2003, 141-146

[10] Swift, H.W. (1952): *J. Mech. Phys. Solids*, **1**, p. 18

[11] El-Magd, E. (2004) In: *Modeling and Simulation for Material Selection and Mechanical Design,*. Totten, G. E., Xie, L., Funatani, K. (Eds.), Marcel Dekker Inc., New York, pp. 195-300

[12] Swift, H.W. Plastic instability under plane stress, J. Mech. Phys. Solids, 1, 1952, 18

WHY IS MESOMECHANICS NECESSARY TO PREDICT THE DAMPING PROPERTIES OF POLYMER COMPOSITES?

Professor R D Adams
Department of Mechanical Engineering,
University of Bristol, Bristol, BS8 1TR, UK

Abstract

The ability of a material to dissipate vibrational energy can be an important parameter when this material is incorporated into a structure that is exposed to cyclic or random loading. This property is called damping and it is defined here as the ratio of the energy dissipated during a cycle to the maximum stored energy. In addition to its value to the engineer, damping has long been recognised as providing a sensitive tool for studying the structure and condition of materials. In this investigation, a polymeric composite, consisting of a deformable matrix reinforced with relatively rigid inclusions was used. In such advanced fibre composites, high modulus, high strength fibres are carefully aligned in one direction. These composites are anisotropic, not only in their moduli, but also in respect of other physical properties, among these being the damping.

The purpose of the present work was to evaluate the effect of the interface on the damping and moduli in both flexure and torsion. Unidirectional glass fibre reinforced composites were used with a range of volume fractions varying from 0.3 to 0.7. In addition, the fibre diameter was varied from 10 to 50 microns.

In general, micromechanics can be successfully used to predict the properties of advanced fibrous composites. It was found that the experimentally-measured longitudinal Young's modulus fitted the micromechanics theory quite well, as did the shear modulus and damping.

However, when measuring the longitudinal damping (in flexural vibration) a significant effect was found of fibre diameter. The values predicted by micromechanics seriously underestimated the measured values. The larger was the fibre diameter, the smaller was the damping. This correlated with a reduction in the specific area of the composite.

Keywords:

Composites, specific area, damping, fibre diameter, volume fraction.

1. Introduction

The ability of a material to dissipate vibrational energy can be an important parameter when this material is incorporated into a structure that is exposed to cyclic or random loads. This property is called damping and it is defined here as the specific damping capacity ψ, where $\psi = \Delta W/W$, ΔW being the energy dissipated during a cycle, and W being the maximum stored energy as shown in Fig. 1. In addition to its value to the engineer, damping has long been recognised as providing a sensitive tool for studying the structure and conditions of materials. It is in this sense we are here examining the dynamic properties of unidirectional composite materials.

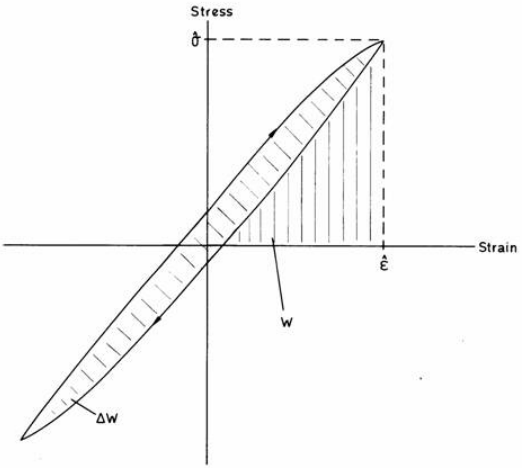

Fig. 1 Definition of specific damping capacity

Generally, composite materials consist of two phases, a deformable matrix which is reinforced with relatively rigid inclusions. Fibre-reinforced materials in which the alignment of the fibres is closely controlled are highly anisotropic, not only in respect of moduli but also other physical properties, among these being damping.

Several authors have studied the damping of fibre-reinforced composites, particularly carbon- and glass-fibre-reinforced plastics (CFRP and GFRP). Among the first were Adams et al [1] who investigated the effect of the volume fraction of fibre, v, in flexure and torsion on unidirectional CFRP and GFRP: this work was extended by Adams and Bacon [2] and new theories were given for predicting the damping from the properties of the fibre and matrix. The above investigations were carried out using fibres of essentially constant diameter, 7-10 μm. Also, in none of these predictions was any account taken of any dissipation associated with the fibre/matrix interface.

The well-known law of mixtures predicts that

$$E_L = v\,E_f + (1-v)\,E_m \qquad (1)$$

where E_L is Young's modulus,
v is the volume fraction,
and the suffices L, f and m refer to the longitudinal direction (parallel to the fibres), the fibre and the matrix respectively.

It can also be shown that the damping ψ_L under direct cyclic stresses and strains in the longitudinal direction is given by

$$\psi_L = \frac{v\psi_f E_f + (1-v)\psi_m E_m}{v\,E_f + (1-v)\,E_m} \qquad (2)$$

Now since ψ_f is very small, compared with ψ_m [3], Eq. (2) reduces to

$$\psi_L = \frac{(1-v)\psi_m E_m}{v\,E_f + (1-v)\,E_m} \qquad (3)$$

If E_f is much greater than E_m (which it is for most cases), Eq. (3) reduces to

$$\psi_L = \left(\frac{1-\nu}{\nu}\right)\frac{\psi_m E_m}{E_f} \qquad (4)$$

Unfortunately, this equation does not fit well the experimental data, and it is the objective of this paper to investigate the discrepancy, and the relative roles of composite micromechanics and mesomechanics.

Experimental programme

Specimens of unidirectional composite were prepared using both glass and carbon fibres embedded in a polymeric resin. The carbon fibres are only available in diameters of about 8 μm, while the glass fibres could be obtained with nominal batch diameters of 10, 20, 30 and 50 μm.

Flexural vibration was used since longitudinal vibration would have been at very high frequencies and given small amplitudes of vibration. Note that if high cyclic stress amplitudes are used at high frequency, there would also be a serious heating effect which would complicate the results. (The author has used such a method to determine the damping properties of metals).

One problem with flexural vibration is that shear stresses arise which can also contribute to the damping. This is discussed later.

Measurements were made not only of the longitudinal damping, but also the longitudinal Young's modulus (E_L) and the longitudinal shear modulus (G_{LT}) and damping (ψ_{LT}). The shear tests were carried out in a torsion pendulum specially developed for testing composites.

Where conventional micromechanics works

For the longitudinal Young's modulus, as given in Eq. (1), there is a lot of evidence, from the author and others, that this equation is robust and accurate for predicting E_L. In the case of shear, several authors, most notably Adams and Doner [6] and Hashin [7] have produced predictions of the longitudinal shear modulus, G_{LT}. Adams and Doner used a numerical technique, and Hashin a correspondence principle. For longitudinal shear, Hashin's expression reduces to

$$G_{LT} = \frac{G_m\left[(G+1)+(G-1)\nu\right]}{(G+1)+(G-1)\nu} \qquad (5)$$

where $G = G_{LTf}/G_m$.

Unfortunately, G_{LTf} is not easily measured, although the author produced some direct results on single carbon fibres [3] and showed that G_{LTf} is approximately 18 GPa. For glass, a value of about 25 GPa is generally accepted. Thus, G_{LTf}/G_m will be of the order of 7 ~ 10. Using these values, Hashin's equation fits quite well the experimental data. This is not surprising as the composite modulus is heavily dominated by the matrix properties.

For the longitudinal shear damping, Hashin's theory gives

$$\psi_{LT} = \frac{\psi_m(1-\nu)\left[(G+1)^2+\nu(G-1)^2\right]}{\left[G(1+\nu)+1-\nu\right]\left[G(1-\nu)+1+\nu\right]} \qquad (6)$$

This expression is again strongly dominated by the matrix damping, and if G = 10 and ν = 0.5, then $\psi_{LT} = 0.8\,\psi_m$. Although, the experimental data are somewhat lower than Hashin's prediction, the discrepancy is not large, and conventional micromechanics is followed reasonably well.

Longitudinal damping – the case where micromechanics fails badly

Adams and Bacon [2] showed that when testing in dynamic flexure, shear effects were not insignificant. By reducing the beam aspect ratio (length/thickness) from 90 to 50, there was a significant reduction (about 5%) in the measured Young's modulus. The discrepancy increased as the proportion of energy stored in shear increased.

From this shear energy, they were able to calculate the energy dissipated due to shear. Since this was highly matrix dependent (as mentioned above), there was a significant contribution from shear damping.

By measuring the damping as the aspect ratio was reduced from 90 to 50, they found that the damping increased by about a half, as shown in Fig. 2. The law of mixtures prediction, as given in Eq. (3), does not allow for this shear effect. However, by calculating the energy dissipated in shear from the mode shape of their specimen, they found that it paralleled the measured trend quite well.

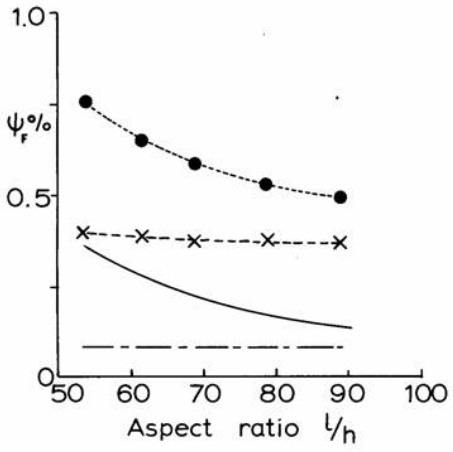

Fig. 2 HM-S carbon fibre in DX-209 epoxy resin; v=0.5; ● measured S.D.C., — theoretical shear S.D.C.; — - — law of mixtures prediction of S.D.C.; × measured minus theoretical shear S.D.C.

But, when the law of mixtures prediction and the shear contribution were subtracted from the experimental data, it was found that there remained a substantial and unexplained contribution which was essentially independent of the aspect ratio. The question then arises as to the source of this additional damping contribution.

The variation of damping with volume fraction was also investigated by Adams and Bacon. Fig. 3 gives their results. A different fibre type was used and two different matrix materials (both epoxy resins) than was the case for the results in Fig. 2. In this experiment, the shear damping contribution was quite small. Even so, they showed that after subtracting the law of mixtures and shear contributions, there remained a substantial additional term which could not be explained, as was also shown in Fig. 2.

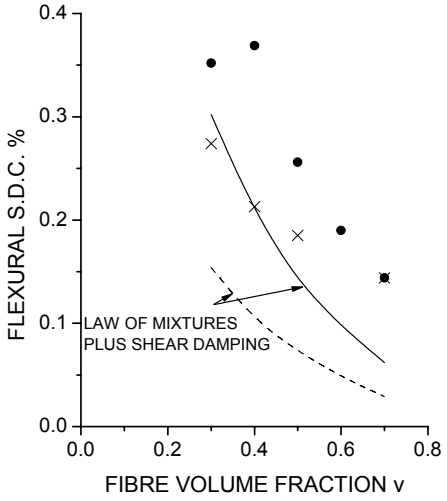

Fig. 3 Variation of flexural S.D.C. with fibre volume fraction in vacuo at 35 MPa maximum surface stress. HT-S fibre: ● LY558; × F/MNA epoxy

It has often been suggested that the presence of fibres affects the nature of the resin matrix compared to that of the neat resin when cured in exactly the

same way. If this is the case, then there should be an effect of volume fraction beyond that given by the law of mixtures prediction for damping. Also, if the fibres have some affect on the matrix cure in the vicinity of the fibres, then there should be an additional damping term which should relate to the surface area of the fibres in a given volume, i.e. the specific fibre area, A_f. Considering a unit cube of composite, we have N fibres of diameter d. The volume fraction, v, is

$$v = \frac{N\pi d^2}{4} \tag{7}$$

Now the area, A, of these fibres will be

$$A_f = N\pi d \tag{8}$$

which is the specific area.

Substituting for N from Eq. (7) gives us

$$A_f = 4v/d \tag{9}$$

With carbon fibres, it is almost impossible to vary the fibre diameter d in any coherent manner. However, with glass fibres, no such restriction is imposed. Adams and Short [8] made up a series of unidirectional glass fibre composites with fibre diameters of 10, 20, 30 and 50 μm, and with volume fractions in the range 0.35 to 0.7. Their results for the longitudinal damping vs. volume fraction are given in Fig. 4. It can be clearly seen that there is a coherent and significant variation of damping with fibre diameter.

Figure 4 shows that ψ_L decreases not only with increasing v but also with increasing fibre diameter d. At the higher volume fractions, the measured difference in damping values for 50 and 10 μm fibres was 0.4-0.5% SDC. This was slightly greater than the total damping predicted by the law of mixtures (0.3-0.4% SDC) at the same volume loading. This indicates that the damping contribution from the interfacial area is of the same order as that from the energy stored in the matrix. Two explanations spring to mind. One concerns the stress concentration around the fibre, the other concerns the change in matrix properties around the fibre.

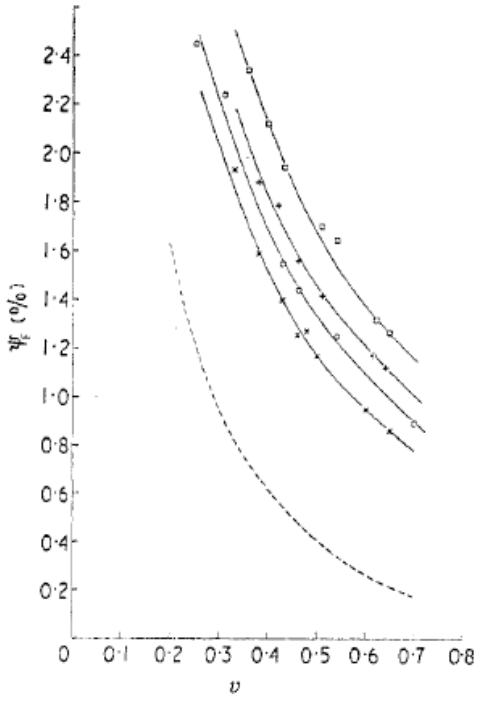

Fig. 4 Specific damping capacity in flexure ψ_F, against fibre volume fraction v for different diameter fibres: --- law of mixtures; □ d = 10 μm; + d = 20 μm; ○ d = 30 μm; × d = 50 μm.

Physically, it may be argued that, for a given volume fraction, the stress concentration in the matrix due to the presence of a fibre decreases as the diameter d of the fibre increases. In addition, the larger the fibre diameter, the fewer will be the number of sites of these stress concentrations $\left(\alpha d^{-2}\right)$. Thus, the strain energy per unit volume in the matrix close to the fibre will be reduced as the fibre diameter is

increased. Further, since the surface area of the fibres (and hence the volume of matrix affected) is inversely proportional to *d*, the total energy stored in the matrix adjacent to the fibres will be reduced roughly as d^{-3} with increase in *d*. The decrease in strain energy with *d* for a given stress is therefore countered to some extent by the increase in the interfacial shear stress for a given load. Very roughly, we should therefore have that the energy stored in the matrix near to the fibre decreases as d^{-1}. Since the strain energy stored in the matrix is not wholly affected by the above, the actual change will be as d^{-n}, where $n<1$. Since the energy dissipated, and hence the damping, is directly proportional to the energy stored in the matrix, then this too will change as d^{-n}.

The fibre-affected cure zone behaves in a similar way. The volume in which the cure might be changed (in some way) will be proportional to the fibre area per unit volume, A_f. In other words, $\psi_L \alpha d^{-1}$. However, since the fibres are not individuals in a large volume of matrix, there will be interactions with the zones around adjacent fibres. As the volume fraction increases, this interaction will increase. It is therefore likely that the damping is not directly inversely proportional to *d* in a similar way to the stress concentration argument.

The data from Fig. 4 have been re-plotted in Fig. 5 to show the variation of ψ_L with A_f. The lines were drawn from interpolated points. The results show an increase of damping with A_f for the range of fibre volume fraction investigated (0.35-0.7). There is a greater sensitivity to an increase in damping with A_f at lower fibre volume fractions.

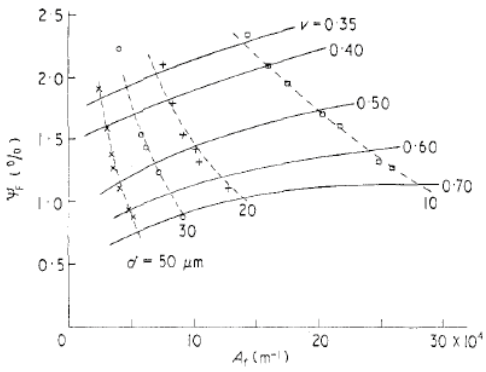

Fig. 5 Specific damping capacity in flexure, ψ_F, against interface parameter A_f for different diameter fibres: □ d = 10 μm; + d = 20 μm; ○ d = 30 μm; × d = 50 μm.

In Fig. 6, the data have been re-plotted to show the variation of $\ln \psi_L$ with $\ln d$. The trend is similar for all volume fractions, and the exponent *n* is of the order of 0.3.

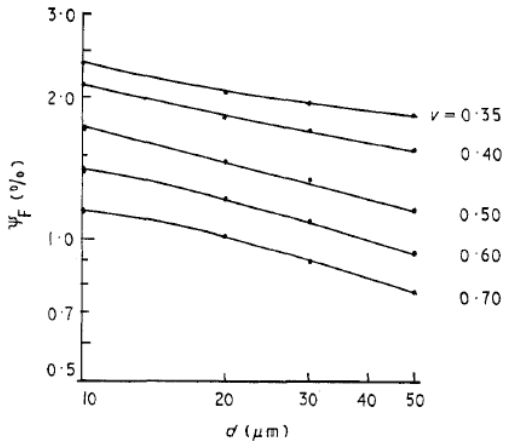

Fig. 6 Specific damping capacity in flexure ψ_F, against fibre diameter *d* at different values of fibre volume fraction *v*.

Conclusions

By testing a series of unidirectional fibre-reinforced plastics in flexural vibration, it has been shown that there is a significant influence of the fibre diameter on the measured damping properties. By subtracting the 'law of

mixtures' damping, and that due to shear (in flexure) it was shown that about half the damping could not be explained by micro and macro mechanics. It was concluded that there was a strong effect of the specific fibre area on the damping, due to actions in the matrix around the fibre. This invoked the need to consider mesomechanics to explain the discrepancy.

References

[1] Adams, R.D., Fox, M.A.O., Fox, R.J.L., Flood, R.J., Friend, R.J., Hewitt, R.L. (1969), *Journal of Composite Materials*, **3**, pp. 594.

[2] Adams, R.D., Bacon, D.G.C. (1973), *Journal of Composite Materials*, **7**, pp. 53.

[3] Adams, R.D. (1975), *Journal of Physics, D: Applied Physics*, **8**, pp. 738.

[4] Adams, R.D., Percival, A.L. (1969), *Journal of Physics, D: Applied Physics*, **2**, pp. 1693.

[5] Adams, R.D. (1972), *Journal of Sound & Vibration*, **23**, pp. 199.

[6] Adams, D.F., Doner, D.R. (1967), *Journal of Composite Materials*, **1**, pp. 4.

[7] Hashin, Z. (1970), International *Journal of Solids & Structures*, **6**, pp. 797.

[8] Adams, R.D., Short, D. (1973), *Journal of Physics, D: Applied Physics*, **6**, pp. 1032.

SCALING ON THE CRITICAL ENERGY RELEASE RATE IN SPRUCE

Nuno Dourado
CETAV/UTAD, Dep. de Engenharias, 5000-911 Vila Real, Portugal

Stéphane Morel
LRBB, UMR 5103 (CNRS/INRA/Univ. Bx1), 69 route d'Arcachon, 33612 Cestas, France

Marcelo F. S. F. de Moura
Fac. Eng. da Universidade do Porto, R. Dr. Roberto Frias, 4200-465 Porto, Portugal

Gérard Valentin
LRBB, UMR 5103 (CNRS/INRA/Univ. Bx1), 69 route d'Arcachon, 33612 Cestas, France

José Morais
CETAV/UTAD, Dep. de Engenharias, 5000-911 Vila Real, Portugal

Abstract

A study is presented focused on the dependence of the *Resistance*-curve (*R*-curve) in Norway spruce (*Picea abies* L.) on the specimen size. Fracture (Mode I) under displacement control is induced in geometrically similar single notched beams loaded in three-point bending (SEN-TPB) of different sizes, and fracture parameters determined from the *R*-curve. Based on experimental data a typical configuration of the *R*-curve in spruce is proposed for different characteristic sizes *h* of the tested specimen shape. Size ranges relative to the ultimate load and the *R*-curve parameters obtained in the experiments are revealed.

Keywords: wood, mode I, *R*-curve, size effect.

1. Introduction

Though initially introduced by Irwin in the fifties [1], the concept of the *Resistance*-curve (*R*-curve), *i.e.* the evolution of the crack growth resistance $\mathcal{R}$ with the crack length increment Δa, has been more extensively treated by Kraft, Sullivan and Boyle [2]. Research involving theoretical and experimental studies in materials which exhibit toughening behaviour as wood revealed that the *R*-curve is not an inherent material property but depends on the specimen geometry [3], relative crack size [4], loading type [5], and specimen size [6]. To the authors knowledge the effect of the specimen size on the *R*-curve is not well understood in wood.
Therefore, a campaign of experiments has been got through using Norway spruce (*Picea abies* L.) as testing material, inducing fracture (Mode I) in geometrically similar single

notched beams loaded in three-point bending (SEN-TPB). Specimens were prepared composing a total of 6 homothetic series with the size range of 1:12 and the loading span-to-depth (L/h) ratio fixed to 6. *R*-curves were obtained according to a recently proposed method [7] by means of an LEFM approach based on the unloading compliance together with FE analysis, using the elastic properties of wood. Influence of the specimen size h is shown comparing fracture parameters determined from the *R*-curve.

Conclusions are drawn on the typical configuration of the *R*-curve in wood (*Picea abies* L.) for different characteristic sizes h of the SEN-TPB. Plotting of size ranges relative to the *R*-curve parameters and the ultimate load are made known.

2. Experiments

The material examined in the present study is cleaned dried (11-13% moisture content) Norway spruce (*Picea abies* L.) sawn to meet the nominal dimensions and wood axis presented in Fig. 1. Taking due note to the reference characteristic structure size (referred to as $h4$ in Table 1) five additional homothetic series were machined composing a size range of 1:12. Composing parts were stuck on with the epoxy adhesive ref. ARALDITE® AW106/953U before introduction of starter notches (1 mm thick) with total extensions set to $h/2$.

Series label	h	b	a_0
$h1$	280	80	140
$h2$	210	60	105
$h3$	140	40	70
$h4$	70	20	35
$h5$	35	10	17.50
$h6$	23.33	6.67	11.67

Table 1: Series label and corresponding dimensions (in mm). *h4* is the reference characteristic structure.

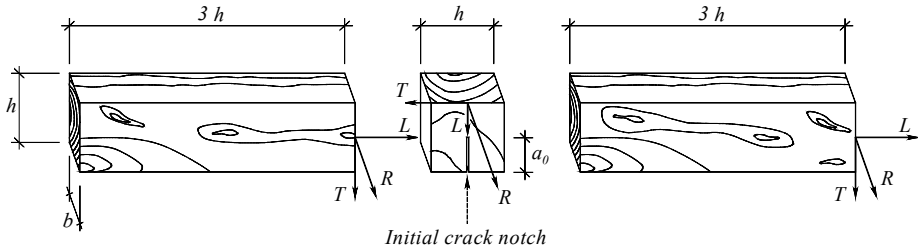

Figure 1: *Composing parts set-up of the SEN-TPB specimen before bonding. Anatomic axis directions in wood: (L) Longitudinal, (R) Radial and (T) Tangential. h : characteristic structure size. a_0: initial crack length. b: thickness*.

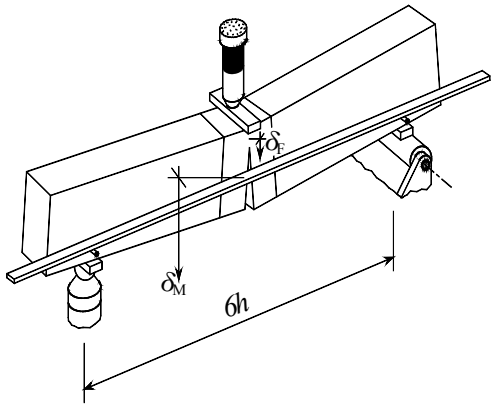

Figure 2: *Sketch of TPB test setup. δ_F: Load-point displacement; δ_M: Metal bar mid-span displacement; h: analysed characteristic structure size. Displacement: $\delta = \delta_F - \delta_M$.*

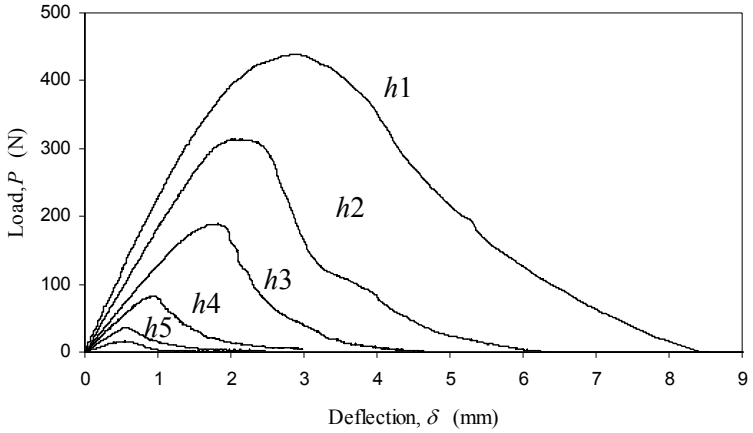

Figure 3: *Superposition of typical load-deflection curves obtained in wood (Picea abies L.) fracture tests (under displacement control) for each tested series using specimen shape SEN-TPB.*

3. The *R*-curve

The procedure proposed by Morel *et al.* [7] was used in this work to determine the *Resistance*-curve in wood. In this approach wood fracture behaviour is described on the basis of an equivalent linear elastic problem. Accordingly, the crack length is understood to be the equivalent crack, which agreeing with LEFM, gives the same unloading stiffness.

Stiffness evolution as a function of the crack length $R(a)$ is computed through FEM calculations using the elastic properties of wood (Table 2). Stiffness dependence with crack length a is determined by means of linear elastic (FEM) analysis for different values of a in the interval: $a_0 \le a < h$ (Fig. 1). Accounting for scattering always present in wood mechanical properties, stiffness evolution $R(a)$ is corrected for each specimen using a multiplicative correction factor $\beta = R(a_0)/R_{\exp}(a_0)$, with $R(a_0)$ representing the initial stiffness given by FEM computations, and $R_{\exp}(a_0)$ the stiffness obtained experimentally, before propagation onset. Factor β is evaluated once per specimen since the only known value of a is the initial crack notch extension a_0. Indeed, for values of $a > a_0$, the damage extension which develops ahead of the crack tip leads to equivalent crack length extents (evaluated from the experimental stiffness of the specimen) unlike the actual crack length. A corrected numerical stiffness function $R_{cor}(a)$ is therefore obtained computing $R_{cor}(a) = R(a)/\beta$.

As a result of this stiffness correction procedure, the equivalent linear elastic crack length a, corresponding to any point of the experimental load-deflection curve, is evaluated. Hence, for a given point of the load-deflection curve (Fig. 4) the unloading stiffness $R_{\exp}(a)$ is determined and the corresponding equivalent linear elastic crack length computed through a dichotomic process applied to the corrected numerical stiffness function $R_{cor}(a)$ previously evaluated. This corrected function enables to perform continuous computations of the elastic energy release rate for each load-deflection values recorded all along the fracture tests.

E_L (MPa)	E_R (MPa)	E_T (MPa)	ν_{TL}	ν_{RL}	ν_{TR}	G_{TL} (MPa)	G_{RT} (MPa)	G_{RL} (MPa)
9 900	730	410	0.018	0.032	0.306	610	22	500

Table 2: Elastic properties of Spruce (Picea abies L.) according to [8].

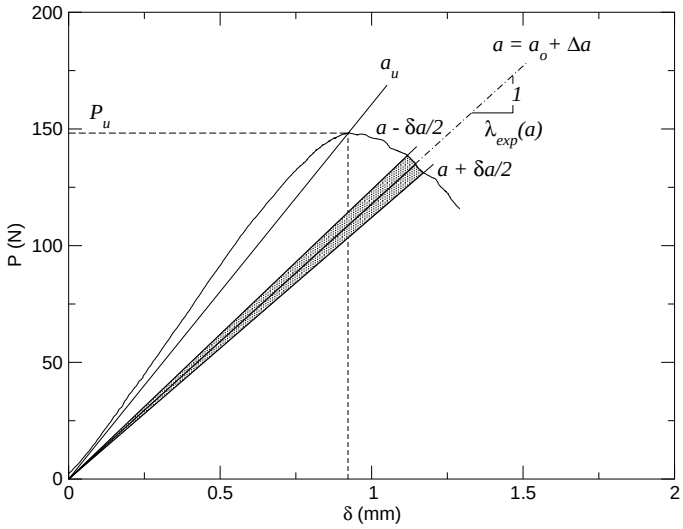

Figure 4: *Procedure used to assess the elastic energy release rate,* $G_R(a)=W(a)/(b\,\delta a)$ *in wood.* P_u *: ultimate load;* a_u *: corresponding equivalent crack length.*

As represented in Fig. 4, for a given experimental equivalent crack length, a, the elastic energy release rate, G_R, is calculated dividing the elastic strain energy $W(a)$, released during a small crack extension δa (dashed area) by the corresponding crack surface $b\,\delta a$ (b: specimen thickness). The small crack extension δa has been set to 1 % of the initial notch extension, since it has been found as the average value for which the estimated R-curves converge to a single curve. The strain energy $W(a)$ was evaluated using the experimental load-deflection curve and the straight lines passing through the points corresponding to equivalent crack lengths: $a-\delta a/2$ and $a+\delta a/2$ (both deduced by dichotomy from the corrected stiffness values: $R_{cor}(a-\delta a/2)$ and $R_{cor}(a+\delta a/2)$, respectively).

As shown in Fig. 5, for which the energy release rate G_R has been represented as a function of the relative crack length ($\alpha = a_{eq}/h$), subsequent to a characteristic relative crack length α_c (or more precisely, an equivalent relative crack length), the R-curve is levelled off, revealing that the energy release rate is independent of the relative crack length α. The critical energy release rate G_{RC} is the horizontal asymptotic value obtained for the $G_R(\alpha)$. It has also been noted through the experiments, that the energy release rate corresponding to the ultimate load $G_R(\alpha_u)$, is always smaller than G_{RC}.

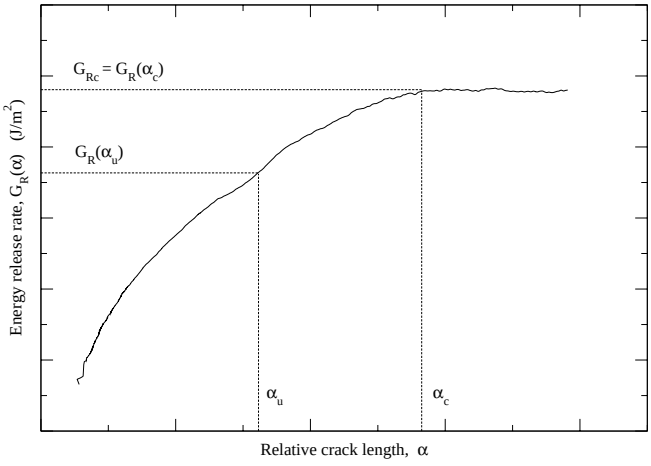

Figure 5: *Typical R-curve obtained for the SEN-TPB in wood.*

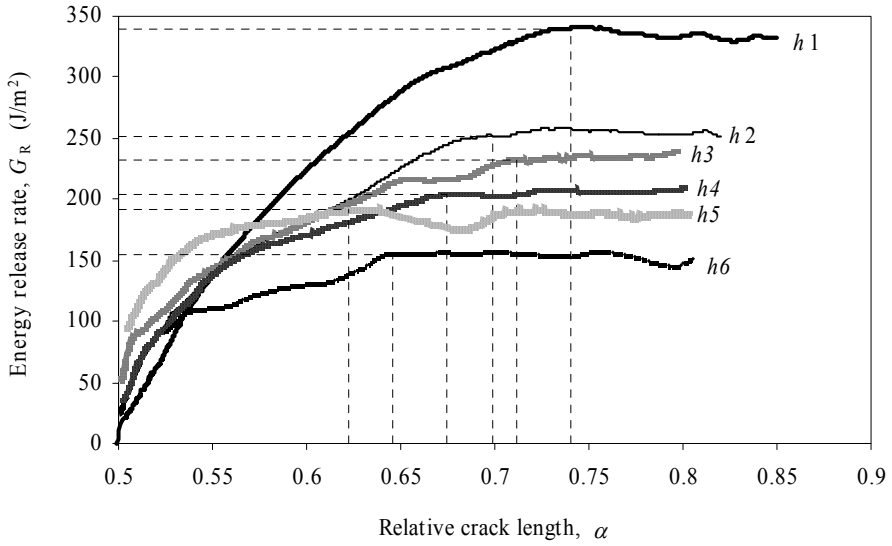

Figure 6: *Superposition of typical R-curves in spruce (Picea abies L.).*

4. Results and discussion

Fig. 6 exhibits the superposition of typical *Resistance*-curves got hold of the procedure proposed by Morel *et al.* [7] showing the characteristic rising tendency of the *R*-curve $G_R(\alpha)$, revealing a quasi-brittle behaviour of wood during fracture. This representative illustration clearly reports what has been noticed by many researching studies documented in the literature pointing out the dependence of the *R*-curve on the specimen size *h*.

Based on the set of results obtained for the totality of the tested specimens, it has been discerned a reduction in the growth rate of the resistance to crack propagation on the specimen size *h*, in the first half of the ascending branch of the *R*-curve.

Though denoting scattering in the parameters of a few tested series (COV assessments higher than 20%), the resume of mean values shown in Table 3 turns out an obvious upward trend in the *R*-curve parameters on the specimen characteristic size *h*. This tendency has been accounted and documented in Figs. 7 and 8 where the equivalent crack lengths a_u and a_c follow a linear behaviour with *h* (or *D*). The growing trend exhibited by the characteristic equivalent crack length a_c (or, which equivalent, the characteristic relative crack length α_c) clearly puts into evidence that the critical size of the damage zone in wood grows with the specimen size.

Series	Qtty.	$R_{exp}(a_0)$ (N/mm)	α_u	$G_R(\alpha_u)$ (J/m²)	α_c	G_{RC} (J/m²)
*h*1	5	283.7 (24.0)	0.578 (2.2)	192.4 (14.2)	0.774 (4.3)	372.0 (18.9)
*h*2	20	258.9 (23.5)	0.572 (4.0)	220.5 (46.0)	0.724 (8.8)	347.8 (47.8)
*h*3	20	167.5 (18.9)	0.543 (2.1)	156.6 (16.1)	0.657 (11.6)	223.3 (30.2)
*h*4	20	123.9 (20.3)	0.542 (1.9)	133.3 (14.5)	0.637 (7.5)	171.5 (14.7)
*h*5	20	49.2 (16.7)	0.535 (2.1)	146.1 (22.3)	0.629 (9.0)	178.1 (19.4)
*h*6	20	45.9 (15.1)	0.529 (2.2)	100.1 (11.7)	0.669 (7.7)	149.5 (15.7)

Table 3: *Resume of mean values obtained in performed fracture tests. $R_{exp}(a_0)$: initial experimental stiffness; α_u: relative crack length corresponding to the ultimate load P_u; $G_R(\alpha_u)$: energy release rate corresponding to P_u; α_c : characteristic relative crack length; G_{RC}: critical energy release rate. Values in parentheses represent the coefficient of variation (COV)*

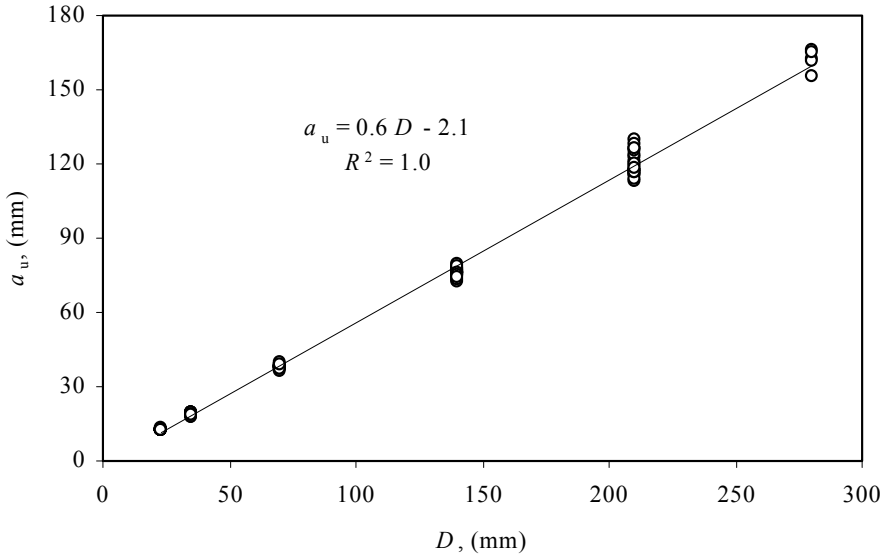

Figure 7: *Linear behaviour revealed by the equivalent crack length corresponding to the ultimate load obtained in the experiments, P_u.*

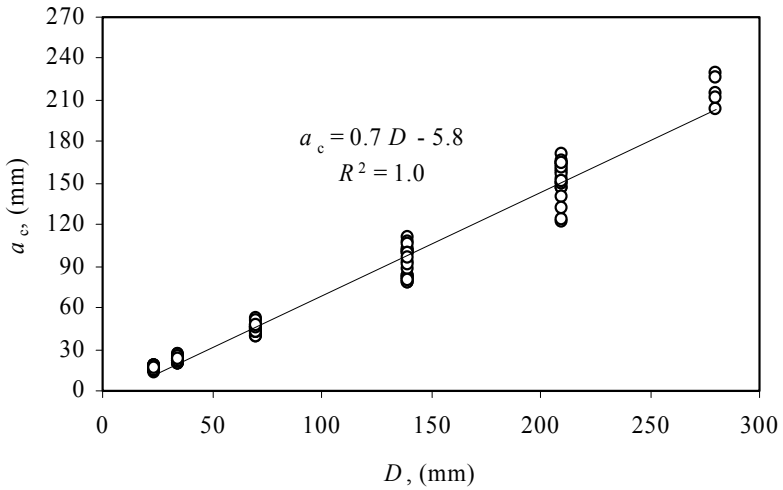

Figure 8: *Linear behaviour revealed by the characteristic equivalent crack length.*

Contrarily, Figs. 9 and 10 denote a clear non-linearity in the values of the remaining *R*-curve parameters (i.e., G_{RC} and $G_R(\alpha_u)$), which has been found not surprising since these values are strongly affected by scattering (Table 3).

Fig. 11 reveals the dependence of the ultimate load on the specimen size, revealing a quite acceptable size range relative to the scatter of the results.

5. Conclusions

Resistance-curves were obtained in spruce (*Picea abies* L.) performing fracture tests (Mode I) in SEN-TPB with different sizes. Characteristic rising tendency of the *R*-curve $G_R(\alpha)$ was noticed, revealing an evolution of the resistance to crack growth as a function of the relative crack length α. Typical configuration of the *R*-curve was revealed for the specimen size *h* (size range 1:12), denoting a reduction in the growth rate of the resistance to crack propagation on the specimen size *h*, in the first half of the ascending branch of the *R*-curve. Plotting of size ranges relative to the equivalent crack length corresponding to the peak load, a_u, and the characteristic crack length a_c have been found to behave linearly with the specimen size. This fact puts into evidence that the critical size of the damage zone in wood grows with the specimen size.

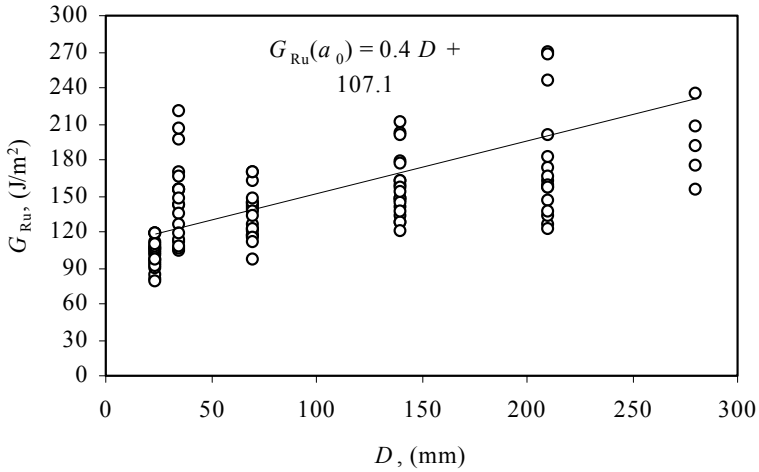

Figure 9: *Size ranges relative to the scatter of results of the energy release rate corresponding to the ultimate load.*

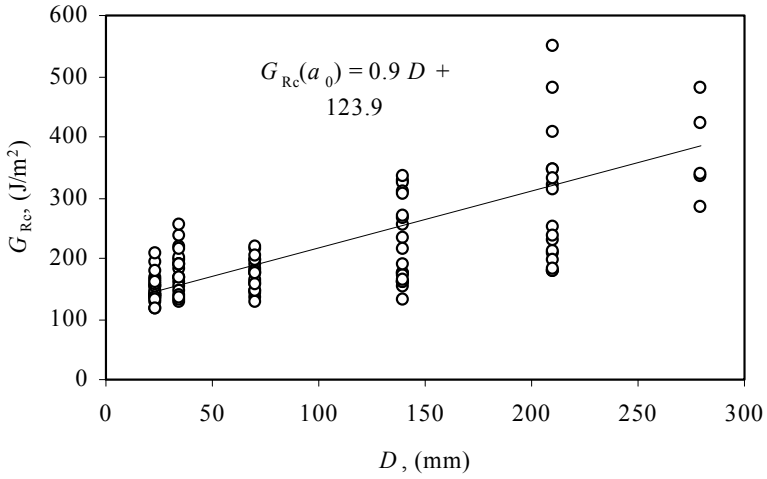

Figure 10: *Size ranges relative to the scatter of results of the critical energy release rate.*

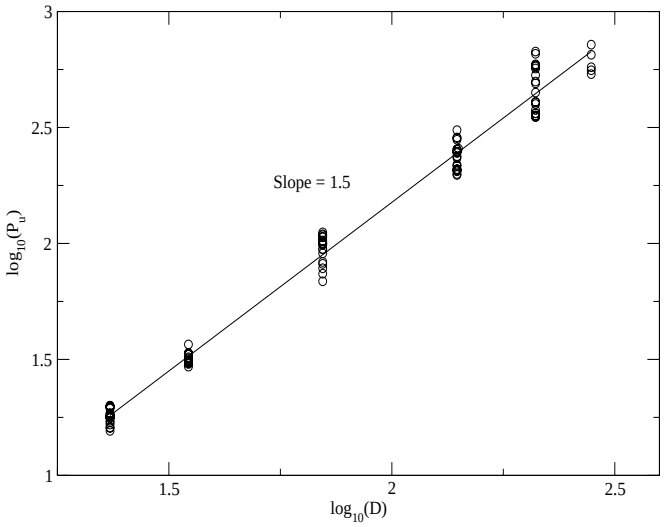

Figure 11: *Size ranges relative to the scatter of results of the ultimate load.*

Acknowledgements

The author acknowledges the *Université de Bordeaux 1* and *Laboratoire de Rhéologie du Bois de Bordeaux* (LRBB) for the scientific and technical support delivered during the fracture experiments.

Acknowledgments are also addressed to the Management Committee of the COST Action E35, for the attribution of a Short Term Scientific Mission within the COST scientific programme on *Fracture mechanics and micromechanics of wood and wood composites with regard to wood machining* (reference code COST-STSM-E35-01573).

References

[1] Irwin G. R., Kies J. A. and Smith H. L. (1958), *Proc ASTM*, 58: 640-657.

[2] Krafft J. M., Sullivan A .M. and Boyle R. W. (1961), *Proc Crack-Propag Symp*, Vol. 1, 8-28.

[3] Morel S., Mourot G., Schmittbuhl, J. *Int J Fract* 2003. 121: 23-42.

[4] Fett T., Munz D., Geraghty R. D., White K. W. (2000), *Eng Fract Mech* 2000. 66: 375-386.

[5] Munz D., Fett T. (1999) CERAMICS, Heidelberg: Springer.

[6] Bažant Z. and Planas J. (1998), CRC Press LLC; ISBN 0-8493-8284-X.

[7] Morel S., Dourado N., Valentin G. and Morais J. (2005), *Int J Fract*, 131: 385-400.

[8] Guitard D (1987). *Mécanique du matériaux bois et composites*. Cepadues-Editions; ISBN 2.85428.152.7: 108-123.

IV. Modeling: Molecular and Continuum

MOLECULAR DYNAMICS SIMULATIONS OF CU/AL DIFFUSION BONDING

Shangda Chen [1,2], Fujiu Ke [1,2], Hui Pan[1,2], Min Zhou[3], Yilong Bai[2]

1. Department of Physics, Beihang University, Beijing China 100083
2. State Key Laboratory of Non-linear Mechanics (LNM), Institute of Mechanics, Chinese Academy of Sciences, Beijing, China, 100080
3. The George W. Woodruff School of Mechanical Engineering, Georgia Institute of Technology, Atlanta, GA 30332-0405, USA

Abstract

A series of molecular dynamics (MD) simulations are performed to analyze the diffusion bonding at Cu-Al interfaces. Embedded atomic method (EAM) potential functions are adopted to describe the atomic interactions. The results indicate that the thickness of the interfaces is temperature dependent, with higher temperatures yielding larger thicknesses. At temperatures below 750 K, the interface thickness is found to increase in a stepwise manner as a function of time. At temperatures above 750 K, the thickness increases rapidly and smoothly. The bonding process consists of three stages. In the first stage, the rough surfaces deform under stress, resulting in increased contact areas. The second state involves significant plastic deformation at the interfaces as temperature increases, resulting in the disappearance of interstices and full contact of the surface pair. The last stage entails the diffusion of atoms under constant temperature. The bonded specimens show very good mechanical properties with the tensile strength reaching 88% of the ideal Cu/Al contact strength.

Keywords: Diffusion bonding, Molecular dynamics, Temperature, Tension, Cu, Al

1. Introduction

Diffusion bonding is a solid-state welding process wherein contacting surfaces are bonded via diffusion-controlled processes under pressure and at elevated temperatures with minimum macroscopic deformation [1]. Almost all materials with compatible chemical and metallurgical properties can be diffusion-bonded [2]. Since unexpected phase propagation may appear at the bond interface of some advanced materials in conventional welding [2-6], diffusion bonding has an inherent advantage in this respect. Recently, many theoretical and experimental studies have been carried out on diffusion bonding [1-8]. However, investigation of diffusion bonding at atomic scale has scarcely been carried out. Molecular dynamics (MD) simulations has become one of the most widely used tools in nanomechanics primarily because it is not limited by uncertainties in sample preparation and test condition and can be used to analyzed a range of issues concerning mechanical behavior at the nanoscale. Weissmann et al. [9] used MD simulations to investigate interface amorphization in the Co-Zr system. Their analysis showed clear development of interface amorphization as temperature increases. Chen et al. [10] calculated the interfacial energy of an fcc/bcc interface in Ni-Cr alloys. Cherne et al. [11] investigated the amorphization of the Ni/Zr system. The microstructures of a Cu-Ta interface [12] and a SiO_2/Si interface [13] have also been analyzed by means of MD simulations. The conditions analyzed in these papers are significantly different from the conditions of diffusion bonding which involve combined high temperature and high pressure. As a result, interfacial diffusion does not occur and no transition regions are seen. Since temperature and pressure play important roles in diffusion bonding, MD simulations accounting for such conditions can provide significant new insight into the not obtainable by other means. Another factor motivating MD analyses of diffusion bonding processes is

the lack of quantification of the effects of surface roughness which also plays an important role. MD simulations also offer the advantage of extensive parametric studies, potentially avoiding the need of long and expensive experiments. Recently, Chen et al. [14] reported an MD study of the pressure effect in diffusion bonding. In the present paper, we consider the coupled pressure-temperature-roughness effects in the diffusion bonding of a Cu/Al surface pair.

2. Simulation procedure

Interatomic potentials play a very important role in MD simulations. Considerable progress has been made in recent years in the development of empirical and semi-empirical many-body potentials. Well established embedded atomic method (EAM) potentials [15, 16] have been successfully used in analyzing elastic properties, defect formation energy and fracture mechanisms of various close-packed bulk metals. The modified EAM model proposed by Johnson [17,18] is adopted in the simulations here.

As shown in Fig. 1, the system analyzed consists of mono-crystal copper (top) and mono-crystal aluminum (bottom) slabs. The contact surfaces of copper and aluminum are both (100) planes. The total numbers of Cu and Al atoms in the model are 52488 and 46080, respectively. A parallel algorithm is used. Periodic boundary conditions are implemented in the two transverse (i.e., x and y) directions. Two layers of atoms at the bottom of the Al slab and two layers at the top of the Cu slab serve as boundary atoms for the purpose of load or displacement application. The initial thermal velocities of atoms are assumed to follow the Maxwellian distribution. The Newton's equation of motion for the atoms is numerically integrated using the Leap-Frog algorithm [19] with a fixed time step of 2 fs. The external transverse pressure is maintained at atmospheric pressure, while the vertical (i.e. z-axis) pressure is 20 MPa. The structures are first equilibrated at the temperature of 1 K for 10 ps. Subsequently, the structure is heated up from 1 K to a desired temperature at a rate of 5×10^{13} K/s. Subsequently, the temperature is kept constant at the desired value through the scaling of atomic momenta. To achieve sufficient interfacial diffusion, all MD runs are performed for 600 ps at the desired temperature.

3. Results and discussions

3.1 Effect of temperature

Atoms on the two sides of the interface can diffuse into the opposite sides only if temperature is sufficiently high. Necessary levels of temperatures are usually between $0.6T_m$~$0.8T_m$ (where T_m represents the melting points of the materials involved). Since the melting point of Al is 933 K, four different temperatures (600 K, 650 K, 700 K and 750 K) are considered here.

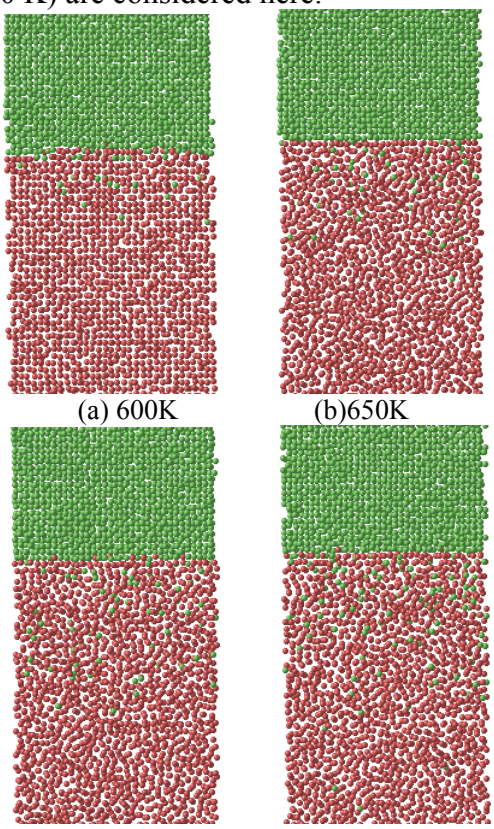

Fig. 1 A cross-section at (a) 600 K, (b) 650 K, (c) 700 K, and (d) 750 K after 600 ps, only atoms near the interface are shown. Copper atoms are green and aluminum atoms are red.

Fig. 1 shows a cross-section of the structure after 600 ps of diffusion at different temperatures. At 600 K, there is no observable diffusion between Cu and Al which retain their initial fcc structures (see Fig. 1(a)). At 650 K (Fig. 1(b)), a few Cu atoms have diffused into the Al side. When the temperature is higher than 650 K, obvious interfacial diffusion of Cu atoms into Al is seen, forming an Al-rich interfacial region. Figure 1 shows that this interfacial region and the Al block with an amorphous structural order. This

observation agrees well with the observation by Weissmann et al. [9] of a similar disordered interface in a Co-Zr system at high temperatures. Figure 1 also shows that the diffusion is primarily one-way, from the Cu side into the Al side. This is because Cu atoms have a smaller radius (2.556 Å) than that of Al atom (2.886 Å). It is well established that it is easier for smaller atoms to diffuse into a region of larger atoms [20]. On the other hand, the melting point of copper is higher than that of aluminum, making it harder to break the bonds between copper atoms than those between aluminum bonds. The effect is to make it more difficult for Al atoms to diffuse into the copper lattice. Because the bonds in aluminum are weaker, vacancies form more easily in Al. All the above factors enhance the opportunity of copper atoms to diffuse into aluminum, and not the other way around.

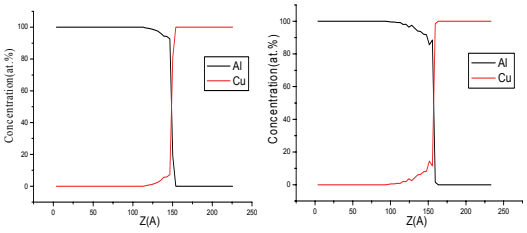

(a) 600K (b) 650K

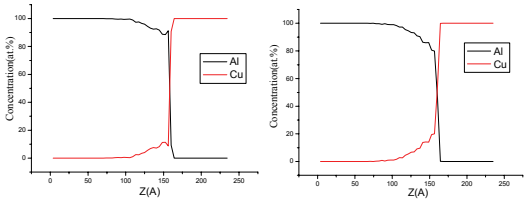

(c) 700K (d) 750K

Fig. 2 Concentrations of Cu and Al atoms along the z-direction at (a) 600 K, (b) 650 K, (c) 700 K, and (d) 750 K after 600ps

Figure 2 shows the concentrations of Cu and Al atoms along the z direction after 600 ps at different temperatures. The region where the concentrations of Cu and Al atoms are both over 5% is defined as the interfacial region. These curves allow the thickness of this interfacial region to be estimated. At 600 K, the thickness is approximately 6 Å (Fig. 2(a)), indicating very little diffusion across the interface. The thickness increases as temperature increases, with the values being 11, 19 and 30 Å at 650, 700 and 750 K, respectively.

Figure 3 shows the thickness of the interfacial region as a function of time at different temperatures. At 600 K, the thickness fluctuates between 0~4 Å in the initial stage (smaller than two atomic layers). After about 400 ps, the thickness reaches about 6 Å and does not show further increase except for minor fluctuations. At 650 K, the thickness shows stepwise increases to 11 Å by about 550 ps and shows no further increase thereafter. The profile for 700 K is similar to that for 650 K, except that the maximum thickness value is higher (18 Å). At 750 K, the thickness increases rapidly and continuously with no saturation over the duration of the calculation.

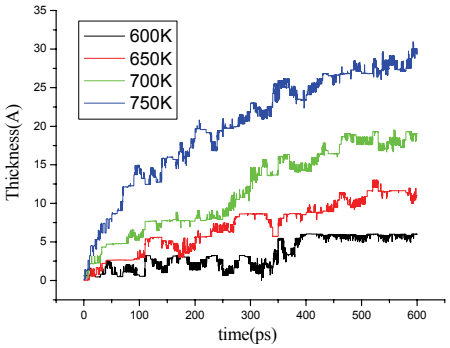

Fig. 3 Thickness of the interfacial region as a function of time at different temperatures

3.2 Effect of surface roughness

Experiments have shown that the roughness of the contact surfaces has a significant impact on the diffusion bonding process [21]. In this section, we consider three different cases:

(i). smooth copper surface and rough aluminum surface with two protuberances of a height of 4 lattice constants for aluminum;

(ii). smooth aluminum surface and rough copper surface with two protuberances of a height of 4 lattice constants for copper;

(iii). Both of surfaces are rough.

In all three cases, the highest temperature is 700 K and the applied stress in the z direction is 20 MPa.

Figure 4 shows a cross-section at different temperatures for case (i). Obviously, the protuberances on the aluminum surface undergo significant deformation under the stress (Fig. 4(b)) even at 200K. However, interstices remain between the two sides. At 300K, the protuberances are completely flattened and fully intimate contact is achieved. Because aluminum is softer than copper, aluminum shows more pronounced deformation. From Fig. 4(c), it can also be seen that a layer of Al close to the interface becomes amorphous. The picture at 700 K is similar

to that at 300 K, with no obvious diffusion of atoms between the interfaces.

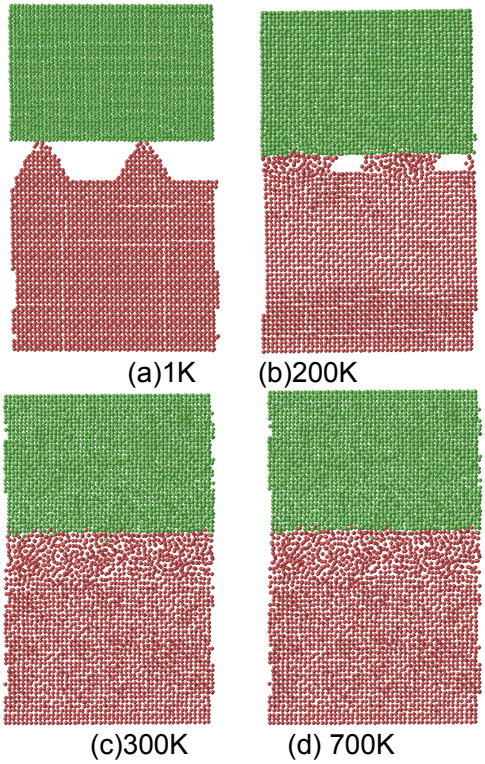

Fig. 4 A cross-section at different temperatures for case (i) (the stress is kept at 20 MPa)

Figure 5 shows the same cross-section for case (ii). The smooth aluminum surface undergoes significant deformation under the applied stress when the temperature is increased to 200 K. Some of aluminum atoms fill the interspaces of the cooper surface (Fig. 5(b)). This process intensifies as temperature increases (Fig. 5(c)). At 400 K, the interspaces on the copper surface are fully filled. The image at 700 is similar to that at 400 K, with no obvious diffusion between the two sides.

Figure 6 shows the results for case (iii). The top of the aluminum protuberances are flattened by the applied stress even before temperature is increased. At 200 K, the aluminum side shows significant deformation, similar to what is seen in the previous cases. Some of aluminum atoms fill in the interspaces of the copper surface (Fig. 6(b)) and the protuberances on the copper side show slight deformation. As temperature increases, more aluminum atoms move into interspaces on the copper surface (Fig. 6(c)). At 400 K, the interspaces are completely filled.

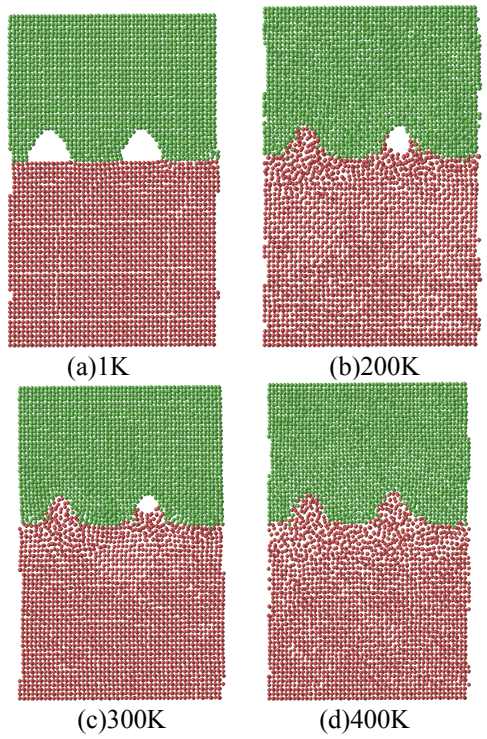

Fig. 5 A cross-section at different temperatures for case (ii) (the stress is kept at 20 MPa)

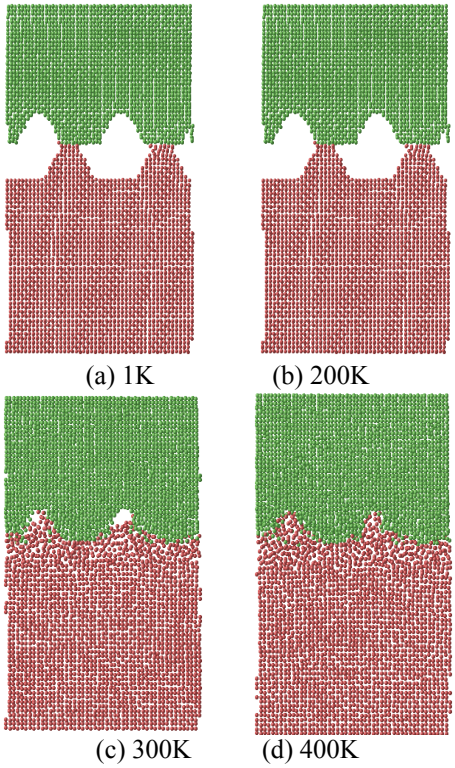

Fig. 6 A cross-section at different temperatures for case (iii) (the stress is kept at 20 MPa)

The results in Figs. 4-6 show that deformation primarily occurs in the Al, regardless of the configuration of the Cu surface. This is because Cu has a higher strength and a higher melting point.

Figure 7 shows the same cross-section after 600 ps at 700 K for cases (i) and (ii). As pointed previously, the rough aluminum

surface is flattened during heating before diffusion (Fig. 4(d)). Consequently, the diffusion pattern in Fig.7(a) at 600 ps is similar to that in the situation with perfectly smooth surfaces (Fig. 1). The diffusion pattern in Fig. 7(b) is very different from those in Fig. 7(a) and Fig. 1. The difference arises because aluminum atoms have previously filled the interspaces during heating and the contact profile is similar to those in cases (ii) and (iii) when the copper surface is rough before diffusion (Fig. 5(d) and Fig. 6(d)). Specifically, after 600 ps diffusion the contact profile is very similar to the initial profile of the copper surface, except that it has become flatter (Fig. 7(b)).

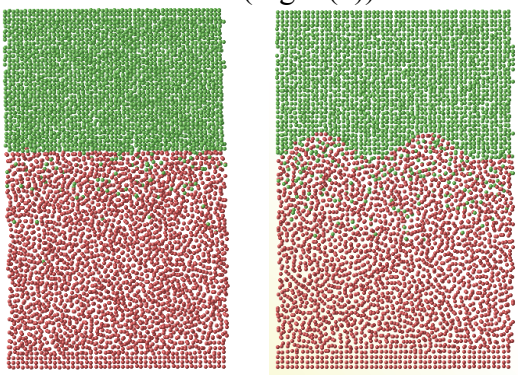

(a) (b)

Fig. 7 A cross-section after 600 ps at 700 K; (a) case (i), (b) case (ii)

The three sets of results show that the diffusion bonding process can be divided into three stages. In the first stage, the rough surface deforms under stress before heating causing the contact area to increase. In the second stage, the softer (Al) surface undergoes significant deformation temperature increases, causing the interstices to disappear leading to fully intimate contact of the surfaces. The last stage is diffusion of atoms at constant temperature.

3.3 Tensile deformation

In order to examine the mechanical properties of the diffusion-bonded Cu/Al sample, tensile loading is applied at room temperature to mono-crystal copper, mono-crystal aluminum, Cu/Al pair with ideal contact and diffusion-bonded Cu/Al pair (diffusion bonding condition is as follows: temperature is 750 K, stress is 20 MPa and cooling rate is 5×10^{13} K/s). Three layers of atoms at both the top and bottom surfaces are taken as boundary atoms for load application. The displacement of the boundary atoms is controlled by time step. Each increment corresponds to a strain of 0.25% and is followed by a period of 8 ps of equilibration at constant strain. The strain rate for the loading step is approximately 3×10^{8}/s, several orders of magnitude higher than the rate in a typical tensile test. However, as shown in a previous investigation [22], the equilibration periods following the load step allows the calculation here to approximate quasistatic loading.

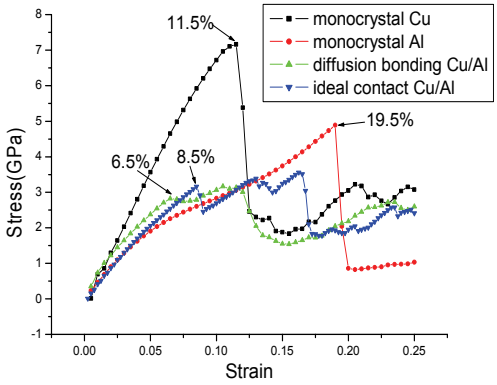

Fig. 8 Tensile stress-strain curves of monocrystal copper and aluminum, Cu/Al pair with ideal contact and diffusion-bonded Cu/Al pair

Figure 8 shows the nominal stress-strain curves for monocrystal copper and aluminum, Cu/Al pair with ideal contact and diffusion-bonded Cu/Al pair. It can be seen that the stress reaches a maximum of 7.2 GPa at a strain of 11.5% for monocrystal copper. Beyond the strain of 11.5%, the stress drops precipitously to 2.5 GPa and plastic flow occurs at stresses of around 2.5 GPa. The curve for monocrystal aluminum has similar feature as that for monocrystal copper, with a maximum stress of 4.9 GPa at a strain of 19.5%. When strain is over 19.5%, the stress drops precipitously to 0.8 GPa and plastic flow occurs at stresses around 1 GPa. The curve for the ideal-contact Cu/Al pair is different from those for monocrystal copper and aluminum. A sudden drop of stress appears first when strain reaches 8.5%, followed by a second drop at a strain of 13%. The stress reaches a maximum of 3.6 GPa at a strain of 16%. When the strain is over 16%, stress drops from 3.6 GPa to 1.6 GPa and the sample shows plastic flow. The flow stress is about 2 GPa. Finally, the case of the diffusion-bonded Cu/Al pair is similar to that of the ideal-contact Cu/Al pair, with no obvious sudden stress drop as strain increases. The stress curve is flatter than

that of the ideal-contact case. When the strain is over 6.5%, the stress shows a small drop and then increases as strain increases. The curve yields a tensile strength of 3.2 GPa which occurs at a strain of 10.5%. Since the tensile strength can reach 88% of that for the ideal-contact Cu/Al case, the diffusion-bonded Cu/Al pair demonstrates very good mechanical properties in terms of strength. The stress drops from 3.2 GPa to 1.5 GPa as strain increases from 10.5% to 15%, and the increase 15% to 22.5% is very gradual due to the plastic flow.

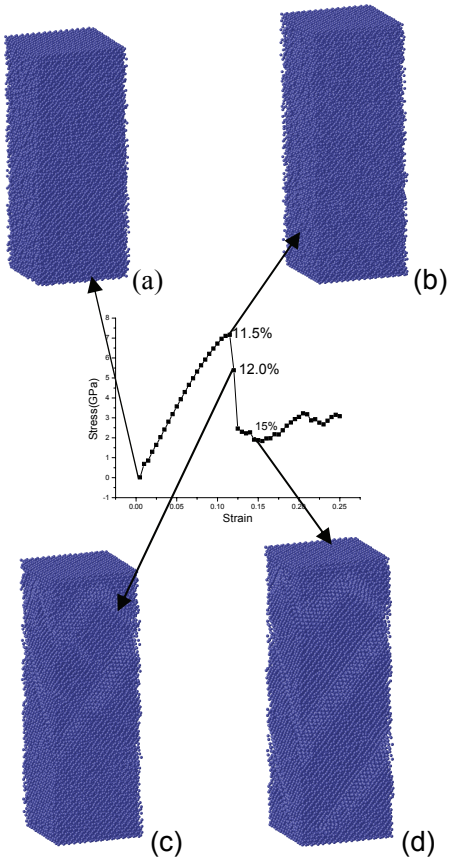

Fig. 9 Deformed configurations of the monocrystal copper at different levels of stain;
(a) 0%, (b) 11.5%, (c) 12%, and (d) 15%

We now turn our attention to the deformed structures inside the samples to gain better insight into the observed mechanical behaviors.

Figure 9 shows the deformed configurations of monocrystal copper at different strains. There is no obvious change as strain increases from 0 to 11.5%, except for the elongation of the sample. The situation becomes very different at a strain of 12% when many slip bands appear on side surfaces. The slip bands on the surfaces form an angle of 45° relative to the loading axis and the horizontal directions (Fig. 9(c)). The formation of these slip bands results in the sudden drops of stress in the stress-strain curves discussed earlier. As strain increases, more bands appear (Fig. 9(d)). The deformation of monocrystal aluminum is very similar to that of monocrystal copper. When strain is over 19%, many slip bands appear on the side surfaces.

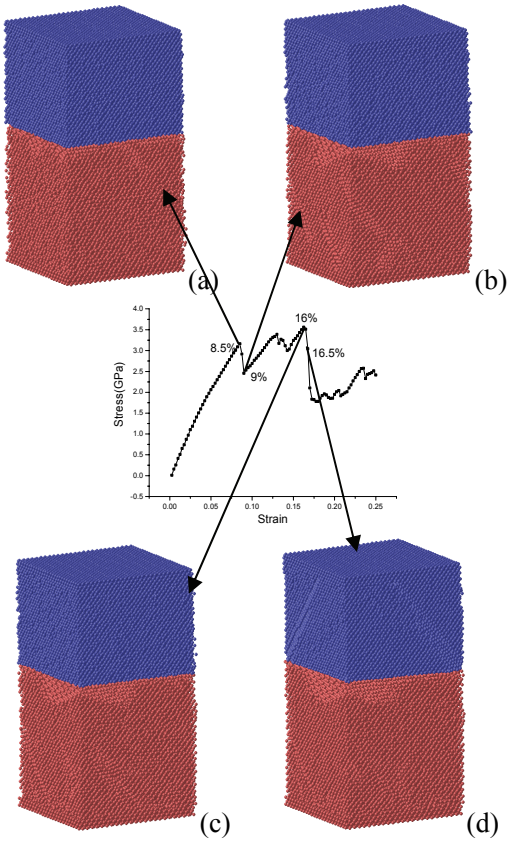

Fig. 10 Deformed configurations of ideal-contact Cu/Al pair at different strain levels;
(a) 8.5%, (b) 9%, (c) 16%, and (d) 16.5%

Figure 10 shows the deformation configurations of the ideal-contact Cu/Al pair at different strains. Figure 10(a) shows that there is no obvious change before a strain of 8.5%. When strain increases to 9%, a few slip bands appear on the side surfaces on the aluminum side and the Al layer adjacent to copper becomes amorphous (Fig. 10(b)). The appearance of slip bands on the aluminum side results in the sudden drop of stress at a strain of 8.5%. Some of the slip bands disappear and new slip bands appear as strain increases (Figs. 10(b)-(d)). When the strain is over 16% (Fig. 10(d)), some slip bands appear on the copper side, resulting in another sudden drop in stress. More and more slip bands appear on the copper side (not shown) as strain further increases, indicating further plastic flow (Fig. 8).

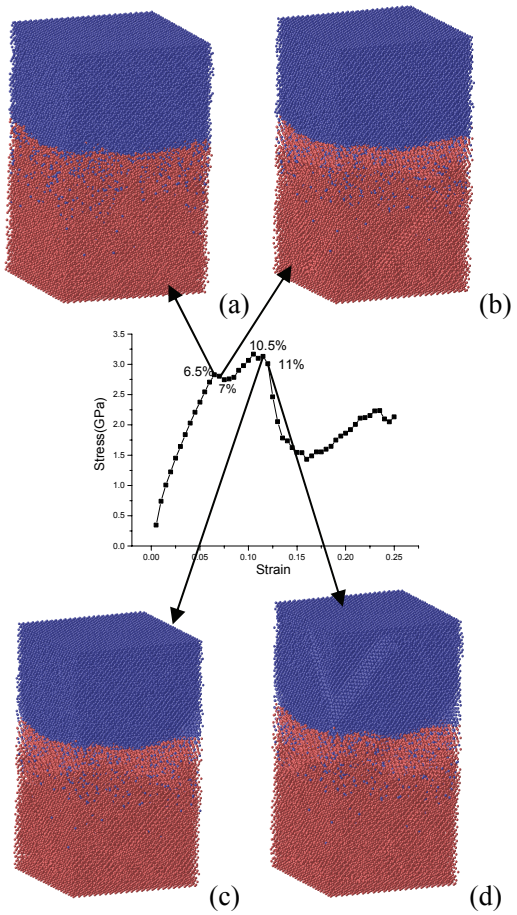

Fig. 11 Deformed configurations of diffusion-bonded Cu/Al pair at different strain;
(a) 6.5%, (b) 7% , (c) 10.5%, and (d) 11%

Figure 11 shows deformed configurations of the diffusion-bonded Cu/Al pair at different strains. The results are similar to those for the ideal-contact cases in the following ways. There are no obvious changes on the side surfaces before the strain of 7% (Fig. 11(a)). A few slip bands appear on the side surface on the aluminum side when strain increases to 7%, and the Al region close to the interface becomes amorphous (Fig. 11(b)). The appearance of slip bands on the aluminum side and the amorphous structure result in the drop of stress when the strain is over 6.5%. Figure 11(c) shows that the slip bands on the aluminum side surfaces can not cross the interface. The occurrence of additional slip bands are associated with only slight stress decreases. The interactions between different dislocations form a Lomer-Cottrel junction [23] as strain increases. Slip dislocations form dislocation pile-ups which induce strain hardening of the aluminum which causes the stress to increase as strain increases (Fig. 8). When the strain is over 10.5%, obvious slip bands appear on the copper side surfaces, resulting in the second drop of stress.

To summarize, the stress-strain curves show that the tensile strengths of monocrystal copper, monocrystal aluminum; ideal-contact Cu/Al and diffusion-bonded Cu/Al are 7.2 GPa, 4.9 GPa, 3.6 GPa and 3.2 GPa, respectively. Although these strength values are one order of magnitude higher than those from experiments [24], their relative magnitudes demonstrate the effectiveness of the diffusion bonding process. The higher strength values relative to experimental values is at least partly due to the fact that there are no defects (dislocations, voids, grain boundaries, etc.) in the model here.

4 Conclusions

MD simulations of the Cu/Al diffusion bonding process and the subsequent tension tests are performed. The primary findings are:

(1) Temperature plays a very important role in the bonding process. When the temperature is lower than 600 K, there is no obvious diffusion. The higher temperatures yield thicker interfacial layers. The thickness of the interfacial region increases in stepwise manner when the temperature is lower than 750 K. When temperature is higher than 750 K, the thickness of interfacial region increases rapidly and continuously;

(2) The bonding process can be divided into three stages. In the first stage, the rough surface deforms under stress before heating, resulting in increases in contact area. In the second stage, the surface deforms significantly as temperature increases. Also, interstices disappear and fully intimate contact is achieved in this stage. The last stage entails diffusion of atoms;

(3) The diffusion-bonded Cu/Al surface pair demonstrates very good mechanical properties, with a tensile strength of about 88% of the ideal-contact Cu/Al pair. The deformation mechanism of diffusion-bonded Cu/Al interfaces is not the same as those for single crystal copper and aluminum. The interface between the dissimilar materials blocks the propagation of dislocations from the aluminum

region into the copper region and strain hardening is also observed.

Acknowledgement

This project is supported by National Natural Science Foundation of China (grant Nos.10372012, 10432050, and 10528205). The computations are performed on the PC clusters of the State Key Laboratory for Scientific and Engineering Computing of the Chinese Academy of Sciences.

References

[1] Owczarski W A and Paulonis D F, (1981), *Weld. J.* 62, pp 22.
[2] Z.X. Guo, N. Ridley, (1987), *Mater. Sci. Technol.* 3 No.11, pp945.
[3] S. Fukumoto, A. Hirose, K. Kobayashi, (1989),Prod. Eng. 46.
[4] Aleman, B.; Gutierrez, I.,(1995), *Mater. Trans. A* pp. 437
[5] B .Aleman, I. Guterrez, J.J. Urcola, (1997), *Scripta Mater*. 36, No,5, pp509
[6] Askeland DR. (1989), The science and Engineer of Materials, Hong Kong, Van Nostrand Reinhold,
[7] O. Yilmaz, H. Celik, (2003), *Journal of Materials Processing Technology*, 141, pp67
[8] Airu Wang, Osamu Ohashi, Norio Yamaguchi, et al. (2004), *Journal of Electron Microscopy*, 53, No.2, pp157.
[9] M Weissmann, R Ramfrez and M Kiwi, (1992). *Phys Rev B*, 46, pp2577
[10] JK Chen, D Frakas and WT Reynolds. (1997), *Acta mater*, 45, pp4415
[11] Cherne FJ, Baskes MS, Schwarz RB. (2003), *Journal of Non-crystalline solids*, 317, pp45.
[12] P Heino, (2001), *Computational materials science*, 20, pp157
[13] T Watanabe, K Tatsummura and I. Ohdomari, (2004), *Applied surface science*, 237(1-4), pp125
[14] S.D. Chen, A.K. Soh, F.J. Ke. (2005), *Scripta Materialia*, 52, pp1135.
[15] Daw MS, Baskes MI. (1983), *Phys Rev Lett,1983*, 50, No.17, pp1285
[16] S.M. Foiles, M.I. Baskes, M.S. Daw, (1986), *Phys. Rev B,* 33, No.12, pp7983
[17] R.A. Johnson, (1989), *Phys. Rev. B* 39, pp 12554.
[18] X.W.Zhou, H.N.G. Wadley, R. A. Johnson, etc. (2001), *Acta mater*. 49, pp4005
[19] R.W.Hockney. (1970) , *Methods in Computational Physics* 9, pp136
[20] O. Richmond et al,(1974), *Int. J. Mech. Sci*
[21] A.S. Zuruzi, H. Li, G. Dong. (1999), *Materials Science and Engineering A*, 270, pp244.
[22] Xu Z, Liang HY, Wang XX. (2003), *Acta Mechanica Solida SINCA*, 24, No.2, pp229.
[23] Meyers M.A□Chawla K.K, (1983), Mechanical Metallurgy, Prentice Hall, Inc.
[24] Y.F. Shen, L. Lu, Q.H. et al. (2005), *Scripta Materialia*, 52, No.10, pp989

CRACKING MODELS FOR SOLVING PROBLEMS OF FRACTURE IN ENGINEERING COMPOSITES

Peter W R Beaumont
Department of Engineering, University of Cambridge
Trumpington Street, Cambridge CB2 1PZ, UK

Hideki Sekine
Aeronautics and Space Engineering, Tohoku University
Aoba-yama 01, Aoba-ku, Sendai 980-8579, Japan

Abstract

Oversights in designing with composite materials at the micro-structural level of size, has resulted in the evolution of cracking mechanisms and the catastrophic fracture of laminated components under cyclic stress. The fracture micro-mechanics and underlying physical processes of failure in engineering composite materials are presented. Modelling techniques are described, which quantify this accumulation of damage over time in terms of the important structural features of the composite material, constituent properties, stress-state, temperature, and environment. Particular emphasis is placed on the material internal state variable method of modelling, which relates failure mechanism and material property change. Proof of identity of individual failure processes based on their direct observation and an understanding of coupling between them are the first steps in the formulation of a completely physical model of fracture.

Keywords: composites, fracture, cracking, failure mechanisms, physical modelling, fatigue

1. Introduction

The expectation is for aerospace materials to last longer and for structures to operate safely and reliably at increasingly higher stresses. In the case of engine components, we expect the material to work successfully at greater elevated temperature and enhanced power. The requirement is to push the performance of the structure to its limit thereby stretching the composite material to its boundary of strength and endurance.

Currently, we see airframes made from composites, arriving at the probability of a successful outcome of a safe design by using intuition and our experience of circumstances that we have encountered before. But if we are to imagine the future differently, disaster as an act of God or of bad luck has to go. Predictive engineering design by intelligent-informed empiricism is the only “show in town”.

2. Empiricism vs Predictive Modelling

For half a century, factors that influence the limits of performance of engineering composite materials and the capability of

large structures and components to sustain high stress without failure, have been the subject of many analytical and theoretical investigations, validated by observations and precise measurement of property data.

Yet despite this acquisition of vast collections of information and compelling evidence, and an experienced designer's intuition based on "feel", "know-how" or "folklore" – *phenomenology* - our ability to fully understand composite material behaviour remains restricted. This is because our knowledge is built on empirical observation.

Oversight in design across orders of magnitude of size of structure has led to undesirable matrix-dominated load paths. In composite structures under load, this has resulted in the cumulative evolution of a complexity of inter-acting small defects. This is material failing on the nanometre or micron size scale, and we notice its consequences at the component level.

An invisible college of continuum mechanicians

There is an invisible college of continuum mechanicians, scattered in universities, who have for decades studied the behaviour of composite materials based on an idealization of what behaviour is all about, and coming up with countless models without any reference whatsoever to microstructure; neither do they care about mechanisms that act at the small end of the size-scale, or structurally-based constitutive equations. Consequently, current design codes for composite material structures in critical loading situations do not take creep, fatigue or environmentally-induced crack growth into account.

Understanding mechanisms

To understand the consequences of damage in composite material systems requires the design process at each size level of structure to include the dominant (meaning most influential) crack growth mechanism(s). Thus, to predict a result, say lifetime or a stress response by a numerical method, there must be a self-evident truth that the mechanism regime in which the component is operating must be known. In other words, the important design issues must all be embedded in the same model of material and component behaviour that must also include the dominant mechanism(s) of structural change over orders of magnitude of size.

Furthermore, what makes for a successful and safe application varies from one material system to the next. The diversity of failure characteristics stems from the differences between fibre-matrix systems and the nature of bonding between the constituent phases. It is not surprising then, that identifying the dominant failure mechanism(s), meaning the one (or more) that has the most influence on the material's or component's limit of performance is not straightforward and sometimes the problem contains several sub-problems. To model each sub-problem separately and to combine the results later, if that is possible, requires that phenomenology experience and those comprehensive collections of data, etc- a knowledge based on intelligent observations.

Intelligent-informed empiricism

Predictive engineering design by intelligent-informed empiricism has as its principal objective the identification and avoidance of all conceivable sources of weakness in the material and misfortune of structure.

What are needed, of course, are constitutive equations for design that encapsulate all of those intrinsic (material) and extrinsic (experimental or working) variables. The problem is that the experimental programme from which these constitutive laws are to be devised becomes too formidable. And if that is not enough, spatial variation appears when stress and temperature or other field

variables are non-uniform. Worse still, when mechanisms of cracking and fracture interact, superposition becomes important, which can lead to a breakdown in the simple constitutive law.
While simple geometries can be treated analytically, using, for example, the modelling tools of fracture mechanics, more complex geometries require discrete methods. The finite element method of modelling is an example. Internal material state variable formulations for constitutive laws are embedded in the finite element computations to give an accurate description of spatial behaviour.

3. Hierarchy of Multi-scale Modelling

Multi-scale problems have to be addressed by appropriate inter-disciplinary multi-scale modelling methods. The entire range of length scale has to be probed if we are to understand issues that limit the performance of the engineering structure. Understanding processes or mechanisms that operate in the material at all length scales and reconciling them with component durability and reliability is one of the ultimate challenges. Of particular interest is how damage transfers from a lower scale to a higher scale.

The framework upon which the modelling processes can be placed, and the connections and continuity between them, is illustrated in Fig. 1 below. This size (or length) scale, which spans several orders of magnitude, provides a framework for understanding the failure characteristics of the material on the one hand and performance limitation of the component on the other.

We observe the hierarchy of structural scales from the nanometre to the micron to the metre (or greater) level of size. Also, the discrete methods of analysis ranging from micro-mechanical (mechanism) modelling to the continuum levels of mathematical prediction of the complete design process. Almost always, behaviour at one level can be passed to the next level up as one or more parameters or as a simple mathematical function. The methods shown in Fig. 1 provide us with scope for optimisation, where composite material properties vary continuously with some internal parameter that relates to composite architecture in some way.

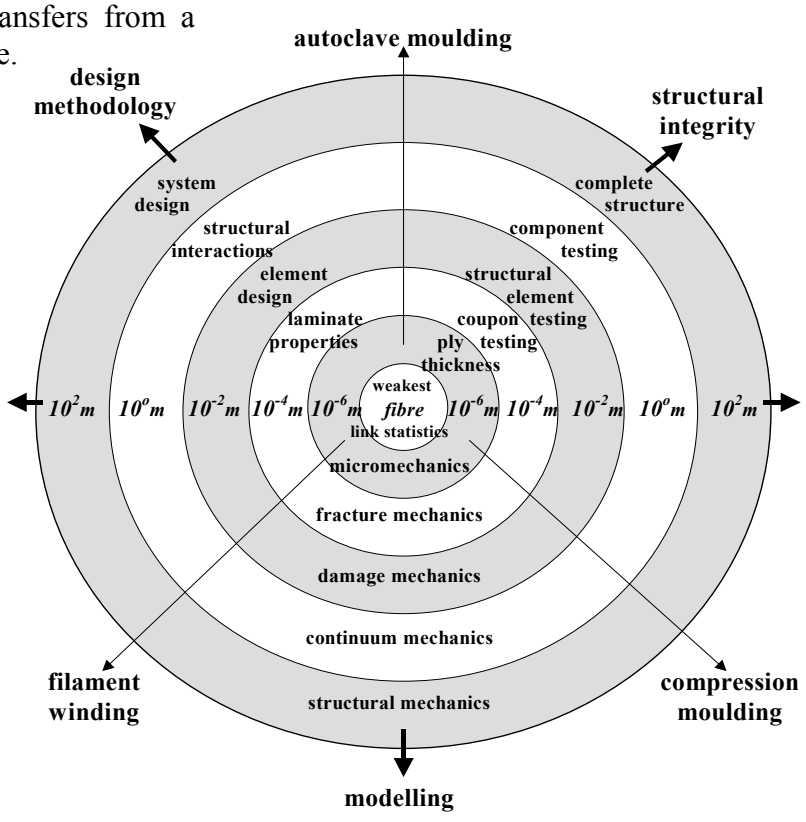

Figure 1 Hierarchy of structural scales from the single fibre to the fully assembled structure, and discrete methods of analysis in design methodology from micro-mechanics to the higher structural levels of modelling.

Then, when a set of properties is specified, it should be possible to select a particular lay-up or weave of an appropriate composite material system, and processing conditions, to meet that specification. This is to follow the path of intelligent design in a functional direction.

Problem posing and solving are essential components of modelling studies, adding value to our current understanding of the application of predictive modelling of composite material behaviour. The style and level of modelling depends on the problem, and they must all have that right degree of sophistication for the task in hand. The model must be simple but not too simple (Albert Einstein). There is elegance in successful physical modelling.

Physical-based damage and failure models can be incorporated into empirical or continuum methods of modelling that would lead to more efficient and reliable experimental programmes and the safe design of composite structures.

4. Physical Modelling

There is a direction, a path, which, if taken, we come upon the well-known laws or principles of physics and chemistry. This is to move in the direction of physical modelling, applying the laws of micro-mechanics in the process of formulating a route map called predictive design. In an engineering context, at first attempt, the physical model could describe concisely a body of fatigue or fracture stress data. But a better model, however, would be one that captures the essential physics of the engineering problem of cracking and fracture. By identifying the dominant microscopic process(es) responsible for failure in the first place, we can then model it (them) using the tools of micro-mechanics and our understanding of the theory of defects, of reaction rates, diffusion (and so forth). This time, such modelling does have powers of prediction derived from those established rules of physical behaviour. But even then, a complete physical treatment isn't always possible.

For example, a model of a thermally activated chemical reaction, using the law of Arrhenius, has its basis in statistical mechanics. Sometimes the activation energy, which enters that law, can be predicted from molecular models, but the value of the pre-exponential in the equation more often than not eludes current modelling methods; it must be inserted empirically. An example is stress corrosion cracking of glass fibre-epoxy composites (of which more is said in another paper of this Meeting by Sekine and Beaumont).

But most importantly, the physical model would illuminate the basic principles that underline the key elements of the total fracture process. By these means, the micro-mechanical model establishes a physical framework on which empirical descriptions of the behaviour of some of the intrinsic and extrinsic variables could be attached. However, a physical model points to something else, and it is of the greatest value; it suggests the proper form that constitutive equations should take and for the significant groupings of the variables that enter them. Empirical methods can then be used to establish the precise functional relations between these groups. The result is a constitutive equation that contains the predictive powers of physical modelling with the precision of ordinary curve-fitting.

5. Constitutive Models: The Internal State Variable Method

Constitutive models are best derived using the internal state variable method. Briefly, the key ideas are based on the fact that constitutive models have two aspects: response equations and structural evolution equations. The response equation describes the relationship of

(say) current modulus, E_c, of the laminate, (a measure of the effect of damage), to the applied stress, σ, or stress range, $\Delta\sigma$, load cycles, N, and to the current value of the internal state variable, D. We call the internal state variable *damage* because it describes a change in the state of a material, brought about by an applied stress or by load cycling. It (meaning D) uniquely defines the current level of damage in the material, for a given set of test variables.

The response equation describes this change of (damage) modulus, E_c, to the stress magnitude, temperature, time (number of load cycles), and to the current value of the internal state variable D:

$E_c = f(\sigma, \Delta\sigma, \lambda, T, \Delta T, t, \nu_\sigma, \nu_T, D,$ material properties, environment) (1)

Consider for example, matrix cracking only: D is usually defined as $D = 1/s$, where s is matrix crack spacing. Damage due to de-lamination, on the other hand, can be defined as total (meaning actual or measured) de-lamination crack area normalised with respect to the total area available for de-lamination, i.e., $D = A/A_o$. Or it might be useful to couple matrix crack spacing, s, with de-lamination crack length l_d, (i.e., s/l_d), because more often than not these two mechanisms are inseparable, the former triggers the latter.

Since the internal state variable, D, evolves over time with the progressive nature of the damaging processes, its rate of change can be described by:

$D' = g(\sigma, \Delta\sigma, \lambda, T, \Delta T, t, \nu_\sigma, \nu_T, D,$ material properties, environment) (2)

Competing mechanisms

Where several mechanisms contribute simultaneously to the response, (e.g., where modulus degradation is the result of de-lamination and matrix cracking combined), this time there are two internal state variables, one for each mechanism. Consequently, the model suggests a constitutive equation having a completely different form than before. Instead of trying to characterize the modulus, E_c, as a function of the complete set of independent variables (although we could), we now seek to fit data to a coupled set of differential equations, one for the modulus E_c', and two (or more), depending on the number of damaging mechanisms, for damage propagation, namely D_1' and D_2':

$E_c' = f(\sigma, \lambda, T, D_1, D_2,$ etc, material properties, environment) [3a]

$D_1' = g_1(\sigma, \lambda, T, D_1, D_2,$, etc, material properties, environment) [3b]

$D_2' = g_2(\sigma, \lambda, T, D_1, D_2,$ etc, material properties, environment) [3c]

D_1 describes the damage due to one mechanism and D_2 describes a different damaging mechanism that, when combined with the first, eventually lead to composite failure. E', D_1' and D_2' are their *rates of change* with time (or numbers of load cycles); f, g_1, g_2 are simple functions yet to be determined.

There are now three independent variables, $(\sigma, T,$ and stress-state, $\lambda)$, whereas before there were eight. These equations can be integrated to track out the change of modulus with the accumulation of damage, and ultimately used to predict fracture of a component or the design life in fatigue. Thus, the modulus-time (cycles) response is found by integrating the equations as a coupled set, starting with $E = E_o$ (the undamaged modulus) and $D = 0$ (no damage). Step through time (cycles), calculating the increments, and the current values, of E_c and D, and using these to calculate their change in the next step. Equation [3a] can now be adopted as the constitutive equation for fatigue, and empirical

methods can be used to determine the functions f, g_1, g_2.

6. An Example: Physical Model of Cracking in GRP

Consider the fatigue of a cross-ply glass fibre-epoxy composite. With increasing numbers of cycles (at low applied stress), the modulus falls slowly as the result of progressive transverse ply matrix cracking (Fig. 2). (This is called high cycle fatigue). As the stress amplitude, $\Delta\sigma$ increases, a noticeable change in slope of the modulus degradation curve designates the onset and domination of de-lamination (inter-laminar) cracking. And if the stress amplitude increases even further, (now called low cycle fatigue), the overwhelming mode of failure becomes fibre fracture.

Modelling coupled mechanisms

For the cross-ply $(0^o/90^o)_{ns}$ glass fibre-epoxy laminate, under monotonic (or cyclic) tensile loading, failure is first and foremost by the evolution of a multiplicity of cracks in the matrix of each transverse (90^o) ply. These closely spaced cracks lie parallel to one another, and in a plane that is perpendicular to the direction of applied stress; and they span the thickness and width of every transverse ply.

More often than not, a microscopic-sized de-lamination crack, (sometimes called an inter-laminar crack), nucleates by de-cohesive failure of the $(0^o/90^o)$ interface, in front of the tip of an advancing matrix crack. This de-lamination crack extends by *mode II* (shear) deformation and stable interfacial fracture. There are two possible alternative reactions to the localised stress field surrounding the matrix crack tip: either, the de-lamination crack forms, blunting the matrix crack tip and thereby reducing the tip stress intensity, or the interfacial bond remains intact and there is no de-lamination.

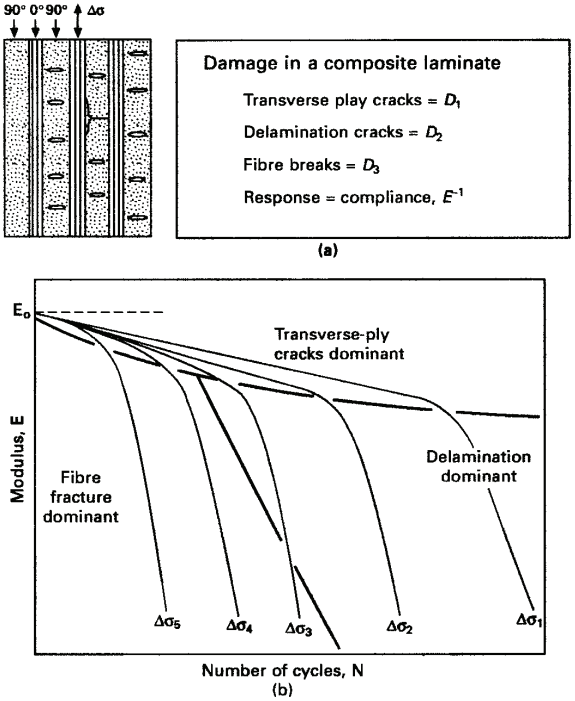

Figure 2(a) A model of the composite laminate subjected to repeated load cycling, with transverse ply cracks, de-lamination cracks, and fibre fractures – state variable D_1, D_2, D_3, measure the extent of these damaging mechanisms;
(b) the response E with the dominant failure mechanisms identified on the map.

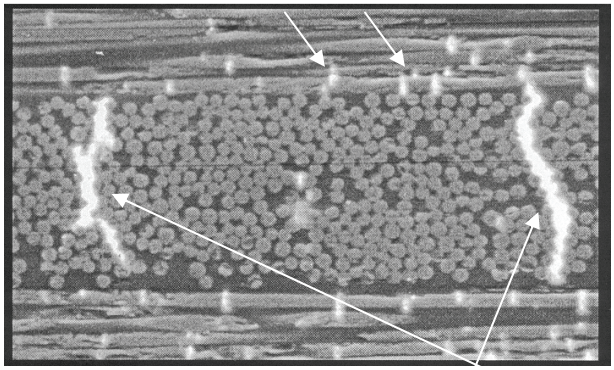

Figure 3 Transverse ply (matrix) cracks and fibre breaks in the outside longitudinal plies. De-lamination cracks can form at the tip of the transverse crack.

If the latter prevails, the magnification of local tensile stress can initiate the breakage of fibres, (in the adjacent load bearing (0^o) ply), on or close to the matrix crack plane.

The physical model

Figure 4 shows the physical picture, a matrix crack intersecting a de-lamination crack (shown circled). Spacing between a pair of adjacent matrix cracks is depicted *2s* (*D = 1/2s*); de-lamination crack length is ℓ_d.

This model of a "damage zone" consists of two parts: that portion of material that is cracked, designated (*a*) (shown circled in Fig. 4), and that portion between two adjacent matrix cracks where the *(0^o/90^o)* interface remains intact, designated (*b*).

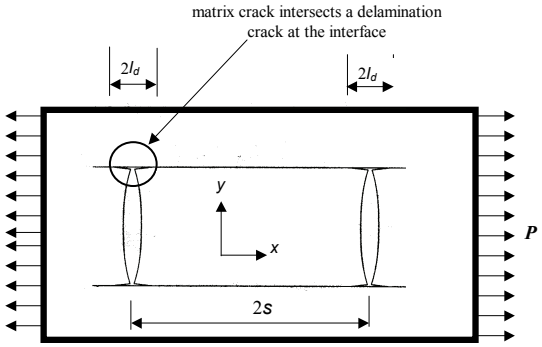

Fig. 4 A damaged $(0^o/90^o)_s$ cross-ply laminate under tensile load *P* (edge view). The geometry shows two neighbouring transverse ply cracks (of spacing 2*s*) interacting with local de-lamination (inter-laminar) cracks of length $2l_d$. (*b* is the thickness of the (outside) longitudinal ply; *d* is the thickness of the transverse ply).

In effect, as damage accumulates the matrix crack spacing gets smaller, while the de-lamination crack gets longer. Consequently, the distribution of load between portion (*a*) and portion (*b*) continuously re-adjusts.

Estimating the damage modulus E_c

To begin with, let us assume matrix cracking only; ignore for the time being the possibility of de-lamination cracking. From knowledge of the elastic strain in the longitudinal ply, and, consequently, the mean stress in the longitudinal ply with respect to distance x, from the matrix crack, we determine the following expression for damage (reduced) modulus, E_c, of a matrix-cracked laminate:

$$\left[\frac{E_c}{E_0}\right] = \frac{1}{\left[1+\left(\frac{d\,E_2}{b\,E_0}\right)\frac{\tanh(\lambda s)}{\lambda s}\right]} \qquad [4]$$

It is convenient to make equation [4] dimensionless by normalising E_c with respect to the undamaged modulus E_o. Roughly speaking, the modulus of an undamaged laminate, (meaning there are no matrix cracks), can be determined using a simple rule of mixtures:

$$E_0 = \left[\frac{b\,E_1 + d\,E_2}{b+d}\right] \qquad [5]$$

E_1, E_2 are the moduli of (0^o) and (90^o) plies, respectively.

We extend this model to include microscopic de-lamination cracking at the matrix crack tip as follows. Begin with the assumption that the reduced or damage modulus, E_c, of that de-laminated portion of laminate, (designated *(a)* in Fig. 4), depends essentially on the modulus of the longitudinal ply only:

$$\left[\frac{E_c}{E_0}\right]_a = \left[\frac{b\,E_1}{b\,E_1 + d\,E_2}\right] \qquad [6]$$

(As before, equation [6] is made dimensionless by normalising E_c with respect to the undamaged modulus, E_o, of the laminate (equation [5]).

Next, consider that the damage zone now has an "effective" matrix crack spacing *(s-ℓ_d)*. Thus, when we substitute *(s-ℓ_d)* into equation [4], we obtain for the modulus of that portion of (undamaged) laminate (designated *(b)* in Fig. 4):

$$\left[\frac{E_c}{E_0}\right]_b = \frac{1}{1+\left(\frac{d\,E_2}{d\,E_1}\right)\frac{\tanh(\lambda(s-\ell_d))}{\lambda(s-\ell_d)}} \qquad [7]$$

Finally, for a given applied tensile stress, the longitudinal modulus of the damaged laminate is calculated by using a rule of mixtures for $(E_c/E_o)_a$ and $(E_c/E_o)_b$:

$$\left[\frac{Ec}{E0}\right]_{lam} = \frac{\left[\frac{Ec}{E0}\right]_a \left[\frac{Ec}{E0}\right]_b (s)}{\left[\left[\frac{Ec}{E0}\right]_b (s-\ell d)+\left[\frac{Ec}{E0}\right]_a (\ell d)\right]} \qquad [8]$$

Mapping stiffness change

Adaptation of the transverse ply cracking model to include de-lamination cracking, (equation [8]), is shown in Fig. 5. Contours of (normalised) damage modulus, E_c, as a function of de-lamination crack length, ℓ_d, (normalised with respect to matrix crack spacing, *s*), are computed for selected spacing of matrix cracks for different ratio of *s/d*. In the absence of de-lamination cracking, the damaged modulus is indicated on the left axis. Thus, the modulus of a laminate, in which the de-lamination crack has extended completely between two neighbouring matrix crack tips, is equivalent to there effectively being a multiplicity of closely spaced matrix cracks. In this case, the damaged modulus would be given by equation [6]. We see that the damaged modulus is a non-linear function of de-lamination crack length for all crack geometries.

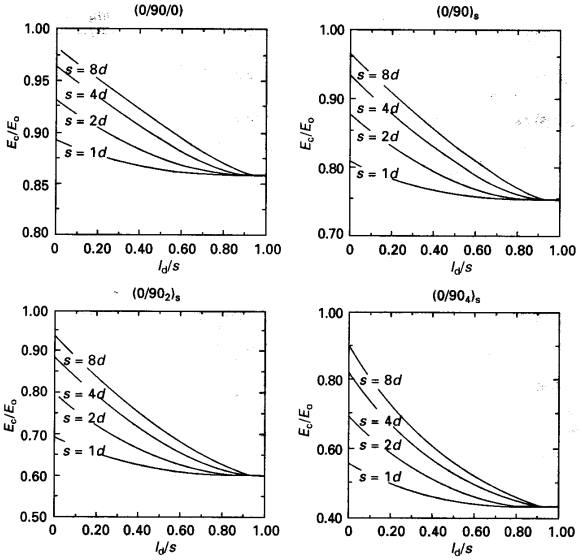

Figure 5 Reduced (damage) modulus change of glass fibre-epoxy laminate with the coupling of matrix and de-lamination cracking (eqn (8)).

This is pronounced in laminates having "thick" transverse plies, (meaning more than two plies). Similar behaviour exists for both glass fibre and carbon fibre-epoxy laminates.

6. Final Remarks

Knowing more about materials in modern design is becoming increasingly more important. This knowledge is partly contained in the constitutive equations of continuum design, in empirical "know-how", and experience. There are three possible routes towards an engineering solution to a complex design problem involving materials: the route of improved empiricism, that of physical modelling, and the coupled route of model-informed empiricism. The last appears to be the most promising. Furthermore, multi-scale modelling has emerged where multi-function materials can be designed from the microstructure upwards to satisfy several design criteria simultaneously. There is more scope for optimisation of when material properties vary continuously with some internal parameter. Composites are the obvious example.

MECHANICAL AND CRACK PROPERTIES OF NANOSCALE MATERIALS BY AB INITIO MOLECULAR DYNAMICS AND TEMPERATURE LATTICE GREEN'S FUNCTION METHODS

K. Masuda-Jindo
Department of Materials Science and Engineering,
Tokyo Institute of Technology, Nagatsuta, Midori-ku, Yokohama 226-8503, Japan

Vu Van Hung
Hanoi National Pedagogic University,
km8 Hanoi-Sontay Highway, Hanoi, Vietnam

M. Menon
Department of Physics and Astronomy,
University of Kentucky, Lexington, Kentucky 40506, U.S.A.

Abstract

The crack nucleation and propagation processes in nanoscale materials are studied using the ab initio constraint molecular dynamics (c-MD) method and the lattice Green's Function method. We investigate the strength and fracture behaviors of carbon related nanoscale materials, especially the graphen sheets in comparison with those of carbon nanotubes (CNT). The linear elastic parameters, nonlinear elastic instabilities, thermal lattice expansion and fracture behaviors are studied in detail. We will show that the thermodynamic and strength properties of the nanoscale materials exhibit characteristic features and they are different from those of the corresponding bulk materials.

Keywords: Lattice Green's function method, molecular dynamics, nanoscale material, carbon nanotube, fracture, crack

1. Introduction

Recently, there has been a great interest in the study of nanoscale materials since they provide us a wide variety of academic problems as well as the technological applications [1-6]. Now, it has been observed that the introduction of lattice defects and mechanical deformation influence quite significantly on the electronical properties of nanoscale materials [7,8]. CNT's have been thus identified as one of the most promising building blocks for future development of functional nanostructures.

The purpose of the present paper is to investigate the strength and fracture behaviors of nanoscale materials using the ab initio tight-binding molecular dynamics method [9,10] and the temperature Lattice Green's function method [11-14]. We calculate the atomic configurations and strength properties of nanocrystals including extended defects (dislocations and cracks) using the new version of the molecular dynamics method, constraint molecular dynamics (c-MD) method, on the basis of the analysis of the Lattice Green's function theory.

In the present study, we also study the temperature effects on the fracture behavior of nanoscale materials using this temperature Lattice Green's function method [15-22]. To derive the force constant matrix and non-linear cohesive forces at the finite temperature T, we use

the statistical moment method [23-25]. We go beyond the quasi-harmonic approximation of the lattice vibration and apply the formalism of statistical moment method to the fracture problem.

2. Principle of Calculations

For treating mechanical properties of nanoscale materials we will use the ab initio tight-binding molecular dynamics methods [7,8], which have been very successful in the calculations of various chemical and physical properties of nanoscale materials. In the present article, we also use the lattice Green's function (LGF) approach to study the mechanical properties of nanoscale materials, like graphene sheets, nanographites and nanotubes. In the treatment of LGF, we generalize the conventional LGF theory to take into account the temperature effects by including the temperature dependence of force constant matrices and non-linear cohesive forces.

2.1. Lattice Green's Function Methood

We will start with the equilibrium lattice equation is given in terms of force constant matrix Φ by

$$\Phi u = F. \qquad (1)$$

Then, Green's function is defined from (2) as the inverse of the force constant matrix,

$$G = \left(\Phi\right)^{-1}. \qquad (2)$$

This is the Green's function for the perfect lattice and can be found by conversion to reciprocal space in the standard manner.

The force constant matrix Φ^* of the cracked lattice is obtained from that of the perfect crystal by introducing the force terms on the cleavage surface that annihilate the bonds there. Thus one can write the change in the force constant matrix Φ^* as

$$\Phi^* = \Phi - \delta\Phi, \quad \delta\Phi = \left[\Phi\right]_{\text{crack forces}}. \qquad (3)$$

The formal solution of the problem is then given by the Dyson equation,

$$G^* = G + G\delta\Phi G^*, \qquad (4)$$

together with the "master equation" for the Green's function,

$$u = G * F. \qquad (5)$$

The crack geometry of the present study is taken to be a "double ended" crack of length $2L_x+1$. The crack is periodic in the z direction, with repeat distance, which allows us to work with an infinite crack in the z direction. The kinks are symmetrically disposed at the ends of the crack on the x axis and repeated in the z direction. The kink pairs are each $2L_k+1$ in length. Another special feature of the problem in the double ended crack is that the "real" external force distribution is a single force dipole situated at the origin and repeated along the z axis with the repeat distance. If the kink length L_k is small compared to the half crack length L_x, then a stress intensity K field is well defined over the entire kink region, so the crack problem is well defined. After the appropriate Lattice Green's functions of the cracked lattice are obtained, it is straightforward to investigate the crack extension events, i.e., kink nucleation and kink migration processes, by solving the coupled linear equations, with temperature dependent force constants, nonliniear cohesive forces and surface tensions.

For treating the discrete crack, all quantities must be Fourier analyzed in order to obtain the Green's functions. Because of the periodicity in the z direction, reciprocal space in that direction will be a Brillouin zone with a finite number of points, while q space in the other directions will be continuous. Thus we have a mixed Fourier representation, which we write for any function f in the form.

$$f(q) = \sum_{l_x, l_y = -\infty}^{\infty} \sum_{l_z = -(L_z - 1)}^{L_z} f(\mathbf{l}) e^{-i\mathbf{q}\mathbf{l}} \qquad (6)$$

$$f(\mathbf{l}) = \frac{1}{8\pi^2 L_z} \sum_{q_z = -(Q-1)}^{Q} \int_{-\pi}^{\pi}\int_{-\pi}^{\pi} f(\mathbf{q}) e^{i\mathbf{q}\mathbf{l}} dq_x dq_y \,, \qquad (7)$$

$$q_z = \pi p / L_z \,, \qquad (8\text{-a})$$

$$p = 0, \pm 1, \pm 2, \ldots, \pm(L_z - 1), +L_z \,, \qquad (8\text{-b})$$

$$Q = \pi / L_z \,. \qquad (8\text{-c})$$

In these equations we have used a notation in which bold face characters represent vectors in the full 3-D space and Fourier decompose the 2-D space in

x-y, where the q space is continuous, separate from the z decomposition. We shall always distinguish the function in real space and its transform in q space by nothing its independenct variable. Variables in real space will be labeled l, n, etc., while variables in reciprocal space will be labeled q, p, etc.

2.1.1 LGF Treatment at finite temperature. The present LGF theory includes the temperature effects on the defect properties: For the LGF treatment at finite temperatures, we take explicitly account the changes in the lattice spacing (thermal lattice expansions), interatomic force constants and non-linear cohesive forces near the crack tip region, simultaneously. To derive the temperature dependent ingredients in the LGF theory, we use the statistical moment method (SMM) in the quantum statistical mechanics [21-23]. This method allows us to take into account the anharmocicity effects of thermal lattice vibrations on the thermodynamic quantities in the analytic formulations.
Using the SMM, one can get the Helmholtz free energy of the system in the following form

$$\Psi = U_0 + \Psi_0 + \Psi_1 \qquad (9)$$

where Ψ_0 denotes the free energy in the harmonic approximation and Ψ_1 the anharmonicity contribution to the free energy. We calculate the anharmonicity contribution to the free energy Ψ_1 by applying the general integral formula

$$\Psi = U_0 + \Psi_0 + \int_0^{\lambda} \left\langle \hat{V} \right\rangle_{\lambda} d\lambda, \qquad (10)$$

where $\lambda\hat{V}$ represents the Hamiltonian corresponding to the anharmonicity contribution. Then the free energy of the system is given by

$$\begin{aligned}\Psi = U_0 &+ 3N\theta\left[x + \ell n\left(1 - e^{-2x}\right)\right] \\ &+ 3N\left\{\frac{\theta^2}{k^2}\left[\gamma_2 x^2 \coth^2 x - \frac{2}{3}\gamma 1\left(1 + \frac{x\coth x}{2}\right)\right]\right., \\ &+ \frac{2\theta^3}{k^4}\left[\frac{4}{3}\gamma_2^2 x\coth x\left(1 + \frac{x\coth x}{2}\right)\right. \\ &\left.\left. - 2\gamma_1(\gamma_1 + 2\gamma_2)\left(1 + \frac{x\coth x}{2}\right)(1 + x\coth x)\right\}\right.\end{aligned} \qquad (11)$$

where the second term denotes the harmonic contribution to the free energy.

With the aid of the "real space" free energy formula Ψ=E-TS, one can find the thermodynamic quantities of given systems (including nanoscale materials). The thermodynamic quantities such as specific heats and elastic moduli at temperature T are directly derived from the free energy Ψ of the system.

3. Results and Discussions

3.1 Temperature dependence of material parameters

Recently, the extensive experimental and theoretical studies have been done for the mechanical properties of carbon related nanotubes and nanomaterials and some information on the dislocation nucleation and plastic flows have been demonstrated [2]. For instance, in the strained nanotubes at high temperatures one observe the spontaneous formation of double pentagon-heptagon defect pairs [26-28]. Firstly, we study the thermodynamic and elastic properties of single wall carbon nanotubes (CNT), using the statistical moment method [11-14].

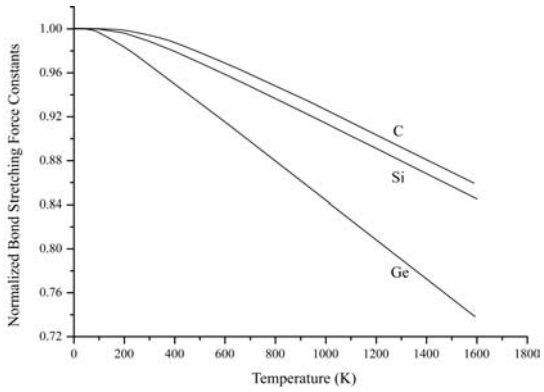

Fig.1: *Temperature dependence of bond stretching force constants of diamond cubic semiconductors C, Si and Ge.*

In Fig.1, we show the temperature dependence of bond stretching force constants of diamond cubic semiconductors C, Si and Ge, calculated by using the generalized TB and the SMM scheme. One can see in Fig.1 that the bond stretching force constants are decreasing function of the temperature and the strongest decreasing characteristics are observed for Ge crystal, while the modest ones for C crystal, Si

crystal being the intermediate. The temperature dependence of the force constant matrices is the important ingredients in the analysis based on the "temperature Lattice Green's Function" method, as will be discussed in the subsequent section 3.6.

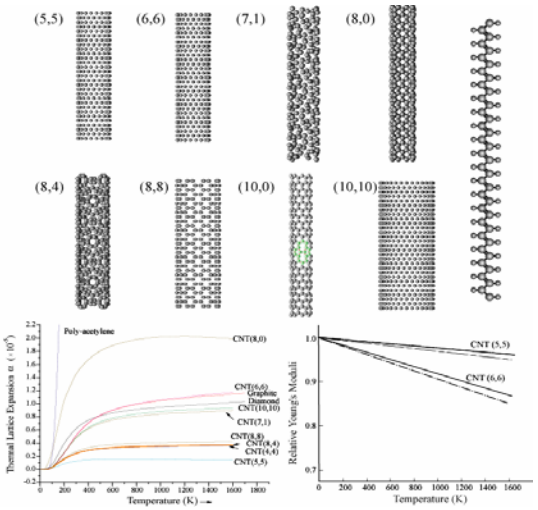

Fig.2: *Thermal lattice expansion coefficients α and the Young's moduli of CNTs.*

The calculated thermal expansion coefficients and Young's moduli of CNTs are shown in Fig.2. One sees in Fig.2 that the thermal and elastic properties depend strongly on the type of CNT. It is interesting in Fig.2 that the Young's moduli of CNT containing a pair of edge dislocations (characterized by 5/7 defects), dot-dashed lines, are smaller than those containing no dislocations and SW defects.

3.2. Constraint-MD method

In the present study, we will focus on the properties of cracks with atomistically smaller sizes, because the "large" macroscopic cracks are non-exsistence in the nanoscale materials. We have calculated the atomic configurations around the crack tips in the graphen sheets, using the constraint molecular dynamics and the lattice Green's function (LGF) method. In these calculations, the small double ended cracks are introduced by annihilating the interatomic bonds across the cleavage plane both for the c-MD and LGF treatments.

3.3. SW defects and nucreation of micro cracks

Firstly, we calculate the formation energies of the Stone-Wales defects in the graphen in the application of the tensile strain. We have obtained the negative values in the tensile strain as in the case of CNT. In this respect, we note that, in the strained nanotubes at high temperatures one observe the spontaneous formation of double pentagon-heptagon defect pairs [26-28]. We have found that the transverse arrays of SW defects is the most stable compared to those of the vertical and 45º declined arrays [13].

We now present our calculation results of dislocations in carbon related nanomaterials. Whe have calculated atomic configurations of pair of edge dislocations in two-dimensional (2D) graphen sheet, and found that bond switching defects dissociate into a pair of edge dislocations. In a pristine nano-molecule and graphen, the 5/7 dislocations have to first emerge as a dipole, by a prime SW transformation. Topologically, the Stone-Wales (SW) defect is equivalent to either one of the two dipoles, each formed by a ~ a/2 slip. The core structure of the edge dislocation is characterized by the five- and seven-membered rings in the 2D small carbon crystallites. The excess energies due to introduction of the edge dislocation are also estimated by comparing the energies of carbon nanocrystals with and without the edge dislocations. We have found that there are no marked differences in the stability between the nanographens with and without edge dislocations.

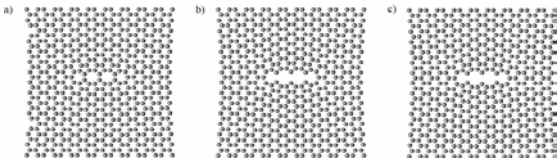

Fig.3: *Initiation of micro cracks from SW defects in 2D graphen sheets under mode I loadings.*

We have also studied the crack opening processes initiating from SW defects in graphen sheets using the c-MD method.

In Fig.3, we present the calculated atomic configurations around the micro cracks in the graphen sheets: Figures 3a and 3b show the atomic configurations of cracks before and after the opening atomic displacements, respectively. The micro cracks initiated in the core region of the SW defects open under mode I loading and the "constraint" of bond breaking at the initial MD stage. Figure 3c shows the atomic geometry of the micro crack after increasing the mode I loading about 2% in the crystallites. We have found that the further increase of the mode I loading does not extend the cracks, and the crack length remains constant. In other words, quite large lattice trapping occurs for this type of "impotent" micro cracks. Terefore, in order to extend the micro crack it is necessary to accumulate further the SW defects in the crack plane.

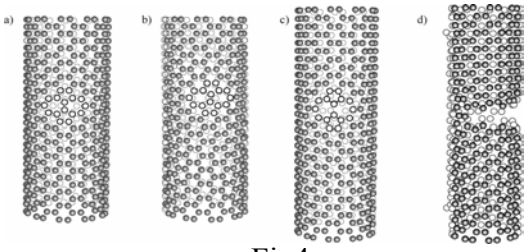

Fig4

For comparison, we have also calculated the atomic configurations of SW defects in the (10,10) carbon nanotubes and presented the results in Fig.4. In Fig.4a and 4b, we present the (10,10) CNT structures including the SW defects without and with twisting deformations (by $\theta = \pi/10$), respectively. In both figures, we see that the SW defects are stable and do not induce the crack like defects, in contrast to the deformed structures of graphen sheets under the shear loadings.

3.4. Micro crack nucleation from vacancy defects

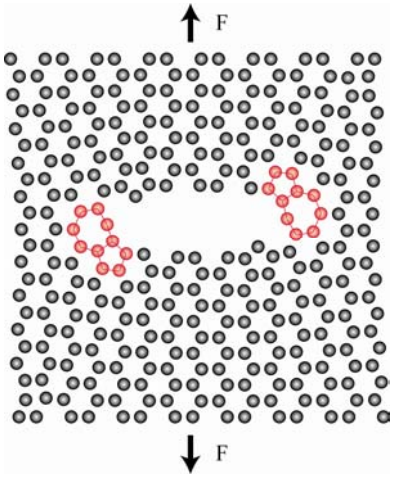

Fig.5: *Atomic configurations of vacancy type micro cracks introduced by removing certain number of atoms in the graphen sheets. Nucleation of dislocations is observed for at the both ends of double ended crack.*

We have also studied the properties of double ended cracks introduced by removing lines of vacancies, "vacancy type" cracks, in the nanoscale materials. The calculated atomic configurations of the "vacancy type" double ended cracks are shown in Fig.5. The double ended cracks shown in Fig.5a and 5b are necleated by introducing the 10 and 12 vacancies, respectively. In Fig.5a, it can be seen that the edge-type dislocations, characterized by pentagon-heptagon pair, are nucleated at both ends of the cracks. Here, it is remarkable that dislocation nucleation occurs without sizeable external shear loadings. The nucleation of dislocations at the end of the cracks depends on the atomic configuration of the unrelaxed vacancy defects, and the relative crack size with respect to the crystallite dimensions. Therefore, we do not find for instance the dislocations at the both ends of the cracks in Fig.5b.

3.5. Micro cracks in the cleavage plane

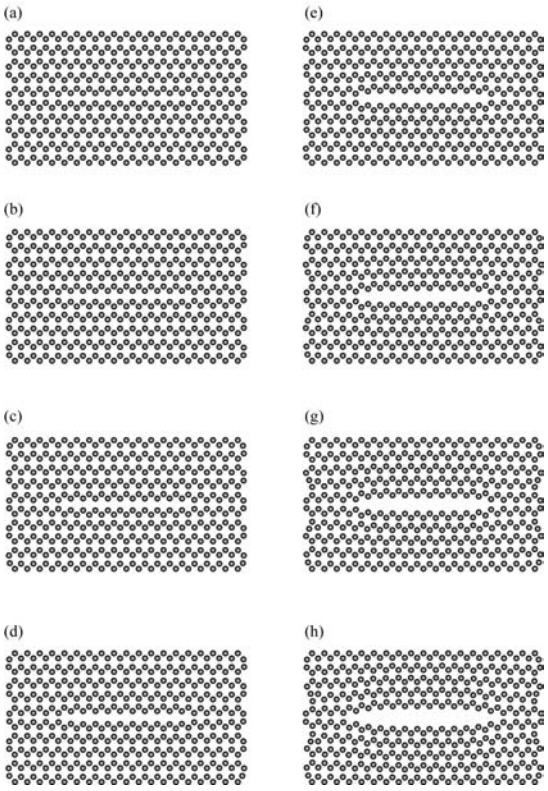

Fig.6: *Atomic configurations of micro cracks in the cleavage plane: (a), (b), (c), (d), (e), (f), (g) and (h) are atomic configurations of MD steps 10, 20, 30, 50, 100, 150, 200 and 250, respectively.*

Finally, we present in Fig.6 the atomic configurations around the double ended cracks in the cleavage plane of the 2D graphen sheets, under applied tensile stresses. In this calculation, we have assumed that the certain bonds across the cleavage plane are broken at the initial stage of MD relaxation processes. Near the end of MD simulation, however, no assumptions on the bond breakings are made for the whole crystallites. Using such MD procedure, i. e. so-called constraint MD (c-MD), one can get the stable equilibrium cracks in the crystallites, which are essentially the similar results as those obtained by the analytic LGF method. As in the infinite three dimensional crystals, the double ended cracks are trapped in the small crystallites at certain mode I loadings. However, upon the increase of the mode I loading to some extent, the micro cracks do extend, by one atomic distance, to the next stable positions (as shown in Fig.8h). This is in marked difference to those of the "impotent" nonpropagating cracks in the previous subsections.

During the c-MD calculations, the change (reduction) in the "strain energy" of 2D graphen sheets habe been monitored. The strain energies of graphen sheets including the cleavage crack are reduced rapidly at the initials stage of the MD processes. Here, it is important to note that the surface excess energies due to the cleaved surface in the crystallites are approximately constant during the c-MD calculations, even when the crack opening displacements are nearly zero, since the "bond annihilation" operations are active from the beggining of the calculations. This is one of the advantages of the c-MD approach in the analysis of crack problems.

3.6. Kink pair nucleation and migration processes in 3D system

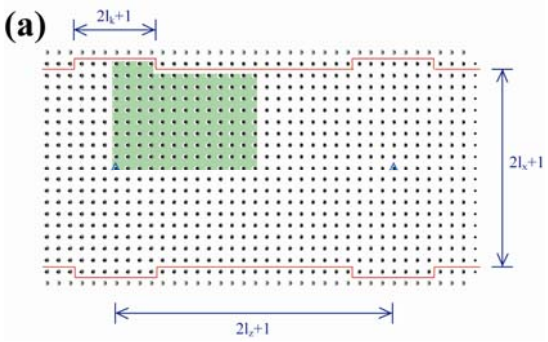

Fig.7: *Atomic geometry of the kinked crack.*

In the three dimensional (3D) crystals (including nanocrystals), the fundamental process of the crack extension events is composed of kink pair nucleation and kink migration processes, as schematically shown in Fig. 7. This type of crack extension process is a thermally assisted ones and it can be analyzed successfully with the use of the Lattice Green's Function method. To derive the Green's functions of the kinked crack at the absolute zero temperature, we follow the procedure developed by Thomson, Tewary and Masuda-Jindo [19]. We place the nonlinear bonds only at the kink sites, and all the other bulk atoms in their linear regimes.

Then the master equations for determining the (vertical opening) displacements at the origin u_0 and the displacements at the kink sites u_k are given by

$$u_0 = g_{oo}F_0 - \sum_k g_{ok} f(u_k), \qquad (11)$$

$$u_k = g_{oc}F_0 - \sum_{k'} g_{kk'} f(u_{k'}), \qquad (12)$$

where F_0 deuotes the external force dispole, excerted on the central atom sites.

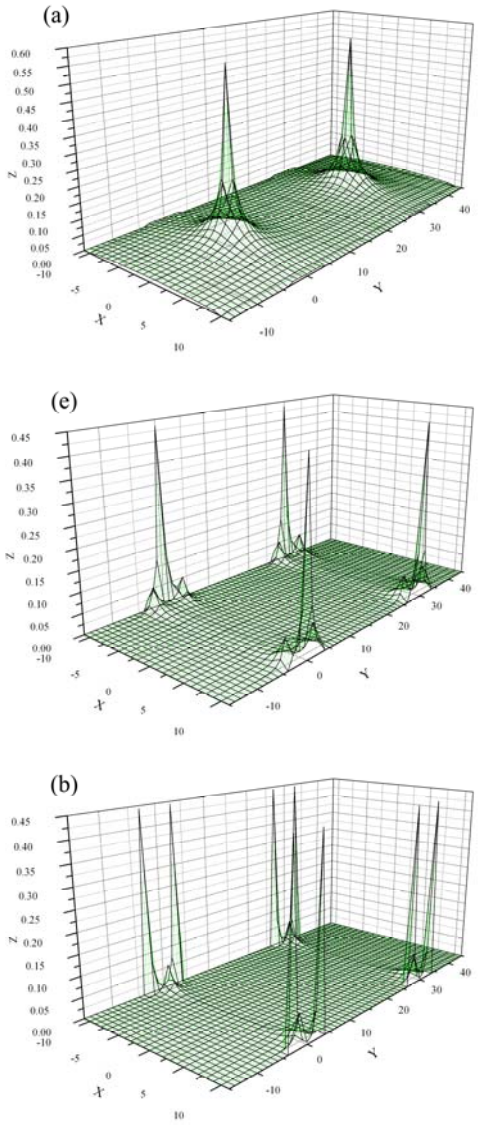

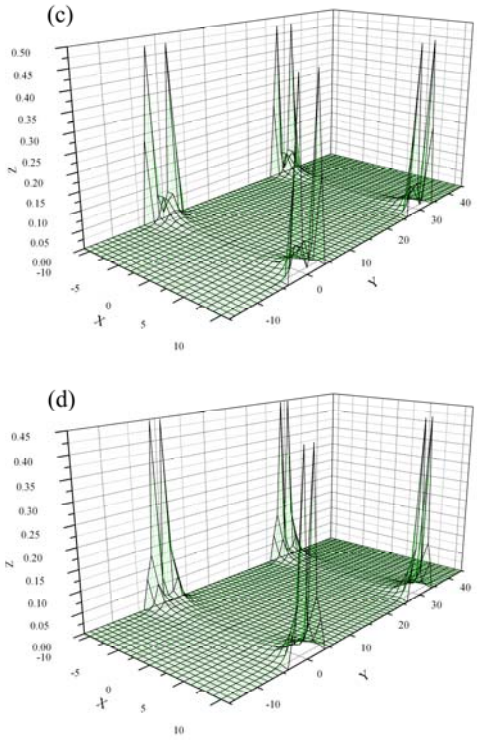

Fig.8: *Kinked crack Green's functions of the geometry with l_x=10, l_z=15 and l_k=3.*

After the appropriate lattice Green's functions of the cracked lattice are obtained, it is straighforward to investigate the crack extension events, i.. e.., kink nucleation and kink migration processes, by solving the coupled linear equations, with temperature dependent force constants, non-linear cohesive forces and surface tensions. In Fig. 8(a), we present the atomic geometry of kinked crack in simple cubic lattice with dimensions of l_x=10, l_z=15 and l_k=3. The lower figures 8b, 8c, 8d, 8e, and 8f are the kinked crack Green's functions originated from the atomic sites of the external loadings, kink sites k_1, k_2, k_3 and k_4, respectively. It is noted that the atomic displacements due to the external force dipoles F_0 are much smaller and more localized in the perfect lattice than those in the cracked lattice. Figure 9 shows the atomic displacements, self-consistently solved, both for the atomic sites of external loadings and for the kink sites. We have found, for model Si crystal (by the ratio between the bond stretching and bending force constants) that both kink formation and migration energies have the weak temperature dependence, decreasing function of the temperature and nucleation energies are

predominant for the whole temperature range. The ratio of the nucleation energy to migration energy is less than ~0.05, and also decreasing function of the temperature.

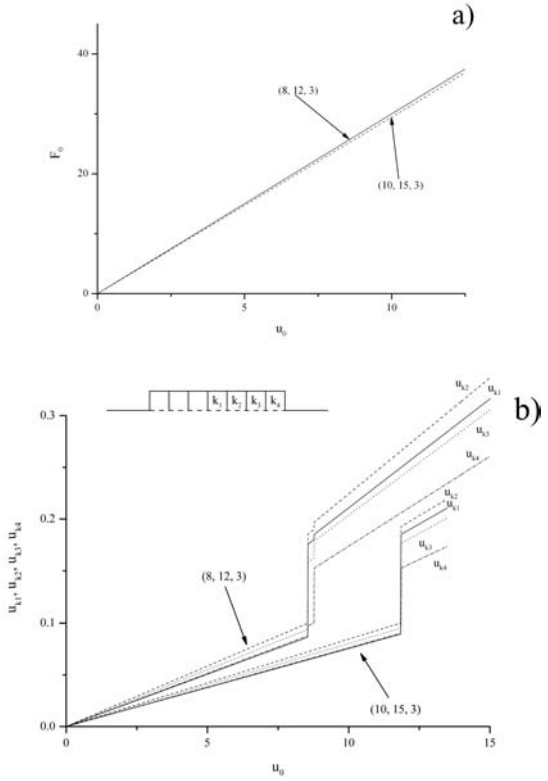

Fig.9: *Atomic displacements u_0, u_{k1}, u_{k2}, u_{k3} and u_{k4} as a function of the external loadings.*

4. Conclusions

Using a minimal parameter ab initio TBMD scheme we have studied the properties of lattice defects and cracks in the nanoscale materials, i.e., quasi-1D and 2D carbon related materials. In the analysis of the crack opening and extension events, we have introduced the new c-MD (constraint Molecular Dynamics) method. It has been shown that there are two kinds of cracks in the nanoscale materials, i. e., strongly lattice trapped "impotent" cracks and the propagating cleavage cracks under the modest external loadings.

In the 3D crystallites, we have studied the crack extension events through the kink pair nucleation and migration processes using the temperature Lattice Green's Function method. We have shown that the kink pair nucleation and migration energies have negative temperature dependence and nucleation energies are predominant for the whole temperature range.

References

[1] *J. P. Hirth and J. Lothe*, "Theory of Dislocations", (Wiley, New York, 1982).

[2] "Trends in Nanoscale Mechanics", ed. By *V. M. Harik and M. D. Salas*, (Kluwer Academic Publishers, 2003).

[3] "Nanoscale Materials", ed. By *L. M. Liz-Marzán and P. V. Kamlat*, (Liuwer Academic, 2003).

[4] "Semiconductor Nanocrystals", ed. By *D. J. Lockwood,* (Kluwer Academic/Plenum, 2003).

[5] *S. Iijima*, Nature 354 (1991) 56.

[6] *K. Masuda-Jindo and R. Kikuchi*, Int. J. of Nanoscience, 1, (2002) 357-371.

[7] *A. Hansson, M. Paulsson and S. Stafström*, Phys. Rev. B62, (2000) 7639.

[8] *A. J. Lu and B. C. Pan*, Phys. Rev. Lett., 92 (2004) 105504.

[9] *M. Menon, E. Richter and K. R. Subbaswamy*, J. Chem. Phys. 104, (1996) 5875.

[10] *R. W. Nunes and D. Vanderbilt*, Phys. Rev. B50, (1994) 17611.

[11] *K. Masuda-Jindo and Vu Van Hung*, Physical Mesomechanics, Vol.7, No.4 (2004) 77.

[12] *K. Masuda-Jindo, Vu Van Hung and M. Menon*, Phys. stat. sol. (c) 2, No. 6, (2005) 1781.

[13] *K. Masuda-Jindo and Vu Van Hung*, J. Phys. Soc. Jap. 73 (2004) 1205.

[14] *Vu Van Hung, K. Masuda-Jindo and Pham Thi Minh Hanh*, J. Phys. Condens. Matter 18 (2006) 283.

[15] *T. J. Matsubara*, J. Phys. Soc.Jpn., 7 (1952) 270.

[16] *H. Kanzaki*, J. Phys. Chem. Solids, 2 (1957) 24.

[17] *V. K. Tewary*, Adv. Phys. 22, (1973) 757.

[18] *D. M. Esterling*, J. Appl. Phys., 47 (1976) 486.

[19] *K. Masuda-Jindo, V. K. Tewary and R. Thomson*, J. Mater. Res., 2 (1987) 631.

[20] *K. Masuda-Jindo, V. K. Tewary and R. Thomson*, J. Mater. Res., 6 (1991) 1553.

[21] *V. K. Tewary and R. Thomson*, J. Mater. Res., 7 (1992) 1018.

[22] *V. K. Tewary, E. R. Fuller Jr. and R. M. Thomson*, J. Mater. Res., 4 (1989) 309.

[23] *V. V. Hung and K. Masuda-Jindo*, J. Phys. Soc. Jap. 69 (2000) 2067.

[24] *K. Masuda-Jindo, Vu Van Hung and Pham Dinh Tam*, Phys. Rev. B67 (2003) 094301.

[25] *K. Masuda-Jindo, S. Nishitani and Vu Van Hung*, Phys. Rev. B70 (2004) 184122.

[26] *M. B. Nardelli, B. I. Yakobson and J. Bernholc*, Phys. Rev. B57, (1998) R4277.

[27] *M. B. Nardelli, B. I. Yakobson and J. Bernholc*, Phys. Rev. Lett. 81, (1998) 4656.

[28] *B. I. Yakobson*, Appl. Phys. Lett., 72, (1998) 918.

EFFECTS OF MICROCRACK INTERACTION ON THE COMPLETE STRESS-STRAIN RELATION FOR BRITTLE ROCK SUBJECTED TO UNIAXIAL TENSILE LOADS

X. P. Zhou
School of Civil Engineering, Chongqing University Chongqing 400045, P R China

Abstract

A micromechanics-based model is proposed to describe unstable damage evolution in microcrack-weakened brittle rock material. The influence of all microcracks with different sizes and orientations are introduced into the constitutive relation by using the statistical average method. Effects of microcrack interaction on the complete stress-strain relation as well as the localization of damage for microcrack-weakened brittle rock material are analyzed by using effective medium method. Each microcrack is assumed to be embedded in an approximate effective medium that is weakened by uniformly distributed microcracks of the statistically-averaged length depending on the actual damage state. The elastic moduli of the approximate effective medium can be determined by using the dilute distribution method. Micromechanical kinetic equations for stable and unstable growth characterizing the ‘ process domains ’ of active microcracks are taken into account. These ‘process domains’ together with ‘open microcrack domains’ completely determine the integration domains of ensemble averaged constitutive equations relating macro- strain and macro-stress. Theoretical predictions have shown to be consistent with the experimental results.

Key words: Microcrack interaction, the complete stress-strain relation, localization of damage, uniaxial tensile loads.

1. Introduction

Determination of the strength and constitutive relation of rock subjected to uniaxial tensile loads is important in analyzing the damage of a rock structure, and hence for designing of rock support. In rock materials, countless microcracks are generally distributed over the bulk of rock material and propagate under loading. Through scanning electron microscope (SEM) and acoustic emission (AE) examinations, it is revealed that the growth and nucleation of these cracks dominate the failure and the macroscopic mechanical properties of rock material[1,2].The estimation of constitutive relation of rock material is the most important problem in micromechanics. This is not only because constitutive relation are needful for the simulation of mechanical response of rock materials, but also because constitutive relation is often applied as the description of stability of rock structure.

Various methods have been proposed to describe the effective moduli of crack-weakened rock. Simplest method is the approximation of noninteracting microcracks, which is referred to as dilute distribution method. In the limit of the dilute distribution of microcracks, the Taylor model(sometimes referred to as the dilute distribution model), which completely neglects the microcrack interaction, offers a simple and efficient

path for the determination of effective moduli[3]. When damage consists of weakly interacting microcracks, estimations of the effective moduli of rock with stationary microcracks may be obtained using the self-consistent method[4] [5], Mori-Tanaka method[6-7] , differential method[8], generalized self-consistent method[9], and other such "effective medum" approaches[10,12,13]. The statistical micromechanical damage theory in [11], and some other theories can be adopted to take strong microcrack interaction into account. If the strong interaction among cracks is considered, a rigorous solution can be sought numerically, but the final numerical results, which may be very accurate, are of limited use.

However, investigations on the effective constitutive relation of brittle materials with evolutionary damage are still very limited. Some effective medium models have been suggested to describe stable damage evolution in brittle solids[12-13]. Neglecting effects of microcrack interaction, the damage and constitutive relation of brittle rock materials under uniaxial tensile loading, dynamic uniaxial tensile loading, compressive loads, dynamic compressive loads and unloading were developed[14-18]. To the author's knowledge, no micromechanical model has been presented to describe the effective constitutive relation with microcrack interaction for brittle rock material with localization of damage under unaxial tensile loading or dynamic uniaxial tensile loading. Therefore, it is the intent of this paper to develop such an approximate micromechanical model for implementing effects of microcrack interaction on the complete stress-strain relation as well as localization of damage for brittle rock material under unaxial tensile loading.

2. Theoretical model

Establish the global coordinate system (x_1,x_2)and corresponding local coordinate system (x_1', x_2') ,in which x_2' –axis is parallel to the normal vector n. It is assumed that the preexisting microcrack sizes is $2c_0$, its normal forms an angle θ with respect to the x_2 -axis as depicted in Fig.1.

Under static uniaxial tensile loading ,the stress intensity factors at the crack tip take the following form

$$\begin{cases} K_I = \sigma_{22}\cos^2\theta\sqrt{\pi c_0} \\ K_{II} = \sigma_{22}\sin\theta\cos\theta\sqrt{\pi c_0} \end{cases} \quad (1)$$

where K_I and K_{II} is the mode I and II stress intensity factors , respectively.

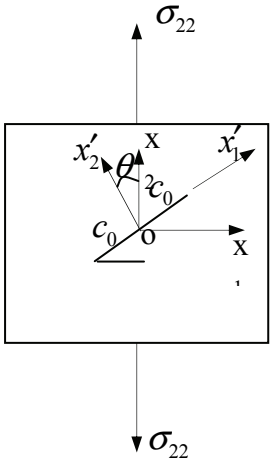

Fig.1 microcrack-weakened rock subjected to uniaxial tensile stress

Since Eq.(1) contains the SIFs for mode I and mode II, the strain energy density theory [19, 20] is applied to solving the mixed mode problem.The criterion of microcrack growth under static uniaxial tensile loading in a stable fashion is[19,20]

$$S = a_{11}K_I^2 + 2a_{12}K_I K_{II} + a_{22}K_{II}^2 = S_c \quad (2)$$

in which

$$S_c = r_c\left(\frac{dW}{dV}\right)_c = \frac{(1+v_0)(1-2v_0)}{2\pi E_0}K_{IC}^2$$

$$a_{22} = \frac{1+v_0}{8\pi E_0}[4(1-\cos\varphi)(1-v_0)+ (1+\cos\varphi)(3\cos\varphi-1)]$$

$$a_{11} = \frac{1+v_0}{8\pi E_0}[(3-4v_0-\cos\varphi))(1+\cos\varphi)]$$

$$a_{12} = \frac{1+v_0}{8\pi E_0}(2\sin\varphi)[\cos\varphi-(1-2v_0)]$$

is the critical strain energy density factor at weak plane , K_{IC} is the mode I critical stress intensity factor at weak plane.The crack growth angles can be obtained from the strain energy density factor

criterion[19,20]. It is assumed that the crack tends to run in the φ_0-direction for which $S_{\min}$ prevails.

Once a microcrack satisfies the criterion(2), it will propagate increasing its radius from the initially statistically-averaged value c_0 to a certain characteristic value c_1 and then being arrested by energy barriers with higher strength than interfaces. The radius c_1 depends on the microscopic structures of rock materials, such as size and shapes of grains or aggregates. Because the contribution of a micrcrack into the effective compliance tensor is proportional to the second power of its radius, the average radii c_0 and c_1 are determined by

$$c_0 = \frac{1}{N_0}\sum_{\beta=1}^{N_0}\left(c_0^{(\beta)}\right)^2, c_1 = \frac{1}{N_1}\sum_{\beta=1}^{N_1}\left(c_1^{(\beta)}\right)^2 \quad (3)$$

where N_0 is the total number of microcracks in the RVE at the initial undamaged state, N_1 the number of micrcracks that have propagated, and the subscript (β) signifies the $\beta-$ th microcrack. The critical domain of unstable microcrack growth can be defined by Eqs(1) and (2). All microcracks whose orientations is defined by Eqs(1) and (2) must have propagated and have the radius c_1.

With a further increase in the applied stresses, some microcracks normal to the tension direction may pass through the higher energy barriers and experience the secondary growth. Similar to Eq.(2), the criterion of secondary growth of a microcrack may the following form[19,20]

$$S = a_{11}K_I^2 + 2a_{12}K_IK_{II} + a_{22}K_{II}^2 = S_{cc} \quad (4)$$

where

$$S_{cc} = r_{cc}\left(\frac{dW}{dV}\right)_{cc} = \frac{(1+v_0)(1-2v_0)}{2\pi E_0}K_{ICC}^2$$

is the critical strain energy density factor describing the resistance of rock material against microcrack growth, K_{ICC} is the critical value of mode I describing the resistance of rock material against microcrack growth.

In this paper, an approximate scheme is applied to estimate the effects of microcrack interaction on constitutive relation of rock material subjected to uniaxial tensile loads. It is assumed in the approximate scheme that all microcracks are in an infinite, damaged effective medium, whose elastic moduli are different from those in the self-consistent method and can be calculated approximately from the actual damage state by using the dilute distribution method[13].

To determine the influences of microcrack interaction on the constitutive relation, the effective medium surrounding the microcracks is here approximate to be isotropic. Thus, its effective moduli can be expressed by Young's modulus $\bar{E}$ and Poisson's ratio $\bar{v}$, the following expression can be obtainted

$$\bar{S}_{ijkl} = \frac{1}{\bar{E}}\left[\frac{(1+\bar{v})}{2}(\delta_{ik}+\delta_{jl}) - \bar{v}\delta_{ij}\delta_{kl}\right] \quad (5)$$

The effective compliance tensor of the approximate effective medium is calculated by assuming that the number of density of microcracks in it remains the actual value,but all micrcracks are with the same radius, $\bar{c}$, which is related to the actual damage state.

Since the contribution of a microcrack to the compliance tensor is proportional to the second power of its radius, $\bar{c}$ is defined as the average of radii of all actual microcracks, that is

$$\bar{c} = \frac{1}{N}\sum_{\beta=1}^{N}\left(c^{(\beta)}\right)^2 \quad (6)$$

where N denotes the total number of microcracks in RVE, and $c^{(\beta)}$ the radius of the β-th microcrack.

The radius of all microcracks that have not propagated are c_0, and those having propagated have the radius c_1, then, $\bar{c}$ can obtained as

$$\bar{c}^2 = \int_0^{\frac{\pi}{2}} p(c)p(\theta)c_0^2\sin\theta d\theta + \int_{\Omega} p(c)p(\theta)(c_1^2 - c_0^2)\sin\theta d\theta \quad (7)$$

where Ω is domain of microcrack propagation, $p(\theta)$ and $p(c)$ are the probability density function describing the distribution of orientations and sizes of microcracks in rock material, respectively.

If all microcracks are uniformly distributed in the orientation space, Eq.(7) is rewritten as

$$\bar{c}^2=c_0^2+\frac{1}{\pi}(c_1^2-c_0^2)\int_{\Omega}\sin\theta d\theta \qquad (8)$$

Thus, the effective moduli of the assumed effective medium surrounding microcracks are approximated by those of an isotropic rock material in which microcracks with the same radius $\bar{c}$ are uniformly distributed with the number density of ρ . They can be readily obtained by using the dilute distribution method. For such a medium subjected to uniform traction on its external surfaces, the results from dilute distribution method are as follows

$$\frac{\bar{E}}{E_0}=\frac{2}{2+\pi^2\bar{\omega}^2} \qquad (9)$$

$$\bar{v}=\frac{2}{2+\pi^2\bar{\omega}^2}\left(\pi^2\bar{\omega}^2+1+v_0\right)-1 \qquad (10)$$

where E_0 is Young's modulus of intact rock, v_0 is Poisson's ratio of intact rock, $\bar{\omega}=\rho\bar{c}^2$ being the conventional scalar microcrack density parameter.

The total strain tensors may be splitted into the elastic strain part ε_{ij}^0, which is the strain in the rock material if there are not cracks, and the inelastic strain part ε_{ij}^m, which accounts for the inelastic deformation of the pre-existing cracks and their preferential growth, i. e.

$$\varepsilon_{ij}=\varepsilon_{ij}^0+\varepsilon_{ij}^m \qquad (11)$$

According to Eq.(11), the compliance tensor can also be decomposed by

$$S_{ij}=S_{ij}^0+S_{ij}^m \qquad (12)$$

where S_{ij}^0 is the compliance tensor of the matrix, and S_{ij}^m the contribution of all microcracks to the effective compliance tensor. Similarly, S_{ij}^m can be splitted into two parts

$$S_{ij}^m=S_{ij}^{m1}+S_{ij}^{m2} \qquad (13)$$

where S_{ij}^{m1} denotes the isotropic component of S_{ij}^m and is defined in Eq.(5), and S_{ij}^{m2} denotes the difference between S_{ij}^m and S_{ij}^{m1} . Then, Eq.(13) can be rewritten as

$$S_{ij}=S_{ij}^0+S_{ij}^{m1}+S_{ij}^{m2} \qquad (14)$$

As the key assumption of the suggested scheme, the compliance tensor of the postulated effective medium surrounding a microcrack is approximated by

$$\bar{S}_{ij}=S_{ij}^0+S_{ij}^{m1} \qquad (15)$$

All microcracks in the microcracked rock material are assumed to be in the isotropic effective medium with compliance $\bar{S}_{ij}$ in Eq.(15), and then used to compute the anisotropic overall compliance tensor S_{ij} in Eq.(12) of the actual damaged rock material.

For an open microcrack in the iosotropic effective medium with Young's modulus $\bar{E}$ and Poisson's $\bar{v}$,the compliance tensor induced by the elastic deformation of the β -th microcrack of length $2c$ and orientation θ is obtained as

$$\bar{S}_{ij}^{b(\beta)}=\frac{2\pi c^2(1-\bar{v}^2)}{A_0\bar{E}}(g_{2i}g_{2j}+g_{3i}g_{3j}) \qquad (16)$$

where A_0 is the representative element area of rock material , g_{ij} are the components of the transformation matrix between the two coordinate system[14].

$$[g]=\begin{bmatrix}\cos^2\theta & \sin^2\theta & \sin 2\theta\\ \sin^2\theta & \cos^2\theta & -\sin 2\theta\\ -\frac{\sin 2\theta}{2} & \frac{\sin 2\theta}{2} & \cos 2\theta\end{bmatrix} \qquad (17)$$

The strains induced by a single microcrack are

$$\bar{\varepsilon}_{ik}^{b(\beta)}=\bar{S}_{ij}^{b(\beta)}\sigma_{jk} \qquad (18)$$

If the tensile stress σ_{22} is less than the critical value $\sigma_{22(c)}=\frac{S_{cc}}{\sqrt{a_{11}\pi c_0}}$, no microcrack has propagated in the rock material, all microcracks are open. In such a case, the average microcrack length $\bar{c}=c_0$. The constitutive relation is

$$\varepsilon_{ik}=S_{ij}\sigma_{jk}=\left(S_{ij}^0+S_{ij}^{b1}\right)\sigma_{jk} \qquad (19)$$

where S_{ij}^{b1} denotes the contribution to the compliance tensor due to all open microcracks that have not propagated,

$$S_{ij}^{b1}=\int_0^{\pi/2}\rho p(\theta)\bar{S}_{ij}^{b}(c_0,\bar{c})\sin\theta d\theta \qquad (20)$$

Once the tensile stress σ_{22} reaches the critical value $\sigma_{22(c)}$ and it is less than $\sigma_{22(cc)}=\dfrac{S_{cc}}{\sqrt{a_{11}\pi c_1}}$,where $\sigma_{22(cc)}$ is the maximal tensile stress the material can bear, some microcracks will propagate increasing their length from $2c_0$ to $2c_1$. The microcrack length $2\bar{c}$ as well as the contribution of a single microcrack to the compliance tensor, $\bar{S}_{ijkl}^{b}(c_1,\bar{c})$, can be easily determined from Eq.(8) and Eq.(16), respectively. Then, the effective constitutive relation can be obtained as

$$\varepsilon_{ik}=S_{ij}\sigma_{jk}=\left(S_{ij}^{0}+S_{ij}^{b1}+S_{ij}^{b2}\right)\sigma_{jk} \qquad (21)$$

where S_{ij}^{b2} denotes the contribution of elastic deformation of microcracks with length $2c_1$ to the compliance tensor, and

$$S_{ij}^{b1}=\int_0^{\pi/2}\rho p(\theta)\bar{S}_{ij}^{b}(c_0,\bar{c})\sin\theta d\theta-\int_{\Omega}\rho p(\theta)\bar{S}_{ij}^{b}(c_0,\bar{c})\sin\theta d\theta \qquad (22)$$

$$S_{ij}^{b2}=\int_{\Omega}\rho p(\theta)\bar{S}_{ij}^{b}(c_1,\bar{c})d\theta \qquad (23)$$

If $\sigma_{22}=\sigma_{22(cc)}$,that is ,the stage of rapid stress drop, some microcracks nearly normal to the tension direction propagate in an unstable fashion.As mentioned above, the distribution of sizes and orientations of microcracks in rock material can be described by the probability density function $p(c)$ and $p(\theta)$, respectively. If the number of microcracks normal to tensile direction is zero, it is assumed that microcracks whose orientations are within a small orientation scope $0\le\theta\le\theta_{cc}$ propagate in an unstable fashion.

Once Eq.(4) is satisfied by microcracks whose orientations are within a small orientation scope $0\le\theta\le\theta_{cc}$, they will experience the secondary unstable growth ,which may cause a transition from the distributed damage to the localization of damage and a rapid stress drop at the transition strain $\varepsilon_{22(cc)}$ .During the stage ,only microcracks whose orientations are within a small orientation scope $0\le\theta\le\theta_{cc}$ propagate further and other microcracks undergo elastic unloading.

The relation between the microcrack length c_2 and the tensile stress σ_{22} can be obtained approximately from the criterion Eq.(4) ,we have

$$c_2=\frac{(K_{ICC})^2}{\pi\sigma_{22}^2} \qquad (24)$$

During the stage of stress drop, the average microcrack length $2\bar{c}$ an be easily obtained as

$$\bar{c}^2=\int_0^{\frac{\pi}{2}}p(c)p(\theta)c_0^2\sin\theta d\theta+\int_{\Omega}p(c)p(\theta)(c_1^2-c_0^2)\sin\theta d\theta+\int_0^{\theta_{cc}}p(c)p(\theta)(c_2^2-c_1^2)\sin\theta d\theta \qquad (25)$$

During the stage of stress drop, the effective constitutive relation can be given as

$$\varepsilon_{ik}=S_{ij}\sigma_{jk}=\left(S_{ij}^{0}+S_{ij}^{b1}+S_{ij}^{b2}+S_{ij}^{b3}\right)\sigma_{jk} \qquad (26)$$

where S_{ij}^{b3} denotes the contribution of elastic deformation of unstable propagating microcracks with length $2c_2$ to the compliance tensor, and

$$S_{ij}^{b1}=\int_0^{\pi/2}\rho p(\theta)\bar{S}_{ij}^{b}(c_0,\bar{c})\sin\theta d\theta-\int_{\Omega}\rho p(\theta)\bar{S}_{ij}^{b}(c_0,\bar{c})\sin\theta d\theta-\int_0^{\theta_{cc}}\rho p(\theta)\bar{S}_{ij}^{b}(c_0,\bar{c})\sin\theta d\theta \qquad (27)$$

$$S_{ij}^{b2}=\int_{\Omega}\rho p(\theta)\bar{S}_{ij}^{b}(c_1,\bar{c})d\theta-\int_0^{\theta_{cc}}\rho p(\theta)\bar{S}_{ij}^{b}(c_1,\bar{c})d\theta \qquad (28)$$

$$S_{ij}^{b3}=\int_0^{\theta_{cc}}\rho p(\theta)\bar{S}_{ij}^{b}(c_2,\bar{c})d\theta \qquad (29)$$

During the stage of stress drop, the strain maintains constant, we have

$$\varepsilon_{22}=\varepsilon_{22(cc)} \qquad (30)$$

where $\varepsilon_{22(cc)}$ is the axial strain at peak loads $\sigma_{22(cc)}$, ε_{22} is the axial strain during stage of stress drop.

According to Eq.(30),the magnitude of the stress drop can be determined. It is assumed that the stage of rapid stress drop intersects that of tension softening at the point where the value of stress is $\sigma_{22(sc)}$.

If $\sigma_{22} \le \sigma_{22(sc)}$,that is, the stage of strain softening. During the stage of strain softening, some of the microcracks which have undergone the secondary growth will propagate further, while other microcracks will simultaneously experience unloading. Meanwhile the growth criterion Eq.(4) must be satisfied by microcracks whose orientations are within a small orientation scope $0 \le \theta \le \theta_{cc}$. The compliance tensor due to the microcracks experiencing the secondary growth unstable microcracks and stable microcracks S_{ij}^{b2} ,S_{ij}^{b3} can be evaluated by Eq.(28)and Eq.(29),respectively. The compliance tensor due to open microcracks can be computed by Eq.(27).

During the stage of strain softening, the effective constitutive relation can be given as

$$\varepsilon_{ik} = S_{ij}\sigma_{jk} = \left(S_{ij}^{0} + S_{ij}^{b1} + S_{ij}^{b2} + S_{ij}^{b3}\right)\sigma_{jk} \qquad (31)$$

It is assumed that all microcrack are distributed uniformly in the orientations and sizes space. The stress-strain relation for microcrack - weakened rock under uniaxial tensile loading can be expressed as

$$\varepsilon_{22} = \begin{cases} F_0\sigma_{22}, & (0 \le \sigma_{22} \le \sigma_{22(c)}) \\ [F_0 + F(\theta_1)]\sigma_{22}, & (\sigma_{22(c)} \le \sigma_{22} \le \sigma_{2(cc)}) \\ [F_0 + F(\theta_2)]\sigma_{22(cc)}, & (\sigma_{22(sc)} \le \sigma_{22} \le \sigma_{22(cc)}) \\ [F_0 + F(\theta_2) + F(\theta_{cc})]\sigma_{22}, & (0 \le \sigma_{22} \le \sigma_{22(sc)}) \end{cases} \qquad (32)$$

where:

$$F(\theta_1) = \frac{1-\bar{v}_1^2}{4\pi\bar{E}_1}\rho(c_1^2 - c_0^2)(2\theta_1 + \sin 2\theta_1)$$

$$F(\theta_2) = \frac{1-\bar{v}_2^2}{4\pi\bar{E}_2}\rho(c_1^2 - c_0^2)(2\theta_2 + \sin 2\theta_2) \quad ,$$

$$\frac{\bar{E}_0}{E_0} = \frac{2}{2+\pi^2\bar{\omega}_0^2}\ ,\ \bar{\omega}_0 = \rho c_0^2\ ,\ \frac{\bar{E}_1}{E_0} = \frac{2}{2+\pi^2\bar{\omega}_1^2}$$

$$\bar{v}_1 = \frac{2}{2+\pi^2\bar{\omega}_1^2}\left(\pi^2\bar{\omega}_1^2 + 1 + v_0\right) - 1$$

$$\frac{\bar{E}_2}{E_0} = \frac{2}{2+\pi^2\bar{\omega}_2^2}\ ,\ \frac{\bar{E}_3}{E_0} = \frac{2}{2+\pi^2\bar{\omega}_3^2}\ ,$$

$$\bar{v}_2 = \frac{2}{2+\pi^2\bar{\omega}_2^2}\left(\pi^2\bar{\omega}_2^2 + 1 + v_0\right) - 1$$

$$\bar{\omega}_1 = \rho\left[c_0^2 + \frac{1}{\pi}\left(c_1^2 - c_0^2\right)(1 - \cos\theta_1)\right],$$

$$\bar{\omega}_2 = \rho\left[c_0^2 + \frac{1}{\pi}\left(c_1^2 - c_0^2\right)(1 - \cos\theta_2)\right]$$

$$c_2 = \frac{K_{ICC}^2}{\pi\sigma_{22}^2}\ ,\ F_0 = \frac{1-\bar{v}_0^2}{\bar{E}_0}\left(1 + \frac{1}{4}\rho c_0^2\right)$$

$$\theta_2 = \arccos\left(\frac{\sigma_{22(c)}}{\sigma_{22(cc)}}\right)^{1/2}\ ,\ \theta_1 = \arccos\left(\frac{\sigma_{22(c)}}{\sigma_{22}}\right)^{1/2},$$

$$\sigma_{22(sc)} = \frac{[F_0 + F(\theta_2)]\sigma_{22(cc)}}{[F_0 + F(\theta_2) + F(\theta_{cc})]}$$

$$F(\theta_{cc}) = \frac{1-\bar{v}_3^2}{4\pi\bar{E}_3}\rho(c_2^2 - c_1^2)(2\theta_{cc} + \sin 2\theta_{cc}),$$

$$\bar{v}_0 = \frac{2}{2+\pi^2\bar{\omega}_0^2}\left(\pi^2\bar{\omega}_0^2 + 1 + v_0\right) - 1$$

$$\bar{v}_3 = \frac{2}{2+\pi^2\bar{\omega}_3^2}\left(\pi^2\bar{\omega}_3^2 + 1 + v_0\right) - 1$$

$$\bar{\omega}_3 = \rho[c_0^2 + \frac{1}{\pi}\left(c_1^2 - c_0^2\right)(1 - \cos\theta_2) + \frac{1}{\pi}\left(c_2^2 - c_1^2\right)(1 - \cos\theta_{cc})]$$

3.Comparison with experimental results

In order to illustrate the four stages of the stress-strain relation predicted by the theoretical model, experimental results [21,22] for Sanjome andesite and Inada granite specimens subjected to uniaxial tensile loading is selected. Sanjome andesite and Inada granite is a relatively

homogeneous and nearly brittle, compact rock.The following material parameters were used in computations for Sanjome rock:

$$E_0 = 11600MPa, c_0 = 8.7\times10^{-4}\,m,$$
$$c_1 = 5.0\times10^{-3}\,m, K_{IC} = 0.14MPa\sqrt{m},$$
$$v_0 = 0.135, \sigma_{22(cc)} = -4.2MPa,$$
$$\rho = 2.1\times10^{5}, \theta_{cc} = 0.1^0,$$
$$K_{ICC} = 0.635MPa\sqrt{m}, p(\theta) = 1/\pi$$

(33)

The following material parameters were used in computations for Inada granite

$$E_0 = 37600MPa, c_0 = 7.5\times10^{-4}\,m,$$
$$c_1 = 5.0\times10^{-3}\,m, K_{IC} = 0.10MPa\sqrt{m},$$
$$v_0 = 0.23, \sigma_{22(cc)} = -6.7MPa,$$
$$\rho = 4.5\times10^{5}, \theta_{cc} = 0.1^0,$$
$$K_{ICC} = 0.85MPa\sqrt{m}, p(\theta) = 1/\pi$$

□34□

In Eqs(33)and (34), the numerical values of E_0 , v_0 , $\sigma_{22(cc)}$ were read off from the tests [22]. ρ,c_0,c_1 were estimated by SEM observations , K_{IC} □ K_{ICC} were estimated by the three-point bend tests. The solid curves depicted in Fig.2 and Fig.3 represent the stress-strain relation predicted by the present model, while dots are the experimental results [22].It can be seen in Fig.2 and Fig.3 that the agreement between theoretical and experimental results is fair good.

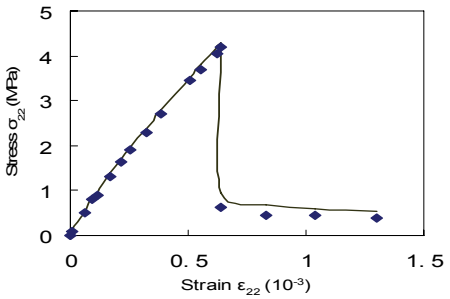

Fig2 The present model vs testing result for Sanjome andesite

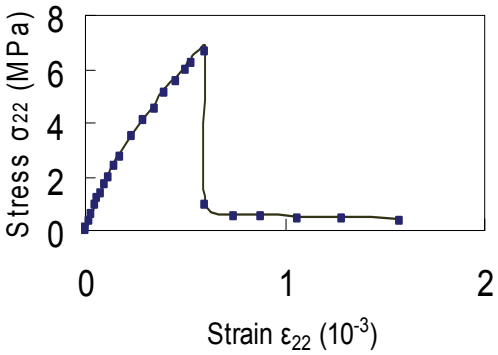

Fig3 The present model vs testing result for Inada granite

4. Conclusion

An approximate scheme is proposed to determine the complete stress-strain relation of brittle rock materials weakened by uniformly distributed microcracks that may propagate in an unstable fashion. The influence of all microcracks with different sizes and orientations are introduced into the constitutive relation by using the statistical average method. Effects of microcrack interaction on the complete stress-strain relation as well as the localization of damage and deformation are taken into account by assuming that all microcracks are embedded in an approximate, isotropic effective medium. The effective moduli of the approximate effective medium are easily determined by using dilute distribution method. The present effective medium model can be applied to study the complete stress-strain relation and the localization of damage and deformation for a statistically homogeneous brittle rock material containing a low-to-mediate density of microcracks.

Acknowledgements

The author would like to express his sincere thank to Professor G.C.Sih for his kind help and remarks.

References

[1] H.Horii, S. Nemat-Nasser (1985), Compression induced microcrack growth in brittle solides:axial splitting and shear

failure,.*J. Geophys. Res,* **90**,pp.3105.

[2] T.F.Wong(1985),Geometric proba-bility app-roach to characterisation and analysis of microcracking in rocks, *Mech. Mater,* **4**,pp.261.

[3] M. Kachanov(1993), Elastic solids with many cracks and related problem, Advances in Applied Mechanics, New York, Academic Press,**30,**pp. 259.

[4] B. Budiansky, R. J. O' Connell(1976), Elastic moduli of a cracked solids, *Int. J. Solids Struct*.**12,**No.1,pp. 81.

[5] H.Hori, S. Nemat-Nasser (1983), Overall moduli of solids with microcracks, load-induced anisotropy, *J. Mech Phys*. Solids,**31** .pp.55.

[6] T.Mori, K. Tanaka(1973), Average stress in matrix and average elastic energy of materials with misfitting inclusions, *Acta Metall*. **21**,pp.571.

[7] G. J. Weng(1990), The theoretical connection between Mori-Tanaka's theory and Hashin-Shtrikman-Walpole bounds, *Int. J. Eng. Sci.* **28**,pp.1111.

[8] Z. Hashin(1988), The differential scheme and its application to cracked materials, *J. Mech. Phys Solids* **36**,pp.719.

[9] Y. Huang, K. X. Hu(1994), A.Chandra, A generalized self-consistent mechanics method for microcracked solids, *J. Mech. Phys. Solids* **42**,No.8 pp.1273.

[10] D. Krajcinovic(1997), Damage mechanics, Amsterdam, Elsevier.

[11] J. W. Ju, T. M. Chen(1994), Effective moduli of two- dimensional brittle solids with interacting microcracks, *J. Appl. Mech*.**61**,pp. 349.

[12] S. W. Yu, X. Q. Feng(1995), A micromechanics-based model for microcrack-weakenedbrittle solids,*Mech. Mater.* **20**,pp.59.

[13] X. Q. Feng, D.Gross(2000), An approximate scheme for considering effects of microcrack interaction on the overall constitutive relation of brittle solids under complex loading, *Acta Mech.***139,**No.1-4,pp.143.

[14] X. P. Zhou, J.H. Wang, Y.X.Zhang, Q.L.Ha(2004), Analysis of the localization of damage and the complete stress-strain relation for mesoscopic heterogeneous rock under uniaxial tensile loading *Applied Mathematics and Mechanics,* **25**,No.9,pp.1031.

[15] X. P. Zhou(2004), Analysis of the localization of deformation and the complete stress-strain relation for mesoscopic heterogeneous brittle rock under dynamic uniaxial tensile loading, *Int. J. Solids Struct.***41**, No.5-6, pp.1725.

[16] X.P.Zhou,Y.X.Zhang, Q.L.Ha, J.H. Wang(2004), Analysis of the localization of damage and the complete stress-strain relation for mesoscopic heterogenous rock subjected to compressive loads, Applied Mathematics and Mechanics, **25**, No.9,pp.1039.

[17] X.P.Zhou, Q.L.Ha, Y.X.Zhang, K.S.Zhu(2004), Analysis of deformation localization and the complete stress-strain relation for brittle rock subjected to dynamic compressive loads, *Int. J. Rock Mech. Min. Sci.***41**,No.2,pp.311.

[18] X.P. Zhou(2005), Localization of deformation and stress-strain relation for mesoscopic heterogenous brittle rock materials under unloading, *J. Theor. Appl. Fract. Mech.* **44**,No.1,pp. 27.

[19] G. C. Sih (1973), A special theory of crack propagation: methods of analysis and solutions of crack problems In: G.C. Sih, Editors, Mechanics of Fracture I, Noordhoof, Leyden.

[20] G. C. Sih(1991), Mechanics of Fracture Initiation and Propagation, Kluwer Academic Publishers, Netherlands.

[21] S.Okubo, K. Fukui(1996), Complete stress-strain curves for various rock types in uniaxial tension, *Int. J. Rock Mech. Min. Sci.* **35,**pp.549.

[22] F. Jin (2001), The non-linear rheological behavior of rock, Hohai University Press,China,.

ANALYSIS OF CRACKS IN TWO-DIMENSIONAL PIEZOELECTRIC MEDIA

MingHao Zhao*, MinShan Liu, Na Li, Xing Wei

Department of Engineering Mechanics, Zhengzhou University, Henan, 45002, P.R. China

Abstract

The analytical solution of an elliptical cavity in an infinite piezoelectric medium under remotely applied combined mechanical-electric loading is obtained under exact boundary conditions by Stroh formalism. Based on the solution and the self-consistent method, the exact solution for a crack is derived. The strain energy density factors of mode I and II cracks are calculated for different mechanical and electric loadings, as well as under different electric boundary conditions. It is demonstrated that the widely used impermeable crack and permeable cracks are two extremes, and the value of the minimum strain energy density factor of the real crack model considering the crack opening is between those of the impermeable and permeable crack models. The minimum strain energy density factor of impermeable crack is larger than that of permeable crack for positive applied electric field, but is less than that of permeable crack for negative applied electric field.

Keywords: Piezoelectric medium, Elliptical cavity, Crack, Exact solution, Strain energy density factor.

1. Introduction

Due to the mechanical-electrical coupling phenomenon, piezoelectric materials are widely used in advanced technologies such as high power sonar transducers, electromechanical actuators, etc. The fragility is the inherent weakness of the piezoelectric ceramic. Therefore, fracture study of this kind material has been attracting many efforts. A lot of work has been done, which can be referred to the review articles [1-5]. Generally speaking, there are two key problems in fracture mechanics. One is the setting up and solving of the boundary value problem. And the other is the fracture criterion. With regard to the insulating crack in piezoelectric materials, several electric boundary conditions, e.g., electrically

* Correspoding author.
E-mail address: memhzhao@zzu.edu.cn

impermeable, electrically permeable and exact boundary conditions, are frequently used. The first two commonly used conditions are only two extremes to treat the crack as an electrically impermeable or permeable slit [3]. In general, different electrical boundary conditions result to different solutions. For a Griffith crack under remotely uniformly applied combined mechanical-electric loadings in an infinite piezoelectric material, the stress intensity factors are only related to the mechanical loadings, while the electric displacement intensity factor is only related to the electric loading under the impermeable conditions. Under the permeable conditions, however, the stress factor intensity and electric displacement intensity factors are all related to the mechanical loading. The electric displacement intensity factor is produced through the piezoelectricity effect. So, the intensity factors are not appropriate to be used directly as fracture criterion as for the conventional elastic material. Both of the energy release rate and the J- integral increase with the absolute value of electric field increasing, which contradict to the experimental results for condition of negative electric field [3]. The researches [6-8] demonstrate that the J-integral is not path independent because of the electric field in the crack cavity. The energy density factor criterion for piezoelectric ceramics is studied [9-13], and show that this criterion takes greatly advantages in explaining the failure behavior under combined mechanical-electrical loadings. In these studies, only the impermeable condition is used. In this paper, the crack in a two-dimensional piezoelectric medium is analyzed under combined mechanical-electrical loadings and different electric boundary conditions.

2. Stroh formalism

For a two-dimensional piezoelectric medium in the ox_1x_2 plane, the general solution of the generalized displacement vector $\mathbf{u} = (u_1 \quad u_2 \quad u_3 \quad \varphi)^{\mathrm{T}}$ and the generalized stress function vector $\mathbf{\Phi} = (\phi_1 \quad \phi_2 \quad \phi_3 \quad \phi_4)^{\mathrm{T}}$ can be expressed as

$$\mathbf{u} = \mathbf{A}\mathbf{f}(z) + \overline{\mathbf{A}}\overline{\mathbf{f}(z)} \tag{1}$$

$$\mathbf{\Phi} = \mathbf{B}\mathbf{f}(z) + \overline{\mathbf{B}}\overline{\mathbf{f}(z)} \tag{2}$$

where $\mathbf{A}$ and $\mathbf{B}$ are two 4×4 matrixes related to the material constants, and

$$\mathbf{f}(\mathrm{z}) = \left(f_1(z_1) \quad f_2(z_2) \quad f_3(z_3) \quad f_4(z_4)\right)^{\mathrm{T}}$$

$z_\eta = x_1 + p_\eta x_2$ with $\eta = 1 \sim 4$, and p_η is the eigenvalue with positive imaginary part [1,3].

Then, the stress vectors are

$$\mathbf{\Sigma_2} = (\sigma_{21} \quad \sigma_{22} \quad \sigma_{23} \quad D_2)^{\mathrm{T}} = \mathbf{\Phi}_{,1} \tag{3a}$$

$$\mathbf{\Sigma_1} = (\sigma_{11} \quad \sigma_{12} \quad \sigma_{13} \quad D_1)^{\mathrm{T}} = -\mathbf{\Phi}_{,2} \tag{3b}$$

3. Solution for an elliptical cavity

Consider an elliptical cavity with the semi major-axis of a and semi minor-axis of b in an infinite piezoelectric plane under remotely uniformly combined mechanical-electric loading of σ_{ij}^{∞}, D_i^{∞} (or E_i^{∞}), as schematically shown in Figure 1. The center of the cavity is located at the origin of the coordinate system.

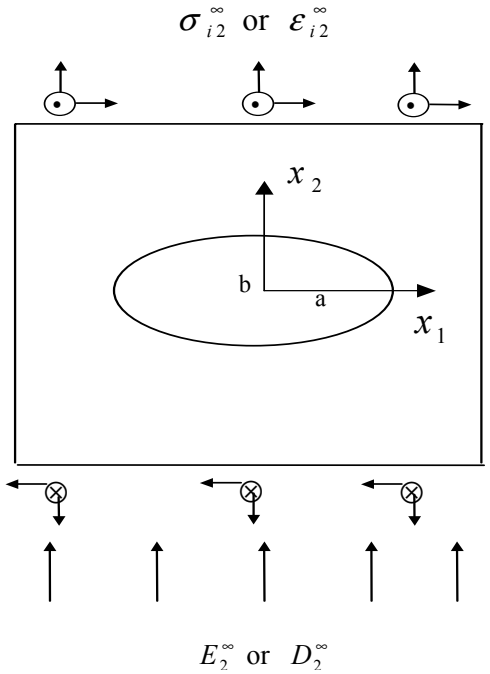

Figure 1 Elliptic cavity in an infinite piezoelectric medium.

The solution is given by [3]

$$\mathbf{f}(z) = \mathbf{c}^{\infty} z + \mathbf{f}_0(z) \tag{4}$$

$$\mathbf{K}_0(z) = \mathbf{B}\mathbf{f}_0(z) \tag{5}$$

where $z = x_1 + \mathrm{i}x_2$, $\mathbf{c}^{\infty}$ is determined by the remotely uniformly applied loading, and

$$\mathbf{K}_0(\varsigma) = -\frac{\mathbf{p}^{\infty}\varsigma^{-1}}{2} \tag{6}$$

where ς is related to z_η by the mapping function

$$z_\eta(\varsigma) = R_\eta(\varsigma + m_\eta \varsigma^{-1}), \quad R_\eta = \frac{a - \mathrm{i}p_\eta b}{2}$$

$$m_\eta = \frac{a + \mathrm{i}p_\eta b}{a - \mathrm{i}p_\eta b}, \quad \eta = 1 \sim 4 \tag{7}$$

and

$$\mathbf{p}^{\infty} = \left(a\sigma_{21}^{\infty} - \mathrm{i}b\sigma_{11}^{\infty} \quad a\sigma_{22}^{\infty} - \mathrm{i}b\sigma_{12}^{\infty} \quad a\sigma_{23}^{\infty} - \mathrm{i}b\sigma_{13}^{\infty} \quad a\Delta D_2^{\infty} - \mathrm{i}b\Delta D_1^{\infty}\right)^T \tag{8}$$

where

$$\Delta D_2^{\infty} = -\frac{\beta\dfrac{\mathrm{Re}[\mathbf{Y}_{4*}\mathbf{M}^{\infty}/a]}{Y_{44}} - \alpha D_2^{\infty}}{\alpha + \beta}$$

$$\Delta D_1^{\infty} = \frac{-\varepsilon_0 E_1^{\infty} + D_1^{\infty} + \beta\,\mathrm{Im}[\mathbf{Y}_{4*}\mathbf{M}^{\infty}/a]/Y_{44}}{1 + \alpha\beta}$$

$$\mathbf{Y} = \mathrm{i}\mathbf{A}\mathbf{B}^{-1}, \ \mathbf{Y}_{4*} = (Y_{41}, Y_{42}, Y_{43}), \ \mathrm{i} = \sqrt{-1}$$

$$\mathbf{M}^{\infty} = \left(a\sigma_{21}^{\infty} - \mathrm{i}b\sigma_{11}^{\infty} \quad a\sigma_{22}^{\infty} - \mathrm{i}b\sigma_{12}^{\infty} \quad a\sigma_{23}^{\infty} - \mathrm{i}b\sigma_{13}^{\infty}\right)^T$$

$$\alpha = b/a, \quad \beta = -\kappa^{c}\,\mathrm{Re}[Y_{44}] \tag{9}$$

where Y_{ij} is the element of the matrix $\mathbf{Y}$.

It can be seen that the solution is not only related to the mechanical loading and the size of the elliptic cavity, but also to the dielectric coefficient κ^c of the medium in the elliptic cavity.

4. Exact solution of the real crack

If b approaches zero, the cavity is shrunk to a crack. From Eq. (8) one has,

$$\mathbf{p}^{\infty} = a\left(\sigma_{21}^{\infty} \quad \sigma_{22}^{\infty} \quad \sigma_{23}^{\infty} \quad \Delta D_2^{\infty}\right)^T \tag{10}$$

where the first three components are applied mechanical loadings, and the last one will be determined by self-consistent method. This component is the function of the mechanical loadings, material constants, and the two non-dimensional parameters α and β. If b approaches zero, α is a small parameter. On the other hand, the dielectric coefficient κ^c of the medium in the crack cavity is generally several magnitudes smaller than that of the piezoelectric media. So, β is also a

small parameter. Then, ΔD_2^{∞} is related to α/β, which can be written as

$$\Delta D_2^{\infty} = D_2^{\infty} - \frac{(\mathrm{Re}[\mathbf{Y_4}]/Y_{44})\boldsymbol{\Sigma}_2^{\infty}}{1+\alpha/\beta} \tag{11}$$

When $b \to 0$, from Eq. (7) we have for the upper and lower center points

$$\varsigma = \pm \mathrm{i} \tag{12}$$

where the sign "+" and "-" denote, respectively, the "upper" and "lower" crack faces. Substituting Eq. (12) into Eq. (6) and then into Eqs. (4) and (1) leads to the displacements of the upper and lower center points

$$\mathbf{u} = \pm\frac{1}{2}\left(\mathrm{i}\mathbf{A}\mathbf{B}^{-1} + \overline{\mathrm{i}\mathbf{A}\mathbf{B}^{-1}}\right)\mathbf{p}^{\infty} = \pm\mathrm{Re}[\mathbf{Y}]\mathbf{p}^{\infty} \tag{13}$$

The self-consistent method requires the displacement u_2 of the upper center point equal the semi minor axis of the elliptical cavity, which leads to

$$\begin{aligned}\alpha = {} & \mathrm{Re}[Y_{21}]\sigma_{21}^{\infty} + \mathrm{Re}[Y_{22}]\sigma_{22}^{\infty} + \\ & \mathrm{Re}[Y_{23}]\sigma_{23}^{\infty} + \mathrm{Re}[Y_{24}]\Delta D_2^{\infty}\end{aligned} \tag{14}$$

where ΔD_2^{∞} is a function of α, as expressed in Eq. (11).

Combining Eqs. (11) and (14) obtains

$$\alpha^2 + h_1\alpha + h_2 = 0 \tag{15}$$

where

$$h_1 = \beta - \sum_{i=1}^{4}\mathrm{Re}[Y_{2i}]\sigma_{2i}^{\infty}$$

$$h_2 = \beta\sum_{1}^{4}(\mathrm{Re}[Y_{24}]\mathrm{Re}[Y_{4i}]/Y_{44} - \mathrm{Re}[Y_{2i}])\sigma_{2i}^{\infty}$$

$$\sigma_{24}^{\infty} = D_2^{\infty} \tag{16}$$

Solving Eq. (15) gives the real crack opening

$$\alpha = \frac{1}{2}(-h_1 + \sqrt{h_1^2 - 4h_2}) \tag{17}$$

5. Strain energy density factor

According to the definition of stress intensity factor and electric displacement intensity factor on the right crack tip

$$\begin{aligned}\mathbf{K} &= \begin{pmatrix} K_{\mathrm{II}} & K_{\mathrm{I}} & K_{\mathrm{III}} & K_{\mathrm{D}} \end{pmatrix}^{\mathrm{T}} \\ &= \lim_{x_1 \to a}\sqrt{2\pi}(x_1 - a)^{1/2}\boldsymbol{\Phi}_{,1}(x_1)\end{aligned} \tag{18}$$

From the solution obtained in Section 3, it is not difficulty to get the intensity factor

$$\mathbf{K} = \sqrt{\pi a}\begin{pmatrix}\sigma_{21}^{\infty} & \sigma_{22}^{\infty} & \sigma_{23}^{\infty} & \Delta D_2^{\infty}\end{pmatrix}^{\mathrm{T}} \tag{19}$$

The stress intensity factor is the same as classical material one, but the electric displacement intensity factor is

$$K_D = \sqrt{\pi a}\left(D_2^{\infty} - \frac{(\mathrm{Re}[\mathbf{Y_4}]/Y_{44})\boldsymbol{\Sigma}_2^{\infty}}{1+\alpha/\beta}\right) \tag{20}$$

The electric displacement intensity factor is related to α/β. Substituting the real crack opening in Eq. (17) into (20) gives the electric displacement intensity factor of the real crack.

As an extreme of $\alpha/\beta \to \infty$, Eq. (20) is reduced to

$$K_D = \sqrt{\pi a}D_2^{\infty} \tag{21}$$

which is the electric displacement intensity factor of the impermeable crack.

While $\alpha/\beta \to 0$, Eq. (20) becomes

$$\begin{aligned}K_D = {} & -(\mathrm{Re}[Y_{11}]/Y_{44})K_{II} - (\mathrm{Re}[Y_{21}]/Y_{44})K_I \\ & -(\mathrm{Re}[Y_{31}]/Y_{44})K_{III}\end{aligned} \tag{22}$$

which is the electric displacement

intensity factor of permeable crack.

Moving the origin of the coordinate system to the right crack tip and introducing new variables $z_\eta^* = z_\eta - a = r(\cos\theta + p_\eta \sin\theta)$, as shown in Fig.2, we can express the stress

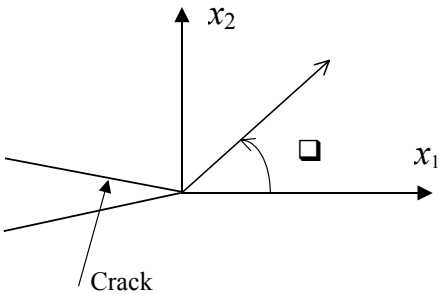

Figure 2 The polar coordinate system at the crack tip.

and displacement fields near the right crack tip in terms of the intensity factor [3]

$$\boldsymbol{\Sigma}_2 = \frac{1}{2}\left[\mathbf{B}\Lambda\mathbf{B}^{-1} + \overline{\mathbf{B}}\overline{\Lambda}\overline{\mathbf{B}^{-1}}\right]\mathbf{K}$$

$$\boldsymbol{\Sigma}_1 = \frac{1}{2}\left[-\mathbf{B}\Delta\mathbf{B}^{-1} - \overline{\mathbf{B}}\overline{\Delta}\overline{\mathbf{B}^{-1}}\right]\mathbf{K}$$

$$\Lambda = \left\langle \frac{1}{\sqrt{2\pi z_\alpha^*}} \right\rangle, \quad \Delta = \left\langle \frac{p_\alpha}{\sqrt{2\pi z_\alpha^*}} \right\rangle \tag{23}$$

$$\mathbf{u} = \frac{1}{2}\left[\mathbf{A}\left\langle \frac{\sqrt{2z_\alpha^*}}{\sqrt{\pi}} \right\rangle \mathbf{B}^{-1} + \overline{\mathbf{A}}\left\langle \frac{\sqrt{2\overline{z_\alpha^*}}}{\sqrt{\pi}} \right\rangle \overline{\mathbf{B}^{-1}}\right]\mathbf{K} \tag{24}$$

The strain energy density function is given [9-11]

$$\frac{\mathrm{d}W}{\mathrm{d}V} = \frac{1}{2}\sigma_{ij}\varepsilon_{ij} + \frac{1}{2}E_i D_i \tag{25}$$

Finally, the strain energy density factor S is obtained

$$S = \frac{1}{2} r\left(\boldsymbol{\Sigma}_1^T \mathbf{I}_{\_}\mathbf{u}_{,1} + \boldsymbol{\Sigma}_2^T \mathbf{I}_{\_}\mathbf{u}_{,2}\right) \tag{26}$$

where

$$\mathbf{I}_{\_} = \begin{bmatrix} 1 & 0 & 0 & 0 \\ 0 & 1 & 0 & 0 \\ 0 & 0 & 1 & 0 \\ 0 & 0 & 0 & -1 \end{bmatrix} \tag{27}$$

The strain energy density factor S is only a function of angle θ and independent of r. Then, the strain energy density factors of different models can be calculated.

6.Numerical results and discusion

The used piezoelectric material is PZT-4, with the material constants given below:

Elastic constants $(\times 10^9\, N/m^2)$

$$c_{11} = 139, \quad c_{12} = 77.8, \quad c_{13} = 74.3$$
$$c_{33} = 113, \quad c_{44} = 25.6, \quad c_{66} = 30.6$$

Piezoelectric constants (C/m^2)

$$e_{15} = 13.44, \; e_{31} = -6.98, \; e_{33} = 13.84$$

Dielectric constants $(\times 10^{-9}\, F/m)$

$$\kappa_{11} = 6.0, \; \kappa_{33} = 5.47, \; \kappa^c = 8.85 \times 10^3$$

The applied loading at infinity is

$$\boldsymbol{\Sigma}_1^\infty = \begin{pmatrix} 0 & 0 & 0 & 0 \end{pmatrix}^T$$

$$\boldsymbol{\Sigma}_2^\infty = \begin{pmatrix} \sigma_{11}^\infty & \sigma_{22}^\infty & 0 & D_2^\infty \end{pmatrix}^T \tag{28}$$

The strain and electric field at infinity are determined by the constitutive equation

$$\begin{aligned} 0 &= c_{11}s_{11}^\infty + c_{13}s_{22}^\infty - e_{31}E_2^\infty \\ \sigma_{22}^\infty &= c_{13}s_{11}^\infty + c_{33}s_{22}^\infty - e_{33}E_2^\infty \\ D_2^\infty &= e_{31}s_{11}^\infty + e_{33}s_{22}^\infty + \varepsilon_{33}E_2^\infty \end{aligned} \tag{29}$$

Introduce the following parameters to present the calculated results

$$R_\sigma = \sigma_{21}^\infty / \sigma_{22}^\infty$$
$$R_E = E_2^\infty / \sigma_{22}^\infty (m^2/C) \quad (30)$$

Influence of stress on strain energy density factors

Figure 3 displays the strain energy density factor for $\sigma_{21}^\infty = 0$, where the strain energy density factor S is normalized as S^*

$$S^* = \frac{S}{a(\sigma_{22}^\infty)^2 \times 10^{-12}} \quad (31)$$

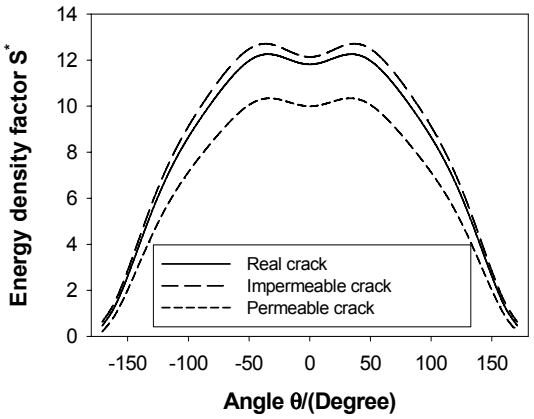

Figure 3 The strain energy density factor versus the angle for $R_\sigma = 0, R_E = 0.01$.

It can be seen that the strain energy density factor of impermeable crack is larger than that of permeable crack, while the strain energy density factor of the real crack is between those of the impermeable and permeable cracks. In this mode I case, the strain energy density factor take the minimum value $S_{\min}^*$ at θ=0°.

Plotted in Figs. 4 and 5 are the normalized minimum energy density factors $S_{\min}^*$ versus the mechanical loadings for a given positive and negative electric fields, respectively. The value of strain energy density factor of impermeable crack is larger than that of permeable crack for positive applied electric field, but is less than that of permeable crack for negative applied electric field**.** The relative error

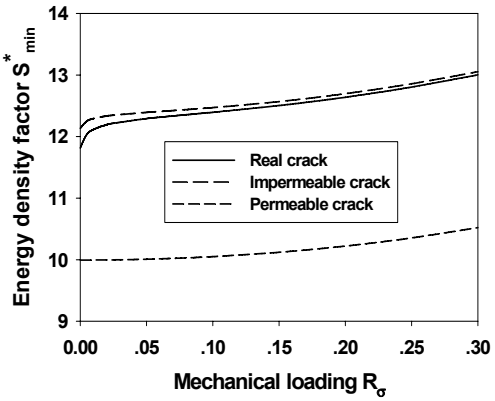

Figure 4 Normalized energy density factor $S_{\min}^*$ verse the stress R_σ for $R_E = 0.01$.

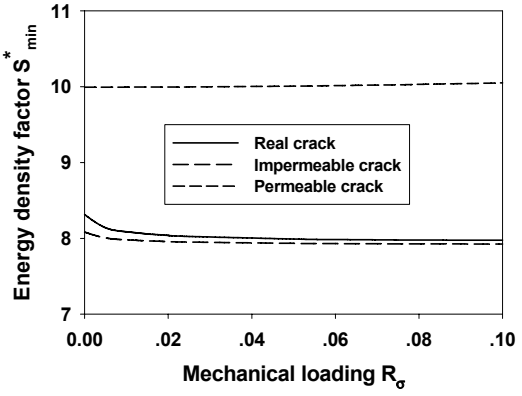

Figure 5 Normalized energy density factor $S_{\min}^*$ verse the stress R_σ for $R_E = -0.01$.

between the values based on the permeable crack and the real crack is about 23% for the positive electric field, and about 20% for negative electric field. The discrepancy between the minimum strain energy density factors calculated by the impermeable crack and the real crack

is not very large, and the gap decreases with the shear mechanical loading increasing.

Figure 6 shows the strain energy density factor variation of the real crack. The maximum of the minimum value increases with the shear mechanical loading increased.

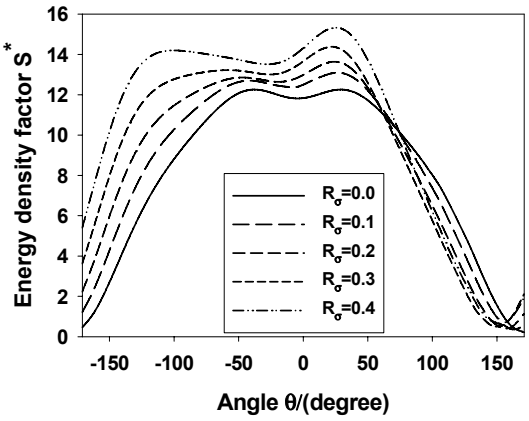

Figure 6 Normalized energy density factor S^* of the real crack verse the angle for different mechanical loading for R_E=0.01.

Influence of electric field on strain energy density factors

For a given mechanical loading, the minimum strain energy density factor versus the electric field is depicted in Figure 7.

The maximum of minimum of strain energy density factor of the permeable crack is independent of the applied electric field. The results of the impermeable crack are very close to those of the real crack, but the discrepancy increases with the absolute value of electric field increasing.

Figure 8 displays the variation of normalized energy density factor of the real crack with the angle for different electric field. The larger the electric field is, the larger the maximum of minimum of strain energy density factor is.

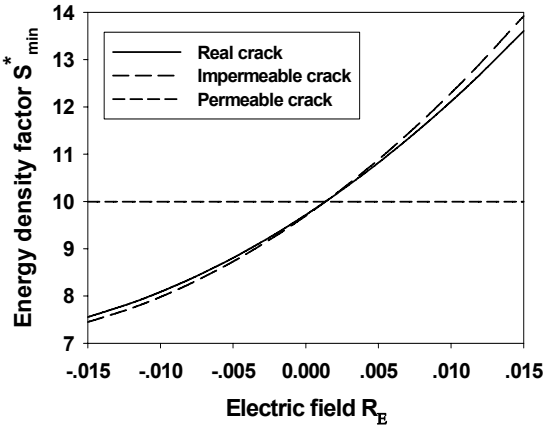

Figure 7 Normalized minimum energy density factor $S^*_{\min}$ versus the electric field R_E for R_σ=0.01.

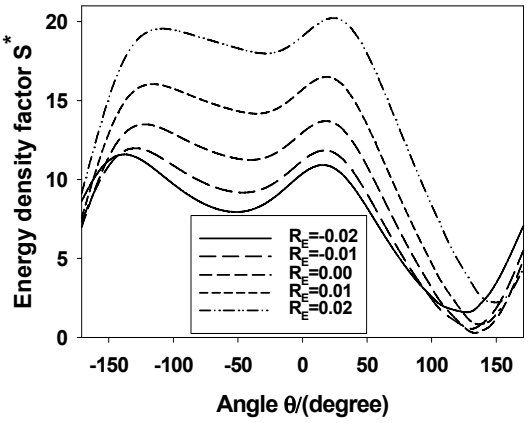

Figure 8 Normalized energy density factor S^* of the real crack verse the angle for R_σ=0.5.

7. Concluding remarks

The exact solution is obtained and the strain energy density factors are calculated for mode I and II cracks in a piezoelectric medium under different combined mechanical-electric loadings.

The results show that the impermeable and the permeable crack models are the upper and lower bounds of the real crack and the impermeable crack model is very close to the real crack model in the used applied loadings. The minimum strain energy density factor of impermeable crack is larger than that of permeable crack for positive applied electric field, but is less than that of permeable crack for negative applied electric field.

Acknowledgement

The work was supported by the National Natural Science Foundation of China (No. 10572131) and the Program for New Century Excellent Talents in University of HeNan Province (HANCET).

References

[1] Suo, Z., Kuo, C.M., Barnett, D.M., Willis, J.R., (1992), J Mech Phys Solids, **40**, pp.739.

[2] Fang, D.N., Soh, A.K., Liu, J.X., (2001), Acta Mech Sinica, **17**, pp.193.

[3] Zhang, T.Y., Zhao, M.H., Tong, P., (2001), Advances in Applied Mechanics, **38**, pp.147.

[4] Chen, Y.H., Lu, T.J., (2002), Advances in Applied Mechanics, **39**, pp.121.

[5] Zhang, T.Y., Gao, C.F., (2004), Theor Appl Fract Mech, **41**, pp.339.

[6] Li, L., (2003), ASME J Appl Mech, **70**, pp.246.

[7] McMeeking, R.M., (2004), Engng Fract Mech, **71**, pp.1149.

[8] Gao, C.F., Zhao, M.H., Tong, P., Zhang, T.Y., (2004), Int J Engng Sci, 42, pp.2175.

[9] Sih, G.C., Zuo, J.Z., (2000), Theor Appl Fract Mech, **34**, pp.123.

[10] Sih, G.C., (2002), Theor Appl Fract Mech, **38**, pp.1.

[11] Sih, G.C., Chen, E.P., (2003), Theor Appl Fract Mech, **40**, pp.1

[12] Lee, K.L., Soh, A.K., Fang, D.N., Liu, J.X., (2004), Theor Appl Fract Mech, **41**, pp.125.

AN RBF-PSEUDOSPECTRAL APPROACH FOR THE ANALYSIS OF FUNCTIONALLY GRADED PLATES

C. M. C. Roque
Faculdade de Engenharia da Universidade do Porto,
Departamento de Engenharia Mecânica e Gestão Industrial,
Rua Dr. Roberto Frias, 4200-465 Porto, Portugal

A. J. M. Ferreira
Faculdade de Engenharia da Universidade do Porto,
Departamento de Engenharia Mecânica e Gestão Industrial,
Rua Dr. Roberto Frias, 4200-465 Porto, Portugal

G. E. Fasshauer
Department of Applied Mathematics, Illinois Institute of Technology, Chicago 60616, USA

R. M. N. Jorge
Faculdade de Engenharia da Universidade do Porto,
Departamento de Engenharia Mecânica e Gestão Industrial,
Rua Dr. Roberto Frias, 4200-465 Porto, Portugal

Abstract

Functionally graded materials are a class of advanced materials where the mechanical and thermal properties in one direction can be tailored so that its variation is gradual. The gradient nature of properties can avoid failure by delaminations due to the absence of interfaces as in laminated composites.

An interesting application of such materials are functionally graded plates obtained from combination of metals and ceramics (i.e. aluminum and zirconia). Metals provide stiffness and ductility whereas ceramics provide mainly thermal protection. This combination of properties may be very useful for aerospace applications.

In this paper we perform the analysis of static deformations and free vibrations of functionally graded plates by a recent meshless method, based on the combination of pseudospectral methods and radial basis functions [1,2].

The method is quite stable and allows excellent accuracy in terms of transverse displacements and natural frequencies.

Keywords: Numerical methods, meshless methods, pseudospectral, radial basis functions, functionally graded plates.

1. Introduction

Vibration of thick and thin composite plates is an important subject in the design of mechanical, civil and aerospace applications. The thickness of most parts

of composite plates makes the transverse shear and the rotatory inertia not negligible as in classical theories. Therefore the first-order shear deformation theory for plates should be considered in general analysis. The analysis of free vibration of isotropic and composite plates is best performed by numerical techniques. The differential quadrature method by Bert [3], the boundary characteristic orthogonal polynomials by Liew [4] and the pseudospectral method by Lee [5] were used in recent years. More recently the free vibration analysis of Timoshenko beams and Mindlin plates by Kansa's non-symmetric radial basis function (RBF) collocation method [6,7] was performed by Ferreira [8].

In the present work we illustrate the application of the combination of radial basis functions and pseudospectral methods to the static and eigenvalue analysis of functionally graded plates.

2. The RBF- pseudospectral method

Pseudospectral (PS) methods (see [9] for an introduction to the subject) are known as highly accurate solvers for PDEs. Generally speaking, one represents the spatial part of the approximate solution u^h of a given PDE by a linear combination of certain smooth basis functions, (i, j represents the N grid points).

$$u^h(x_i) = \sum_{j=1}^{N} c_j \phi_j(x_i), \quad i = 1,\ldots,N \qquad (1)$$

or in matrix-vector notation

$$\mathbf{u} = A\mathbf{c} \qquad (2)$$

with $\mathbf{c} = \left[c_1,\ldots,c_N\right]^T$ and $A_{ij} = \phi_j(x_i)$
Traditionally, polynomial basis functions are used. In this paper, however, we will use radial basis functions (RBFs). The inverse multiquadric we use is of the form:

$$\phi_j(x) = \Phi(r) = \frac{1}{\sqrt{r^2 + \varepsilon^2}} \qquad (3)$$

where r is the euclidian norm between grid points, $r = \| x \|$ and ε is a shape parameter.
The derivatives of u^h are easily computed. For example,

$$\mathbf{u}' = A_x \mathbf{c} = A_x A^{-1}\mathbf{u} \equiv D\mathbf{u} \qquad (4)$$

with $A_x = \frac{d}{dx}\phi_j(x_i)$

where matrix D is the *differentiation matrix*. Details about this formulation can be found in [1,2].

3. First-order shear deformation plate theory (FSDT)

Equations for Reddy's (FSDT) are presented bellow and are derived by using the dynamic version of the principle of virtual work. Further details are presented in [10]

$$a)\quad \frac{\partial N_{xx}}{\partial x} + \frac{\partial N_{xy}}{\partial y} = I_0 \frac{\partial^2 u_0}{\partial t^2} + I_1 \frac{\partial^2 \phi_x}{\partial t^2}$$

$$b)\quad \frac{\partial N_{xy}}{\partial x} + \frac{\partial N_{yy}}{\partial y} = I_0 \frac{\partial^2 v_0}{\partial t^2} + I_1 \frac{\partial^2 \phi_y}{\partial t^2}$$

$$c)\quad \frac{\partial Q_x}{\partial x} + \frac{\partial Q_y}{\partial y} + q = I_0 \frac{\partial^2 w_0}{\partial t^2} \qquad (5)$$

$$d)\quad \frac{\partial M_{xx}}{\partial x} + \frac{\partial M_{xy}}{\partial y} - Q_x = \frac{\partial^2}{\partial t^2}\left(I_1 u_0 + I_2 \phi_x\right)$$

$$e)\quad \frac{\partial M_{xy}}{\partial x} + \frac{\partial M_{yy}}{\partial y} - Q_y = \frac{\partial^2}{\partial t^2}\left(I_1 v_0 + I_2 \phi_y\right)$$

where q is the external distributed load and

$$\begin{Bmatrix} N_{\alpha\beta} \\ M_{\alpha\beta} \end{Bmatrix} = \int_{-h/2}^{h/2} \sigma_{\alpha\beta} \begin{Bmatrix} 1 \\ z \end{Bmatrix} dz \qquad (6)$$

$$\{Q_\alpha\} = \int_{-h/2}^{h/2} \sigma_{\alpha z} \{1\} dz \qquad (7)$$

$$I_i = \sum_{k=1}^{N} \int_k^{k+1} \rho^{(k)} (z)^i dz, \quad i = 0,1,2 \qquad (8)$$

4. Homogenization of material properties

We assume that the plate is made of two randomly distributed isotropic constituents, the macroscopic response of the composite is isotropic, and the composition of the composite varies only in the z direction. Qian and Batra [11] have studied free vibrations of a FG plate with material properties varying smoothly in two directions.

The volume fraction of constituent 1 is given by:

$$V_1 = \left(\frac{1}{2} + \frac{z}{h} \right)^p \qquad (9)$$

Thus $V_1 = 0$ at the bottom surface $z = -h/2$ and $V_1 = 1$ at the top surface $z = h/2$ of the plate. Two homogenization techniques are used to find the effective properties at a point. According to the rule of mixtures, the effective property P, at a point is given by

$$P = P_1 V_1 + P_2 V_2 \qquad (10)$$

where V_1 and $V_2 = 1 - V_1$ are the volume fractions of constituents 1 and 2 respectively, and P_1 and P_2 are values of P for the two constituents.

According to the Mori-Tanaka [12] homogenization method the effective bulk modulus, K, and the effective shear modulus, G, of the composite are given by

$$\frac{K - K_1}{K_2 - K_1} = \frac{V_2}{1 + (1 - V_2) \dfrac{K_2 - K_1}{K_1 - \frac{4}{3} G_1}} \qquad (11)$$

$$\frac{G - G_1}{G_2 - G_1} = \frac{V_2}{1 + (1 - V_2) \dfrac{G_2 - G_1}{G_1 + f_1}} \qquad (12)$$

where $f_1 = \dfrac{G_1 (9K_1 + 8G_1)}{6(K_1 + 2G_1)}$.

The effective values of the Young's modulus, E, and the Poisson's ratio, ν, are found from:

$$E = \frac{9KG}{3K + G}, \nu = \frac{3K - 2G}{2(3K + G)} \qquad (13)$$

Fig. 1 shows the variation of volume fraction, V_1, along the plate thickness, z, for different p parameters.

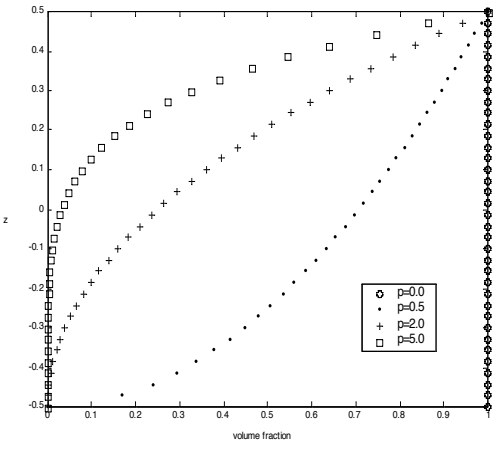

Figure 1: *Volume fraction variation in the z direction.*

5. Numerical examples

We use functionally graded square plates of length a and total thickness h to present some numerical examples.

Static analysis
We first compute the central deflection for a simply-supported FG aluminum/zirconia plate, with material properties:

$$E_1 = 70\ \text{GPa},\ \nu_1 = 0.3$$
$$E_2 = 151\ \text{GPa},\ \nu_2 = 0.3$$

A convergence study is made for various values of p, and compared with a meshless solution by Qian and colleagues, based on the meshless local Petrov-Galerkin method (MLPG) [13], and a meshless Kansa collocation using a multiquadric (MQ) [13]. Results are presented in Table 1, with normalization $\bar{w} = w/h$.

n (points/side)	$p=0$	$p=0.5$	$p=1$
9	0.0086	0.0110	0.0124
11	0.0271	0.0368	0.0405
13	0.0201	0.0269	0.0298
15	0.0205	0.0275	0.0305
17	0.0208	0.0279	0.0309
19	0.0208	0.0279	0.0309
21	0.0208	0.0279	0.0309
[13] MQ	0.0208	0.0279	0.0309
[13] MLPG	0.0212	/	0.0315
n (points/side)	$p=2$	metal	
9	0.0139	0.0184	
11	0.0431	0.0584	
13	0.0322	0.0433	
15	0.0329	0.0443	
17	0.0334	0.0449	
19	0.0333	0.0448	
21	0.0333	0.0448	
[13] MQ	0.0333	0.0448	
[13] MLPG	0.0334	0.0458	

Table 1: Central deflection $\bar{w}$, for various p parameters, with $a/h = 20$, $\varepsilon = \sqrt{n}/2$.

As seen in Table 1, results are in close agreement with other meshless methods, the meshless local Petrov-Galerkin method (MLPG) and the multiquadric radial basis function (MQ). In fact, our formulation gives similar results to the MQ-RBF formulation.

Free vibration analysis
A free vibration analysis is made using a simply supported FG aluminum/zirconia plate with the following material properties:

$$E_1 = 70\ \text{GPa},\ \nu_1 = 0.3,\ \rho_1 = 2702$$
$$E_2 = 200\ \text{GPa},\ \nu_2 = 0.3,\ \rho_2 = 5700$$

All presented values are adimensionalized by: $\bar{\omega} = \omega\left(a^2/h\right)\left(\sqrt{\rho_1/E_1}\right)$.

The first natural normalized frequencies, $\bar{\omega}$ are presented in Table 2 and Table 3, for different ratios a/h (Table 2) and different p parameters (Ttable 3).

In Fig. 2, the first four flexural vibration modes are represented, for $a/h = 20$ and $p = 0$.

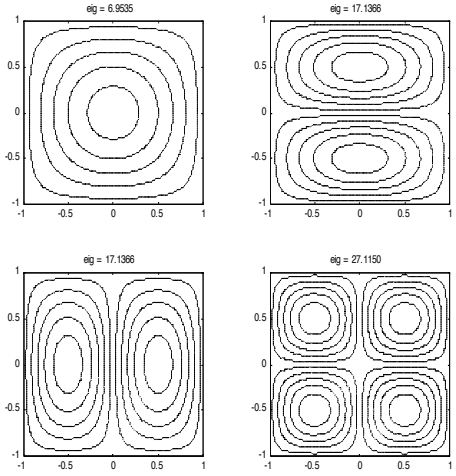

Figure 2: Vibration modes for $a/h = 20,\quad p = 0,\quad \varepsilon = \sqrt{n}/2$

n (points/side)	$\frac{a}{h}=5$	$\frac{a}{h}=10$	$\frac{a}{h}=20$
11	5.5077	5.8135	5.3699
13	5.5494	6.0027	6.1732
15	5.5455	5.9894	6.1626
17	5.5426	5.9776	6.1042
19	5.5429	5.9787	6.1081
[14]	5.4806	5.9609	6.1076

Table 2: Convergence of first natural frequencies $\bar{\omega}$ for various a/h, with $p=1, \varepsilon=\sqrt{n}/2$.

n (points/side)	$p=2$	$p=3$	$p=5$
11	5.5448	5.5936	5.6333
13	5.5844	5.6320	5.6706
15	5.5806	5.6283	5.6670
17	5.5779	5.6257	5.6644
19	5.5782	5.6260	5.6647
[14]	5.4923	5.5285	5.5632

Table 3: Convergence of first natural frequencies $\bar{\omega}$ for various p parameters, with $a/h=5, \varepsilon=\sqrt{n}/2$.

From Tables 2 and 3 we can conclude that our formulation agrees well with the exact solution of Vel and Batra [14]. The agreement is higher for thinner plates, as the exact solution has higher order modes that our formulation does not consider, in particular in the thickness direction. In Table 3 for $a/h=5$ (thick plate) the results are quite comparable. Again, differences lie in the higher-order theory used in both cases.

6. Conclusions

This paper considers the analysis of functionally graded plate with an hybrid formulation. In this formulation we consider radial basis functions (RBFs) with pseudo spectral (PS) to form a new, accurate meshless solution for functionally graded composite plates.

We briefly presented the formulation and tested it in static deformation and free vibration of simply supported functionally graded plates.

Results show very good accuracy for moderately thick plates and thin plates. For very thick plates differences with exact solution increases, proving the need of higher-order shear deformation theories.

References

[1] Ferreira, A. J. M., Fasshauer, G. E., (2005), Natural frequencies of symmetric composite plates by a RBF-Pseudospectral method, *Compos. Struct.*, to appear.

[2] Ferreira, A. J. M., Fasshauer, G. E., (2005), Natural frequencies of shear deformable beams and plates by a RBF-Pseudospectral method, *Comput. Meth. Appl. Mech. Eng.* to appear.

[3] Bert, C. W., Malik, M., (1996), Differential quadrature method in computational mechanics: a review, *Appl. Mech. Rev.*, **49**, pp. 1.

[4]. Liew, K. M, Hung, K. C., Lim, M. K., (1995), Vibration of Mindlin plates using boundary characteristic orthogonal polynomials, *J. Sound. Vib.*, **182**, pp. 77.

[5] Lee, J., Schultz, W. W., (2004), Eigenvalue analysis of Timoshenko beams and axisymmetric Mindlin plates by the pseudospectral method, *J. Sound. Vib.*, **269**, pp. 609.

[6] Kansa, E. J., (1990), Multiquadrics- a scattered data approximation scheme with applications to computational fluid dynamics. i: Surface approximations and partial derivative estimates, *Comput. Math. Appl.*, **19**, pp. 127.

[7] Kansa, E. J., (1990), Multiquadrics- a scattered data approximation scheme with applications to computational fluid dynamics. ii. Solutions to parabolic, hyperbolic and elliptic partial differential equations, *Comput. Math. Appl.,* **19**, pp. 147.

[8] Ferreira, A. J. M., (2005) Free vibration analysis of Timoshenko beams and Mindlin plates by radial basis functions, *Int. J. Comput. Meth.*, **2**, pp. 15.

(9] Trefethen, L. N, (2000), *Spectral Methods in MATLAB*, Siam, Philadelphia, PA.

[10] Reddy, J. N., (1997), *Mechanics of laminated composite plates*, CRC Press, New York.

[11] Qian, L. F., Batra, R. C., Chen, L. M.., (2004), Static and dynamic deformations of thick functionally graded elastic plate by using higher-order shear and normal deformable plate theory and meshless local Petrov-Galerkin method, *Compos. B Eng.*, **35**, pp. 685.

[12] Mori, T., Tanaka, K., (1973), Average stress in matrix and average elastic energy of materials with misfitting inclusions, *Acta Metall.*, **21**, pp. 571.

[13] Ferreira, A. J. M., Batra, R. C., Roque, C. M. C., Qian, L. F., Martins, P. A. L. S., (2005), Static analysis of functionally graded plates using third-order shear deformation theory and a meshless method, *Compos. Struct.*, **69**, pp. 449.

[14] Vela, S., Batra, R. C., (2004), Three-dimensional exact solution for the vibration of functionally graded rectangular plates, *J. Sound. Vib.*, **272**, pp. 703.

DYNAMIC PROPAGATION PROBLEM ON THE SURFACES OF MODE Ⅰ SINGLE DIRECTION CRACK SUBJECTED TO MOVING LOADS

N. C. Lü*
Department of Astronautics and Mechanics, Harbin Institute of Technology, Harbin 150001, P R China;

Y. H. Cheng
Department of Civil Engineering, Northeastern University, Shenyang 110006, P R China;

J. Cheng
Department of Astronautics and Mechanics, Harbin Institute of Technology, Harbin 150001, P R China;
*School of Material Science and Engineering, Shenyang Ligong University, Shenyang 110168, P R China

Abstract: By the approaches of the theory of complex functions, dynamic propagation problems on the surfaces of mode Ⅰ single direction crack subjected to moving loads were studied. Analytical solutions are very readily attained by application of the methods of self-similar functions. The problems researched can be facilely changed into Riemann-Hilbert problems, and analytical solutions to single direction crack under the actions of constant moving loads and unit-step moving loads respectively, are obtained.
Key words: mode Ⅰ single direction crack, dynamic problem, self-similar functions, analytical solution

1. Introduction

Dynamic problems play an important role in modern fracture mechanics. They will play a still greater role in the future, in connection with the possibility in principle of using dynamic stress waves generated by internal local fracture for detection of the power and nature of a fracture focus. Only an adequate theory of such a focus, whose development is one of the missions of fracture mechanics, can help to resolve this great problem [1]. Single direction crack often occurs in factual engineering structure; and a number of researchers studied its statics problems on edge crack and only gained numerical solutions[2-4]. However, many engineering machineries work under the conditions of dynamic loadings, and statics researches can't effectually settle a series of dynamic problems appearing in the dynamic conditions, so it is essential to investigate their fracture dynamics problems. On account of the difficulty in mathematics, numerical solutions and half analytical solutions were attained by literatures [5-10], moreover analytical solutions were obtained much less [11-12]. Therefore it is necessary to study mode I single direction crack dynamic extension problem. General expressions of solutions are given by the approaches of the theory of complex functions in this article. The problems considered can be changed into a Riemann-Hilbert problem by application of this method, which is very readily resolved by the usual Muskhelishvili's measures[13-14].

2. The correlative representations of self-similar functions

In order to resolve availably fracture dynamics problems concerning single direction crack, solutions will be obtained under the condition of variable loads for

mode I single direction crack. In terms of the theorem of generalized functions, the unlike boundary condition problems researched will be easily transformed into Keldysh-Sedov mixed boundary value problem by the methods of self-similar functions, and the correlative solutions will be attained.

Postulating at $y=0$ there are any number of loaded sections and displacement sections along the *x*-axis, and the ends of these sections are running with different constant velocity. At the initial moment t=0 the half-plane is at rest. In these segments the loads and displacements are arbitrary linear combination of the undermentioned functions [1, 11, 15-17]:

$$\frac{d^k f_{k_1}(x)}{dx^k}\cdot\frac{d^s f_{s_1}(t)}{dt^s} \qquad (1)$$

Where $$f_i(\xi)=\begin{cases}0 & \xi<0\\ \xi^i & \xi>0\end{cases} \qquad (2)$$

Here k, k and s, s_1 are arbitrary integer positive numbers.

An arbitrary continuous function of two variables x and t may be represented as a linear superposition of Eq.(1), therefore solving loads or displacements with the modality of Eq.(2) will possess significance in principle. Let us introduce the linear differential operator as well as inverse:

$$L=\frac{\partial^{m+n}}{\partial x^m\partial t^n}\quad \text{inverse: } L^{-}=\frac{\partial^{-m-n}}{\partial x^{-m}\partial t^{-n}} \qquad (3)$$

Here $+m+n$, $-m-n$ and 0 denote the $(m+n)$th order derivative, the $(m+n)$th order integral and function's self. It is facile to testify that there exist constants m and n, when L is put into Eq.(3), homogeneous functions of x and t of zeroth dimension (homogeneous) are attained. The coefficients m, n will be called the indices of self-similarity [1,11].

Utilizing correlative representations of elastodynamics equations of motion for an orthotropic anisotropy [1,11,15-17]:

for the case when functions Lu and Lv are homogeneous

$$u^0=Lu\ ,\quad v^0=\quad Lv\ ,\sigma_y^0=L\sigma_y \qquad (4)$$

for the case when functions $L\sigma_y$ and $L\tau_{xy}$ are homogeneous

$$u^0=\frac{\partial}{\partial t}Lu\ ,\qquad v^0=\frac{\partial}{\partial t}Lv\ ,$$

$$\sigma_y{}^0=\frac{\partial}{\partial t}L\sigma_y\ , \qquad (5)$$

The relevant self-similar functions are as follows [15-17] :

$$\sigma_y^0=(1/t)\,\mathrm{Re}\,F(\tau)\ ,\quad v^0=\mathrm{Re}\,W(\tau)\ , \qquad (6)$$

$$W'(\tau)=[D_1(\tau)/D(\tau)]F(\tau) \qquad (7)$$

where: $\tau=x/t$ $F(\tau)$ and $W(\tau)$ are self-similar functions. The values of $D_1(\tau)/D(\tau)$ can be ascertained from Appendix 1 of literatures [15-17], shown only here: $D_1(\tau)/D(\tau)$ at the interval of the subsonic speeds is purely imaginary for the values which we are considering. Thus, elastodynamics problems for an orthotropic anisotropic body researched can be translated into seeking the single unknown function problems on $F(\tau)$ and $W(\tau)$ sufficing the boundary-value conditions. In the universal case this is Riemann-Hilbert problem in the theory of complex functions (in the simplest cases we have Keldysh-Sedov or Dirchlet problem), this kind of problem is facilely solved by the usual methods, for example, in the books by Muskhelishvili [13-14].

Fracture dynamics problems will be investigated for an infinite orthotropic anisotropic body. Assume at the initial moment $t=0$ a crack occurs at the origin of coordinates and begins running at constant velocity V (for the subsonic speeds) along the positive direction of $x-$axis; and at $t<0$, the half-plane was at rest. The surfaces of the crack are subjected to the unlike types of loads under the plane strain states.

3. Basic modality of the solution to single direction crack propagation problem

Postulate at the initial moment $t=0$, a micro-crack abruptly appears at an orthotropic anisotropic body, we shall choose the Cartesian co-ordinate axes to be coincident with the axes of elastic symmetry of the body, and the problems considered are restricted to motion in the $x-y-$plane. The crack is propagating with constant velocity V in the positive direction of x-axis, the problem studied will be translated into the following boundary condition problems as:

$$\sigma_y(x,0,t)=f_1(x,t)\qquad 0<x<\qquad Vt$$

$$v(x,0,t)=0, \qquad x>Vt \qquad (8)$$

Introducing the formula $\tau = x/t$. By application of the above corresponding expressions and $t\delta(x)=\delta(x/t)$ in the theory of generalized function[18-20], the previous boundary conditions can be transformed into the following boundary value issues:

$$\begin{aligned} &\mathrm{Re}\,F(\tau)= f_2[\tau,\delta(\tau)], \qquad 0<\tau< V \\ &\mathrm{Re}W'(\tau)=0 \qquad \tau> V \end{aligned} \qquad (9)$$

According to the relationship of $F(\tau)$ and $W'(\tau)$ in Eq. (7) and the above conditions, the format of single unknown function $W'(\tau)$ can be confirmed:

$$W'(\tau)= f_3[(\tau,\xi(\tau)] \qquad (10)$$

Then the problem researched can be come down to Keldysh-Sedov problem:

$$\begin{aligned} &\mathrm{Re}\,\xi(\tau)=0, \qquad \tau> V \\ &\mathrm{Im}\,\xi(\tau)=0, \qquad 0<\tau< V \end{aligned} \qquad (11)$$

Considering synthetically asymmetry and the conditions of the infinite point of the plane corresponding to the origin of coordinates of the physical plane as well as singularities of the stress at the crack tip[21-22], the modality of the solution of the above problems can be attained:

$$\xi(\tau)=T[(V-\tau),\ \tau] \qquad (12)$$

Then utilizing Eqs. (6) or (7), we will easily deduce the stress, the displacement and the stress intensity factor under the conditions of single direction crack propagation problems.

4. Solutions to idiographic problems

In order to resolve efficiently dynamics problems on an orthotropic anisotropic body, solutions will be gained under the action of the concentrated force for mode I moving single direction crack. In terms of the theorem of generalized functions, the dissimilar boundary condition problems investigated will be changed into Keldysh-Sedov mixed boundary value problem by the methods of self-similar functions, and the correlative solutions will be acquired.

1) Postulate at the initial moment $t=0$, an single direction crack suddenly occurs and begins to run with constant velocity V along the positive direction of x-axis. The surfaces of the crack are subjected to normal point force P, moving at a constant velocity $\beta<V$ along the positive direction of x-axis. On the half-plane at $y=0$, the boundary conditions will be as follows:

$$\begin{aligned} &\sigma_y(x,0,t)=-P\delta(x-\beta t) \qquad 0<x< Vt \\ &v(x,0,t)=0, \qquad x>Vt \end{aligned} \qquad (13)$$

In this case the displacement will obviously be homogeneous functions, in which $L=1$, Utilizing $\tau = x/t$, the theory of generalized function[18-20] as well as Eqs. (4) and (6), the first of Eq. (13) can be rewritten:

$$\mathrm{Re}\,F(\tau)=-Pt\delta(x-\beta t)=-P\delta(\tau-\beta) \qquad 0<\tau<V \qquad (14)$$

In terms of Eq. (7), boundary conditions (14) will be further rewritten as :

$$\begin{aligned} &\mathrm{Re}[\frac{D(\tau)}{D_1(\tau)}\cdot W'(\tau)]=-P\delta(\tau-\beta), \qquad 0<\tau<V \\ &\mathrm{Re}W'(\tau)=0 \qquad \tau>V \end{aligned} \qquad (15)$$

Deducing from the above formulas, the solution of $W'(\tau)$ must have the format:

$$W'(\tau)=\xi(\tau)/(\tau-\beta) \qquad (16)$$

In the formula $\xi(\tau)$ has no singularity in the extension of $0<\tau<V$,while $D(\tau)/D_1(\tau)$ is purely imaginary for the subsonic speeds, therefore $\xi(\tau)$ must be purely real in the area of $0<\tau<V$ .Thus, question (15) becomes:

$$\begin{aligned} &\mathrm{Re}\,\xi(\tau)=0 \qquad \tau>V \\ &\mathrm{Im}\,\xi(\tau)=0 \qquad 0<\tau< V \end{aligned} \qquad (17)$$

According to dissymmetry and the conditions of the infinite point of the plane corresponding to the origin of coordinates of the physical plane as well as singularities of the crack tip [21-22], the unique solution of the Keldysh-Sedov problem (17) can be obtained:

$$\xi(\tau)=\frac{A}{\sqrt{(V-\tau)\tau}} \qquad (18)$$

Where A is an unknown constant.

Substituting Eq. (18) into Eqs. (16) and (7), we can gain:

$$W'(\tau)=\frac{A}{(\tau-\beta)\sqrt{(V-\tau)\tau}} \qquad (19)$$

$$F(\tau)=\frac{AD(\tau)/D_1(\tau)}{(\tau-\beta)\sqrt{(V-\tau)\tau}} \qquad (20)$$

Then putting Eq. (20) into Eq. (14), at $\tau\to\beta$, constant A can be confirmed:

$$A=-\frac{P\sqrt{(V-\beta)\beta}}{\pi\,\mathrm{Im}[D(\beta)/D_1(\beta)]} \qquad (21)$$

Substituting Eqs. (20) and (19) into (6) and (4), at the surface $y=0$, we will

attain the stress, the displacement and the stress intensity factor, respectively:

$$\sigma_y = \frac{1}{t}\mathrm{Re}\,F(\tau) = \frac{1}{t}\mathrm{Re}\frac{AD(\tau)/D_1(\tau)}{(\tau-\beta)\sqrt{(V-\tau)\tau}}$$

$$= \mathrm{Im}[\frac{D(\tau)}{D_1(\tau)}]\cdot\frac{A}{(x-\beta\, t)\sqrt{(\tau - V\,)\tau}}$$

$$x > Vt \qquad (22)$$

$$v = v^0 = \mathrm{Re}W(\tau) = \mathrm{Re}\int_{\infty}^{x/t}\frac{A}{(\tau-\beta)\sqrt{(V-\tau)\tau}}d\tau$$

$$= \frac{A}{\sqrt{l}}\ln\left|\frac{-\sqrt{(Vt-x)x}+t\sqrt{l}}{x-\beta t}+\frac{V+2\beta}{2\sqrt{l}}\right|$$

$$0 < x < V\,t \qquad (23)$$

Where: $l = V\beta - \beta^2$, the result is gained by making use of integral formulas in Literature [23].

$$K_{\mathrm{I}}(t) = A\cdot\frac{\sqrt{2\pi}\,\mathrm{Im}[D(V)/D_1(V)]}{(V-\beta)\sqrt{Vt}} \qquad (24)$$

Known from Eq. (24), dynamic stress intensity factor $K_{\mathrm{I}}(t)$ decays inchmeal to slow and has obvious singularity on account of sole variable t in the denominator, and the rest quantities are all real constants.

2) With all conditions remaining the same as those in the above example, a unit step load is applied along the positive direction of *x*-axis starting at the point $x = \beta t$ where β is the speed of the moving load. The boundary conditions will be as follows:

$$\sigma_y(x,0,t) = -PH(x-\beta t) \qquad 0 < x < \quad Vt$$

$$v(x,0,t) = 0, \qquad x > Vt \qquad (25)$$

where $H(x)$ is *Heaviside* function, with $H'(x) = \delta(x)$.

In this case the stress will evidently be homogeneous functions, in which $L = 1$. Applying Eqs. (5) and (6), the first expression of the boundary conditions (25) can be written as follows:

$$\mathrm{Re}\,F(\tau) = -PtH'(x-\beta t) = -P\delta(\tau-\beta)$$

$$0 < \tau < V \qquad (26)$$

According to Eq.(7), Eq.(26) will be further rewritten as:

$$\mathrm{Re}[\frac{D(\tau)}{D_1(\tau)}W'(\tau)] = -P\delta(\tau-\beta), \quad 0 < \tau < V$$

$$\mathrm{Re}W'(\tau) = 0 \qquad \tau > V \qquad (27)$$

From the above formulas, the solution of $W'(\tau)$ can be easily deduced:

$$W'(\tau) = \xi(\tau)/(\tau-\beta) \qquad (28)$$

In the formula $\xi(\tau)$ has no singularity at the interval of $0 < \tau < V$,while $D(\tau)/D_1(\tau)$ is purely imaginary for the subsonic speeds, therefore $\xi(\tau)$ must be purely real in the range of $0 < \tau < V$ .Thus, question (27) takes:

$$\mathrm{Re}\,\xi(\tau) = 0 \qquad \tau > V$$

$$\mathrm{Im}\,\xi(\tau) = 0 \qquad 0 < \tau < V \qquad (29)$$

In terms of asymmetry and the conditions of the infinite point of the plane corresponding to the origin of coordinates of the physical plane as well as singularities of the crack tip [21-22], the unique solution of the Keldysh-Sedov problem (29) can be attained:

$$\xi(\tau) = \frac{A}{[(V-\tau)\tau]^{3/2}} \qquad (30)$$

Where *A* is an unknown constant.

Then substituting Eq. (30) into Eqs. (28) and (7), we can obtain:

$$W'(\tau) = \frac{A}{(\tau-\beta)[(V-\tau)\tau]^{3/2}} \qquad (31)$$

$$F(\tau) = \frac{D(\tau)}{D_1(\tau)}\cdot\frac{A}{(\tau-\beta)[(V-\tau)\tau]^{3/2}} \qquad (32)$$

Putting Eq. (32) into Eq. (26), at $\tau \to \beta$, constant *A* can be ascertained:

$$A = -\frac{P\,[(V-\beta)\beta]^{3/2}}{\pi\,\mathrm{Im}[D(\beta)/D_1(\beta)]} \qquad (33)$$

In an orthotropic isotropic body, the disturbance range of elastic wave can be denoted by the circular area of radius $c_1 t$ and $c_2 t$. In an orthotropic anisotropic body, the disturbance range of elastic wave is not the circular zone and can not exceed threshold value $C_d = \sqrt{C_{11}/\rho}$ of elastic body, where C_{11} is an elastic constant of materials. At $|x| > C_d t$, with $\mathrm{Im}[D_1(\tau)/D(\tau)] = 0$, thus the stresses and the displacements are zero; and this depicts that disturbance of elastic wave can not overrun $C_d t$.

Now putting Eq. (32) into (6) and (5), at the surface $y = 0$, the stresses and the dynamic stress intensity factor are gotten:

$$\sigma_y = \int_{\infty}^{x}\frac{1}{t}\mathrm{Re}\frac{AD(\tau)/D_1(\tau)}{(\tau-\beta)[(\tau-V)\tau]^{3/2}}dt$$

$$= -\mathrm{Re}\int_{C_d}^{\frac{x}{t}}\frac{A\,\mathrm{Im}[D(\tau)/D_1(\tau)]}{\tau(\tau-\beta)[(\tau-V)\tau]^{3/2}}d\tau$$

$$x > Vt \qquad (34)$$

$$K_1(t) = \lim_{x\to Vt}\sqrt{2\pi(x-Vt)}\cdot\sigma_y$$

$$= 2\sqrt{2\pi t}\cdot\frac{A\,\mathrm{Im}[D(V)/D_1(V)]}{(V-\beta)V^{5/2}} \qquad (35)$$

The limit of Eq.(35) remains with the format $0\cdot\infty$, which should be changed

into the modality of ∞/∞, then its result can be worked out by the measures of L'Hospital theorem[24]. Dynamic stress intensity factor $K_I(t)$ gently increases from zero and trends to a constant in virtue of only variable t in the numerator of the above expressions, so the rest quantities are also regarded as real constants.

For the sake of expedience, we postulate:

$$X=(V-\tau)\tau=V\tau-\tau^2 \tag{36}$$

Known from the above: $a=0$, $b=V$, $c=-1$, $D=4ac-b^2=-V^2$

Denominator in Eq. (31) has this item $(\tau-\beta)X^{3/2}$, computation is not fulfilled by application of integral formulae, so integral format must be changed into integral which can be performed. By variable substitution: $\tau_1=\tau-\beta$, Eq. (36) can be rewritten as:

$$X=(V-\tau)\tau=V\beta-\beta^2+(V-2\beta)\tau_1-\tau_1^2 \tag{37}$$

From Eq. (37), the following relation is:

$a_1=V\beta-\beta^2$, $b_1=V-2\beta$, $c=-1$

$D=4a_1c-b_1^2=-V^2=D_1$

Integrating Eq. (31), we obtain $W(\tau)$:

$$W(\tau)=\int\frac{Ad\tau}{(\tau-\beta)X^{3/2}}=\int\frac{Ad\tau_1}{\tau_1 X^{3/2}}$$

$$=\frac{A}{a_1}[\frac{1}{\sqrt{X}}+\int\frac{d\tau_1}{\tau_1\sqrt{X}}-\frac{b_1}{2}\int\frac{d\tau_1}{X^{3/2}}]=\frac{A}{a_1}[\frac{1}{\sqrt{X}}$$

$$-\frac{1}{\sqrt{a_1}}\ln\left|\frac{\sqrt{X}+\sqrt{a_1}}{\tau_1}+\frac{b_1}{2\sqrt{a_1}}\right|-\frac{b_1(b_1-2\tau_1)}{D\sqrt{X}}]$$

$$=\frac{A}{a_1}[\frac{D-b_1^2}{D\sqrt{X}}-\frac{1}{\sqrt{a_1}}\ln\left|\frac{\sqrt{X}+\sqrt{a_1}}{\tau_1}+\frac{b_1}{2\sqrt{a_1}}\right|$$

$$+\frac{2b_1\tau_1}{D\sqrt{X}}]=\frac{A}{a_1}[\frac{D-b_1^2-2b_1\beta}{D\sqrt{X}}+\frac{2b_1\tau}{D\sqrt{X}}$$

$$-\frac{1}{\sqrt{a_1}}\ln\left|\frac{\sqrt{X}+\sqrt{a_1}}{\tau-\beta}+\frac{b_1}{2\sqrt{a_1}}\right|]+C \tag{38}$$

Eq. (38) is gained by relevant formulae in Literature [23].The crack runs along the *x*-axis, so $W(\tau)$ can be calculated in the definite integral, we take constant $C=0$. Then putting Eq. (38) into Eqs. (5), (6), the displacement v is attained:

$$v=\int_0^t \mathrm{Re}W(\tau)dt=\mathrm{Re}\int_\infty^{x/t}-\frac{x}{\tau^2}W(\tau)d\tau$$

$$=\frac{-Ax}{a_1}\mathrm{Re}\int_\infty^{x/t}\frac{1}{\tau^2}[\frac{D-b_1^2-2b_1\beta}{D\sqrt{X}}+\frac{2b_1\tau}{D\sqrt{X}}$$

$$-\frac{1}{\sqrt{a_1}}\ln\left|\frac{\sqrt{X}+\sqrt{a_1}}{\tau-\beta}+\frac{b_1}{2\sqrt{a_1}}\right|]d\tau \tag{39}$$

Appling integral formulas in Literature [23], we can acquire the following:

$$\int\frac{d\tau}{\tau\sqrt{X}}=-\frac{2\sqrt{X}}{b\tau},\quad (\text{for } a=0) \tag{40}$$

$$\int\frac{d\tau}{\tau^2\sqrt{X}}=-\frac{2}{V^2}\sqrt{\frac{V-\tau}{\tau}}(1+\frac{V-\tau}{3\tau}) \tag{41}$$

Where $a=0$, Eq. (41) is deduced by this relationship: $\tau=V\sin^2\theta$.

The integral of the second term of Eq. (39) without coefficient can be written:

$$\int-\frac{1}{\tau^2\sqrt{a_1}}\ln\left|\frac{\sqrt{X}+\sqrt{a_1}}{\tau-\beta}+\frac{b_1}{2\sqrt{a_1}}\right|d\tau$$

$$=\frac{1}{\sqrt{a_1}}\int\ln\left|\frac{\sqrt{X}+\sqrt{a_1}}{\tau-\beta}+\frac{b_1}{2\sqrt{a_1}}\right|d(\frac{1}{\tau})$$

$$-\frac{1}{\sqrt{a_1}}\int\frac{1}{\tau}\cdot\frac{1}{\frac{\sqrt{X}+\sqrt{a_1}}{\tau-\beta}+\frac{b_1}{2\sqrt{a_1}}}$$

$$\times[\frac{\frac{b-2\tau}{2\sqrt{X}}\cdot(\tau-\beta)-(\sqrt{X}+\sqrt{a_1})}{(\tau-\beta)^2}]d\tau$$

$$=\frac{1}{\tau\sqrt{a_1}}\ln\left|\frac{\sqrt{X}+\sqrt{a_1}}{\tau-\beta}+\frac{b_1}{2\sqrt{a_1}}\right|$$

$$-\frac{1}{\sqrt{a_1}}\int\frac{1}{\tau}\cdot\frac{2\sqrt{a_1}(\tau-\beta)}{2\sqrt{a_1X}+2a_1+b_1(\tau-\beta)}$$

$$\times\frac{(b-2\tau)(\tau-\beta)-2X-2\sqrt{a_1X}}{2\sqrt{X}\cdot(\tau-\beta)^2}\cdot d\tau$$

$$=\frac{1}{\tau\sqrt{a_1}}\ln\left|\frac{\sqrt{X}+\sqrt{a_1}}{\tau-\beta}+\frac{b_1}{2\sqrt{a_1}}\right|+\int\frac{d\tau}{\tau(\tau-\beta)\sqrt{X}}$$

$$=\frac{1}{\tau\sqrt{a_1}}\ln\left|\frac{\sqrt{X}+\sqrt{a_1}}{\tau-\beta}+\frac{b_1}{2\sqrt{a_1}}\right|+\frac{1}{\beta}(\frac{2\sqrt{X}}{b\tau}$$

$$+\frac{1}{\sqrt{a_1}}\ln\left|\frac{\sqrt{a_1}-\sqrt{X}}{\tau-\beta}+\frac{b_1}{2\sqrt{a_1}}\right|) \tag{42}$$

Then inserting Eqs. (40), (41) and (42) into (39), the displacement v will be obtained:

$$v=\frac{-Ax}{a_1}\mathrm{Re}\{\frac{D-b_1^2-2b_1\beta}{D}[-\frac{2}{V^2}\sqrt{\frac{V-\tau}{\tau}}$$

$$\times(1+\frac{V-\tau}{3\tau})]+\frac{1}{\tau\sqrt{a_1}}\ln\left|\frac{\sqrt{X}+\sqrt{a_1}}{\tau-\beta}+\frac{b_1}{2\sqrt{a_1}}\right|$$

$$+\frac{2b_1}{D}(-\frac{2\sqrt{X}}{b\tau})+\frac{1}{\beta}[\frac{2\sqrt{X}}{b\tau}$$

$$+\frac{1}{\sqrt{a_1}}\ln\left|\frac{\sqrt{a_1}-\sqrt{X}}{\tau-\beta}+\frac{b_1}{2\sqrt{a_1}}\right|]\}\Big|_{\infty}^{x/t}$$

$$=\frac{A}{a_1}\mathrm{Re}\{\frac{D-b_1^2-2b_1\beta}{D}\cdot\frac{2}{3V^2}\sqrt{\frac{V-\tau}{\tau}}(2x+Vt)$$

$$-\frac{t}{\sqrt{a_1}}\ln\left|\frac{\sqrt{a_1}+\sqrt{X}}{\tau-\beta}+\frac{b_1}{2\sqrt{a_1}}\right|-\frac{2t\sqrt{X}}{b}(-\frac{2b_1}{D}$$

$$+\frac{1}{\beta})-\frac{x}{\beta\sqrt{a_1}}\ln\left|\frac{\sqrt{a_1}-\sqrt{X}}{\tau-\beta}+\frac{b_1}{2\sqrt{a_1}}\right|\}\Big|_{\infty}^{x/t}$$

$$=\frac{A}{a_1}\{\frac{D-b_1^2-2b_1\beta}{D}\cdot\frac{2}{3V^2}\sqrt{\frac{Vt-x}{x}}(2x+Vt)$$

$$-\frac{t}{\sqrt{a_1}}\ln\left|\frac{t\sqrt{a_1}+\sqrt{(Vt-x)x}}{x-\beta t}+\frac{b_1}{2\sqrt{a_1}}\right|$$

$$-\frac{x}{\beta\sqrt{a_1}}\ln\left|\frac{t\sqrt{a_1}-\sqrt{(Vt-x)x}}{x-\beta t}+\frac{b_1}{2\sqrt{a_1}}\right|-(\frac{1}{\beta}$$

$$-\frac{2b_1}{D})\cdot\frac{2\sqrt{(Vt-x)x}}{b},\qquad 0<x<Vt \qquad (43)$$

where $a=0$ $b=V$ $c=-1$
$D=4ac-b^2=-V^2$, $a_1=V\beta-\beta^2$
$b_1=V-2\beta$, $D=4a_1c-b_1^2=-V^2=D_1$

5. Description of dynamic stress intensity factor with crack velocity

In terms of real case of concrete problems, variations of the normalized dynamic stress intensity factor as a function of crack velocity should be described better when time t is ascertained. The relevant parameters are put into Eqs. (24) and (35) to plot $K_1(t)$ with crack velocity V/c_r respectively, and the numerical solutions of them are facilely attained. Consider a composite solid made of a unidirectional rein-forced material. The corresponding parameters are given as follows[25-26]:

$C_{11}=149.25Gpa$; $C_{22}=12.202Gpa$;
$C_{12}=3.9047Gpa$; $C_{66}=5.45Gpa$
$\rho=1.478\times9.8\times10^3N\cdot m^{-3}$; $\beta=0.4V$
$c_r=\sqrt{C_{66}/\rho}=613.40m\cdot s^{-1}$; $P=200N$;
$V<c_r$; $t=1.0\times10^{-4}\sec$.

Where c_r is Raleigh wave velocity of elastic body.

Known from Eq. (24), the effect of crack speed on $K_1(t)$ is displayed graphically in

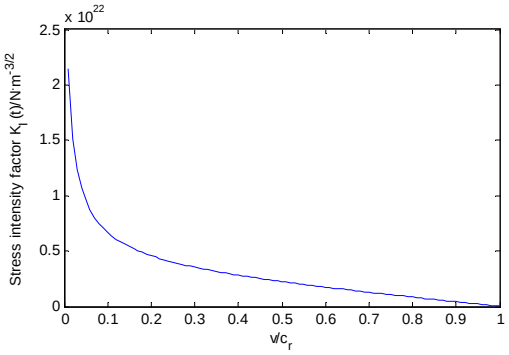

Figure.1: *Dynamic stress intensity factors with crack velocity .*

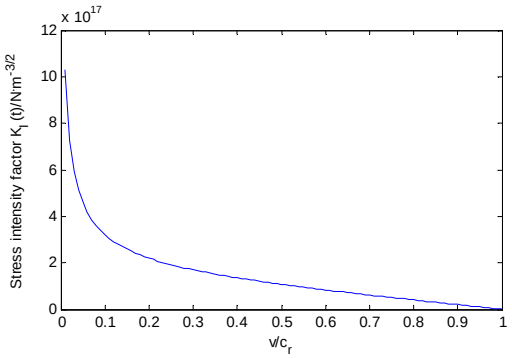

Figure 2: *Dynamic stress intensity factors with crack velocity .*

Table.1 Relevant numerical values between $K_1(t)$ and V/c_r

V/c_r	0.1	0.2	0.3	0.4
$K_1(t)\times10^{21}$ $/N\cdot m^{-3/2}$	6.698	4.588	3.545	2.827
V/c_r	0.6	0.7	0.8	0.9
$K_1(t)\times10^{21}$ $/N\cdot m^{-3/2}$	1.747	1.283	0.843	0.418

Table.2 Relevant numerical values between $K_1(t)$ and V/c_r

V/c_r	0.1	0.2	0.3	0.4
$K_1(t)\times10^{17}$ $/N\cdot m^{-3/2}$	3.215	2.202	1.702	1.357
V/c_r	0.6	0.7	0.8	0.9
$K_1(t)\times10^{17}$ $/N\cdot m^{-3/2}$	0.838	0.616	0.405	0.200

Fig.1 at $t = 1.0 \times 10^{-4}$ sec. It is seen that dynamic stress intensity factor decreases gradually with crack velocity and reaches zero when the crack velocity coincides with the Rayleigh wave speed, i.e., $V = c_r$. According to Eq. (35), variations of $K_1(t)$ with crack velocity V/c_r are similar to the above-mentioned cases when time also equals 1.0×10^{-4} sec. This illustrates that dynamic stress intensity factor tends to reduce in magnitude with the crack velocity until it vanishes at the Rayleigh wave speed when time is finite. Hence, in the time as $t \to \infty$ and $V \to 0$, no comparison between the static and dynamic results can be made [21,27]. The numerical values between $K_1(t)$ and crack velocity V/c_r are represented in Tables.1, 2 in terms of curves in Figs.1, 2, respectively.

6. Conclusion

Analytical solutions to mode Ⅰ dynamic single direction crack extension problem were obtained by the measures of the theory of functions of a complex variable. The approach based on the methods of the self-similar functions makes it possible to attain the idiographic solution of the dynamic single direction crack propagation problem. This is regarded as the analogous class of dynamic problem of the elasticity theory. The measure of solution is based exclusively on techniques of analytical-function theory and is straightforward and concise. By making some observations regarding the solution of the mixed boundary value problem we have reasonably decreased the amount of the computational work needed to settle such a single direction crack propagation problem.

Reference

[1] G. P. Charepanov, (1973),Mechanics of brittle fracture, Nauka Moscow, 732-792.

[2] Hasebe N, Inohara S. (1980),Stress analysis of a semi-infinite plate with an oblique single direction crack. Ingen Arch, 49(1):51-62.

[3] Hasebe N. (1981),An edge direction crack in semi-infinite plate welded to a rigid stiffener. Proc Japan .Soc. Civil. Engrs, 314(10):149-157.

[4] Chen Yi-Zhou, Norio Hasebe. (2001), An edge direction crack problem in a semi-infinite plane subjected to concentrated forces. App. Math. Mech. 22(11):1279-1290.

[5] Yao xuefeng, Jin Guanchang, et al. (2002), Experimental studies on dynamic fracture behavior of thin plates with parallel single edge direction cracks. Polymer Testing. 21(8):933-940.

[6] G. C. Sih, B. MacDonald. (1974), Fracture of mechanics applied to engineering problems. Strain energy density fracture criterion. Eng. Frac. Mech. 6(2): 361-386.

[7] Rice J R. (1967), Comment on stress in an infinite strip containing a semi-infinite cracks. J. App. Mech. (34):248-249.

[8] Hartranft R J, Sih G C. (1973), Alternating method applied to edge and surface crack problems[A].In:. G C Sih(Ed.) Mech. Frac [C], Vol,(1): 177-238

[9] Solommer E, Soltesz U. (1971), Crack-opening-displacement measurements of a dynamically loaded crack. Eng. Frac. Mech. **(**2): 235-241.

[10] G. C. Sih, (1973), *Handbook of stress intensity factors*. Inst. Frac. Solid. Mech. Lehigh University, Bethlehem, Pa.

[11] G. P. Charepanov, E. F. Afanasov, (1970), Some dynamic problems of the theory of elasticity—A review. Int. J. Engng Sci. (12)**:** 665-690.

[12] B. R. Baker. (1962), Dynamic stresses created by moving crack. J. App. Mech. 29(3):449-458.

[13] N. I. Muskhelishvili. (1968), Singular Integral Equations. Nauka Moscow,

[14] N. I. Muskhelishvili. (1968), Some fundamental problems in the mathematical theory of elasticity. Nauka Moscow,

[15] C. Atkinson, (1965),The Propagation of A Brittle Crack in Anisotropic Material. Int. J. Engng Sci.(**3):** 77-91,

[16] Lü Nian-Chun, Cheng Jin, Cheng Yun-Hong. (2005),.Models of fracture dynamics of bridging fiber pull-out of composite materials. Mech. Res. Commun. 32 (1): 1-14

[17] Cheng Jin. (1985), Problems on elastodynamics of some orthotropic

anisotropic bodies. *J. Harbin. Inst. Tech.* Eng. Mech, Supplement: 8-21,(in Chinese)

[18] R.F.Hoskins, (1979), Generalized Functions, Ellis Horwood,

[19] F. D. Gahov. (1963),Boundary-Value Problems. Fitzmatigiz, Moscow,

[20] Wang Xie-shan. (1993), *Singular functions and their applications in mechanics*. Beijing: Scientific Press, 3-45 (In Chinese)

[21] G. C. Sih, (1977),Mechanics of Fracture 4. Elastodynamics Crack Problems, Noordhoff, Leyden. 213-247

[22] R.P .Kanwal, D.L.Sharma, (1976), Singularity methods for elastostatics, J. Elasticity, 6 (4): 405-418.

[23] Editorial group of mathematics handbook. (2002), *Mathematics handbook*. Beijing: Advanced Education Press, 244-300. (in Chinese).

[24] Teaching office of mathematics of Tongji University. (1994), *Advanced mathematics* (Vol.1). Beijing: Advanced Education Press,. 167-172. (in Chinese)

[25] Y. Huang, W Wang, C Liu etc. (1999), Analysis of intersonic crack growth in unidirectional rein-forced materials. J. Mech. Phy. Solids.(47):1893-1916.

[26] K C Wu, (2000), Dynamic crack growth in anisotropic material. Int. J. Frac.,(106):1-12

[27] G. C. Sih, (1991), *Mechanics of Fracture Initiation and Propagation, Kluwer* Academic Publisher, Boston

MULTI-SCALE HIERARCHICAL APPROACH FOR MECHANICAL ANALYSIS OF POLYMERIC MATERIALS

Ricardo Simões
IPC - Institute for Polymers and Composites
University of Minho, Campus de Azurem, 4800-058 Guimarães, Portugal; rsimoes@dep.uminho.pt ; *and*
School of Technology, Polytechnic Institute of Cávado and Ave (IPCA), 4750-117 Barcelos, Portugal; rsimoes@ipca.pt

Gustavo R. Dias
IPC - Institute for Polymers and Composites
University of Minho, Campus de Azurem, 4800-058 Guimarães, Portugal; grdias@dep.uminho.pt

Júlio C. Viana
IPC - Institute for Polymers and Composites
University of Minho, Campus de Azurem, 4800-058 Guimarães, Portugal; jcv@dep.uminho.pt

António M. Cunha
IPC - Institute for Polymers and Composites
University of Minho, Campus de Azurem, 4800-058 Guimarães, Portugal; amcunha@dep.uminho.pt

Abstract

In the past decade there has been an increasing interest in multi-scale approaches for predicting the macroscopic constitutive response on the basis of the underlying microstructure. The overall physical behavior of micro-heterogeneous materials depends strongly on the size, shape, properties and spatial distribution of the microstructural constituents.

In polymeric materials, the microstructure is influenced by processing and material type (e.g. amorphous or semi-crystalline). There is also a structural hierarchy in the mechanical behavior: the macro-scale response is related to the local microstructure, which in turn depends on the structure at the nano-scale. In this work, a three level multi-scale approach has been employed to investigate the mechanical properties of polymeric materials. The approach couples finite-element modeling (continuous milieu) and molecular dynamics (discrete milieu) in an iterative procedure.

This approach does not lead to closed-form overall constitutive equations, but it computes the stress-strain relationship at every analysis point of the macro component by detailed modeling of the underlying micro- and meso-scale deformation phenomena.

Keywords: multiscale modelling, polymer mechanics, molecular dynamics, FEM, computer simulations, structure-properties relationships, nanocomposites.

1. Introduction

Being able to understand the deformation mechanisms and behavior of a polymer under an external load is not only of interest from the academic point of view but also from the industrial standpoint. Much of the process optimization, for example in injection molding, is still being achieved based on empirical data. These methods create problems when something as simple as a change of material batch occurs. Moreover, understanding the behavior of polymers is of interest to the society in general, since ultimately we all depend on the reliability and performance of plastic parts.

This paper follows previous simulation work at the meso-scale to study the crack formation and propagation phenomena [1], deformation mechanisms at the nano-scale [2], true stress development [3], and the influence of the loading conditions on the material behavior [4].

One of the main issues with polymers is their complex structure at multiple length-scales. For example, semi-crystalline polymers form molecular arrangements (crystalline lamellas), which combine to give rise to supralamellar structures, such as spherulites and shish-kebab arrangements, which in turn constitute the morphology at the microscopic level. The size, shape, and other features of these microscopic structures determine the behavior at the macro-scale.

There are several advantages to a Computational Materials Science and Engineering approach: (1) minimizing the cost of trial-and-error experiments, occasionally termed the "Edisonian" approach; (2) increased confidence on the materials' properties, which also means easier scale-up from the laboratory scale; (3) new knowledge-based structures can be devised and tested in comparatively shorter times; (4) ability to study phenomena which are inaccessible experimentally due to current technology limitations.

While there are emerging experimental techniques that allow the manipulation of structures at the micro- and nano-scale, allowing for example the measurement of electrical current through a single nano-tube, there are still many unknowns and uncertainties regarding the response of materials at those levels. Conversely, computer simulations require input data which is typically obtained experimentally (although theoretically on occasion). Furthermore, simulation results must be validated through experimental testing. Even if the micro- and nano-scale models cannot be validated individually, the macro-scale results must be representative of the real material behavior.

The goal of this work is thus to concomitantly employ simulation and experiments to increase our knowledge about the polymeric material properties and the key phenomena responsible for their behavior.

2. Multiscale approach

The developed multiscale approach is based on three hierarchical levels. These levels span from the mesoscale (polymer macromolecular chains) to the macro-scale (test specimen or part). The methodology employed in this work is described next.

Conceptual methodology.
A schematic representation of the methodology is shown in Figure 1. The lowest scale level (hierarchical level 3) corresponds to the mesoscale, where amorphous or semi-crystalline regions can be studied. Each region is comprised of individual polymeric chains, with each chain consisting of a set of statistical segments. This scale level is simulated using the molecular dynamics method. In molecular dynamics, a statistical segment represents a series of repeating units of a real polymer chain.

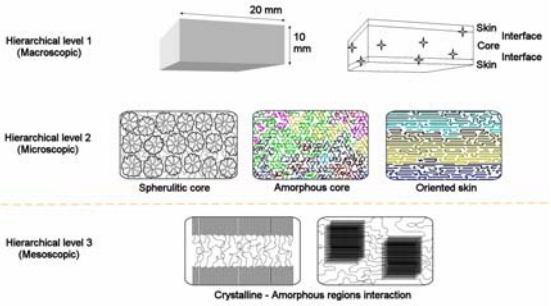

Figure 1 – Schematic representation of the conceptual methodology used in this work.

Hierarchical level 2 corresponds to the micro-scale, where it is possible to find specific microstructural features such as spherulites in semi-crystalline polymers, or highly oriented and coiled chain arrangements in amorphous polymers.

The highest length scale (hierarchical level 1) corresponds to the macroscopic molded test specimen or part. For a molded component it is possible at this scale to distinguish between regions of high molecular orientation (skin) and lower orientation (core) in the specimen (skin-core microstructure). However, typical simulations performed at this level are unable to discern and take into account the effect of the local microstructure. Although macroscopic FEM model can model the mechanical response of laminated structures (such as the skin-core microstructure), it is further necessary to study the local response at a lower length scale (hierarchical level 2). For that, it is necessary to know the local morphology of each element in the model.

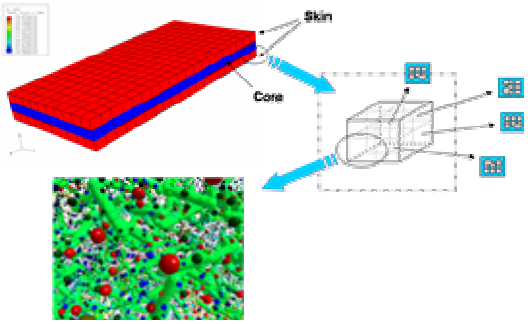

Figure 2 – Schematic representation of the practical implementation of the employed methodology.

Implementation.
The macro-scale and micro-scale simulations are performed using the Finite Element Method (FEM). The coupling algorithm was implemented on a commercially available software package (Abaqus), using the open subroutines available for material definition. The molecular dynamics code was developed by the authors, as was the meso-scale visualization software. A schematic representation of the implemented methodology is shown in Figure 2.

As previously mentioned, while the lowest scale level (HL3) is simulated using a discrete approach, the two highest scale levels are simulated using a continuum approach. It is therefore necessary to bridge between hierarchical levels 2 and 3. This is done by creating a record of the mechanical behavior of a variety of structures at the mesoscale level (HL3), through simulation of each of those structures under different loading modes (tension, compression, shear). Each of these structures represents a specific constituent at the microscopic level (HL2).

The HL3 simulations can be performed *a priori*, and the results stored for later retrieval (offline approach). Thus, the simulation at the HL2 level can obtain information from that record regarding the specific response associated with each microstructural arrangement. The response under complex loading modes, which will be the typical case, can be inferred from combining simple loading modes.

Analogously, gathering mechanical information from HL2 performs the simulations at the HL1 level. However, the HL1-HL2 coupling strategy is executed recursively during the simulation, with the mechanical problem being solved locally at a smaller length scale for each time (or deformation) increment. This incorporates the microstructural diversity into the model. The coupling is implemented in the user material subroutine UMAT, starting from a HL1 perturbed elastic solution. The kinematical variables (displacement field gradient) are passed to HL2 in each material evaluation point of HL1 (Gauss Points) and are an input for the microstructural (HL2) model assigned to a particular element of HL1. The response from HL2 is the complete Cauchy stress tensor response in the material point. This approach enables an implicit form for the stress response.

3. Molecular dynamics simulations

The molecular dynamics (MD) method has been employed to simulate the response of the polymeric materials at the mesoscale. At this level, three main types of structures are considered: (a) coiled chains in amorphous polymers; (b) interlamellar regions in semi-crystalline

polymers; and (c) nano-filled polymers. Further details and some results at this length scale are presented in the next sections.

Model details.

The MD method was developed by Alder and Wainwright at the Lawrence Livermore Laboratory, initially with the purpose of studying systems of hard spheres. Other commonly used simulation methods for polymeric materials include the Monte Carlo method, the Brownian dynamics (BD) and the kinetic model of fracture. A detailed description of all these methods, along with comparative analysis in terms of applications and limitations, has been provided by Fossey [5].

In the MD method, the system is comprised of a set of statistical segments in three-dimensional space. These segments can be individual or linked as part of a macromolecular chain. Each segment is characterized at any instant by its three Cartesian coordinates and three momentum components along the main axes. These six variables are calculated at every time step of the simulation, using a leap-frog algorithm, effectively describing the time-dependent response of the system.

As time is an explicit variable in MD simulations, all particles are moved simultaneously at each time step. Thus, the method can be employed to simulate not only equilibrium properties but also time dependent ones. This is a particularly important feature when dealing with viscoelastic materials.

Segments interact according to a set of interaction potentials, which are function of the inter-segmental distance. Different potentials are defined for the different types of interactions present in the material. In single-phase polymeric systems there are two types of interactions: intra-chain bonds (primary chemical bonds in the polymeric chain), and inter-chain bonds (secondary bonds between chains), the later also termed non-bonded interactions. In the case of nano-filled polymers, there are additional interactions: between the fillers and the polymeric chains, and between fillers.

Before performing a simulation, a model representative of the polymeric system under study must be created. The procedure used to create the computer generated material (CGM) is described in the next section. In the case of on-lattice creation, and before performing the simulation, all segments are perturbed from their original ideal lattice positions by a small displacement (on the order of one-hundredth of the equilibrium inter-segmental distance). After this stage, the simulation begins with an equilibration step with no external force applied.

As in previous work, a coherent dimensionless system of units was employed. The length of a non-strained bond corresponds to a unit of length, the mass of a single statistical segment corresponds to a unit of mass, and the energy needed to dissociate a bond corresponds to a unit of energy. All other quantities can be derived from these; e.g. a unit of force is given by the ratio of one unit of energy to one unit of length.

A detailed description of the MD model, including the main simulation parameters, has been provided elsewhere [2].

Material generation.

The creation of amorphous and semi-crystalline regions follows a lattice-based approach, whereas nano-filled regions are created off-lattice. Notice however, that even when the creation of the CGM is done on-lattice, the simulation itself is always performed off-lattice.

In the case of on-lattice generation, all segments are initially positioned at the equidistant lattice positions, each segment representing a polymeric chain of length 1. These chains then grow similarly to the step-wise polymerization process. The system is searched for neighboring end-of-chain segments that can be bonded, resulting in larger chains. This procedure is repeated until no more such segments exist.

At the earlier generation stages, there are many available neighboring end-of-chain segments that can be bonded. When that happens, one such pair is randomly selected for bonding, giving rise to systems of coiled chains that exhibit no preferential orientation. Alternatively,

systems can be created with a specified preferential orientation with a certain chain growth direction.
While this is a relatively simple procedure, it results in systems with several realistic features, such as molecular weight distribution and the presence of chain entanglements.

In the case of the off-lattice generation, used for nano-filled systems, the first stage is to create the nano-fillers (either nano-particles or nano-fibers) inside the CGM bounding box. For the nano-fibers, a random position is first selected for one end of the fiber. Then, a random direction is assigned, which defines the position of other end of the fiber. It is also possible to predefine a preferential direction for the fiber vector, which allows the creation of systems with different degrees of nano-fiber orientation along a particular axis. The length of the fibers can be set as a fixed value or a random value within a certain range.

After the nano-fillers have been placed in the bounding box up to a specified concentration, the box is filled with individual statistical segments, by random sequential addition. Each of these segments represents a polymeric chain of length 1. The procedure then employed for chain growth is equivalent to that previously described for on-lattice generation.

Naturally, the off-lattice procedure results in a lower degree of packing of the bounding box, with many bonds extended beyond their equilibrium configuration. Therefore, during the first stage of the simulation procedure it will be necessary to equilibrate the system for a substantially longer time than in the case of on-lattice generation.

A detailed description of some of the procedures used for creating the CGMs and a detailed analysis of the resulting systems has been provided before [6].

Simulation of amorphous polymeric systems.
Amorphous polymeric systems comprised of coiled chains are one of the main types of structures relevant to the present work. In these systems it is possible to study the influence of chain orientation, loading conditions, and loading mode.

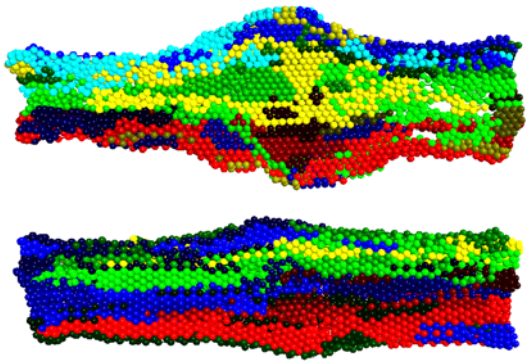

Figure 3 – Deformation of materials with different initial preferential orientation of the chains with the external load direction.

The degree of preferential orientation of the chains with a specific axis can be controlled during the material generation process, and the evolution of the orientation along time can be established [7]. It is also possible to study the influence of the loading conditions for a fixed material structure [4], including the deformation (or force increase) rate, the magnitude of creep force (deformation under constant load), and the time during which the external load is maintained. An example of the deformation of two materials with different preferential chain orientations is shown in Figure 3.

Simulation of semi-crystalline polymeric systems.
In the case of semi-crystalline polymers, the model attempts to represent the phenomena taking place at the lamellar level, specifically the interface between the crystalline lamella and the amorphous region. The lamellae are comparatively rigid with respect to the flexible amorphous chains.

Aside from the variables that were already mentioned for the amorphous regions, it is also possible in these materials to study the influence of the lamella thickness, amorphous region thickness, and the degree of packing (free volume) of the amorphous region [8].

The material can also be deformed under a variety of loading modes, including uniaxial tensile load or simple shear; see Figure 4).

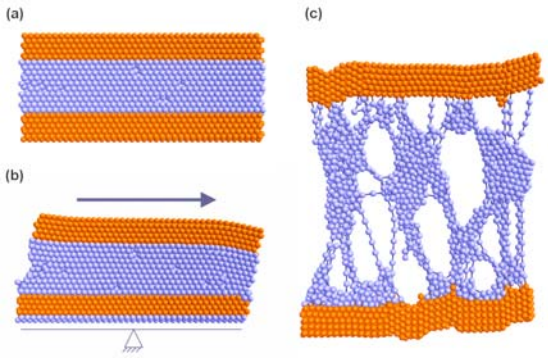

Figure 4 – Deformation of a sample material under different loading modes: (a) initial geometry; (b) deformation under shear; (c) deformation under tensile load.

Simulation of nano-filled polymers.
When considering two-phase systems, such as nano-filled polymeric materials, the number of variables that can be studied increases considerably. This is obviously related to the fact that the fillers are dispersed in an amorphous matrix, which in itself can have several parameters. In nano-filled systems, additional material parameters include the filler concentration, filler orientation, type of filler, filler size (fiber length and width, and particle diameter), and filler spatial dispersion.

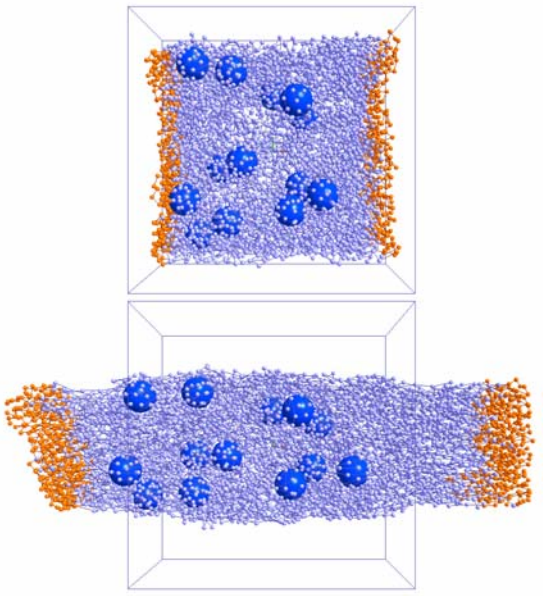

Figure 5 – Deformation of a sample material containing approximately 2 vol-% of randomly distributed nano-particles (each with a diameter three times that of the statistical segments).

There are also model parameters that can be studied, such as the extent of interaction between the fillers and the polymeric chains, which is related to the type of bonds (chemical or physical) that form in the material.

An example of the deformation of a sample material reinforced with nano-particles is shown in Figure 5.

4. Macro-micro coupling

The macro-micro coupling is performed assigning at each particular zone of the macro model HL1 the corresponding microstructural architecture. This implies that finite elements that are on each assigned zone have a FEM HL2 model of the underlying microstructure, and the stress response will be obtained from the solution of the corresponding HL2 model. The response is obtained starting from an elastic perturbed solution of the HL1 model, enabling the calculation of the kinematic field variables that will be passed for the solution of HL2 models.

The perturbed solution is only a starting method for the coupled problem. The core methodology is coded using the available subroutine for generic material behavior in Abaqus. The process works as follows: in each material point of each element of the HL1 mesh the subroutine UMAT is called and the kinematical variables are transformed in boundary conditions for the microstructural model HL2 assigned to the material point. The corresponding model is then launched and the stress response is obtained.

In UMAT, the material Jacobian matrix for this material implicit response is also calculated, enabling the correct integration in the non-linear solution algorithm for higher-scale model.

An example of a deformed microstructural model is presented in Figure 6. The framework for this approach to macro-micro coupling can be found in [9] and [10].

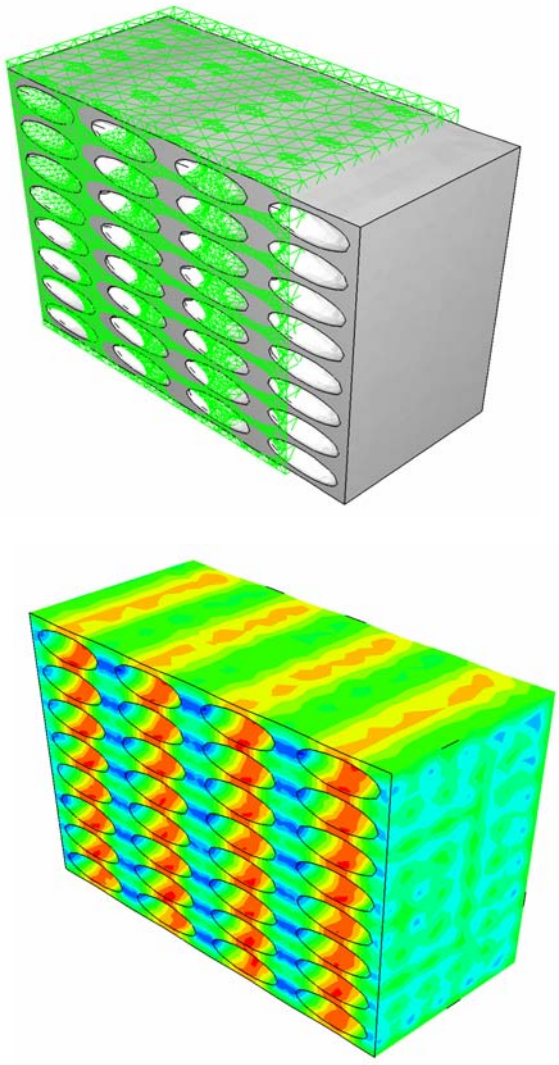

Figure 6 – Deformation profile (top) and strain mapping (bottom) of a HL2 microstructural model.

5. Preliminary results

Validating the developed methodology is a three-stage process. First, it is necessary to create the models at each length scale. Then the models must be simulated individually to verify their adequacy to the envisioned analyses. This is particularly critical for the molecular dynamics models since they will determine the response of the material at the lowest length scale. Finally, the macroscopic-microscopic iterative routine must be tested for simple geometries.

The molecular dynamics simulations have shown that the material behavior is particularly affected by some structural aspects, while other parameters have small or negligible influence.

As an example, the concentration of a rigid second-phase dispersed on the flexible matrix was found to affect considerably the stiffness of the material [1]. However, the distribution of that second-phase only affects the material response at large deformations, namely the crack initiation and propagation phenomena.

In semi-crystalline polymers, the thickness of the lamellas appears to be the most significant factor determining the mechanical response [8], while the thickness of the amorphous phase as well as its degree of orientation have smaller impact on the material response.

The degree of preferential orientation of the macromolecular chains with respect to the axis of external loading was also shown [7] to greatly influence both the stiffness and the deformation at break of the simulated systems.

Also, the rate at which an amorphous material is forced to deform was found [4] to be a critical factor in both the nature of the mechanical response (localized deformation) and the mechanical properties (stiffness and deformation at break).

6. Concluding remarks

The predictive capability of the simulation of polymers at the macro-scale is limited by their complex structure at different length scales. Furthermore, commercial software has not been developed specifically for the study of these materials, ignoring for example the morphology developed at a local level.

A hierarchical approach to the multiscale simulation of polymeric materials has been developed coupling FEM (continuous milieu) and MD methods (discrete milieu). The macroscopic part can be divided into regions with a characteristic local microstructure (which can be predicted from mold-filling simulations), and each of those regions can be simulated in more detail at the micro-scale. The properties and behavior

of each morphological feature at the micro-scale are obtained from molecular dynamics simulations at the mesoscale.

Although this methodology still needs to be validated, it has a strong potential to solve one of the critical issues in multiscale simulations – the seamless bridging between length scales.

Results of the developed methodology (with the three coupled hierarchical levels) will be presented at the conference.

7. Acknowledgements

Financial support for this research has been provided by the Fundação para a Ciência e a Tecnologia, Lisbon, through the 3° Quadro Comunitário de Apoio and through the POCTI and FEDER programmes.

8. References

[1] Brostow, W., Cunha, A.M., Quintanilla, J., Simoes, R., (2002), *Macromol. Theory & Simul.*, **11**, pp. 308.

[2] Simoes, R., Cunha, A. M., Brostow, W., (2004), *e-Polymers*, no.**067**.

[3] Simoes, R., Cunha, A. M., Brostow, W., (2005), *Computat. Mater. Sci.*, **35**, in press (available online 18 July 2005).

[4] Simoes, R., Cunha, A. M., Brostow, W., (2006) *Modelling Simul. Mater. Sci. Eng.*, **14**, pp. 157.

[5] Fossey, S. (2000) In: Performance of Plastics, pp. 63, Brostow, W. (Ed.). Hanser, Munich.

[6] Brostow, W., Cunha, A. M., Simoes, R., (2003), *Mater. Res. Innov.*, **7**, pp. 19.

[7] Simões, R., Viana, J. C., Dias, G. R., Cunha, A. M., (2004), *Proc. Internat. Conf. On Comput. & Exper. Eng. & Sci.* (ICCES), ISBN 0-9657001-6-X, pp. 1663.

[8] Simoes, R., Brostow, W., Dias, G. R., Viana, J. C., Cunha, A. M., (2005), *Proc. Ann. Tech. Conf. Soc. Plastics. Engrs.*, **63**, pp. 3507.

[9] Kouznetsova, V., Geers, M., Brekelmans, (2002), *Int J. Numer. Meth. Engng.*, **54**, pp. 1235.

[10] Terada, K., Kikuchi, N., (2001), *Comp. Meth. Appl. Engng.*, **190**, pp. 5427.

DAMAGE ANALYSIS OF A CRACKED NANOBEAM AS PREDICTED BY SCALE INVARIANT CRITERION

Lucio Nobile
Department DISTART, University of Bologna, Viale Risorgimento 2, 40136 Bologna-Italy

Christian Carloni
Department DISTART, University of Bologna, Viale Risorgimento 2, 40136 Bologna-Italy

Abstract

Nanobeams are used in several engineering applications either as components of nanoelectromechanical systems or to strengthen composite materials. The mechanical properties of such small structures determine their utility and are therefore of considerable interest.
Based on nanometer scale tests, a theoretical model to predict the bending strength of a nanobeam is proposed.
A fracture approach which takes into account imperfections on the beam surface and crack growth is employed.

Keywords: Nanobeam, atomic force microscope, fracture mechanics, strain energy density function, failure.

1. Introduction

The rapid advances in nanotechnology, nanomaterials and nanomechanics will make manufacturing technologies and infrastructure more sustainable in terms of reduced energy usage and environmental pollution. Recent advances in the research community on this topic have stimulated research activities in science and engineering devoted to their development and their applications.
A macroscopic and microscopic material damage description ahead of a crack in a single formulation that satisfies the continuum mechanics axioms with consistency has been made by Sih & Tang [1,2,3]. Different order and strength of singularity are uniquely associated with the boundary conditions, loadings and geometries of the defects under consideration. The character of the volume energy density function was found to be fundamental in scale shifting. To this end, the energy density function for the dual scale model has been determined and discussed in connection with what was emphasized.
The salient features of the model can be summarized as follows:
• Singularity representation is applied to simulate the effects of loading, boundary constraint and geometry at each scale level.
• Equilibrium mechanics is used in each segment of scaling such that the error of approximating non-equilibrium can be controlled.
• Connection can be made from segment to segment by a scale invariant criterion that corresponds to the quantity of "force".
• The one-dimensional line crack model can be extended to two-dimensions by application of the volume energy density function in conjunction with the introduction of a length or area parameter.
Recently, the analysis of validity of the continuum beam models for the constitutive behaviour of carbon nanotubes and nanorods, and other nano-beams of non-carbon materials has been

presented by Wong et al.[4] and Harik [5], among others. It is a common notion that small whiskers have strengths considerably greater than those observed in macroscopic crystals. The increase in strength is normally attributed to a reduction in the number of defects that lead to mechanical failure. The crystal may indeed contain more defects but if they are distributed uniformly the strength can be high. The strength depends upon the degree of system homogeneity that can be represented by a characteristic length parameter [3].

In this paper, the scale invariant criterion is applied to cracked nanobeams to describe material damage. It makes use of the strain energy density factor, *S*, which is a function of the stress intensity factors [10]. As stated above, the strain energy density theory provides a more general treatment of fracture mechanics problems by virtue of its ability in describing the multiscale feature of material damage and in dealing with mixed mode crack propagation problem. A simple method for obtaining approximate stress intensity factors is also applied [7]. It takes into account the elastic crack tip stress singularity while using the elementary beam theory. Some basic loading conditions can be studied.

2. Nanometer-scale testing

A method for the direct determination of the bending force in small SiC whiskers as a function of displacement has been proposed by Wong at al. [4]. Atomic force microscope (AFM) was used on carbide (SiC) nanorods pinned at one end to molybdenum disulfide surfaces. The determination of the Young's modulus has been performed in the framework of beam theory. A cantilever beam model was adopted for nanorod subjected to a point load and a distributed friction force. Besides, the force-displacement plots allowed the determination of the strength and toughness. Different failure mechanisms were observed. In the determinations of the strengths, it was observed that the nanorods fractured either at the pinning site or at some distance from the pinning site. It was argued that defects can limit the strengths of such nanorods. In a recent paper, Sundararajan et al.[9] described nanometer-scale quasi-static bending tests performed on fixed single-crystal silicon (Si) and silicon dioxide (SiO_2) nanobeams with widths ranging from 200 to 800 nm using atomic force microscope (AFM). Typical load-displacement plots were derived. All the beams showed linear elastic behaviour until abrupt failure. In reference to a fixed elastic beam loaded at the centre of the span, the Young modulus and the maximum tensile stress have been calculated. The values of Young modulus calculated for the Si ranged between 171 and 195 Gpa which approximate the bulk value of 169 Gpa. The values for SiO_2 ranged between 72 and 98 Gpa, which approximate the bulk value of 73 GPa. From the SEM images of the broken beams it was observed that the beams fractured near the fixed ends and values of the bending strength calculated are an order of magnitude higher than bending strengths reported for larger micrometer and millimeter scale silicon and silicon dioxide beams, confirming a size effect. Since surface roughness were observed on the beam surfaces, a comparison was made between the critical value of the edge crack length calculated by Griffith theory and the peak-to-valley distances measured by AFM. The calculated values are smaller than measured ones. However it was concluded that the surface roughness affects the value of the bending strength.

As well known, fracture mechanics is widely used to describe many aspects of crack behaviour. Knowledge of the stress intensity factors plays an important role in fracture control. In structural applications, combined standard loading conditions often involve simultaneously K_{I}, K_{II} and K_{III}. Within the framework of fracture, the well-known *strain energy density factor theory* [10] allows to predict stable and unstable crack growth in mixed mode. The strain energy density function is positive definite and the rapid decay character of energy density next to a crack can best describe the multiscale feature of material damage.

In this paper, the scale invariant criterion for describing the failure of such a beam is employed. If the total energy is used as the scale invariant, then the ratio of the volume energy densities at two different scales depend upon a parameter defining the degree of system inhomogeneity. It can be found analytically by defining the

degree of system inhomogeneity. For a homogeneous system the parameter is equal to 1 and dW/dV versus l is a perfect hyperbola.

Stress intensity factors for many configurations are available. In most cases the results were obtained by means of analytical and numerical methods. In many cases the results were obtained by finite element methods and boundary element methods. Experimental methods have been applied to simple cases in order to determine the fracture toughness K_{IC} of engineering materials. Solutions for many structural configurations are not available in the handbooks. Simple engineering methods which allow a fast but approximate determination of the stress intensity factors are highly valued to a design engineering. Remarkably simple methods for close approximation of stress intensity factors in cracked or notched beams were proposed by Gao and Herrmann [6] and by Nobile [7,8]. The former has been based on elementary beam theory estimation of strain energy release rate as the crack is widened into a fracture band, the latter has been based on elementary beam theory equilibrium condition for internal forces evaluated in the cross-section passing through the crack tip, taking in account the stress singularity at the tip of an elastic crack. The derived simple formulas for stress intensity factors are in reasonable agreement with the more accurate calculations in literature. In this paper the latter method [7] is applied to compute stress intensity factors for basic loading condition.

3. Approximate evaluation of stress intensity factors

Consider a straight beam of constant cross-section. The z-axis coincides with the geometrical axis, and the x- and y-axes coincide with the principal axes of the cross-section. The stress components due to stress resultants are well known. Suppose that the presence of an edge crack of initial length a does not alter the stress resultant on the cross-section passing through the crack tip. The singular stress distribution at the crack tip takes the form

$$\sigma_{ij}^{s} = \frac{K_i}{\sqrt{2\pi r}} \tag{1}$$

with the condition that σ_{ij}^{s} acts at a distance $r=b$ from the tip. The nominal stress is evaluated by the known stress distribution on the reduced solid cross-section passing through the crack tip (ligament). The stress distribution does not take into account the presence of the crack. Then, the equivalent condition between singular stress and nominal stress resultant at the crack tip determines K_i approximately. Note that K_i-values are better approximated for $b<a$ such that the elastic singularity governs stresses at a distance from the tip lower compared to the geometric dimension of crack length.

3.1 Pure bending

The distribution of normal stresses on the reduced cross-section passing through the crack tip is

$$\sigma_z = \frac{M_x}{I_x^*} y \tag{2}$$

where M_x is the bending moment and I_x^* is the moment of inertia for the reduced part of the cross-section. The singular stress component is related to the mode I stress intensity factor as follows:

$$\sigma_z^s = \frac{K_I}{\sqrt{2\pi r}} \tag{3}$$

The stress resultant arising at the crack tip is equal to

$$\int_0^b \frac{K_I}{\sqrt{2\pi r}} dr = \sqrt{\frac{2b}{\pi}} K_I \tag{4}$$

According to the condition that $\sigma_z=\sigma_z^s$ at $r=b$, K_I can be expressed as

$$K_I = \sqrt{2\pi b}\,\sigma_{z|y=\bar{y}-b} \tag{5}$$

The distance b can be determined from the equivalence condition for forces in the direction of the geometrical axis z:

$$\int_0^b \frac{K_I}{\sqrt{2\pi r}} dr = \int_{\bar{y}-b}^{y} \sigma_z dy \tag{6}$$

where $\bar{y}$ is the distance from the neutral axis of the reduced cross-section to the tip. Introducing b into Eq. (5), the approximate intensity factor K_I can be obtained.

Consider the case when a cracked trapezoidal beam (Fig.1) is subjected to a bending moment M_x.

The equivalent condition between singular stress and nominal stress resultant at the crack tip determines K_I approximately:

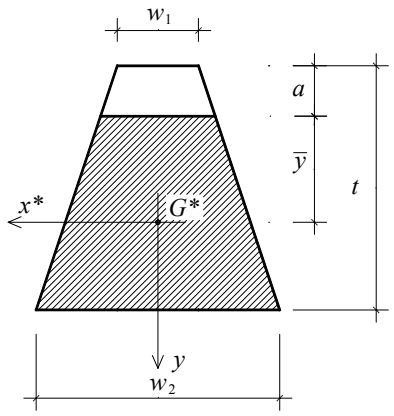

Figure 1:*Cross Section*

$$K_I = \frac{M_x}{h^{5/2}} F_I(\alpha, \omega_1, \omega_2) \tag{7}$$

where

$$F_I = \frac{8.18}{(1-\alpha)^2}\left[(\omega_1 - \alpha\omega_1 + \alpha\omega_2 + 2\omega_2)/ (\omega_1^2 + 4\omega_1\omega_2 + \omega_2^2 + \omega_1^2\alpha^2 - 2\omega_1^2\alpha + \omega_2^2\alpha^2 + 4\omega_2^2\alpha - 2\omega_1\omega_2\alpha^2 - 2\omega_1\omega_2\alpha)\right] \sqrt{\left(\frac{1-\alpha}{3}\right)\frac{\omega_1 - \alpha\omega_1 + \alpha\omega_2 + 2\omega_2}{\omega_1 - \alpha\omega_1 + \alpha\omega_2 + \omega_2}}$$

with

$$\alpha = \frac{a}{h}; \omega_1 = \frac{w_1}{h}; \omega_2 = \frac{w_2}{h}.$$

A plot of geometric function F_I as function of *a/h* is shown in Fig.2.

4. Scale invariant criterion

Based on experimental evidence, the behaviour can be assumed brittle and described in terms of coincidence of local and global failure. According to Griffith criterion the condition of incipient brittle fracture has been calculated in [9] as

$$\sigma_f = \sqrt{\frac{2E\gamma_f}{\pi a}} \tag{8}$$

where γ_f is the specific surface energy at nanometer scale and E is the Young modulus. It was observed that the values σ_f obtained are an order of magnitude higher then bending strengths reported in literature for micrometer scale.

Force and total energy are quantities that can be used to bridge the gap between different material damage models.

The description of high stress magnification at the crack tip can be conveniently characterized by the ratio of the local stress σ_l to the global stress σ_f [11]

$$\frac{\sigma_l}{\sigma_f} = \frac{\gamma_l}{\gamma_f} = \frac{\Delta L}{\Delta l} \tag{9}$$

The quantity $\Delta L/\Delta l$ represents the ratio of lengths at different scales. It is clear that the specific surface energy γ_l at the smaller scale is higher than the specific surface energy γ_f at the bigger scale This explains the measurements of a in [9] that are higher than the calculated values.

The S-theory is applied to determine crack initiation and direction for the trapezoidal fixed centrally loaded beam.

It makes use of the so called strain energy density factor S which is a function of the stress intensity factors

$$S = a_{11}K_I^2 + 2a_{12}K_I K_{II} + a_{22}K_{II}^2 + a_{33}K_{III}^2 \tag{10}$$

where

$$a_{11} = \frac{1}{16\pi\mu}\left[(3 - 4\nu - \cos\theta)(1 + \cos\theta\right],$$

$$a_{12} = \frac{1}{16\pi\mu} 2\sin\theta\left[\cos\theta - (1 - 2\nu)\right],$$

$$a_{22} = \frac{1}{16\pi\mu}[4(1-\nu)(1-\cos\theta) + (1+\cos\theta)(3\cos\theta - 1)],$$

$$a_{33} = \frac{1}{4\pi\mu}.$$

with ν being the Poisson's ratio and μ the shear modulus of elasticity.

The stress resultant at both the ends are $M_x = fl/8$ and $V_y = f/2$.

Mixed mode crack growth on the top surface at both ends can be determined according to the fundamental hypotheses

The edge crack will spread in the direction of maximum potential energy density.

The critical intensity S_{cr} of this potential field governs the onset of edge crack propagation.

Although the plane normal to the geometric axis has a surface energy higher as compared to the plane oriented at 35° from it, crack has been observed to run in

its own plane [9]. In this case, it is reasonable to consider only mode I.
Setting $K_{II}=0$ and $K_{III}=0$ and referring to Eq.(10), S becomes

$$S = a_{11}\frac{M_x^2}{h^5}F_I^2(\alpha,\omega_1,\omega_2) \qquad (11)$$

The relative minimum of S corresponds to θ =0 which implies that the edge crack runs in its own plane.
A plot of normalized strain-energy-density-factor as a function of θ for constant ν is shown in Fig.3.
Crack instability is then assumed to take place when $S_{\min}$ equals the critical value S_c that depends only on the material and is related to K_{IC} and γ_f as

$$S_c = \frac{(1+\nu)(1-2\nu)}{2\pi E}K_{IC}^2 \qquad (12)$$

$$S_c = \frac{(1-2\nu)}{\pi(1-\nu)}\gamma_f \qquad (13)$$

In particular, the relation

$$\left(\frac{dW}{dV}\right)_c = \frac{S_c}{r_c} \qquad (14)$$

allows the determination of S_c from the area under the true stress-strain curve, being r_c the critical ligament.
The critical load can be determined as

$$f_c = 16\sqrt{\frac{\pi\mu S_c}{(1-2\nu)}}\frac{h^{5/2}}{lF_I} \qquad (15)$$

Thus the critical crack length obtained using Eq.(15) can be compared to the values measured by AFM.

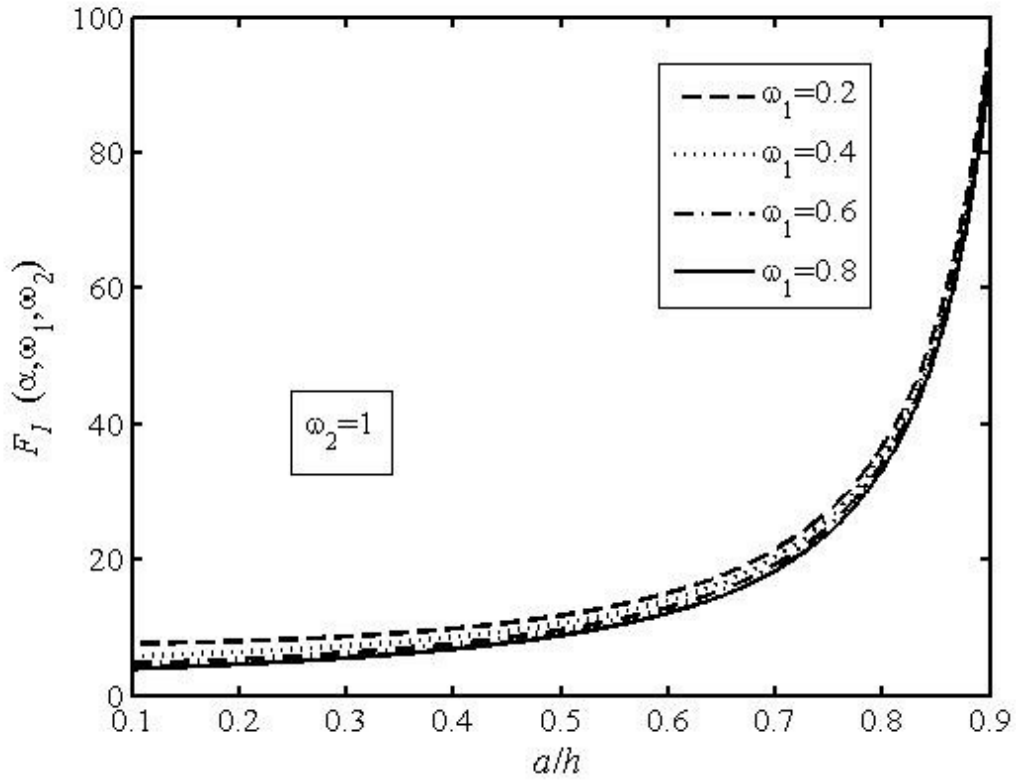

Figure 2 : *Stress intensity factors versus a/h*

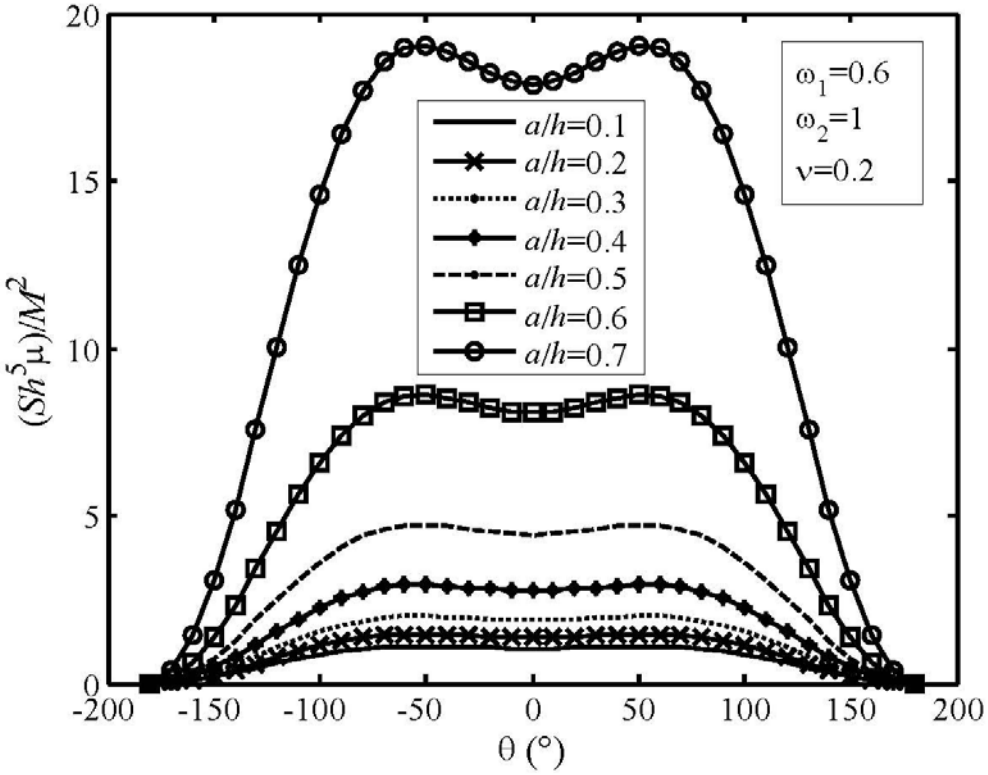

Figure 3 : *Normalized strain energy density factor versus angle θ*

Acknowledgements

The authors gratefully acknowledges the financial support rendered by Italian Ministry of Instruction, University and Research (MIUR).

References

[1] Sih, G.C. and Tang, X.S. , (2004), *Theor. Appl. Fract. Mech.* **42** (1), pp. 1–24.

[2] Tang, X.S. and Sih, G.C. ,(2004), *Theor. Appl. Fract. Mech.* **42**(3), pp. 199–225.

[3] Sih, G.C. and Tang, X.S. , (2005), *Theor. Appl. Fract. Mech.* **43**(2), pp. 211–231.

[4] Wong, E.W., Sheehan, P.E., Lieber, C.M. ,(1997), *Science* **277**, pp. 1971-1974.

[5] V.M. Harik, (2002), *Comput. Mater. Sci.* **24**, pp. 328-342.

[6] Gao, H. and Herrmann, G., (1992), *Eng. Fract. Mech.* **41**, pp. 695–706.

[7] Nobile, L., (2000), *J. Theor. Appl. Fract. Mech.* **33**, pp. 107–116.

[8] L. Nobile,L., Carloni, C., Nobile, M., (2004), *Theor. Appl. Fract. Mech.*, **41** (1-3), pp.137-145.

[9] Sundararajan, S., Brushan, B., Namazu, T., Isono, Y., (2002), *Ultra-microscopy*, **91**, pp. 111-118.

[10] Sih, G.C., (1991), Mechanics of Fracture Initiation and Propagation, Kluwer Academic Publishers, Dordrecht.

[11] Sih, G.C., (1984), In Modelling Problems in Crack Tip Mechanics, pp. 65-90, J.T. Pindera (Ed.). Martinus Nijhoff Publishers,Dordrecht.

A MULTIAXIAL DAMAGE-ENHANCED CREEP MODEL OF POLYCRYSTALLINE ICE

Dong Ho Choi, Hoon Yoo, Jay In Shin
Department of Civil Engineering, Hanyang University
17 Haengdang-dong Sungdong-gu, Seoul, 133-791, Korea

Abstract

A multiaxial constitutive damage-enhanced creep model for orthotropic polycrystalline ice is presented within the framework of the thermodynamic theory of irreversible processes. This paper formulates material anisotropy and damage anisotropy to describe the importance of the directional nature of material behavior. Many deformation mechanisms operate at the microstructural scale to induce flow and damage due to microcracking, and depend highly on loading rate, temperature and crystalline structure. Flow is attributed to the motion and production of dislocations and an interaction between the basal and non-basal systems of a constituent single crystal ice. The local internal stresses cause many stable microcracks under far field compression. Several mechanisms are involved in microcracking. These include dislocation pile-up, grain boundary sliding and elastic anisotropy; the dominant mechanism depends on loading conditions. Experimental results under various loadings show the occurrence of microcracking, which enhances the inelastic deformation of polycrystalline ice during the damage process. A multiaxial dissipation potential for the inelastic deformation is proposed for kinematic hardening, isotropic hardening and damage due to microcracks. Finally, comparison of the model with available experimental data shows good agreement and demonstrates the effectiveness of the model.

Keywords: Polycrystalline ice, Creep, Damage, Microcracking, Inelastic deformation, Kinematic hardening, Isotropic hardening

1. Introduction

In most engineering problems, polycrystalline ice exists at homologous temperatures exceeding $0.9T_M$. At these high temperatures, the creep of polycrystalline ice cannot be completely suppressed even at relatively high loading rates. Many constant stress or constant strain-rate tests and studies of deformation mechanisms have characterized polycrystalline ice behavior during the last several decades [4, 11]. Most of these studies have emphasized the stress dependence of the steady-state creep rate under constant stress following the empirical power-law creep.

Both the elastic and inelastic behavior of polycrystalline ice are of great importance in broad range of ice engineering problems. Sinha [16] has studied the transient creep of ice, since engineering applications invariably involve complex thermal and mechanical histories.

Constitutive models for polycrystalline ice based on internal state variables have been developed for monotonic constant stress. These internal state variables are used to describe phenomenologically various states of intracrystalline processes

associated with dislocation activities. Internal state variables have been used in constitutive models for metallic materials.

The present study presents a multiaxial damage-enhanced creep of polycrystalline ice. The most significant aspect of the proposed model is the formulation of kinematic equations which are firmly based on physical processes that reflect salient microstructural aspects. In this study, the primary mechanism is considered to be the motion and production of dislocations and the creep anisotropy of single crystal ice. Major features of the model include the hardening and recovery processes within evolution functions of kinematic stress and of isotropic drag stress. The damage effects due to microcracking are taken into account mainly for the enhancement od creep properties. The information obtained from experiments for the cracking activities during the deformation are used.

2. Creep model

This section describes a mathematical representation of the elastic and inelastic responses of polycrystalline ice. Following the contracted Voigt notation, vector notation is used instead of tensor notation. The total strain rate vector $\dot{\varepsilon}_{ij}$ is decomposed as follows

$$\dot{\varepsilon}_{ij} = \dot{\varepsilon}^e_{ij} + \dot{\varepsilon}^c_{ij} \tag{1}$$

where $\dot{\varepsilon}^e_{ij}$ and $\dot{\varepsilon}^c_{ij}$ are the elastic and inelastic strain rate "vectors" (in the sense of the contracted Voigt notation), respectively. The elastic strain rate vector is written as

$$\dot{\varepsilon}^e_{ij} = \mathbf{S}\dot{\sigma}_{kl} \tag{2}$$

where σ is the applied stress vector and $\mathbf{S}$ is the elastic compliance matrix of polycrystalline ice [15]. The vector form of the strain and stress components are written as $\varepsilon_{ij} = [\varepsilon_{11}\varepsilon_{22}\varepsilon_{33}\varepsilon_{23}\varepsilon_{13}\varepsilon_{112}]^T$ and $\sigma_{ij} = [\sigma_{11}\ \sigma_{22}\ \sigma_{33}\ \sigma_{23}\ \sigma_{13}\ \sigma_{12}]^T$, where superscript T denotes the transpose operation.

Flow Equation

The mechanical behavior of crystalline solids at high temperatures is controlled by activated rate processes. Thus, the inelastic behavior of polycrystalline ice is very sensitive to rate and temperature variations. Experimental observations suggest that the deformation of polycrystalline ice without microcracks is controlled by several processes, such as the motion and production of dislocations on slip planes within grains, and grain boundary sliding. The resistance to shear on the basal plane is at least 60 times less than that on the non-basal planes, such as prismatic and pyramidal planes at $-10\,^oC$. This great difference in resistance is known as creep anisotropy, which plays a major role in controlling the macroscopic behavior of polycrystalline ice.

The flow equation describes the dependence of the inelastic strain rate on applied stress, temperature, and internal stresses. In particular the macroscopic inelastic strain rate in the incremental form is a function of applied stress, isotropic drag stress is related to isotropic hardening, and kinematic back stress is related to kinematic hardening. The change in microstucture is described by the evolution equations of these internal stresses.

In the rate-dependent context, there is no yield/failure fuction and an inelastic dissipation function serves in deriving constitutive relations. If inelastic flow in polycrystalline ice is taken to follow Glen's power law, a scalar-valued dissipation potential $\Phi(\sigma_{ij}, X_{ij}, B, T)$ of the Norton-Hoff type can be defined as

$$\Phi = \frac{\dot{\varepsilon}_0 B}{n+1}\left(\frac{\sigma_{d,eq}}{B}\right)^n \tag{3}$$

where n is the stress exponent, taken as 3 in the experimental literature, the internal variable B represents the isotropic drag

stress, and $\dot{\varepsilon}_0$ is a temperature-dependent reference strain rate. The effect of temperature on the reference strain rate is represented by an Arrhenius relationship:

$$\dot{\varepsilon}_0 = A_0 \exp\left(-\frac{Q}{RT}\right) \tag{4}$$

where A_0 is a temperature-independent constant, Q is the activation energy, R is the universal gas constant, and T is the absolute temperature in degrees Kelvin. The reduced equivalent stress $\sigma_{d,eq}$ may be expressed in matrix notaion as

$$\sigma_{d,eq}^2 = \frac{3}{\beta}\sigma_{d,ij}^T \mathbf{G} \sigma_{d,ij} \tag{5}$$

where $\beta = a_1 + a_2$ and the matrix $\mathbf{G}$ transforms stresses into their deviatoric components [15]. The reduced stress is defined as

$$\sigma_{d,ij} = \sigma_{ij} - X_{ij} \tag{6}$$

and the internal variable X_{ij} represents the kinematic back stress. Normality between $\dot{\varepsilon}_{ij}^c$ and $\sigma_{d,ij}$ requires

$$\dot{\varepsilon}_{ij}^c = \frac{\partial \Phi}{\partial \varepsilon_{d,ij}}. \tag{7}$$

The inelastic strain rate is determined by substituting Eq. (3) into Eq. (7):

$$\dot{\varepsilon}_{ij}^c = \dot{\varepsilon}_0 \frac{3}{\beta}\left(\frac{\sigma_{d,eq}}{B}\right)^n \frac{\mathbf{G}\sigma_{d,ij}}{\sigma_{d,eq}}. \tag{8}$$

Isotropic drag stress

Since isotropic hardening is a result of the way dislocations interact and trap each other and thus depends on the statistics of their distributions and motion, the processes contributing to isotropic hardening are dipole formation, Forest hardening, the formation of kink bands of cell boundaries, and combinations of these. The dislocation density in ice increases in transient creep during constant stress loading; thus the isotropic hardening effect of the average dislocation density describes the characteristics of the resistance to inelastic flow. The following evolution equation of isotropic drag stress B is proposed

$$\dot{B} = \frac{h_2 E}{\sigma_{d,eq}}\left(B_{sat} - B\right)\left|\dot{\varepsilon}_{eq}^c\right| \tag{9}$$

where h_2 is the isotropic hardening constant, B_{sat} is the saturated value of B, and $\dot{\varepsilon}_{eq}^c$ is the equivalent strain rate expressed in matrix form as [15]

$$\dot{\varepsilon}_{eq}^{c\,2} = \frac{2}{3}\dot{\varepsilon}_{ij}^{c\,T}\mathbf{H}\dot{\varepsilon}_{ij}^c \tag{10}$$

where the matrix $\mathbf{H}$ transforms strains into their deviatoric components.

Kinematic back stress

Kinematic hardening is attributed to the directional internal stress caused by the creep anisotropy of single crystal ice, the great difference in resistance to creep between the basal plane and non-basal planes. When ice is unloaded, this internal stress is responsible for recoverable strain. For monotonic increasing deformation, the back stress increases from zero, and saturates when the creep strain rate reaches its steady-state value. The increase of the back stress results in kinematic hardening. The following evolution equation of kinematic back stress X is proposed

$$\dot{X}_{ij} = h_1 E\left(\dot{\varepsilon}_{ij} - r_1 X_{ij}^n\right) \tag{11}$$

where E is the isotropic Young's modulus, h_1 is the kinematic hardening constant, and r_1 is the recovery constant.

2. Damage-enhanced creep model

In metals, microcracks have some influence on inelastic strain rate, but this influence is generally weaker than the influence of microcracks on the elastic properties of the material. Unlike the case of metals, however, the effect of microcracks in polycrystalline ice on inelastic creep can be too large to ignore. This influence is taken into account in the ensuing discussion of the formulation of a dissipation potential function.

In the following formulation, the kinematic and isotropic hardenings as well

as the damage due to microcracks are taken into account. In order to incorporate damage due to microcracks into inelastic flow, the following form of dissipation potential for damage-enhanced inelastic flow is considered:

$$\Phi = \Phi_0 F = \frac{\dot{e}_0 B}{n+1}\left(\frac{\sigma_{d,eq}}{B}\right)^n F(n, D, Y) \quad (12)$$

where Φ_0 is the dissipation potential for inelastic flow without microcracks, n is the stress exponent, the scalar function F is described below, D is a measure of damage, and Y is a measure of stress states.

Rodin and Parks [13] suggested a similar form of dissipation potential for inelastic flow in which hardening effects due to dislocations are ignored. The description of the material includes the construction of a scalar function $F(n, D, Y)$ of three dimensionless variables: the first variable describes the matrix response, the second is the averaged characteristic of the microstructure, and the last identifies a measure of stress state. For the dissipation potential to be convex, F must satisfy the condition

$$FF'' - \frac{n}{n+1}F'^2 > 0 \quad (13)$$

where a prime denotes partial derivative of F with respect to Y. The later symbol is defined in Eq. (14) A variety of forms for F have been proposed for isotropic porous metals experiencing void growth and for isotropic material with cavitating grain-boundary facets.

Previously published experimental results [12, 17] in ice indicate that microcracks occur mainly in the direction of the maximum principal compressive stress. Considering material damage due to a population of aligned microcracks, it can be argued that under proportional load histories the material preserve isotropy. We consider microcracks by specifying a scalar microcrack density ($D = \omega$). The damage anisotropy, however, can be implicitly taken into account by the introduction of the maximum principal stress σ_1 into the dissipation potential with the following relation:

$$Y = \frac{\sigma_1}{\sigma_{d,eq}} \quad (14)$$

For the enhancement of creep due to microcracks in polycrystalline ice, the following function F is considered, according to Rodin and Parks [13]:

$$F = \left(1 + \alpha(n, W)Y^2\right)^{(n+1)/2} \quad (15)$$

The function $\alpha(n, W)$ reflects material behavior and is independent of stresses at a point. The following forms, which satisfy convexity of the potential Eq. (12), are given as

$$\alpha(n, W) = 2\pi n^{1/2}\omega \quad (16)$$

for slit microcracks in columnar-grained S2 ice and

$$\alpha(n, W) = 8\left(\frac{n}{n+3}\right)^{1/2}\omega \quad (17)$$

for penny-shaped microcracks in equiaxed-granular ice. The theoretical basis for these forms is discussed for slit microcracks by He and Hutchinson [8], and for penny-shaped microcracks by Rodin and Parks [13].

The inelastic strain rate is obtained by

$$\dot{\varepsilon}_{ij}^c = \frac{\partial \Phi}{\partial \sigma_{d,ij}} \quad (18)$$

For the given dissipation potential in Eq. (12), the inelastic strain rate is determined as

$$\dot{\varepsilon}_{ij}^c = \dot{\varepsilon}_0\left(\frac{\sigma_{d,eq}}{B}\right)^n \left(1 + \alpha(n,\omega)Y^2\right)^{(n-1)/2} \left\{\frac{3}{\beta}\frac{\mathbf{G}\sigma_{d,ij}}{\sigma_{d,eq}} + \alpha(n,\omega)Y\frac{\partial \sigma_1}{\partial \sigma}\right\} \quad (19)$$

For the case of isotropic polycrystalline ice under uniaxial stress, Eq. (19) reduces to

$$\dot{\varepsilon}^c = \dot{\varepsilon}_0\left(\frac{\sigma - X}{B}\right)^n \left(1 + \alpha(n,\omega)\right)^{(n+1)/2} \quad (20)$$

And for the case of isotropic polycrystalline ice where there is no

damage (i.e., $F(n,\omega=0,Y)=1$), Eq. (19) reduces further to the well-known relation

$$\dot{\varepsilon}_{ij}^{c}=\dot{\varepsilon}_0\frac{3}{2}\left(\frac{\sigma_{eq}}{B}\right)^n\frac{\sigma'_{ij}}{\sigma_{eq}} \qquad (21)$$

where σ'_{ij} is the deviatoric stress. It is worth noting that a wide variety of specific microstructural damage process for different materials can be described by similar mathematical expressions of the material damage.

Microcrack Density

We characterize the microcracks only by specification of their density ω defined as [1]

$$\omega=\frac{2N}{\pi}\left\langle\frac{A^2}{P}\right\rangle \qquad (22)$$

where N is the number of microcracks per unit volume, A is the area of the microcrack, P is the perimeter, and the angle brackets denote an average. Experimental results indicate that the size of microcracks are of the order of the grain size [3]

Consider columnar-grained S2 polycrystalline ice containing a population of aligned slit cracks of width $2c$ and length l, with a constant aspect ratio $l/2c >> 1$, under compressive loading. Noting that A is $2cl$ and P is approximately $2l$, Eq. (24) results in $\omega=\frac{4}{\pi}N\langle c^2 l\rangle$. Assuming the average microcrack size, $2c$, to be equal to the length of the average grain facet and assuming the cross-sectional geometry of the grain to be hexagonal, it can be calculated by equating the area of a circle of the average grain diameter d with the area of the hexagon: $c\approx 0.275d$. The microcrack density is written as

$$\omega=\frac{N}{10.39}\langle d^2 l\rangle \qquad (23)$$

We now consider equiaxed-granular ice and a population of aligned penny-shaped cracks of diameter $2c$ under compressive loading. Noting that A is πc^2 and P is $2\pi c$, Eq. (22) results in $\omega=N\langle c^3\rangle$. Assuming the volume geometry of the grain to be dodecahedron, and assuming the average diameter of microcracks, $2c$, to be equal to the diameter of a circle inclosed by the pentagon surface of a dodecahedron, it can be shown that $c\approx 0.354d$, where d is the average grain diameter, having the same volume $(4/3)\pi(d/2)^3$ as that of the dodecahedron. The microcrack density is written as

$$\omega=\frac{N}{22.54}\langle d^3\rangle \qquad (24)$$

Microcrack Evolution

Microcrack activity in ice has been monitored both visually and acoustically. Visual examination of microcrack formation during uniaxial compression has been performed in both columnar-grained freshwater ice [12, 17] and equiaxed-granular freshwater ice [7, 10]. These experimental results show that the majority of microcracks are oriented parallel to the maximum principal loading axis [6, 17].

Gold [5] first monitored acoustic emissions for microcracking in columnar-grained freshwater ice under constant compressive stresses at -10 ^oC . Gold's results showed that the rate of microcrack formation is dependent on duration time and on the magnitude of applied stress. Later, extensive studies on acoustic emissions were conducted in both columnar-grained freshwater ice [6, 16] equiaxed-granular freshwater ice [3] under a range of temperatures, stress levels and grain sizes. These studies showed that when the applied stress is greater than the critical stress, microcracks form. Plotting the strain dependence of microcracking density shows that microcrack density increases with applied stress. According to the results of these acoustic emissions for constant strain rate loading, the rate of microcracking is highest when the stress reaches its peak, and then diminishes significantly. These results demonstrate that microcracking is highly rate-sensitive and depends strongly on grain size.

In order to describe the microcracking dependence on stress and time, the following equation for the number of microcracks is proposed as a result of a study of the literature:

$$N=\begin{cases} N_0\left[1-\exp\left(-\left\langle\frac{\sigma-\sigma_c}{\sigma_0}\right\rangle^2\left(\varepsilon^c\right)^m\right)\right] & \sigma\geq\sigma_c \\ 0 & \sigma<\sigma_c \end{cases} \quad (25)$$

where N_0 is a reference constant, σ_c is the critical stress for microcrack nucleation defined in Eq. (26) and σ_0 is the reference stress, defining the sharpness of the transition. Microcrack nucleation is a fundamental phenomenon in the failure process of polycrystalline ice, since it occurs in both the ductile and brittle domains of deformation. The experiments of Gold [5, 6], Cole [3], and Schulson [14] suggest a form for microcrack nucleation as:

$$\sigma_c=\sigma_{c1}+\sigma_{c2}\exp\left(-\frac{Q}{RT}\right)\frac{K_{IC}d^{-1/2}}{(1-\mu)} \quad (26)$$

where $\sigma_{c1},\sigma_{c2},K_{IC},\mu$ are material constants depending on the type of ice (equiaxed-granular or columnar-grained). For a range of grain sizes (d=1~8 mm) and temperatures (T=-2~-40 ^0C), the measured microcrack nucleation stress lies between 0.5 and 1.5MPa.

3. Model Parameters and Predictions

Creep Parameters

The values of material parameters n, A, Q, B_0, k_1, k_2, h_1, h_2 and r_1 for any given material may be determined from isothermal constant stress tests [2]. The model parameters c_1, c_2 and c_6 are used to represent the creep anisotropy of ice single crystals. Without loss of any generality, c_2 can be taken as 1. Thus only two parameters need to be determined from constant stress tests on single crystal ice.

Damage Parameters

The damage parameters N_0, σ_c, σ_o and m may be estimated from experimental measurements. However, due to a lack of data for ice, the parameters are determined by fitting the model response to data.

In Table 1, a summary of the damage-enhanced model parameters is given for the different ice examined by Jordaan and MeKenna [9], Mellor and Cole [11].

Parameter	Jordaan and MeKenna [9]	Mellor and Cole [11]
E(MPa)	9000	9000
n	3	3.43
Q($kJmol^{-1}$)	67	67
A($MPa^{-3}s^{-1}$)	3.57×10^{6}	2.23×10^{6}
$A_0(s^{-1})$	1	1
$B_0(MPa)$	1.73×10^{-3}	7.92×10^{-3}
k_1	0.15	0.27
k_2	3.2	1.30
h_1	1/10	1/70
h_2	1/1.5	1/10
$r_1(MPa^{-3}s^{-1})$	5.21×10^{-5}	1.73×10^{-5}
$N_0(m^{-3})$	2500	400
σ_c	0.5	0.5
σ_o	1.0	3.0
m	2.0	2.0

Table 1: Model parameters

Model Comparisons

Jordaan and McKenna [9] measured the stress strain curve of granular polycrystalline ice in compression at -10 ^oC under an applied strain rate of 10^{-4} s^{-1}. The strain softening response due to microcracks without strain hardening is observed at this high strain rate. Figure 1 compares the prediction of the model with the data of Jordaan and McKenna [9]. The model prediction is in excellent agreement with the data, when the parameters in Table 1 are used.

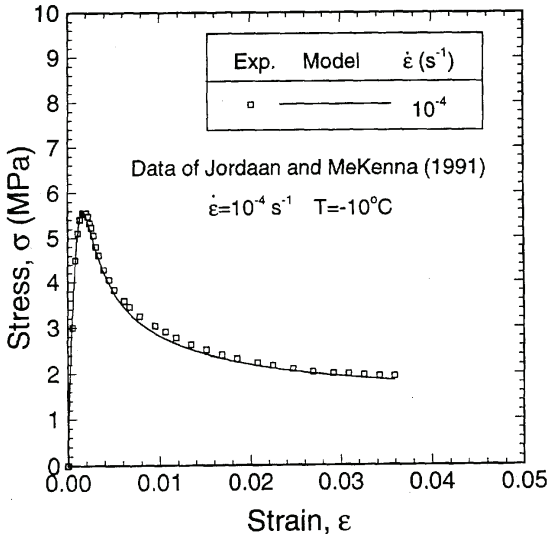

Figure 1: Stress-strain curve under constant strain-rate: the model prediction is compared with the data of Jordaan and McKenna [9]

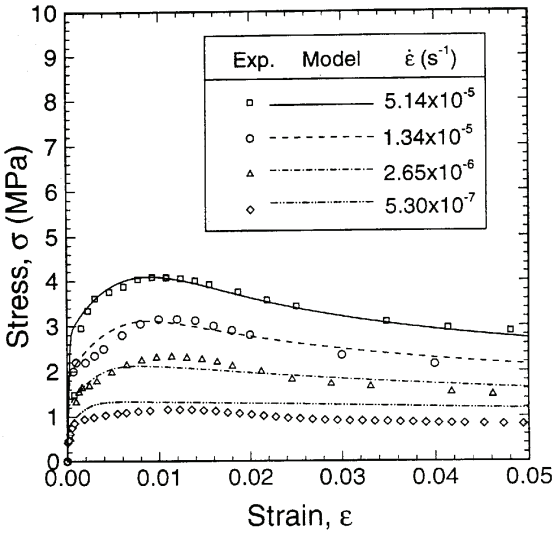

Figure 2: Stress-strain curve under constant strain-rates: the model prediction is compared with the data of Mellor and Cole [11]

Figure 2 shows the comparison of the model predictions and experimental data of Mellor and Cole [11] under applied strain rate tests. The model predictions using the parameters in Table 1 show quite good agreement with the data. The stress-strain curves exhibit strain hardening as well as strain softening behavior. It is worth noting that the model response slightly overpredicts the data at the strain rate of $5.30\times10^{-7}\ s^{-1}$. This might be due to recrystallization at very low loading rates, which is not modeled.

4. Conclusions

A comprehensive damage-enhanced creep model for orthotropic polycrystalline ice is formulated within the framework of thermodynamics theory of irreversible process. In this model, highly rate- and temperature-dependent mechanical behavior is described by the changing microstructures due to the movement and production of dislocations and microcracking. The proposed damage-enhanced model can simulate the distributed damage process due to microcracking under compressive loading.

Constitutive equations are proposed to help bridge the physical processes within the material and the macroscopic behavior observed in experiments. The evolution functions of internal stresses are formulated with hardening and recovery functions due to the production and annihilation of dislocations, respectively. The damage effects due to microcracking are taken into account mainly for the enhancement of creep properties. The information obtained from experiments for the cracking activities during the deformation are used in this damage-enhanced creep formulation. The response of the model captures the experimentally measured stress-strain and strain-time curves.

As mentioned by Duval et al. [4], a detailed analysis is necessary to determine how microcracking really affects the creep rate. Much work remains to be done to develop fully anisotropic damage evolution equation which accounts for microcrack growth, coalescence, and brittle fracture at high strain rates. The proposed orthotropic model, however, is useful for simulation of creep deflection of ice sheets under static loading and slow

fracturing processes in ice-structure indentation.

References

[1] Budiansky, B., O'Connell, R.J. (1976), *International Journal of Solids and Structures*, **12**, pp. 81-97.

[2] Choi, D.H. (1997) In: Proceedings of The Seventh International Conference on Computing in Civil and Building Engineering (ICCCBE-VII), **2**, pp. 835-840.

[3] Cole, D.M. (1986), *Effect of grain size on the internal fracturing of polycrystalline ice*, U.S. Army Corps of Eng., Cold Reg. Res. Eng. Lab., Report 86-5.

[4] Duval, P., Ashby, M.F., Anderman, I. (1983), *The Journal of Physical Chemistry*, **87**, No. 21, pp. 4066-4074.

[5] Gold, L.W. (1960), *Canadian J. Phys.,* **38**, No. 9, pp. 1137-1148.

[6] Gold, L.W. (1972), *Philosophical Magazine A*, **26**, No. 2, pp. 311-328.

[7] Hallam, S.D., Duval. P., Ashby, M.F. (1987), *Journal de Physique*, **48**, pp. C1-303- C1-311.

[8] He, M.Y., Hutchinson, J.W. (1981), *J. Appl. Mech.,* **48**, pp. 830-840.

[9] Jordaan, I.J., McKenna, R.F. (1991) In: Proc. IUTAM/IAHR Symp. on Ice-Structure Interaction, pp. 283-309, Jones, S.J., MeKenna, R.F., Tillotson, J. and Jordaan, I.J. (Ed.), Springer-Verlag.

[10] Kalifa, P., Duval, P., Richard, M. (1989) In: Proc. 8th Int. Conf. on Offshore Mechanics and Arctic Engineering, **4**, pp.13-21, The Hague, The Netherlands.

[11] Mellor M., Cole, D. (1982), *Cold Regions Science and Technology*, **5**, pp. 201-219.

[12] Nixon, W.A., Wasif, M.A. (1992) In: IAHR 92 Proceedings of the 11th International Symposium on ice, **2**, pp. 1167-1175.

[13] Rodin, G.J., Parks, D.M. (1988), *J. Mech. Phys. Solids*, **36**, pp. 237-249.

[14] Schulson, E.M. (1990), *Acta metall.,* **38**, pp. 1963-1976.

[15] Shyam Sunder, S., Wu, M.S. (1990), *Cold Reg. Sci. Tech*., **18**, 267-294.

[16] Sinha, N.K. (1984), *Journal of Materials science*, **19**, pp. 359-376.

[17] Sinha, N.K. (1988), *Journal of Materials science*, **23**, pp. 4415-4428.

V. Fatigue Behavior

FATIGUE LIFE ASSESSMENT OF 2024 ALUMINUM ALLOY SPECIMENS BY HARDNESS MEASUREMENTS AT THE MESO-SCALE

Sp.G. Pantelakis, P.V. Petroyiannis
Laboratory of Technology & Strength of Materials, Department of Mechanical Engineering and Aeronautics, University of Patras, Panepistimioupolis Rion, 26 500 Patras, Greece

K.D. Bouzakis, I. Mirisidis
Laboratory for Machine Tools & Manufacturing Engineering, Mechanical Engineering Department, Aristoteles University of Thessaloniki, Thessaloniki, Greece

Abstract

Present work aims to exploit recent advancements on methodologies for the accurate and reliable measurements of nano- and meso-hardness measurements, in order to measure the evolution of the surface hardness of 2024 aluminum alloy specimens subjected to high cycle fatigue loading with increasing number of fatigue cycles. The fatigue tests were interrupted at specified percentages of the fatigue life for each stress level. With the aid of nanoindentations, on the specimen's surface, hardness increase at the meso-scale due to fatigue has been measured at different areas of the specimens. As expected, with increasing the number of fatigue cycles the superficial hardness increases. The dependency of hardness increase on the number of fatigue cycles is not linear and seems to tend to a hardness saturation value. The entire process is accelerated at higher fatigue stress amplitudes.

Keywords: Fatigue loading, surface hardness increase, nanoindentations, fatigue damage accumulation, 2024 aluminum alloy.

1. Introduction

Failure by fatigue continues to remain the most serious concern for structural failure of aircraft components despite the exhaustive amount of past research. Fatigue life of a material can be divided into a number of subsequent fatigue damage phases, characterized by cyclic slip, crack nucleation, micro-crack growth and macro-crack growth up to the final material failure. Yet, although considerable progress has been made in understanding the mechanisms of fatigue failure, an accurate fatigue failure prediction is difficult because the different physical processes which prevail to the gradual fatigue damage accumulation during the fatigue life of a metallic component are complex and interrelated, develop with increasing number of fatigue cycles from atomic, over nano-, meso- and micro-, to macro-scale damage

mechanisms and also entail a host of material, geometric and loading parameters [1]. Their interaction cannot be easily assessed in quantitative terms. Mechanistically, the fatigue damage phases mentioned above maybe summarized to a crack initiation and a crack growth period, with the latter starting once cracks become visible. Different parameters are essential to assess crack initiation or crack growth respectively, which for the former period of relevance is the severity of stress concentration, while crack growth is dominated by the intensity of the crack-tip stress distribution. As a consequence, different fatigue prediction methods have been suggested for the two periods [e.g. 2]. Damage tolerance which is the present day design concept for modern metallic aircraft structures [2], relies on fracture mechanics, i.e. accounts for fatigue damage accumulation after the structure under consideration involves fatigue macrocracks. It is at this stage that the fatigue crack growth models in fracture mechanics become valid. Yet, growth of a fatigue macrocrack represents the last stage of the entire fatigue damage accumulation process. This stage of fatigue damage refers to a small percentage of the material's fatigue life and decreases further with decreasing fatigue stress level.

It is known that cyclic loading of metals leads to the formation of bands of concentrated slip. Cyclic slip occurs almost immediately after a cyclic stress above the fatigue limit is applied. The occurrence of surface slip markings lying along traces of the active slip planes is a general feature of cyclic plastic deformation.

Cyclic plasticity of engineering polycrystalline alloys is complex and depends on a host of parameters including type of unit cell, value of stacking fault energy, heat treatment, grain size, precipitate geometry, distribution and coherence to the matrix etc., [e.g. 3-7], thus making the prediction of the mechanisms of cyclic damage and the associated cyclic hardening or softening difficult. A vast amount of empirical information could be gathered to date on the cyclic stress-strain behaviour of a wide spectrum of engineering alloys [e.g. 3-10]. With regard to the engineering alloy under consideration and the aims of the present study the following observations are of importance:

- Experiments on FCC single crystals subjected to fully reversed fatigue loading, have shown a rapid hardening already in the initial few cycles [4].
- In [3] cyclic hardening was observed for annealed pure polycrystalline aluminum subjected to cyclic strains.
- The high value of stacking fault energy favors the activation of multiple glide systems and the formation of three-dimensional dislocation structures, which result in cyclic hardening during plastic deformation.
- Microhardness measurements by means of Vickers micro-hardness tests conducted on 2024 T42 alloy specimens fatigued at reversed bending have confirmed the increase of hardness at the microscale following fatigue loading [11]. Yet, as the changes are limited within a narrow surface material layer classical hardness measurements lack the necessary sensitivity to reliably quantify this phenomenon. Recall that, the depth of penetration for the square pyramid indenter used for the Vickers micro-hardness test is more than 0.5mm. The lack on sufficient sensitivity of the performed hardness measurements has been reflected into appreciable scatter of the experimental data presented in [11] thus making it difficult to exploit the technique for practical purposes.

The primary objective of this work was to exploit the ability of measuring material hardness changes at the nano- and meso-scale in order to develop a concept for the early detection of fatigue damage accumulation for the aircraft aluminum alloy 2024 T3. To accomplish the goal, interrupted fatigue tests followed by

nanohardness measurements were performed. The convection adopted in the present investigation for the scales is: $1\cdot10^{-4}$ to $1\cdot10^{-3}$ atomic-scale, $1\cdot10^{-3}$ to $1\cdot10^{-1}$ nano-scale, $1\cdot10^{-1}$ to 10 meso-scale, 10 to ≈ 200 micro-scale and $\rangle 200$ macroscale. The determination of the specimen hardness was carried out accurately by means of nanoindentations [12]. Up to now nanoindentation measurements were used widely for the determination of elastic and plastic properties of thin films and coatings [13,14]. The nanohardness measurement is a precise indentation method to register continuously the course of the applied force versus the occurring penetration depth.

2. Experimental Investigation

The experiments were conducted for the 2024 alloy and included fatigue tests which were interrupted at predefined number of fatigue cycles to carry out surface hardness measurements. The alloy was received in the form of 3mm thick bare sheets in T3 condition. For the experiments, fatigue specimens as shown in Fig. 1, were prepared according to the ASTM E466-96 specification. Machining of the specimens was made according to the specification ASTM E466-96. All specimens were cut in longitudinal (L) orientation relative to the rolling direction.

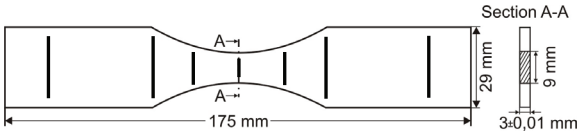

Figure 1: *Fatigue specimen geometry*.

The fatigue tests were performed according to the ASTM E466-96 specification. An overview of the performed fatigue tests is given in Table 1. The tests were performed for constant stress ratio $R = 0.1$ for three different applied fatigue stresses. The frequency used was 25Hz while all tests were conducted at constant room temperature $(25 \pm 3^0 C)$.For the mechanical testing two servohydraulic MTS machines of 100 and 250kN were used.

Maximum Applied Stress σ_{max} [MPa]	Direction/Number of tests performed
180	L3
200	L3
250	L3

Table 1: Fatigue tests performed on 2024 T3 aluminium alloy specimens.

In order to investigate the hardness increase during fatigue loading, the fatigue tests were interrupted at certain numbers of fatigue cycles which refer to different percentages of the fatigue life and surface hardness measurements were carried out at different specimen locations. Each fatigue test has been interrupted 6 times to conduct nanohardness measurements. The selected numbers of cycles for interrupting the fatigue tests are given in Table 2; they refer to different percentages of the consumed fatigue life of the specimens.

σ_{max} [MPa]	Cycles for interrupting fatigue tests [x10^3]	Expected fatigue life according to [15]
180	150, 300, 450, 700, 1050, 1250	1000000
200	60, 120, 180, 280, 420	400000
250	15, 30, 45, 70, 105, 125	100000

Table 2: Selected numbers of cycles for interrupting the fatigue tests.

The determination of the specimen hardness can be carried out accurately by means of nanoindentations [12]. The nanoindentation is a precise method of registering continuously the course of the applied force on a diamond indenter versus the occurring penetration depth. This measurement consists of two steps, the so-called loading stage and the unloading one. During the loading stage, a

load forces the diamond indenter to penetrate into the specimen. The load is gradually applied and at the same time the indentation depth is measured. When the load is fully removed, there remains, as the result of material plastic deformation, a depth h_p that is dependent on the material properties as well as on the applied load and the indenter geometry [12].

3. Results and Discussion

3.1 Results of the Fatigue Tests

The fatigue lives obtained for the performed interrupted fatigue tests are summarized in Table 3.

σ_{max} [MPa]	Experimental fatigue life - N_f [cycles]
180	5000000 (interrupted)
	1577460
	5000000 (interrupted)
200	428600
	919865
	1349290
250	208692
	184582
	182365

Table 3: Experimental fatigue lives.

The S-N curve corresponding to the data of Table 3 is displayed in Fig. 2. The fitting curve has been calculated using the Weibull equation:

$$\sigma_{max} = C_1 + \frac{C_2 - C_1}{e^{\left(\log N / C_3\right)^{C_4}}} \qquad (1)$$

where C_1, C_2, C_3, C_4 are the fatigue strength amplitude, tensile strength amplitude and regression coefficients, respectively. The derived coefficients for the fitting curve are given in Table 4.

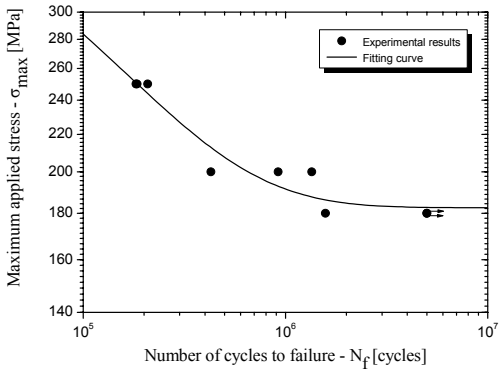

Figure 2: *S-N curve resulted from the interrupted fatigue tests*.

Fitting Coefficient	Value
C_1	182.60 MPa
C_2	425 MPa
C_3	5.09
C_4	7.29

Table 4: Derived fitting coefficients for the S-N curve.

3.2 Results of the Hardness Measurements

The specimens used were thoroughly investigated concerning initial nanohardness deviations on various areas before the fatigue loading procedure. These measurements were exploited to provide a reference for deriving hardness changes after certain numbers of applied fatigue cycles at the different fatigue loads. Nanoindentation results on the unloaded area 1 for one of the specimens used are shown in Fig. 3.

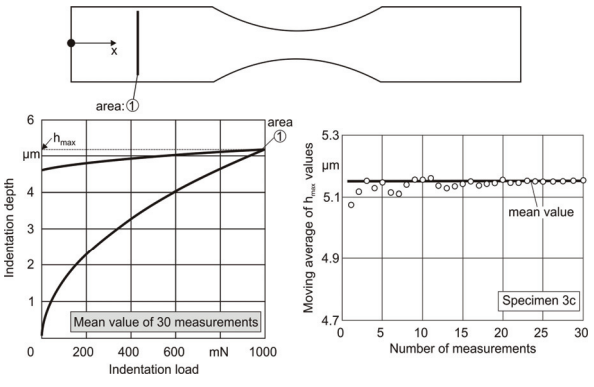

(a) (b)

Figure 3: *Nanoindentation results conducted in area 1 before specimen loading*.

Displayed in Fig. 3(a) has been the course of the applied indentation load versus the corresponding penetration depth for one measurement. h_{max} and h_p in Fig. 3(a) stand for the maximum penetration depth corresponding to the maximum applied load and h_p for the remaining penetration depth after the load is fully removed, respectively. Previous investigations [14], have shown that in order to derive the average value of the maximum penetration depth with confidence a number of approximately 15 nanoindentations in the same specimen region is sufficient. In the present study all values given for the penetration depth are average of 30 nanoindentations.

Plotted in Fig. 3(b) is the average value of the maximum penetration depth h_{max} as a function of the number of measurements involved to derive this average value. As it can be seen by a number of measurements exceeding 20 the average h_{max} value remains practically constant and equal to 5.154μm. Nanoindentation results performed in area 1, for all specimens used, show that the indentation depth fluctuation in area 1, does not exceed 60 nm. This scatter can be considered as sufficiently low.

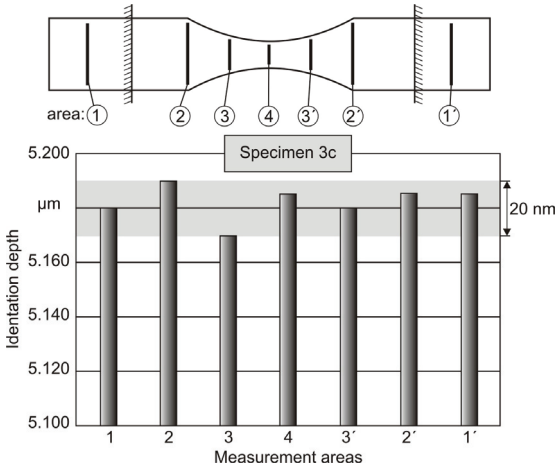

Figure 4: *Measurement areas and corresponding nanoindentation results for one specimen prior to fatigue loading*.

Fig. 4 shows nanoindentation results, obtained in various regions in the axial direction of one of the specimens, before cyclic loading. It can be observed that the indentation depth remains practically constant all over the specimen surface, within a small scatter of 20 nm, indicating a uniform superficial material structure. Nanoindentations were conducted on all specimens and the scatter of results had approximately the same value. The registered nanoindentation results over the surfaces of the unloaded specimens, are considered in the followings as reference values. The derived nanoindentation depths after certain operational cycles are compared to the corresponding reference values and the related indentation depth alterations are monitored.

The hardness change with the number of applied fatigue cycles is shown in Figs. 5-7 for the maximum applied stresses 180, 200 and 250MPa, respectively.

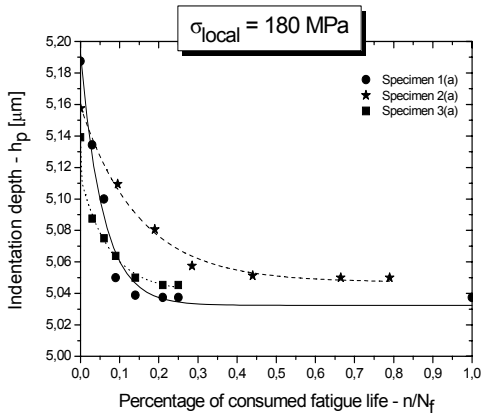

Figure 5: *Nanoindentation depth results for σ_{max}=180MPa at various percentages of the consumed fatigue life for all specimens used.*

Displayed in the figures has been the indentation depth as a function of the percentage of the consumed fatigue life. All figures involve measurements obtained for three different specimens subjected to the same fatigue conditions (Table 3). As it can be seen in the figures a clear hardness increase with increasing number of applied fatigue cycles could be monitored for all specimens investigated. At the early stages of fatigue, a rapid hardness increase is observed. With increasing number of applied fatigue

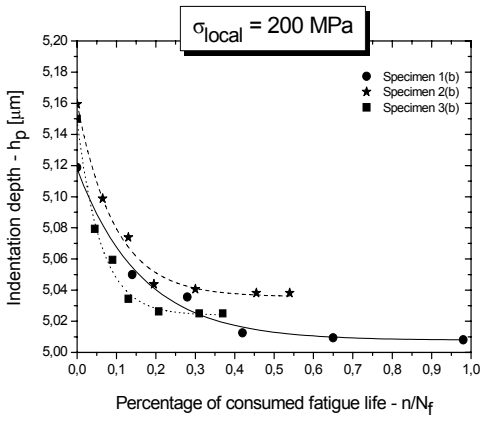

Figure 6: *Nanoindentation depth results for σ_{max}=200MPa at various percentages of the consumed fatigue life for all specimens used.*

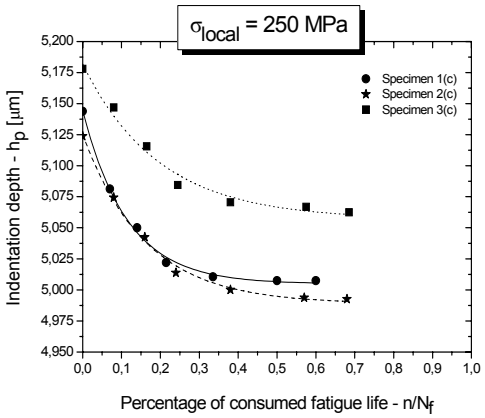

Figure 7: *Nanoindentation depth results for σ_{max}=250MPa at various percentages of the consumed fatigue life for all specimens used.*

cycles the material's hardness continues increasing yet with a decreasing rate. The indentation depth alteration with increasing percentage of consumed fatigue life for all loading cases investigated can be seen in Fig. 8. In the figure, a clear decrease of the indentation depth change, corresponding to a lower increase of hardness, can be observed with increasing number of applied fatigue cycles. By consumed percentages of fatigue life of the order of 50% the observed hardness increase becomes marginal but still occurs. The absence of Persistent Slip Bands on fatigued pure aluminum [5,7], which if present, would favour the localisation of cyclic plasticity within these bands formed by the transformation of the saturated matrix dislocation structure [9], may explain the decreasing but present hardness increase also at percentages of consumed fatigue life where mechanisms such as crack nucleation or even micro-crack growth are expected to be dominant.

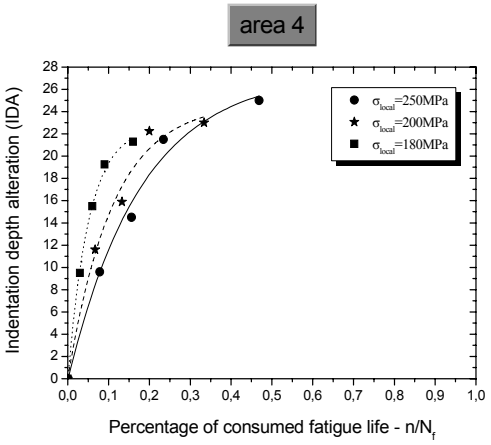

Figure 8: *Indentation depth alteration versus the percentage of consumed fatigue life.*

The comparison of the results in Figs. 5-7 makes the dependency of the observed hardness increase on the applied fatigue stress evident. As shown also in Fig. 9 a higher applied fatigue stress causes also a higher hardness increase. The penetration depth $h_{p50\%}$ values displayed in Fig. 9 refer to the maximum penetration depth value observed experimentally at a consumed fatigue life of 50% by the respective value of the maximum fatigue stress at the areas 2, 3 and 4 for all specimens investigated.

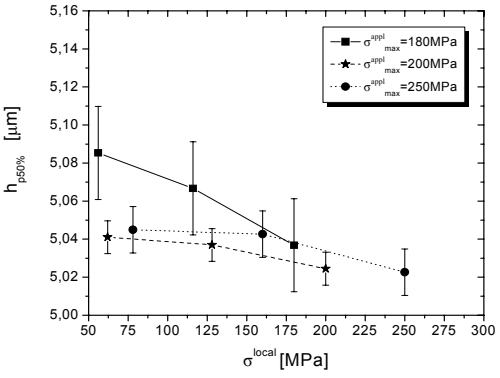

Figure 9: *Penetration depth value at 50% consumed fatigue life.*

The plotted $h_{p50\%}$ values represent average values and scatter is indicated. As expected, the hardness increase at the various locations of the specimen's surface depends on the stress applied on this location. The hardness increase along the x-direction of the specimen has a maximum at area 4, which is the area of maximum applied fatigue stress and decreases gradually to reach a minimum at area 2, which is the area of minimum applied fatigue stress. The results confirm the expectation that the degree of hardening increases with increasing applied fatigue stress. Noticeable is the observed increase in scatter with increasing maximum applied fatigue stress σ_{max} at area 4 (Fig. 9).

4. Conclusions

From the above investigation the following conclusions can be drawn:

- The surface hardness of the alloy 2024 increases when the material is subjected to fatigue loading.
- With increasing number of applied fatigue cycles, the surface hardness increases. The dependency of hardness increase on the number of applied fatigue cycles is non-linear and can be expressed by involving experimental functions. Further experimental investigation is needed to derive reliable fitting equations of the evolution of hardness increase with the number of applied fatigue cycles.
- The surface hardness increase process is accelerated at higher fatigue stress amplitudes. Further experimental investigation is needed to derive the dependency of hardness increase on the applied fatigue stress value.
- It is remarkable that the increase of hardening at two material volumes subjected to the same local applied fatigue stress for the same number of fatigue cycles but lying at different locations of two different specimens which are fatigued by different fatigue loads may deviate significantly.

References

[1] Suresh, S. (1998), *Fatigue of Materials*, 2nd. Ed. Kluwer Academic Publishers, Dordrecht, The Netherlands.

[2] Gallagher, D.A., Giessler, F.J., Berens, J.P., Engle, R.M. (1984), *Damage Tolerant Design Handbook,* Air Force Wright Aeronautical Labs, USA.

[3] Feltner, C.E., Laird, C., (1967), *Acta Metall.*, **15**, pp. 1621.

[4] Mughrabi, H., (1978), *Mater. Sci. Engng.*, **33**, pp. 207.

[5] El-Madhoum, Y., Mohamed, A., Bassim, M.N., (2003), *Mater. Sci. Engng.*, **A359**, pp. 220.

[6] Brown, L.M., (2000), *Mater. Sci. Engng.*, **A285**, pp. 35.

[7] Hopperstad, O.S., Langseth, M., Remseth, S., (1995), *Int. Jour. Plast.*, **11**, No. 6, pp. 725.

[8] Landgraf, R.W., Morrow, J., Endo, T., (1969), *Jour. Mater.*, **4**, No. 1, pp. 176.

[9] Lukas, P., Kunz, L., (2004), *Phil. Mag.*, **84**, No. 3-5, pp. 317.

[10] Feltner, C.E., Laird, C., (1967), *Acta Metall.*, **15**, pp. 1633.

[11] Kermanidis, Th.B,, Pantelakis, Sp.G., Pavlou, D.G., (1990), *Theor. Appl. Fract. Mech.*, **14**, pp. 43.

[12] Bouzakis, K.D., Michailidis, N., Hadjiyiannis, S., Skordaris, G., Erkens, G., (2002), *Zeitschrift für Metallkunde*, **93**, pp. 862.

[13] Oliver, W.C., Pharr, G.M., (1992), *Jour. Mater. Res.*, **7**, No. 6, pp.1564.

[14] Chudoba, T., Scwarzer, N., Richter, F., (2000), *Surf. Coat. Technol.*, **127**, pp. 9.

[15] ASM Handbook (1996), *Fatigue and Fracture - Volume 19*, Antonio C. Ruffin (Ed.), ASM International.

POLYCRYSTAL DEFORMATION: MODELLING AND DIFFRACTION MEASUREMENTS FOR THE DEVELOPMENT OF MICROSCOPIC ENERGY-BASED FATIGUE PREDICTION CRITERIA

Daniele Dini
Department of Engineering Science, University of Oxford, Parks Road, OX1 3PJ, Oxford, UK
Current address: Department of Mechanical Engineering, Imperial College London, Exhibition Rd, SW7 2AZ, London, UK

Gabriel M. Regino, Fionn P.E. Dunne, Alexander M. Korsunsky
Department of Engineering Science, University of Oxford, Parks Road, OX1 3PJ, Oxford, UK

Abstract

Structural materials in practice are most widely used in polycrystalline form, i.e. as an agglomerate of a large number of crystallites, or grains, each possessing its own distinct orientation and separated from its neighbours by grain boundaries. Both elastic and plastic deformation properties of these crystallites depend on their orientation, leading to complex load transfers and interaction within the solid. While classical treatments of solid deformation achieve remarkable success even ignoring these aspects, this neglect is likely to become unacceptable if the issue of crack initiation is to be addressed. The present paper discusses the application of energy-based crack initiation criteria to the prediction of crack initiation in polycrystalline solid, using a particular implementation of finite element-based modelling scheme that does not represent grain boundaries explicitly, but assigns crystal orientation at the level of integration points on a simple fixed mesh. This has implications for both elastic and plastic deformation behaviour that in the present approach are accounted for within a fully three-dimensional formulation. Modelling results are compared with neutron diffraction measurements of orientation-specific diffraction strains, obtained during *in situ* cyclic loading of a sample of a nickel-base superalloy. The advantages and limitations of the modelling approach are discussed.

Keywords: Polycrystal deformation, crystal plasticity, neutron diffraction, crack initiation, fatigue prediction criteria, microscopic dissipated strain energy.

1. Introduction

Modern engineering often applies phenomenological laws to describe the physical phenomena that govern fatigue failure of industrial components. All

classical fatigue criteria can be expressed in the form [1, 2]:

$$\Phi(\varepsilon, \varepsilon_{pl}, \sigma, ...) N_f^b = c \qquad (1)$$

where b and c are material parameters, N_f is the number of cycles to failure[1] and $\varepsilon, \varepsilon_{pl}$ and σ are strain, plastic strain and stresses respectively.

However, in these criteria, instead of being in the form of a *functional* (i.e. a function of *deformation history*, an expression depending on stresses and strains at all previous points in time), Φ becomes a *function*, i.e. an expression depending only on certain *values* of stress and strain. These values are usually taken at the extreme points in a stabilised fatigue cycle. The alternative proposed here arises from the analysis of classical criteria that reveals that they are *all* in some way related to the dissipated energy per cycle, as they combine products of strains and stresses. Therefore, following the explanations offered in [1] and the work of Skelton and co-workers (e.g. [3]), the functional form Φ may be written as:

$$\Phi(x) = \int_{cycle} \sigma(x,t) : \dot{\varepsilon}(x,t) dt \qquad (2)$$

where the stress and strain fields should be considered at the stabilized cycle and x is the field point where the elastic quantities are computed. It is proposed to regard the dissipated energy per cycle as the damage indicator. It can be interpreted as an upper bound of the energy dissipated on damage, and is proportional to the damage parameter itself, if a fixed fraction of dissipated energy actually contributes to the decrease of the material's load bearing capacity. The authors are fully aware that this represents an approximation, as yet unverified, and intend for this assumption to be confirmed or refuted through comparison with experimental observations. Within the proposed framework quantitative assessment of localised energy dissipation at the microscopic level (i.e. the scale at which cracks initiate and failure begins) plays a fundamental role in fatigue durability prediction.

In order to assess the energy dissipated at the microscopic level it is necessary to consider only a representative volume element (RVE) of material and to use polycrystal micro-mechanics to model the details of grain morphology and elastic-plastic anisotropy induced by the crystallographic orientation. In this way, the relationship between the macroscopic stress state and the stress state at the grain level can be investigated in detail. The model adopted in this work is briefly introduced here. Furthermore, the use of diffraction measurements is discussed for the validation of the proposed numerical modelling employed for the development of microscopic energy-based fatigue prediction criteria.

Finally, a preliminary investigation of the capabilities of micro-level energy-based criteria for the prediction of crack initiation within the crystal plasticity framework are also presented.

2. Modelling crystal plasticity using finite elements

The plasticity formulation implemented within the finite element (FE) framework used to reproduce the stress-strain fields induced by external loading is similar to that developed by Manonukul and Dunne [4]. The model has been extended to three-dimensional RVEs and anisotropic elasticity has been included. The choice of the finite element method to solve the considered boundary value problem also requires the design of a finite element mesh discretising the geometry of the

[1] Note that for the material considered in this work, the number of cycles to crack initiation is larger than that for propagation. Therefore the number of cycles to failure will be used instead of the number of cycles to initiation (more difficult to determine) to formulate crack initiation prediction laws.

microstructure. A straightforward and systematic way for representing the interfaces is by using Voronoï polyhedra for 2D and 3D free meshing techniques [5]. Crucially, in order to obtain an implementation that is efficient both in terms of numerical solution and input preparation, the grain structure of the RVE is prescribed by way of assigning crystal orientation at the level of integration points within a fixed regular hexahedral mesh.

The crystal orientation properties at a given integration point are inherited from the nearest 'seed' point which notionally represents the source of a growing grain during crystallisation. This is equivalent to specifying Voronoï polyhedra 'centred' at seed points. In the current implementation the polyhedra can be specified at any chosen resolution, defined by the size of the three-dimensional domain (cubic RVE). The simplest way to distribute the centres of polyhedra is to use a Poisson process. In this case, points are independently distributed, leading to uniform spatial density. The grain shape can be adjusted by varying the density of the distribution along different axes, leading to the average grain shape changing from sphere to oblate or prolate ellipsoids.

Texture is the term used to describe the statistics of grain orientation distribution function (ODF). Texture of the polycrystal is reflected in the specific orientations prescribed at 'seeds', and can be varied from random to strong by selecting appropriate generating functions.
A particular set of 'seed' point positions together with prescribed crystal orientations will be referred to as 'microstructure implementation'.

Once the microstructure implementation has been generated within the RVE, the polycrystalline volume is next discretised using a regular cubic mesh, with material properties associated with each Gauss point. The main advantage of this technique is that a flexible description of the polycrystalline structure is obtained, and automatically an arbitrary number of microstructure implementations can be readily generated. Periodic microstructure can also be generated using this technique as shown in Fig. 1(a). Furthermore, once the model has been calibrated, a number of structural realisations can be studied without further experimental input. In this way statistical analyses might be carried out within the crystal plasticity framework.

Viability of the solution for damage studies at meso/microscopic level

As a result of this approach to discretisation, grain boundaries become 'smeared out' (see Fig. 1(a)). However, this does not constitute a problem when computing average values within the grains, and may only present a limitation for the computation of the localisation of deformations at grain boundaries. This methodology is perfectly suitable for meso-scale analyses, in that the model allows computing physical quantities at the grain level. An example of distribution of accumulated plastic slip within the RVE during the stabilised cycle, also highlighting the presence and the formation of persistent slip bands is shown in Fig. 1(b).

Damage initiation in heterogeneous materials is not driven by the mean values of stress and strain in each constituent but by some maximum values reached at a specific location of the heterogeneous microstructures. The computation of explicit microstructures also provides these local data and can be coupled to damage criteria or damage evolution equations to predict initiation and propagation of damage or cracks.

However, the model needs to be calibrated at a microscopic level. X-ray or neutron diffraction can therefore be employed to

correlate the finite element results for specific grain sub-sets.

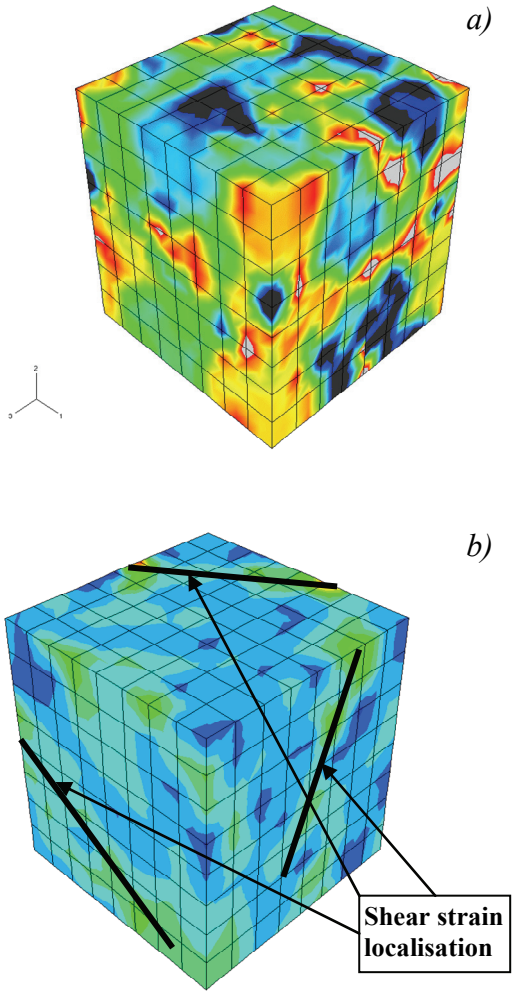

Figure 1. (a) Periodic microstructure: grain boundaries are smeared out due to the characterisation of the grain orientation at integration points; (b) Accumulated plastic slip within the RVE after 3 loading cycles.

3. Diffraction Measurements

In diffraction measurements (either X-ray [6] or neutron [7] diffraction) elastic lattice strain components in chosen directions can be determined during uniaxial *in situ* loading.

In situ measurements were made of the lattice plane response of C263 Nickel based superalloy during uniaxial tensile loading using the ENGIN-X strain measurement instrument at the ISIS spallation neutron source at Rutherford Appleton Laboratory. The instrument has two detector banks that are centred on horizontal scattering angles of ±90º. The detectors measure time-resolved spectra, each Bragg peak being produced by reflection from a different family of grains, oriented such that the *{hkl}* plane normal lies at ±45º to the incident beam (to within a few degrees). The load axis was aligned horizontally at +45º to the incident beam, allowing simultaneous measurement of lattice strains in directions both parallel and perpendicular to the applied load. Cyclic strain controlled fatigue loading was carried out using a 50kN horizontal servo-hydraulic INSTRON stress rig. A clip extensometer was used to obtain accurate record of the macroscopic total strain during loading. Conventionally measurements of diffraction strains are performed at fixed externally applied load. However, it frequently leads to relaxation effects that are particularly prominent under the conditions of plastic deformation. Therefore in the present series of experiments measurements were made during constant rate continuous straining, using count times of approximately 6 min per point.

TOF patterns contain large numbers of diffraction peaks, each representing the scattering from a group of grains sharing the orientation of a normal to a set of lattice planes. The analysis of the relative peak shift during loading with respect to the initial position provides a highly sensitive method of evaluating the mesoscale (grain sub-group average) elastic lattice strains. The diffraction spectra were analysed by single peak fits of individual *{hkl}* reflections and by Rietveld refinement of the complete spectrum, using the GSAS software package [8].

4. Model tuning and comparison with experimental results

One of the central challenges of model validation for complex constitutive laws arises from the fact that acceptable agreement with macroscopic stress-strain data can be obtained using different and distinct combinations of material parameters, such as the yield stress, hardening rate, ratio between latent and self-hardening of slip systems, etc. The motivation for the use of diffraction measurement of orientation-specific elastic strains is to utilise this mesoscopic scale information to determine optimal values of system parameters [9]. If it is discovered that not only the macroscopic strains and stresses, but also the elastic lattice strains for several Miller indices are adequately predicted by the model, then it may be reasonably assumed that the plastic strains associated with energy dissipation are also captured accurately, and confident prediction of fatigue durability can be attempted.

Figure 2 shows a comparison between the experimental data (markers) for the first fatigue cycle with the model prediction (continuous curve). It is interesting to note that the hardening slope of the real material's stress-strain curve is overestimated by the model. We believe this effect to be associated with the fundamental nature of the finite element solution that is equivalent to Rayleigh-Ritz potential energy minimisation across the family of piecewise continuously differentiable statically admissible displacement fields. Excessive 'stiffening' observed in the simulation is the consequence of displacement shape functions being forced to maintain continuous differentiability between neighbouring dissimilar grains. Note that the hardening law used at the level of individual slip system was elastic-ideally plastic.

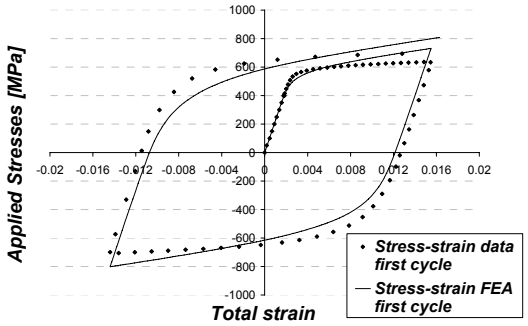

Figure 2. Comparison between experimentally measured points on the stress-strain curve during the first fatigue cycle (markers) with the prediction of the 3D anisotropic polycrystal plasticity-based finite element model (continuous curve).

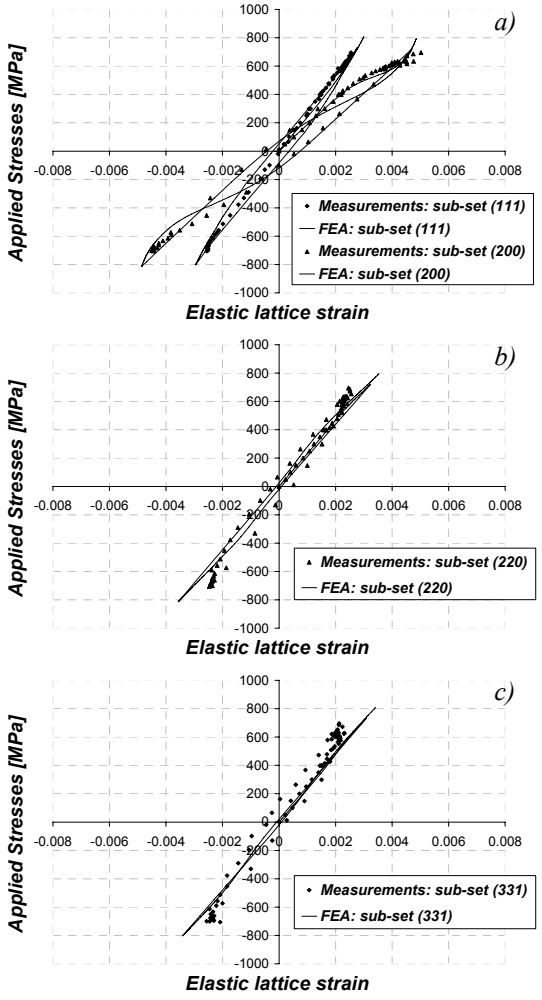

Figure 3. Comparison between orientation-specific elastic lattice strain measured experimentally by neutron diffraction (markers) and the predictions of the finite element model (continuous curves).

Consideration of Fig. 2 and Fig. 3 in combination suggests that the elastic strain partitioning between differently oriented grains is adequately captured by the existing model. However, this cannot be said about the plastic strain, that is invisible in the diffraction experiment, but has a particularly prominent effect on the macroscopic stress-strain curve. Further improvement of the agreement between model and experiment should be sought through better choice of displacement field representation.

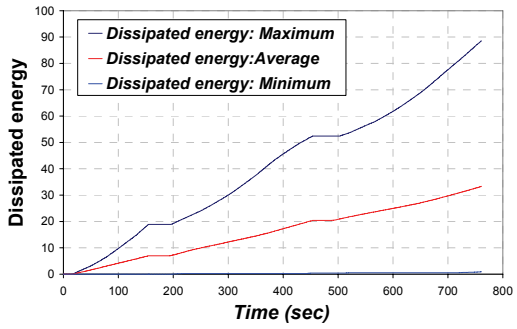

Figure 4. Illustration of dissipated energy evolution during fatigue cycling as a function of time. Note the significant difference observed between locations that display most significant and least dissipation.

5. Energy dissipation and prediction of fatigue crack initiation

Based on any particular polycrystal plasticity model it is possible to evaluate the rate of energy dissipation by plastic slip at any chosen location (integration point) within the model. Dissipation rate can be defined as the sum total of plastic work of shear stresses on slip displacements in an increment over all active slip systems. It is then discovered (e.g. Figure 4) that all points are not equal in this respect: some points appear to dissipate significantly, while others show negligible dissipation rate, i.e. primarily deform elastically. This is an explicit manifestation of the inhomogeneity of damage in real materials that serves as the starting physical premise for some fatigue criteria (e.g. Dang Van), but is rarely utilised directly in the prediction of life to fatigue crack initiation.

In the approach utilised by the authors this aspect of the problem is tackled directly, i.e. crack initiation prediction is based on the local estimate of energy dissipation – although in principle other parameters of the *local* fatigue loop can also be used.

Table 1. (a) Experimental data and (b) life prediction

a)

Experiment number	ε_{min} (%)	ε_{max} (%)	$\Delta\varepsilon_{tot}$(%)
1	-0.635	0.635	1.27
2	0	1.05	1.05
3	-0.42	0.42	0.84
4-Calibration	-0.307	0.308	0.615

b)

Experiment number	N_f	*Predicted* N_f
1	1218	1321
2	4216	4038
3	9670	9533
4-Calibration	34877	34877

Here we state that the functional form Φ in Eq. (1) corresponds to the spatial maximum of the energy dissipated during a loading cycle, E_{cycle}, within the studied RVE. Therefore the lifing Eq. (1) can be written in terms of the maximum across all points of the sum of energy dissipation over each of the M slip systems, i.e.:

$$E_{cycle}(x) = \sum_{j=1}^{M} \int_{cycle} \tau(x,t)\dot{\gamma}(x,t)dt \,,$$

$$\hat{E}_{cycle} = \max_{x} E_{cycle}(x)$$

$$\hat{E}_{cycle} N_f{}^{b} = c \qquad (3)$$

where the material constant c is extracted from a single calibration test as follows:

$$c = \left(\hat{E}_{cycle} N_f{}^{b}\right)_{calibration\,test}, \qquad (4)$$

and b is obtained as best fitting parameter for the available experimental data.

The 3D anisotropic polycrystal finite-element model was used to calculate the maximum energy dissipated during a stabilised loading cycle for a range of applied macroscopic strain amplitudes and load ratios (see Table 1) using the microstructural model for C263 described in section 2. Only data for low cycle fatigue (LCF) tests at 300ºC will be considered here as an example application of how to perform life predictions using the proposed methodology.

Test data are reported in Table 1(a) and the comparison between experimental and predicted lives (obtained using Eq. (3)) for the tested specimens is tabulated in Table 1(b). A plot comparing the predictive trend and the experimental results is also shown in Fig. 5. The data points align well according to a simple power law represented graphically by the linear relationship between $\log(\boldsymbol{E}_{cycle})$ and $\log(\boldsymbol{N}_f)$. Good agreement between the prediction and the experimental data is observed. It is worth noting that the lifing data used for comparison span almost two decades of the numbers of cycles to failures, suggesting that the proposed approach captures well the underlying damage mechanism, and that the latter mechanism is likely to remain unchanged across this range of cyclic lives.

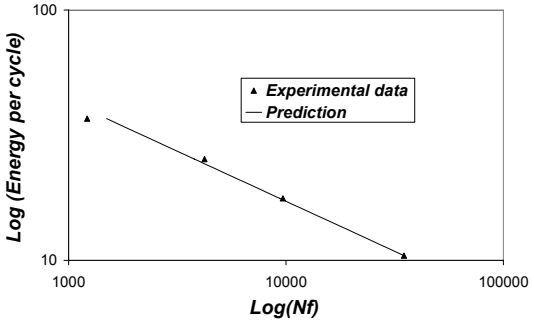

Figure 5. Comparison between experimental and predicted cycles to failure with maximum energy dissipated per cycle. LCF tests carried out at 300ºC (see Table 1).

6. Discussion

The preliminary results obtained in this study suggest that the combination of three-dimensional, FE-based, elastically anisotropic polycrystal plasticity modelling, in combination with energy based fatigue criteria provide a viable route for the development of improved life prediction approaches for structural design.

A particular feature of the proposed approach is its ability to address the probabilistic and statistical aspects of structural strength. The numerically 'lean' formulation allows numerical simulation of cyclic loading of significant numbers of distinct 'implementations' of the microstructure. This in turn provides a measure of the spread of behaviour as a function of particular grain arrangement within the highly stressed regions of the sample.

It is the authors' hope that once the model has been tuned up using e.g. fatigue lifing data for a randomly textured sample, the predictions can then be obtained without any further parameter adjustment for other textures. This expectation is based on the hypothesis that single crystal plastic slip response is not affected by the changes in the overall texture; and that the model adjustment carried out for an untextured sample provides sufficiently accurate and reliable estimates of the parameters. Of course, this hypothesis requires verification by comparison with sufficient experimental data on fatigue durability of samples possessing different textures.

One of the difficulties encountered in the implementation of the finite element plasticity model involving crystal orientation assignment at integration points turned out to be excessive 'stiffening' of the polycrystalline response. This phenomenon is ascribed by the authors to the particular choice of trial

displacement fields within the formulation. This problem may be overcome by allowing greater discontinuity between displacements at neighbouring nodes within a single finite element. Although the authors have not attempted to develop such a formulation, they are aware of several approach found in the literature that aim to achieve such a solution.

6. Conclusion

The use of polycrystal deformation models for the prediction of crack initiation has been investigated. In particular, a three dimensional anisotropic elastic-plastic material model has been implemented within the FE framework in order to study failure mechanisms at mesoscopic level.

The formulation based on crystal plasticity theory was validated both at macro- and mesoscopic level. The proposed model calibration at mesoscopic level was performed via comparison with neutron diffraction data obtained experimentally. In order to compare the numerical predictions of the FE model with these experimental data, the corresponding mesoscale average elastic strains were extracted from the results of the simulation.

Comparisons between the FE model and experimental results show that the elastic strain partitioning between differently oriented grains is adequately captured by the proposed model. However, the FE polycrystal formulation does not produce a rigorous match of the elasto-plastic behaviour of the material at all levels. Advantages and limitations of the present methodology have been thoroughly discussed and solutions to overcome the limitations of the FE implementation have been proposed.

Finally, the capabilities of micro-level energy-based criteria for the prediction of crack initiation have been assessed. The proposed approach seems to capture well the underlying damage mechanism, hence providing good agreement between experiments and predictions.

Acknowledgments

The authors gratefully acknowledge the help of Dr. E.C. Oliver in carrying out the experiments performed on the ENGIN-X instrument at the Rutherford Appleton Laboratory, and would like to express their particular gratitude to Mike Walsh and Combustion Systems Engineering, Rolls-Royce plc.

References

[1] Constantinescu, A., Charkaluk, E., Lederer, G., and Verger, L. (2004), *Int. J. Fatigue*, 26, No.8, pp. 805.

[2] Socie, D. and Marquis, G. (2000), *Multiaxial fatigue*, Society of Automotive Engineers, Warrendale, Pa.

[3] Skelton, R.P., Vilhelmsen, T., and Webster, G.A. (1998), *Int. J. Fatigue*, 20, No.9, pp. 641.

[4] Manonukul, A. and Dunne, F.P.E. (2004), *Proc. R. Soc. London Ser. A-Math. Phys. Eng. Sci.*, 460, No.2047, pp. 1881.

[5] Barbe, F., Decker, L., Jeulin, D., and Cailletaud, G. (2001), *Int. J. Plast.*, 17, No.4, pp. 513.

[6] Korsunsky, A.M., Collins, S.P., Owen, R.A., Daymond, M.R., Achtioui, S., and James, K.E. (2002), *J. Synchrot. Radiat.*, 9, 77.

[7] Lorentzen, T., Daymond, M.R., Clausen, B., and Tome, C.N. (2002), *Acta Mater.*, 50, No.6, pp. 1627.

[8] Larson, A.C. and Von Dreele, R.B. (1994), *GSAS – General Structure Analysis System.* , in *Technical Report LA-UR-86-748*: Los Alamos National Laboratory, USA.

[9] Korsunsky, A.M., James, K.E., and Daymond, M.R. (2004), *Eng. Fract. Mech.*, 71, No.4-6, pp. 805.

A MULTISCALE APPROACH OF HIGH CYCLE FATIGUE OF METALS INCLUDING PLASTICITY AND MICROVOIDS GROWTH

V. Monchiet, E. Charkaluk & D. Kondo

LML, UMR8107 CNRS, USTL, Lille, France

ABSTRACT : A micro-macro approach of multiaxial fatigue in unlimited endurance is proposed. It allows to take into account plasticity and damage mechanisms which occur at the scale of Persistent Slip Bands (PSB). The damage is modelled as the consequence of microvoids growth along PSBS and so can be coupled or uncoupled with plasticity. The proposed macroscopic fatigue criterion, which corresponds to microcracks nucleation at the PSB-matrix interface, is derived for different homogenization schemes (Sachs, Lin-Taylor and Kröner). The role of a mean stress and of the hydrostatic pressure in high cycle fatigue is shown; this dependence is related here to the damage micro-mechanisms. Finally, the particular case of affine and out of phase loadings are presented as an illustration. Comparisons between the predictions of the coupled and uncoupled plasticity-damage models are shown and allow to illustrate the relevance of the approach.

Keywords : Fatigue, Micromechanics, Unlimited endurance, PSB.

1 Introduction

Structures and mechanical components submitted to cyclic loadings can fail after a finite number of cycles, even the macroscopic response remains elastic. Fracture is the result of fatigue macrocracks nucleation and growth. Classically, in uniaxial experiments, a fatigue limit can be distinguished, i.e. there is a maximum value of the stress amplitude under which no fatigue crack can be observed whatever the applied number of cycles.

It has been earlier recognized that, under high cycle fatigue loadings, metals fracture is the result of the cyclic plastic strain; at the microscale, some grains (in very low proportion), favorably oriented, undergo plasticity. This local plasticity is however confined and has no significant effect on the macroscopic response which remains elastic. Dang Van and Papadopoulos (see [(2)]) formalized this multiscale framework. The resulting criterion is based on the consideration that a sufficient condition for non nucleation of fatigue cracks is to ensure elastic shakedown at all the scales. Nevertheless, plastic activity alone is not able to account for the role of pressure on the fatigue criterion. In order to take into account the mean stress effect, Papadopoulos [(2)] postulated a "generalized multiaxial fatigue criterion" (which corresponds to the elastic shakedown limit) depending on the hydrostatic pressure. But in fact, the phenomenon of grain level plasticity is accompanied with the development of localized damage.

The explicit incorporation of damage in HCF modelling has been the subject of several recent studies among which [(7)]. Although this work allows to account for the role of the pressure in fatigue, the principal criticism is that the concept of a scalar variable d, used to describe damage, cannot be explicitly related to a particular physical micro-mechanism. Moreover, in the two scale model proposed by [(7)], no plasticity occurs at the grain scale

below the macroscopic fatigue limit, and this does not correspond to experimental observations [(1)].
Based on experimental results obtained in the context of faced-centered-cubic structures (FCC) [(3)], and following the multiscale approach of Dang Van [(2)] in HCF, we propose a new micromechanical approach of HCF criterion in which plasticity and damage are coupled at the grain scale (section 2). Considering such coupled micro-mechanisms, the present study aims to provide a fatigue criterion in which an explicit dependence on the pressure and on the mean stress is shown (section 3). Finally, through an application to affine and out of phase cyclic loadings, we investigate the role of the homogenization scheme and the local hardening rule in the qualitative predictions of the approach (section 4).

2 Cyclic plasticity and damage at grain level

2.1 Basic principles of the modelling

Let us introduce $\boldsymbol{\sigma}$ and $\boldsymbol{\varepsilon}$ respectively the microscopic (i.e. at the grain level) stress and strain fields. As classically, an additive decomposition of the total strain $\boldsymbol{\varepsilon}$ into elastic strain, $\boldsymbol{\varepsilon}^e$, and plastic strain, $\boldsymbol{\varepsilon}^p$, at the microscopic scale is adopted : $\boldsymbol{\varepsilon} = \boldsymbol{\varepsilon}^e + \boldsymbol{\varepsilon}^p$. Plastic activity at the grain scale is classically characterized by the activation of slips systems defined by a unit normal vector $\underline{n}^r$ and a slip direction $\underline{m}^r$. The microscopic plastic strain tensor reads :

$$\boldsymbol{\varepsilon}^p = \sum_{r=1}^{r=N} \gamma^r \boldsymbol{\Delta}^r; \;\; \boldsymbol{\Delta}^r = \underline{n}^r \overset{s}{\otimes} \underline{m}^r \qquad (1)$$

Where N is the number of slip system activated. We assume that the plastic strain is described, as classically, by Schmid's law :

$$f^r = |\tau^r - X_g^r| - \tau_0 - h^{rs} R^s \qquad (2)$$

where X_g^r is the kinematic hardening variable; a linear law is chosen : $X_g^r = c\gamma^r$. The isotropic hardening variable, R^r, is function of the cumulated plastic strain $\gamma_{cum}^r = \int_0^t |\dot{\gamma}^r| dt'$. Either a linear and a non linear isotropic law are considered in the following :

$$R^s = \begin{cases} R_0 \gamma_{cum}^s \\ \\ R_s \left\{1 - \exp(-r_0 \gamma_{cum}^s)\right\} \end{cases} \qquad (3)$$

where R_0, R_s and r_0 are three model parameters.
h^{rs} is the interaction matrix classically introduced in order to take into account latent hardening and supposed defined by : $h^{rs} = h + (1-h)\delta_{rs}$. Under low macroscopic loading as in the context of HCF, in the case of FCC structures, the plastic behavior is generally characterized by the activation of a predominant slip system and more precisely by the formation of strain localization band which are the potential sites for microcracks nucleation.
This predominant slip system activated is denoted by the use of the notations : $r = p$ (for "predominant"). The strain localization into the PSBs is also accompanied by a dislocations annihilation mechanism which lead to the formation of vacancies along PSBs. A phenomenological model for points defects production by dislocations annihilation has been already proposed by Essmann et al. [(3)]. The porosity associated to this mechanism, denoted η_a, is function of the cumulated plastic slip strain on the predominant system activate, γ_{cum}^p, and is given by :

$$\eta_a = A_0 \Big\{ k_a \gamma_{cum}^p - 1 + \exp\left(-k_a \gamma_{cum}^p\right) \Big\} \qquad (4)$$

Unfortunately, the transition from vacancy production to the formation of microvoids or microcracks along the PSBs is not yet well understood. Nevertheless, we assume that the formation of these microvoids is the result of the agglomeration and the growth of vacancies formed by the dislocation annihilation process. It follows that damage along PSBs is the result of both two mechanisms : vacancies production and voids growth which is the result of the combined effect of the slip-like plastic activity and pressure. The total porosity at the grain scale, η, is then decomposed into two terms corresponding respectively to nucleation and the growth part as follows :

$$\eta = \eta_a + \eta_g \qquad (5)$$

As it have been pointed out by [(4)], void growth in single crystal is the result of the activation of multiple slip activity around the circumference of the void. More precisely the deformation state takes the form of angular slip sectors in which only one slip system is activated. As voids growth induces volume change, the plastic strain at the grain scale can be decomposed in the following form, $\mathbf{1}$ being the second order identity tensor :

$$\boldsymbol{\varepsilon}^p = \gamma^p \boldsymbol{\Delta} + \varepsilon_h^p \, \mathbf{1} \tag{6}$$

in which the volumetric plastic strain ε_h^p

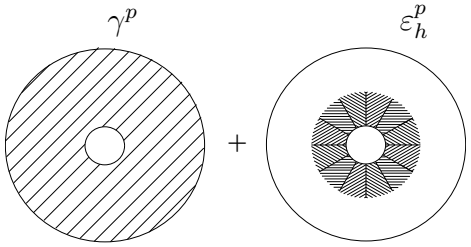

Figure 1: Considered cell : Additive decomposition of the microscopic plastic strain

due to the voids growth is related to η_g by using mass balance equation :

$$\eta_g = 1 - \exp(-3\varepsilon_h^p) \tag{7}$$

It appears that the determination of the total porosity η requires the calculation of ε_h^p. For this purpose two approach of void growth in single crystal, a non coupled and a coupled model, are considered for the present study. Comparisons between the prediction of these two models will be presented in section 4.

2.2 An uncoupled plasticity-damage model (UPDM)

In order to derive a void growth model, single crystal is replaced by an equivalent von Mises materials. A first step of the modelling consists to consider a single void growth in an infinite perfectly plastic medium using the well known Rice and Tracey approach [(10)]. Plastic activity is assumes to be decomposed into an homogeneous plastic strain (the predominant slip system activated) and a heterogeneous symmetric plastic strain which accounts for multiple slip activity around the circumference of the void. The volumetric plastic strain ε_h^p, is the result of the combined action of pressure and the predominant slip plastic strain activity and is given by (see [(8)] for more details) :

$$\dot{\varepsilon}_h^p = \eta \frac{1}{2\sqrt{3}} \sinh \left\{ \frac{\sqrt{3}}{2} \frac{\sigma_h}{\tau_0} \right\} \dot{\gamma}_{cum}^p \tag{8}$$

where σ_h is the hydrostatic part of the microscopic stress tensor and γ^p is described here by Schmid'law (2). Two limitations must be pointed out in this type of modelling. First it does not take into account the hardening in the void growth law. The second shortcomings is that the yield function is not coupled with damage. That's why a more elaborated model is due.

2.3 A coupled plasticity-damage model (CPDM)

For this purpose we consider a single void (of radius a) embedded in a sphere (of radius b) defining a porosity $\eta = a^3/b^3$. As in the previous section, single crystal is replaced by an equivalent von Mises materials. Adapting the limit analysis proposed by [(5)], in the context of rigid ideally hollow sphere, leads to the following yield function :

$$f = \frac{\tau^2}{\tau_0^2} + 2\eta \cosh \left\{ \frac{\sqrt{3}}{2} \frac{\sigma_h}{\tau_0} \right\} - 1 - \eta^2 \tag{9}$$

It is worth noticing that for $\eta = 0$ the Schmid'law (2) in the particular case of rigid ideally plastic single crystal is recovered. An extension of the original Gurson model to isotropic and kinematic hardening has already been performed by [(6)]. Following their approach we propose an extension of (9) to single crystal hardenable behavior. Similarly to [(6)], the critical shear stress τ_0 is replaced by τ_1 and τ_2, into the square and the hyperbolic cosine in order to take into account isotropic hardening. Kinematic hardening rule is introduced by replacing $\boldsymbol{\sigma}$ by $\boldsymbol{B} = \boldsymbol{\sigma} - \boldsymbol{X}$ where $\boldsymbol{X}$ denotes the center of the elasticity domain, which includes an hydrostatic part, X_h, and a deviatoric part such that : $\boldsymbol{X} = 2X_g \, \boldsymbol{\Delta} + X_h \mathbf{1}$. Taking into account

this change, (9) reads :

$$f = \frac{(\boldsymbol{B} : \boldsymbol{\Delta})^2}{\tau_1^2} + 2\eta \cosh\left\{\frac{\sqrt{3}}{2}\frac{B_h}{\tau_2}\right\} - 1 - \eta^2 \tag{10}$$

The identification of those different hardening variables require the knowledge of the matrix hardening in the hollow sphere. As in [(6)], the hardening parameters are identified by considering two particular loading cases, the first is the purely deviatoric loading (obtained by putting $\sigma_h = 0$) for which no void growth may occur; plastic activity is then only constituted of the predominant slip system. The second is the purely hydrostatic loading (obtained by putting $\tau = 0$) for which plastic activity is then only constituted of the heterogeneous slip activity around the circumference of the void. This procedure allows to identify X_g, X_h, τ_1 and τ_2 (see [(9)] for more details), which read :

$$\begin{aligned} X_g &= (1-\eta)c\gamma^p; \quad X_h = \frac{2c}{\sqrt{3}}\beta \\ R_d &= R(\gamma^p_{cum}) + hR\Big(\frac{\alpha_{cum}}{1-\eta}\Big) \\ R_h &= hR(\gamma^p_{cum}) + R\Big(-\frac{\beta_{cum}}{\ln(\eta)}\Big) \end{aligned} \tag{11}$$

where α and β are such that :

$$\begin{aligned} \alpha &= \frac{2}{\sqrt{3}}\Big\{(1-\eta_g)\ln(1-\eta_g) \\ &+\eta_a \ln(\eta_a) - \eta\ln(\eta)\Big\} \\ \beta &= \frac{2}{\sqrt{3}}\Big\{\text{dilog}\left\{\frac{\eta_a}{\eta}\right\} \\ &- \text{dilog}(1-\eta_g)\Big\} \end{aligned} \tag{12}$$

α_{cum} and β_{cum} are respectively the cumulated value of α and β and defined by : $\alpha_{cum} + \int_0^t \alpha(t')dt'$ and $\beta_{cum} + \int_0^t \beta(t')dt'$. dilog is the dilorithm function defined by :

$$\text{dilog}(x) = \int_1^x \frac{\ln(x')}{1-x'}dx' \tag{13}$$

The slip and volumetric plastic strain rate, $\dot{\gamma}^p$ and $\dot{\varepsilon}^p_h$ are obtained by using the normality rule associated to f :

$$\begin{aligned} \dot{\gamma}^p &= 2\dot{\Lambda}\frac{\boldsymbol{B} : \boldsymbol{\Delta}}{\tau_1^2} \quad (i) \\ \dot{\varepsilon}^p_h &= \frac{\dot{\Lambda}}{\sqrt{3}}\frac{\eta}{\tau_2}\sinh\left\{\frac{\sqrt{3}}{2}\frac{B_h}{\tau_2}\right\} \quad (ii) \end{aligned} \tag{14}$$

$\dot{\Lambda}$ is the plastic multiplier. It is deduced from (i), in (14) : $\dot{\Lambda} = \dot{\gamma}^p \frac{\tau_1^2}{2\boldsymbol{B}:\boldsymbol{\Delta}} = \dot{\gamma}^p_{cum}\frac{\tau_1^2}{2|\boldsymbol{B}:\boldsymbol{\Delta}|}$. Reporting the expression of $\dot{\Lambda}$ into (ii), one obtains :

$$\dot{\varepsilon}^p_h = \frac{\eta}{2\sqrt{3}}\frac{\tau_1^2}{\tau_2|\boldsymbol{B} : \boldsymbol{\Delta}|}\sinh\left\{\frac{\sqrt{3}}{2}\frac{B_h}{\tau_2}\right\}\dot{\gamma}^p_{cum} \tag{15}$$

2.4 fatigue crack nucleation criterion

A local approach of fatigue crack nucleation at the PSB-matrix interface consists in introducing a critical value of the porosity, η_c :

$$\eta_a + \eta_g = \eta_c \tag{16}$$

The damage-dependent criterion (16) is the threshold below which no crack nucleation could be observed. From (4) and (7), it is readily seen that this criterion depends explicitly on the cumulated slip plastic strain γ^p_{cum} and on the volumetric plastic strain ε^p_h.

3 Micro-macro based determination of the fatigue criterion

3.1 The local fatigue criterion.

For the determination of the fatigue criterion, following [(2)], we assume that a necessary condition for non nucleation of cracks is that the monocrystal shakedowns elastically. In our HCF approach, elastic shakedown is a necessary but not a sufficient condition for non nucleation of cracks : *in the elastic shakedown regime, a crack may nucleate if a critical porosity along the PSB-matrix interface is attained (see condition (16))*. Therefore, as the grain shakedowns elastically, γ^p_{cum} is bounded and so the porosity is very low; the following approximations can then be done : $\eta_g \ll 1$, then mass balance equation (7) reads : $\eta_g \simeq 3\varepsilon^p_h$. The local fatigue criterion, deduced from (16), reads :

$$A_0(k_a p - 1 + \exp(-k_a p)) + 3\varepsilon^p_h < \eta_c \tag{17}$$

Since γ^p_{cum} and ε^p_h are defined at the grain scale, in order to establish a macroscopic expression of the fatigue criterion, a non linear homogenization approach is due.

3.2 The macroscopic fatigue criterion

Let us first recall that the macroscopic behavior remains elastic. Therefore, the macroscopic stress tensor, $\mathbf{\Sigma}$, and the macroscopic elastic strain tensor, $\boldsymbol{E}$, are given by : $\mathbf{\Sigma} = \mathbb{C} : \boldsymbol{E}$ where $\mathbb{C}$ is the stiffness tensor of the aggregate. For simplicity, $\mathbb{C}$ is assumed isotropic : $\mathbb{C} = 3k\mathbb{J} + 2\mu\mathbb{K}$, k and μ being respectively the bulk and shear modulus of the matrix, $\mathbb{J} = \frac{1}{3}\mathbf{1} \otimes \mathbf{1}$ and $\mathbb{K} = \mathbb{I} - \mathbb{J}$ with $\mathbb{I}$ the fourth order symmetric identity tensor. In the particular case of high cycle fatigue, the plastic strain being confined into a few number of grains embedded in the elastic matrix, the overall behavior is close to the one of polycrystal near the yield limit. For such situation, three homogenized schemes, namely Lin-Taylor, Sachs and Kröner models, are considered; they can be written in the following general form :

$$\boldsymbol{\sigma} = \mathbf{\Sigma} - \mathbb{C}^* : \boldsymbol{\varepsilon}^p \tag{18}$$

where the fourth order tensor $\mathbb{C}^*$ reads for the different homogenized scheme : $\mathbb{C}^* = 0$ for Sachs model, $\mathbb{C}^* = \mathbb{C}$ for Lin-Taylor scheme and $\mathbb{C}^* = \mathbb{C} : (\mathbb{I} - \mathbb{P} : \mathbb{C})$ for the Kröner estimation. $\mathbb{P}$ is the Hill tensor; defined for a spherical inclusion, as :

$$\begin{aligned} &\mathbb{P} = \tfrac{a}{3k}\mathbb{J} + \tfrac{b}{2\mu}\mathbb{K} \\ &\text{with : } a = \tfrac{3k}{3k+4\mu} \quad \text{and} \quad b = \tfrac{6}{5}\tfrac{k+2\mu}{3k+4\mu} \end{aligned} \tag{19}$$

It follows that the hydrostatic pressure σ_h and the shear stress τ, which enter into the local criterion, (16), are given by :

$$\begin{aligned} \tau &= \mathbf{\Sigma} : \mathbf{\Delta} - \mu^* \gamma^p \\ \sigma_h &= \Sigma_h - 3k^* \varepsilon^p_h \end{aligned} \tag{20}$$

with $\mu^* = \mu(1-b)$, $k^* = k(1-a)$. Lin-Taylor estimate is obviously recovered for $a = b = 0$ and the Sachs model for $a = b = 1$.

As previously shown, the transition from microscale to macroscopic level of the fatigue criterion (17) requires the expression of γ^p_{cum} and ε^p_h as function of the macroscopic fields.

For the UPDM, γ^p_{cum} is related to τ by means of the Schmid's law $f = 0$ (2) and then to the macroscopic shear stress by the interaction law (20), son one has :

$$f = |\mathbf{\Sigma} : \mathbf{\Delta} - X^*_g| - \tau_0 - R(\gamma^p_{cum}) \tag{21}$$

with : $X^*_g = (c + \mu^*)\gamma^p$. ε^p_h is obtained from (8) in which the expression of σ_h, given by (20), is used :

$$\dot{\varepsilon}^p_h = \eta \frac{1}{2\sqrt{3}} \sinh\left\{ \frac{\sqrt{3}}{2} \frac{\Sigma_h - 3k^* \varepsilon^p_h}{\tau_0} \right\} \dot{\gamma}^p_{cum} \tag{22}$$

For the CPDM, γ^p_{cum} and ε^p_h are related to τ and σ_h by means of the yield function f, and the normality rule associated to plastic criterion f. Their relation with the macroscopic stress is then given by the interaction law (20), reads :

$$\begin{aligned} f &= \left(\frac{\mathbf{\Sigma} : \mathbf{\Delta} - X^*_g}{\tau_1} \right)^2 \\ &+ 2\eta \cosh\left\{ \frac{\sqrt{3}}{2} \frac{\Sigma_h - X^*_h}{\tau_2} \right\} - 1 - \eta^2 \\ \dot{\varepsilon}^p_h &= \frac{\eta}{2\sqrt{3}} \frac{\tau_1^2}{\tau_2 |\mathbf{\Sigma} : \mathbf{\Delta} - X^*_g|} \times \\ &\sinh\left\{ \frac{\sqrt{3}}{2} \frac{\Sigma_h - X^*_h}{\tau_2} \right\} \dot{\gamma}^p_{cum} \end{aligned} \tag{23}$$

with : $X^*_g = X_g + 2\mu^* \gamma^p$ and $X^*_h = X_h + 3k^* \varepsilon^p_h$. In a general case, the macroscopic stress tensor $\mathbf{\Sigma}$ is a time dependent function which describes a closed curve in the stress space corresponding to the cyclic loading path. γ^p_{cum} and ε^p_h can be determined by using a numerical procedure in order to determine the elastic shakedown state and the critical condition corresponding to crack nucleation (17). For an illustration purpose, we consider now the particular case of affine and out of phase loadings.

4 Applications

4.1 Applications to affine loadings

The macroscopic stress tensor, $\mathbf{\Sigma}(t)$, associated to an affine loading is decomposed

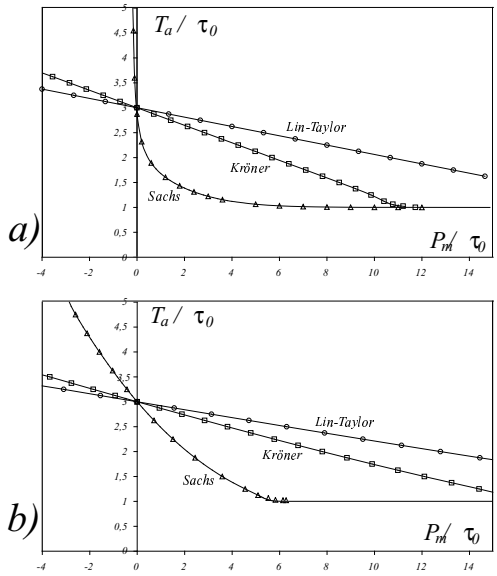

Figure 2: Fatigue criterion in the plane T_a, P_m : a) for non coupled model (UPDM), b) for coupled model (CPDM), using a linear isotropic hardening rule.

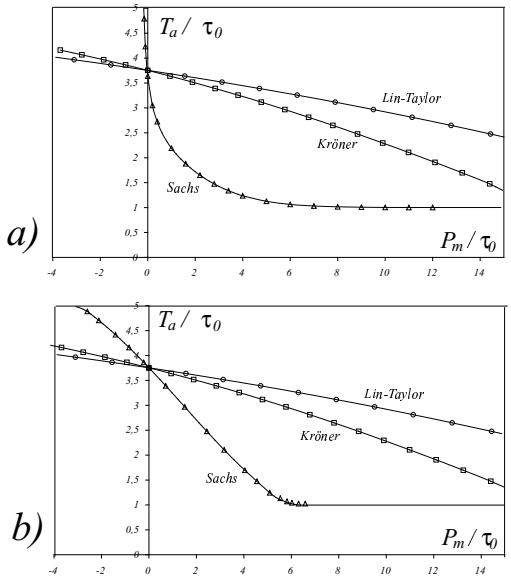

Figure 3: Fatigue criterion in the plane T_a, P_m : a) for non coupled model (UPDM), b) for coupled model (CPDM), using a non linear isotropic hardening rule.

into an alternative and a mean part :

$$\mathbf{\Sigma}(t) = \mathbf{\Sigma}_a \, \sin(\omega t) + \mathbf{\Sigma}_m \tag{24}$$

The macroscopic shear stress, $C(t)$, and the hydrostatic pressure, P(t), associated to (24), are defined by :

$$\begin{aligned} C(t) &= \mathbf{\Sigma}(t) : \mathbf{\Delta} = C_a \sin(\omega t) + C_m \\ P(t) &= \Sigma_h(t) = P_a \sin(\omega t) + P_m \end{aligned} \tag{25}$$

with : $C_a = \mathbf{\Sigma}_a : \mathbf{\Delta}$, $C_m = \mathbf{\Sigma}_m : \mathbf{\Delta}$, $P_a = \mathbf{\Sigma}_a : \mathbf{1}/3$ and $P_m = \mathbf{\Sigma}_m : \mathbf{1}/3$.
When the grain shakedowns elastically, numerical resolution shown that the center of the elastic domain coincide with the mean stress component. This implies for the UPDM model that :

$$\begin{aligned} C_m &= X_g^* = (c + \mu^*)\gamma^p \\ C_a &= \tau_0 + R(\gamma_{cum}^p) \end{aligned} \tag{26}$$

In the UPDM, the γ_{cum}^p is related to the alternated part of the macroscopic shear stress C_a; ε_h^p is deduced by integrating (8). For Lin-Taylor and Kroener's models, numerical resolution of equation (8) shows that, for moderate values of the pressure, ε_h^p reaches a saturation state corresponding to $\dot{\varepsilon}_h^p = 0$ and then to $P_m = 3k^* \varepsilon_h^p$.
Similarly, for the CPDM we have :

$$\begin{aligned} C_m &= X_g^* = (c + \mu^*)\gamma_m^p \\ P_m &= X_h^* = \frac{2c}{\sqrt{3}}\beta + 3k^* \varepsilon_h^p \\ \frac{C_a^2}{\tau_1^2} &+ 2\eta \cosh\left\{ \frac{\sqrt{3}}{2} \frac{P_a}{\tau_2} \right\} - 1 - \eta^2 = 0 \end{aligned} \tag{27}$$

It can be observed that the fatigue criterion is independent of γ_m^p and then independent of the mean shear stress C_m. This is consistent with experimental data provided by [(11)]. Considering now the CPDM, the same remarks concerning the mean shear stress can be done. However, in this approach, γ_{cum}^p depends not only on the alternated shear stress tensor C_a but also on the alternated part of the macroscopic hydrostatic pressure P_a. Contrarily to the UPDM, ε_h^p is deduced from shakedown condition ($P_m = X_h^*$). As a first illustration let us consider the following particular affine loading, $C_m = P_a = 0$. Different parameters are taken as $k = 200000MPa$, $\mu = 75000MPa$, $c = 500MPa$, $R_0 = 20MPa$, $\tau_0 = 60MPa$, $A_0 = 4.10^{-4}$, $k_a =$

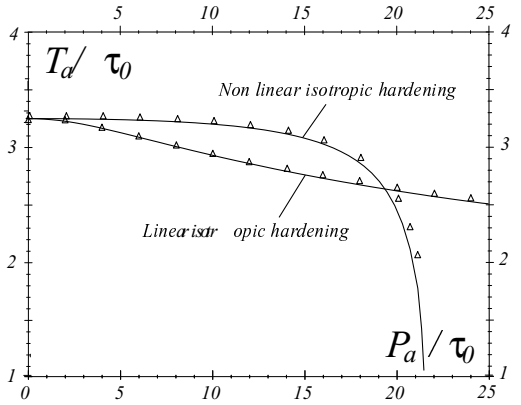

Figure 4: Fatigue criterion in the plane C_a, P_a.

2, $\eta_c = 0.006$. The fatigue criterion is plotted in the plane C_a, P_m, on figures 2a and 3a (for UPDM, using linear and non linear isotropic hardening) and figures 2b and 3b (for CPDM, using linear and non linear isotropic hardening) and for the different homogenization schemes (Lin-Taylor, Sachs and Kröner). Besides the influence of the homogenization scheme and of the hardening rule, the results show a remarkable effect of the pressure on the fatigue criterion. However, for negative pressure, the results of Sachs approach for UPDM seem to be physically inconsistent.
Let us consider now an alternated torsion with an alternated pressure, $C_m = P_m = 0$: $P(t) = P_a\ \sin(\omega t)$ and $C(t) = T_a\ \sin(\omega t)$. Parameters used are the same as previously. It is worth noticing that the UPDM is unable to account for the effect of an alternated pressure on the fatigue criterion. The results obtained in the context of the CPDM are reported on figure 4 in the plane T_a, P_a. It can be observed that all homogenized schemes coincide for this particular loading case. However it can be shown a clear influence of the isotropic hardening rule on the fatigue criterion (linear or non linear rule).

4.2 Application to out of phase loadings

The great majority of non affine fatigue tests in the relevant literature corresponds to the out of phase sinusoidal loading : $\Sigma_{ij}(t) = \Sigma_{a,ij}\sin(\omega t + \psi_{ij}) + \Sigma_m$, in which the summation convention on repeated indices may not be applied. ψ_{ij} are the out phase terms associated to each stress components Σ_{ij}. We propose here an another notations, using the following identity : $\sin(\omega t + \psi_{ij}) = \sin(\omega t)cos(\psi_{ij}) + \cos(\omega t)sin(\psi_{ij})$. $\mathbf{\Sigma}(t)$ can therefore be defined, for out of phase loadings, by introducing two second order tensors, denoted $\mathbf{\Sigma}_a^1$ and $\mathbf{\Sigma}_a^2$:

$$\mathbf{\Sigma}(t) = \mathbf{\Sigma}_a^1\ \sin(\omega t) + \mathbf{\Sigma}_a^2\ \cos(\omega t) + \mathbf{\Sigma}_m \quad (28)$$

where $\mathbf{\Sigma}_a^2 = 0$ and $\mathbf{\Sigma}_a^1 = \mathbf{\Sigma}_a$ when $\psi_{ij} = 0$. The macroscopic shear stress and the hydrostatic pressure reads :

$$\begin{aligned} C(t) &= C_a^1\ \sin(\omega t) + C_a^2\ \cos(\omega t) + C_m \\ P(t) &= P_a^1\ \sin(\omega t) + P_a^2\ \cos(\omega t) + P_m \end{aligned} \quad (29)$$

with : $C_a^1 = \mathbf{\Sigma}_a^1 : \mathbf{\Delta}$, $C_a^2 = \mathbf{\Sigma}_a^1 : \mathbf{\Delta}$, $C_m = \mathbf{\Sigma}_m : \mathbf{\Delta}$, $P_a^1 = \mathbf{\Sigma}_a^1 : \mathbf{1}/3$, $P_a^2 = \mathbf{\Sigma}_a^2 : \mathbf{1}/3$ and $P_m = \mathbf{\Sigma}_m : \mathbf{1}/3$. Expression (29) can be rewritten as :

$$\begin{aligned} C(t) &= \widetilde{C}_a \sin(\omega t + \phi_g) + C_m \\ P(t) &= \widetilde{P}_a \sin(\omega t + \phi_h) + P_m \end{aligned} \quad (30)$$

with :

$$\begin{aligned} \phi_g &= \arccos\left(\frac{C_a^1}{\widetilde{C}_a}\right) \\ \widetilde{C}_a &= \sqrt{(C_a^1)^2 + (C_a^2)^2} \\ \phi_h &= \arccos\left(\frac{P_a^1}{\widetilde{P}_a}\right) \\ \widetilde{P}_a &= \sqrt{(P_a^1)^2 + (P_a^2)^2} \end{aligned} \quad (31)$$

Using now the following change of variable : $t = t' - \phi_g/\omega$ and $\Phi = \phi_h - \phi_g$, (30) reads :

$$\begin{aligned} C(t) &= \widetilde{C}_a \sin(\omega t') + C_m \\ P(t) &= \widetilde{P}_a \sin(\omega t' + \Psi) + P_m \end{aligned} \quad (32)$$

Numerical resolution of equation (23) for out of phase loading (32) shown that :
- as in the context of affine loadings, the UPDM is not able to take into account the role of the alternated pressure ($\widetilde{P}_a$). The fatigue criterion associated to this model is only dependent of $\widetilde{C}_a$ and P_m.

- The CPDM is not only dependent of $\widetilde{C}_a$ and P_m but also on $\widetilde{P}_a$ and Ψ. Numerical resolution of (23) shows that, when the grain shakedown elastically, one has :

$$\begin{aligned} C_m &= X_g^* = (c+\mu^*)\gamma_m^p \\ P_m &= X_h^* = \frac{2c}{\sqrt{3}}\beta + 3k^*\varepsilon_h^p \end{aligned} \tag{33}$$

$$\frac{\widetilde{C}_a^2}{\tau_1^2} + 2\eta\cosh\left\{\frac{\sqrt{3}}{2}\frac{\widetilde{P}_a\cos(\Psi)}{\tau_2}\right\} - 1 - \eta^2 = 0$$

As an application let us consider an alternated torsion (T_a) with an alternated pressure (P_a) : $P(t) = P_a\ \sin(\omega t + \psi)$ and $C(t) = T_a\ \sin(\omega t)$. Then the different quantities introduced previously are defined by : $\widetilde{C}_a = C_a$, $\widetilde{P}_a = P_a$, $\Psi = \psi$. The influence of the dephasing term ψ on the fatigue criterion is clearly shown.

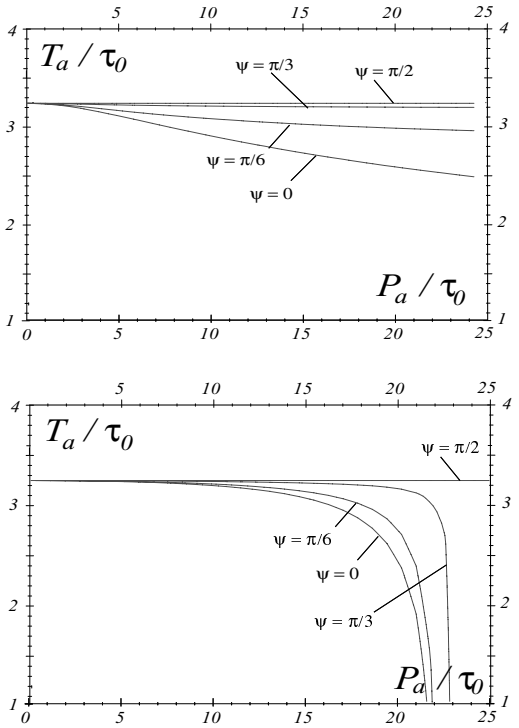

Figure 5: Fatigue criterion in the plane T_a, P_a for different values of ψ.

5 Conclusion

A multiscale approach for the determination of a High Cycle Fatigue criterion has been proposed. It allows to take into account, not only plasticity activity in some grains, but also damage due to microvoids growth along PSB-matrix interface. An uncoupled plasticity-damage model (UPDM) and a coupled plasticity-damage model (CPDM) are devellopped at the grain scale. The proposed criterion, as non crack nucleation condition at the PSB-matrix interface, shows a significant effect of the pressure which is due to the considered damage mechanism. For a complete validation of the approach a comparison with experimental existing data will be done.

REFERENCES

[1] **P. Cugy, A. Galtier**.
Microplasticity and temperature increase in low carbon steels. *Proceedings of the 8th International Fatigue Congress, Stockholm, Ed. A. F. Blom*, 2002.

[2] **K. Dang Van, I.V. Papadopoulos (eds)**.
High cycle metal fatigue. From Theory to Applications. *CISM Courses and Lectures, no. 392, eds. : Ky Dang Van and I.V. Papadopoulos*

[3] **U. Essmann, H. Mughrabi**.
Annihilation of dislocations during tensile and cyclic deformation and limits of dislocation densities. *Philosophical Magazine A*, Vol. 40, No. 6, pp. 731-756, 1979.

[4] **J. W. Kysar, Y .X. Gan, G. Mendez-Arzuza**.
Cylindrical void in a rigid ideally plastic single crystal. Part I: Anisotropic slip line theory solution for faced-centered cubic crystals. *Philosophical Magazine A*, Vol. 44, No. 2, pp. 405-426, 1991.

[5] **Gurson, A.L., 1977**.
Continuum theory of ductile rupture by void nucleation and growth: part I - yield criteria and flow rules for porous ductile media. *ASME J Engng Materials Technol* 99, 2-15.

[6] **J.B. Leblond, G. Perrin, J.Devaux**.
An improved Gurson-type model for hardenable ductile metals .

EUR. J. Mech. A/Solids, Vol. 14, No. 4, pp. 499-527, 1995.

[7] **J. Lemaitre, J.P. Sermage, R. Desmorat**.
A two scale damage concept applied to fatigue. *Int. J. Fracture*, Vol. 97, pp. 67-81, 1999.

[8] **V. Monchiet, E. Charkaluk, D. Kondo**.
Plasticity-damage based micromechanical modelling in high cycle fatigue. *C. R. Acad. Sci. Paris* , Série IIb 334, pp. 129–136, 2006.

[9] **V. Monchiet, E. Charkaluk, D. Kondo**.
A microvoids growth approach applied to high cycle fatigue. submitted, 2006.

[10] **J.R. Rice, D.M. Tracey**.
On the ductile enlargement of voids in triaxial stress fields. *J. Mech. Phys. Solids*, Vol. 17, pp. 201-217, 1969.

[11] **G. Sines**.
Behavior of metals under complex static and alterning stresses. *In Metal Fatigue, ed. G. Sines and J.L. Waisman. McGraw Hill, New York*, pp. 145-159, 1959.

A COMPREHENSIVE STUDY OF CRACK OPENING AND CLOSING STRESSES IN FATIGUE CRACK CLOSURE PROBLEMS

Paulo F. P. de Matos
University of Oxford, Department of Engineering Science,
Parks Road, Oxford OX1 3PJ, United Kingdom

David Nowell
University of Oxford, Department of Engineering Science,
Parks Road, Oxford OX1 3PJ, United Kingdom

Abstract

In general, fatigue cracks in ductile materials grow thorough plastically deformed material. Material ahead of the crack will be left with a residual strain after a cycle of loading and this strained material will remain as the crack tip passes it. Elber [1] found out that this phenomenon gave rise to crack closure. At the microscopic level, crack tip deformation takes place through dislocation motion on appropriate glide planes. In the present work a mesomechanics approach is used to capture the underlying microscopic processes without modelling them explicitly. An analytical model developed by Nowell formulated with dislocation dipoles will be used to describe the crack tip deformation at a macroscopic level making use of continuum elasticity and plasticity. In addition some finite element analysis work is presented. FE Analysis is one of most successful techniques which have been used to quantify the closure effect. However, there are many difficulties associated with this modelling work, since the results depends on a variety of input parameters such as mesh refinement, node release scheme and modelling of the contact between the crack faces etc. Even after a great deal of modelling work, an arbitrary decision usually has to be made concerning the technique employed for assessing the opening and closing stresses. Many techniques have been developed along the last few years. This work will assess and compare techniques such as the nodal displacement method, the change in stresses at the crack tip and the weight function technique. These techniques will be used in conjunction with a finite element model of a plane stress propagating crack. The analytical 'mesomechanics' model will then be used to discuss the accuracy of the different methods.

Keywords: Finite elements, Opening stresses, Closing stresses, Weight function.

1. Introduction

The aim of this work is the understanding of different techniques often used to assess the level of plasticity-induced crack. The plastic deformation of a growing crack is studied using an analytical mesomecanics model [2] and a finite element simulation of the same problem, a crack under cyclic

loading (σ_0/σ_{yield}=0.5 and R=0) for plane stress conditions. At a microscopic scale the plastic deformation at the crack tip occurs due to the breaking and reforming of atomic bonds in a material. The breaking and reforming of bonds allows *dislocations* to slide through crystalline materials, the slippage causes permanent deformation and ultimately failure [3]. In the present work both analytical and numerical model are used to describe the crack tip deformation at a macroscopic level making use of continuum elasticity and plasticity. This approach captures the underlying microscopic processes of plastic deformation without modelling them explicitly. After modelling the deformation mode of the crack the closure behaviour is quantified. Usually three different techniques are used to assess the closure level in plasticity-induced crack closure: the displacement method, the contact stress method and the change in stress at the crack tip. Most researchers using FEM to simulate crack closure have used the first node behind the crack tip to assess the crack opening stresses [4-7]. An alternative technique consists of using the contact stresses along the crack faces to compute the opening stresses [8]. Sun and Sehitoglu [9] introduced an alternative criterion to estimate the crack opening based on the assumption that when the stress at the crack tip node changes from compressive to tensile, the crack is fully open. This technique has subsequently been adopted by other researchers [10-13]. Wu and Ellyin [11] defined the opening stress as the remote applied stress for which the stresses perpendicular to the crack plane change from compressive to tensile at the crack tip node. Similarly, during unloading the load at which the tensile stress at the crack tip changes from tensile to compressive is taken as the closing stress. The results obtained with this approach can differ significantly from those obtained by other methods. The general trend exhibits higher closing stresses than opening stresses. Moreover the opening stresses themselves are larger than the predictions made by the contact stress and nodal displacement approaches [10, 13].

In the present work the analytical mesomechanics model developed by Nowell [2] will used to show some of the limitations inherent to the finite element approach. It will be shown that displacement method, contact stress method and change in stress at the crack tip (for crack opening) are equivalent provided that the displacement and stress at the crack tip are assessed accurately.

2. Finite element modelling

Geometry and material model

Figure 1 a) presents the geometry of the problem modelled. It consists of a square plate with a finite central crack, W=45mm and a_0=1mm. An elastic perfectly plastic material model was used with isotropic hardening and the von Mises yield criterion. The material properties used were appropriate to the titanium alloy Ti-6Al-4V. The yield stress is 1000 MPa, Young's modulus 110 GPa and Poisson's ratio is 0.34.

Mesh and boundary conditions

Figure 1 b) and c) presents the mesh of a quarter of the plate modelled. An increasing level of mesh refinement was used towards the crack region. Four node quadrilateral linear displacement elements were used in the present study, since Dougherty *et al.* [14] have observed a saw tooth pattern of the residual stresses on the crack faces of quadratic elements, whereby corner nodes were subjected to compressive stresses whereas mid-side nodes were carrying tensile stress. Symmetry boundary conditions were used (along both axes x and y). A cyclic remote applied load was applied. Along the crack plane a rigid line was created and contact conditions between this an the elements

along the crack plane were prescribed. The rigid line does not simulate any real surface but only accounts for symmetry and the prohibition of crack face interpenetration.

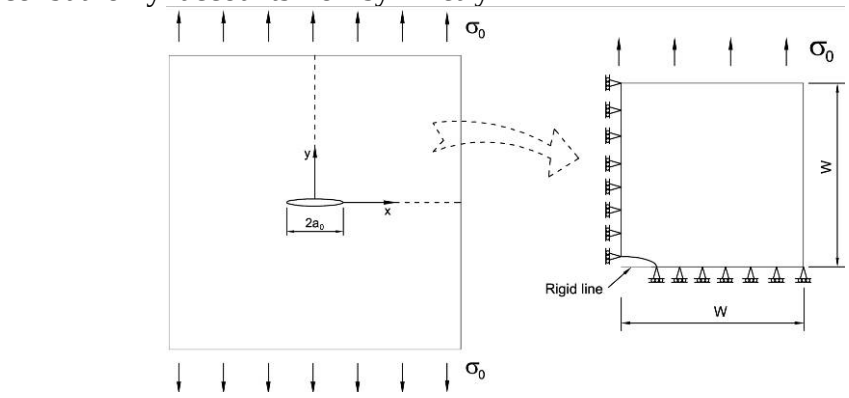

a)

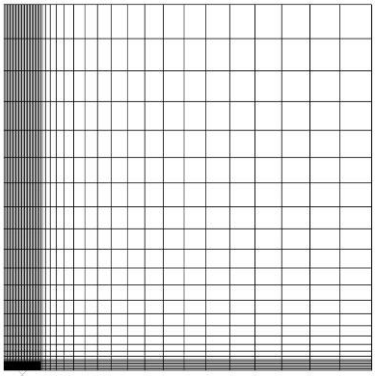

b)

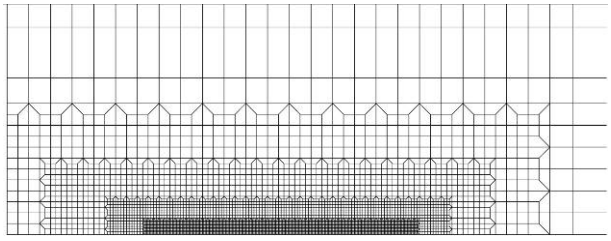

c)

Figure 1. a) Geometry and boundary conditions; b) Mesh; c) Mesh detail (minimum element size 10 μm).

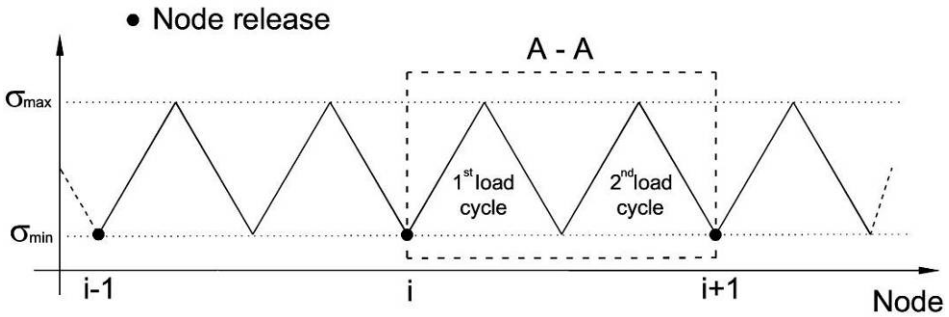

Figure 2. Crack growth scheme.

Crack growth modelling

The simulation of crack growth was performed by sequential node release of the nodes ahead of the initial crack. Recent work has shown that satisfactory results are obtained, irrespective of whether the nodes are released at minimum or maximum load, provided a suitable mesh refinement is used [15]. In the current study, the node release takes place at minimum load and the increment of crack growth was defined by the element size. Figure 2 presents the crack growth scheme adopted. One node is released every two cycles; the first load cycle is applied to stabilize the plastic region close to the crack tip. During the second load cycle the opening and closing stresses are measured. In order to reach steady state closure behaviour it is required to grow the crack for some distance, necessitating the simulation of a significant number of load cycles.

Crack opening and closing stresses, description of the different techniques

The opening and closing stresses were calculated using the displacement method (based on the displacement of nodes behind the crack tip, see Figure 3); the change in stress at the crack tip; and the weight function method based on the contact stress along the crack surfaces. These methods are described in the following subsections.

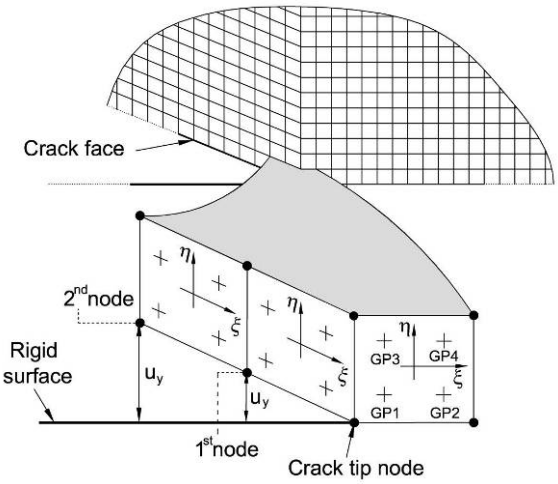

Figure 3. Elements close to the crack tip.

Nodal displacement method. This method is the most popular method for computing opening and closing stresses. It consists of monitoring the displacement of a node (either the first or second node behind the crack tip) as the load is applied (see Figure 3). The opening stresses are found when the displacement of the node monitored becomes positive during the loading stage of a load cycle and the closing stresses are found when the displacement of this node is zero during the unloading stage.

Change in stress at the crack tip. The change in stress at the crack tip was first proposed by first introduced by Sehitoglu and Sun [16] for studying plane strain fatigue crack closure. In a later work Sun and Sehitoglu [9] defined crack opening stress as the external applied stress for which the stress at the crack tip node changes from compressive to tensile, at this stage the crack is fully open. An extension of this technique was proposed by Wu and Ellyin [11]. In addition to using the definition of crack opening, they proposed that the closure stress could be obtained from the point in the unloading cycle where the crack tip stress changes from tensile to compressive. The analytical model presented in the next section shows that this technique has some limitations, indeed the closing stresses should not be estimated by this approach. Nevertheless, in order to compare the results obtained by the different techniques both opening and closing stresses will be calculated using this method.

Weight function technique. In the presence of closure after unloading, a compressive stress state exists along part of the crack faces. This residual stress can be used to calculate a (negative) residual stress intensity factor using a simple method such as the weight function method, introduced by Bueckner [17]. A negative residual stress intensity factor does not make any physical sense on its own, but by employing a superposition argument it may be equated to the change in (nominal) opening stress intensity K_{op} needed to overcome the residual stress field along the crack faces and open the crack to the tip. For R=0, the required opening stress intensity factor can be expressed as follows,

$$K_{op} = -K_{res} = \int_0^a \sigma(x) \cdot h(x,a)\, dx \qquad (1)$$

For more general R ratios, the opening stress, σ_{op}, may therefore be calculated as follows:

$$\sigma_{op} = \frac{K_{res} + C\sigma_{\min}\sqrt{\pi \cdot a}}{C\sqrt{\pi \cdot a}} \qquad (2)$$

where C is the usual geometric factor in the stress intensity expression (equal to 1 in the geometry studied here). This technique is simple and does not rely on measurements performed at a single point (or node). It is not particularly mesh

dependent since the approach is not over-dependent on a measurement taken close to the crack tip.

FEM results

Figure 4 and Table 1 present some of the FEM results obtained for σ_0/σ_{yield}=0.5 and R=0. Pictures a) and b) show the evolution of the opening and closing stresses (respectively) as the crack grows. As expected, the opening stresses give slightly different results depending on the technique adopted. The closing stresses obtained with the tensile tip stress method are differ a great deal from those estimated using the displacement of the 1st and second nodes behind the crack tip. Picture c) shows the variation of stress σ_{yy} at the Gauss point GP1 (see Figure 3) throughout a complete load cycle for a/a_0=2. The opening load is taken to correspond to the point (O) where σ_{yy} changes from compressive to tensile (loading stage) and similarly, the closing load is estimated from the unloading stage when the stress at the crack tip changes from tensile to compressive (C). Picture d) shows the variation of displacement (u_y) for the first and second nodes behind the crack tip for a/a_0=2. Here, the opening load corresponds to the point where the displacement becomes greater than zero and the closing load when the displacement becomes zero during the unloading stage. Table 1 summarises the results obtained by the different approaches.

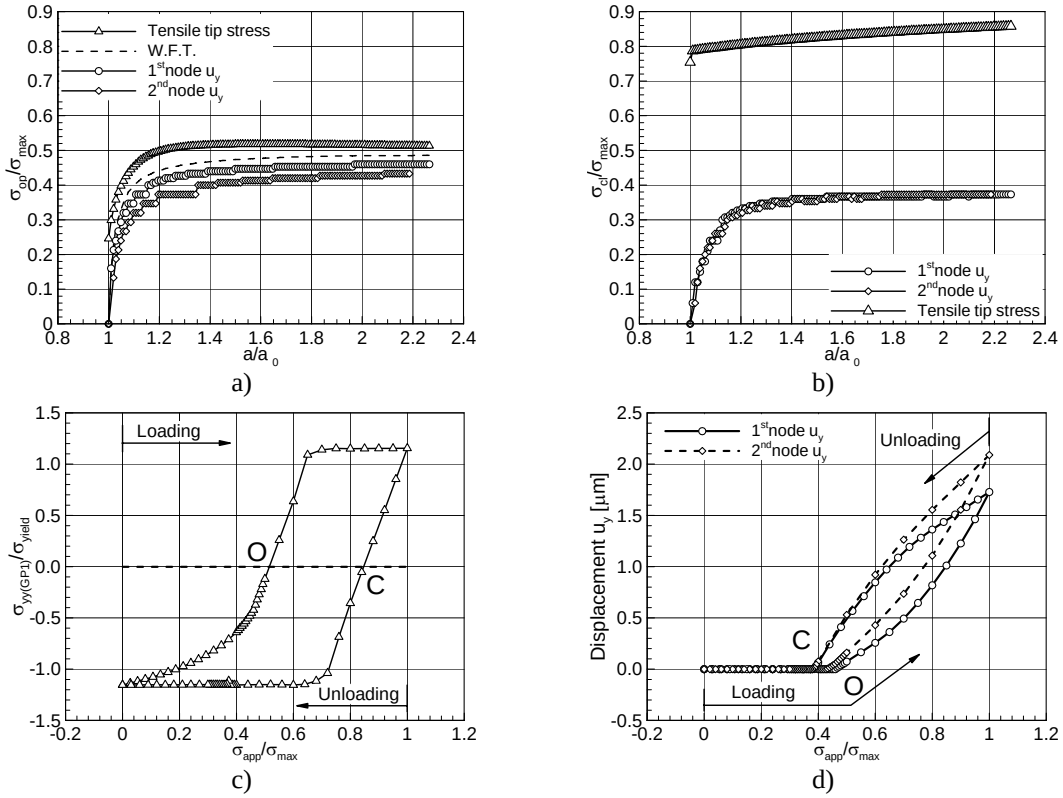

Figure 4. Finite element results for σ_0/σ_{yield}=0.5 and R=0: a) Opening stresses; b) Closing stresses; c) Stress σ_{yy} at GP1 and a/a_0=2.0; d) Displacement of the 1st and 2nd nodes behind the crack tip, a/a_0=2.0.

Table 1. Steady state closure results (a/a_0=2.2), FE modelling

Method	σ_{op}/σ_{max}	σ_{cl}/σ_{max}
Tensile tip stress	0.514	0.855
Weight function technique	0.485	---------
1st node u_y	0.460	0.373
2nd node u_y	0.433	0.373

3. Analytical modelling

The analytical mesomechanics model used was developed by Nowell [2] for crack closure under plane stress conditions. The model is formulated using dislocation dipoles making use of continuum elasticity and plasticity. In the present work only cracks growing under constant amplitude loading will be addressed. The model is formulated by defining an object function which incorporates the required boundary conditions. This is minimized, subject to constraints, using a standard quadratic programming approach. Full details are presented in [2]. In the model, a crack of length 2*a* exists in an infinite plate under conditions of plane stress. Three different sets of dislocation dipoles are used. The first represents the crack itself, the second represents the yield zone, ahead of the crack along a thin strip from $x = a$ to $x = d$ (see Figure 5). The third set of dipoles is used only for growing cracks, and represents the plastic wake which arises from the crack growing through the plastic zone.

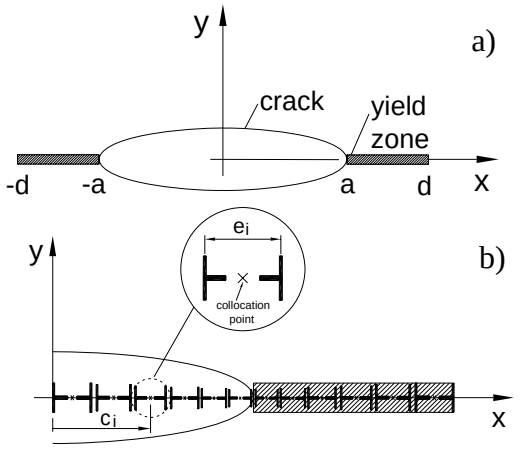

Figure 5. Nowell's model: a) co-ordinate system; b) displacement discontinuity dislocation dipoles.

Analytical model results

Figure 6 compares the results obtained for a growing crack under a remote applied load of σ_0/σ_{yield}=0.5 and R=0. Pictures a_1, b_1 and c_1 were obtained by placing the first collocation point very close to the crack tip (equivalent to 0.001 μm in the FE model). Picture a_2 was obtained by placing the first collocation point ahead the crack tip, corresponding to the position of the first gauss point in the FE model (2.5 μm from the crack tip (see Figure 3)). Similarly, b_2 is obtained by placing the collocation point 2.5 μm behind the crack tip. The results presented in Figure 6 b_2 have the same trend as the FE results presented in Figure 4c. It will be seen that the distance of the reference point from the crack tip means that yield does not occur immediately after opening (Figs 4c, $6a_2$. In contrast, Fig $6a_1$ shows an immediate onset of yield.

Figure 6c shows the variation of residual stress intensity factor (Eq (1)) with applied load. Comparing with Fig. $6b_1$ it can be seen that the sharp change in gradient makes identification of the opening and closing loads particularly straightforward. It is also clear that closure occurs earlier in this plot than is apparent in Fig $6b_1$. This is due to initial contact taking place remote from the crack tip itself.

Comparing Figure 6 a_1 and a_2 it may be seen to conclude that the opening load obtained from typical Gauss point locations overestimates the true opening load. Moreover it is clear that the closure load should not be calculated using the crack tip stress technique since the stresses at the crack tip are compressive during the whole unloading stage. In addition the analytical model shows that all these techniques of calculating opening and closing stresses are equivalent provided that the stresses and displacement fields are assessed sufficiently close to the crack tip, as presented in Table 2.

Conclusions

The results of the mesomechanics model presented here have shown that tensile tip stress method, node displacement method and the weight function technique are equivalent for predicting crack opening load, provided that the displacement and stresses are valuated at a very small

distance from the crack tip. It was also shown that as soon as a crack opens the implied elastic stresses at the crack tip are singular and tensile yielding is therefore predicted. The closing stresses should not be calculated using the tensile tip stress technique since compressive yield stresses are predicted during the whole unloading stage. Similar results have been obtained for other levels of remote applied loading, but space constrains preclude their presentation here.

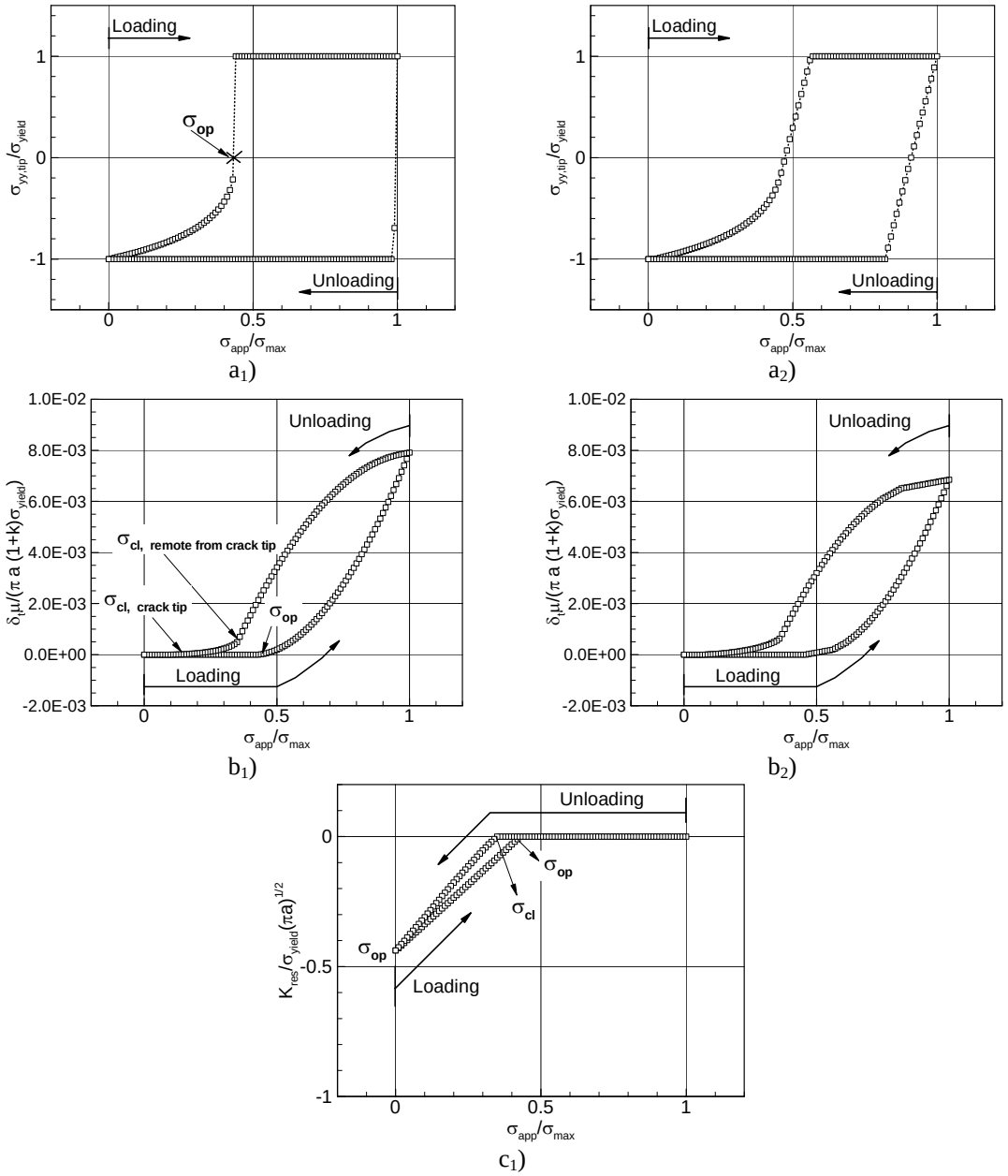

Figure 6. Analytical model results, σ_0/σ_{yield}=0.5 and R=0. In a_1 and b_1 the first collocation point is at 0.0001 μm from the crack tip; in a_2 and b_2 the first collocation point is at 2.5 μm from the crack tip. a_1 and a_2 – stress at the crack tip as a function of the applied stress; b_1 and b_2 - crack tip opening displacement as a function of the applied stress; c shows the residual stress intensity factor (caused by the contact stress) as a function of the applied stress.

Table 2. Closure steady state results, analytical model

Method	σ_{op}/σ_{max}	σ_{cl}/σ_{max}
Tensile tip stress	0.437	--------
Weight function technique	0.438	0.350
Displacement method u_y	0.439	0.350

Acknowledgements

Acknowledgements are due to the Portuguese Fundação para a Ciência e a Tecnologia (FCT) for providing a D.Phil. scholarship for P.F.P. de Matos (reference SFRH/BD/12989/2003, financed by POSI). Finite element calculations were carried out using the Oxford Supercomputing Centre (OSC).

References

[1] Elber, W., *Fatigue crack closure under cyclic tension.* Engineering Fracture Mechanics, 1970. 2(1): p. 37-44.
[2] Nowell, D., *A boundary element model of plasticity-induced fatigue crack closure.* Fatigue & Fracture of Engineering Materials & Structures, 1998. 21(7): p. 857-871.
[3] Hull, D. and D.J. Bacon, *Introduction to dislocations*. 4th ed. 2001, Oxford: Butterworth-Heinemann. 242 p.
[4] Solanki, K., S.R. Danaiewicz, and J.C. Newman Jr., *Finite Element modelling of plasticity-induced crack closure with emphasis on geometry and mesh refinemet effects.* Engineering Fracture Mechanics, 2003. 70: p. 1475-1489.
[5] McClung, R.C. and H. Sehitoglu, *On the finite element analysis of fatigue crack closure - 1. Basic modeling issues.* Engineering Fracture Mechanics, 1989. 33(2): p. 237-252.
[6] McClung, R.C. and H. Sehitoglu, *On the finite element analysis of fatigue crack closure - 2. Numerical results.* Engineering Fracture Mechanics, 1989. 33(2): p. 253-272.
[7] Fleck, N.A., *Finite element analysis of plasticity-induced crack closure under plane strain conditions.* Engineering Fracture Mechanics, 1986. 25(4): p. 441-449.
[8] Solanki, K., S.R. Danaiewicz, and J.C. Newman Jr., *A new methodology for computing crack opening values from finite element analyses.* Engineering Fracture Mechanics, 2004. 71: p. 1165-1175.
[9] Wei, S. and H. Sehitoglu, *Residual stress fields during fatigue crack growth* Fatigue & Fracture of Engineering Materials & Structures, 1992. 15(2): p. 115-128.
[10] González-Herrera, A. and J. Zapatero, *Influence of minimum element size to determine crack closure stress by finite element method.* Engineering Fracture Mechanics, 2005. 72: p. 337-355.
[11] Wu, J. and F. Ellyin, *A study of fatigue crack closure by elastic-plastic finite element analysis for constant-amplitude loading.* International Journal of Fracture, 1996. 82: p. 43-65.
[12] Ellyin, F. and J. Wu, *A numerical investigation on the effect of an overload on fatigue crack opening and closure behaviour.* Fatigue & Fracture of Engineering Materials & Structures, 1999. 22: p. 835-847.
[13] Wei, L.W. and M.N. James, *A study of fatigue crack closure in polycarbonate CT specimens.* Engineering Fracture Mechanics, 2000. 66: p. 223-242.
[14] Dougherty, J.D., J. Padovan, and T.S. Srivatsan, *Fatigue crack propagation and closure behaviour of modified 1070 steel: Finite lement study.* Engineering Fracture Mechanics, 1997. 56(2): p. 189-212.
[15] Solanski, K.N., *Two and three-dimensional finite element analysis of plasticity-induced fatigue crack closure - A comprehensive parametric study*, in *Department of Mechanical Engineering*. 2002, Mississsipi State University. p. 195.
[16] Sehitoglu, H. and W. Sun, *Modelling of Plane Strain Fatigue Crack Closure.* Journal of Engineering Materials and Technology, 1991. 113: p. 31-40.
[17] Bueckner, H.F., *A novel principle for the computation of stress intensity factors.* Zeitschrift fur Angewandte Mathematik und Mechanik, 1970. 50(529-545).

INFLUENCE OF OXIDE FILM ON CRACK INITIATION IN LOW CYCLE FATIGUE

Z. Azari

Laboratoire de Fiabilité Mécanique, Enim, 57045 Metz, France

M. Abbadi

LTI, Research Center Henri Tudor, 70 Rue de Luxembourg, L-4221 Esch-sur-Alzette, Luxemburg

H. Moustabchir, M. Lebienvenu

Laboratoire de Fiabilité Mécanique, Enim, 57045 Metz, France

Abstract

The influence of fatigue cycling on the oxidation kinetic and crack initiation of a Cr-Mo steel has been studied. For this purpose, high temperature low cycle fatigue tests were performed in both the absence and presence of mechanical cycling. Then the number of cycles to crack initiation has been determined using two methods based on the evolution of the oxide penetration and the crack length, and the activation energy. Based on microscopic observations and experimental results, a new criterion assimilating the average thickness of the oxide layer to a microcrack is proposed. It appears that the number of cycles to crack initiation corresponds to a microcrack equivalent to the average size of the grain.

***Keywords*:**
Low cycle fatigue;Temperature; Oxide film; Crack initiation; Life duration

1. Introduction

Several works devoted to oxidation phenomena [1-7] showed that from a temperature higher than 550°C, steel oxidation in air contributes, at gas/metal interface, to the formation of three oxide compact layers Fl_2O_3, Fe_3O_4 and FeO.

The tests performed by the last authors pointed out that oxide films take place with the aid of a diffusive dual flow from the steel towards the exterior and from the oxygen towards the interior.

The oxidation kinetics of many metals and alloys, capable to develop oxide layers at high temperatures, are essentially of linear, parabolic or logarithmic form.

The parameters needed for the formulation of different equations are:

D_i (i=1-3): diffusion coefficients,

t: time, and

X_i: oxide layer thickness.

The linear law is defined by the following equation:

$$X_1 = D_1 t \qquad (1)$$

The parabolic law is applied at high temperatures and is formulated as:

$$X_2^2 = D_2 t \qquad (2)$$

In low temperature domain, the oxidation of a large number of materials respects the following logarithmic evolution:

$$X_3 = D_3 \log(B\,t+1) \qquad (3)$$

where B is a constant.

The diffusion coefficient D follows the Arrhenius law, given by:

$$D = D_0 \exp\left(-Q/RT\right) \qquad (4)$$

where D_0 is the diffusion coefficient, Q the activation energy characterizing the oxidation, R the universal gas constant and T the absolute temperature.

If we plot log D vs. $1/T$, for different temperatures, a linear curve is obtained whose slope enables to determine Q.

In the case of steel materials, Paidassi and Bernard [8] found an activation energy of 36000 cal/mole, for a temperature range varying from 400 to 600°C. However, Birchenal [9] found a higher activation energy of 45000 cal/mole for the same temperature range.

According to Tikhomirov et al. [10], the mass increase Δm (mg/cm^2) in isothermal conditions, follows a parabolic law of the form:

$$\Delta m^2 = k\,t \qquad (5)$$

The growth constant k, function of the diffusion coefficient value D and the effect of temperature, is formulated as:

$$k = k_0 \exp(-Q/RT) \qquad (6)$$

where k_0 is a constant.

At high temperature, the environment plays an important role in crack initiation. The oxidation in air, at temperatures varying from 500 to 1000°C, encourages the diffusion kinetic of the oxide inside the metal causing, in the case of a mechanical loading, a crack initiation. The latter occurs at the specimen surface.

The microstructural embritlment of grain boundary due to the environment (oxidation during high temperature fatigue) leads to the formation of initiation sites especially privileged as the strain is important according to Boettner, Laird and Evily [3], Vernault et al. [11] and Molins et al. [12].

According to Levaillant et al. [13], the detailed examination of crack initiation in low cycle fatigue comes up against the definition of even a microcrack length, which is directly related to the resolution of the microscopic means used. So, in the absence of a general agreement on the crack initiation definition, it is preferable to report the number of cycles to crack initiation N_a for a crack conventional length. This length might be of 25 μm , which corresponds to a defect size comparable to the grain size.

2. Experimental procedure

2. 1. Testing apparatus description

The real working conditions of the components here investigated are T= 610°C and $\Delta\varepsilon_t$ =0.74%. Traction-compression tests were performed on a 10 t servo-hydraulic testing machine. The heating system of the specimen is ensured by a resistance furnace and the temperature measurement is controlled by a thermocouple fixed on the specimen by means of an asbestos cord.

2. 2. Material

The tests were performed on chromium steel material whose grain mean diameter is 18 μm . The chemical composition of this material is given in Table 1 while the mechanical properties at room temperature, are illustrated on Table 2.

Steel	C	Cr	Mn	Mo	Si
wt.%	0.27	0.98	0.53	0.98	0.26

Table 2: Chemical composition of the material used (in wt.%).

Material	chromium steel
σ_R (MPa)	769
σ_e (MPa)	350

Tableau 2: Material mechanical properties at room temperature.

The tests were achieved at imposed total strain amplitude $\Delta\varepsilon_t = 0.74\%$ and a strain rate of 3.2 x 10^{-3} s^{-1}. The imposed signal is triangular ensuring thus a constant strain rate. Specimens are assumed to be fractured if a 50% rapid drop of the load recorded at the first cycle is observed.

3. Results and discussion

3. 2. Determination of oxidation parameters

3. 2. 1. In the absence of mechanical cycling

The oxidation of specimens was performed at three different temperatures, namely 610, 800 and 1000°C and various durations in order to manifest the effect of oxidation in air at high temperature of the chromium steel. This purpose enabled to quantify the average thickness of the oxide film at the material-oxide interface and the growth kinetic of the material.

Observations made on the cross section of three specimens showed the nature of oxide penetration inside the material. Fig. 1, related to an oxidation duration of two hours at 610°C, shows no penetration of the oxide into the material.

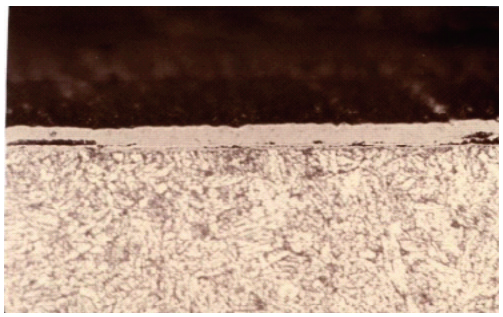

Fig. 1: Oxide layer evolution for two hours at T= 610°C in the absence of mechanical loading.

Afterwards, five tests were performed at various temperatures in order to determine:

- the kinetic law of the specimen mass evolution,
- the activation energy Q_0, (Eq. 6).

From (Eq. 6), the plot of ln$k$ versus 1/T for different temperatures and various cycles is characterized by a straight line whose slope enables to calculate the activation energy Q of the phenomenon.

The activation energy value, in the absence of cycling denoted Q_0, is 40100 cal/mole.

3. 2. 2. In the presence of mechanical cycling

In the case of isothermal tests, with external loading, the oxidation kinetic may be written as:

$$X_1^2 = D_1\, t = D_0\, t \exp(-Q_1 / RT) \quad (7)$$

The activation energy Q_1 is assumed to be variable and to evolve at each cycle, see Table 3. This evolution of the activation energy may be formulated as:

$$Q_1 = Q_0\,(1 - A\,N^{\alpha}) \qquad (8)$$

where A and α are constants, and N is the number of cycles.

The evolution kinetic of the specimen mass, at each cycle, is a law of the form:

$$\Delta m_1^2 = k_1\, t = k_0\, t \exp(-Q_1 / RT) \quad (9)$$

The values of A and α are found to be 18x10^{-4}/cycle and 0.77, respectively.

The study of the kinetic and oxidation laws for the steel material of the present investigation was completed by microscopic observations.

The evolution of the oxide during mechanical cycling has been achieved with respect to the following conditions:

- the virgin specimen is placed into the oven at a temperature of 610°C during a constant period of two hours. No oxide penetration in the material was revealed (Fig. 1). It is observed that for the chromium steel the oxide saturation time is around one hour,
- the virgin specimen is then cycled and tests are stopped regularly at 100, 200 and 500 cycles. The oxide growth during cycling is observed by means of slight microscopy. The results are shown in Figs. 2, and
- at 550 cycles, the crack initiates in the oxide and advances inside the material over a depth of 0.21 mm.

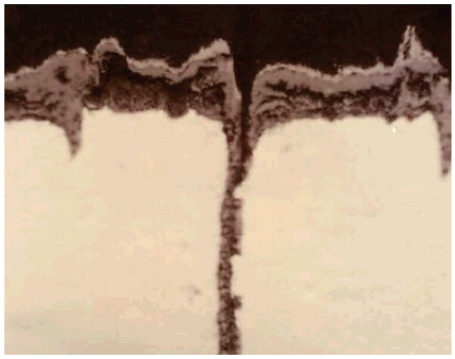

Fig. 2: Influence of the oxide on the chromium steel in the presence of mechanical cycling.

Three stages are observed:

- a first stage where the oxide presence is abundant, which proves its harmfulness in the beginning of cycling and shows the significant role of the chemical damage in the initiation phenomenon: the aspect of stage I is analogous to an intergranular cleavage,
- a second stage where the growth of an oxidized crack is observed. This growth is due to two mechanisms, one mechanical and the other chemical. The interaction between the two last phenomena is characterized by an acceleration of the crack growth: the aspect of stage II is mixed between the first and the third stage that are locally juxtaposed,
- a third stage, where the presence of the oxide is not so considerable, the effects of mechanical cycling are predominant and the crack propagation is very fast: the aspect of stage III is characterized by the formation of fatigue striations whose convexity is turned in the propagation direction.

4. Proposition of a new criterion taking into account the oxide thickness preceding the cycling onset

Based on the previous experimental results, a new approach which determines the number of cycles to crack initiation was developed. This number of cycles is defined as that corresponding to stage I and characterized by the oxide film growth and fracture. This criterion is based on two assumptions:

The first takes into consideration the presence of an adhesive oxide layer from the first cycle. This layer will crack when the loading is reversed (compressive stage). A new penetration of the oxide takes place during the mechanical cycling. This phenomenon is assumed to evolve during each mechanical cycling.

For the second, the average thickness of the adhesive oxide layer is assimilated to a microcrack.

Beyond a thickness X^* corresponding to the time necessary for the crack initiation, the mechanism is modified. A mechanical crack strongly oxidised will be then substituted for the crackled oxide.

T C°	k_0 $g^2/cm^4.s$	k $g^2/cm^4.s$	D_0 cm^2/s	D cm^2/s
924		$2.63x10^{-8}$		$1.056 x10^{-7}$
795		$3.872x10^{-9}$		$1.4x10^{-8}$
704	0.516	$6.36x10^{-10}$		$2.45x10^{-9}$
610		$7.1x10^{-11}$	1.89	$2.78x10^{-10}$
560		$1.8x10^{-11}$		$6.65x10^{-11}$

Table.4:The different diffusion parameters in the absence of mechanical cycling.

Four fatigue tests were carried out at a temperature of 610°C for a total strain amplitude of $\Delta\varepsilon_t$=0.74%. Then, the tests were stopped at a number of cycles determined for each test, namely 100, 200, 400 and 550 cycles. The objective consists in measuring the length evolution of the largest crack and computing the oxide penetration (Eq. 10).

$$X_2 = \left(D_0 \exp\left(\frac{-Q_0\left(1 - A N^{\alpha}\right)}{R\,T} \right) t \right)^{1/2} \quad (10$$

with Q_0=40100 cal/mole, R=2cal/mole/K, D_0=1.89 cm^2/s, α=0.77, A=18x10^{-4}/cycle and N indicates the number of cycles.

To take into account the preliminary holding temperature of one hour and before the starting of the test, the initial thickness of the oxide layer will be assimilated to a microcrack of length $X_0 = a_0 = 9.64\ \mu m$, as justified by Fig. 3.

For various numbers of cycles N, the crack length a will be the sum of the crack length a_i measured after N cycles increased by a_0.

$$a = a_0 + a_i(N) \qquad (11)$$

where $a_i(N)$ indicates the crack length measured after N cycles.

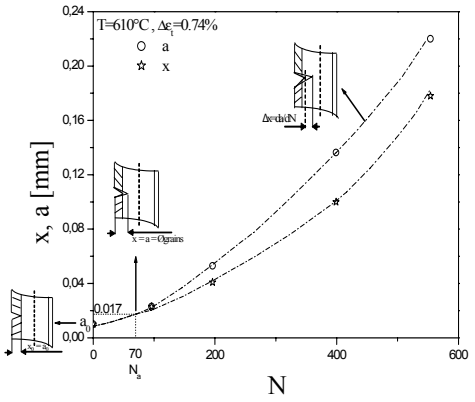

Fig. 3: The growth of the oxide layer and crack length at T=610°C for stages I and II.

The evolution of both the crack length and the oxide penetration shows a nonlinear behaviour. Moreover, this curve shows that from a number of cycles greater than 100, the crack growth is faster than oxide penetration.

A first method for the determination of the number of cycles to crack initiation consists in detecting the separation point between the two curves of Fig. 3. This separation occurs at 17 μm, which corresponds to a number of cycles to crack initiation of 70 cycles.

The second method consists in plotting the variations of the activation energy Q as a function of the applied load. The curve fitting of data at low and high loading regimes shows a transition point of coordinate (18420 N, 38525 cal/mole). From the value of the activation energy corresponding to the previous point, the number of cycles to crack initiation of 64 cycles, corresponding to 16 μm, is derived (Fig. 15b). It is important to note that the two methods give similar results. Moreover, the length of crack initiation corresponds to the mean grain diameter (~18 μm).

The hypotheses take into account:

- the presence of an oxide layer since the first cycle. This layer increases by the mechanism of oxygen diffusion with the preliminary holding time,
- the average thickness of the oxide layer is assimilated to a microcrack.

These two hypotheses, completed by the application of an Arrhenius growth law of the oxide layer permitted to illustrate the variations of the oxide film during the mechanical cycling.

During the stage initiation (stage I), these two curves are similar. However, beyond the number of cycles to crack initiation N_a, the crack growth is faster than that of the oxide.

Fig. 4 depicts the evolution of the crack length during three stages. Right from the first cycles (stage I), the oxide film growth follows a parabolic law. The diffusion coefficient obeys the Arrhenius law. The cracking is then triggered by the failure of the oxide film which evolves until reaching a critical size equivalent to the average grain size of the material. The number of cycles corresponding to this grain size is considered to be the number of cycles to crack initiation.

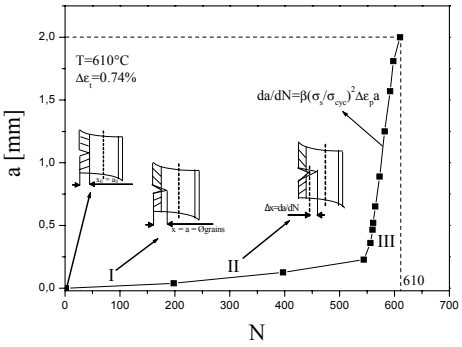

Fig. 4:Crack length evolution during the three stages.

Considering the oxide thickness X, the crack length a and the number of cycles to failure N_a:

N=0, X=X_0=a_0=the initial thickness of the oxide film,

during the test: $N < N_a$ and a=X,

at the initiation stage: $N = N_a$, X=X^*≈ the average grain size of the material.

Stage II is governed by the interaction between the oxide film and the mechanical loading. The crack growth is due to the external mechanical loads applied to the specimen and the oxidation chemical phenomena. After each cycle, the oxide film cracks and propagates on the order of ΔX value.

The penetration rate of the cycled oxide layer (per cycle) is then written:

$$\frac{da}{dN} = \Delta X \qquad (12)$$

In stage III, the crack growth propagation is so high that the oxide influence is minimized. This stage is controlled by the only effect of the mechanical loading.

An equation that defines the crack growth propagation is suggested by Tomkins [14] under the following formulation:

$$\frac{da}{dN} = \beta \left(\frac{\Delta\sigma}{\sigma_T} \right)^2 \Delta\varepsilon_p \, a \qquad (13)$$

where:

β = 1+2n, with n indicating the work hardening coefficient; here n=0.2,

$\Delta\sigma$ = the variation of the applied load,

σ_T = the ultimate strength,

$\Delta\varepsilon_p$ = plastic strain amplitude, and

a = the crack length.

According to [14], σ_T may be equal to the ultimate load [5] or the cyclic tensile strength [13].

Concerning the steel here studied, the crack growth rate has the following form:

$$\frac{da}{dN} = \beta \left(\frac{\sigma_s}{\sigma_{cyc}} \right)^2 \Delta\varepsilon_p \, a \qquad (14)$$

σ_s = the monotonic yield stress,

σ_{cyc} = the cyclic elastic stress.

5. Conclusion

Fatigue tests at a temperature of 610°C and a strain range of 0.74% were carried out on comercial steel. The effect of the oxide on the life time reduction prompted us to propose a criterion based on the existence of a microcrack having the same size as the thickness of the mean oxide layer.

The parameters that define the diffusion such as the activation energy and the initial coefficient of diffusion are determined.

An evolution law of the activation energy was given in order to take into account the deterioration of the material during the mechanical cycling. Afterwards, the values of the oxide penetration were derived.

The real crack length and oxide penetration, during cycling, are compared and allowed to define the number of cycles to crack initiation.

Another method, based on the variations of the activation energy as a function of the number of cycles, is proposed.

We show, for the material here investigated, that the number of cycles to crack initiation calculated from the two methods, namely 64 and 70 cycles, corresponds to a crack of 17 μm length which matches the average grain size.

Fig.5 depicts the crack growth propagation as a function of the number of cycles. This curve grows linearly with respect to a weak slope in a first stage until 544 cycles. Then, it increases abruptly until the failure. Furthermore, the crack growth propagation in stage III is around 43 times that of stage II.

The evolution of crack growth propagation during stage III is found to be in good agreement with results predicted by Eq. (14).

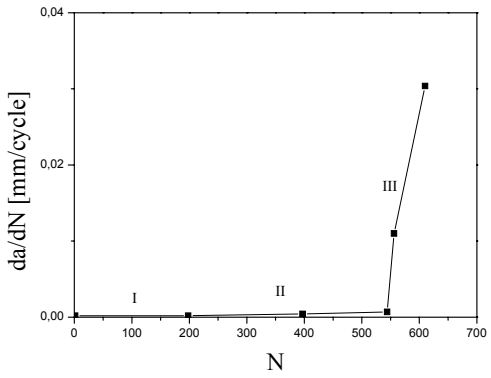

Figs. 5 Crack growth propagation as function of the number of cycles.

References

[1] T. Broom, A. Nicholson, Journal "Institute of metals 89", 83,1960.

[2] C. Laird, D.J. Duquette, "Corrosion Fatigue", Nice, Edition Huston, 82, 1972.

[3] R.C. Boettner, C. Laird, A.J. Mc Evily, "Trans AIME 223", 379, 1965.

[4] C. Levaillant, B. Rezgui, "Effec of environnement and hold times on high temperatures low cycles fatigues behaviour of 316 L stainless steel", 3rd Int. Conf. on Mechanical Behaviour, Cambridge, 1978.

[5] K.U. Snowden, Acta Met. 12, 265, 1964.

[6] J.W. Swanson, H.L. Marcus, Met. Trans., Vol. 9A, 29, 1978.

[7] J.L. Remy, J. Reuchet, Rev. Metall., 439, 1982.

[8] Paidaissi, J. Bernard, Bull. Soc. Chim. F., 1958, 1964.

[9] C.E Berchenall, Trans. AIME, 197, p. 889, 1951.

[10] V.I. Tikhomirov, V.V. Ipatiev, Nauk. URSS, 95 (1954), 305.

[11] C. Vernault and J. Mendez, "Fatigue damage in a 316L type stainless steel induced by surface oxide layers", Annales de Chimie Science des Matériaux, Vol. 24, Issues 4-5, 1999, pp. 351-362

[12] R. Molins, G. Hochstetter, J. C. Chassaigne and E. Andrieu, "Oxidation effect on the fatigue crack growth behaviour of alloy 518 at high temperature", Acta mater., Vol 45, N°2, 1997, pp. 663-674.

[13] C. Levaillant, B. Rezgui, "Effet of environnement and hold times on high Temperatures low cycles fatigue Behaviour of 316 L Stainless Steel", Third. Int. Conf. on mechanical, Behaviour, Cambridge, 1978.

[14] B. Tomkins, "Fatigue crack propagation and analysis", Philip. Mag. 16 (1969), pp. 1041.

FRICTION STIR WELDED ALUMINIUM ALLOY 6063-T6: MECHANICAL CHARACTERIZATION, FATIGUE TESTS AND DEFECTS IDENTIFICATION

P.M.G.P. Moreira, F.M.F de Oliveira, P.M.S.T. de Castro
Departamento de Engenharia Mecânica e Gestão Industrial,
Faculdade de Engenharia da Universidade do Porto, Portugal

Abstract

Friction stir welding (FSW), a solid-state welding process developed and patented by the TWI in 1991, is finding increasing use. It emerged as a welding technique to be used for high strength alloys that were difficult to join with conventional techniques. The process was developed initially for aluminium alloys, but since then FSW was found suitable for joining a large number of materials.
In the aircraft manufacturing industry, riveting is currently the preferred manufacturing process for fuselage structures.
Nevertheless, FSW is emerging as an appropriate alternative technology due to low distortion, high strength of the joint and high processing speeds.
In this work a study of the influence of the FSW technique on the fatigue life of the aluminium alloy 6063-T6 is carried out. Fatigue tests on notched specimens were carried out further to examination of microstructure and microhardness measurements. Scanning electron microscopy (SEM) is used to identify microscopic features, as striations and welding defects.

Keywords: Friction Stir Welding, Fatigue life, Scanning electron microscopy, Microstructures.

1. Introduction

In order to evaluate the influence of friction stir welding (FSW) on the fatigue life of notched aluminium 6063-T6 specimens, similar base material and welded specimens were fatigue tested at several stress levels. Specimens were loaded perpendicular to the rolling direction and fatigue life was defined as the number of cycles to failure. Hardness tests were also performed and scanning electron microscopy (SEM) analysis was performed in order to identify welding defects and metallurgical details of fatigue cracks such as fatigue striations.

2. Specimens

Welded specimens

Aluminium alloy 6063-T6 plates were friction stir (FS) welded with the parameters: 1000*rpm* pin-tool rotation speed; 9.17*mm/s* welding speed; 4.5*kN* axial force. The welded sheet dimensions are 300 *x* 100 *x* 3 *mm*. From this sheet 13 fatigue specimens, Fig. 1 were machined. To ensure that a fatigue crack initiates and propagates through the specimens middle line two notches were introduced in the specimens. The notch machined in the specimens

introduces a stress concentration factor of 2.82, calculated using the Dual Boundary Element Method software "Cracker" [1].

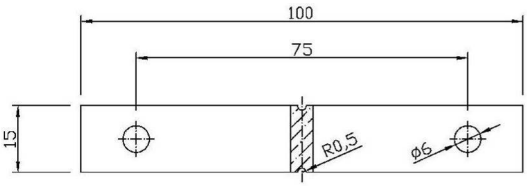

Figure 1**:** Specimens geometry, 3*mm* thickness

Unwelded specimens

To estimate the influence of FSW on the fatigue lives, base material specimens, without welding, were manufactured. The 6063-T6 alloy was only available as a rectangular tube with 4*mm* of thickness. To compare the results of the welded and unwelded specimens the thickness of the specimens machined from the tube had to be reduced to 3*mm*.

3. Material characterization

The material used in this study is the aluminium alloy 6063-T6 with Mg and Si as major alloying elements. T stands for products that had an increase in strength due to thermal treatments, with or without supplementary strain-hardening operations and the digit 6 after the T means that it is a solution heat-treated and artificially aged, [2]. The mechanical properties of the aluminium alloy 6063-T6 can be found in [3].

4. Hardness tests and metallographic analysis

Friction stir weld visual analysis

The nomenclature shown in Fig. 2 was used to identify the different surfaces of specimens.

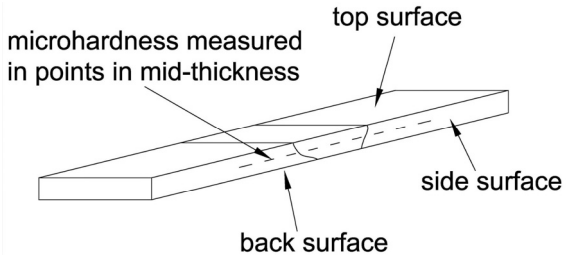

Figure 2: Specimens surface definition.

The first step was the visual analysis of the FS weld. Flaws or defects were not detected on the top and back surface of the weld, as shown in Fig. 3.

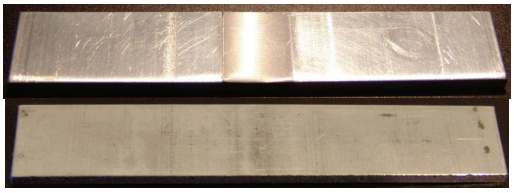

Figure 3: Visual inspection of FSW joints, front and back surfaces.

Since the sheet side faces perpendicular to the weld line were cut by guillotine it is possible to identify the different hard zones in each face, Fig. 4. This type of examination is well documented by several authors, e.g. [4, 5].

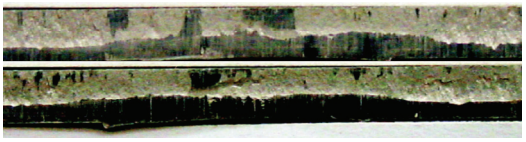

Figure 4: The two side surfaces of the plate, cut by guillotine.

In both figures the darker zone, in the centre of the image, indicates the material that was affected by the welding process. The increase in the darker area in the weld region is expected to be a characteristic of lower values of hardness when compared to those of the base material.

Hardness tests

The hardness profiles can assist in the interpretation of the weld microstructure and mechanical properties. Since the welded and unwelded specimens were machined from material from different sources, welded sheet and 4*mm* thickness tube respectively, hardness tests were performed in all sources of material. The results of hardness Brinell (HB) tests performed with parameters $F = 62.5kg$ and diameter $\phi = 2.5mm$ and hardness Vickers (HV) with 1*kgf* are presented in Table 1. Results of these measurements are in the range of properties presented in the literature. Also, when comparing HV results, material of tube 3*mm* thick and welded sheet material present quite similar values of hardness.

	HB	HV
Tube 3 mm thick	72.9	77.2
Tube 4 mm thick	70.2	73.8
Welded sheet	78.2	76.2

Table 1: Al 6063-T6 hardness test results.

After the hardness characterization of the material, microhardness tests were performed in order to characterize the hardness profile in the vicinity of the weld affected area in the FSW specimens. The microhardness tests were performed with a 200*gf* load. The microhardness tests were performed in the top surface and in the side surface at half of the specimen thickness after polishing the specimen. The HV microhardness results are presented in Fig. 5. Hardness drastically decreases in the weld-deformed zone; the average hardness of the nugget zone being significantly lower than the hardness of the base alloy. It was also possible to identify higher hardness values when measuring the hardness at the side surface.

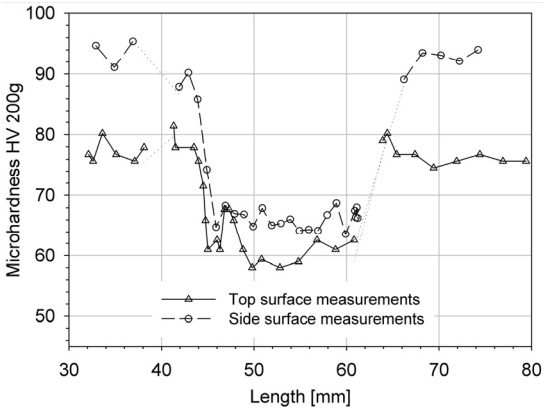

Figure 5: Microhardness profile.

Metallographic analysis

The aim of this work is the analysis of microstructural changes due to the FSW process. A specimen of the welded material (MW) and another from the base material (MB) were analyzed. Microstructures were acquired according to the scheme presented in Fig. 6.

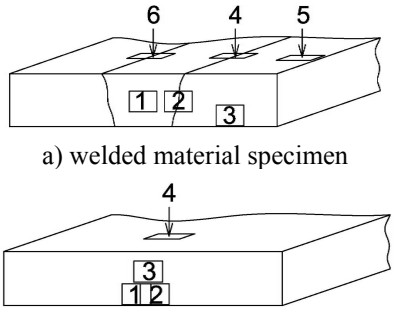

a) welded material specimen

b) base material specimen

Figure 6: Scheme of microstructural analysis.

Microstructures of the FS welded specimen. Microstructures MW1, MW2 and MW3 of the FS welded specimen were acquired in the side surface and microstructures MW4, MW5 and MW6 were acquire in the top surface, as presented in Fig. 2. Microstructures MW2, MW4 and MW6 correspond to zones of transition between material affected by the welding and base material. Microstructures MW3 and MW5 represent the base material.

Microstructures MW2 and MW3 are shown in Fig. 7. In microstructure MW2 it is possible to identify the transition between the zone affected by the welding process and the base material, delimited by the black line. The material affected by the welding process presents a fine stir grain structure, and the material near the heat affected zone (HAZ) presents regular grains. In the FS welded zone very fine recrystallized grains are present due to the high deformation and high temperature during the process. Microstructure MW3 shows larger grains near the plate free surface and smaller grains outside this layer.

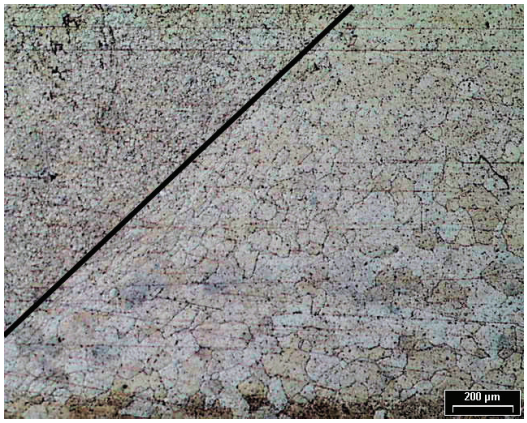

a) microstructure MW2

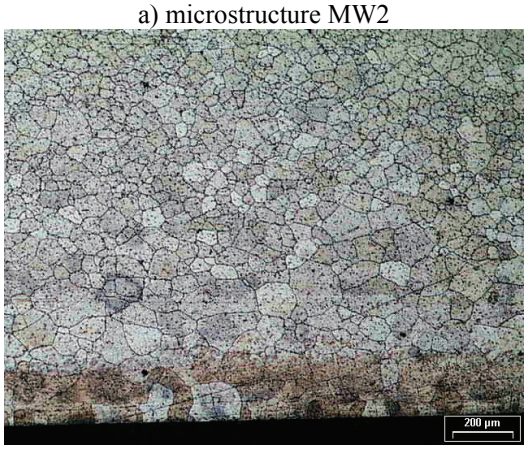

b) microstructure MW3

Figure 7: Welded specimen microstructures, surface perpendicular to the top surface.

To determine the grain size diameter, microstructure MW3 was divided in two zones, zone 1 near the plate edge and zone 2 outside the plate edge. In each zone the grain diameter was measured in 5 grains. In each grain an average of three measurements was calculated. The results obtained are presented in Table 2.

zone 1	Diameter [mm]			
grain	1	2	3	average
1	125.4	187.4	167.6	160.1
2	94.8	103.4	132.8	110.3
3	107.2	174.7	125.8	135.9
4	262.3	193.7	109.6	188.6
5	124.0	136.1	114.4	124.8
average				144.0
zone 2	Diameter [mm]			
grain	1	2	3	average
1	67.2	82.7	72.8	74.2
2	66.6	77.2	84.0	76.0
3	50.4	60.2	57.5	56.0
4	71.0	79.1	68.8	72.9
5	77.1	73.1	65.5	71.9
average				70.2

Table 2: Grain size in microstructure MW3.

Microstructures of the base material specimen. Microstructures MB1, MB2 and MB3 of the base material specimen were acquired near the plate free edge in the side surface and microstructure MB4 was acquired in the top surface near the middle width plane, as presented in Fig. 6. Fig. 8 presents the microstructures MB2 and MB3.

To determine grain size diameter in microstructure MB2, the microstructure was divided in two zones, zone 1 near the plate edge and zone 2 outside the plate edge. The results obtained are presented in Table 3.

a) microstructure MB2

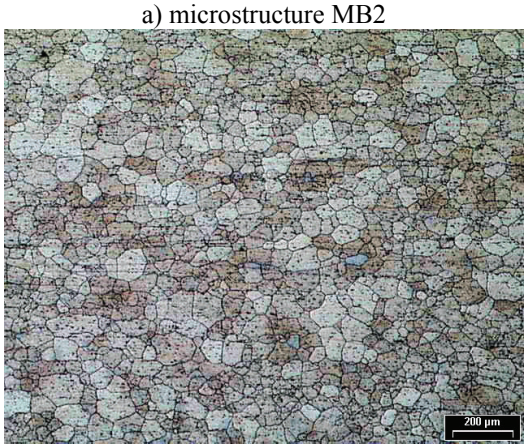

b) microstructure MB3

Figure 8: Base material specimen microstructures, side surface.

zone 1	Diameter [mm]			
grain	1	2	3	average
1	269.8	226.2	257.2	251.1
2	193.8	179.0	171.5	181.5
3	211.4	184.1	158.3	184.6
4	252.2	248.0	245.7	248.6
5	289.6	197.6	204.0	230.4
average				219.2
zone 2	Diameter [mm]			
grain	1	2	3	average
1	97.4	68.1	90.8	85.4
2	70.9	71.9	62.6	68.5
3	76.0	67.9	74.5	72.8
4	64.5	45.3	47.7	52.5
5	130.8	53.9	73.5	86.0
average				73.1

Table 3: Grain size in microstructure MB2.

The grain size diameter obtained in microstructure MB3 is presented in Table 4.

	Diameter [mm]			
grain	1	2	3	average
1	112.2	130.5	110.6	117.8
2	76.7	42.1	67.7	62.2
3	117.4	80.8	100.3	99.5
4	38.1	38.9	42.4	39.8
5	42.4	42.4	104.9	63.2
average				76.5

Table 4: Grain size in microstructure MB3.

Notes on the microstructural analysis. Although base material microstructures, MB, were obtained from a rectangular tube, and FS welded plate was supplied in a sheet form, it was verified that the grain size diameter on top or back surface has similar average diameters, between 70.2*mm* and 76.5*mm*, in all microstructures. Middle thickness grain diameters of 219.2*mm* and 144.0*mm* were measured in the unwelded specimen, and in the base material region of the welded specimen, respectively. This difference is explained by the different fabrication processes. Grains at surface of extrusion have recrystallized because of more working and heating, while grains in the interior of the extrusion are unrecrystallized [6]. FS welded specimens were supplied in sheet shape with the thickness of 3*mm*. Base material specimens were machined from a rectangular tube profile with an initial thickness of 4*mm* that was reduced to a final thickness of 3*mm*.

Interpretation of hardness results. An increase of the hardness profile when measuring the hardness at the side surface was identified in Fig. 5. This difference is identified in the zone not affected by the welding process, base

material. It is concluded that this difference is due to the different grain size of these two regions. The grain near the top or back surface has average diameters between 70.2*mm* and 76.5*mm*. Grains near the external surfaces have an average diameter of 144.0*mm* in the FS welded specimen, and 219.2*mm* in the base material specimen.

5. Tensile tests

Tensile tests were performed to determine the mechanical properties of the material. Five welded specimens were tested. In the first three welded specimens, strain was measured in an area which includes welded and unwelded material (area with 25*mm* length). Since the welded zone is 14 *mm* wide, in the other two welded specimens strain values were only acquired in a 6*mm* range, only inside the welded material area. This procedure was carried out to obtain the material behaviour of only the welded material. Six specimens of unwelded material were tested, three with 3*mm* thickness, and three with 4*mm* thickness. The tensile test specimens were identified with three letters followed by two numbers separated by a dot. The first letter is a T which indicates that it is a tensile test specimen; the other two letters, UW for the unwelded specimens and FW for the FS welded specimens, indicate the specimen type. The first number after the letters indicates the specimen thickness. In the case where strain values were acquired in a 6*mm* length zone, the reference '.6' was included at the end of the numbering. In FS welded specimens the rupture occurred in the external part of the weld line, in a transition between welded and unwelded material zone. Also, a decrease in resistant area in the other side of the weld line was noticed.

To identify the influence of FS weld on the specimen tensile properties, the σ *vs* ε records of all tensile tests are plotted in Fig. 9. Similar results were obtained in tests of base material with 3 and 4*mm* thickness. It can be concluded that the operation of thickness reduction did not affect the material properties. Yield stress and rupture stress of FS welded specimens have lower values than unwelded specimens. The welding process leads to a decrease of the material mechanical properties.

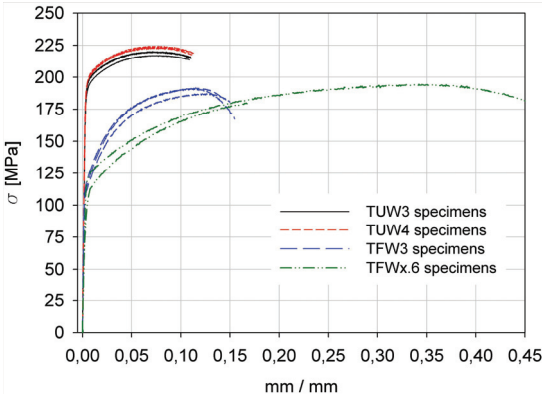

Figure 9: Tensile test results of unwelded and welded specimens.

6. Fatigue tests

The fatigue tests were carried out in a MTS servo-hydraulic machine of 250*kN* capacity. Fatigue tests were performed at several different percentages of the minimum yield stress welded material. In fatigue tests the following parameters were used: $\sigma_{min}/\sigma_{max}=R = 0.1$ and frequency $f = 8Hz$. Due to the lack of availability of larger amounts of welded material and since the objective was to obtain a S-N plot for each stress level a few specimens of each type of material (unwelded and welded material) were tested, making a total of 25 tests. The parameters used for each level are

presented in Table 5 [% s_y refers to material properties of welded material yield stress (s_y=113*MPa*)]. As example, the chosen values of remote stress used in tests 90%, 75% and 60% correspond to 53.1%, 44.2% and 35.4% of the base material s_y stress.

s_y	s_{remote} [*MPa*]	s_y	s_{remote} [*MPa*]
140%	158.2	80%	90.4
100%	113.0	70%	79.1
90%	101.7	60%	67.8

Table 5: Fatigue tests parameters.

In the fatigue tests carried out it was found that FSW specimens displayed longer fatigue lives than similar non-welded specimens tested under the same loading conditions, Fig. 10. Even at 158.2*MPa* maximum stress level, 140% of the s_y of the FS welded specimens, FS welded specimens presents longer fatigue lives. Biallas *et al.* [7] found in their study for another aluminium alloy that using high welding speeds similar fatigue lives were obtained testing FS welded specimens and base material specimens.

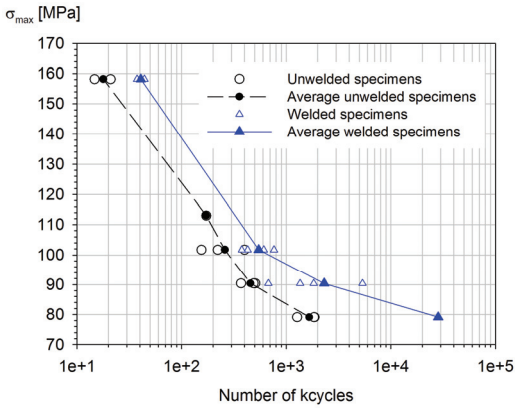

Figure 10: Fatigue life results.

7. Scanning electron microscopy analysis

SEM was used to identify microscopic features, as welding defects and metallurgical details of fatigue cracks such as fatigue striations. Two welded specimens and two unwelded specimens were analysed. Notwithstanding the good properties obtained in welded specimens fatigue tests, some defects were identified. Inner defects, such as cavities, cannot be seen on the surface though it was revealed that a defect linearly exists along the joint line by SEM inspection, Fig. 11. The defects are regularly spaced in a distance similar to the advance per revolution. It can be speculated that the pin shape is not optimum for such a high advance per revolution, leading to a cavity or groove-like defect caused by insufficient heat input. Defects are situated at mid thickness so they are not a root flaw or lack of penetration. Defects are formed outside the optimum FSW conditions. Studying FS welded specimens of aluminium 2024-T6, Biallas *et al.* [7] concluded that this defect don't affect the tensile strength as well as high cycle fatigue performance.

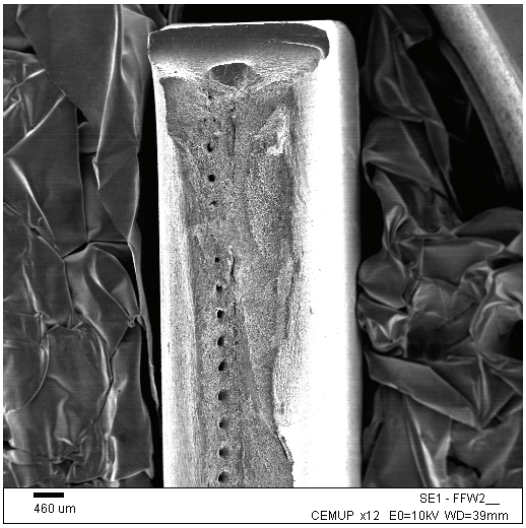

a) specimen FFW2, crack surface

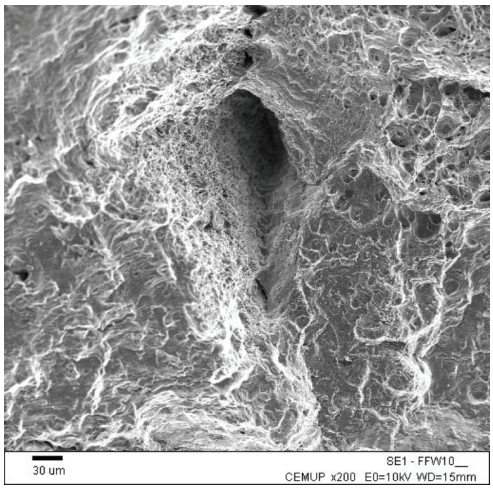

b) inner welding defect, specimen FFW10

Figure 11: SEM analysis of a crack surface on a friction stir welded specimen.

In the FS welded specimens, due to the stir effect, the crack propagation area is harder to identify. The fatigue crack growth area of the unwelded specimen UW6 is presented in Fig. 12.

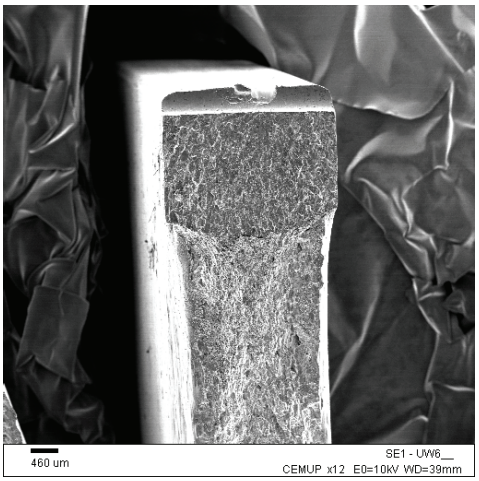

Figure 12: SEM analysis of an unwelded specimen (specimen UW6).

Metallurgical details of fatigue cracks such as fatigue striations were identified in both welded and unwelded specimens, Fig 13. Nevertheless, due to the more heterogenic fracture surface, fatigue striations were difficult to be identified on the welded specimens.

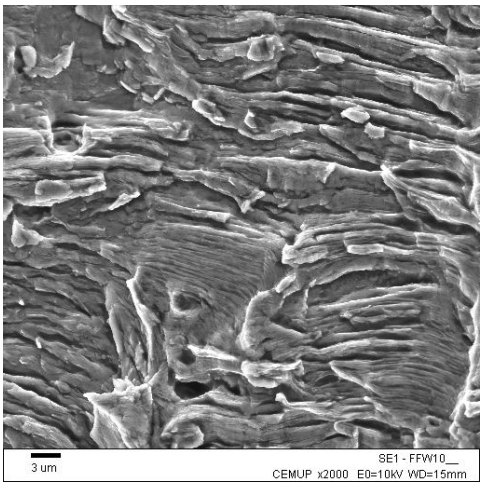

a) fatigue striations, welded specimen FFW10

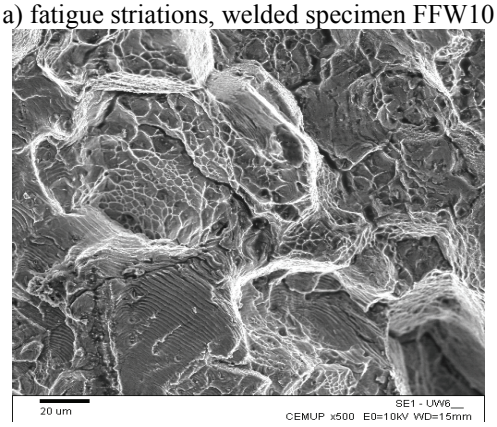

b) fatigue striations, unwelded specimen UW5

Figure 13: SEM analysis of crack surfaces, fatigue striations identification.

8. Conclusions

This study quantifies the influence of the FSW technique on the fatigue life of aluminium alloy 6063-T6 notched specimens. SEM analysis was performed in order to identify welding defects and metallurgical details of fatigue cracks such as fatigue striations.
To study the influence of FSW on the fatigue strength, specimens with and without welding were fatigue tested at different stress levels. It was found that hardness drastically decreases in the weld-deformed zone; the average hardness of the nugget zone is significantly lower than the base alloy. It was also possible to identify an increase of the hardness profile when

measuring the hardness at the side surface due to the different grain size diameter of both surfaces.
FSW specimens displayed longer fatigue lives than similar non-welded specimens tested under the same loading conditions. Despite this good performance, defects were identified in the SEM inspection of the weldments. These inner defects, such as cavities, that cannot be seen on the outside surface were caused by insufficient heat input.

9. Acknowledgements

The FSW plate was kindly supplied by Prof. A. Loureiro, Universidade de Coimbra, Portugal. Work partially supported by PhD scholarship FCT SFRH/BD/19281/2004 and FP6 project DaToN (contract No. AST3-CT-2004-516053 of the European Union).

10. References

[1] A. Portela and M. H. Aliabadi. Crack Growth Analysis Using Boundary Elements. Computational Mechanics Publications Southampton UK and Boston USA, 1993.

[2] Department of Defence, United States of America. Military Handbook, Metallic Materials and Elements for Aerospace Vehicle Structures. MIL-HDBK-5H, 1 December 1998

[3] Automation Creations MatWeb.com. http://www.matls.com.

[4] M. Ericsson and R. Sandstrom. Influence of welding speed on the fatigue of friction stir welds, and comparison with MIG and TIG. International Journal of Fatigue, 25(12):1379-1387, 2003.

[5] L. E. Svensson, L. Karlsson, H. Larsson, B. Karlsson, M. Fazzini, and J. Karlsson. Microstructure and mechanical properties of friction stir welded aluminium alloys with special reference to AA 5083 and AA 6082. Science and Technology of Welding & Joining, 5(5):285-296(12), 2000.

[6] ASM. ASM Handbook: Metallography and microstructures, volume 9. ASM, Materials Park, OH, 1995.

[7] G. Biallas, C. Dalle Donne, C. Juriçic. Monotonic and cyclic strength of friction stir welded aluminium joints. Advances in Mechanical Behaviour, Plasticity and Damage; D. Miannay, P. Costa, D. François and P. Pineau (Eds.), Elsevier Science, Oxford, Vol. 1, 115-120 (2000)

CHARACTERIZATION OF ROLLING CONTACT FATIGUE DAMAGE ON ARTIFICIALLY DENTED SURFACES

V.M.M.B. da Mota, L.A.A. Ferreira
Department of Mechanical Engineering and Industrial Management, University of Porto,
Rua Dr. Roberto Frias, 4200-465 Porto, Portugal

Abstract

A study on the effects of surface dents on rolling contact fatigue (RCF) of a bearing steel has been undertaken on a twin disc machine with both grease and oil lubrication. In order to select the adequate type of dent, a previous study was performed. After it, dents were artificially introduced in one of the contacting disc surfaces, and the damage process was monitored by means of surface video microscopy. At the end of the tests surface perfilometry analysis was used to characterize eventual spall craters, and scanning electron microscopy (SEM) was used to identify crack propagation under the surface layer. Finally, the damaging mechanism due to the dent is discussed and conclusions are also taken on the influence of grease and base oil lubrication in RCF.

Keywords: rolling contact fatigue, artificial dents, video-microscopy, scanning electron microscopy.

1. Introduction

It is widely known that rolling contact fatigue (RCF) affects the performance of several machine elements such as gears, roller bearings, railway wheels and rails, etc. Many factors influence the mechanism of failure. Among those, the presence of surface defects is known to be an important one. These defects are usually originated from the entrainment of debris in the lubricant supply. Their presence changes the contact conditions, leading to high stress concentrations that may result in a significant reduction in the life of the component. Different types of shapes can be found for these defects, although the conical dent shape is often the one that better characterizes them. These dents have been shown to modify significantly the formation of elastohydrodynamic lubricant films between rolling elements [1]. Furthermore, when they are overruled high pressure peaks are generated. Consequently, the maximum shear stress moves closer to the surface contributing to a premature damage.

Several workers [2-8] have created artificial defects on contact surfaces and studied the effect that these have on contact fatigue. Most studies are based on observation and analysis of failed specimens.

This work is aimed at investigating the effect of surface defects on RCF both under oil and grease lubrication. Experiments are based on twin-disc simulation of the rolling contact. Prior to the tests, artificial dents were

introduced on one of the contacting disc surfaces. To choose the adequate type of dent, a previous study was carried out. During the experiments, periodic stops were programmed and the dents damage evolution was monitored using video-microscopy. At the end of the tests surface perfilometry analysis was used to characterize eventual spall craters, and scanning electron microscopy (SEM) was used to identify crack propagation under the surface layer.

2. Artificial dent analysis

Various authors [2-8] tested different types of artificial defects such as conical, spherical and diamond dents, among others. For this work, the Rockwell C type of dent (Fig. 1) was the chosen one for several reasons: its dimensions can be controlled by the indent load, the stress level concentration is high due to a high plastic strain and they are easily reproducible. Furthermore, Rockwell C dents are useful for modeling due to their symmetrical morphology.

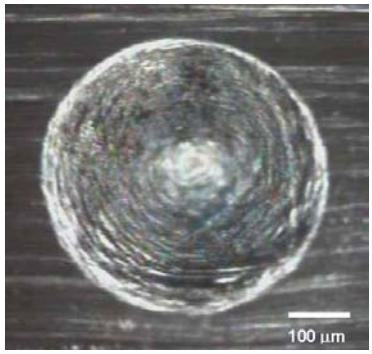

Figure 1: Initial aspect of a Rockwell C dent.

As shown in Fig. 2, the dent is analytically characterized by its depth denoted h_d, its diameter D, the diameter between peaks D' and the height of its shoulders h_s. Another important parameter that should also be considered is the shoulder sharpness S_s given by:

$$S_s = \frac{h_s}{\frac{D' - D}{2}} \quad (1)$$

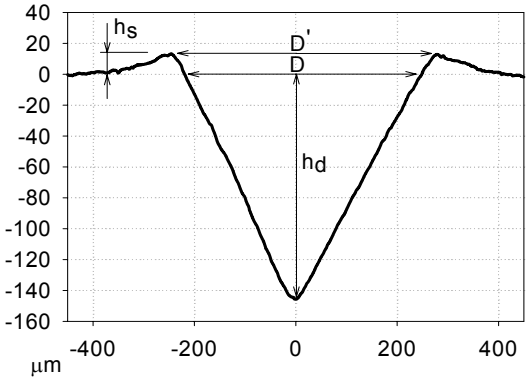

Figure 2: Profile of a Rockwell C dent.

To generate dents on the discs surface, a diamond Rockwell C penetrator was manufactured and adapted to a tensile test machine. The design of the penetrator was such that the location of the dent and the applied load were controlled with great accuracy. The disc was fastened on a rotable and adjustable plate so that the penetrator could be pressed at the required location on the discs surface. The necessary indent load for getting the required dent could be adjusted by the load cell of the test machine.

To choose the adequate indent load, several tests with indent loads from 1500 N to 5000 N were performed in order to evaluate the dent size characteristics. Fig. 3 presents the obtained dent profiles while Figs. 4 to 6 respectively present the evolution of the diameter D, the depth h_d and the shoulder height h_s. As it can be observed, D and h_d growth tendencies change after 3000 N and recover it after 3500 N. On the other hand, h_s increases till 3500 N and then decreases till 4500 N after which a small increase can be

observed. The evolution of S_s (Fig. 7), which depends on the shoulder height, accompanies the growth tendency till 3000 N after which reaches an almost constant value, and then decreasing after 4500 N.

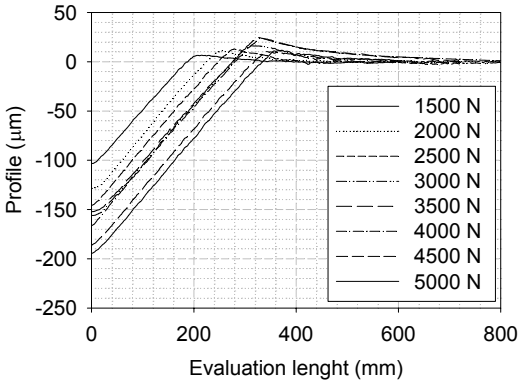

Figure 3: Comparison of the dent profiles for different loads.

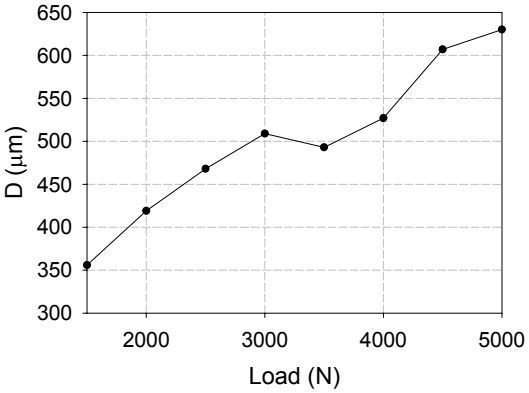

Figure 4: Evolution of the diameter D with the indent load.

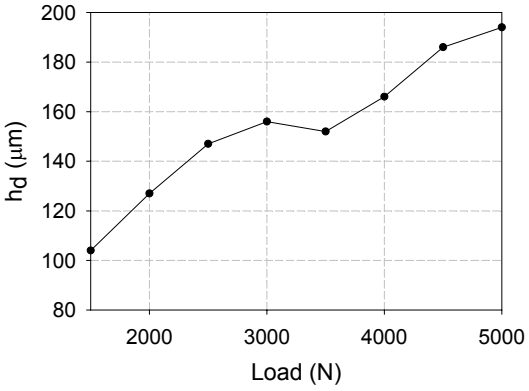

Figure 5: Evolution of the depth h_d with the indent load.

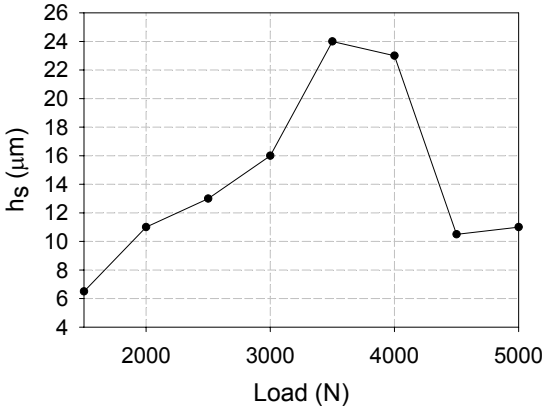

Figure 6: Evolution of the shoulder height h_s with the indent load.

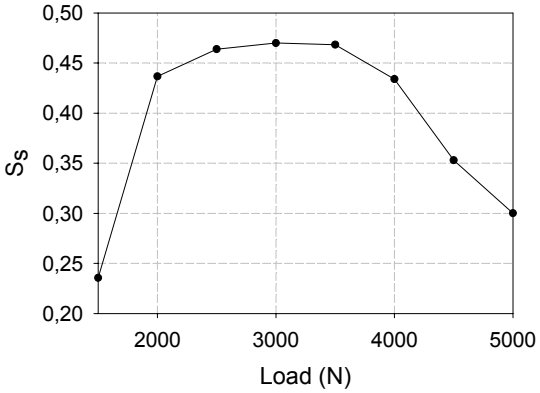

Figure 7: Evolution of the shoulder sharpness S_s with the indent load.

These tests at different loads helped in choosing the load that produces the most suitable dent for the fatigue tests. The best dent is the one that gathers the following characteristics:

- small diameter (it must be as small as possible when compared with the contact ellipse);
- low depth (a big depth might produce an exaggerated plastic deformation);
- a sufficiently high shoulder height and consequent shoulder sharpness (the stress concentration is highly affected by the dent's shoulder height).

Analyzing the results for different loads, one can conclude that the preferable loads are the 2500 and 3000 N loads. The choice was the 2500 N load because, even having a slightly lower shoulder height and shoulder sharpness than the 3000 N load, it produces a dent with a smaller diameter (and also a smaller depth). This fact is very important because the dent area dimension must not approach in size the elliptical contact area.

3. Experimental procedure

3.1. Disc machine test apparatus

A twin disc testing machine was utilized to carry out the rolling contact experiments. The machine was designed to perform surface contact fatigue and wear resistance tests. Its principle consists of two discs normally loaded and rolling against each other under pure rolling or rolling and sliding conditions (see Fig. 8). In the used machine, the discs can be oil or grease lubricated and permanent feeding of the lubricant is ensured.

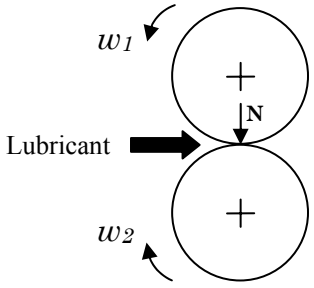

Figure 8: Working principle of the twin-disc machine.

3.2. Test specimens

The discs were manufactured in AISI 52100 bearing steel. The chemical composition and mechanical properties are given in Tables 1 and 2 respectively.

Chemical Composition (wt %)	
C	1.00
Si	0.25
Mn	0.30
Cr	1.50

Table 1: Chemical composition of the AISI 52100 steel.

Mechanical Properties (units)	
Average Hardness (HRc)	58
Yield Stress (MPa)	1747
Rupture Stress (MPa)	2106
Young modulus (GPa)	207

Table 2: Mechanical properties of the AISI 52100 steel.

3.3. Lubricants used

The lubricants used were a grease and its correspondent base oil (see properties in Table 3).

Grease properties	
NLGI number	3
Thickener	Lithium
Soap concentration (%)	12

Base oil properties	
Chemical form	Naphthenic
Cinematic viscosity 40ºC (cSt)	124
Cinematic viscosity 100ºC (cSt)	18

Table 3: Properties of the lubricants used.

3.4. Contact severity

To assess the severity of the contact, the film thickness ratio λ (Eq. 2) was calculated for the lubricants tested.

$$\lambda = \frac{\Phi_T h_0}{\left(\sigma_A^2 + \sigma_B^2\right)^{0.5}} \quad (2)$$

In Eq. 2, h_0 is the minimum film thickness in μm, calculated using the Hamrock and Dowson equation [9], σ_A and σ_B are the RMS surface roughness of body 'A' and 'B' respectively in μm

and Φ_T is the thermal effects correction factor.

In Table 4, the relationship between λ and the lubrication regime, in elastohydrodynamic lubrication for rolling bearings, is presented.

λ	Lubrication regime
$\lambda \geq 1.5$	Full film
$1.0 < \lambda < 1.5$	Mixed film
$\lambda \leq 1.0$	Boundary film

Table 4: Regimes of EHD lubrication [10].

Grease film thickness was calculated under fully-flooded using Eq. 3, which is the result of previous research from workers that attempted to estimate the film thickness of greases [11].

$$h_0 = 1.5 h_0^{baseoil} \quad (3)$$

The results of λ for the grease and correspondent base oil are presented in Table 5.

Lubricant	h_0	σ	λ	Lubr. regime
Grease	5,4	1,6	1,9	Full film
Base oil	3,6	1,5	1.3	Mixed film

Table 5: Contact severity for the grease and base oil.

3.5. Operating conditions

The tested discs were loaded to achieve a maximum contact pressure of 2 GPa. Due to their geometry, when the discs are loaded against each other, an elliptical contact area is generated (see Fig. 9). The dimensions of the ellipse can be determined using the Hertzian contact theory (see for instance Johnson [12]) and in this case are: a = 0.52 mm and b = 0.83 mm.

The discs rolled against each other under pure rolling conditions with a rotational speed of 3000 rpm.

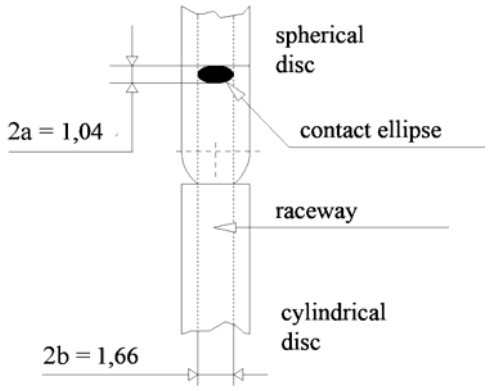

Figure 9: Contact geometry of and surface contact area.

3.6. Test procedure

Three dents separated 120º from each other were manufactured on the spherical discs. Following the dent analysis, the chosen and applied indent load was 2500 N.

Fully-flooded conditions were assured for both lubricants during the tests. Oil lubrication was assured by permanent oil injection into the contact zone and grease lubrication was assured by a reservoir installed around the discs that supplies grease into the contact.

Tests were planned for a total duration of 12 million cycles with regular interruptions. At each interruption the discs were removed from the machine, their surfaces were cleaned and analyzed by video-microscopy.

In the end of the tests, perfilometry was used to characterize the profile of the damaged site. Discs were also cut into samples to be observed using SEM.

4. Characterization of the dents damaging mechanism

The test under grease or base oil lubrication showed similar behaviors on the dents damage mechanism.

Fig. 10 shows a series of micrographs from the grease lubricated test captured at different stages during the test.

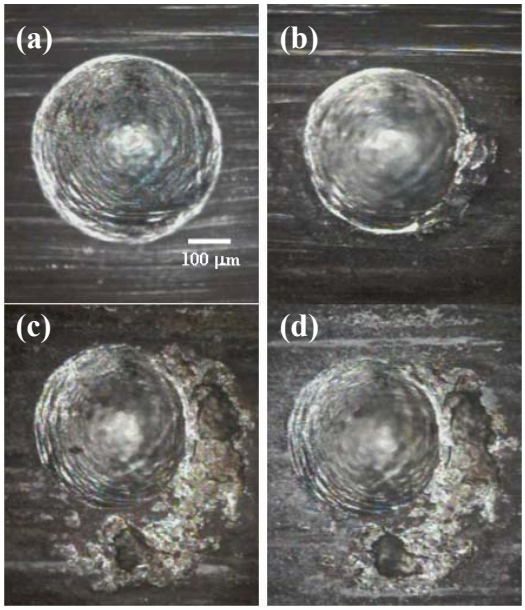

Figure 10: Sequence of micrographs of the dent damage process for the grease lubricated test (a) at the start of the test, (b) after 5×10^5 cycles, (c) after 4×10^6 cycles, and (d) after 12×10^6 cycles. Rolling direction is from left to right.

The initial dent is rapidly reduced in size during the first few cycles. This process occurs by plastic flow of the dent side walls. The dent shoulders and the side walls collapse under contact loading. The dent then shakes down to a stable shape and little further deformation occurs (see Fig. 11).

A fatigue crack initiates at the trailing edge of the dent (Fig. 12) and later propagates to a spall (Fig. 13). A finite element simulation of the indent process showed that the highest stress values are found in that site [13]. Additionally, the pressure distribution is modified by the dent shoulders [1] and high pressure spikes appear leading to an increasing stress concentration. The pressure peak is higher at the trailing edge due to the slope change which is more favorable for generation of fluid pressure. This location then suffers a higher stress and is consequently the initiation point.

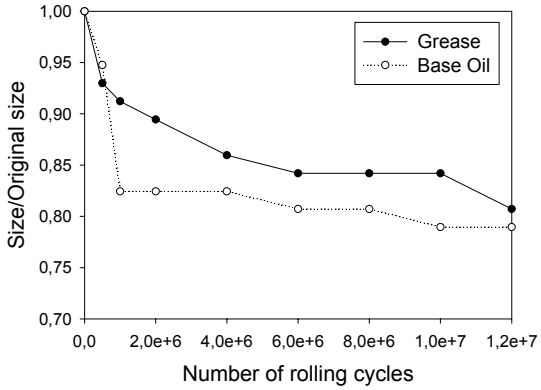

Figure 11: Cross section Contact geometry of and surface contact area.

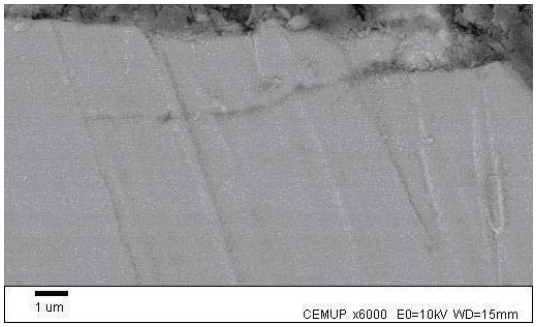

Figure 12: Cross section through the running surface observed using SEM.

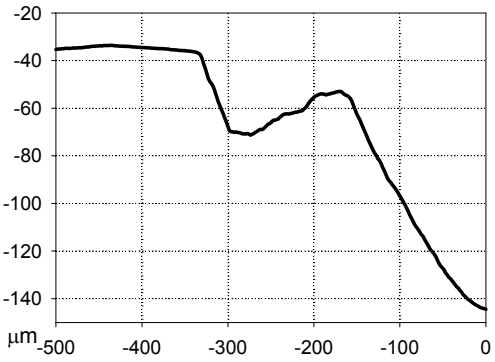

Figure 13: Profile of a spall obtained using perfilometry.

If the oil is used as the lubricant, a similar process takes place (see Fig.14). Again the dent is deformed but this time the damaged area propagation does not lead to a spall in the end of the tests. This can be justified on the value of

film thickness ratio λ that under fully-flooded conditions is expected to be smaller for the test using oil than for the one using grease (see Table 5). Therefore, the loss of material due to wear is higher, as presented in Fig. 11.

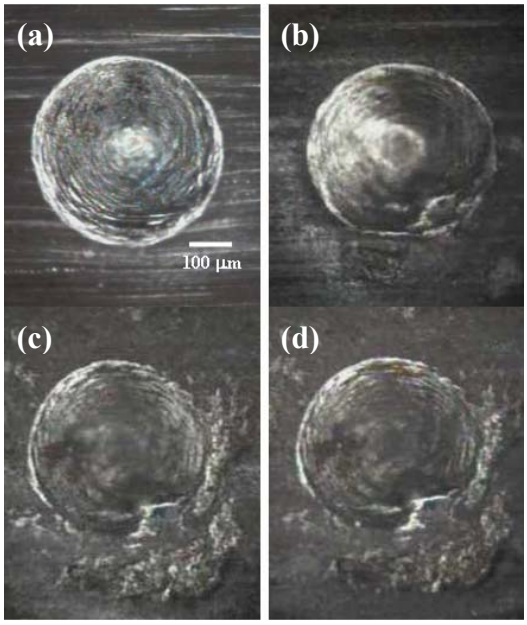

Figure 14: Sequence of micrographs of the dent damage process for the oil lubricated test (a) at the start of the test, (b) after 5×10^5 cycles, (c) after 4×10^6 cycles, and (d) after 12×10^6 cycles. Rolling direction is from left to right.

5. Conclusions

A study on the effects of artificial dents surfaces on RCF has been undertaken on a twin disc machine with both grease and oil lubrication. The surface damaged area around the dents was monitored by means of video-microscopy throughout the tests.

It was found that either the contact is grease or oil lubricated, a similar damaging mechanism takes place. In a first phase, the dent shoulder is flattened by the high pressure spikes generated when the contacting surface moves on the dent edge. The shoulder height decreases very quickly and becomes quite stable long after. Then, due to the accumulated plastic strain resulting from the high pressure spikes and the high stress concentration beneath the edge dent, cracks are initiated on or close to the surface at the dent edge.

Under grease lubrication cracks propagate to form a spall in the end of the tests. However, when oil is used as the lubricant, cracks propagation does not lead to a spall in the end of the tests. This can be justified on the value of λ that under fully-flooded conditions is expected to be smaller for the test using oil than for the one using grease. The oil lubricated contact runs under a mixed film lubrication regime while the grease lubricated contact runs under a full film lubrication regime. Therefore, the amount of material removed by wear in the case of the oil lubricated contact is higher and the formed cracks that tended to propagate to form a spall are consequently worn out.

6. References

[1] Coulon, S., Jubault, I., Lubrecht, A.A., Ville, F., Vergne, P., "Pressure profiles measured within lubricated contacts in presence of dented surfaces. Comparison with numerical models", Tribology International, Vol. 37, pp. 111-117, 2004.

[2] Fan, H., Keer, L. M., Cheng, W., Cheng H. S., "Competition between fatigue crack propagation and wear", J. Trib., Vol. 115, pp. 141-147, 1993.

[3] Cheng, W., Cheng, H.S., Keer, L.M., "Longitudinal crack initiation under pure rolling contact fatigue", STLE Trib. Trans., Vol. 37, nº1, pp. 51-58, 1994.

[4] Nélias, D., Dumont, M.-L., Couhier, F., Dudragne, G., Girodin, D., "Experimental and theoretical investigation on rolling contact fatigue of AISI 52100 and M50 steels under EHL o Micro-EHL conditions", ASME J. Tribol., Vol.124, pp. 653-667, 1997.

[5] Nélias, D., Ville, F., "Detrimental effects of debris dents on rolling contact fatigue", ASME J. Tribol., Vol.122, pp. 55-64, 2000.

[6] Magalhães, L., Seabra, J., Sá, C., "Experimental observations of contact fatigue crack mechanisms for austempered ductile iron (ADI) discs", Wear, Vol. 246, pp. 134-148, 2000.

[7] Girodin, D., Ville, F., Guers, R., Dudragne, G., "Rolling contact fatigue tests to investigate surface initiated damage using surface dents", Bearing Steel Technology, ASTM STP 1419, J.M. Beswick, Ed., ASTM, pp. 1-19, 2002.

[8] Diab, Y., Coulon, S., Ville, F., Flamand, L., "Experimental investigations on rolling contact fatigue of dented surfaces using artificial defects: subsurface analyses", Tribological Research and Design for Engineering Systems, D. Dowson et al. (Editors), pp. 359-366, 2003.

[9] Hamrock, B.J. & Dowson, D., "Ball Bearing Lubrication: The Elastohydrodynamics of Elliptical Contacts", John Willey & Sons, 1981.

[10] Seabra, J., Campos, A. & Sottomayor, A., "Lubrificação elastohidrodinâmica" (in portuguese), FEUP, 2002.

[11] Jonkisz, W. & Krzeminski-Freda, H., "The properties of elastohydrodynamic grease films", Wear, Vol. 77, pp. 277-285, 1982.

[12] Jonhson, K.L., "Contact mechanics", Cambridge University Press, 1985.

[13] Mota, V., Moreira, P. & Ferreira, L., "Stress intensity factor calculation for inclined surface-breaking cracks initiated in an artificial indentation under rolling contact fatigue using the edge Green Functions", 10th Portuguese Conference on Fracture, 2006.

FATIGUE ANALYSES OF AERONAUTICAL STRUCTURAL DETAILS OF DIFFERENT COMPLEXITY

Paulo M. S. T. de Castro[1], Paulo F. P. de Matos[1,2], Pedro M. G. P. Moreira[1], Lucas F. M. da Silva[1]

1 - IDMEC, Departamento de Engenharia Mecânica e Gestão Industrial, Faculdade de Engenharia da Universidade do Porto, Portugal
2 – presently: University of Oxford, Department of Engineering Science, Parks Road, Oxford OX1 3PJ, United Kingdom

Abstract

This communication discusses the fatigue behaviour of specimens with different levels of geometrical and mechanical complexity, including the effects of residual stresses due to the cold-working process of rivet holes, load transfer and stress intensity factor calibration of riveted lap-joints, and finally the problem of multiple site damage.
A finite element analysis of the different structural details was performed in order to model the residual stresses, the stress intensity factor, the load transfer and finally fatigue crack propagation. Analyses of fracture surfaces were carried out in order to measure the location and extent of fatigue damage and the spacing between fatigue striations.

Keywords: cold-working, crack growth, fatigue striations, finite element analysis, load transfer, multiple site damage, open hole, residual stress, riveted lap-joint, SEM analysis.

1. Introduction

Aircraft manufacturers aim at lighter structures, possibly susceptible to multiple site damage (MSD) and widespread fatigue damage (WFD). The improvement of the fatigue behaviour of these structures includes techniques such as the cold-working of rivet holes [1]. WFD, as an effect MSD, can be regarded as the major structural problem of ageing aircraft, comprising three stages: 1) the initiation of MSD, which determines the initial damage scenario, 2) the crack growth stage of MSD, when cracks grow simultaneously at different sites, and 3) the residual strength in the presence of MSD and possible further deteriorating effects like corrosion, debonding or manufacturing defects, [2].
This communication gives an overview of studies on open-hole specimens, single rivet lap joints, and riveted panels:
(i) firstly, the influence of residual stresses due to the cold-working process on the fatigue behaviour of 2024-T3 Al open hole specimens is discussed.
(ii) secondly the fatigue behaviour of a single rivet lap joint is studied. This specimen can be regarded as a slice of a riveted lap joint with various columns of rivets, for a specific pitch. The stress intensity factor calibration of symmetrical/asymmetrical cracks was quantified using three-dimensional finite element analysis (FEA) and equivalent initial flaw size (EIFS) results are presented. The estimation of rates of crack

propagation based on fatigue striation measurements is presented.
(iii) the third part consists on the analysis of a riveted lap joint panel with 3 rivet rows and 15 rivet columns. At this stage, the problem of MSD is discussed and an approximate predictive model for fatigue crack propagation, initially proposed by Silva *et al.* [2] and based on the FRANC2D/L [3] finite element programme is presented.
The emphasis of the communication is on the present authors' own experimental or modelling work.

2. Fatigue behaviour of open-hole specimens

Residual stresses due to the cold-working process

Fastener hole fatigue strength may be increased by creating compressive residual circumferential stresses around the hole. Research has been concentrated on modelling the residual stress field using analytical [4, 5] or numerical two- or three-dimensional (2D or 3D) methods [6-8], and on the experimental measurement of the residual stress field [9, 10].
A study of in-service fatigue failures in aircraft structures revealed that seventy per cent of fatigue cracks originated from the holes of riveted or bolted joints [11]. Most of the experimental observations suggest that cold expansion can increase fatigue life to failure by a factor ranging from 3 to 10, depending upon the fatigue stress level [13, 14].

Specimens characterization

Figure 1 shows the 2mm thick specimen configuration. The holes were reamed after drilling and were subsequently expanded (4.5% of the hole diameter) using a mandrel.
In prior studies [17, 18] the residual stresses resulting from hole expansion were determined by X-ray diffraction. The aluminium alloy used in this work is the 2024-T3 Alclad. The yield and tensile strengths are 312MPa and 440MPa respectively, the Young's modulus and Poisson's ratio are 78GPa and 0.33 respectively.

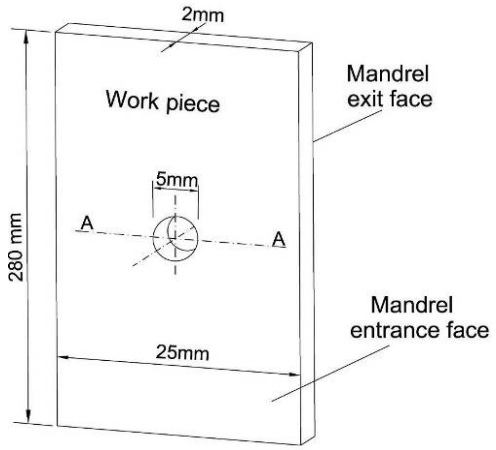

Figure 1. Open hole specimen, geometry.

Fatigue tests

In the fatigue test program a total of 45 open hole specimens (24 with and 21 without residual stresses) were tested. The fatigue tests were carried out at an R ratio of 0.1 (R = min. load/max. load) in air at room temperature and at a frequency of 10Hz. In the fatigue test program constant maximum stress levels of 120, 140, 160, 180 and 200MPa were used.
The results presented in Figure 2 agree with expected trends [13, 14].

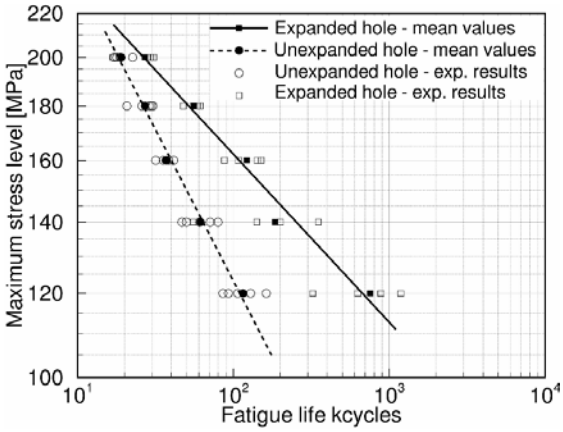

Figure 2. *S-N* curves for open hole specimens with and without cold expansion, after [19].

Scanning electron microscopy

The fracture surfaces of four of the specimens tested were examined by scanning electron microscopy (SEM).

Two of these specimens had normal holes – *ie*, non cold-worked - and two had cold-worked holes. The maximum stress used in the fatigue tests was σ_{max}=140MPa and σ_{max}=200MPa. A SEM equipped with a Field Emission Gun (FEG) was used to measure the fatigue striations spacing (*s*); details concerning the techniques involved can be found in [20, 21]. The fatigue striations spacing measurements were made in two different directions: one in the direction of crack growth (see Figure 3a), and the other in the transverse direction, 0 to 2mm from the edge of the hole, in an attempt to estimate the crack nucleation site. Figure 3b) shows the right side of the fatigue crack measured by SEM, where the dashed line represents the fatigue crack area. Figures 3 c) and d) show some fatigue striations measured in the specimens tested at σ_{max}=140MPa for a fatigue crack length of 0.580mm. For both directions, five measurements of striations spacing were made in each SEM screen and the average value was calculated for purposes of plotting the results.

Figure 4 presents some quantitative measurements of the fatigue striation spacing along the crack length and crack depth. Along the crack length the space between fatigue striations decreases due to the effect of the residual stresses induced by the hole expansion. Along the crack depth the measurements trend is not as clear as along the crack length. Moreover, in the specimens tested at σ_{max}=200MPa it seems that the fatigue crack nucleated at the surface of the specimen since the fatigue striations spacing increases along the crack depth from 0 to 2mm (it is again mentioned that specimen thickness is 2mm). Fatigue striation spacing can be directly related to the rate of crack propagation [22, 23], therefore these measurements indicate a braking effect in the rate of crack propagation due to the residual stresses.

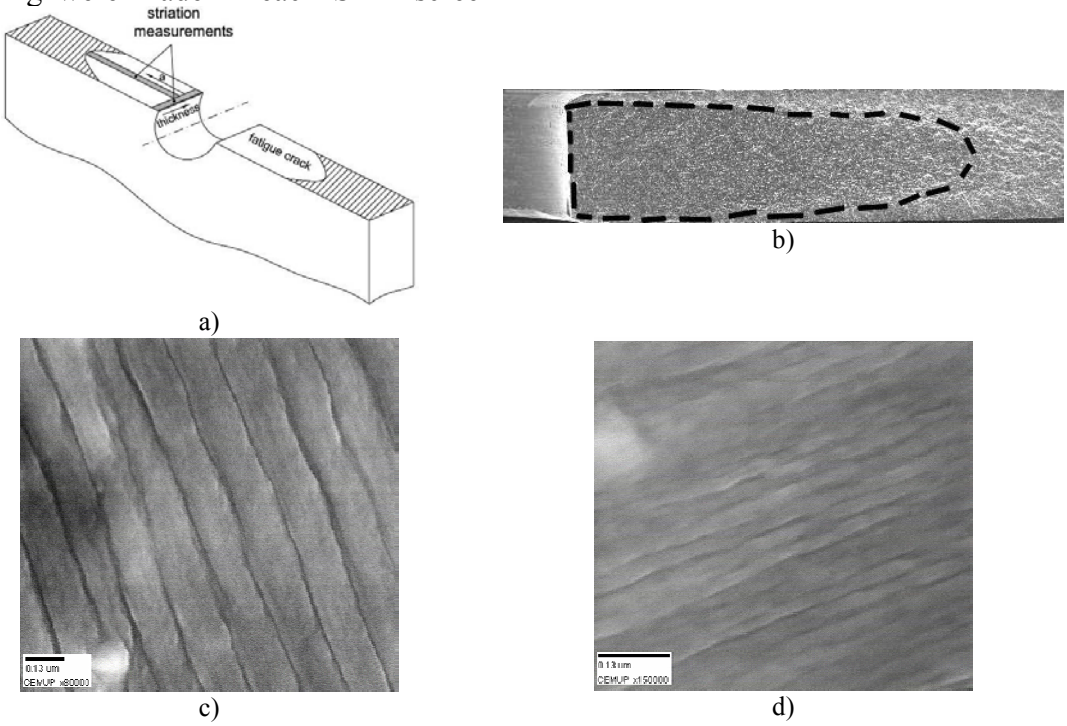

a) b)

c) d)

Figure 3. a) Fratography analysis; b) Fracture surface; c) Fatigue striations along the crack length σ_{max}=140 MPa, normal hole *a*=0.580 mm; d) Fatigue striations along the crack length σ_{max}=140 MPa, cold-worked hole *a*=0.580 mm, de Matos *et al.* [24].

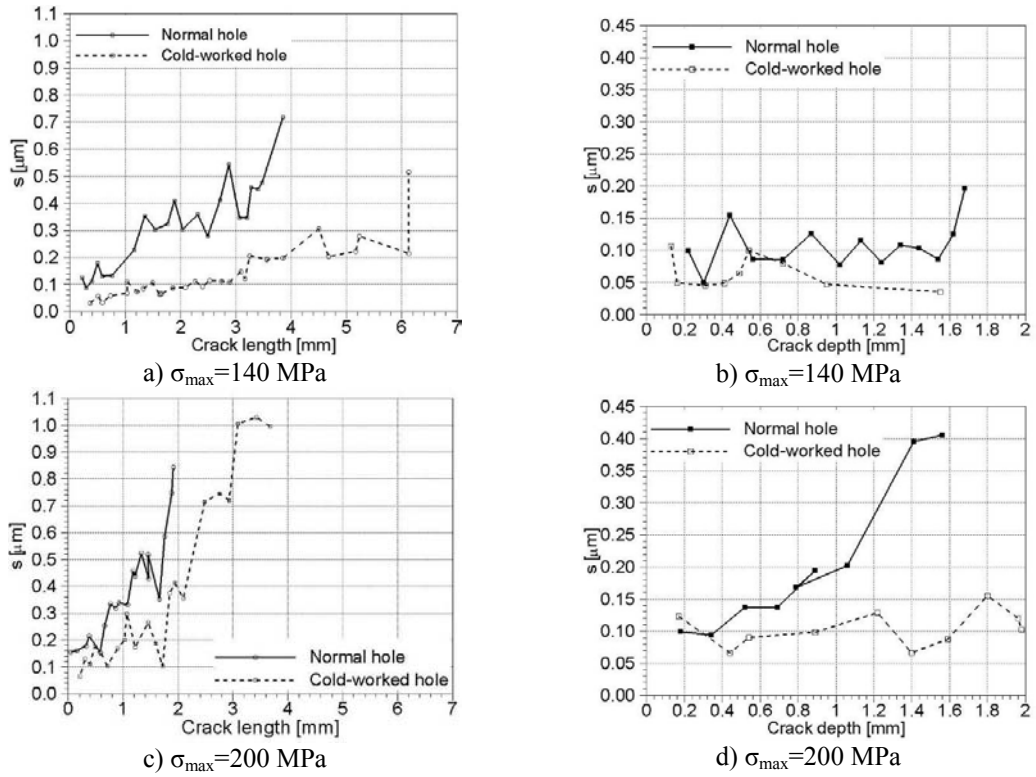

a) σ_{max}=140 MPa b) σ_{max}=140 MPa

c) σ_{max}=200 MPa d) σ_{max}=200 MPa

Figure 4. Fatigue striation spacing measurements.

3. Single-rivet lap-joint

Several geometric configurations are used to study riveted joints, such as those discussed in [25]. Load transfer (LT) is defined as the percentage of the applied load which is transferred from one plate to the other by means of the fasteners and friction between the plates [26].

A lap splice with three rivet rows and one rivet column is one of these configurations, consisting of a "slice" of an aircraft lap joint. This specimen was tested in for the development of statistical data on the fatigue behaviour of single-shear joints. Detailed analyses involving crack propagation require a stress intensity factor (SIF) calibration which is not commonly available. A 3D FEA of the load transfer behaviour as a function of crack length, and a SIF calibration is presented.

Specimens characterization

The specimen is a lap splice with three rivet rows and one rivet column, subjected to tensile load. Two cracking scenarios were studied - a single crack and two symmetric cracks – for the critical cross section, which contains the first rivet as shown in Figure 5.

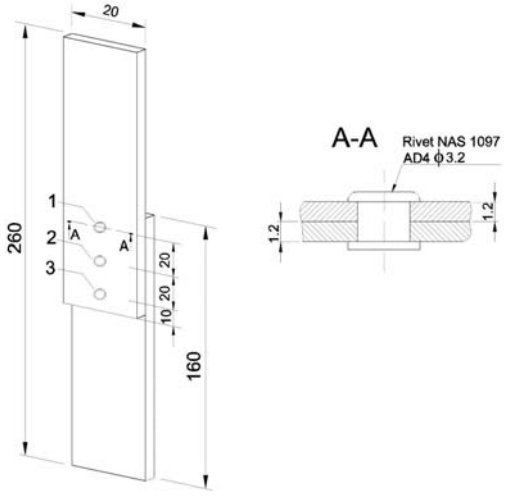

Figure 5. Single rivet lap-joint geometry.

Fatigue tests

Forty five specimens were tested at σ_{max}=160MPa, R=0.05 and at a frequency of 10Hz. An average value of 77688 cycles to failure with a standard deviation of 18320 cycles was obtained.

SEM analysis

The fatigue crack in the right side of

specimen #224 is schematically presentedin Figure 6.

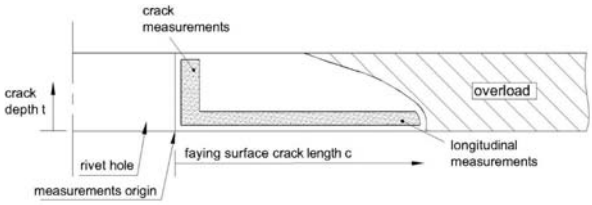

Figure 6. Fatigue crack area and crack length measurements.

Measurements of the fatigue striations were carried out on four specimens. The measurements were done in the longitudinal and transversal directions considering the origin at the bottom side of the hole. Fatigue striation spacing for a given point (coordinate value) was obtained by the average of five measurements along a line perpendicular to striation orientation. Figure 7 present the striation spacing *versus* crack length and crack depth respectively for specimen 224.

According to [20] the longitudinal crack growth rate can be fitted with reasonable correlation using an exponential approximation, and this was confirmed in the present work. The exponential fit and the corresponding correlation factor for the longitudinal and transverse crack growth are presented in Figure 7. Fatigue striations give useful information on the rate of crack propagation [22, 23] as they offer a potential basis for the fractographic reconstitution of fatigue crack characteristics in terms of growth kinetics [27, 28] as well as in terms of crack front geometry [29], particularly in the mid-regime of fatigue crack propagation. Based on fatigue striation measurements it is possible to perform the fatigue life reconstitution of structural components; some examples are given in [22, 24, 30].

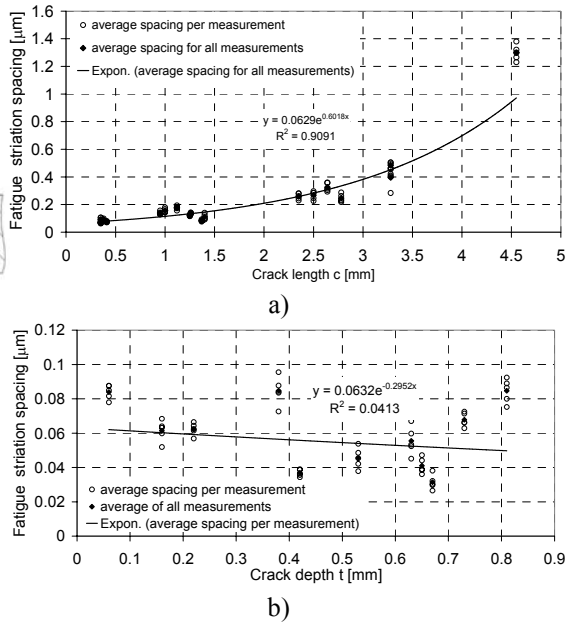

Figure 7. Fatigue striation spacing measurements.

Finite element analysis

The finite elements package ABAQUS was used to perform a 3D stress analysis. The joint was modelled with no interference (perfect fit joint). Friction between the lap joint components was not taken into account. Several contact surfaces were modelled: contact between the two plates to avoid the interpenetration due to bending; contact between the rivet and the plates; and contact between the rivet head and each plate.

The load transfer problem is a key point in the study of riveted lap-joints since the stress intensity factor calibration depends on the level of applied load transmitted by each rivet, [32]. According to [33], for typical lap joints with three rivet rows, it is expected that 37% of the load is carried by the first rivet and 63% of the load is the by-pass load, a result approximately verified in the 3D FEA of the present specimens, where the load carried out by the first rivet was found to be 38%.

Stress intensity factor evaluation

Following techniques discussed for example in [34], the node nearest to the crack tip of each element was moved to quarter point position in order to model the $1/r$ singularity at the crack tip. The

results are obtained in two consecutive moments. Firstly, SIF results for 5 coordinates along the thickness were obtained.

Afterwards, using the three results of SIF for each element, and equation (1), an average value of SIF is calculated, as specified in [34].

$$K_{average} = \frac{K_A + 4K_B + K_C}{6} \qquad (1)$$

where A, B and C are three nodes along the element edge (and along the crack front). Since this is a mixed mode situation, the effective stress intensity factor K_{eff}, as suggested in [35], is used:

$$K_{eff} = \left(K_I^2 + K_{II}^2 + \frac{K_{III}^2}{1-\nu^2} \right) \qquad (2)$$

The SIFs K_I, K_{II} and K_{III} were calculated using the J-integral [36]. It was concluded that K_I is dominant, and K_{II} and K_{III} have values which are one order of magnitude smaller, with the only exception of K_{III} in the vicinity of the faying surface. The results in terms of the non-dimensional K_{eff} for several crack lengths are presented in Figure 8. The results, published in detail in [37], show that the SIF is maximum at the faying surface and minimum at the outside surface, for all crack lengths. This result is related with the bending of the plate, which tends to open more the edge of the crack located at the faying surface than the edge of the crack located at outside surface. For a symmetric crack, the major difference between the stress intensity factor at the faying and outside surfaces is 17%, and occurs for a crack length of 4 mm. For an asymmetric crack, the major difference is 21%, also occurring for a crack length of 4mm.

It can be concluded that, for a given crack length and surface, the SIF of a symmetric crack is always higher than the one of an asymmetric crack.

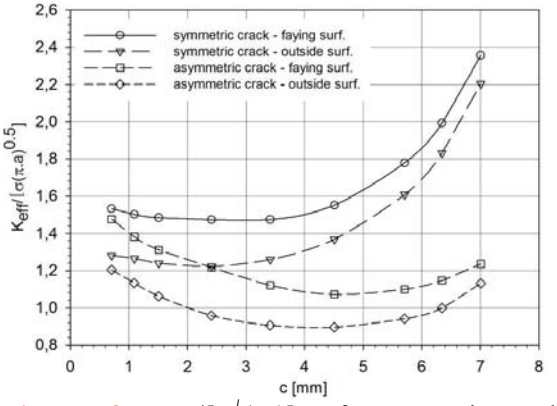

Figure 8. $K_{eff}/[\sigma\sqrt{(\pi a)}]$ of symmetric and asymmetric cracks, for several crack lengths, after [37].

Using the Paris law the fatigue crack growth propagation between the EIFS and the rupture moment was rebuilt, as shown in Figure 9. A statistical analysis of the IFS distribution is presented in Figure 10. The distribution that best fitted the EIFS results was the Weibull two parameters. The probability density function (PDF) is presented in Figure 10.

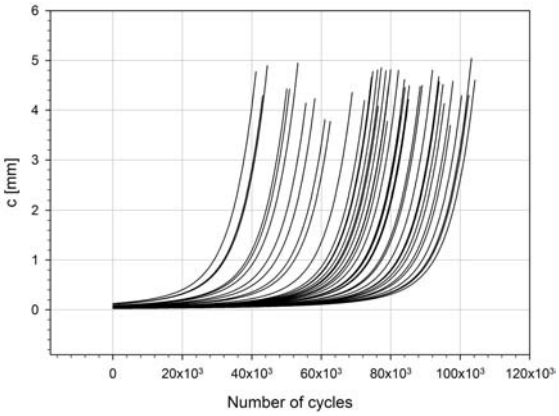

Figure 9. Fatigue crack propagation according to the Paris law.

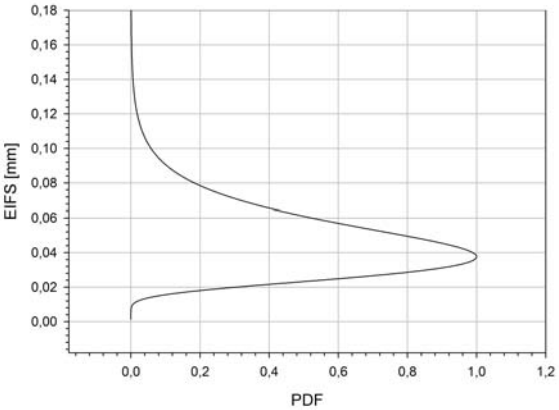

Figure 10. EIFS probability density function.

SEM analyses could not confirm these EIFS values, a fact that is not unexpected, given the approximate nature of the crack growth law used (Paris) and of the SIF solutions (for through cracks). In the present circumstances, EIFS was found to lack real physical significance, being just another way of presenting the distribution of fatigue test results.

4. Lap joint panel

The last part of this paper deals with fatigue crack propagation in a more complex structural detail, consisting of a riveted lap joint panel with three rows of 15 columns of rivets. The fatigue analysis of this type of structural component has received special attention since the Aloha Airlines accident in 1988, *e.g.* [38-41].

According to Schmidt and Brandecker [38, 39], an aircraft structure containing multiple cracks can be categorised into one of three different classes of damage: Widespread Fatigue Damage (WFD), Multiple Site Damage (MSD) and Multiple Element Damage (MED). It should be noted that in general WFD, MSD and MED may act simultaneously on aircraft structures, and therefore it is difficult to establish a boundary between these interactive phenomena.

Problems such as loading and stress distribution, crack initiation, crack growth and residual static strength play an important role on this type of structural component. These topics have been addressed in detail by Eastaugh *et al.* [42] and Schijve [32].

One of the major issues is the calculation of stress intensity factors representative of the state of stress in this type of structural detail. It is known that fatigue cracks start at riveted lap joints of the fuselage skin [32]. Under such conditions, the analysis of fatigue riveted lap joints is difficult because: 1) the load transmission in riveted lap joints is a highly complex phenomenon as it involves load transmission by friction, fretting, secondary bending and residual stresses, and 2) the relevance of stress intensity solutions for small part through cracks in riveted joints is questionable in view of the complex nature of the load transmission and failure modes [32]. A flavour of the level of complexity of this type of problems was presented in section 3 for the case of a single rivet lap joint, which is representative only of a "slice" of the riveted lap joint panel.

This final part of the paper addresses the modelling of the crack growth process in a riveted lap joint panel, for a given multiple site damage scenario obtained experimentally by Cavallini and Lazzeri [43]. The crack growth modelling was done using the finite element program FRANC2D/L and the Paris law, following a methodology proposed by Silva *et al.* [2]. FRANC2D/L is a finite element program for the small deformation analysis of two dimensional structures. As such, a lap joint is modelled in two dimensions, without considering the bending effect. Linear Elastic Fracture Mechanics (LEFM) analyses can be performed with automatic re-meshing as crack grows. The layered capability allows the user to model riveted and adhesively bonded structures, such as lap joints and bonded repairs.

Specimen geometry and details of the experimental work

The geometry of the lap joint panel modelled is presented in Figure 11 a). The sheets are 1.6 mm thick and made of aluminium alloy 2024-T351. The rivets used were the MS 20426D5-6 in Al 2017-T31. The lap joint panel contains three rows and fifteen columns of rivets. The two columns of holes at each side of the specimen were cold-worked to avoid early nucleation of fatigue cracks. The lap joint panel (BJ3) was fatigue tested at σ_{max}=110 MPa and R=0.1.

Crack growth was measured using the Image Analysis Technique described in

[46]. The sites inspected are marked from 1 to 22 in Figure 11 b). No crack growth was recorded at positions A, B, C, D, E and F because these holes were cold expanded in order to delay the fatigue crack propagation, a subject discussed in section 2 of this paper.

The growth of fatigue cracks was monitored from 132450 cycles until rupture at 138450 cycles. Figure 11 b) shows schematically the crack scenario at different stages of the fatigue test.

Cavallini and Lazzeri [43] reported that fatigue cracks in this structural detail grow with quarter ellipse shape.

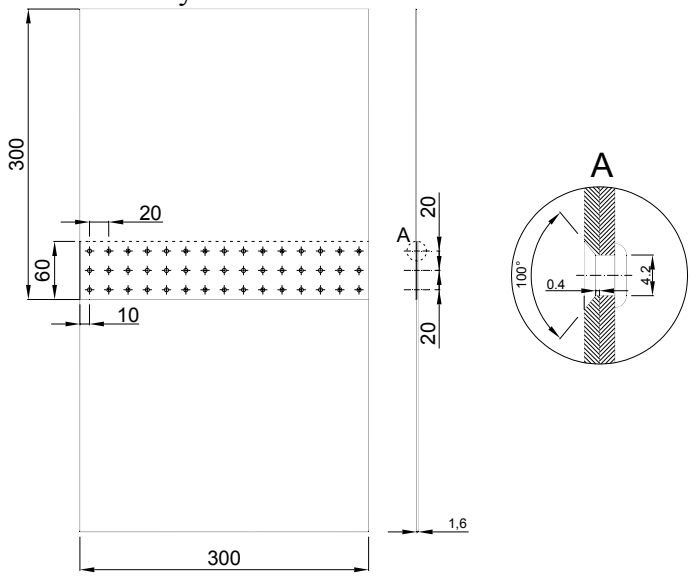

a)

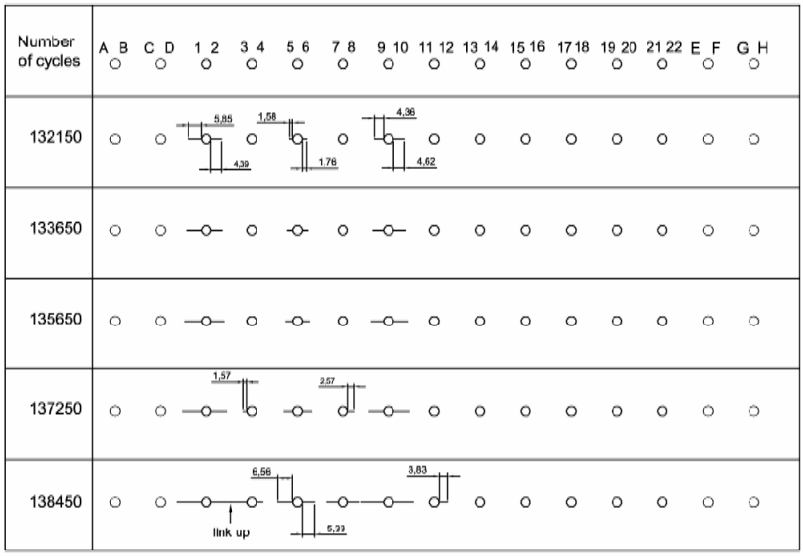

b)

Figure 11. a) Riveted lap-joint panel, and rivet detail (rivet type MS 20426D5-6); b) Crack scenario at different stages of the fatigue test.

MSD crack growth modelling

The crack growth problem was performed using the Paris Law [44]. The Paris Law constants were taken from reference [45], C=7.46×10^{-8} and m=3.333 (Paris law with da/dN in mm/cycle and ΔK in MPa m$^{1/2}$). The Young's modulus and Poisson's ratio

are 70 GPa (approximately) and 0.33 respectively.

A layered structure, such as a riveted lap-splice joint or a bonded lap joint, is actually a three-dimensional structure. A three-dimensional finite element or mathematical modelling of such a structure involves several degrees of complexity. In FRANC2D/L simplifying assumptions are made allowing us to capture the essential features of the response [3]. The assumptions include:

- each layer is considered as an individual two-dimensional structure under a state of plane-strain;
- cracks are approximated as through cracks along a line passing exactly through the rivets;
- individual layers can be connected with rivets or adhesive bonds;
- a rivet is treated as an elastic shear spring between two nodes of each layer (in our case $P/\delta = 33052N/mm$).

An algorithm based on the Paris Law was used to model the crack propagation, as used by Silva *et al.* [2]. The crack propagation modelling was done from 132150 cycles until rupture at 138450 cycles.

A new crack was included in the FEM model after being experimentally detected. Figure 11 compares the experimental measurements with the predictions from the model previously described. The numerical results presented in Figure 12 are in good agreement with experimental measurements. The largest differences were noticed for cracks 3, 5 and 8, although cracks 5 and 8 show the same trend than the experimental measurements.

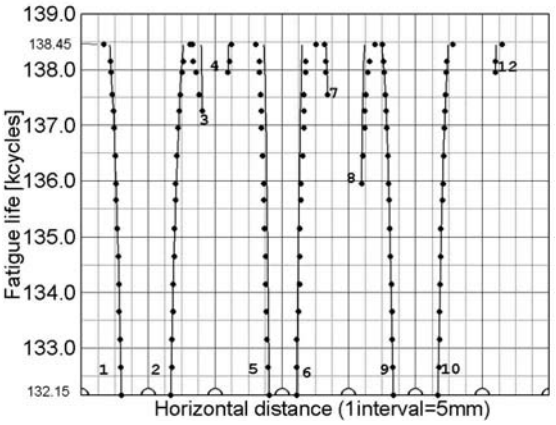

Figure 12. Crack growth in the lap-joint panel (bullets are experimental results and continuous lines are predicted results).

MSD crack growth - comments

Good agreement was found between the experimentation and the prediction using the FE package FRANC2D/L. However there are important limitations that must be mentioned:

- The cracks were modelled as through cracks, although it was found experimentally that they grow with a complex shape (*e.g.*, quarter of ellipse or half ellipse);
- The rivets are treated as spring elements. It is only a simplification that has some limitations. The problem actually solved is in fact closer to a lap joint fastened by welded points than to a riveted lap joint. The typical stress distribution of a hole is not considered;
- FRANC2D/L allows only a 2D model ignoring the secondary bending expected in a typical lap joint. There is no doubt that a 2D model gives a good indication of the lap joint stresses but there is stills controversy about how important the bending stresses in the joint are and how they affect the crack growth. Secondary bending may not be required for an approximation of the stresses, and consequent fatigue life or strength.

5. Concluding remarks

The fatigue behaviour of different types of specimens with increasing level of

complexity (geometrical and mechanical) was discussed. Selected testing data of open-hole, single column rivet lap-joint, and lap joint panel specimens was surveyed, and some key lessons were drawn for each one of these types of specimens.

The residual stresses induced by the cold-working process improve significantly the fatigue life of structural details. This improvement in life might be up to 10 times, depending on the level of applied stress. The residual stresses due to the cold-working decrease the space between fatigue striations, which indicates a braking effect on the rate of crack propagation.

Single rivet lap joint geometry were tested and analysed. SEM examination and conversion of striation spacing into crack growth rate da/dN, showed that the longitudinal crack growth rate can be fitted with reasonable correlation using an exponential approximation; transversal crack growth rates were almost constant and similar to the longitudinal rates for small cracks.

A detailed stress analysis of a single column rivet lap joint was conducted using three-dimensional elastic finite element analysis. The stress intensity factors for this geometry with through symmetric and asymmetric cracks were determined. It was concluded that K_I is dominant, and K_{II} and K_{III} have values which are one order of magnitude smaller, with the only exception of K_{III} in the vicinity of the faying surface. This suggests that first approximations to modelling may be based on mode I only.

The EIFS concept was applied to these tests, using the SIF solutions obtained and the Paris law. EIFS values could not be confirmed by the SEM analyses; they have no proper physical meaning, being just another way of presenting the distribution of fatigue lives.

Regarding the lap joint panel, a good agreement was found between the experimental measurement of crack growth and the prediction using the FE package FRANC2D/L. However, this simple model involves simplifications concerning for example crack geometry, the behaviour of rivets (holes not modelled) and the bending effects is not taken into account.

This paper briefly presented studies with various levels of detail or complexity, either experimental or numerical, including very detailed SEM analysis of crack surfaces, X-ray residual stress field measurement in textured Al alloys, and macroscopic modelling of crack growth without concern to fine details. Time consuming experiments and/or detailed modelling *versus* comparatively rough approximations: each level of study must be understood, and it is up to the designer and stress analyst to decide what depth of analysis to use for each intended case. The results concerning lap joints presented in the paper suggest that acceptable answers for some complex problems may be obtained using simplifications as, for example, 2D models or consideration of mode I only.

Acknowledgements

The overview presented in this paper is based upon the contribution of IDMEC – Porto to the European Union projects 'SMAAC' (project BE95-1053) and 'ADMIRE' (project GRD1-2000-25069; contract no. G4RD-CT-2000-0396).

Professor Giorgio Cavallini (Dipartimento di Ingegneria Aerospaziale, Università di Pisa), kindly gave permission to use the experimental data of the riveted lap joint panel discussed in section 4.

References

1. FTI, *Cold Expansion Holes Using the Standard Split Sleeve System and Countersink Cold Expansion*. 2002, Fatigue Technology INC.: 150 Andover Park West, Seatle, Washinton, USA.

2. Silva, L.F.M., et al., *Multiple-site damage in riveted lap-joints: experimental simulation and finite element prediction.* International Journal of Fatigue, 2000. **22**(4): p. 319-338.
3. Swenson, D. and J. Mark, *Franc2D/L: A crack Propagation Simulator for Plane Layered Structures. Version 1.4 User's Guide*.
4. Pinho, S.P., et al., *Residual stress field and reduction of stress intensity factors in cold-worked holes.* Theoretical and Applied Fracture Mechanics, 2005. **44**: p. 168-177.
5. Ball, D.L., *Elastic-Plastic Stress-Analysis of Cold Expanded Fastener Holes.* Fatigue and Fracture of Engineering Materials and Structures, 1995. **18**(1): p. 47-63.
6. Pavier, M.J., C.G.C. Poussard, and D.J. Smith, *A finite element simulation of the cold working process for fastener holes.* Journal of Strain Analysis for Engineering Design, 1997. **32**(4): p. 287-300.
7. Lanciotti, A. and C. Polese, *The effect of interference-fit fasteners on the fatigue life of central hole specimens.* Fatigue & Fracture of Engineering Materials & Structures, 2005. **28**: p. 587-597.
8. Kang, J., W.S. Johnson, and D.A. Clark, *Three-dimensional finite element analysis of the cold expansion of fastner holes in two aluminium alloys.* Journal of Engineering Materials and Technology, 2002. **124**: p. 140-145.
9. Webster, G.A. and A.N. Ezeilo, *Residual stress and their influence on fatigue lifetimes.* International Journal of Fatigue, 2001. **23**: p. S375-S383.
10. Priest, M., et al., *An assessment of residual stress measurements around cold-worked holes.* Experimental Mechanics, 1995: p. 361-366.
11. Bauxbaum, O. and H. Huth, *Expansion of cracked fastener holes as a measure of extension of lifetime to repair.* Engineering Fracture Mechanics, 1987. **28**: p. 689-698.
12. McNeill, W.A. and A.W. Heston. *Coldworking fastner holes - theoretical analysis, methods of coldworking, experimental results*. in *ASM Conference on Residual Stresses in Design, Process and Materials Selection*. 1987. Cincinnati, OH, USA.
13. Phillips, J.L., *Sleeve coldworking fastner holes*. 1974, Air Force Materials Laboratory: Wright-Patterson Air Force Base.
14. Ozedemir, A.T., R. Cook, and L. Edwards. *Residual stress distributions around cold expanded holes*. in *18th ICAF Symposium on Estimation, Enhancement and Control of Aircraft Fatigue Performance*. 1995. Stockholm.
15. Grandt Jr., A.F. and T.E. Kullgren, *A compilation of stress intensity factor solutions for flawed fastner holes*. 1981, Materials Laboratory, Air Force Wright Aeronautical Laboratories: Wright-Patterson Air Force Base, Ohoio, USA.
16. Grandt Jr., A.F., *Stress intensity factors for some trhought-cracked fastner holes.* International Journal of Fracture, 1975. **5**(2): p. 283-294.
17. Pina, J.C.P., et al., *Residual Stress Analysis Near a Cold Expanded Hole in a Textured Alclad Sheet Using X-ray Diffraction.* Experimental Mechanics, 2004. **45**(1): p. 83-88.
18. de Matos, P.F.P., et al., *Residual stress effect on fatigue striation spacing in a cold-worked rivet hole.* Theoretical and Applied Fracture Mechanics, 2004. **42**: p. 139-148.
19. de Matos, P.F.P., *The influence of residual stresses on the fatigue bahaviour of 2024-T3 Al specimens*, in *Faculdade de Engenharia, Departamento de Engenharia Mecânica e Gestão Industrial*. 2004, Universidade do Porto: Porto. p. 281.
20. Wanhil, R.J.H., T. Hattenberg, and W.v.d. Hoeven, *A practical investigation of aircraft pressure cabin msd fatigue and corrosion*, in *NLR-CR-2001-256*. 2001, NLR.
21. Eijkhout, M.T., *Fractographic analysis of longitudinal fuselage lapjoint at stringer 42 of Fokker 100 full scale test article TA15 after 126250 simulated flights*, in *Fokker RT2160*. 1994, Fokker Aircraft Ltd.: Amsterdam.
22. Nedbal, I. *One Lecture on Fractography of Fatigue Failures*. in *Proc. École d'Été sur la Fatigue*. 1997. Saint-Pierre-d'Oléron, Paris: EC Paris / FJFI CVUT.
23. Bathias, C. and J.-P. Bailon, *La fatigue des matériaux et des structures*. Collection Université de Compiégne. 1980, Paris, Montréal,Presses de l'Université de Montréal, 547 p.
24. de Matos, P.F.P., et al., *Reconstitution of Fatigue Crack Growth in Al-alloy 2024-T3 Open-hole Specimens Using Microfratographic Techniques.* Engineering Fracture Mechanics, 2005. **75**: p. 2232-2246.

25. Schijve, J., *Fatigue of Structures and Materials*. 2001, The Netherlands: Kluwer Academic Publishers.
26. Schijve, J. *The significance of flight-simulation fatigue tests*. in *13th Symposium of the International Committee on Aeronautical Fatigue (ICAF)*. 1985. Pisa, Italy.
27. Nedbal, I., J. Siegl, and J. Kunz. *Fractographic study of fatigue crack kinetics in bodies and structures*. in *6th International Conference on Fracture (ICF6)*. 1984. New Delhi, India: Pergamon Press.
28. Nedbal, I., J. Siegl, and J. Kunz. *Quantitative Fractography - Possibilities and Applications in Aircraft Research*. in *International Colloquium "Basic Mechanics in Fatigue of Metals"*. 1988. Prague: Publishing House of the Czechoslovak Academy of Sciences.
29. Laushmann, H. and M. Blahout, *A Fractographic Reconstituion of a Fatigue Crack Front.* Fatigue and Fracture of Engineering Materials and Structures, 1994. **17**(12): p. 1391-1396.
30. Nedbal, I., J. Siegl, and J. Kunz. *Relation Between Striation Spacing and Fatigue Crack Growth Rate in Al-Alloy Sheets*. in *7th International Conference on Fracture (ICF7)*. 1989. Houston: Pergamon Press.
31. ABAQUS User's Manueal. 2004 [cited; Version 6.5:[.
32. Schijve, J., *Multiple-site damage in aircraft fuselage structures.* Fatigue & Fracture of Engineering Materials & Structures, 1995. **18**(3): p. 329-344.
33. Harris, C.E., R.S. Piascik, and J.C. Newman Jr. *A practical engineering approach to predicting fatigue crack growth in riveted lap joints*. in *In International Conference on Aeronautical Fatigue (ICAF)*. 1999. Seattle, W.A.
34. Karlson, H. and I. Sorensen, *Abaqus, Fracture Mechanics (course notes)*. 1991.
35. Broek, D., *The practical use of fracture mechanics*. 1988, Dordrecht ; Boston: Kluwer Academic Publishers.
36. Rice, J.R., *A path independent integral and the approximate analysis of strain concentrations by notches and cracks.* Journal of Applied Mechanics, 1968. **35**: p. 379-386.
37. Moreira, P.M.G.P., et al., *Stress intensity factor and load transfer analysis of a cracked riveted lap joint.* Materials and Design, 2006. **in press**.
38. Schmidt, H.J. and B. Brandecker. *On widespread fatigue damage, durability of metal aircraft structures*. in *International Workshop on Structural Integrity of Aging Airplanes*. 1992. Atlanta: Springer-Verlag.
39. Pitt, S. and R. Jones, *Multiple-site and widespread fatigue damage in againg aircraft.* Engineering Failure Analysis, 1997. **4**(4): p. 137-257.
40. Diamantakos, I., et al., *A model to assess the fatigue behaviour of ageing aircraft fuselage* Fatigue & Fracture of Engineering Materials & Structures, 2001. **24**(10): p. 677-686
41. Zuo, J., A. Kermanidis, and S. Pantelakis, *Strain energy density prediction of fatigue crack growth from hole of aging aircraft structures* Theoretical and Applied Fracture Mechanics, 2002. **38**(1): p. 37-51
42. Eastaugh, G.F., et al., *A special uniaxial coupon test specimen for the simulation of multiple site fatigue crack growth and link-up in fuselage skin splices*, . Editor. 1995.
43. Cavallini, G. and R. Lazzeri, *Report on experimental fatigue crack growth in medium and complex components*. 2003, University of Pisa - Dep. Aerospace Eng.
44. Paris, P.C., P.M. Gomez, and W.E. Anderson, *A Rational Analytic Theory of Fatigue.* The Trend in Engineering, 1961. **13**(1): p. 9-14.
45. *Fracture Mechanics of Aircraft Structures*, H. Liebowitz, Editor. 1974, AGARDograph No. 176, AGARD, p. 234.

VI. Thermal Effects: Thermal and Electrical

NUMERICAL SIMULATION OF H-TYPE STRUCTURE IN HEAT EXCHANGER WITH LONGITUDINAL FLOW OF SHELLSIDE FLUID

Qi-wu Dong*, Min-shan Liu, Xin Gu, Guang-hui Xu
Thermal Energy Engineering Research Center, Institute of Technology, Zhengzhou University, Zhengzhou 450002, China

Abstract

Shell-and-tube heat exchanger is widely used in oil refinery, chemical industry, power plant, light industry and so on. In the New-type high-efficiency heat exchanger with longitudinal flow of shellside fluid, difform new support structures, such as rod, ring, whole circular plate and so on, replace traditional segmental plate. The direction of fluid flow is changed from cross flow to longitudinal flow in shellside and there are extraordinary advantages such as higher heat transfer coefficient, lower pressure drop and better antivibration performance. Especially it is successfully used in engineering for heat exchanger with longitudinal flow of shellside fluid in which there is a new three-elements combination structure including rod-baffle support structure, distributor with varying cross section and jacket.

In above new type heat exchanger, H-type welded combination structure, which consists of the three-element including inner cylinder, ring plate and outer cylinder, is formed. Under the multi-factor coupling loading of pressure, temperature and medium erosion, the structure design method could not be found from common shell-and-tube heat exchanger design criterions and handbooks. It is critical for safe use of new type heat exchanger. So it is needed to search a scientific design method for designing and checking the structure strength.

In this paper, a detailed analysis of stress and temperature field is completed in the whole structure of the New-type heat exchanger and an instructional proposal is provided to design ring plate. A formula calculating the biggest stress of new heat exchanger is presented and is used in engineering design.

Keywords: numerical simulation, heat exchanger, H-type structure

1. Introduction

Shell-and-tube heat exchangers are widely used in process industries such as petroleum industry, chemical industry, power industry and light industry etc. In recent years, a new type of high-efficiency heat exchanger with longitudinal flow of shellside fluid has been used in such industries. The traditional segmental baffle is replaced by various kinds of new support structures such as rod-baffle, ring-baffle and whole-circle plate baffle and so on in the shellside of the new kind of heat exchanger. The direction of fluid flow in the shellside changes from cross flow to longitudinal flow. This new kind of heat exchanger has some advantages such as higher

* Crresponding author: Qi-wu Dong, Thermal Energy Engineering Research Center, Institute of Technology, Zhengzhou University, 97 Wenhua Road, Zhengzhou, Henan, 450002, China. Email address: qwdong@zzu.edu.cn

efficiency of heat transfer, lower pressure drop of fluid flow and better anti-vibration performance.

Distributors are equipped at the inlet, as well as at the outlet in the shellside of the new type heat exchanger with longitudinal flow of shellside fluid, which not only prevent the direct impact on the tube bundle from the high-velocity fluid flow at the inlet, but also benefit to the relative uniform fluid distribution in the shellside. Consequently, the heat transfer area at the inlet and outlet fields of tube bundle is well used and the inefficacious heat transfer area is decreased, at the same time, the possible flow-induced vibration of the tube bundle at the inlet and outlet fields is reduced. Especially, the heat exchanger with longitudinal flow of shellside fluid (HELFSF) with the varying cross-section distributor has been successfully used in process industry.

The HELFSF is usually attached with the jacket in order to meet some processes' requirements. For example, during the heat exchange between the semiwater gas and the converter gas in fertilizer industry, the semiwater gas is usually preheated from 130^0C to $160\sim170^0C$ before it enters tubeside of heat exchanger, which benefits to abate the dewpoint corrosion in heat exchanger. Upon that, a new type of structure is presented composed of inside distributor, ring-plate and outside cylinder. The new type of structure looks like the character H, so it can be called H-type structure. The H-type structure is shown in Fig.1.

With the couple load action of various factors such as pressure, temperature difference and corrosion medium etc, the design method of the structure strength of the new type of HELFSF with H-type structure is complex. Furthermore, there are not reference book and design principle about the new type of heat exchanger. So, in order to ensure the safety of the whole process of design, manufacture and operating, the method of scientific and reasonable design should be further developed.

2. Basic parameters of heat exchanger

The new type of heat exchanger has been widely applied in fertilizer industry and its basic technical parameters are as follows. The design pressure of both tubeside and shellside is $1.6MPa$. The semiwater gas enters tubeside through the jacket at the temperature 130^0C and the converter gas enters shellside through distributor at the temperature 470^0C. The tubes are weldless steel tubes ($\Phi25\times2.5$), which is 6 meters long. The outside cylinder diameter is $1000mm\sim1400mm$ and the inside cylinder diameter is $800mm\sim1200mm$. The materials of the main components are high quality mild steel or mild alloy steel.

3. Numerical simulation of stress in heat exchanger

The ANSYS software is used to perform the numerical analysis of the heat exchanger with longitudinal flow of shellside fluid and the H-type structure.

3.1. Model establishing

The geometric form of the H-type structure in the HELFSF is quite complex and its

geometric dimension is too big to be simulated directly. Furthermore, the stress resulted from the interaction of quite a few component parts of the heat exchanger is to be taken into account. So, the process of calculation and analysis is rather complex. Based on the actual condition of the heat exchanger, for simplifying the assumptions about the structure and material of heat exchanger are made as follows:

1) The end of the varying cross-section distributor with the jacket can freely displace along the axial direction without constraint. The incline section of the distributor is regarded as plane section and vertical with the axial direction. The whole structure of heat exchanger is an axisymmetric body, therefore, it is feasible to extract a quarter of the whole body as the model.

2) The material of the component parts of heat exchanger is isotropic, homogeneous and continuous. The physical character of the two kinds of main material is almost the same as each other, so they are dealt as the same material in the process of numerical analysis.

3) With regarding the arithmetic mean temperature of the medium at inlet and outlet of the heat exchanger as the qualitative temperature, so the physical and mechanical character of medium and material can be determined.

4) The tubesheet and the cylinder are jointed together with the welding means, as well as the tube bundle and the tubesheet jointed together. There is not slip between the component parts of heat exchanger.

5) The action between the support structure and tube bundle in the shellside of the HELFSF is ignored.

6 The influence of the action of the equipment weight and outside constraints on the strength of heat exchanger is ignored.

7) The outside wall of heat exchanger is adiabatic, that is to say $dt / dr = 0$.

Because structure discontinuity and edge effectiveness at the linkage of cylindrical shell and cover in heat exchanger, the edge stress occurs at the area of connection. The effect scope of edge in the cylindrical shell is estimated by using Eq. $2.5\sqrt{RS}$ and the length of model is to be chosen felicitously.

According to the above consideration, the 3D model and the physical model of heat exchanger are established, which is shown in Fig. 1 and Fig. 2 respectively.

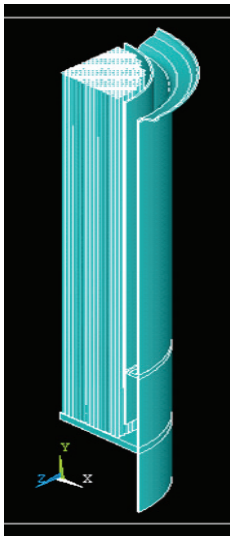

Fig.1 Heat exchanger 3D model

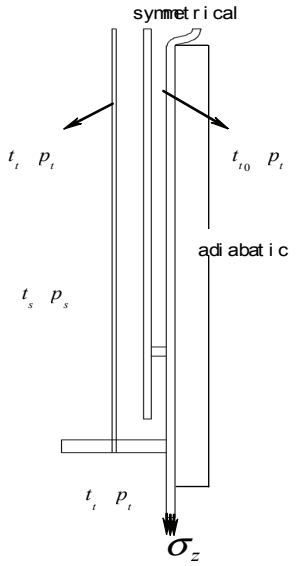

Fig. 2 Heat exchanger physical model

3.2 Elements and mesh

It is very important to select element type for getting the correct analysis results. The following elements are used in this paper, shown in Table 1.

Table 1 element selection

element type	element name	remark
structure solid element□2D□	PLANE 82	8-node quadrangle element
structure solid element□3D□	SOLID 45	8-node hexahedron element
thermal solid element□2D□	PLANE 77	8-node quadrangle element
thermal solid element□3D□	SOLID 70	8-node hexahedron element

In the paper, the method of indirect coupling is applied for calculation and analysis. Those elements presented in Table 1 are enough to deal with the temperature field and stress analysis of the H-type structure in this kind of heat exchanger. The 3D model and the 2D model are analyzed respectively. The 2D model analysis is responsible for calibration of the 3D model analysis result.

It is important to partition mesh reasonably for ensuring the dependability of analysis result. If the mesh is too dense or the number of the nodes is too many, it is difficult to perform the calculation. The mesh is generated by the order flow program of the ANSYS software. Fig. 3 and Fig. 4 show the whole structure mesh and the H-type structure mesh of heat exchanger, respectively.

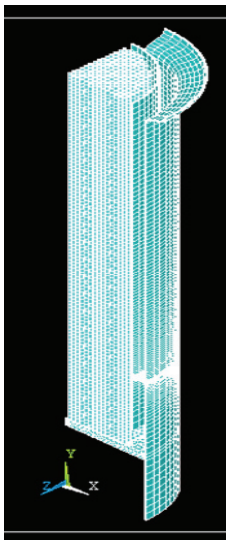

Fig. 3 Whole structure mesh of heat exchanger

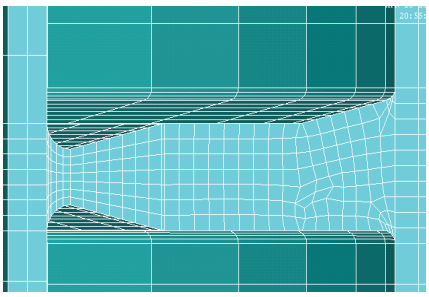

Fig.4 H-type structure mesh of heat exchanger

3.3 Temperature load

In order to analyze the distribution of the temperature field, the surface temperatures of the component parts of heat exchanger are reasonably estimated. The fluid flow velocity on the up surface and down surface of the tubesheet are estimated and the flow modality on the two sides of surfaces of tubesheet are determined (turbulent flow or laminar flow). Sequentially, the temperature is obtained by calculating the heat transfer coefficients. Because the locality of the ring-plate is invalid area for fluid flow, flow modality on the two sides of surfaces is quite different from that of the tubesheet. The free convection heat transfer equation is used to perform the calculation in this area and the reasonable result is obtained. At the same time, the reasonable result is also obtained in the jacket outside cylinder and the equation referred from the traditional heat transfer book is applied to calculating the heat transfer coefficient. The layout of walls for heat exchange is shown in Fig. 5. The temperature estimated is shown in Table 2.

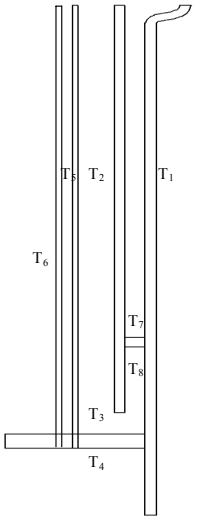

Fig. 5 Temperature estimated for wall of heat exchanger

Table 2 temperature estimated for the walls of the component parts in heat exchanger

location	code	heat transfer	wall temp. ^0C
jacket outside cylinder	T_1	237.3	233.5
shellside	T_2	233.2	237.0
	T_6		297.5
tubeside	T_5	199.4	297.3
ring-plate	T_7	16.1	250.7
	T_8	23.7	251.5
tubesheet	T_3	127.3	298.5
	T_4	82.8	297.1

3.4 Numerical simulation of thermal stress

Firstly, numerical simulation of the temperature field of the HELFSF is performed by the following steps. The 8-node hexahedron 3D thermal elements are selected, as well as the material codes of component parts. All of the models of component parts of heat exchanger are linked by the functions of glue and overlap of Boolean operation in the ANSYS software. By using three functions of mapping, scan and freedom, the partition, inspection and modification of mesh are performed to decrease the error occurrence when the calculation is proceeded. The results of numerical simulation of temperature field in the whole body of heat exchanger, the ring-plate of H-type structure and the expansion joint are shown in Fig. 6, Fig. 7 and Fig. 8, respectively.

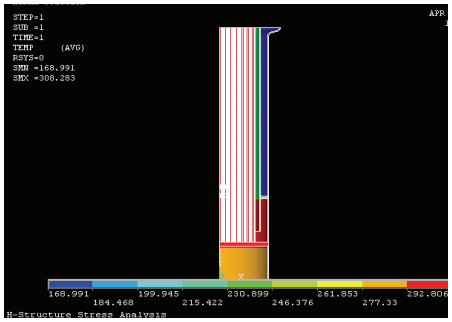

Fig. 6 Temperature contour of whole heat exchanger

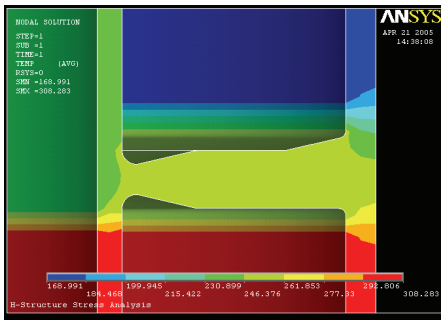

Fig.7 Temperature contour of H-type

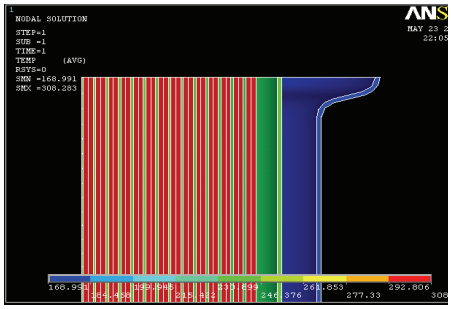

structure

Fig.8 Temperature contour of expansion joint

Secondly, the 8-node hexahedron 3D thermal elements are replaced by the 8-node hexahedron 3D structure elements. The boundary conditions and the results of temperature field obtainded in above section are led into the calculation process of the stress field. The results of numerical simulation of stress field in the whole body of heat exchanger, the ring-plate of H-type structure and the expansion joint are shown in Fig. 9, Fig. 10 and Fig. 11, respectively.

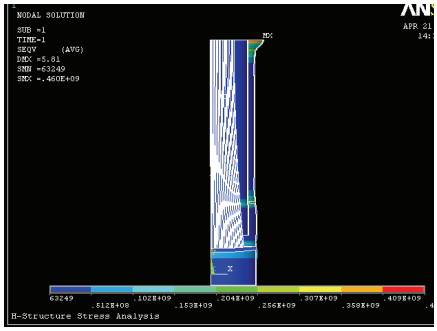

Fig. 9 Stress and deformation distribution of whole heat exchanger

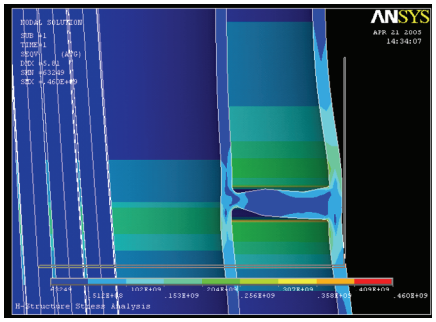

Fig. 10 Stress and deformation distribution of H-type structure

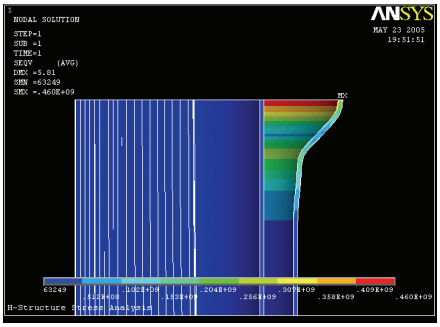

Fig. 11 Stress and deformation distribution of expansion joint

4. Numerical simulation results and synthesized analysis

Base on the series of this kind of heat exchanger and the same process condition, which are applied in the fertilizer industry, the numerical analysis of the biggest stress of heat exchanger, as well as the ring-plate are completed in this research, including five series of different cylinder diameters and nine kinds of different ring-plate thickness.

A heat exchanger with the outside cylinder diameter of $1200mm$ and the inside cylinder diameter of $1000mm$ is given as an example. The influence of ring-plate with different thickness on the biggest stress of the heat exchanger, ring-plate and expansion joint is analyzed. Analysis results are shown in Fig. 12, Fig. 13 and Fig.14, respectively.

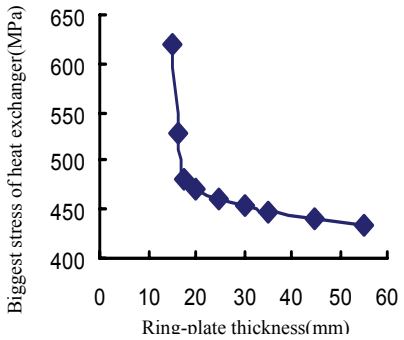

Fig. 12 Ring-plate thickness and biggest stress of heat exchanger

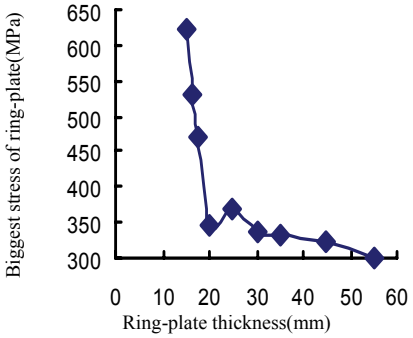

Fig. 13 Ring-plate thickness and biggest stress of ring-plate

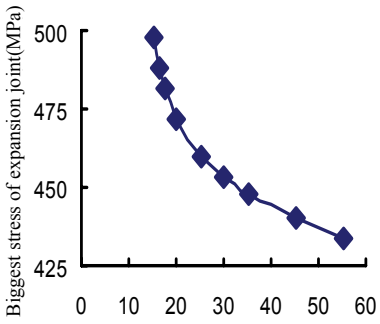

Ring-plate thickness(mm)

Fig.14 Ring-plate thickness and biggest stress of expansion joint

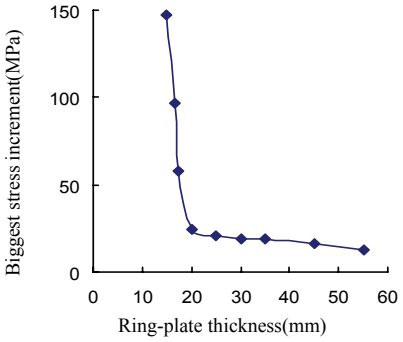

Fig.15 Ring-plate thickness and biggest stress increment

By use of the dimensional analysis method the numerical simulation results and curve diagrams are analyzed and concluded. The relational expression between the biggest stress of heat exchanger and the cylindrical shell diameter D, the thickness of ring-plate S is presented, shown in the following equation.

$$\sigma = c_1 + \frac{c_2 + c_3 . D}{S - c_4}$$

where

parameters:

$c_1 = 434 , c_2 = -694 , c_3 = 0.8 , c_4 = 13.7$

D = shell diameter (mm)

S = ring-plate thickness (mm)

σ = the biggest stress of heat exchanger (MPa)

The biggest relative error between the calculation result by the above equation and the analysis result by the ANSYS software is less than 5%. When the ring-plate is too thin, which oversteps the scope of practical engineering application, the biggest relative error is less than 10%. This kind of error can meet the practical engineering requirement.

From the above studies, some conclusions can be got as follows:

1) The thickness of the ring-plate in the H-type structure in this kind of heat exchanger has a notable influence on the biggest stress of the heat exchanger, the ring-plate and the expansion joint. So, it is significant to select reasonably the thickness of the ring-plate for the safety of heat exchanger (shown in Fig.15). Within the scope of process condition and cylindrical shell dimension of this research, when the thickness of the ring-plate is less than $20mm$ the stress in heat exchanger, ring-plate and expansion joint will be significantly increasing. The thickness of the ring-plate is usually selected within the scope of $25mm \sim 30mm$.

2) The biggest stress of heat exchanger occurs at the area of the middle of the expansion joint which connects with outside shell and the area where the ring-plate connects with outside shell and inside shell.

3) Besides the axial stress, the stress is membrane stress in the outside cylindrical shell of heat exchanger. Temperature difference has a notable influence on the axial stress, which is overlapped by the membrane stress resulted from the pressure and the thermal stress resulted from the temperature difference, as well as the axial direction stress in the inside shell. The biggest stress is increased with increasing the shell diameter.

References

[1] Qiwu Dong, Minshan Liu, Chaxiu Guo, Qingjun Hu and Xuesheng Wang. Characteristic research of the new type energy-saving tubular heat exchanger with longitudinal-flow of shellside fluid, Proceedings of ICEE Beggell House Press, 1996, PP. 448-454

[2] Guanghui Xu. Numerical simulation of H-type structure in heat exchanger with longitudinal flow of shellside fluid and secondary development,[M], Zhengzhou University, 2005

[3] Qiwu Dong, Minshan Liu, Xiaodong Zhao and Yongqing Wang. Research on the characteristic of shellside support structures of heat exchange with longitudinal flow of shellside fluid, IASME Transactions, Issue8, Volume2, October 2005, PP. 1491-1498

[4] C. C. Gentry, Rod baffle heat exchanger technology, Chemical Engineering Progress, Vol86, No71,1990

[5] Vincent Manet. The use of ANSYS to calculate the behaviour of sandwich structures, Composites Science and Technology, vol56, 1998

[6] Shuguang Gong. ANSYS basic application and example analysis, Beijing: Mechanical Industry Press, 2004. 01

[7] Shuguang Gong. ANSYS analysis of engineering application example, Beijing: Mechanical Industry Press, 2003. 04

[8] Minshan Liu, Qiwu Dong and Dingbiao Wang. Numerical simulation of thermal stress in tube-sheet of heat transfer equipment, International Journational Pressure, Vessels and Piping, 1999

DAMAGE BEHAVIOR OF TiAl ALLOY UNDER THERMAL FATIGUE AND DEAD-LOAD THERMO-MECHANICAL FATIGUE

Li Jun, Qiao Sheng Ru*, Han dong, Li Mei
Ultra-high-temperature structural composites laboratory of Northwestern Polytechnical University, Xi'an, 710072, China

Abstract

The investigated γ-TiAl was of the nominal composition Ti-46.5Al-2.5V-1.0Cr (at%) and was radiant heated in air. Thermal fatigue tests were performed in the temperature ranges of 200-700□and 200-900□. Tests of dead-load thermo-mechanical fatigue were conducted under the following conditions: 200-700□with 70MPa and 140MPa dead-load tensile stress, respectively, and 200-900□ with 70MPa. At the vested cycle, the dynamic elastic modulus and electrical resistance were measured at room temperature. The relative change of modulus D_E and that of electrical resistance D_R were employed to characterize damage. In the shorter thermal cycling, the damage parameters increased intensely, and the discrepancy between D_E and D_R was very limited. Then, the damage parameters increased very slowly as the number of cycles increased and approached a constant, and the discrepancy also trended to a stable constant. The negative increase of D_E at 200-700^oC with 70MPa and 140MPa dead-load stress occurred at the very start, and increased after a few cycles. Then, the negative increase emerged again, and D_E increased slowly as the number of cycles increased and finally reached a constant value; At 200-900 ^oC with 70MPa dead-load stress, at the beginning of cycling, D_E increased intensely, and decreased slightly at the 20th cycle. Thereafter, D_E increased slightly and then remained at a constant. D_R did not increase negatively like D_E. D_R increased intensely in the first few cycles and followed by fluctuation. Then the stable damage stage occurred. Temperature drop affected D_R more than dead-load stress. The fine and dark γ phase increased and the size of lamellar colony reduced obviously after thermal cycling. This occurs not only in thermal fatigue but also in dead-load thermo-mechanical fatigue. After thermal cycling the damage appear as micro-pores and micro-cracks, etc.

Keywords: γ-TiAl; Thermal Fatigue; Dead-load Thermo-mechanical Fatigue; Damage; Elastic Modulus; Electrical Resistance.

1. Introduction

γ-TiAl alloys have low density, high specific strength and specific modulus, and excellent creep and oxidation resistance. Such properties make them come to be one of the candidate high-temperature structural materials. However, the applications of γ-TiAl alloys are impeded by their poor machinability and ambient temperature ductility. At present, the majority of research work has focused on alloy modifications through compositional controls by alloying with additional metallic elements and by improving fabrication techniques, which improve the low temperature ductility and toughness, high temperature creep resistance, and processing properties, etc [1-4].

It's inevitable that the service environments for γ-TiAl alloys, as a high-temperature structural material, involve thermal transients or in combination with mechanical stress or strain. The laws governing γ-TiAl alloys under thermal fatigue and dead-load thermo-mechanical

*Corresponding author: Prof. Qiao Sheng Ru.
Tel: +86-029-88492084; Fax: +86-029-88492084; E-mail: blao@nwpu.edu.cn.

fatigue, to the authors` knowledge, are still unclear. There exists only limited publication regarding these aspects [6-10]. The present work aimed to develop a basic understanding of the laws governing γ-TiAl alloys under thermal fatigue and combination of thermal cycling and dead-load stress, including the transformations of microstructure and phases, the damage behavior and the effect of mechanical stress, etc. In addition, the damage mechanisms were also discussed.

2. Experimental procedures

The investigated alloy was of the nominal composition of Ti-46.5Al-2.5V-1.0Cr (at%). The ingots, prepared by vacuum induction magnetic suspension melting technology, were hot isostatically pressed (HIP) at 1290°C under 150MPa in an argon atmosphere for 2.2h to remove casting porosity and to increase sample uniformity. The as-received microstructure of alloy was nearly lamellar, consisting of lamellar colonies containing alternating γ and α_2 platelets, and equiaxed γ phase in the lamellar colony boundaries. The cross-section macrostructure of ingot and the sketch map of sampling were shown in Fig. 1.

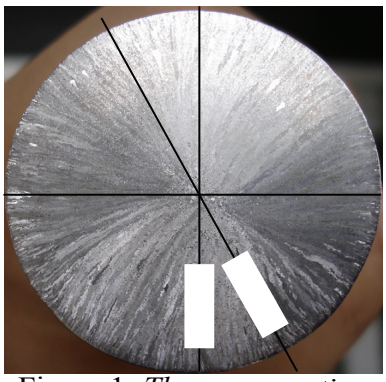

Figure 1: *The cross-section macrostructure of ingot and sampling schematic diagram (cross-section)*

Columnar crystals grew along the radial direction, which can ensure the microstructures of samples were consistent. The samples, 65mm (length)x2mmx3mm in size for thermal fatigue and 85mm(length)x2mmx3mm for thermal-mechanical fatigue ,were cut using Electrical Discharge Machine (EDM), and annealed at 100°C in oven for 2h to remove any machining stress.

The specimen was radiant heated in air, and the apparatus, employed to tests, was described in Refs [9]. Thermal fatigue tests were carried out in the temperature ranges of 200-700 and 200-900°C. Three different testing conditions for dead-load thermo-mechanical fatigue were used. They were temperature range of 200-700□with 70MPa and 140MPa dead-load tensile stress, respectively, and 200-900□ with 70MPa.

A platinum-rhodium thermocouple was used to measure the surface temperature. The heating and cooling time of thermal cycles are shown in table 1.

Temperature ranges	Heating time	Cooling time
200-700□	16[s]	50[s]
200-900□	25[s]	55[s]

Table 1: The parameters of thermal cycling

At a predetermined number of cycles, the dynamic elastic modulus of sample was measured by forced resonance techniques. The resolution of resonance frequency is 0.1 Hz. A QJ84 digital constant-current electric bridge was employed to measure electrical resistance. The measurement range and precision of electric bridge is 0~20KΩ and 10^{-6}Ω, respectively. Electrical resistance was measured five times at the same position on the sample, and the average was reported as the measurement value.

Samples were etched in a solution of 1%HF+2%HNO_3+97%H_2O (vol%), and Scanning Electron Microscopy (SEM) was employed to observe the microstructure pattern of the samples. XRD analysis was carried out on a D/Max-3C X-ray Diffraction apparatus for primary and subsequent phase identification and for quantitative analysis of the specimens.

3. Damage assessment

Two non-destructive examination methods were employed to characterize the damage under thermal cycling.

The extent of damage can be represented by the retained elastic modulus after thermal cycling and was defined in Eqs. (1) [10-13]:

$$D_m = 1 - \frac{E_N}{E_0} = 1 - \frac{f_N^2}{f_0^2} \quad (1)$$

Where E_0 is the elastic modulus of as-received sample, E_N is elastic modulus after N cycles; f_0 is the resonance frequency of as-received sample, f_N is the resonance frequency after N cycles. The right hand side of the above equation is obtained in accordance with the law of elastic modulus which states that the elastic modulus is proportional to f^2 [10-13]. D_E is a modulus damage parameter. D_E can vary from 0 to 1.

Another damage parameter D_R can be defined to represent the relative change of electrical resistance after thermal cycling [14-15]:

$$D_R = 1 - \frac{R_0}{R_N} \quad (2)$$

Where R_N is electrical resistance after N cycles, R_0 is the electrical resistance of as-received sample, and D_R is electrical resistance damage parameter. D_R also can vary from 0 to 1.

4. Results

4.1 Damage curve

4.1.1 The thermal fatigue

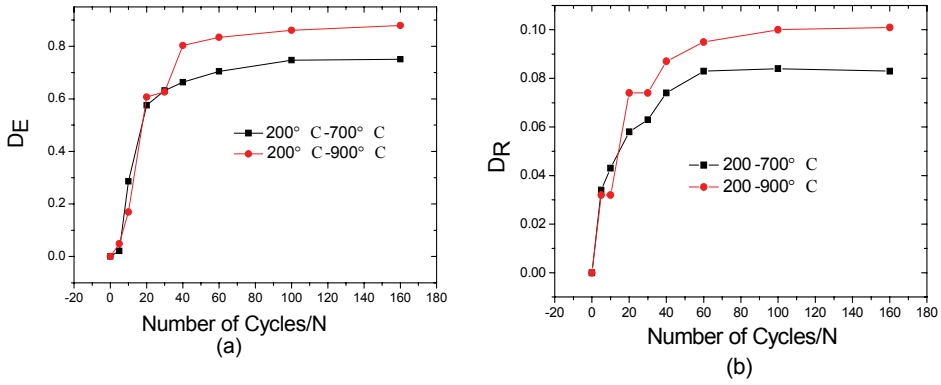

Figure 2: *Damage parameters as a function of the number of cycles under thermal fatigue: (a) Modulus damage parameter D_E; (b) Electrical resistance damage parameter D_R.*

The damage parameters D_E and D_R as a function of the number of cycles under thermal fatigue were shown in Fig. 2. As can be seen, the trend of the two damage curves, determined by the two non-destructive examination methods, was consistent. In the shorter cycles, the damage parameter increased intensely, and the discrepancy between two damage parameters was very limited. Then, the damage parameter increased very slowly after a few cycles and approached a constant. This is referred to as the stable damage stage. At this stage, the discrepancy between D_E and D_R increased as the number of thermal cycling increased, and trended to a stable constant. Fig. 2 also shows that the damage of the specimen with big temperature difference (or high maximum temperature), at the stable damage stage, was greater than that with small one. The higher the temperature difference the sample had, the larger the thermal stress in the sample, caused by temperature gradient, and the larger the damage generated. Such phenomena coincide with the general law of thermal fatigue. In addition, the inflexions appeared at about the 30th cycle on the two damage curves of thermal fatigue at 200-900^{o}C. It is revealed that D_E and D_R had well corresponding relationships, and could be used to characterize the damage of γ-TiAl under thermal fatigue.

4.1.2 dead-load thermo-mechanical fatigue

Fig. 3 shows the damage parameter D_E and D_R as a function of the number of cycles under three different dead-load thermo-mechanical fatigue conditions *(It was found that the damage parameter D_E*

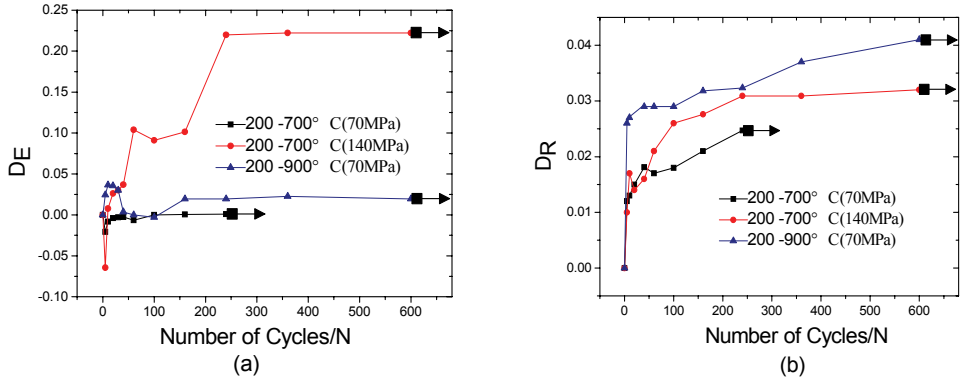

Figure 3: *Damage parameters as a function of the number of cycles under dead-load thermo-mechanical fatigue*: *(a)* D_E; *(b)* D_R.

showed limited rise after examination at 200-700 °C *with 140MPa dead-load stress and 200-900*°C *with 70MPa, so the measurement of 200-700* °C *with 70MPa ceased at 240*th *cycle)*. As can be seen from fig. 3a, the damage parameters D_E, at some stage in the shorter cycles, also increased negatively. The differences among three testing conditions are as follow: The negative increase of D_E of 200-700°C with 70MPa and 140MPa dead-load stress occurred at the very start, and increased after a few cycles. Then, the negative increase emerged again when the number of cycles increased, and D_E increased slowly and almost held at a constant; D_E of 200-900°C with 70MPa dead-load stress, at the beginning of cycling, increased intensely, and descended slightly after the 20th cycle. Thereafter, D_E increased slightly and maintained at a constant.

At the stable damage stage, D_E hardly changed. The D_E at 200-700°C with 140MPa dead-load stress was the biggest among three testing conditions, and that of 200-900°C with 70Mpa was larger than 200-700°C with 70MPa. It was shown that the samples with bigger stress presented larger damage than that with lesser stress under the same temperature drop; and, the samples with bigger temperature drop (higher maximum temperature) exhibited larger damage than that with lower one under the same stress. It was also shown that the temperature drop (or maximum temperature), at the shorter cycles, was more sensitive to the damage parameter D_E, and the effect of dead-load stress on D_E was remarkable as the number of cycles increased,

As can be seen form Fig. 3b, the negative increase of D_E did not occur on D_R. The trend of the three curves was consistent with each other, and all of them increased intensely in the first few cycles and followed by fluctuation. Then, the stable damage stage occurred. At the stable damage stage, D_R at 200-900°C with 70MPa dead-load stress, among the three testing conditions, was the biggest, and that at 200-700°C with 140MPa and 70MPa took second and third place, respectively. It is obvious that the influence of temperature drop on D_R was more pronounced to dead-load stress. Comparing to the two plot of Fig. 3, it was concluded that the D_E, for dead-load thermo-mechanical fatigue with lower stress (70MPa), was smaller than D_R and the D_E, for that with bigger stress (140MPa), was also smaller than D_R at the earlier cycles, the opposite is true at the stable damage stage.

4.2 Microstructure observation

Fig.4 shows microstructures of the as-received sample and that of the samples after thermal cycling. Comparing to as-received microstructure, the fine and dark γ phase increased and the size of lamellar colony reduced obviously after thermal cycling, which occurred not only in thermal fatigue tests but also in dead-load thermo-mechanical fatigue tests. This was

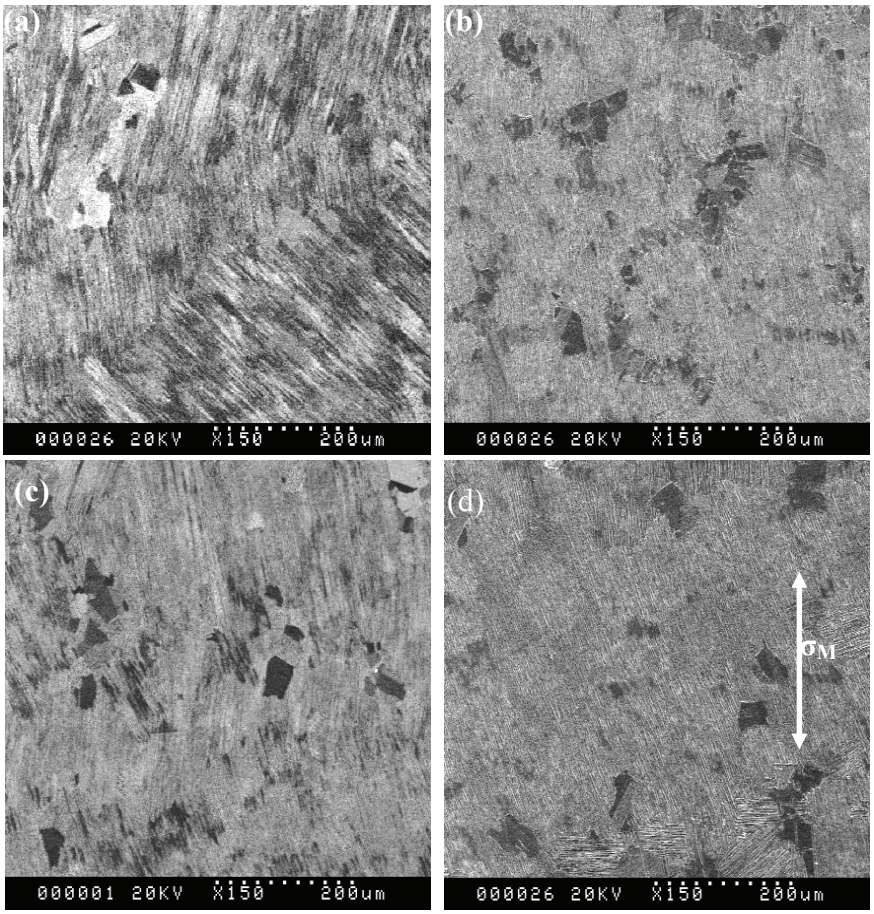

Figure 4: *The microstructures of γ–TiAl: (a) As-received ;(b)200-700□ after160 cycles; (c) 200-900□ after160 cycles;(d) 200-700□ with 140MPa dead-load tensile stress after160 cycles.*

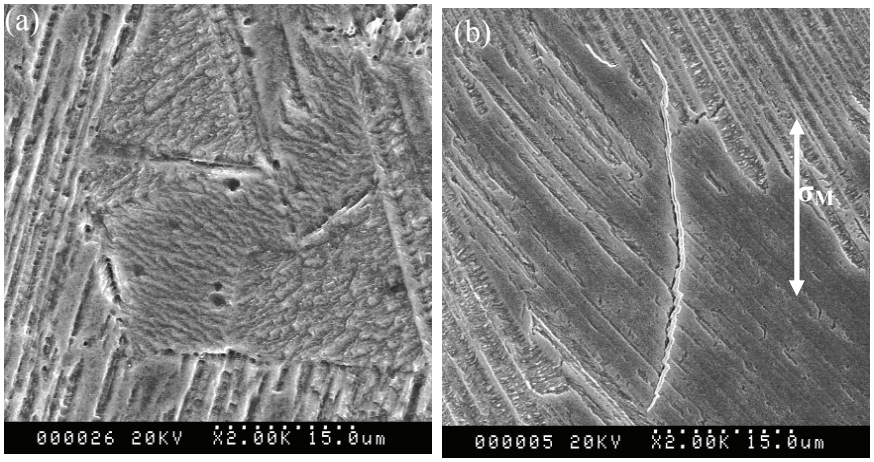

Figure 5: *The microstructures of γ–TiAl after thermal cycling: (a) 200-700□; (b) 200-700□ with 140MPa dead-load tensile stress.*

subsequently validated by XRD analysis. The more fine transformations were found by higher power microstructure observation. After thermal fatigue Micro-pores emerged in equiaxed γ phase and the lamellar colony, micro-cracks did not come forth. Nevertheless, micro-cracks appeared across the whole lamellar colony after dead-load thermo-mechanical fatigue

5. Discussion

Based on the Ti–Al alloy phase diagram (Fig. 7), the content of γ phase is large, and that of α_2 is very small at 46.5%Al content. At the heating stage of thermal cycling, the content of γ phase enhanced relatively, and that of α_2 decreased

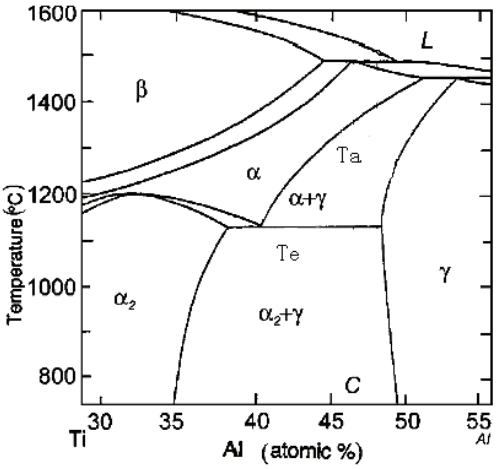

Figure 7: *Ti-Al alloy phase diagram* [1]

correspondingly; this phase change is reversible and the reverse occurs during the cooling stage. α_2 is an ordered phase of hexagonal symmetric structure , and γ is an ordered type of face-centered tetragonal structure. Owing to the difference in crystal structure, the stack faults at the interfaces of γ/α_2 transferred, driven by the volume free energy, to the direction of decreasing α_2 and increasing γ at the heating stage of thermal cycling [17]. In addition, the heating and cooling rates were fast during testing, which made the material stay at a non-equilibrium state at all times. The γ and α_2 were ordered phases, and formed by diffusion. During thermal cycling, the elastic strain energy generated by thermal stress becomes the driving force for diffusion [18]. The enthalpy of γ phase formation is lower than that of α_2 phase [19]. Therefore, it is difficult for α_2 phase to form by diffusion, and α_2 phase dissolved into γ phase during thermal cycling. The thermal stress generated by heating and cooling could also induce the break up of lamellar colony, and thinner lamellar colony would form. Therefore, after thermal cycling, the content of γ phase increased, and α_2 decreased accordingly (Fig. 4). The size of lamellar, simultaneously, reduced (Fig. 4), and flaws, such as micro- pores and micro-cracks (Fig. 5), appeared. The increase of γ phase generated by heating and cooling can also be found during elevated temperature dynamic stretching of γ-TiAl alloy [20].

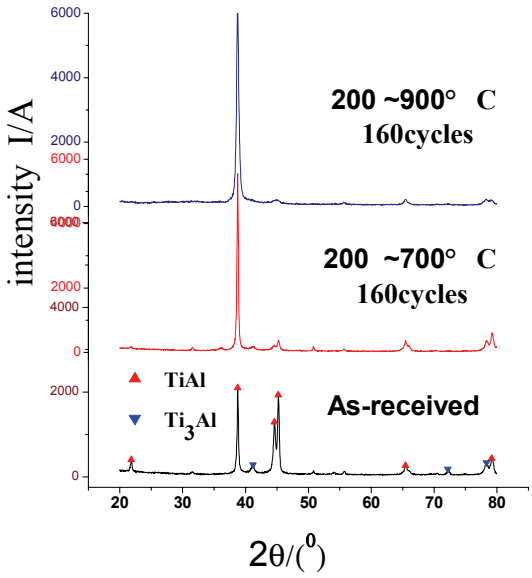

Figure 8: *The XRD pattern of samples before and after thermal fatigue*

XRD analysis further validated these conclusions and microstructure observations. Fig. 8 shows the XRD pattern of samples before and after thermal cycling. Since the main factor influencing the phase transformation was temperature not dead-load stress, we did not perform XRD analysis of samples after dead-load thermo-mechanical fatigue. As can be seen, diffraction peak of γ-TiAl was still obvious after thermal cycling, and its intensity enhanced. The diffraction peak intensity of 200-900°C was bigger than that of 200-700°C after the same number of thermal cycles. After thermal cycling, the diffraction peak intensity of α_2 reduced dramatically in samples tested at 200-700°C, and nearly disappeared in samples tested at 200-900°C. It was concluded that the content of γ phase increased and the integrity of crystal elevated at the same time. And the content of α_2 phase decreased accordingly. The contents of γ and α_2 phases before and after thermal cycling were analyzed by XRD quantitatively, and the results are shown in Table. 2**.**

Generally, the mode of release for thermal stress is as follow: when the elastic misfit strain of the two phases, generated by thermal stress, is high enough, dislocation would launch from the phase boundary to

Microstructures states	Contents of γ	Contents of α_2
As-received microstructure	88□	12□
200-700□ 160 Cycles	90□	10□
200-900□ 160 Cycles	95□	5□

Table 2: The contents of γ and α_2 in microstructure before and after thermal fatigue

the bulk phase; If dislocations could not activate due to unfavorable crystal orientation, stack faults and deformation twins will form first [18]. Thermal stress and volume internal stress generated due to the changes of phase content increased the probability for the formation of dislocations and twins [21]. Such changes caused the increase in the electrical resistance damage parameter D_R. On the one hand, the probability of conductive electron scattering increased because of the reduction in size of the lamellar colonies and because of the microscopic flaws, this in turn caused an increase in electrical resistance [22]. On the other hand, the electrical resistance of alloy also increased owing to the decrease of effective loaded area because of the formation of micro-pores [15]. In addition, the increase in micro-pores and the intragranular and interphase damages could also weaken interatomic combining force and reduce the elastic modulus simultaneously, resulting in an increase in the elastic modulus damage parameter D_E.
In the present work, we have shown that the damage of thermal fatigue mainly emerged in the form of micro-pores. According to the damage mechanics, the damage measured by the electric method should be less than that by the mechanical method [22]. The damage characterized by the elastic modulus indicates the overall damage of material [23], while that characterized by electrical resistance is usually related to the influence of flaws on electron conduction. Therefore, D_E is larger than D_R,and there were differences existed on the damage curves between D_E and D_R(Fig. 2).
The damages caused by dead-load thermo-mechanical fatigue appear in the form of micro-cracks (Fig. 5b). Micro-cracks have more significant influence than micro-pores on electrical resistance value [22]. Considering other factors affecting damage, D_R would become larger when there are micro-cracks. Comparing the two damage curves of dead-load thermo-mechanical fatigue, it is concluded that the D_E, measured by mechanical method, was more sensitive to dead-load stress, while temperature drop (or higher maximum temperature) has a more significant effect on D_R measured by the electric method.
In our opinion, the negative increase of D_E shown in the Fig. 3 could be caused by cyclic hardening. Cyclic hardening occurs in many materials after thermo-mechanical fatigue, and decreases at higher temperatures [6, 20]. The reduction of cyclic hardening was found in dead-load thermo-mechanical fatigue at 200-900□ with 70MPa stress, which coincides with that reported in Refs [6]. However, further research is needed to determine the validity of such hypothesis.

6. Conclusion

1. During shorter thermal cycles, the damage parameter increased intensely, and the difference between the two damage parameters was very limited□Then, the damage parameter increased very slowly as the number of cycles increased gradually and finally approached a constant, and the difference between D_E and D_R also become stable.
2. The negative increase of D_E at 200-700^{o}C with 70MPa and 140MPa dead-load stress occurred at the very start, and increased after the first few cycles. Then, The negative increase of emerged again, and D_E increased slowly as the number of cycles increased until reaching a constant; D_E at 200-900^{o}C with 70MPa dead-load stress, at the beginning of cycling, increased intensely, and decreased slightly at the 20th cycle. Thereafter, D_E increased slightly until reached a constant. The negative increase of D_E did not occur in D_R. D_R increased intensely in the first few cycles and followed by fluctuation. Then the stable damage stage occurred. Temperature drop affected D_R more than dead-load stress.
3. The fine and dark γ phase increased and the size of lamellar colony reduced obviously after thermal cycling. This occurs not only in thermal fatigue but also

in dead-load thermo-mechanical fatigue. After thermal cycling the damages appear as micro-pores and micro-cracks, etc.

Acknowledgement

The authors wish to acknowledge Prof. Li Shi Qiong of Central Iron & Steel Research Institute of China for providing the material. The authors also would like to acknowledge the support of Program for Changjiang Scholars and Innovative Research Team in University (PCSIRT).

References

[1] Y-W. Kim, (1989), *JOM*, 41, No.7, pp. 24.
[2] Y-W, Dennis M.Dimiduk, (1991), *JOM*, 43, No.8, pp. 40.
[3] Liu CT, Maziasz PJ, (1998), *Intermetallics*, 6, pp. 653.
[4] Y-W. Kim, (1995), *Mat Sci Eng A*, A192–193, pp. 519.
[5] William Dunfee, Ming Gao, Robert P, (1995), *Scripta Mater*, 33, No.2, pp.245.
[6] H.-J. Christ, F.O.R. Fischer, H.J. Maier, (2001), *Mater Sci Eng* A, 319-321, pp. 625.
[7] Marcel Roth, Horst Biermann, *Scripta Mate*, (2006), 54, pp.137.
[8] Li jun, Qiao Sheng Ru, Li Shi Qiong, Zhang bin, (2006), *Journal of Aeronautical Materials*, to be published. *(in chinese)*
[9] Du Shuang Ming, Qiao Sheng Ru, LV Bao Tong (2000) In: Proceedings of the seventh national conference on thermal fatigue, pp.154-159, Shao-lun Liu (Eds).Chinese Society of Metals, Hai kou. *(in chinese)*
[10] J.C. Goldsby, (2000), *Mater Sci Eng* A, 279, pp. 266.
[11] Won Jae Lee, Eldon D.Case. (1992), *Mater Sci Eng* A, 154, No.1, pp. 1.
[12] H.Wang, R.N.Singh, (1994), *Int Mater Rev*, 39, No.6, pp.228-.
[13] C. Kaya, F. Kaya, H. Mori, (2002), *J Eur Ceram Soc*, 22, pp.447.
[14] Lemaitre J, Dufailly J, (1987), *Eng Fract Mech*, 28, No.5, pp.643.
[15] Binxiang Sun, Yimu Guo, (2004), *Int J Fatigue*, 26, pp.457.
[16] Y. Mishin, Chr. Herzig, (2000), *Acta Mater*, 48, No.3, pp.589.
[17] P. Pouly, M. -J. Hua, C. I. Garcia and A. J. DeArdo, (1993), *Scripta Mate*, 29, No.12, pp.1529.
[18] Geng Hong Bin □ He Shi Yu □ Lei Ting Quan, (1997), *The Chinese Journal of Nonferrous Metals*, 7, No.3, pp.99.*(in chinese)*
[19] Murry J, (1987), *Binary Alloy Phase Diagram*, American Society for Metals, Metals Park, Ohio.
[20] Ou Wen Pei, Huang Bo Yun, HE Yue Hui. et al, (1997), *Mining and Metallurgical Engineering*, 17, No.1, pp.68. *(in chinese)*
[21] Li Bao Shan (2000) In: Proceedings of the seventh national conference on thermal fatigue, pp.225-235, Shao-lun Liu (Eds).Chinese Society of Metals, Hai kou. *(in chinese)*
[22] Zang Yong Gang, *Intermetallics Structural Materials*, National Defence Industry Press, Beijing. *(in chinese)*
[23] Li pin, (1992), *Basic Damage Mechanics*, Shandong Science & Technology Press, Shandong. *(in chinese)*
[24] Venkata R. Vedula, David J. Green, John R. Hellmann, (1998), *J Eur Ceram Soc,* 18, pp.2073.

THERMOELECTRIC HYDROGEN SENSOR BASED ON Bi0.5Sb1.5Te3 AND Pt/α-Al_2O_3 FILMS

Weiling Luan, Hu Huang, Jiansong Zhang, Shan-Tung Tu
School of Mechanical and Power Engineering, East China University of Science and Technology, Shanghai 200237, P.R.China

Abstract

A thermoelectric hydrogen sensor was fabricated based on the Seebeck effect of $Bi_{0.5}Sb_{1.5}Te_3$ and the hydrogen oxidation on Pt / α-Al_2O_3 catalyst. $Bi_{0.5}Sb_{1.5}Te_3$ film was deposited by RF magnetron sputtering and then the catalytic layer was dip-coated on its surface. The phase structure and morphology of thermoelectric and catalyst layers were studied. The Seebeck coefficient of $Bi_{0.5}Sb_{1.5}Te_3$ film showed a high value of 400μV/K and excellent temperature stability ranging from RT to 160°C. The porous Pt/α-Al_2O_3 layer increased the reacting area surface and displayed a large temperature difference of 50°C around RT with a short response time of 25s. As-composed sensor demonstrated many merits such as simple structure, low energy consumption, high sensitivity, quick response and recoverability. Experimental results showed that when exposing to 3vol% H_2 / air, the sensor gave out a strong output signal of 26.6mv with response time of 50s and recovering time of 100s.

Keywords: hydrogen sensor, thermoelectric film, $Bi_{0.5}Sb_{1.5}Te_3$, Pt catalyst

1. Introduction

Hydrogen is the most potential energy carrier due to its wide resources, burning cleanness and high exothermic value. At the same time, hydrogen is among the most dangerous gases because of its high propensity to leak, explode, and combustion. The technology for sensors on detection and monitoring of gaseous hydrogen is essentially demanded. Large varieties of hydrogen sensor were designed and fabricated according to their different principle and requirement of applications. Traditional sensors are mostly made from semiconductor, thermal conductor, and optical fiber. Recently, with the increasing development of nano-technology, new kinds of sensors come into appearance, such as carbon nano-tube[1], palladium nano wire[2], and TiO_2 nano-tube[3]. Though conventional hydrogen sensors have been widely commercialized, but their shortages of high operating temperature (200-400°C), low reliability, broad spectrum response to combustible gases like methane and carbon monoxide limited their applications and accuracy. While nano types hydrogen sensors normally respond to very low concentration of hydrogen. Therefore development of new types of hydrogen sensor with compact structure, high sensitivity at low temperature, unitary selectivity is therefore an emergent urgency.

TE hydrogen sensor takes advantages from TE effect and the exothermic reaction of hydrogen oxidation on Pt catalyst. TE materials have attracted much attention as clean energy system on power generation and refrigeration [4-6]. Moreover some special functions have also been reported as temperature monitoring[7], infrared radiation detection[8], fluid flow and pressure measurement[9-10]. In this paper, a small-sized and highly sensitive hydrogen sensor based on TE material was studied.

Figure 1 displayed the structural mechanism of TE hydrogen sensor composing of two layers. The higher part is hydrogen catalyst layer, on the surface of which the hydrogen and oxygen molecules react and

give out certain heat concurrently. The heat generated resulted in a temperature increase. Therefore a temperature difference between the both sides of the TE film substrate is established. Belonging to the Seebeck effect, the TE film generates voltage output as a function of temperature difference and the TE film's Seebeck coefficient. Because the Seebeck coefficient has no relationship with the material's size, TE sensor can be fabricated into a small space. Moreover, theoretical analysis declared that low dimensional materials showed high Seebeck coefficient due to its enhanced phonon scattering. Comparing with other hydrogen sensors, the TE film hydrogen sensor owns advantages of simple structure, low power consumption, high sensitivity and quick response. Shin's [11-12] investigation showed that such sensor has wide sensitive ability from 50ppm to several percents, high voltage of 25.3mv to 3% hydrogen at 28□. In this study, we chose $Bi_{0.5}Sb_{1.5}Te_3$ as the TE film candidate due to its high Seebeck coefficient at room temperature, and a porous structure of catalyst to increase the sensibility. The processing parameters were intensively investigated; the phase structure and morphology were studied. As a result, a small size hydrogen sensor with high sensitivity was obtained.

2. Experimental

2.1 Preparation of hydrogen sensor

Bi_2Te_3-based solid solutions exhibited high TE properties around room temperature and were widely applied for cooling and temperature control. Several methods have been explored to grow their film, including flash evaporation, reactive evaporation, MOCVD, MBE, and magnetron sputtering method. Here RF magnetron sputtering was used to deposit $Bi_{0.5}Sb_{1.5}Te_3$ film owing to the method's high efficiency and easily-controlled operation. Quartz glass was used as the substrate with a dimension of 18×10×1mm. Powder mixture of high purity bismuth, antimony and tellurium composed the sputtering target. Before sputtering, substrate was intensively cleaned with formaldehyde, distilled water and absolute alcohol in ultrasonic agitator.

As for the catalyst layer, magnetron sputtering method was firstly used for fabrication of pure Pt film. But the layer's smooth surface depressed its catalytic reactivity. Wet chemical method was then adopted to increase the contact area, and amount of α-Al_2O_3 was added in to establish a porous structure. Aqueous solution of Pt chloride was used as the starting material of Pt, and it was homogeneously mixed with organic vehicle, a blend of terpineol and ethyl cellulose. Then the mixture was dropped onto the half surface of TE film, and then dried in oven. After several times of dropping and drying, a certain thickness of paste layer was formed. The sample was then sintered to get the porous structure of Pt / α-Al_2O_3 film.

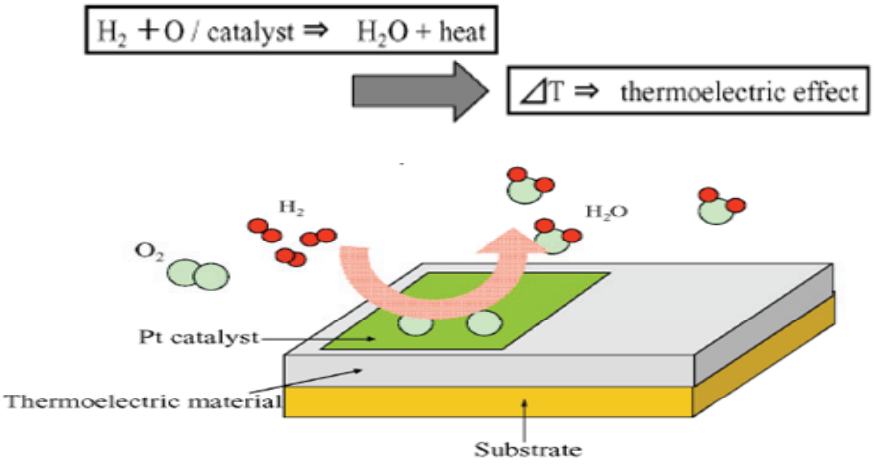

Figure 1: Structure of thermoelectric hydrogen sensor

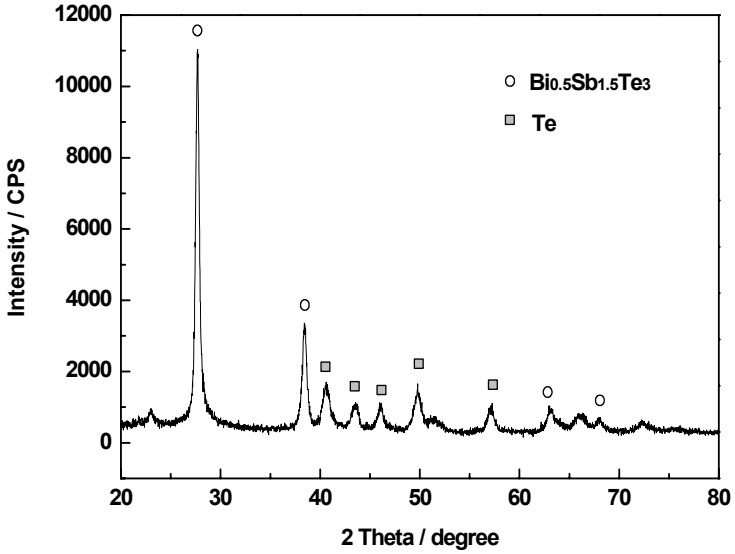

Figure 2: XRD pattern of thermoelectric film prepared by RF magnetron sputtering

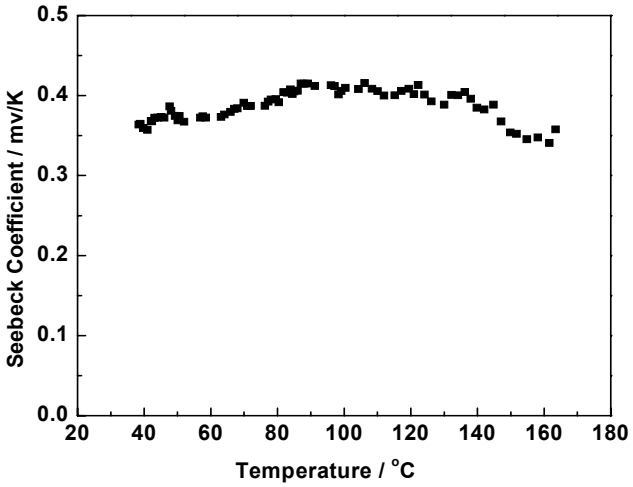

Figure 3: Seebeck coefficient of thermoelectric film as a function of temperature

2.2 Properties observation and measurement

The crystal structure of TE and catalyst films was investigated by XRD (Rigaku D/max 2550, Japan), The surface morphology of Pt ./ α-Al_2O_3 was observed with SEM (JEOL JSM-6360LV). The Seebeck coefficient of $Bi_{0.5}Sb_{1.5}Te_3$ film was measured from RT to 150□ with a temperature difference of 10k between both sides, the temperature was monitored by two thermocouples with an accuracy of 0.1□. The catalytic and sensor activities were performed in a 3vol% H_2 gas flowing system with a pressure of 3Mpa. The gas flow rate was controlled in the regime of 0-100 ml/min by a flow-meter. Acquired data was automatically collected via data collector produced by NI Corp. USA.

3. Results and Discussions

3.1 Thermoelectric film properties

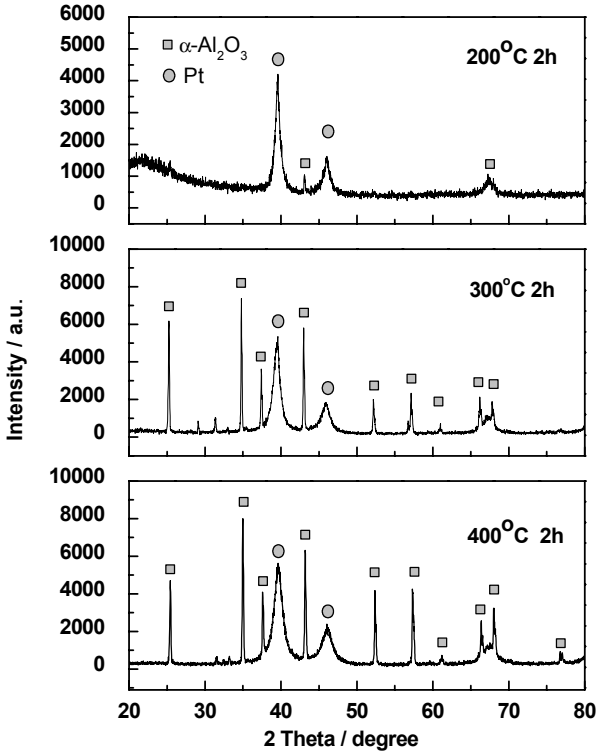

Figure 4: XRD patterns of catalyst film prepared by wet chemical method as a function of sintering temperature

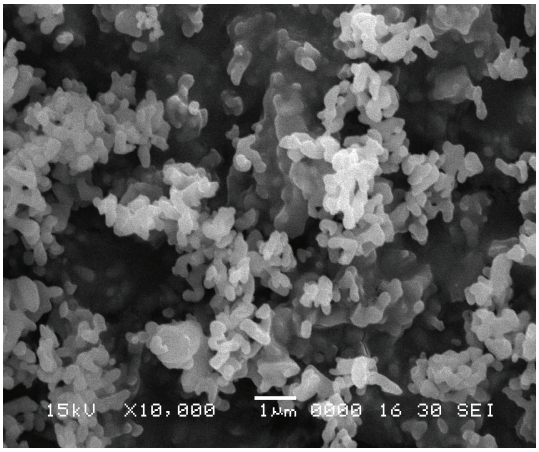

Figure 5: SEM image of catalytic layer sintered at 400 ^{o}C for 2hr

Figure 2 showed the XRD pattern of RF magnetron sputtered $Bi_{0.5}Sb_{1.5}Te_3$. It was found that besides the expected phase of $Bi_{0.5}Sb_{1.5}Te_3$ a little amount of Te was also emerged. This was because that among the three elements of Bi, Sb and Te, Te owned the highest vapor pressure, and displayed a high depositing ratio during sputtering process.

Figure 3 displayed the Seebeck coefficient of TE film between 40 and 160^{o}C. It can be clearly found that the Seebeck coefficient of the TE film were positive in whole range which indicated that the electric hole was the main conducting carrier. And the measuring value of Seebeck coefficient was relatively stabilized at a high value of 400μv/k.

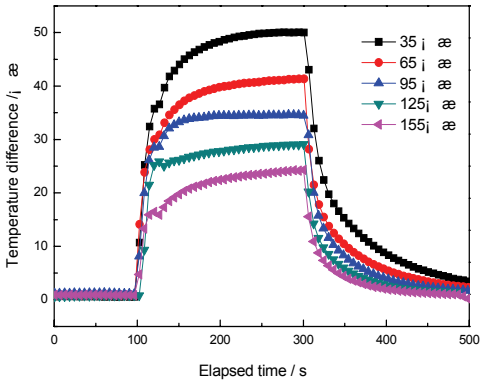

Figure 6: Pt /. α-Al_2O_3 catalytic activity as a function of temperature

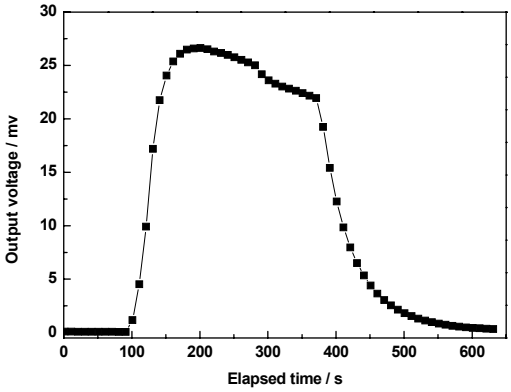

Figure 7: Voltage output of thermoelectric sensor with 3vol% H_2 at RT

3.2 Catalytic properties

Pt is a commonly used catalyst for hydrogen sensor. Here some α-Al_2O_3 was mixed in by wet chemical method in order to increase the active ability. Figure 4 showed the XRD patterns of catalyst sintered at different temperature. It was displayed that at 200°C Pt chloride ($H_2PtCl_6{\cdot}6H_2O$) finished its conversion to Pt, while most of α-Al_2O_3 was still in amorphous state. More α-Al_2O_3 crystals showed up with the increase of sintering temperature. At 400°C, the sample became a crystallized mixture of Pt and α-Al_2O_3.

Figure 5 was the SEM image of catalyst sintered at 400°C for 2hr with magnification 2000. It can be clearly seen that α-Al_2O_3 established a porous structure for Pt powders, and the latter dispersedly overspread on the structure, which offered lots of contacting surface between the reaction gases.

The sensitive catalytic ability was carried out, and the measuring results of temperature difference caused by the exothermic reaction of 3 vol% hydrogen on the catalyst surface as a function of operating temperature was shown in figure 6. A strong sensitivity was found after the catalyst was exposed in 3vol% H_2. An exiting temperature difference (ΔT) was generated along the both sides of substrate with a quick response. The highest value of 50°C was appeared at 35°C. With the increase of operating temperature, ΔT gradually reduced. But even at 135°C, the gave-off heat can still generate a ΔT of 25°C. Moreover, the response time was perfectly short as 25s, and showed no relation with operating temperature. The recovery test declared that the catalyst had a good recoverability of about 50s.

3.3 Hydrogen sensing properties

After combined catalytic layer with the TE film, a simple-structured hydrogen sensor was formed. The sensor's properties depended on the characteristic of both catalyst and TE material. The film-structured TE materials offer a high Seebeck coefficient of 400μv/k. The porous frame Pt catalyst increased the catalytic sensitivity. As composed TE sensor showed a high output voltage of 26.6mv with a quick response time about 50s (in figure 7). The recover properties ensure the repeatability of the sensor. When the mixed gas flow was shut down, the voltage signal quickly reduced to the original state in 100s.

4. Conclusion

In this paper, a TE hydrogen sensor of a composition of $Bi_{0.5}Sb_{1.5}Te_3$ TE film and Pt /. α-Al_2O_3 catalytic layer was demon-

strated. The TE film was fabricated by RF magnetron sputtering. Its phase structure was studied. Seebeck coefficient was measured as a high average value of 400μv/k. Wet chemical method was applied to prepare a porous-structured Pt / α-Al_2O_3, which greatly increased the catalytic properties, and the temperature difference generated was as high as 50^{o}C. As-prepared sensor showed simple structure, low cost and high sensitivity to hydrogen. Output signal of 26.6mv was obtained with a response time of 50s when the sensor was exposed in a mixed atmosphere with 3 vol% hydrogen.

Acknowledgement
This work was supported by the Natural Science Foundation of China and Shanghai Shu'guang Project, China.

References

[1] Kong J., Franklin N. R., Zhou C., et al. (2000), *Science*, **287**, pp. 622.
[2] Walter E. C., Favier F., Penner R. M., (2002), *Analytical Chemistry*, **74**, pp.1546.
[3] Varghese O. K., Gong D., Paulose M., et al. (2003), *Sensors and Actuators B*, **93,** pp.338.
[4] Kyeo H-K., Khajetoorians A., Shi L., (2004), *Science*, **303,** pp. 816.
[5] Hsu K. F., Loo S., Fuo F., et al. (2004), *Science*, **303**, pp.818.
[6] Venkatasubramanian R., Siivola E., Colpitts T., O'Quinn B., (2001), *Nature*, **413**, pp. 597.
[7] Allison S.C., Smith R. L., (2003), *Sensors and Actuators B*, **104**, pp. 32.
[8] Muller M., Budde W., (1996), *Sensors and Actuators B*, **54**, pp.601.
[9] Stachowiak H., Lassue S., (1998), *Flow Measurement and Instrumentation*, **9**, pp.135.
[10] Giani A., Asmail A. B., (2002), *Materials Science and Engineering,* **95**, pp.268.
[11] Tajima K., Qiu F., Shin W., et al. (2005), *Sensors and Actuators B*, **108**, No.1-2, pp.973.
[12] Shin W., Tajima K., Choi Y., et al. (2005), *Sensors and Acutators B*, **108,** No.1-2, pp.455.

STUDY AND LIFE ANALYSIS OF MULTIAXIAL THERMO-MECHANICAL FATIGUE TESTS

Franck Gallerneau, Vincent Bonnand and Didier Pacou
Office National d'Etudes et de Recherches Aérospatiales
Structures and Damage Mechanics Department
BP 72, 29 avenue de la Division Leclerc
F-92322 Châtillon Cedex, France

Abstract

A multiaxial Thermo-Mechanical Fatigue test device has been developed at ONERA to be able to test materials, and also to validate the capability of lifetime prediction methods, under more realistic and complex loading. A detailed description of the testing equipment and of the specific experimental procedure specially developed for tension-torsional TMF test is first given. We present then the experimental results obtained in tension, torsion and in tension-torsion with AM1 single crystal superalloy for turbine blade application. Finally, we discuss about the results of the life analysis of the tests realised by simulating and calculating the response of the material under tension-torsional loading with a specific Finite Element calculation method, before the application, as a post-treatment to the F.E. analysis, of a fatigue-creep-oxidation interaction damage model developed and extended here to account for the specific behaviour of such anisotropic under axial-torsional fatigue loading.

Keywords: Thermo-Mechanical Fatigue, Numerical simulation, Tension-Torsion tests, Single crystal superalloy, Crack initiation, Lifetime prediction model.

1. Introduction

Critical engine components, such as Aircraft Gas Turbine blades, are subjected to multiaxial states of stress under non-isothermal cyclic conditions. Several constitutive models have been proposed to describe the cyclic viscoplastic behaviour of anisotropic material and applied with success for the design of single crystal blades [1-4]. Thermo-Mechanical Fatigue tests were developed for turbine blade alloys over the past 20 years, first to be as close as possible to the real blade in service, and also to validate constitutive equations and damage models. These experiments are generally performed on a material volume element simultaneously submitted to controlled uniaxial load and temperature [5-7]. However, this kind of test may not be sufficiently representative of the multiaxial loading that can be generated in turbine blades, and for which complex experimental tests machines were developed [8-9].

An axial-torsional TMF test device has been developed and designed to be able to test materials, and also to validate the capability of lifetime prediction methods, under more realistic loading [10]. A description of the testing equipment and of the specific experimental procedure specially proposed for multiaxial TMF test is given in the first section. We present then the experimental results obtained in tension, torsion and in tension-torsion. We discuss in a third section about the difficulties to simulate and model the response of the non-isothermal TMF loading particularly with torsional loading for which a specific Finite Element calculation algorithm is needed. Finally, in fourth and last section, we present the fatigue predictions given by the application of a fatigue-creep-oxidation interaction model and the recent developments we propose to account for the resistance of the single crystal specifically in torsion loading.

2. Development of tension/torsion Thermo-Mechanical fatigue test device

Experimental procedure.
TMF consists in applying a mechanical loading during the heating of the specimen in non-isothermal conditions (Fig. 1). The main difficulty is to perform the fatigue test with a mechanical strain control. Thus, the thermal strain has to be subtracted to the measured total strain. The testing procedure we developed is divided in three sequences. We first apply the thermal loading with a force control equal to zero, to record the axial thermal strain. Afterwards, we impose only the thermal strain cycle previously recorded during the heating and verify the thermal compensation. If this is correct, we measure no significant force on the dynamometer. The last sequence consists in launching the real TMF test.

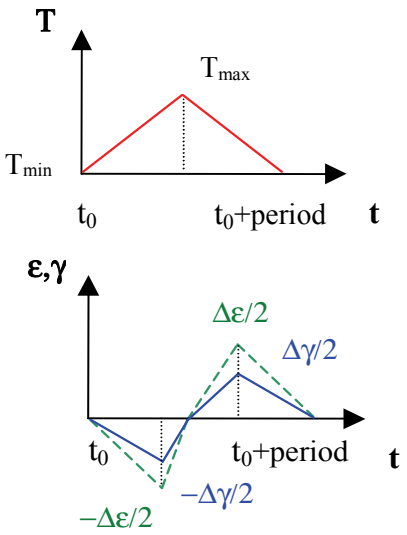

Figure 1: *Schematic description of the standard S axial-torsional TMF cycle.*

In previous papers [11, 12], we described in details the experimental procedure we finalised, concerning particularly the signal treatment to execute a feedback of the real thermal strain signal, extracted from the first sequence, in the servo loop. Two closed-loop control loops are used for mechanical actuators (axial and torsional). The heating of the specimen is obtained by giving the triangular tension command to an induction unit. The procedure has been developed to conduct any axial-torsional loading. In Fig. 2, it is shown the quite good results we obtain on the thermal compensation by reporting the measured stress with time. Indeed, a comparison of the measured stress with the high frequency noise (in black on the figure) of the acquisition-generation cards has been performed in terms of stress. Measured during many cycles, this is about ± 5 MPa, which implies a response of the system equivalent to the error induced by the electronic unit.

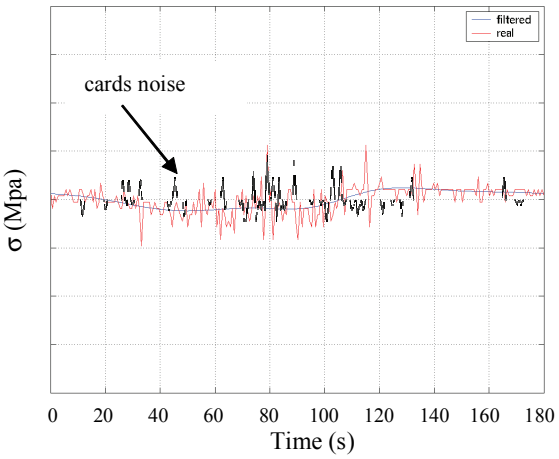

Figure 2: *Validation of the thermal compensation.*

Experimental validation with tension tests.
Validation tests have been performed with the thermo-mechanical cycle defined in Fig. 1, with a minimal temperature of 650°C and a maximum temperature of 1100°C. The period of the cycle is 180 seconds. The tests were carried out on thin wall tubular specimens (1 mm in the thickness) of AM1 Nickel-based single crystal superalloy, with C_1A industrial coating, to be as representative as possible to the real blade in service. Moreover, the substrate exhibits the cubic symmetry and the specimens are oriented along <001> principal crystallographic orientation. The disorientation and secondary orientation have been located by the Laüe method. As a matter of fact, tension-torsion multiaxial test requires noticing the crystallographic orientation along which the torsional strain is applied on and measured. The validation consisted in the realisation of a uniaxial TMF test, in tension. A measurement of the Young's modulus, realised in preliminary with the test, made it possible to obtain the inelastic strain during the fatigue test. The comparison with a Volume Element calculation (specimen with low disorientation along <001>

submitted to tension loading) with viscoplastic single-crystal constitutive models allowed us to validate the TMF device, in term of stress response of the material to the thermo-mechanical loading (Fig. 3), and also in term of life duration (compared to similar tension tests performed in other laboratories [5, 6]).

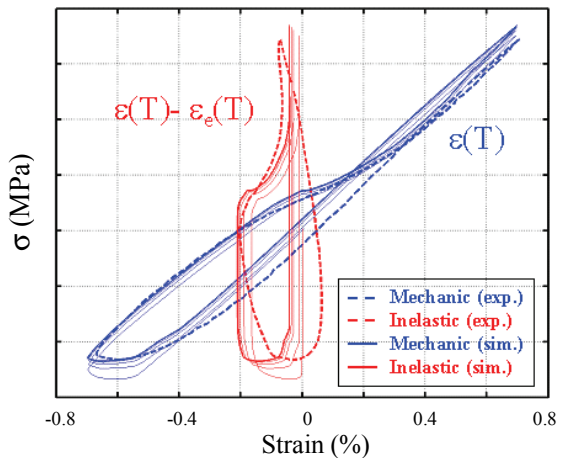

Figure 3: *Tension test: stress/mechanical-inelastic strain loop at stabilised cycle.*

The specificity of TMF tension-torsion tests.

Due to the cubic symmetry, the thermal expansion is hydrostatic and isotropic, and then does not intervene on the torsion strain components. So, two possible definitions can be proposed for a TMF torsion test. The first one consists in compensating the axial thermal strain and in controlling the torsional one. The second one is to keep the axial actuator free, i.e to perform the test with a zero-force control.

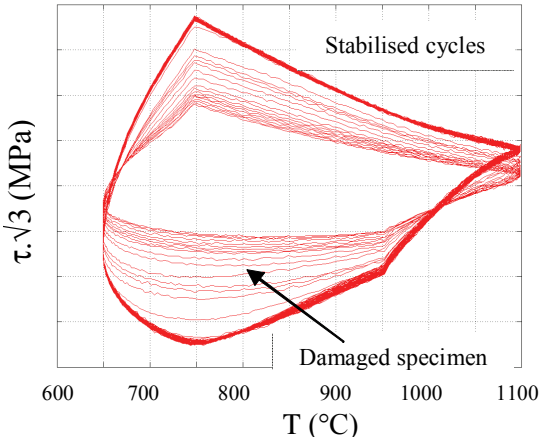

Figure 4: *Torsion test: stress/temperature loops from first to stabilised cycles.*

We verified, in such configuration, that the torsional loading had no significant effect on the axial strain measurement, and so that those two kinds of tests are identical. The first torsion test was carried out by positioning the extensometer arms in the <100> secondary direction. Fig. 4 presents the torsion strain evolution versus the temperature until the end of the test. Whatever the test, the rupture of the specimen is given by a force or torque drop up of to 50 %. In Fig. 5, we can observe the macroscopic crack oriented along the specimen axis, that is not singular for a torsion test, but exactly in the <110> secondary crystallographic orientation. This has to be validated by the prediction of the damage models applied to the results of the Finite Element analysis.

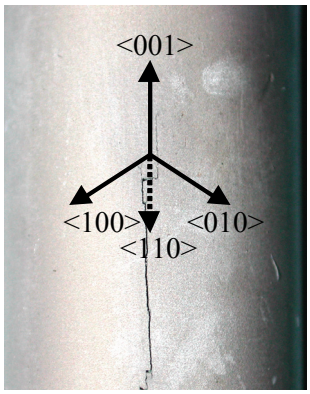

Figure 5: *View of the macroscopic crack observed in pure torsion test for high mechanical strain level.*

3. Simulation and calculation of tension-torsion TMF tests

To simulate the response of the anisotropic material due to a combined thermal and mechanical cycle, a 3D Finite Element simulation is required if a torsion loading is generated in the specimen. The mesh of the problem considers four elements in the specimen thickness to account for accurately the stress and strain gradients in the tube wall as soon as a torsion loading is considered. The difficulty of such calculation concerns the application of specific boundary conditions to obtain locally, in the gage length, the strain imposed experimentally by the axial-torsional extensometer. As a matter of fact, it is no possible to impose, as

boundary conditions, the displacement and angle recorded experimentally, due to the transducers inaccuracy and the existence of a lot of unknowns, like the temperature gradient in the grip of the specimen.

Specific simulation algorithm.
We tried first to proceed in performing the calculation using a computation method with successive approximations, by incorporating patch terms. But such approached calculations and the non linearity induced by plasticity to obtain in the specimen gage length the resulting strain, make this computation technique inadequate. Therefore, to apply the adequate boundary conditions to obtain locally the resulting mechanical strain, it is necessary to build an algorithm of calculation allowing to execute the same control, as the experimental P.I.D. servo. The scheme below (Fig. 6) gives a simplified view of this algorithm we developed in the ZéBuLoN Finite Element code.

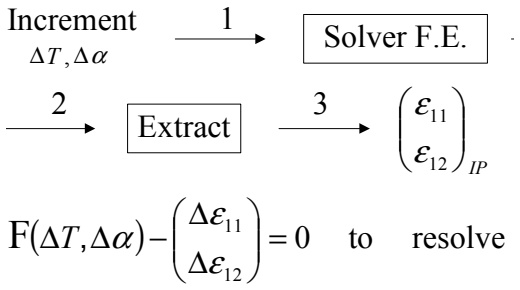

Figure 6: *Specific algorithm developed to simulate tension-torsion TMF tests.*

At each increment of time, the functional to resolve for all the integration points is expressed as F. This algorithm based on a perturbation method is thus the numerical equivalent of the closed-loop servo of the TMF test. Let us notice its general character, i.e. it makes possible to impose the accurate boundary conditions to control any observable variable.

Finite element analysis of tension-torsion TMF tests.
The simulation of around ten successive cycles is required to have a stabilised state of stress and strain in the specimen (Fig. 7). The specific calculation algorithm is more time consuming (factor 2) in comparison to classical calculation, the computation time reaching three days per test simulation. As precised previously, the possible disorientation of the single crystal specimen has to be taken into account for accurate simulation, as well as the exact location of the arms of the extensometer.

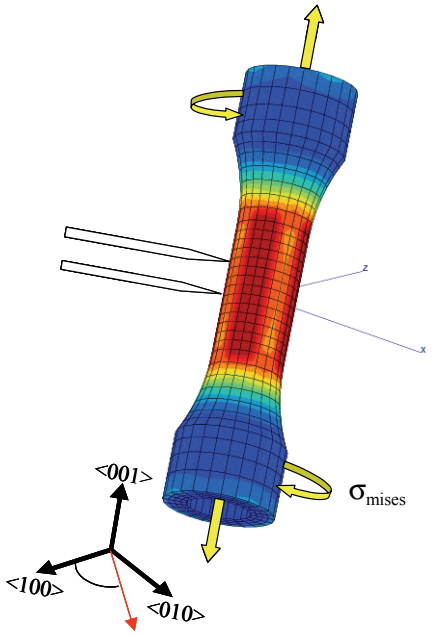

Figure 7: *Example of Finite Element simulation of tension-torsion test with cubic single crystal material.*

To compare the results of the calculations to the experimental data, it is needed to calculate, as a post-treatment, the torsion effort (global value deduced from nodal forces). The inelastic strains are also deduced from the total mechanical strains, from previous calculations of the elastic strains (a dynamic method consisting to apply thermal loading with low force control gives measurements of apparent axial and transversal elastic modulus of the specimen). On Fig. 8 are reported the experimental and calculated cycles at the stabilised state for both axial and torsion components. As it can be observed, there is a very good agreement between the simulation and the experimental data in term of elastic and inelastic strains.

It is worth to note that the constitutive model in tension-torsion, more precisely the Schmid plasticity criterion, with the respect of the cubic symmetries, was only validated in previous works [4] at room temperature. The hypothesis formulated on the evolution of the material properties

under multiaxial loading in then validated on the entire temperature domain by such simulation of complex tension-torsion TMF test.

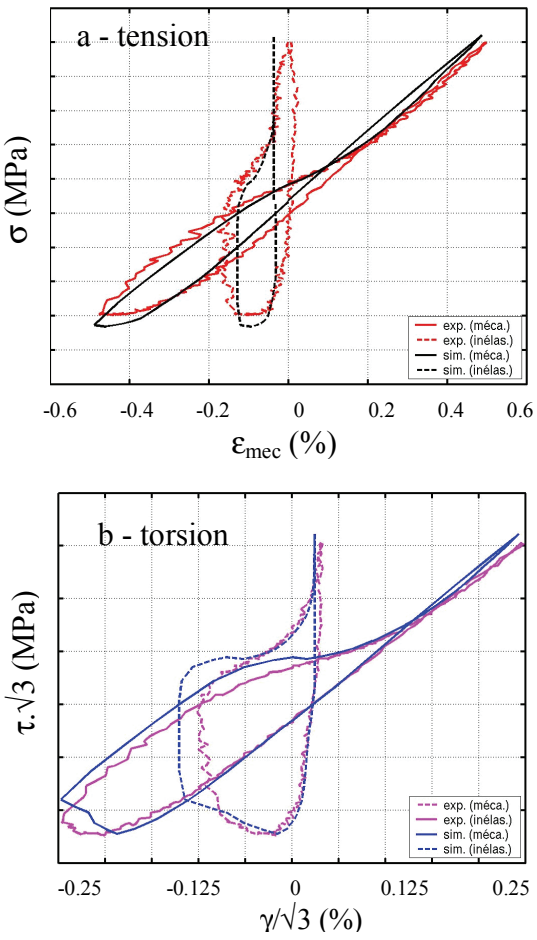

Figure 8: *Comparison of calculated and experimental responses of the material (stress/strain loop) submitted to complex axial-torsional TMF cycle.*

4. Fatigue life analysis of axial/torsional tests in isothermal and non isothermal conditions

General multiaxial non-isothermal writing of the damage model.

This model, specifically developed for coated single-crystal superalloys has already been applied successfully to the fatigue life prediction of isothermal and thermo-mechanical tests but only with tension loading. The model supposes isotropic damage. It has been detailed elsewhere [13-14], and we shortly recall here its main characteristics. To take into account the effect of the coating on the fatigue strength of the superalloy at low temperature, the model differentiates two distinct damage processes: a micro-initiation phase and a micro-propagation phase respectively described by D_I and D_P scalar variables. Interaction effects are introduced between fatigue and oxidation damage process (traduced by D_{ox} variable) during the micro-initiation phase only. The variable D_c is related to creep damage. It can be developed during the micro-initiation phase, but it interacts with the fatigue damage during the micro-propagation phase.

The important assumption for this model concerns the non-isothermal writing. As a matter in fact, micro-initiation and micro-propagation fatigue laws can be suppose temperature independent, by using a notion of reduced stress. These reduced stresses are defined by $S_I = \sigma/\sigma_{uI}(T)$ and $S_P = \sigma/\sigma_{uP}(T)$, and are considered as describing the thermo-mechanical fatigue cycle, where σ_{uI} and σ_{uP} are respectively the ultimate stresses in micro-initiation and in micro-propagation which are temperature dependent, the fatigue laws can then be supposed temperature independent. Only time dependent and thermally activated phenomena, such as creep and oxidation, are described by temperature dependent laws.

Micro-initiation

$$dD_A = \frac{1}{C}\left\langle \frac{S_{IIA} - S_{I_A}(S_{AH})(1-D_{0X})}{(1-D_{0X}) - S_{AeqMax}} \right\rangle^b dN \qquad (1)$$

Micro-propagation

$$dD_P = H(1-D_A)\left[1-(1-(D_C+D_P))^{\beta+1}\right]^{1-a} \cdot \left\langle \frac{S_{IIP} - S_{IP}(S_{PH})}{1-S_{PeqMax}} \right\rangle \left(\frac{S_{IIP}}{M^*(S_{PH})(1-(D_C+D_P))} \right)^{\beta} dN \qquad (2)$$

$$H(D_A - 1) = 0 \text{ if } D_A < 1 \text{ and } H(D_A - 1) = 1 \text{ if } D_A = 1$$

Oxidation

$$dD_{0X} = \frac{1}{2} D_{0X}^{-1} \left(\frac{K^*}{e_0} \right) \left[1 + \frac{\langle X_{0X}(\chi_{0X}) - S_{l_{0X}}(S_{PH}) \rangle}{B^*} \right]^{2m} dt \qquad (3)$$

$$K^{*2} = \frac{1}{\Delta t} \int_0^{\Delta t} \left[K_0 \exp\left(-\frac{Q}{RT_{(t)}} \right) \right]^2 dt \qquad (4)$$

Creep

$$dD_C = \left(\frac{X_C(\chi_C)}{A(t)} \right)^{r(T)} \left(1 - (D_C + D_P)\right)^{-k(T)} dt \qquad (5)$$

Table 1: Equations of the fatigue-creep-oxidation interaction damage model.

Damage evolutions due to micro-initiation (Eq. (1)) and micro-propagation (Eq. (2)) in fatigue, to creep (Eq. (3)) and to oxidation (Eq. (4)) are summarized in Table 1. Indices I and P in the equations stand respectively for initiation and propagation. S_{II} is the octahedral shear amplitude, S_{PH} or S_{IH} is the mean hydrostatic pressure as defined by Sines, S_{eq} is the Hill equivalent stress. Limit stresses S_I are defined by: $S_{II} = S_{IIo}$ (1-h_1 Mean (tr S_P)), $S_{IP} = S_{IPo}$ (1-h_2 Mean (tr S_P)), and $S_{lox} = S_{loxo}$ (1-h_3 Mean (tr S_P)) + Mean (tr S_P). Similar relation is used for the parameter $M^* = M^*_o$ (1-h_4 Mean (tr S_P)). For damage creep law, Hayhurst's multiaxial criterion has been extended to account for material anisotropy of the single crystal.

This writing makes the model attractive for its identification on a large temperature domain. Pure fatigue tests results performed at one temperature are then sufficient to identify all the parameters of micro-initiation and micro-propagation laws. Micro-initiation and micro-propagation laws evolve with temperature through the variations of the ultimate stresses $\sigma_{uI}(T)$ and $\sigma_{uP}(T)$. Fatigue creep tests results conducted at lower frequencies at the same or another temperature allow us to identify the oxidation law. Pure creep tests are nevertheless required to identify the damage creep law at several temperatures. Material anisotropy effects in fatigue regime could be taken into account by four fourth-order tensor introduced in S_{II} and S_{eq} writing. For cubic anisotropy, only two independent material constants are required.

Application to AM1 single crystal superalloy for isothermal and TMF tension-torsion tests.

The identification of the parameters of the different functions of the damage model was realised on the based of tension and isothermal fatigue tests obtained at 950°C and 1100°C. The available fatigue data (tests performed with a force control along three different orientations, <001>, <110> and <111>) did not indicate a significant effect of the anisotropy and the material is supposed here to be isotropic in term of life duration.

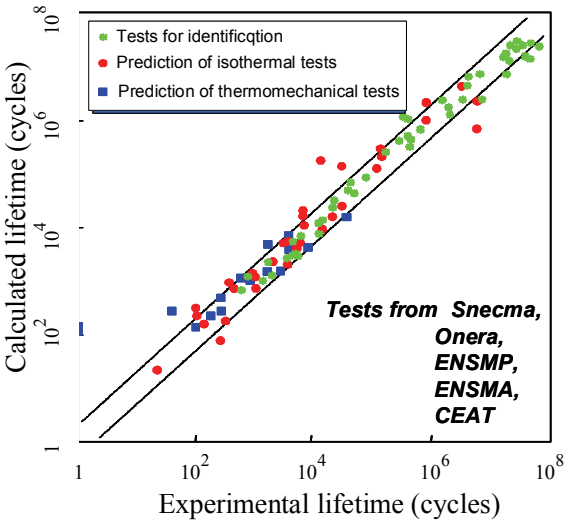

Figure 9: *Comparison between calculated and experimental lifetime for various tension tests in isothermal and TMF conditions.*

We reported in Fig. 9 the results of the lifetime predictions of many isothermal tests (circular symbols) performed in several laboratories at different temperatures and for several loading conditions (loading frequencies from 50 Hz to tests with hold of 90s, different stress ratios). The star symbols represent the tests used for the identification of the model parameters. The square symbols are relative to the prediction of uniaxial TMF tests representatives to critical cycles (two different standard S and W cycles were studied) defined from the analysis of loading applied in blades for both civil and military applications. The predictions are fairly good whatever the loading conditions.

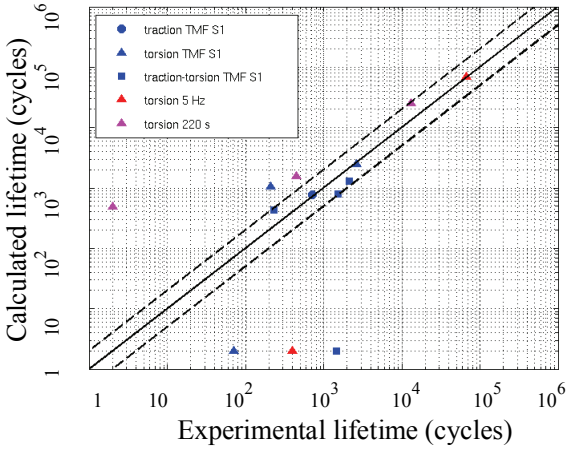

Figure 10: *Calculated and experimental lifetime of tension-torsion tests.*

The results of the predictions of the torsion and tension-torsion tests in isothermal and TMF conditions are given in Fig. 10. As it can be seen, the damage model, applied as the post-treatment to the Finite Element analysis predicts systematically too much long life durations as soon torsion loading is applied. In term of Von Mises equivalent stress, it appears that the single crystal material exhibits a much lower resistance than in tension. We reported in Fig. 11 the Woehler curves obtained at 950°C (total reversed loading, R_σ=-1) for fatigue (5 Hz) and with hold time tests. The hollow symbols represent the results of the tension tests realised with the specimens oriented along different crystallographic orientations.

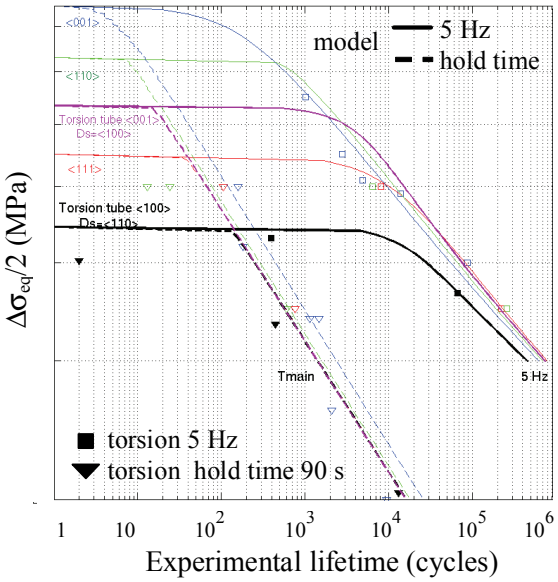

Figure 11: *Calculated and predicted Woehler curves at 950°C.*

The predictions are no more satisfying when the plasticity threshold is reached (perfectly plastic behaviour in torsion). In such a case, the rupture domain is very close. The previous rupture criteria were based on the comparison of the maximum of the Von Mises equivalent stress to the ultimate tension stress σ_{uI} (Eq. (1)) or σ_{uP} (Eq. (2)) supposed to be isotropic and non dependant to the material orientation. A new rupture criterion (Eq. (6)) based on Schmid law can then be proposed to describe more correctly the rupture behaviour of the anisotropic material:

$$\tau_u^i = \tau_{res}^i \quad with \quad \tau_{res}^i = \overline{\overline{\sigma}} : \left(\vec{n}^i \otimes \vec{l}^i \right)_s \qquad (6)$$

τ_u^i is the ultimate shear stress (i is a cubic or octahedral plane) to be compared to the resolved shear stress in plane i. As a mater of fact, for a tube <001> oriented and submitted to torsion loading, the criterion is reached along the secondary orientation <110> in agreement with the localisation of the macroscopic crack (Fig. 5). The model also leads to more conservative predictions, in the way of the security (Fig. 12) as confirmed in Fig. 11 with the calculated Woehler curves.

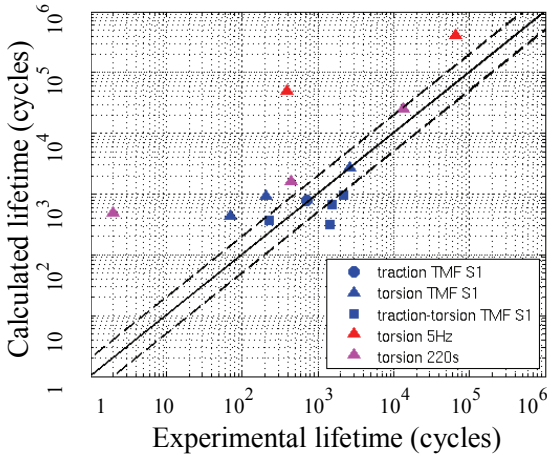

Figure 12: *Calculated and experimental lifetime of tension-torsion tests with the new rupture criterion.*

5. Conclusions

An axial-torsional thermo-mechanical fatigue test device was developed in order to study the effects of multiaxial loading on the fatigue life resistance of anisotropic materials such as single crystal superalloys for turbine blade applications. The experimental procedure has been validated in tension, in torsion and also by considering an in-phase tension-torsion thermo-mechanical loading. The difficulties encountered in the Finite Element simulations in the case of multiaxial loading, have constrained us to develop an algorithm of calculation allowing to apply specific boundary conditions to obtain locally, in the gage length, the strain imposed experimentally by the axial-torsional extensometer. The fatigue life prediction is then given by a creep-fatigue-oxidation interaction model, developed for coated single crystal superalloy, applied as a post-treatment to the Finite Element analysis. To be in the

way of the security, a new rupture criterion, based on Schmid law, has been proposed to describe correctly the specific behaviour of anisotropic material observed under torsion loading.

6. Acknowledgments

Support for this work by SNECMA is gratefully acknowledged.

7. References

[1] Pollicella, H., Paulmier, P., Pacou, D., (1990), Comportement mécanique de l'alliage monocristallin CSMX-2 à haute température : résultats expérimentaux, La Recherche Aérospatiale, n°4, p. 47 -63.

[2] Méric, P., Poubanne, P., Cailletaud, G., (1991), *Single crystal modeling for structural calculations: Part 1-Model presentation*, J. of Eng. Mat. And Techn., p. 113-162.

[3] Nouhailhas, D., Freed, A. D., (1992), *A viscoplastic theory for anisotropic Materials,* J. of Eng. Mat. and Techn., 114, 97.

[4] Nouhailhas, D., Culié, J.-P., Cailletaud, G., Méric L., (1995), *Finite element analysis of the stress-strain behavior of single-crystal tubes,* Eur. J. Mech. , A/Solids, 14, n°1, p. 137 -154.

[5] Malpertu, J.-L., Rémy, L., (1990), In Metall. Trans. A., vol. 21A, pp. 389-399.

[6] Lautridou, J.-C., Guédou, J.-Y., Delautre J., (1995), *Comparison of single crystals superalloys for turbine blades* through *TMF tests*, International Symposium, Fatigue under thermal Mechanical loading, Petten The Netherland, May 22-24.

[7] Beck, T., Hähner, P., Rae, C., Affeldt, E., Andersson, H., Köster, A., Marchionni, M., (2006), *StandardizationThermo-mechanical fatigue – the route to standardization ("TMF-Standard Project"),* PMaterials and Corrosion, 57, No. 1.

[8] Kalluri, S., Bonacuse, P., (1997), *An axial-torsional thermomechanical fatigue testing technique,* Multiaxial Fatigue and Deformation Testing Techniques, STP 1280, p. 184.

[9] Kanoute, P., Pacou, D., Poirier, D. Gallerneau, F., Cardona, J.-M., (2002), *Thin wall thermal gradient: experimental study and fatigue life analysis on multiperforated components,* Temperature Fatigue Interaction, Elsevier Science Ltd. And Esis Publication 29, p. 341-350.

[10] Bonnand, V., (2006), Etude de l'endommagement d'un superalliage monocristallin en fatigue thermo-mécanique multiaxiale, Thesis, School of Mines of Paris, January.

[11] Bonnand, V., Pacou, D., Gallerneau, F., Poirier, D., (2002), *Development of an axial-torsional thermo-mechanical fatigue device,* Symposium on anisotropic behavior of damaged materials, Cracow, September 09-11.

[12] Bonnand, V., Gallerneau, F., Pacou, D., (2004), *A new experimental device for multiaxial thermo-mechanical fatigue,* Journal of Materials Testing, 6/2004, p. 301-205.

[13] Gallerneau, F., (1995), Etude et modélisation de l'endommagement d'un superalliage monocristallin revêtu pour aube de turbine, Thesis, School of Mines of Paris, November.

[14] Gallerneau, F., Chaboche, J.-L., (1999), *Fatigue life prediction of single crystals for turbine blade applications*, International journal of Damage Mechanics, vol. 8, p. 405-427.

RESIDUAL STRESS PREDICTION FOR MULTI-PASS REPAIR WELD

L.K. Keppas, D.E. Katsareas, N.K. Anifantis
Machine Design Lab., Mech. and Aeronautics Engg Dept.,
University of Patras, 26500, Rion, Greece

A.G. Youtsos
High Flux Reactor Unit, Institute for Energy, EC-JRC, PO Box 2,
1755, ZG Petten, the Netherlands

Abstract

Scope of the present work is the determination of the residual stresses in a 2¼CrMo plate, containing an 18-pass repair weld of the same material. The configuration under investigation concerns a 20 mm thick steel plate with dimensions of 200 mm x 100 mm, containing a 15 mm deep machined central cavity, with dimensions of 92 x 30 mm at its opening and 75 mm x 25 mm at its bottom. Uncoupled thermal and mechanical analyses and the "birth and death of elements" technique is the basis of the simulation procedure. Each weld pass is discretized in a number of increments and these are "deposited" sequentially. An optimized finite element mesh of a preliminary 2-D analysis is used as basis for the construction of a 3-D mesh and the implementation of a 3-D analysis where the 18 beads are lumped into 4 passes. The lumping approach is a pre-requisite for the 3-D analysis to be cost effective in terms of CPU time. The proposed modelling technique is assessed through comparison of predicted stresses with neutron diffraction testing data. In general a good agreement between numerical and experimental results was found.

Keywords: Residual Stress, Prediction, Repair Weld, FEM, Sensitivity, Neutron Diffraction.

1. Introduction

Repair welds are a common way in industry of repairing cracks or other forms of defects in steel components and structures. The material around the crack is excavated through machining. The groove, which has usually letterbox geometry, is filled with a weld metal of – mostly - a composition similar to the parent material. Since the welding procedure is of a multi-pass type, a repair weld is considered an extreme case of a multi-pass weld.

Prediction of the residual stress field in repair welds has attracted the researchers. Dong et al [1-2] inferred that residual stresses in such welds typically exhibit strong three-dimensional features, depending on both component and repair geometry. Several repair cases were investigated through 3D computational models and revealed that repair welds increase the magnitude of transverse residual stresses along the weldments and the shorter the repair length the greater the increase in transverse stresses. Moreover, welding parameters such as heat content and pass sequencing play a more important role when analyzing repairs than normal fabrication welds. Lant et al [3] concentrated on practical weld repair procedures for low alloy steels. During the design phase of structures and their components or during evaluation of a potential crack initiation and growth, it is important to have a complete description of the residual stress distribution. In addition, there is the potential for stress distributions to become even more complicated, when weld repairs are performed in regions where other welds are already present. Indeed, in the

construction of new plants and for their continued operation, local repair welds are undertaken, so it is necessary to be able to certify these for safe operation. As a consequence, knowledge of the residual stresses and their distribution is an important input to an overall structural integrity assessment. Weld simulation involves complicated aspects of modelling like metallurgical phase transformation, temperature dependent material properties, creep, phase change, radiation, heat input models, etc. The impact of these on the accuracy of the predicted residual stress has attracted researchers for some time now. Lindgren in his review [4] demonstrates the complexity of weld simulation models if aspects such as solid-state phase transformations and hot cracking are involved in order to achieve a more accurate analysis.

Analysis of multipass welds as a series of single pass welds is probably the most accurate methodology as it can take into account the effect of interpass temperatures for every single bead and the exact heat input in the weldments. Each weld bead increment alters the temperature and displacement fields caused by previous increments and the effects, while cumulative, are not simply additive. As a result, simulation of multi-pass welding can be very time consuming. Lumping successive passes together is one way to reduce the cost. Several researchers adopted this technique in the past. Hong et al [5] evaluated the approximations due to pass lumping. They tried to lump a 5-pass weld into a 3-pass weld. They introduced a weight factor to decrease the heat input and thereby also reduce the zone with large residual stresses so that the results compared with more favourably with the 5-pass simulation. Lumping approach used by Hyde et al [6] in a 3D finite element model to simulate a pressurized CrMoV pipe and the same technique has also been adopted in recent studies [7-8] as costly effective.

Measurement of residual stresses with non-destructive techniques is very important for safety assessment of welded components and the experimental results can be used for verification of numerical models. Ohms et al [9] have used a novel and very promising non-destructive method, in order to evaluate large welded components, such as dissimilar metal welded pipe joints and RPV walls, used in the nuclear industry, within the context of structural integrity assessment. They have used the neutron diffraction method to measure residual stresses, induced in such components during welding and have compared successfully their results to data of other experimental and computational methods. The neutron diffraction technique was also used in [10] to obtain through thickness residual stress profiles in repair welded stainless steel pipes.

Scope of the present work is the determination of the residual stresses in a 2¼CrMo plate, containing an 18-pass repair weld of the same material. Uncoupled thermal and mechanical analyses and the “birth and death of elements” technique is the basis of the simulation procedure. Each weld bead is discretized in a number of increments and these are “deposited” sequentially. “Deposited” means, in numerical terms, activated and that refers to the elements that constitute the weld bead. The deactivation and activation of elements during the simulation is achieved through the well known “birth & death of elements” technique, a feature common to many commercial FE codes. Element deactivation or “death”, as it is called, is not achieved by actual removal of "killed" elements, but by multiplying their stiffness, conductivity, etc, by a severe reduction factor. When an element is reactivated, its stiffness, conductivity, etc. return to their original values. The influence of weld bead lumping on the evaluation of residual stresses field is examined in a sensitivity analysis. Metallurgical phase transformation effects are not included in the model, although it is general knowledge that its role in the formation of a residual stress field can be quite significant.

The proposed modelling technique is assessed through comparison of predicted stresses of 2-D plane strain analysis and lumped 3-D analysis with neutron diffraction testing data. The overall objective of the present study is the development of a residual stress predictive tool for repair welds, based on the evaluation of currently developed finite element techniques, as encountered in industrial applications. Emphasis is given

on the applicability of such a tool in problems of industrial relevance, in respect of the computational cost of its implementation. In fact the work presented in this paper constitutes an exercise towards development of simulation of multi-pass repair welds, which is currently pursued within the NET European Network - Neutron Techniques Standardization for Structural Integrity.

2. Methodology of welding simulation and assumptions

The weld material region consists of 18 beads. (Fig. 2). The weld beads can be modelled one by one separately (Fig. 3), or they can be lumped into 6 layers, each one consisting of 3 sequential beads (Fig. 4). In this case it is assumed that the 3 beads of a layer are laid simultaneously into the weld groove. In a further simplification, the first two layers are lumped to one pass and layers 3 and 4 to another single pass (Fig. 5). In this approach 12 of the original 18 beads have been incorporated into the first 2 lumps (6 and 6) and the other 6 beads are shared between lump 3 and lump 4. The decrement of the initially 18 beads to only 4 distinct lumps aims to the reduction of simulation time, which in case of a 3-D model may be too long for a bead-by-bead analysis. However, before proceeding to a lumped 3-D approach, a 2-D sensitivity analysis concerning the number of distinct weld passes is carried out.

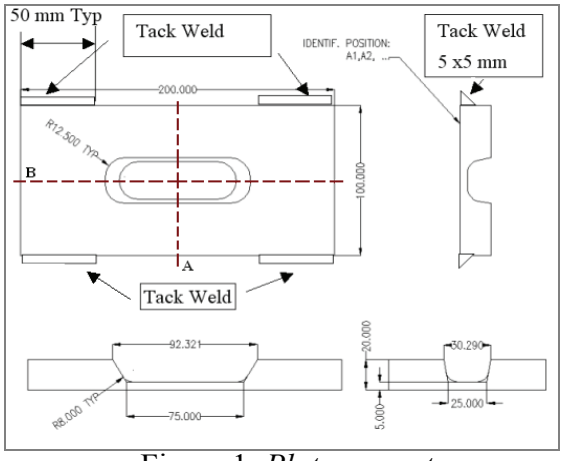

Figure 1: *Plate geometry.*

Thermal analysis

The weld simulation procedure that is followed here is incremental as is the real process of weld bead deposition. 10 increments have been used for each pass (lump) in the present 3-D analysis and the deactivation and activation of elements during the simulation is achieved through the "birth & death of elements" technique. The elements that constitute the each weld pass, although generated from the beginning of the meshing remain inactive until the moment in time T^i_{act} when the pass increment they belong to is "deposited". That time point is calculated by dividing the total bead deposition time T_{tot} by the total number of increments used in the simulation.

$$T^i_{act} = (i-1)\Delta T = (i-1)\frac{T_{tot}}{10} \qquad (1)$$

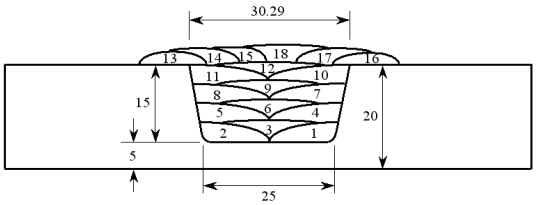

Figure 2: *Bead sequence.*

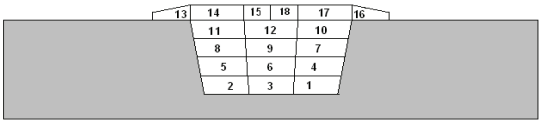

Figure 3: *Bead modelling.*

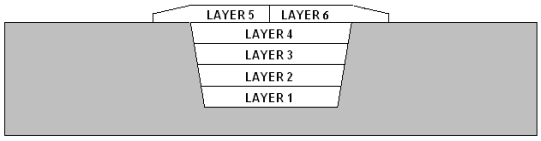

Figure 4: *Layer modelling.*

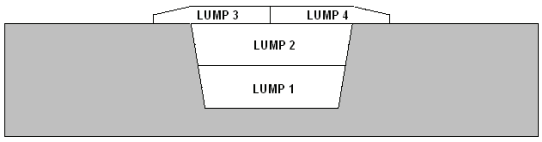

Figure 5: *Lump modelling.*

Before starting the simulation analysis procedure, the whole base plate including the weld region is meshed (Fig. 6). The elements corresponding to the weld material are "killed". To start the 1st weld pass increment analysis, the elements corresponding to this are activated. If the "prescribed temperature approach"[4] is followed then on the nodes of these elements a constant temperature load of 1450°C (melting temperature) is applied

for the duration T^{i}_{act} - T^{i+1}_{act}, where for the 1st increment i=1. This time is in fact the time the weld pool needs to come through a specific cross section and it is taken t_h = 1.5 sec. A free convection boundary condition is assumed over all free surfaces except the longitudinal plane of symmetry. The film coefficient is set to 10 W/m^2 K. The 1st pass increment transient non-linear thermal analysis is performed starting at time point T^{1}_{act} and ending at time point T^{2}_{act}. Before moving to the 2nd pass increment, all temperature loads are removed from the 1st increment elements and nodes, thus allowing it to cool under free convection during analysis of the 2nd increment. For the 2nd increment the procedure is repeated, the only difference being that the resulting temperature distribution of the 1st increment is used as initial condition. The procedure goes on until all increments are analyzed and the fisrt weld pass is complete. The same steps are followed for the simulation of the rest passes. The cooling period after the completion of all passes deposition is regulated from the inter-pass temperature of 250^{o}C. Finally a series of transient thermal analyses that simulate the cooling period in order to achieve a uniform temperature distribution over the plate equal to room temperature.

Mechanical analysis

The mechanical analysis is a close follow-through of the thermal analysis and is constituted by a sequence of static structural analyses, which use as loads the temporal temperature fields predicted in each of the time steps. The final structural analysis, which corresponds to a completely cooled down specimen, produces the residual stress field. To start the 1st weld pass increment analysis, the elements corresponding to this are activated. The temperature field, obtained from the 1st pass increment transient non-linear thermal analysis, is applied as a temperature load and a static non-linear structural analysis is performed. Using as initial stress field the result of the previous structural analysis, the temperature field, obtained of the 2nd increment transient non-linear thermal analysis, is applied as a temperature load and a static non-linear structural analysis is performed for the 2nd pass increment. Procedure goes on until all increments are analyzed and the whole pass is completed. What follows is a series of static structural analyses that simulate the cooling period up to the predefined interpass temperature. The whole procedure is repeated for rest passes and finally a number of static analyses simulating the overall plate cooling are carried out in order to obtain the residual stress field when the temperature over the whole plate has reached room temperature.

It is assumed that the temperature field is independent from the displacement field (the heat produced due to dissipation or internal friction, is negligible when compared to the heat input due to welding). It is also assumed that the thermal transient evolves much faster than the resulting changes in the displacement field, thus the present is treated as an uncoupled quasi-static thermo-elasticity problem. In this treatment the mechanical part of analysis is a series of static analyses that use as an initial displacement field, the one produced by the previous mechanical analysis and as a thermal load, the temperature field at the corresponding time point that was produced by the transient thermal analysis.

Numerical tests have shown that the maximum strain does not exceed 3% (equivalent strain < 5%), which corresponds to negligible changes in geometry. Therefore a small displacement formulation was followed.

Both parent plate and weld bead material behaviors were modeled using a kinematc hardening law. Kinematic hardening assumes that the total stress range is equal to twice the yield stress, so that the Bauschinger effect is included. This option is recommended for generally small-strain use for materials that obey Von Mises yield criteria, which includes most metals, and of course, the case under investigation and it is not recommended for large-strain applications. It is also appropriate for cyclic load histories, which is the case in sequential bead deposition.

3. The multipass repair weld

Twelve identical machined 2¼CrMo base plates, 200 mm x 100 mm x 20 mm, containing a central cavity, 92.3 mm x 30.3 mm at the opening, 75 mm x 25 mm at the base, and 15 mm deep, were manufactured by Belleli Energy, I, (Fig.1). The plates were not heat treated to remove

fabrication residual stresses prior to welding. An 18-bead submerged arc weld was deposited along each cavity, as shown in Fig. 2. The electrodes used were AL CROMO S 225 2¼CrMo, 4 mm diameter,. The welding conditions for each pass are given in Table 1. Each pass was allowed to cool to the specified inter-pass temperature of 250°C, before proceeding with the next. The base plate was pre-heated to 200°C before welding commenced and was strongly restrained on the welding bench by 4 tack welds 5 mm x 5 mm x 50 mm (Fig.1). The base plate material is DIN 17175, grade 10CrMo9-10, low alloy steel and the electrodes used were AL CROMO S 225 2¼CrMo, 4 mm diameter. Stress-strain data, for the base plate parent material and filler material at different temperatures, as well as for thermal and physical properties can be found in reference [11]

Pass	V [volts]	I [amps]	v [mm/s]	d [mm]	Interpass Temp. [C⁰]
1	30	470	8.67	4.0	250
2	30	470	8.67	4.0	250
3	30	470	8.67	4.0	250
4-18	30	570	8.67	4.0	250

Table 1: *Welding parameters.*

4. Finite element mesh

A 2-D model is constructed initially, representing the mid-section of the plate (Fig. 6).

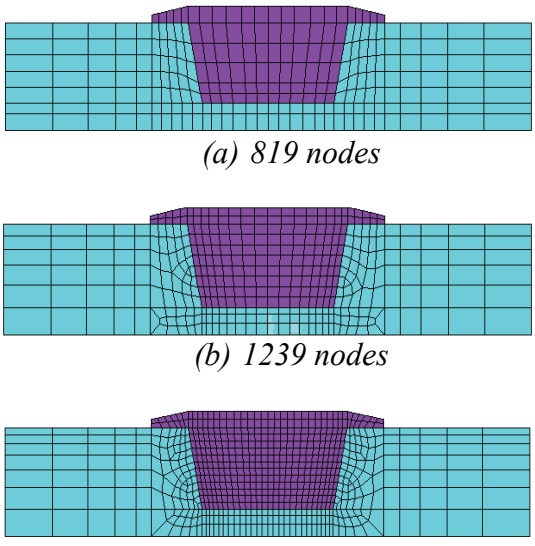

(a) 819 nodes

(b) 1239 nodes

(c) 2145 nodes

Figure 6: *2-D FE meshes.*

Three mesh configurations were examined for convergence as shown in Fig 6. The optimum configuration was used for sensitivity analysis regarding the number of weld passes as described earlier.

Using as basis the 2-D model, a 3-D model is also produced (Fig. 7-8). A total of 11578 brick 20-node thermal elements and totally 51472 nodes having 1 degree of freedom (temperature) each, were used in the thermal analysis. Free convection boundary is assigned over all free surfaces The same mesh was used for the mechanical analysis switching the element type to brick 20-node solid elements having 3 degrees of freedom (x, y, z translation) each. In the transverse to the weld bead direction the optimised mesh configuration from the 2D analysis is maintained. Restraints preventing rigid-body-motion are applied. The plate is considered clamped during welding according to Fig. 1.

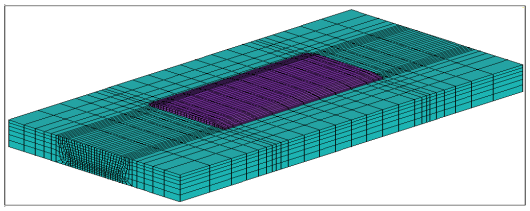

Figure 7: *3-D FE mesh - 51472 nodes.*

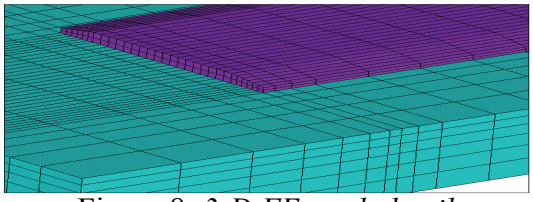

Figure 8: *3-D FE mesh detail*

5. Results and discussion

Mesh convergence

In Fig. 9 the convergence diagram regarding the prediction of the transverse residual stress via different 2-D mesh configurations is provided. The results refer to the mid-section of the plate (line A in Fig. 1), 3 mm below the top surface. The intermediate mesh density of 1239 fits well the finest mesh of 2145 nodes. In the case of 819-nodes mesh stresses are overestimated near the weld-plate interface. Thus the 1239-nodes mesh is indicated as optimum for further investigations. Restricted node numbers is

beneficial for the following 3-D analysis, since the 3-D mesh is based on the converged 2-D mesh.

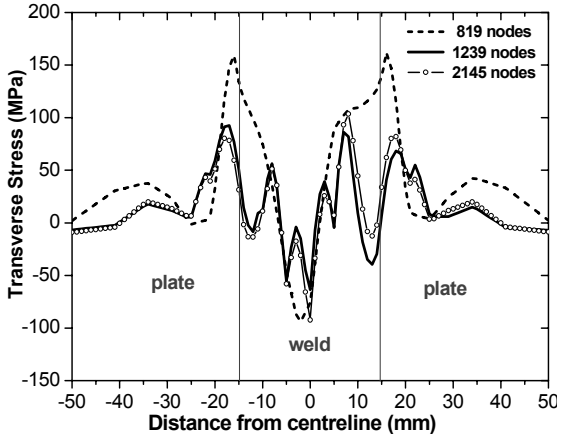

Figure 9*: Mesh convergence.*

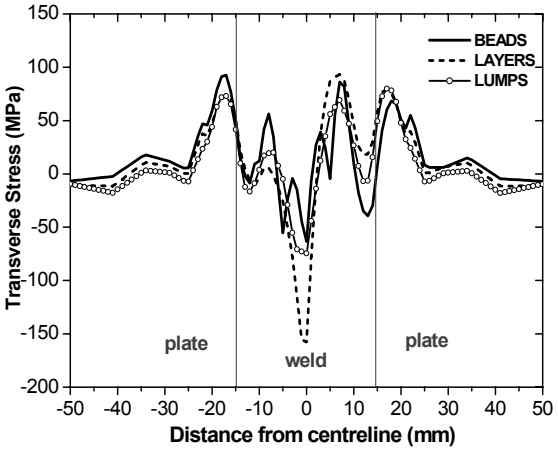

Figure 10: *Effect of bead lumping. Transverse stresses along line A*

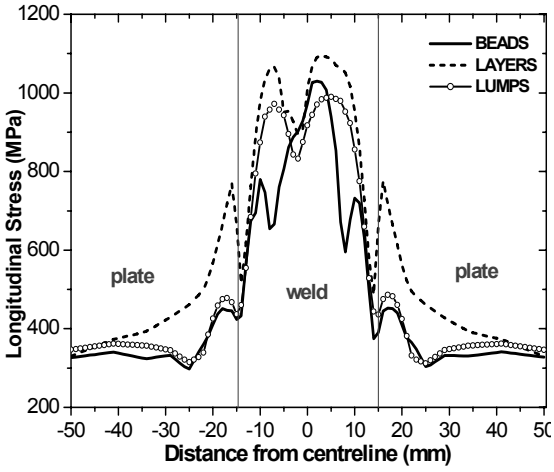

Figure 11: *Effect of bead lumping. Longitudinal stress along line A*

Bead lumping

Fig 10, 11 illustrate the distribution of residual stresses along line A, if bead-by-bead or lump-by-lump approach is used. Concerning the transverse stress, discrepancies are observed only within the welded region (Fig. 10), where the 6-layer case is characterized by a spike of a relatively high compressive stress. Curves for the bead-by-bead approach and 4-lump approach come in better agreement throughout this section. In the case of longitudinal stresses (Fig.11), discrepancies between the 6-layer analysis and the other two cases are most significant near the weld-plate interface on the base metal side. Again the 4-lump curve matches better the bead-by-bead curve. However in all cases, the magnitude of longitudinal stresses is very high due to the hypothesis of plane strain condition.

The total run time (thermal and mechanical analysis) for each simulation, based on a Pentium IV 3.0 GHz with 1Gb of RAM machine is 30 min for the bead-by-bead approach, 11 min for the 6-layer and 6 min for the 4-lump approach. The difference in time between the first and last case is large while the loss in accuracy is not considerable. Therefore, the current conclusions will be reclaimed in the 3-D analysis where the computation time is expected to be very long.

2-D and 3-D finite element analyses vs. neutron diffraction measurements

In Fig. 12-13, residual stress predictions from 2-D and 3-D analyses are directly compared to neutron diffraction (ND) measurements, which were performed at the High Flux Reactor of the Joint Research Centre - Institute for Energy of the European Commission. All measurements have been carried out along the transverse and longitudinal planes of symmetry of the plate (line A and B respectively and), 3 mm beneath the top surface.

For the transverse stress along the mid-section of the plate (Fig 12a), 2-D and 3-D analyses give quite similar results. However, prediction through 3-D modelling is the one, which come in better agreement with the experimental data. It is clear that welding cause relatively low transverse residual stresses in this direction.

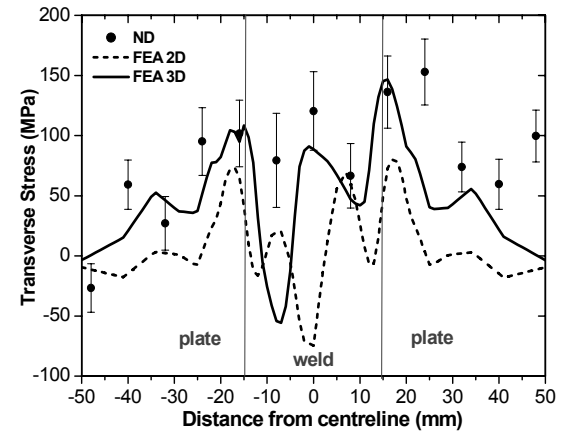

(a)

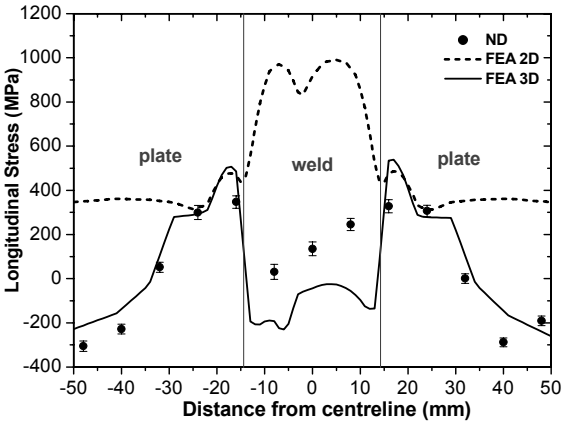

(b)

Figure 12: *Residual stress along line A (a) transverse, (b) longitudinal*

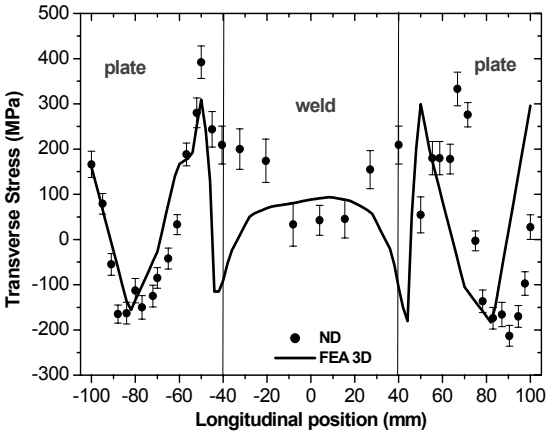

(a)

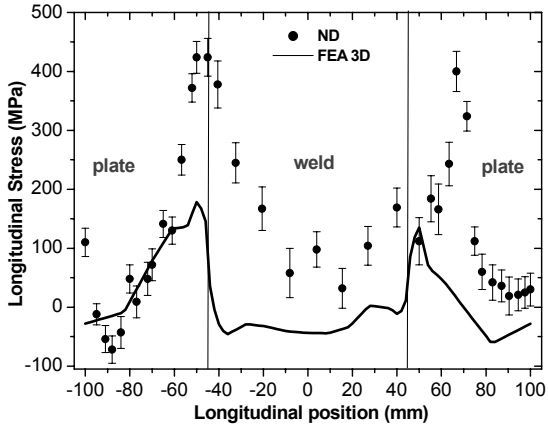

(b)

Figure 13: *Residual stress along line B (a) transverse, (b) longitudinal*

On the other hand, the longitudinal residual stresses are higher with magnitude up to 600 MPa as Fig. 12b presents. In this case, 2-D analysis gives completely unrealistic results with overestimated stress values. This is on account of the plane strain assumption, which neglects the short repair length with regard to the width and the consequent intense edge effect. On the contrary 3-D numerical results fit well the experimental data. Therefore, 3-D analysis is inevitable for reliable determination of longitudinal residual stresses in short repairs welds.

Fig. 13 depicts the comparison of 3-D finite element prediction with ND measurements along the longitudinal plane of symmetry. As measurements reveal, both residual stress components take high values (400 Mpa) in this direction. Transverse stress distribution is determined satisfactorily through the 3-D finite element analysis (Fig.13a), however, concerning the longitudinal stress field, prediction misfits the ND points around the weld-plate interface.

Metallurgical phenomena taking place in this region, the so-called heat affected region (HAZ), may be responsible for this behaviour. When the weld material is deposited, part of the parent material adjacent to the fusion line, which stands at lower temperature, melts. It may be supposed that this region does not conserve its original mechanical properties but it obtains weld material properties. That practically means enlargement of the fusion zone. Actually, this region has mixed material. Moreover, it experiences annealing and solid-state phase transformations. All these phenomena demand intricate finite element models and knowledge of the exact fusion boundary in order to be taken into account. In the present study a simplified lumped 3-D analysis was followed to reduce the computational cost. However the total processing time was about 95 hours, in

fact very long. Neglecting the metallurgical effects and the precise pass sequencing, which increase the modelling complexity, satisfying results for the residual stress field can be derived

A clearer view of what happens in the weld material may be given if transverse and longitudinal scans performed at different distances from the top surface. A revised set of yield strength data is to be released within the project and as soon as this is done, a revised set of simulations based on the new material data will be performed.

6. Conclusions

Numerical analysis of an 18-bead short repair weld has been conducted. 2-D models can give relatively good results for the transverse stress along the weld mid-section but unreliable ones for the longitudinal stress. The main utility of the 2-D models is the numerical optimisation prior to a 3-D analysis, since the performance of the mesh configuration and lumping approach can be assessed. Using a simplified 3-D model with reduced number of weld passes and omitting the complex metallurgical changes, which accompany the welding procedure, a satisfying numerical prediction of residual stresses can be achieved. This is very important if the proposed simulation methodology is to be used in industrial applications.

7. Acknowledgements

The authors would like to thank the steering committee of the NET European Network for making available data from this project, in particular R.C. Wimpory and C. Ohms, who have performed the ND measurements, and Belleli Energy srl (I) for manufacturing the weld specimens. The research presented in this paper was conducted under the financial support of the Institute for Energy, JRC-IE, Petten, NL, through Study Contract SC320226.

References

[1] Dong P., Zhang, J. and Bouchard, P.J., (2002), ASME J. Press. Vessel Technol., **124**, No.1, pp. 74.

[2] Dong P., Hong J.K., Bouchard P.J., (2005) Int. J. Press. Vessels Piping, **82**, pp. 258.

[3] Lant T., Robinson D., Spafford B. and Storesund J., (2001) Int. J. Press. Vessels Piping, **78**, pp. 813.

[4] Lindgren L.E., (2001) J. Therm. Stress., **24**, pp. 141.

[5] Hong J.K., Tsai C.L., and Dong P., (1998), Welding Journal, 77, No 9, pp. 372.

[6] Hyde T., Sun W., Becker A. and Williams, J., (2004) In.t J. Press. Vessels Piping, **81**, pp. 1.

[7] Soanes T.P.T., Bell W., Vibert A.J., (2005), Int. J. Pressure Vessels Piping, **82**, pp. 311.

[8] Sharples J.K., Garrner L., Bate S.K., Goldthorpe M.R., Yate J.R., Bainbridge H., (2005), Int. J. Press. Vessels Piping, 82, pp. 319.

[9] Ohms C., Katsareas D.E., Wimpory R.C., Hornak P., & Youtsos A.G, Proceedings of the 2004 ASME/ JSME Pressure Vessels and Piping Conference, 479, ISBN-0-7918-4674-1, pp. 85-92, San Diego (California)

[10] Bouchard P.J., George D., Santisteban J.R, Bruno G., Dutta M., Edwards L., Kingston E., Smith D.J., (2005), Int. J. Press. Vessels Piping 82, No 4, pp. 299.

[11] NET–TG2, (2005), 18-Bead Repair Weld Finite Element Simulation Protocol.

EFFECT OF MULTIPLE REPAIRED WELDED AND TIG-DRESSING ON WELD BEAD FATIGUE STRENGTH

LI DongXia
Department of Civil Engineering,
ZhongYuan University of Technology,
41 West Zhongyuan Road, Zhengzhou, Henan 450007, P.R.China

JIA Fang
Chu Kechen Honors College, Zhe Jiang University,
Hangzhou 310058, P.R.China

JIA BaoChun
Zhengzhou Research Institute of Mechanical Engineering,
No.81, South Songshan Road, Zhengzhou, Henan 450052,
P.R.China

Abstract:

The effects of multiple repairing-weld and TIG-dressing on the fatigue property of high strength steel weld joints used in platform have been investigated. The principle and technological process of TIG-dressing of welding bead is studied on an important basis for our study of the offshore drilling platform. Through the fatigue tests on high strength welding joint samples, the life estimating formula is obtained after as-weld and TIG-dressing. The S-N curve and the equation after as-weld and TIG-dressing are given. By comparison and analysis tests' results of each time, thus prolong the platform's life and reduce the times of repairing weld has been examined. The work in this paper offers an important basis for the multiple repairing-weld of platforms.

Key words: high strength steel, multiple repairing-weld, TIG-dressing, weld bead, fatigue strength

1. Introduction

The ocean platform is very important structures for ocean oil industry. Due to the alternate loadings, fatigue cracks inevitably appear in its welded parts during service period. The safety operated is critically affected by the cracks of the ocean platforms. As a result,

engineers have immersed themselves in programs about it, and they brought forward varieties of force condition being improved more reasonable to the structure, and also methods to increase the fatigue life of the joints.

Weld bead property of the high strength steel welding joints is studied in this paper. According to the specification of classification society all over the world, the using times after repaired welding high strength steel in general can't exceed twice. And then the service period, the cracks that have been had and already twice repairing weld would be rejected if it can't be repaired. This will lost a lot for the company, instead the using life of the platforms will be prolonged much longer if be repaired over twice. At the same time, studying modern technique and improving fatigue life after repaired welding will reduce production costs and repairing times. Spend on it both in add the working time on platforms and increase financial profit. As a result, it is pressed for that TIG-dressing and improving fatigue strength of weld line. The repaired welding technique also has strong practical significance and both financial and social profit.

2. Types of welding joints and test materials

2.1 Types of welding joints

The fatigue cracks of the ocean platforms emerge in the legs welding joint corresponding to the specific legs. The welding line of the legs welding joint that makes the materials hardly to be welded, but easily to splits there will be severe stress concentration and plenty of cracks after all. This problem is the weak link for the leg of construction consequently. Therefore the T-shape of welding joint is chosen for this experiment of the high strength steel [1] .

2.2 Welding materials

The materials used for the test were high strength steel. The mechanical properties of the steels are given in Table1.

Mechanical properties		
σ_b [MPa]	σs [MPa]	δ
490	343	22%

Tab.1 The mechanical properties of experimental materials

3. TIG-dressing procedure

3.1 The TIG-dressing is fusion repaired in the position of toes used by tungsten inert gas when the structure has already been the first welding repaired. And it is applied using the ordinary TIG-welding equipment by which the metal on the toes of welding line can be remolded and appears as smooth transition. And all above is in a particular way that remands the special dressing sequences and dressing parameters. Consequently the transition will be more smoothly with the remanded metal here more compact and also free of inclusion with better property.

The position of the cracks is actually not certain to appear at one side of the T-shape welding line, instead, both sides of it will undergo the identical fatigue procedure. Therefore for guarantee to experiment of unity, make specimen the both sides is placed in the same groove

all and together, ignoring when which side appear the crack, welding repaired, the both sides all makes same grooves, repair with the same specification proceeding welding repaired and TIG-dressing. See Fig.1.

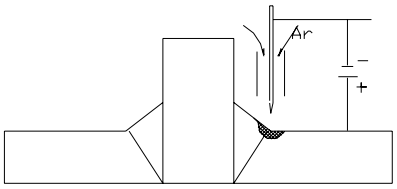

Fig.1 TIG-dressing.

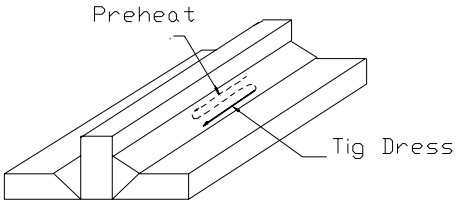

Fig.2. TIG-dressing by translational motion back and forth.

3.2 The TIG-dressing by translational motion back and forth is proceeding after the weld bead cutting apart. And then the weld bead is preheated with electricity before the TIG-dressing, and then is repaired by TIG-dressing. See Fig.2. The purpose of the TIG-dressing by translational motion back and forth is reducing the cooling velocity in heat-affected zone of the weld bead so that the hardness descends and the toughness is made better.

3.3 The technology and parameter TIG-dressing affects the fatigue strength of welding joints awfully. The technology and parameter TIG-dressing is chosen mainly according the base metal property and chemical composition of the weld bead in repairing area so that the better weld bead metal-lographic structure. The energy input is adopted so that the test proceeded by three standards. See Tab.2.

The standard	1	2	
The hardness in heat-affected zone / HV	377	335	328

Tab.2. The energy input.

The metal-lographic structure in heat-affected zone of specimen 3 is bainite +sorbite +ferribite + a little amount martensite, and ones' specimen 1 is more martensite than the specimen 3. The hardness exceeds 350HV and it is 377HV so that it exceeds the construction standard of platform.

4. TIG-dressing procedure of the fatigue specimen and data treatment

4.1 TIG-dressing procedure of the

fatigue specimen

The specimen after weld-repaired is proceeding TIG-dressing in weld toe.

- The crack is cleaned.
- It is repaired welding by the repair welding technology and standard.
- The weld toe is cleaned without corrosion and inclusions.
- The TIG-dressing is proceeding according to the standard technology parameters, and the welding velocity must be even.
- The ultrasonic inspection is proceeding after the TIG-dressing.

4.2. Data treatment of the fatigue specimen

The fatigue test is proceeding for the specimen after TIG-dressing and the welding repair. The fatigue test adopts the system of the 4-point bending test [2]. It is divided two stresses class and the test parameter is following table3.

	High stress	Low stress(TIG-dressed)	Low stress (as-weld)
Mean stress	299.52[MPa]	167.68[MPa]	137.28[MPa]
Stress amplitude	161.28[MPa]	90.38[MPa]	73.92[MPa]
Ratio of stress	0.3	0.3	0.3
Frequency	10[Hz]	95-98[Hz]	

Tab.3. The stresses class for TIG-dressed and as-weld

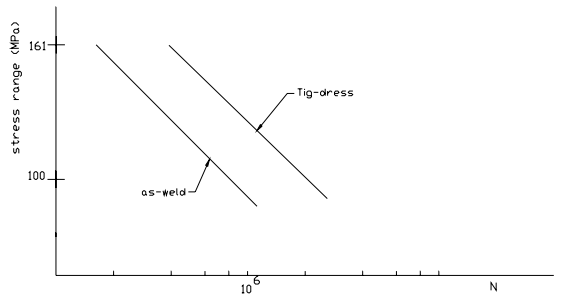

Fig.3 The S-N curves used by TIG-dressing and as-weld

The fatigue test result of the TIG-dressing and as-weld according to each one, the logarithms normal distribution is adopted the proceeding data processing. The fatigue life formulae are given by results of the fatigue test data [3]. The equations are refer to (1), (2). The as-weld and TIG-dressing fatigue based on statistic analysis is shown in Fig.3.

As-weld: $lgN = 12.5141 - 3.3079 lg\sigma$ (1)

TIG-dressing: $lgN = 12.7524 - 3.2420 lg\sigma$ (2)

In figure 3, we can see clearly that the fatigue life of specimen after TIG-dressing is much higher than ones after as-weld.

5. The effect of welding repaired TIG-dressing on fatigue properties of

the weld bead

5.1 The fatigue life of specimen after TIG-dressed increases 1 time than that hasn't been TIG-dressed. From that we can see, not only the fatigue strength, but also the fatigue life after TIG-dressed materials that even are more safety conduct procedure, can still be much more improved. TIG-dressed repairing will obviously increase the fatigue strength. For inspecting the TIG-dressed the effect and the practical applicability, it is shown to us for the practice on a drill platform that was in repairing. After TIG-dressed, the surface of the welding line transited clearly and smoothly, none cracks, none inclusion and none undercut that sort of imperfection. With the perfect result, that platform has already been in use since 1999, the crack did not appear up to now.

5.2 The effect of TIG-dressing repaired on material property of the weld bead:

Because the outside of welding lines prolonged after as-weld, the shape change of welding line made the curve radius of position of welding toe transition and the angle of position of welding toe to change. The position of welding toe transition and the welding toe after TIG-dressed are amplified by 10 times and by 100 times. See Fig.4.5.6.7. In Fig.4, Fig5 and Fig6, we can see clearly to that shape of welding toe is change by TIG-dressing and the transition of welding toe is level and smooth. Therefore the stress concentration is lower. From the formula of Nishida [4], the coefficient of stress concentrations after repaired welding and TIG-dressing are obtained. See the Tab.4.

From the Fig.4 and Fig.5, we can see that the surface of welding toe without TIG-dressing is not smooth and the micro-cracks and micro-imperfections is on welding toe. The fatigue crack source is caused on the weld bead. See Fig.7. But the surface of welding toe after TIG-dressing is more smooth and level. The micro-cracks and micro-imperfections on welding toe are eliminated. See Fig.6. The considerable improvement of welding toe property is obtained by the application of the TIG-dressing. The transition angle of welding toe is changed and the stress concentration is lower by TIG-dressing. The stress concentration after TIG-dressing is lower 30%-75% than that after as-weld. The fatigue crack is not caused on the weld bead and the considerable improvement of the fatigue life is obtained.

Welding toe after as-weld	θ=150--170^{O}	ρ=2—4	h=12	K=2.3—3.1
Welding toe after TIG-dressing	θ=150--170^{O}	ρ=10	h=12	K=1.3—1.7

Tab.4. The coefficient of stress concentrations after as-weld and TIG-dressing

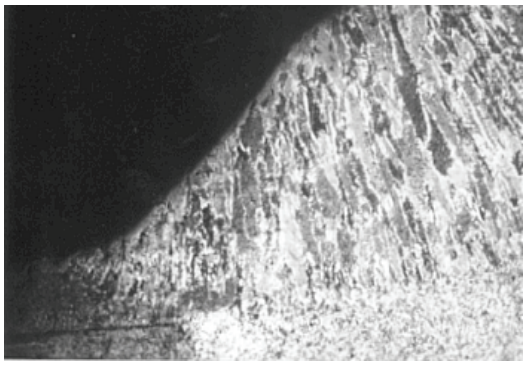

Fig.4 The welding toe shape (a) 10X

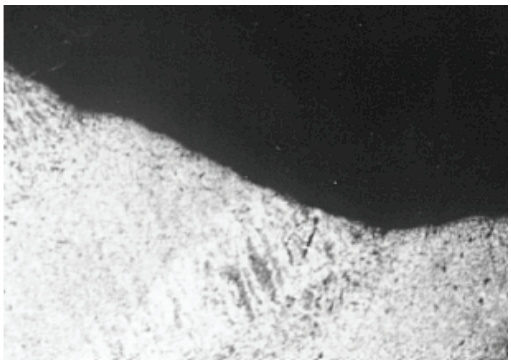

Fig.5 The welding toe shape (b) 10X

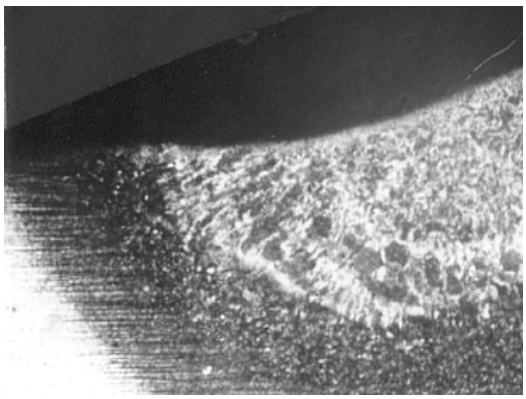

Fig.6 The welding toe shape after TIG-dressing 10X

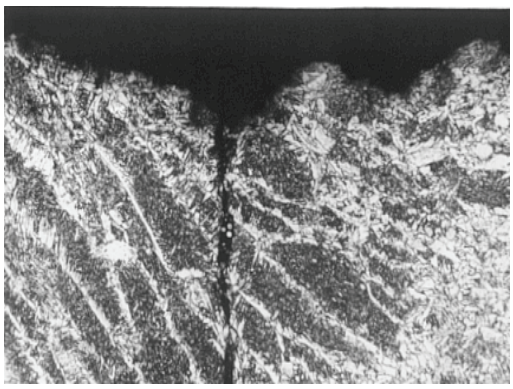

Fig.7 The welding toe shape without TIG-dressing 100X

6. The conclusion

The imperfection in welding toe is the key factor of the fatigue life. The probability of the imperfection appeared on welding toe of welding line under the same technology and condition is equal in amount so that the fatigue life after repaired welding is almost no difference. The strain concentration of thermal cycle stress and residual stress as-weld makes the micro-cracks produced on welding line. The stress concentration is lower by TIG-dressing. Therefore, the stress concentration coefficient by TIG-dressing is lower 30%-75% than that after as-weld.

The considerable improvement of fatigue strength and life is made by TIG-dressed technology in the present test so that the technology is used for offshore drilling platform and the result is better.

References

[1] LI Dongxia, ZHU Yanzhi, JIA Baochun, "Experimental study for fatigue behavior of weld line by secondary TIG dressing", in: Proceedings of 7th International Conference on Mesomechanics, Montreal, Canada, August 1-4, 2005, pp. 460-463

[2] LI Dongxia, JIA Baochun*, et al*, "A study of fatigue strengths and lower temperature properties of TIG dressed welded joints". Journal of Mechanical Strength. 2005, vol.27, (1), pp.126-129.

[3] Z. T. Gao, "Applications of Statistics in fatigue", Beijing: National Defense Industry Press. 1986.

[4] H. H. Minner and T. Seeger, "Investigations on the fatigue strength of welding high strength steel STE 460 and STE 690 in as-welded and TIG-dressed conditions", IIW/IIS document XIII-912-79

VII. Structural Damage

IMPORTANCE SAMPLING FOR MULTIPLE SITE DAMAGE MONTE CARLO SIMULATIONS

Peter Horst
Institute of Aircraft Design and Lightweight Structures
Technical University of Braunschweig
Hermann-Blenk-Str. 35, D 38108 Braunschweig, Germany
e-mail: p.horst@tu-bs.de

Abstract

Multiple Site Damage is a key problem in aging aircraft. The subject has been treated since about 15 years. The author – as some other authors from Europe – looks at the problem as a stochastic problem. A Monte-Carlo Simulation seems to be a good way to treat it, but it needs a very high number of scenarios to be calculated. This has been described in a set of papers. The problem behind this approach is that the deterministic model part of the MCS process must be very time efficient, since many calculations are needed. This is to some extent limiting the accuracy of the model.

One way to save a large amount of time-consuming calculations is to try to use importance sampling in this case. A number of approaches in this direction are presented in this paper.

The current paper looks at the problem by starting from an existing MCS model and tries to combine modern methods of feature detection via wavelet transform with the results of this MCS model in order to find a means for importance sampling, which is not a simple task in MSD cases. The idea is to find patterns of damage in an early stage of the process, which may be used to conclude that the pattern is critical or non-critical. This means that only few scenarios really have to be calculated, and may be calculated by a more sophisticated method.

The method and an example are presented.

Keywords: Multiple Site Damage, Widespread Fatigue Damage, Monte Carlo Simulation, Importance Sampling, Wavelet Transform.

1. Introduction

As pointed out in the paper [1] Monte-Carlo (MC) simulations are the best possible way to assess Multiple Site Damage (MSD) and Widespread Fatigue Damage (WFD) in aerospace structures. Other methods as e.g. first order reliability methods (FORM) etc. are not successful in this case, since too many stochastic parameters are involved. The biggest drawback of the MC approach is the high numerical effort needed in this case. Different methods are at hand to assess the number of scenarios to be simulated in such a MC simulation in order to find a certain probability of failure. As pointed out in [1], the method given by Brodin et al. [3] results in nearly 75,000 scenarios in the case of a probability of failure $p_f = 4 \times 10^{-5}$ and a confidence level of 0.95. This illustrates the problem of pursuing this way. Importance sampling is the way how to try to minimize the number of scenarios, which really have to be analyzed completely. This is not an easy task to set up, as the following sections will show.

The general outline of the MC simulation used in this paper is given in Horst [1] and some other papers. This is also true for several different methods of crack propagation calculation by other authors.

In paper [1] and [2] a wavelet transform has been used to build up typical patterns of MSD critical scenarios. This is a way of performing data compression. A Haar transform (see [4]) has been used in the case of a uniformly loaded/stressed lap joint, which is a classical WFD susceptible part.

In this paper this approach is extended in the way that the effort and possible benefit from this approach is investigated. This is done by using one extensive example, which is given in the next section.

2. The Example

The example consists of a three-rivet row lap joint: pitch 20 mm, rivet diameter 4 mm, material 2024 T3, thickness 1.6 mm and a remote stress of 84 MPa at R = 0.0. The example has 16 rivets at this highly fatigue critical location, as e.g. in the case of a single frame-bay. The number of 16 rivets results in 32 fatigue critical locations. Further details concerning both, the crack initiation parameters as well as crack growth behavior of the material are given in [2].

A typical result of a MC simulation of such an example is given in Figure 1.

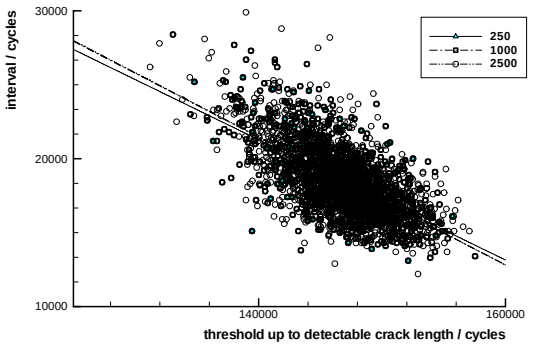

Figure 1*: Typical result of a MC simulation using different numbers of scenarios*

This figure shows the inspection interval plotted versus the threshold up to detectable crack length for the case of a detectable crack length of 5 mm, and only the crack initiation as a stochastic parameter. What can be seen easily is the fact that only a few scenarios are needed to predict the general trend and mean values of the distributions, since the regression line converges quite fast. But this is in general not the point in structural reliability. What mainly is interesting are the extreme values.

Figure 2 shows another typical result of a single scenario, i.e. the crack growth in the case of a minimum inspection interval. This scenario is meant in the way that the left and right hand side position of the fatigue crack is plotted versus the number of loading cycles. In this minimum case, the cracks are typically nearly of the same size in a certain domain.

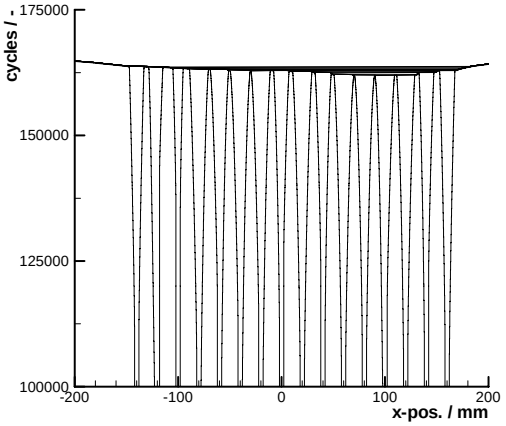

Figure 2: *Typical crack growth pattern in the case of minimum interval*

Data compression by means of a Haar transform.

It is now the question what to use for the importance sampling. A first impulse would be to use the initial damage scenario, which is found by means of a random process, based on fatigue data found by coupon tests. Unfortunately, it turns out that this is not very well linked to the inspection interval, which usually is the most interesting parameter with respect to certification. The next interesting parameters could be the crack scenario at the point in time, when the first crack reaches detectable crack length, i.e. 5 mm in this case.

This second approach still has the advantage that the crack propagation up to this point may be calculated by highly effective means without taking into account the interaction of the cracks, since the interaction effect is quite low at crack sizes below this value.

In the case of 250 scenarios, the Haar transform of the minimum and maximum interval scenario is given in figures 3 and 4.

It is quite simple to see that the two transforms are quite different at higher levels. This is exactly what is intended. Higher levels of Haar transforms may obviously been used for the purpose of feature detection. (for further comments on Haar transform, see [1] and [2]).

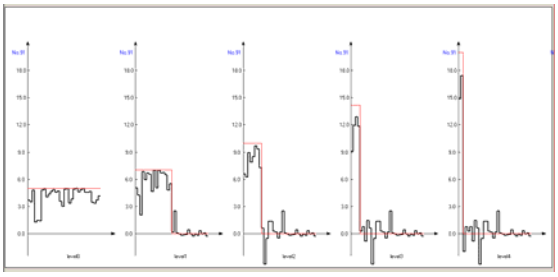

Figure 3: *Haar transform of the minimum interval case*

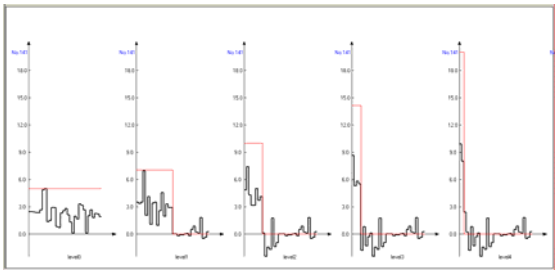

Figure 4: *Haar transform of the maximum interval case*

In order to have a closer look at the performance of the new way of using higher levels of the Haar transform of the 5 mm crack scenario, a simulation of 25,000 different initial damage scenarios has been performed for the case described above. The result of these scenarios is given in figure 5. It may be used as a kind of reference data set for the importance sampling discussed in the following sections.

The problem now is the way to find a minimum level 5 Haar transform number for a given inspection interval to be assessed. The importance sampling method has to decide, which level 5 number will guarantee that all critical inspection interval cases are calculated, while most of the non-critical cases are not looked at.

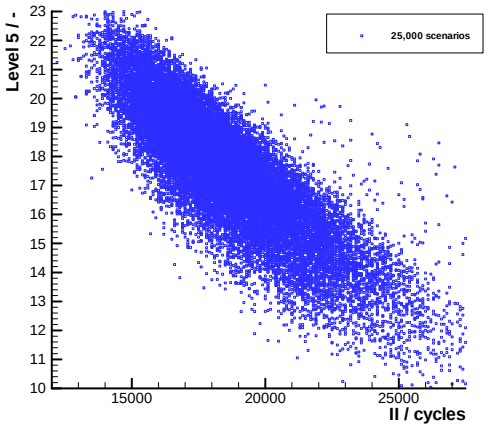

Figure 5: *Results of 25,000 scenarios – inspection interval vs. level 5 Haar transform*

Possible tactic for an optimal importance sampling.

As mentioned above, the tactic must provide a most accurate guess of the minimum level 5 parameter per inspection interval. The question is how to do this. One first attempt must be to use only a small number of scenarios, which are completely calculated, e.g. 1 % of the number of total scenarios as a basis of this prediction. This would be 250 scenarios in this case of 25,000 overall scenarios, as given in figure 1.

Figure 6 shows the minimum level 5 line from 250 calculated scenarios as well as the minimum line from 25,000 scenarios. The question is how to do the extrapolation from one line to the other.

The extrapolation may be performed on the basis of different methods, e.g. Students distribution, Gumbel distribution etc.. Up to now, no optimal criterion has been found. The problem is that the method must provide a conservative extrapolation on the one hand, but a really conservative guess would result in a quite reduced benefit from the importance sampling, i.e. the benefit vanishes quite fast.

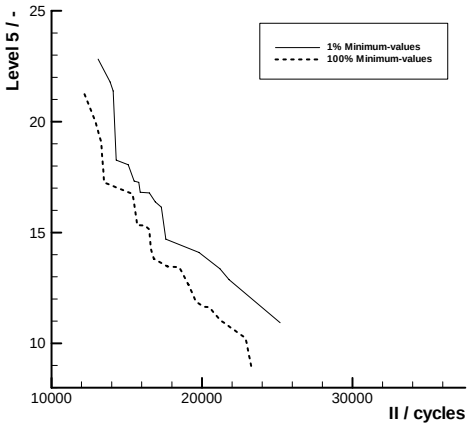

Figure 6: *Minimum values per inspection interval vs. level 5 value*

This last point may be assessed or at least understood by means of figure 7. Figure 7 uses the results of the 25,000 scenarios and just shows the minimum number of scenarios to be analyzed completely, provided an optimal criterion on the criticality would be known. This optimal criterion will not be at hand anyway, i.e. this line shows something like an unreachable limit line.

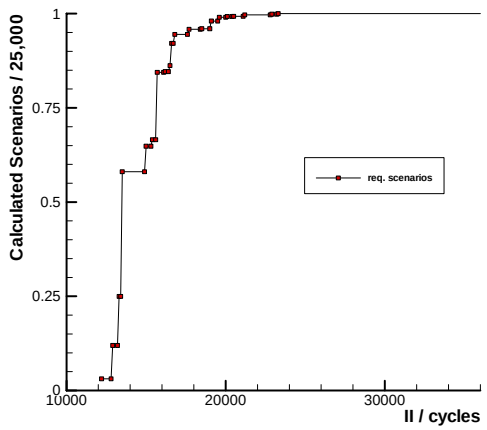

Figure 7: *Relation of critical to overall scenarios in the 25,000 scenario case*

What may be observed from figure 7 is the steep rise in the number of scenarios which have to be analyzed completely, even in the case of a perfect criterion, if the required inspection interval and therefore the probability of failure rises. This is again a hint that this type of work on importance sampling only makes sense, if low probabilities of failure are of interest.

Conclusions

From the short presentation given in this paper, the following conclusions may be drawn:

- a MC simulation is a means to assess certain interesting features of aging aircraft by means of a stochastic approach
- this approach is quite versatile, but it needs a high computational effort
- MC simulations would not change their general outline, if further probabilistic parameters would be included, as e.g. in the probability of detection etc.
- one way to reduce the computational effort is importance sampling by means of a Haar transform of the crack scenario at the point in time, when the first crack reaches 5 mm
- the benefit may only been found in cases where small probabilities of failure are of interest
- a realistic criterion for the extrapolation of results from a few scenarios to a large ensemble is still needed.

References

[1] Horst, P. (2005): Criteria for the Assessment of Multiple Site Damage in Ageing Aircraft, *Structural Integrity & Durability*, **Vol. 1**, pp 49-65, 2005

[2] Horst, P. (2005): Feature Detection for the Assessment of Critical Multiple Site Damage Patterns, Proceedings of the MESOMECHANICS 2005 Conference, Montreal, Canada, 2005

[3] Broding, W.C., Diederich, F.W. and Parker, P.S. (1964): *Structural Optimization and Design Based on a*

Reliability Design Criterion, J. Spacecraft, **Vol. 1**, pp 56-61

[4] Walker, J.S. (1999): *Wavelets and their Scientific Applications*, Chapman & Hall

MICROMECHANICAL DAMAGE MODELLING IN THE THICKNESS DIRECTION OF PIPELINE STEEL

Ayvar, S., Yates, J. R. and Howard, I. C.
The University of Sheffield, Department of Mechanical Engineering, Sheffield, UK

Abstract

Recent developments in micromechanical damage modelling of flat fracture mechanism in X100 gas line pipe steel are reported in this paper. Gurson-Tvergaard-Needleman (GTN) and the Rousselier damage models, with the assumption of isotropic behaviour, were tuned to experimental load-displacement data to calibrate the appropriated micro-mechanical parameters to fracture in the through wall thickness orientation.

Two sets of 3D computational analyses were conducted and the results compared. The first set was a conventional finite element (FE) method in which the element size must be chosen with regard to the micro-structural scale of the ductile damage process. The second set of analyses used the hybrid cellular automata finite element, CAFE, technique. The finite element in this case only needs to be refined enough to capture the deformation behaviour and the cellular automata deal with the evolution of damage at the correct micro-structural scale.

Comparison of the results from the two computational modelling strategies demonstrates the effectiveness of the CAFE technique in reducing the simulation time whilst maintaining satisfactory deformation and damage predictions.

Keywords: GTN model, Rousselier model, micromechanical parameters, finite element (FE), cellular automata (CA), flat fracture, 3D computational analyses, thickness direction, X100 pipeline steel.

1. Introduction

Interest in using micromechanical damage modelling has increased in recent decades. Extensive research on macro and micro mechanic has showed that ductile fracture in metals can be predicted by micro-mechanisms of failure. An example of this interest, in industrial line pipe application, is to control the fracture propagation of gas transmission pipelines by specifying upper shelf Charpy energy. Recently, it has been suggested by e.g. Leis [1] and Andrews et al. [2] that the fracture energy in Charpy impact test of high grade pipeline materials associated with fracture propagation can be split in two parts. One is related to flat fracture at the centre of the typical Charpy fracture surface and the other to slant fracture at the edges. As the dominant failure mechanism in gas line pipes is fast propagating ductile shear, the latter is the most important portion of the fracture energy which can be reasonably attributed to the real failure mode of the pipe.

Accordingly, specimens with different flat and slant fracture characteristics are needed for a comprehensive failure analysis of Charpy specimens. This paper reports on preliminary studies on the application of two damage models, one proposed by Tvergaard - Needleman (GTN model) [3] and that introduced by Rousselier [4], to describe the material behaviour and flat fracture prediction in the assumption of effective material damage isotropy in the through thickness direction of X100 material. There is also a discussion of classic FE modelling compared with the more recent CAFE

technique, as a potential tool to reduce the time of simulation, whilst maintaining a good prediction of damage.

2. Numerical work on ductile fracture

Two damage models, GTN and Rousselier, were employed as the mechanisms to characterise the process of void growth and coalescence driving material failure. The material was assumed to have a Young's modulus E of 210 GPa, a Poisson's ratio υ of 0.3, a yield stress and tensile strength, estimated from the true stress strain curve, of 715 MPa and 840 MPa respectively.

GTN and Rousselier models.
The GTN model is typically expressed in the form of the yield potential [3]:

$$\Phi = \left(\frac{\sigma_{eq}}{\sigma_Y}\right)^2 + 2q_1 f^* \cosh\left(q_2 \frac{3p}{2\sigma_Y}\right) - \left(1 + q_3 (f^*)^2\right) = 0 \quad (1)$$

The function $f^*(f)$ was chosen as:

$$f^*(f) = \begin{cases} f & f \le f_c \\ f_c - \dfrac{f_u^* - f_c}{f_F - f_c}(f - f_c) & f > f_c \end{cases} \quad (2)$$

Where σ_{eq} is the von Mises equivalent stress, σ_Y the material yield strength, p the hydrostatic pressure, q_1, q_2 and q_3 are material constants, f_c is the critical value of void volume fraction, f_F is void volume fraction at final fracture and $f_u^* = 1/q_1$

In this model, fracture propagates when the damage parameter reaches its critical value designated by f_c (threshold of rapid loss of load carrying capacity). So that, the damage elements are removed from the analysis simulating crack growth through the microstructure. The parameters f_c, f_F, q_1 and q_2 have to be determined. As well as these parameters, there is a parameter L_c, the cell size, which is representative of the spacing of the large inclusions in the material. In total five parameters should be calculated to perform the damage simulation.

Another consistent and simple ductile damage theory was introduced by Rousselier [4]. The plastic potential in this model has the form:

$$\frac{\sigma_{eq}}{\rho} - H\left(\varepsilon_{eq}^p\right) + B(\beta) D \exp\left(\frac{\sigma_m}{\rho\sigma_1}\right) = 0 \quad (3)$$

Where:

$$\dot{\beta} = \dot{\varepsilon}_{eq}^p \, D \exp\left(\frac{\sigma_m}{\rho\sigma_1}\right) \quad (4)$$

$$\rho(\beta) = \frac{1}{1 - f_0 + f_0 \exp\beta} \quad (5)$$

$$B(\beta) = \frac{\sigma_1 f_0 \exp\beta}{1 - f_0 + f_0 \exp\beta} \quad (6)$$

Where β is a scalar damage variable, and its evolution is determined by Eq. (4). B is the damage function, ρ is dimensionless, D and σ_1 are material constants and $H\left(\varepsilon_{eq}^p\right)$ is a term describing the hardening properties of the material. The term f_0 is the initial void volume fraction, which can be calculated from Franklin's formula [5]:

$$f_0 = f_v \frac{\left(d_x d_y\right)^{1/2}}{d_z} \quad (7)$$

$$f_v = 0.054\left(S\% - \frac{0.001}{Mn\%}\right) \quad (8)$$

Where d_x, d_y and d_z are the average dimension of the inclusions. If a spherical inclusion shape is assumed, Eq. (7) gives $f_0 = f_v$. From this an initial void volume fraction $f_0 = 3x10^{-5}$ was found for this steel.

CAFE technique.
The main idea of the CAFE approach is to separate the structural analysis from the material properties. This means that a finite element model is constructed only to represent the macro strain gradients adequately. On the other hand, the cellular automata arrays with a suitable cell size represent the appropriate material behaviour. The CAFE model implemented by Shterenlikht [6] for transitional ductile brittle fracture has been used in this work. In this CAFE the brittle mode has been switched off, so the model parameters for ductile fracture have been calibrated independently for an investigation of damage modelling to characterise the flat fracture behaviour of a modern line pipe steel. The general strategy for ductile fracture in this CAFE is that an array of CA is connected to the FE in question. In this array the Rousselier continuums ductile damage model is used, principally because of its combination of simplicity and realism. Therefore the total number of cells per ductile CA, M_D, has to be chosen so that the linear size of an individual CA cell is close to the ductile damage cell size, L_D. If a cubic finite element of size $L_{FE} \times L_{FE} \times L_{FE}$ is assumed then the Eq. (9) can be used to choose M_D

$$\frac{L_{FE}}{\sqrt[3]{M_D}} = L_D \tag{9}$$

Where $\sqrt[3]{M_D}$ is the number of cells per dimension of a cubic ductile CA.

3D finite element modelling and representation of damaged elements.
The numerical calculations were conducted on cylindrical tensile specimens in order to tune the material constitutive parameters and on square tensile samples to validate the calibrated model by reproducing the full field strain deformation of the experimental data [7]. The commercial code ABAQUS/Explicit 6.4 [8] was used to build and analyse the FE models and, for CAFE analysis, a user material subroutine VUMAT was employed. Due to symmetry, only one quarter of the cylindrical tensile specimen was modelled. For the square tensile sample, in spite of symmetry conditions, the complete model was represented to obtain the whole field strain deformation in the damage zone. All analyses were carried out using 3D elements (C3D8R).

In the GTN damage model, fracture starts when the void volume fraction reaches its critical value, simulating the state where the cavities link. This process is simulated in finite element modelling by the extinction of the damage elements. Figs. 1 and 2 show the elements removed in the centre of the 3D cylindrical and square tensile tests due to the severe triaxiality and the initial maximum cavity in that place.

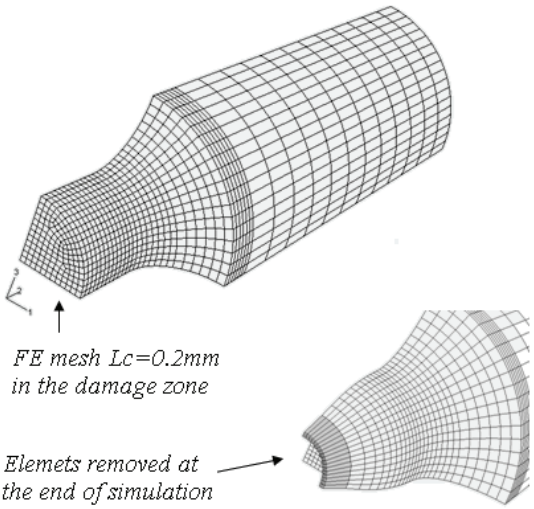

Figure 1: 3D cylindrical tensile FE modelling and crack growth representation for the GTN model.

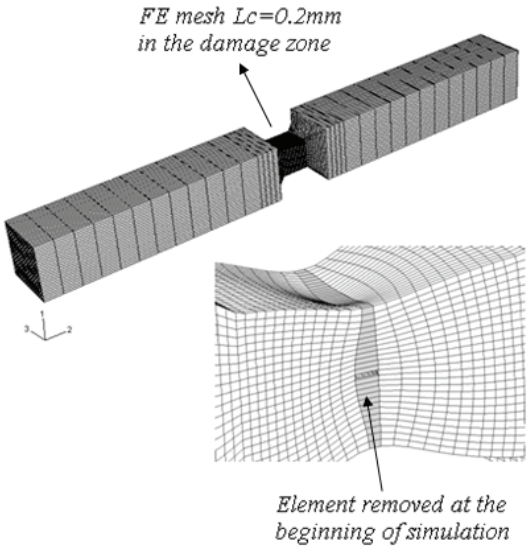

Figure 2: 3D square tensile FE modelling and crack growth representation for the GTN model.

Applying similar computational procedure as used for the classical FE model, in the CAFE technique fracture starts when its damage variable, distributed across a CA cell, exceeds the critical value according to the local strain concentration. When all ductile CA cells assigned at one finite element die at the microscopic level, a dead element at the macroscopic scale is produced as well. Figs. 3 and 4 show the fracture propagation.

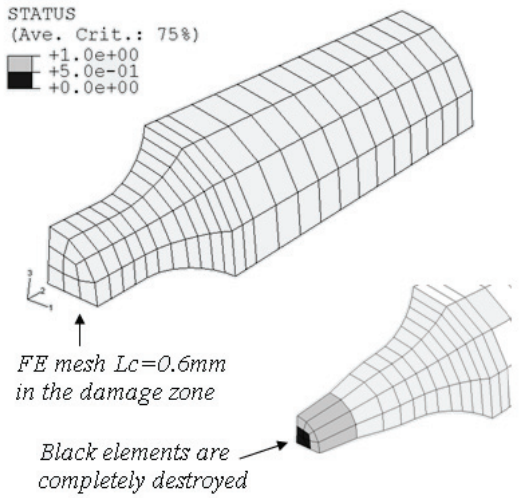

Figure 3: 3D cylindrical tensile FE modelling and crack growth representation for CAFE technique.

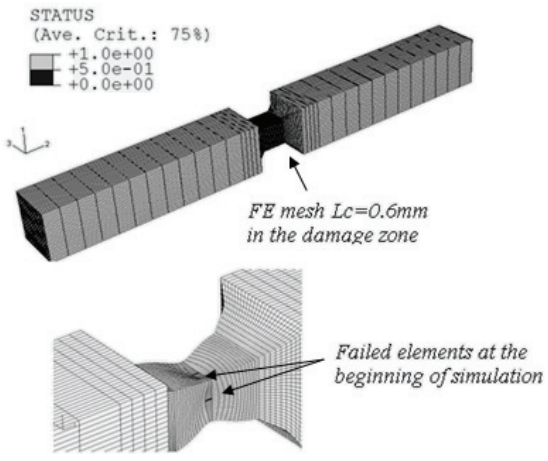

Figure 4: 3D square tensile FE modelling and crack growth representation for CAFE technique.

3. Results and discussion

This section describes and discusses numerical calculations carried out to study the flat fracture in special laboratory tests in the through wall thickness direction of X100 line pipe. Two sets of numerical predictions, GTN damage theory + classic FE modelling and Rousselier damage theory + CAFE technique, were carried out and compared. The effect of the damage parameters and computing time were investigated. All simulations were performed in a PC Pentium 4 CPU 3.2 GHz, 1 GB of ram and 40 GB disk capacity.

In the first set of 3D numerical studies on cylindrical tensile testing, five micromechanical parameters (q_1, q_2, f_c, f_F and L_c) were calibrated. For the initial simulation the critical mesh size ($l_c = 200\mu m$) and typical values of the q parameter ($q_1 = 1.5, q_2 = 1.0, q_3 = q_1^2$) were used. The GTN damage parameters were determined by a series of trial and error finite element analyses comparing the experimental (Load – Diametral contraction) record until the model response matched the experimental data. The load was calculated from the reaction at the top surface of the specimen since displacement loading was used, whilst the contraction was monitored in the damage zone. In the trial and error procedure it has been observed that higher values of q_2 and f_c cause a delay in the material damage process and vice versa smaller values of them accelerate the failure of the material. Values of the final calibration of damage parameters are set out in Table 1. Plots of the test data and result of the best fitted simulation are shown in Fig. 5

q_1	q_2	f_c	f_F	L_c mm	Time min.
1.5	0.87	0.001	0.005	0.2	50:18

Table 1: Damage modelling parameters calibrated for the first set of numerical studies.

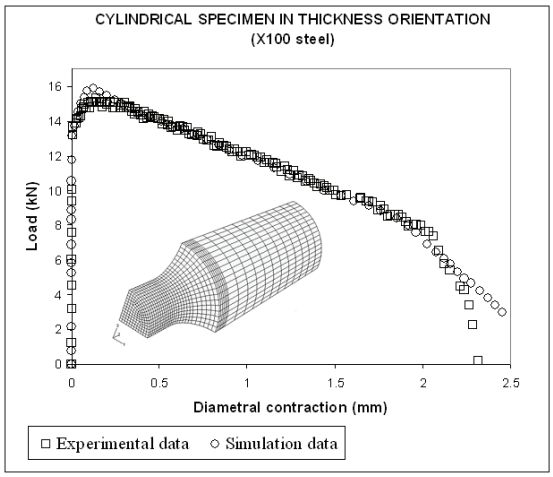

Figure 5: *Experimental and best fitted data for the first set of numerical studies.*

In the second set of 3D numerical predictions, the two micromechanical damage parameters for Rousselier model (D and σ_1) were adjusted by trial and error. It was observed that the general effect of increasing D is to cause the damage at an earlier stage of loading and a higher value of σ_1 delayed the failure process. The initial void volume fraction f_0 was obtained from Franklin's formula [5]. The other three values needed were adjusted for the best prediction of the material behaviour: number of cells per linear FE ($\sqrt[3]{M_D}$), mean critical value of the damage variable (BFM) and standard deviation of the critical value of the damage variable (BFSTD).

A suitable FE size of 0.8mm was chosen to give adequate resolution of the stress-strain field behaviour in the damage zone, such that four ductile cell elements were attached at each FE providing a cell size of 0.2mm, which is representative of the large inclusion spacing in the material. Initial input value of $\sigma_1 = 780MPa$, $BFSTD = 1.25$ and $BFM = 8$ were initially used as proposed in [6]. The best fitted data of damage parameters in CAFE technique are set out in Table 2, and the plot of its final tuning simulation to the experimental data is shown in Fig. 6

σ_1	780 [MPa]
D	3.5
f_0	$3.0x10^{-5}$
L_{FE}	0.8 mm
L_D	0.2 mm
$\sqrt[3]{M_D}$	4
BFSTD	1.3
BFM	8
time	3:29 min.

Table 2: Damage modelling parameters calibrated for the second set of numerical studies.

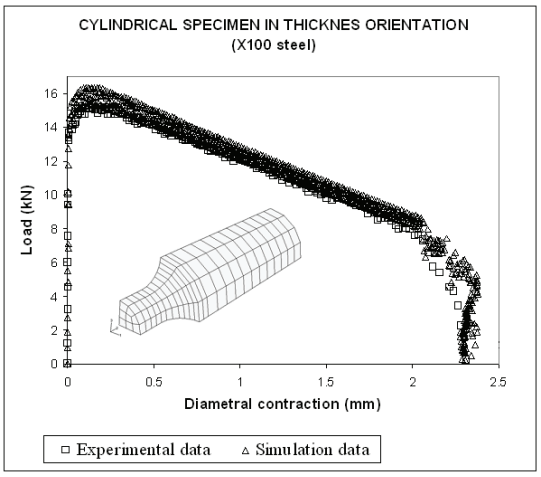

Figure 6: *Experimental and best fitted data for the second set of numerical studies.*

With the aim of showing the effectiveness of the CAFE technique in reducing computing time to obtain comparable results of damage prediction, four cylindrical tensile specimens with different size element, but the same cell size in the damage zone were created. A value of $L_D = 0.1mm$ for the cell size was chosen and models with element size L_{FE} of 0.2mm, 0.4mm 0.6mm and 0.8mm were made. These models decreased the number of FE with VUMAT properties (NEL) in the damage zone from 131 to 30, 15 and 8 elements respectively.

Calibration was achieved using the model with $L_{FE} = 0.8mm$ and the fitted data was input to the other three models. CAFE simulations demonstrated that for the same values of Rousselier damage parameters with different element size but equal internal cell size, the results are comparable and the running time is reduced considerably. Fig. 7 shows the plots of the simulated results and experimental data. Specific values of each

simulation are set out in Tables (3) and (4).

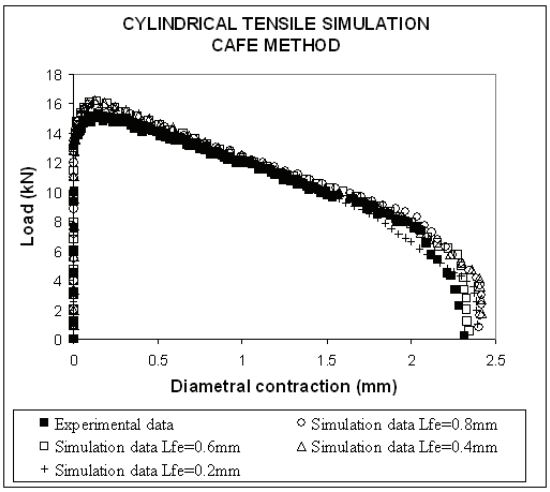

Figure 7: *Plots results of different element sizes* L_{FE}*, but equal cell size* L_D.

	1	2
σ_1	780 [MPa]	780 [MPa]
D	3.5	3.5
f_0	$3.0x10^{-5}$	$3.0x10^{-5}$
L_{FE}	0.8 mm	0.6 mm
L_D	0.1 mm	0.1 mm
$\sqrt[3]{M_D}$	8	6
BFSTD	1.3	1.3
BFM	8	8
NEL	8	15
time	4:10 min.	7:28 min.

Table 3: Damage modelling parameters calibrated for: $L_{FE} = 0.8mm$ and $L_{FE} = 0.6mm$ tensile models.

	3	4
σ_1	780 [MPa]	780 [MPa]
D	3.5	3.5
f_0	$3.0x10^{-5}$	$3.0x10^{-5}$
L_{FE}	0.4 mm	0.2 mm
L_D	0.1 mm	0.1 mm
$\sqrt[3]{M_D}$	4	2
BFSTD	1.3	1.3
BFM	8	8
NEL	30	131
time	15:05 min.	57:38 min.

Table 4: Damage modelling parameters calibrated for: $L_{FE} = 0.4mm$ and $L_{FE} = 0.2mm$ tensile models.

Validation of calibrated micromechanical parameters for the damage prediction was carried out with square tensile section specimens. In these samples, vertical and horizontal lines were marked on the specimen gauge face (Fig. 8) and using an imaging method, grid technique, the whole field strain deformations were extracted [7]. From this experimental information, logarithmic strain deformation in thickness direction was taken and input directly in [9] representing contours at the end of the test (Fig. 9). It was with the aim of validating the numerical damage prediction in terms of comparing deformation contours of experimental and simulation results, having used the previous calibrated micromechanical parameters.

3D numerical simulations on square tensile tests were conducted using the same information listed in Tables 1 and 2. Accordingly FE models in the damage zone with identical characteristics were created. Figs. 10 and 11 show the contour results for the FE model and CAFE model at the end of the simulations.

Taking values e.g. from the final simulations in the centre of the specimen, $\log \varepsilon_{final} = 1.25$ for the classic FE and $\log \varepsilon_{final} = 1.06$ for CAFE technique, demonstrated that the damage parameters previously calibrated were transferable to predict with sufficient accuracy the experimental logarithmic strain in thickness direction ($\log \varepsilon_{\exp erimental} = 1.25$).

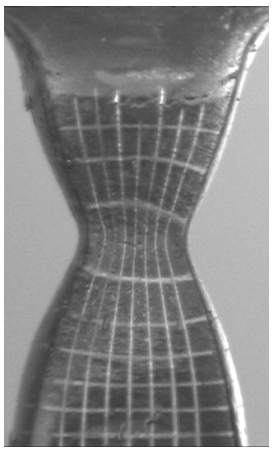

Figure 8: *Experimental data (Shape deformation of the square tensile specimen at fracture initiation in the centre of the test).*

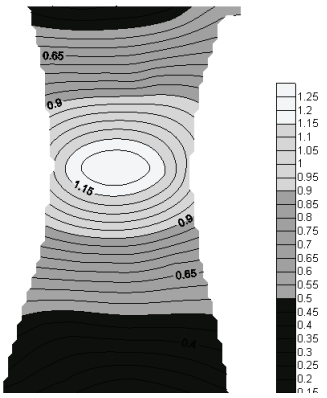

Figure 9: *Contour of the experimental logarithmic strain (thickness direction) at fracture initiation.*

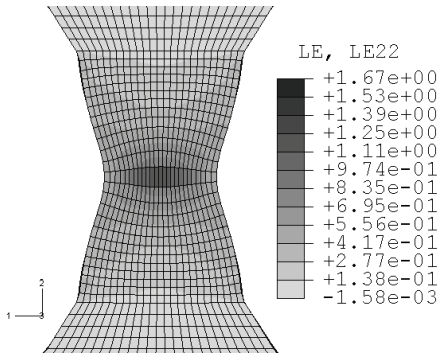

Figure 10: *Contour of the simulated logarithmic strain (thickness direction) at fracture initiation, "FE model"*

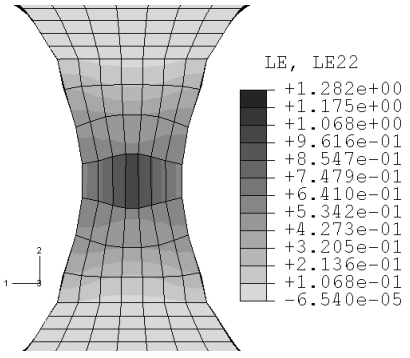

Figure 11: *Contour of the simulated logarithmic strain (thickness direction) at fracture initiation, "CAFE model"*

4. Conclusions

The Cellular Automata – Finite Element (CAFE) technique has been shown to be a powerful tool in reducing simulation time whilst maintaining good predictions of damage. Micromechanical damage parameters tunned to cylindrical tensile test data were transferable to reproduce the experimentally observed data on square tensile samples.

References

[1] Leis, B.N., Eiber, R.J., Carlson, L. and Gilroy-Scott, A. (1998). *Proc. of Int. Pipeline Conf.,* Vol. **II,** ASME, pp. 723.

[2] Andrews, R.M., Howard, I.C., Shterenlikht, A. and Yates, J. R. (2002). *Proc. of the 14th Biennial Conf. on Fract*, ECF14, Edited by Neimitz, A. et al. EMAS Publication, Sheffield, pp. 65.

[3] Tvergaard, V. and Needleman, A. (1984), *Acta Metallurgica,* **32**, pp. 157.

[4] Rousselier G. (1987), *Nuclear engineering and Design,* **105**, No.1, pp. 97.

[5] Franklin, A. G., (1969), *J. Iron and Steel Inst.,* **207**, pp. 181.

[6] Shterenlikht A. (2003), PhD Thesis, Mechanical Engineering Department, The University of Sheffield.

[7] Ayvar, S., Yates, J. R. and Howard, I. C., paper , (2006) *Proc. Int. Conf. 8th Mesomechanics*, Porto, Portugal.

[8] Hibbitt, H. D., Karlsson, B. I. and Sorensen, E. P., (2001) ABAQUS User's Manual, version 6.2.

[9] Surface 8, (2002) Golden Software, Inc.

THROUGH THICKNESS DEFORMATION OF MODERN GAS PIPELINE STEEL

Ayvar, S., Yates, J. R. and Howard, I. C.
The University of Sheffield, Department of Mechanical Engineering, Sheffield, UK

Abstract

The aim of this paper is to report on recent experimental work carried out to measure the deformation behaviour of X100 line pipe steel when loaded in the through wall direction. The laboratory tests were conducted on specially designed cylindrical and square tensile specimens. The through wall pieces were friction welded to steel grip extensions. Scanning Electron Microscope (SEM) photographs were taken before and after the friction welding to confirm that the process did not change the microstructure of the line pipe steel.

Two methods were used to monitor deformation during the tensile loading. Firstly, transverse and axial extensometers were used on cylindrical tension specimens to capture the diametral contraction and axial deformation throughout the loading process. Secondly, a fine grid was marked on the faces of the square section tensile specimens and images were recorded using still and video digital cameras during loading. A full field map of the deformation of the test material was captured using this technique.

The experimental results obtained demonstrate the effectiveness of the proposed specimen designs and deformation measurement techniques to obtain the mechanical properties of modern pipeline steel in the through thickness direction.

Keywords: X100 pipe line steel, thickness direction, friction welding, SEM, grid technique, specimen designs for through wall direction

1. Introduction

For the safe and economical transportation of natural gas, pipelines play a vital role in gas field development. Gas companies have shown increasing interest in the use of higher grade steels for the construction of long distance pipelines. The use of a high strength grade offers potential benefits, in terms of using a higher service pressure without increasing the pipe wall thickness. This in turn offers financial advantages in transportation and fabrication costs. Recent progress in the technology for the controlled-rolling (CR) process and thermo-mechanical control (TMC) process, has allowed high grade line pipes to be obtained, such as API 5L [1] X80, X100 and X120. However, to construct pipelines with those materials, the characteristics of high-strength steel need to be investigated carefully in terms of deformation behaviour and tearing toughness.

The research reported here describes recent results on the experimental work to investigate the effectiveness of the proposed designs and measurement techniques to obtain the deformation behaviour and mechanical properties in the through wall direction of X100 line pipe. The data obtained from these tests is required for a complete analysis of the plastic anisotropic behaviour induced in this modern material by the fabrication process.

2. Design of tensile specimens for thickness direction

The material under investigation was an X100 grade gas pipeline (36" O.D X 19mm W.T). To measure the pipe tensile properties through wall direction, a plate was taken from the original pipe. From this plate, cubic pieces (20×20×18 mm in the thickness direction) and round bars (ϕ=20mm and 100mm long) were machined. The manufacturing process consisted (Fig. 1) of pre-machining the above pieces, then friction welding each sample to the bar extensions, and finally machining the tensile specimens.

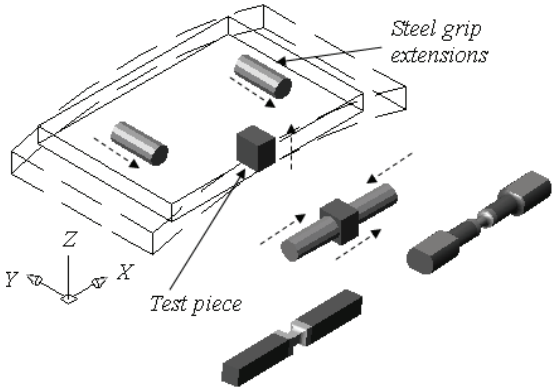

Figure 1: *Specimen manufacture process.*

According to the dimensions of the original gas pipe and the requirement of the friction welding process, two special designs (cylindrical and square section tensile specimens) were proposed as can be seen in Fig. 2.

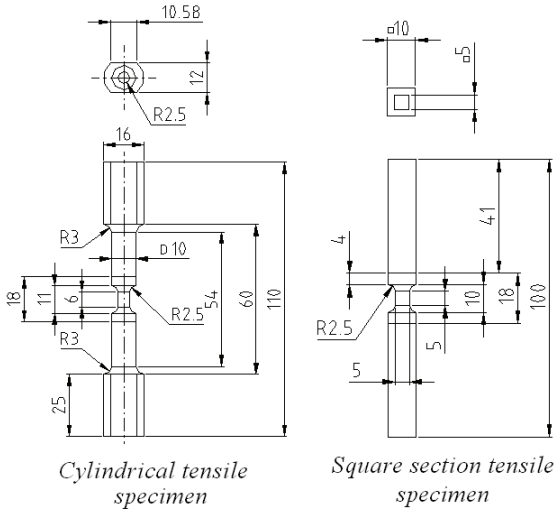

Figure 2: *Designs of the tensile specimens.*

The cylindrical specimen was designed with a 6mm gauge length and a 5mm gauge diameter. The ends of this specimen were machined with flats for a better fit in the hydraulic grips; this also made it possible to identify the thickness direction in the tested specimen. The square section specimen was created with a gauge area of 5×5mm length. Fig. 3 shows the machined specimens.

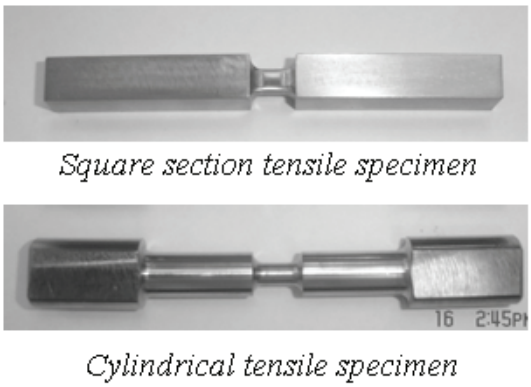

Figure 3: *Machined specimens.*

3. Welded specimens

The friction welding process was carried out in the following steps: a) one component is rotated while the other is advanced into pressure contact with it, b) heat is produced at the faying surface. Overheating of metal can not occur as the weld zone temperature is always stabilised below the melting point, c) softened material begins to extrude in response to the applied pressure, creating an annular upset, d) heat is conducted away from the interfacial area for forging to take place, e) rotation is stopped and a forge force is applied to complete the weld, f) the joint undergoes hot working to form a homogenous, full surface, full diameter, high integrity weld.

Scanning Electron Microscope (SEM) images were taken before and after the friction welding to confirm that the process did not change the microstructure of the line pipe steel. A welded specimen and a steel piece of the original pipeline were taken randomly. These two samples were ground, polished and etched (nital 2%) for metallographic analysis. The microstructure of the welded specimen was revealed in three main zones as is

shown in Fig. 4. Zone one: on the annular upset created by the friction welding process, zone two: on the edge close of the welding and zone three in the centre of the piece test. Fig. 5 shows in detail the microstructures of those zones. In the original pipeline sample, the microstructure was revealed at the centre (Fig. 6).

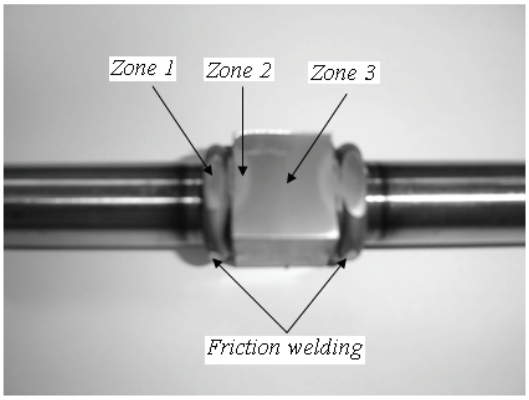

Figure 4: *Welded specimen*

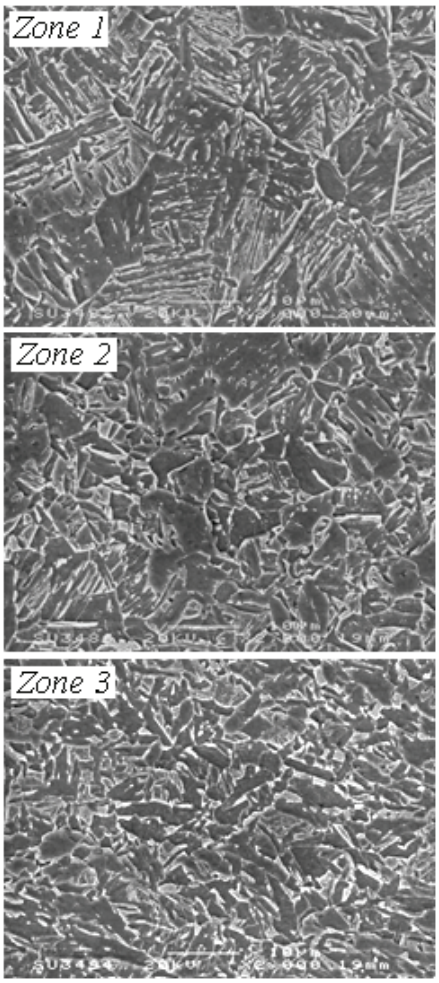

Figure 5: *Microstructure of the three zones in the welded sample (X2000).*

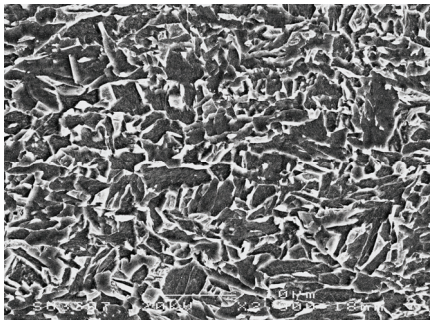

Figure 6: *Microstructure of the original pipeline sample.*

The SEM images showed that the microstructure of zone three is similar to the original microstructure, so that the mechanical properties were not affected in that zone by the friction welding process. The microstructures of zones one and two are different from the original pipeline. However, this is not important as the test area is confined to the centre of the specimen, corresponding to zone three.

4. Experimental work on cylindrical tensile specimen

All cylindrical specimens were loaded in uni-axial tension in a servo-hydraulic Instron 8501 machine under displacement control of 0.01 mm/s. The load, displacement, axial and transverse strains were recorded in each tests. An Instron strain gauge (model 2620-604) and an Epsilon extensometer (model 3575-100-ST) were used to capture the axial and diametral strains respectively. Two grip extensions were made and calibrated with a dial indicator (Fig. 7) for the Instron strain gauge (axial extensometer) due the short gauge length.

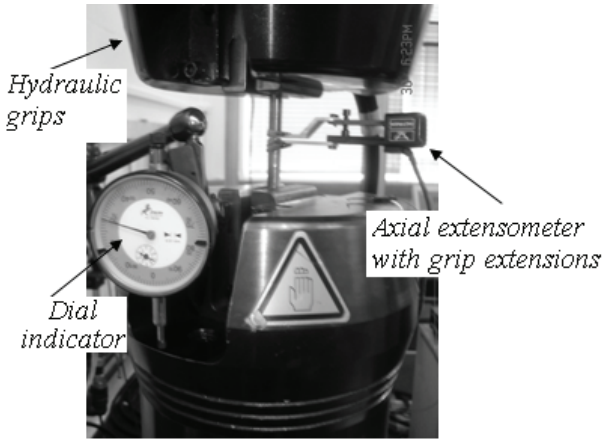

Figure 7: *Calibration set-up.*

5. Experimental work on square section tensile specimen

For the measurement of the displacement field an optical method, using a grid, was utilised [2]. The gauge area (5×5mm) of the sample was prepared using engineering blue spray-paint, and a crossed grating pattern in a series of well-defined parallel lines of 0.5mm pitch was produced on it. The fine pitch of the mesh was created carefully with a height gauge.

The experimental set-up (Fig. 8) for the acquisition of the images consisted of a still camera (EOS 20D Canon) and a digital video camera (NV-GS400 fixed at two perpendicular gauge areas to capture the full displacement field. The gauge surface with the grid pattern was lit by a lamp in order to improve the contrast and consequently the acquisition of the images.

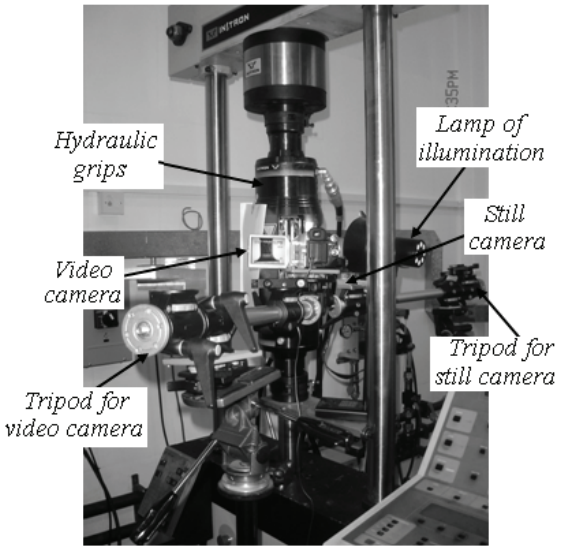

Figure 8: *Experimental set-up.*

The square section tensile specimens were tested on the same servo-hydraulic Instron 8501 and were steadily loaded at the same low strain rate under displacement control 0.1 mm/s as the previous cylindrical tensile samples. In this laboratory test the load, displacement, and images from the still and video cameras were synchronised at the same starting time of the test. Information on load and displacement was recorded by the controlling computer every two seconds. The video frame and the photographs with a time sequence of six seconds were recorded in another computer. Thus at the end of the experiment, the two computers acquired and stored complete load-time and displacement-time curves, together with the video and photographs of the whole field deformation of the specimen.

6. Experimental results and discussions

Four cylindrical and four square section tensile specimens were carried out. Experimental data on axial deformation-load of three cylindrical samples and load-time of four square section specimens have shown that the recorded information was consistent with each other. (Figs. 9 and 10)

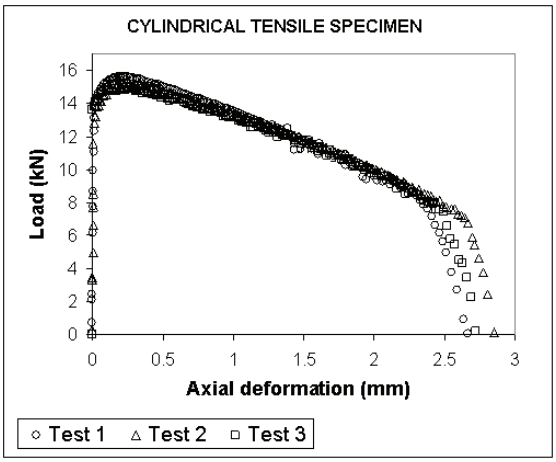

Figure 9: *Axial deformation-load curves.*

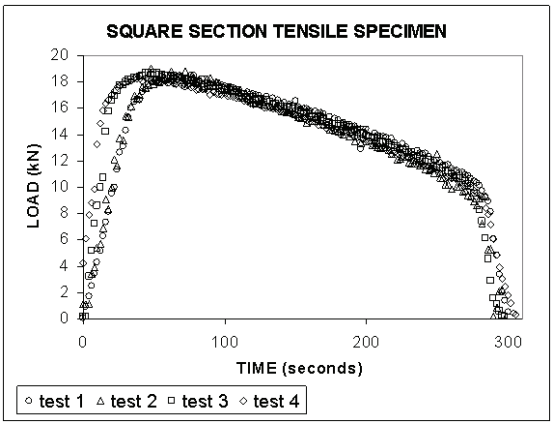

Figure 10: *Load-time curves.*

Regarding the cylindrical tests, the diametral contraction was monitored by the transverse extensometer. It was fixed on the cross section area in two orientations in order to capture the considerable ovalisation of the specimens at the end of the test. In two of the tests, the transverse extensometer was attached in the longitudinal direction. Whilst in the other two tests, it was positioned in the transverse direction. The plotted results (Fig. 11) show that deformation up to the point of hardening displays isotropic behaviour, but softening shows anisotropic damage since the transverse orientation deforms more than the longitudinal direction.

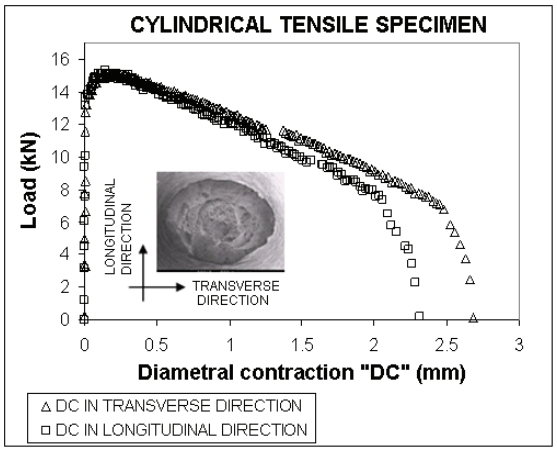

Figure 11: *Load-diametral contraction curves.*

To obtain the full field deformation behaviour in the through wall direction of the line pipe, four square section specimens were tested. The calculation of the displacements was achieved by comparing the deformed grid with the original one. It was possible by the use of video frames (e.g. Fig. 12) and a series of photographs (e.g. Fig. 13) that were taken of the gauge surface. Acquisition of the images from the still camera was not as good as the ones obtained from the video camera, due to the difficulty of focussing on the small grid pattern through the loading process. This is important since the reliability of this method depends firstly upon the quality of the pictures in terms of contrast, uniform and width of the engrave lines.

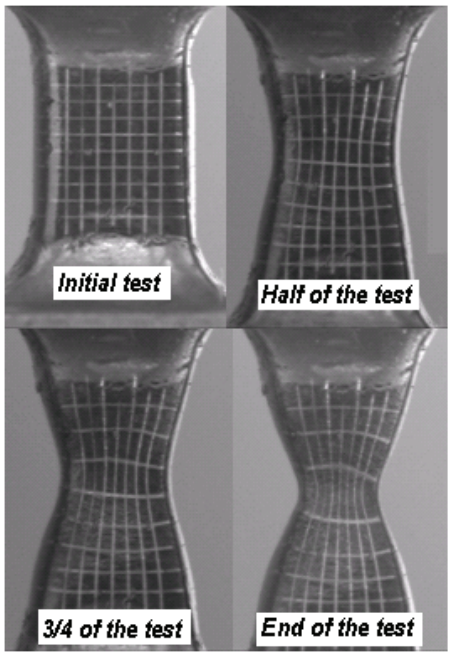

Figure 12: *Example of images from the video camera*

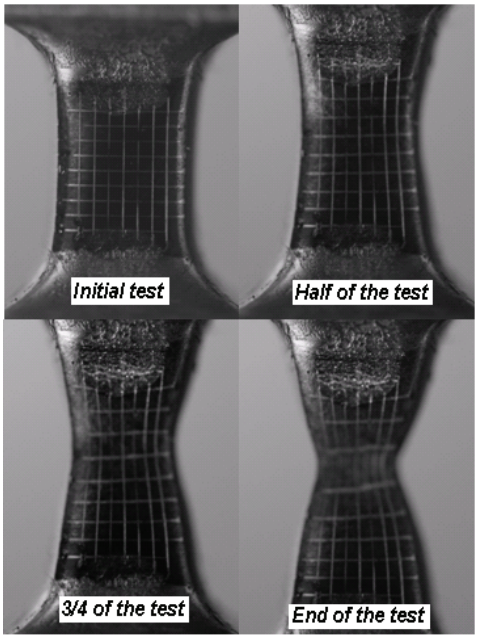

Figure 13: *Example of images from the still camera*

A MATLAB script [3] was used to extract the deformation measurement, at the centroid of each single grating, when clicking on grid intersections. In the script text output files can be created, as deformation gradients, logarithmic and principal strains of the grid. These text output files can be utilised to plot the contours of the whole field deformation

behaviour by using [4]. Fig. 14 shows the logarithmic strain contours produced.

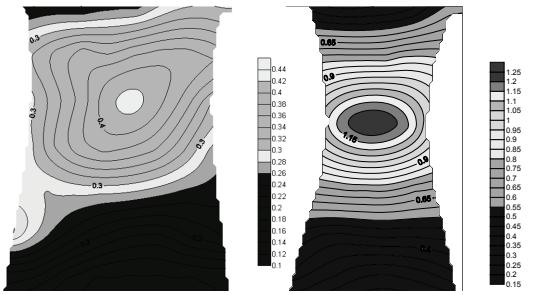

Figure 14: *Contours of logarithmic strains in thickness direction*

A power law function of the form $\sigma_T = K\varepsilon_T^n$ (where n is the strain hardening exponent and K is the strength coefficient), was fitted to the experimental data obtained in the tensile tests in terms of true stress-strain. The power law fit was used to extrapolate the yield curve beyond uniform elongation of the specimen. Fig. 15 shows the fitted stress-strain curves of the cylindrical and square section specimen. Tables 1 and 2 show the values of the measured mechanical properties obtained from the cylindrical and square section specimens.

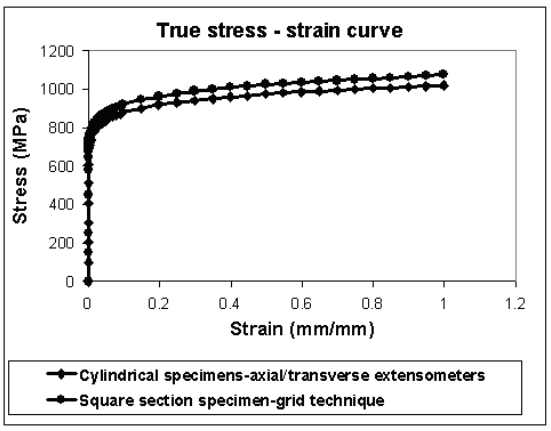

Figure 15: *stress-strain curves.*

Property	Value
Young's modulus	210 [GPa]
Yield strength (0.2% proof stress)	718 [MPa]
Tensile stress	836 [MPa]
Strain hardening law $\sigma_T = K\varepsilon_T^n$	$n = 0.064$
	k =1017

Table 1: Mechanical properties in thickness direction obtained from cylindrical tensile specimen.

Property	Value
Young's modulus	210 [GPa]
Yield strength (0.2% proof stress)	721 [MPa]
Tensile stress	844 [MPa]
Strain hardening law $\sigma_T = K\varepsilon_T^n$	$n = 0.067$
	k =1073

Table 2: Mechanical properties in thickness direction obtained from square section tensile specimen.

The mechanical properties obtained from the two different tensile specimens are comparable, as they can be seen in the Fig 15 and tables 1 and 2. The two designed specimens and the two proposed methods to monitor the deformation during the tensile loading proved to be reliable for an experimental evaluation of the mechanical properties in the through thickness direction.

Conclusions

The stress-strain characteristics of high strength gas line pipe steel were obtained for the through pipe wall thickness direction. Two different techniques were employed: axial and diametral extensometry on cylindrical tensile specimens; and optical deformation mapping on square cross-section tensile specimens. SEM images confirmed that the welding process used to make the specimens did not change the microstructure of the gauge area in the tests. The proposed specimen designs and the data collection technique demonstrated the efficacy of the whole process to get the mechanical properties.

References

[1] Kawaguchi S., Hagiwara N., Ohata M., and Yotoda M., (2004) *Int. Pipeline Conf.*, Calgary, Alberta, Canada,

[2] Boldetti C., Pinna C., Howard I. and Gutierrez G., (2005), *Int. Conf. Adv. in Exp. Mech.,* pp. 111.

[3] Gutierrez G., (2005), Grid-analysis, User's Manual, Department of Mechanical Engineering, The University of Sheffield.

[10] Surface 8, (2002) Golden Software, Inc.

ENVIRONMENT CORROSION AND MECHANICAL BEHAVIOR OF BURIED PIPING

Min-shan Liu*, Qi-wu Dong, Jing Li, Ke Wang
Thermal Energy Engineering Research Center, Institute of Technology, Zhengzhou University, Zhengzhou 450002, China

Abstract

The engineering project of west-to-east gas transportation is carried out in China which covers 4000 kilometers and the piping goes from Xinjiang province to Shanghai city, across nine provinces, including Henan province .

In this paper the damage of buried piping caused by natural environment in Henan district are explored from two aspects. First, destructive factors come from corrosive environment. In this aspect the soil physicochemical properties of Henan district are analyzed. The properties include the type of soil, corrosion rate, PH value, percent moisture content and chemical constitution of soluble salt. The characteristics of soil corrosion in Henan district are generalized and the corrosive actions which are likely to be caused by these physicochemical properties are presented. The mechanism of corrosion and effect generated by stray current corrosion of buried piping are analyzed. Because of the diversity of the scale of public facilities between the large cities and small cities, the different measures depending on stray current corrosion are taken in different cities. The features of main microbes in the soil are analyzed and the corrosive behaviors of buried piping caused by microbes are explored.

Second, destructive factors are from stress environments. At the present, the design pressure of buried piping has reached 10 MPa. The characteristics of environments combination include working stress and conveying medium are analyzed. The potential existence stress corrosion is proofed through experiments. Because of mal-condition constructed buried piping, it is very difficult to do the annealing heat treatment of weld residual stress. The theoretical value of weld residual stresses on joints and weldments are calculated by using of computer program. The author's outlooks of quality monitoring of welds are presented. In this paper the Henan geological structure and 50-years-periodic geological rules of motion are analyzed. The potential existence seismic loads are simulated with cyclic loading by incremental amplitudes. The stress category and estimation of buried piping under limit loads are completed with finite element method analysis. The safety and reliability under the limit loads are forecasted. In the paper, the main influence of buried piping caused by environments are fully analyzed.

Keywords: Buried piping, Environmental corrosion, Stray current, Seismic loads

1. Introduction

The corrosion of buried piping is mainly caused by soil and transported media. The

* Crresponding author: Min-Shan Liu, Thermal Energy Engineering Research Center, Institute of Technology, Zhengzhou University, 97 Wenhua Road, Zhengzhou, Henan, 450002, China. Email address: qwdong@zzu.edu.cn

engineering project of west-to-east gas transportation is carried out in China, which covers 4000 kilometers and the pipeline goes across Xinjiang, Gansu, Ningxia, Shanxi, Shaanxi, Henan, Anhui, Jiangsu, Shanghai. The total investment amounts to 120 billion RMB yuan. Because the gross pipeline is very long and covers various zones with many kinds of environment, it is very important to consider some technical economical assessment such as pipeline management, transportation safety and pipeline protection, etc.

Buried piping are subject to the corrosion of soil. And the soil environments in different zones have different corrosiveness. Henan province is locate in the middle of China and belongs to the river basin of Yellow River. The pipeline of west to east gas transportation goes mainly through the areas of Zhengzhou and Zhoukou in Henan province of China, which belong to the alluvion plain of Yellow River basin and have unique soil environment. The soil environment couples with buried pipes and forms unique corrosion environment, especially for steel buried pipe when compared to other zones. In this paper, based on the physicochemical index that represents the corrosion environment of soil, the macro corrosion battery influencing steel buried pipes, the corrosion action on pipes of stray current in different cities and the corrosion behavior of the major microbes in soil are analyzed. For the destruction factors caused by stress environment, the numerical analysis of design working load, residual stress at welding joint and possible earthquake load is carried out. And the stress evaluation of steel buried pipe under ultimate load is also done.

2. Influencing factors from corrosive environment

Henan zone is located in the middle of China, and the buried piping of west to east gas transportation passes through Zhengzhou and Zhou zone . The two zones lie on the alluvion plain of Yellow River, where the soil is the compoundsubstance of clay, sand ,soil and loam in layer[1].

The corrosion of steel buried piping is primarily decided by the basic properties of soil and the grade scales of soil corrosivity for carbon steel are listed in table 1. The properties of soil in Henan zone have been investigated and the main influencing factors of soil corrosion include salt content, electrical resistivity, moisture content, PH value, ionic component of soil (e.g. SO42-,Cl,CO32-,HCO3-) and the type of soil, etc. According to the experimentation and collected data, the soil physicochemical data of Henan zone are concluded and listed in table 2. The average rate of corrosion approximates to 3.54g/dm2 /a by test, which fits to corrosion grade III.

Table 1 The grade scales of soil corrosivity for carbon steel

Corrosion grade	I	II	III	IV	V
Corrosion rate g/dm^2 •a	<1	1~3	3~5	5~7	>7
Corrosion depth mm/a	<0.1	0.1~ 0.3	0.3~ 0.6	0.6~ 0.9	>0.9

Table 2 The main soil physicochemical data of Henan zone

Zone	Type of soil	PH value	Electrical resistivity Ω•m	Percent moisture content□	Soluble salt □	Chloride ion □	Sulfate radical □	Carbonas □
Zhengzhou	deposit	7.8	32	13.5	0.23	0.005□ 2.4	0.008□ 2.1	2.0□30
Zhoukou	deposit	8.5	30	26	0.15	0.007□ 2.5	0.006□ 1.8	2.5□30

2.1 Influence of soil fractor on macro corrosion battery

Many factors influence macro corrosion battery of steel buried piping, which interact and work together. So it is difficult to estimate the soil corrosiveness accurately. In the below, in allusion to the terrene characteristic of Henan, the properties of soil of Henan zone are analyzed in the aspects of moisture content, salt content, electrical resistivity and PH value.

Moisture Content: The average moisture content approximates 14% in the soil of Henan. Certain moisture content may dissolve Soluble salt and form electrolyte, so moisture content has an important influence on the corrosion and the salt dissolved in soil increases with the increasing moisture content. In the basin of Yellow River, soil is sandy silt having less than 20% moisture content and the ground water appears and disappears on occasion. It causes that the oxygen content is not uniform in the soil. Then the differential oxygen concentration macro corrosion battery is easy to come into being and make the most serious corrosion to steel buried piping[1].

Salt Content: The distribution of salt content is complicated in Henan with the regional imbalance. The content percent of Sulfate, carbonate and chloride is about 0.008□2.1%, 2.0□30□ and 0.005□2.4□ respectively. According to the grade scale of soil corrosivity and salt content, the corrosivity grade of this kind of soil spans a large scale. In common place, the increase of soluble salt in soil causes the enhancement of ionic conductivity. The existing $Cl^{□}$ destroies the passivating film on the surface of melt and increase the electric conductivity. In some local part of Henan, the percent of $Cl^{□}$ content reaches 2.4%, it greatly accelerates the anode process of soil corrosion. The reaction between □ □ $_4^{2-}$ and steel produces sulfide and accelerates the corrosion of steel. This reaction is concerned with the reducibility of sulfate. The accumulation and separation of soluble salt in soil causes the production of differential salt concentration battery and increase the corrosivity of macro corrosion battery.

Electrical Resistivity: Generally there is inverse relation between soil corrosivity and electrical resistivity. Electrical resistivity is affected by soil state, moisture content and salt content. The soil with bigger void fraction has a less moisture content , reversely, the soil with smaller void fraction has a more moisture content and more soluble salt dissolved. So the electrical resistivity of the latter is lower and corrosivity is stronger. The electrical resistivity of soil in Henan is about 30. It belongs to middling corrosivity to soil and has an important influence on the long distance macro corrosion battery.

PH Value:The soil in Henan appears a little

alkaline, which is mainly composed of loam and alkaline saline soil. The PH value of soil in Zhengzhou is almost 7.8 and in Zhoukou the value is 8.5. In common place, buried piping is easy to be corroded in soil with strong acidity. So the direct corrosion behavior caused by PH value is not obvious in Henan.

In conclusion, in Henan the primary soil corrosion is macro corrosion battery caused by the inhomogeneity of moisture content, the rather high level of soluble salt, the low level of electrical resistivity and the proper PH value. There is a rule that where the electrical resistivity of soil is lower, the corrosion electric potential of metal is higher. So the buried piping is generally located at the anode region of corrosion, then punch corrosion occurs very easily; The accumulation and separation of soluble salt in soil causes the production of salinity battery; The difference in moisture content makes the difference in the density of electrolyte and the non-uniform distribution of moisture content produces the differential oxygen concentration macro corrosion battery.

2.2 The corrosion effect of Stray Current on buried piping

Some times the severe damage of steel buried piping is coming from corrosion under stray current .The harm created by direct stray current is the biggest. Under alternate stray current the corrosion is reducing with the increasing of frequency. Generally, the damage of alternating current with 50Hz is as large as the same direct stray current in 1%. Meanwhile, because of the diversity of the cities scale and the plants proportion, the corrosion status of stray current is different. The intensity of stray current has been estimated by measuring electric potential gradient of buried piping. In Zhengzhou, which is the capital of Henan province, the scale of commonality facilities is rather large. The electric potential gradient of the soil near buried piping in Zhengzhou and Zhoukou have been measured separately. The results of measure show that the average value of electric potential gradient is 8.0 mV/m in Zhengzhou. In addition, the biggest value of electric potential gradient of Zhoukou is 0.24mV/m and the least is 0mV/m[3].

According to some degree electric potential gradient, approximate arithmetic is presented to calculate the density of stray current and the rate of corrosion.

$$i_c = U_d \bullet L/(R \bullet A_0)$$

$$R = \rho L/A_0$$

where,

U_d—electric potential gradient （V/m）;

A_0 — cross-section area of electricity conduction (m^2);

ρ —electrical resistivity (Ωm);

L—length changing with electric potential gradient (m);

i_c—the density of current（amp/m^2）.

The corrosion rate of steel is obtained by Faraday's law and is expressed as a quantity of electricity.

If the value of electric potential gradient is 8.0 mV/m, the corrosion rate under stray current is 0.21$\mu m/a$.

This corrosion rate under the stray current belongs to feebleness corrosion. It can be inferred that there is direct current interference in the steel buried piping. Furthermore, because there is less direct current interference in Zhoukou zone, the corrosion rate may belong to less feebleness corrosion.

2.3 The corrosion of main microbes in soil

Generally, it is difficult to generate corrosion when the soil lacks oxygen. On the other hand, the steel was severely corrupted when microbes especially Sulfate Reducing Bacteria (SRB) exist in the soil. The breeding environment of SRB is that the PH value is within 4.5□9.0. Because the PH value of soil in Henan zone is within 7.1□8.5, which is suitable for the reproduction of SRB. The deoxidation reaction is described as follows:

$$SO_4^{2-} \xrightarrow{SRB} H_2S$$

Due to the existence of H_2S and other corrosive gas, Fe was corroded into black FeS and secondary corrosion products $Fe(OH)_2$. The decomposition of Fe caused by SRB is a synthesis galvano-chemistry process. This deoxidation reaction engaged by Sulfate needs hydrogen. The microbes can slowly release hydrogen from soil and then promote the corrosion of steel in soil. The deoxidation reaction can not only corrode the steel surface, but also can corrode through the wall. This process can be narrated as follows:

$$Fe^{2+} + S^{2-} \rightarrow FeS$$

(Fe^{2+} came from the anode dissolving process)

3. Influencing factors from stress-corrosive environment

While it is quite possible to occur potential SCC(stress corrosion cracking) in the gas transportation pipingline under complicated environment, investigations on mechanical and material behavior of long distance transmission pipelines are necessary and important.

Stress corrosion cracking is conducted by coupling actions of tensional stress and medium corrosion, which leads to metal failure. There are many loading type producing the tensional stress. Buried pipelines subjecting a series of loading during service undergo a rather significant tensional stress, such as the operation stress caused by internal pressure, residual stress resulted from nonuniform heating, cooling, transition and constraints when welding, as well as other reasons like seismic waves or local fundamental subsidence.

When stress exceeds yielding strength at material's crack initiation zone, that is one of two necessary conditions to arise SCC. Therefore it is valuable to study the stresses of structure.

Numerical analysis of stresses has been done taking into account residual stress and seismic loading.

3.1 Numerical analysis of welding residual stress

More attentions have been paid to residual stress of pipeline welding. The analysis of residual stress and strain of a welding joint has been performed by using elastoplastic FEM and von Mises yielding criterion. The simulation has illustrated whole evolution process of welding temperature and deformation, which are shown in Fig.1, Fig.2, and Fig.3[4].

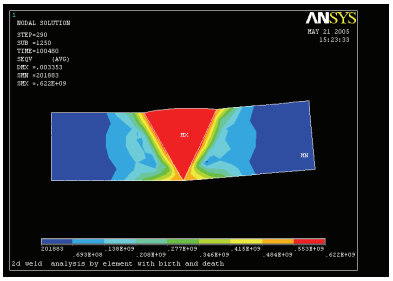

Fig.1 Contour of gross residual stress

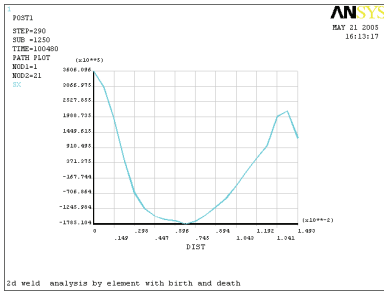

Fig.2 Curve of residual stress in thickness direction

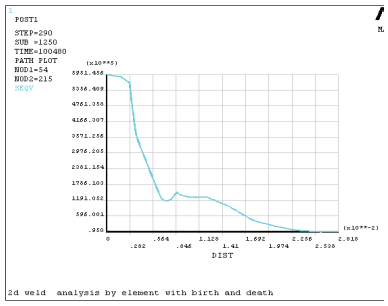

Fig.3 Distribution of longitudinal stress in length direction

Such conclusions can be drawn:

(1) According to Fig.1, the maximum stress is 622 MPa, which has overstepped the yield limit and reached critical value of cracking. At the fusion line, the stress value is 415 MPa and approaches the yield limit.

(2) From Fig.2, it is showed that the weld residual stresses along axis are approximately symmetry between exterior surface and inner surface. The axial tension stress in inner surface is 260 MPa. The stress values is distributing by sequence linearity along wall thickness.

(3)The stress values in inner surface are higher than in exterior surface. The stresses at inner welding line or near it are tension stress, but those are compression stresses at middle part of wall.

(4) From Fig.3, it is showed that the stress value is very low and leaves away from the fusion line. At that time the distance from the middle of welding line is 23mm. Near the fusion line, the stress value reaches a higher level, so that may be a reason for creating easily coll crack.

3.2 Numerical analysis of seismic loads

In terms of records, the highest seismic intensity factor in Henan zone is grade 7. Supposing the period to 0.8s, wave speed Cp = 1.7×10^5mm/s. The maximum axial stress in pipes can be calculated □

$$\sigma_{a\max} = EA\alpha\frac{2\pi}{\lambda_a} = 172.6MPa$$

where

A — amplitude of earthquake displacement wave, mm□

E—Elastic modulus of pipeline□N/mm2;

$$\alpha = (1+\frac{ES}{k_a}(\frac{2\pi}{\lambda_a})^2)^{-1} = 0.37$$

λ_a — — wave length of earthquake displacement wave□mm;

$$\lambda_a = TC_p = 136m$$

3.3 Behavior under co-action of stress and corrosion

Based on difference of PH value in soil environment, SCC can be caused by high or near litmusless PH value. The PH value of soil in Henan zone locates in the range of bringing SCC[6]. First of all, the cracking is formed at the surface of steel under tension stress.

According to the above numerical analysis:

(1). If design pressure of pipeline is 10MPa, the axial tension stress at piping wall is181MPa and the circumferential stress is 362 MPa, which makeup the origin of tensional stress.

(2). The high weld residual stress of pipe connection is another origin of tension stress.

The existence of tension stress is the major factor to generate SCC. The experiment done by MiYunqing et al has shown that critical stress in welding line is near half of the critical stress in base metal if welding joint of high strength pipe is not heat treated. It proves that the zone near welding line is easiest to bring SCC[7].The experiment has shown that the critical stress value of SCC for this pipe steel is about 340MPa, so SCC is very easy to occur at welding line without heat treatment.

(3). In life-span, limit loads that perhaps exist are estimated and sorted by stress. For instance, the potential existence seismic loads in 50 years are calculated. Supposing that 70□ of residual stress can be eliminated, superimposed the working stress, degree of safety is predicted under limiting stress:

$$\sigma_{axis}£¼\sigma_w£«\sigma_{re}£«\sigma_{se}£½81+622\times(1-0.7)+173=540(MP_a)$$

where, σ_{axis} , σ_w , σ_{re} , σ_{se} are total axial stress, axial working stress, axial residual stress and axial seismic stress, respectively.

The prediction results show that the stress value under limit load has overstepped the yield limit and approached the breaking point.

4. Conclusion and measures

(1) It is the synthesizing actions of macro corrosion battery of buried pipes created by soil characteristics in Henan zone□corroding of direct stray current and the rot of microbes in soil that make assessment of soil environment corrosion up to class □, middle corrosion environment□

(2) By use of integrating cathodic protection and outer protection coatings, that is an effective measure for long distance transmission pipelines and the best scheme for avoiding the occurrence of macro corrosion battery.

(3) Epoxy powders are suggested to be used as an anticorrosive coating which is the main part of the combined protection, particularly adapting the soil characteristics in Henan Zone. They have a strong bonding property with steel surface, a preferable corrosion resistance and mechanical properties, mostly be used in intensely corroded environment and a zone consisting of fine soil particles.

(4) The sand clay with well ventilation, mixed or calcareous soils ought to be utilized when filling the buried pipes so as to lower corrosion, prevent the breeding of anaerobic microbes and better the corrosion behavior of soil environment.

(5) It is difficult to select an appropriate annealing technology at grouped construction site for eliminating the welding residual stress which is a principle factor causing stress corrosion cracking. Break arc welding with temperature in melting pool effectively controlled is recommended as it can release the residual stress as welded.

(6) Under limit loading, the calculation result indicates that the magnitude of combined stress has been beyond the yielding strength, close to the value of ultimate strength. Therefore it is particularly significant to apply numerical method to assess the safety margin of the pipeline under limit loading.

References

[1] China soil census office, China Soil[M]. Beijing: China Agriculture Press, 1998.

[2] Wang Zhifang, Investigation and evaluation of the corrosiveness of soil[J]. Corrosion & Protection in Chemical Industry, 1997(4): 17~21.

[3] Lee W, Characklis WG. Corrosion of mild steel under anaerobic biofilm[J]. Corrosion, 1993,49(3): 186~199.

[4] Tan Xianfeng, Zhang Hua. Analysis of temperature and stress fields in welding process by thermo-elastoplastic finite element method[J]. Journal of Plasticity Engineering, 2004, 11(5):71~74.

[5] Wang Shisheng, Zhang Hong et al: Simplified Calculation Method for Strength of Buried Pipeline under the Seismic Load[J]. OGST, 2000,19(11):19~22.

[6] Wang Bing, Liu Shu'e, Zhu Ziyong, Ke Wei, Han Enhou. Stress corrosion cracking of pipeline steel 16Mn in solutions with near neutral PH values[J]. Corrosion Science and Protection Techonology, 2001, 13(2):71~73.

[7] Mi Yunqing, Zhou Guangqi. Stress corrosion cracking research on pipeline steel weld[J]. Journal of Xi'an JiaoTong University, 1996, 30(8): 64~70.

ANALYSIS OF THROUGH CRACKS BEHAVIOUR UNDER RESIDUAL STRESSES

G. Labeas
Laboratory of Technology and Strength of Materials, Department of Mechanical Engineering & Aeronautics, University of Patras, Patras 26500, Greece

I. Diamantakos
Laboratory of Technology and Strength of Materials, Department of Mechanical Engineering & Aeronautics, University of Patras, Patras 26500, Greece

Al. Kermanidis
Laboratory of Technology and Strength of Materials, Department of Mechanical Engineering & Aeronautics, University of Patras, Patras 26500, Greece

Abstract

Numerous engineering structures operate under the presence of residual stresses, arising from various thermo-mechanical processes, such as, welding, forming, cutting, milling etc. In such situations the development of cracks at the influenced regions demands additional attention. In the present work numerical analysis by means of the Finite Element Method (FEM) has been performed for the calculation of two of the main crack parameters, i.e. Stress Intensity Factor (SIF) and strain energy density. Both parameters are required in the prediction of fatigue crack propagation and residual strength of structures under mixed mode loading conditions. The methodology is initially validated in simple loading cases by comparison of numerical results with existing analytical solutions. The numerical procedure is then applied to the study of the effect of more complicated residual stress fields on SIF value and crack propagation angle.

Keywords: Crack behaviour, Residual stresses, FE analysis.

1. Introduction

The application of modern manufacturing techniques, like laser beam welding and forming, friction stir welding, high-speed cutting, milling, etc., leads to the development of residual stresses [1-2]. The effect of these residual stresses may be the undesired distortion of the geometry [3-4], the reduction of structural integrity and fatigue life of the structure [5-6] etc. Furthermore, the behaviour of cracks located near the effected zone may be influenced. Crack initiation period, crack propagation rate and critical crack size may be significantly influenced by the presence of residual stresses at the vicinity of the cracked area.

A common methodology for assessing the behaviour of cracked structures is the utilization of Stress Intensity Factors (SIFs). By knowing the values of SIFs,

crack propagation and residual strength of a structure may be calculated, using simple formulas e.g. Paris law [7] for fatigue crack propagation, or well established laws and criteria, like the strain energy density criterion for stable or unstable crack propagation [8]. For the calculation of SIFs under residual stress fields limited works have been published. Tada et al. [9] and Terada [10-11] have used a customary method based on the superposition principle and Muskhelishvili's stress functions for the calculation of SIFs at cracks situated perpendicular to the welding bead. However, in all the above mentioned works cracks only perpendicular to one-dimensional residual stress field have been considered, which is not realistic in practical applications and does not always represent the most critical situation.

In the present work the influence of a two-dimensional residual stress field on the stress intensity factor of cracks affected by a residual stress field is studied. The residual stress distribution considered for the present analysis is represented by a simple function, which is chosen, such as, to satisfy the requirements for a residual stress field and simultaneous to resemble the commonly observed distribution of residual stresses at welded structures. Finite element analysis is used for the calculation of SIFs at cracks directed at different angles with regard to the weld line. For the validation of the numerical methodology analytical solutions for the case of cracks normal to a one-dimensional residual stress filed, for which analytical SIFs expressions are provided in [12], are used. Excellent agreement is observed between the results of the numerical simulation and the analytical solution. The effect of the various residual stress field parameters on the direction of crack propagation predicted by the minimum strain energy density criterion is also examined. The strain energy density theory, proposed by Sih [13], suggests that a crack propagates when the minimum strain energy density at a specific distance away from the crack tip reaches a critical value. The propagation angle is defined by the angle θ, along which the strain energy density becomes minimum, i.e. crack propagates along the path of minimum resistance. In the present work the required strain energy density values along a cyclic path around the crack tip are numerically calculated.

2. Residual stress field considered

The configuration considered is a square plate of 300 mm edge and 1 mm thickness, resulting from the welding of two plate segments, as shown in Fig. 1. The residual stress field applied at the plate has two components σ_x perpendicular to the weld line and σ_y parallel to the weld line. The variation of σ_y is schematically presented in Fig. 1. The values of σ_x and σ_y are constant at the *y*-direction and vary with the *x*-coordinate. The residual stress distributions are given by the following relationships:

$$\sigma_x(y) = \sigma_{0x}\frac{1-\left(\frac{y}{c_0}\right)^2}{1+\left(\frac{y}{c_0}\right)^4}$$
$$\sigma_y(x) = \sigma_{0y}\frac{1-\left(\frac{x}{c_0}\right)^2}{1+\left(\frac{x}{c_0}\right)^4} \quad (1)$$

where σ_{0x} and σ_{0y} are parameters defining the maximum values of the tensile stresses in the *x*- and *y*-directions, respectively and c_0 is the distance from *y*-axis at which the residual stress value changes from positive to negative, i.e. from tension to compression. The functions $\sigma_x(x)$ and $\sigma_y(x)$, which qualitatively simulate the residual stress field caused by welding [9], fulfil the following conditions:

a) the residual stresses are self-equilibrated (σ_y),

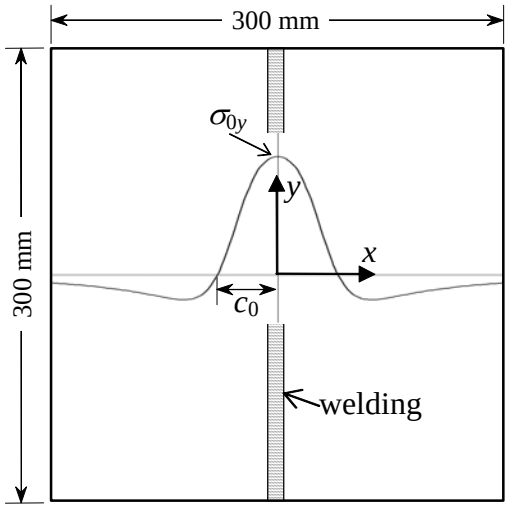

Figure 1: *Residual stress distribution at the plate considered*

b) the functions $\sigma_x(x)$ and $\sigma_y(x)$ produce a symmetric stress field with respect to y-axis, which has maximum value at $x = 0$,
c) the effect of the residual stress vanishes far from the welding
d) the functions $\sigma_x(x)$ and $\sigma_y(x)$ decrease monotonically until they reach some negative minimum values and then increase again to zero without fluctuating, with increasing x.

In the present study a crack of length 2a, inclined at an angle β relatively to the vertical axis is considered at the centre of the plate, as shown Fig. 2. The crack is under the influence of residual stress state in addition to the external plate loading. The values of the residual stress field parameters σ_{0y} and σ_{0x} are considered in this study to be 200 MPa and 100 MPa, respectively, representing typical values observed at welded structures. The remote stress of 100 MPa is applied to the panel in the y-direction. Various residual stress fields, crack lengths and orientations have been studied, in order to evaluate their influence to SIF value and crack propagation angle. More specifically the following parameters have been considered:

a) The crack half-length a is varied from 1 to 20mm.
b) The inclination angle β of the crack with respect to the y-axis has been varied from 10 to 90 degrees, where 90 degrees corresponds to the case when the crack is normal to the external load direction.
c) The distance c_0 where residual stresses changes from tensile to compressive is considered to vary from 2.5 to 10 mm simulating different heat affected zones due to welding.

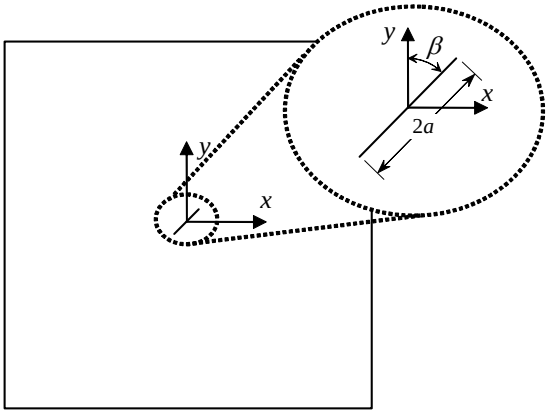

Figure 2: *Position and direction of the crack considered*

3. Numerical Methodology

The Finite Element Method is used in the present study for stress analysis, calculation of Stress Intensity Factors and strain energy densities. The FE model of a plate with a central crack 2a, inclined at different angles β is developed. For the simulation of the cracked plate a Finite Element model is developed using the ANSYS FE code. 'PLANE183' a two-dimensional 8-node structural shell element has been used, having two degrees of freedom at each node, i.e. translations in the nodal x and y directions. The FE model for the case of a crack situated at an angle β=50° is presented at Fig. 3(a). Special care is taken for the discretization of the area around the crack tip, as can be seen in the detail of Fig. 3(b) and (c). Due to the singular nature of the stress field in the vicinity of the crack, singular elements shown in Fig. 3(d) for

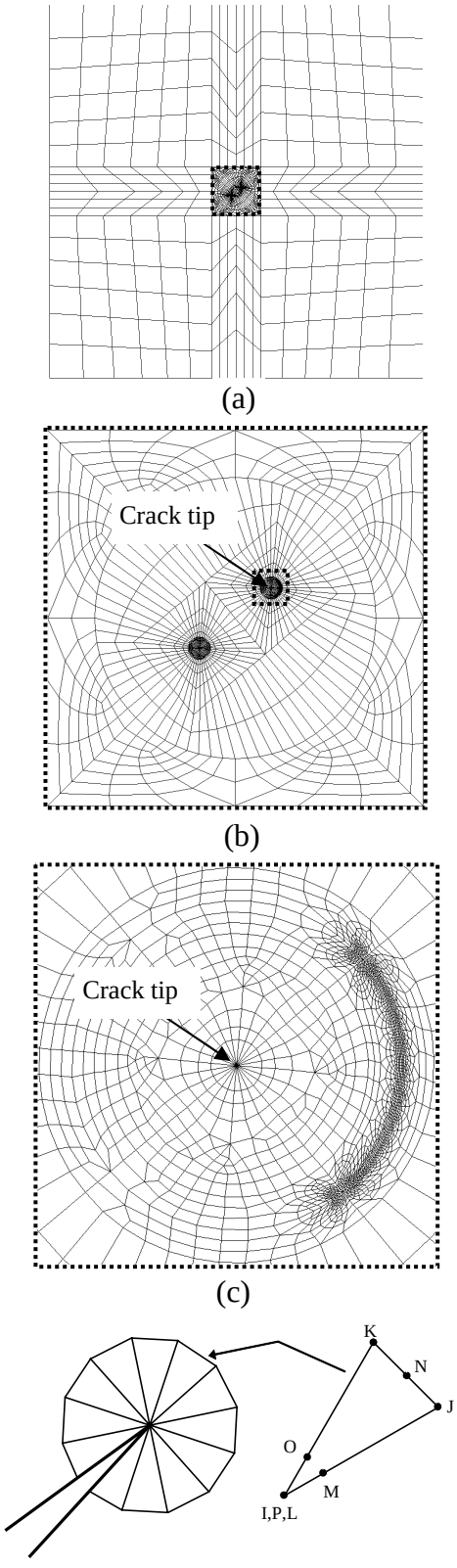

Figure 3: *FE model of the plate*

which the mid-side nodes have been moved to the ¼ of the edge are utilized at each crack tip area.

Consequently, the residual stress values are calculated at element centroids according to Eq. (1) and are introduced in the FE model as initial stresses and the external load is applied at the edges of the plate. Then, linear elastic analysis of the structure is executed, from which stresses, strains and deformations of the plate are computed. For the calculation of SIFs, nodal displacements in the vicinity of the crack tip are used, while strain energy density is computed at a critical distance, where more dense mesh has been developed.

In the literature analytical relationships of SIFs exist for cracks situated into one-dimensional residual stress fields only, i.e. the field σ_y, shown in Fig. 1. Due to this reason, for the numerical model validation, the component σ_x is omitted from the residual stress field and SIFs are numerically calculated for different crack lengths. In Fig. 4, the computed SIFs are compared to those given analytically from [12], indicating an excellent agreement.

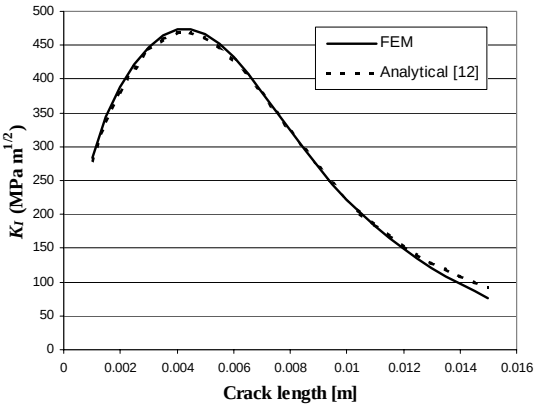

Figure 4: *Comparison of analytical and numerical results for the one-dimensional residual stress field*

4. Investigation of SIFs under residual stress fields

For the cases of mixed mode fracture the efficient stress intensity factor, K_{eff}, as proposed in [14], is currently used:

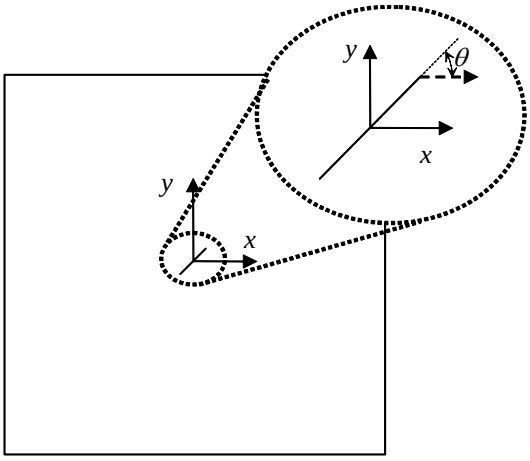

Figure 5: *Definition of crack propagation angle* θ

$$K_{eff} = \sqrt{\frac{16G}{2*(k-1)}} \cdot \cdot \sqrt{\left(a_{11}K_I^2 + 2a_{11}K_I K_{II} + a_{11}K_{II}^2\right)} \quad (2)$$

where:

K_I and K_{II} are mode-I and mode-II stress intensity factors respectively,

G is the shear modulus of the material,

v is the Poisson ratio of the material,

θ is the direction of crack propagation (see Fig. 5), which is calculated in the next section using the minimum strain energy density criterion

$k = (3v)/(1+v)$

$$a_{11} = \frac{1}{16G}\left[(1+\cos\theta)(k-\cos\theta)\right]$$

$$a_{12} = \frac{1}{16G}\sin\theta(2\cos\theta - k + 1)$$

$$a_{22} = \frac{1}{16G}\left[(k+1)(1-\cos\theta) + (1+\cos\theta)(3\cos\theta - 1)\right]$$

The magnitude K_{eff} is normalized by dividing it to its respective value arising from the remote loading only. The results of the analyses concerning the changes of $K_{eff,norm}$ are presented in the diagrams of Fig. 6. From these diagrams the following conclusions may be drawn:

a) The presence of residual stress field is of major importance for the behaviour of small cracks as increases the calculated stress intensity factors significantly.

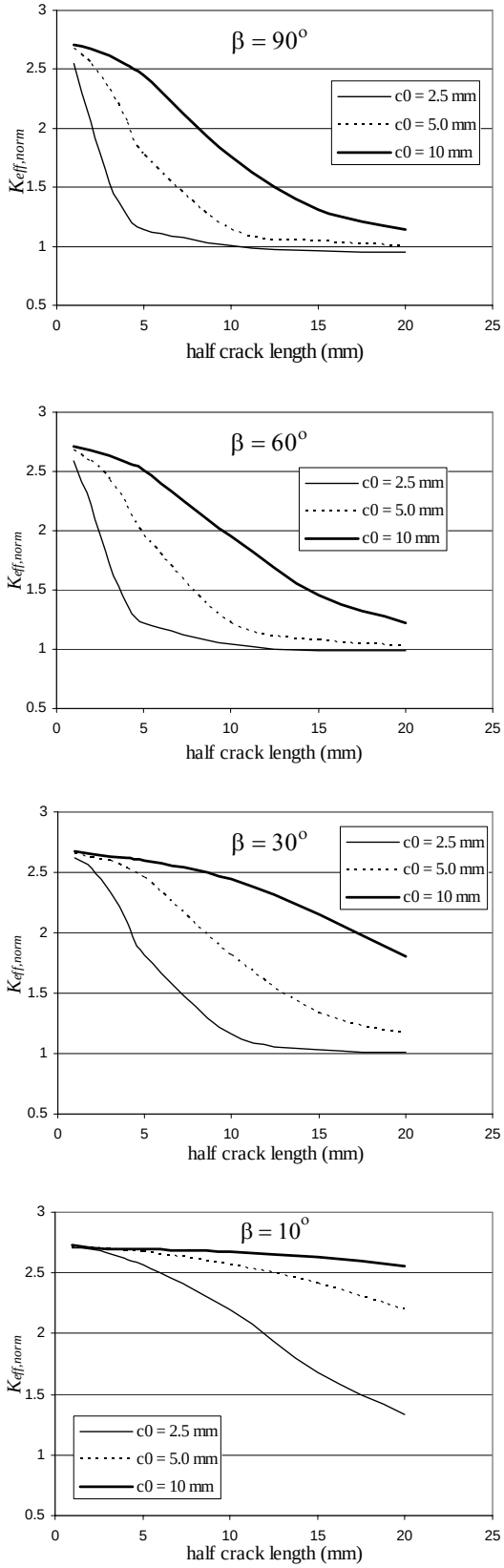

Figure 6: *Normalized efficient Stress Intensity Factor for different crack lengths, directions and* c_0 *values.*

b) The impact of residual stresses on SIFs increases with increased values of parameter c_0 of the residual stress field.
c) Larger values of c_0 lead to a larger crack length range influenced by the residual stress field.
d) The residual stresses impact is influenced by the orientation of the crack, as for lower values of inclination angle β, $K_{eff,norm}$ is shaded with significantly lower rate.

5. Crack propagation angle

The strain energy density theory is widely applied for the prediction of crack evolution, since its introduction in the early 1970's [13]. The basic concept of strain energy density theory is that the strain energy density fluctuates at locations of material properties or geometry changes. The peaks and valleys of the fluctuation can be considered as material failure locations due to material yielding and fracture. Based on the strain energy density criterion, the sequence of fatigue crack growth can be assumed as:

$$\left(\frac{dW}{dV}\right)_c = \frac{S_1}{r_1} = \frac{S_2}{r_2} = \cdots = \frac{S_j}{r_j} = \cdots = \frac{S_c}{r_c} \quad (3)$$

where S_j is the strain energy density factor and S_c its critical value at the distance r_c, which is consider the critical distance from the crack tip. When S_j reaches its critical value S_c, unstable fracture is expected to occur according to the strain energy density theory. For the material type considered in the present study (Al alloy 2024-T3), the value of the critical strain energy factor is 14.31 N/mm, while the critical distance may be calculated to have the value of 0.301mm if equation (4) is applied with K_{Ic} considered to be 1047N(mm)$^{1/2}$:

$$r_c = \frac{3(1-2\nu)}{2\pi}\left(\frac{K_{Ic}}{\sigma_y}\right)^2\left[1+\frac{2(1+\nu)}{1-2\nu}\right]^{-1} \quad (4)$$

For the prediction of crack growth angle θ (Fig. 5) using the strain energy density failure criterion, the strain energy density values have to be calculated at a circular path of radius r_c around the crack tip. The angle for which strain energy density reaches its minimum value is the requested crack propagation angle.

In the present work strain energy density values have been calculated along the above mentioned path using the results of the FE analysis. A typical strain energy density distribution is presented in Fig. 7 for the case of half crack length of 2 mm, angle β = 60º and parameter c_0 = 5 mm. It has to be mentioned that for the presented case the angle θ of crack propagation is at -25° where a local minimum is observed and not around 140° where the overall minimum exists.

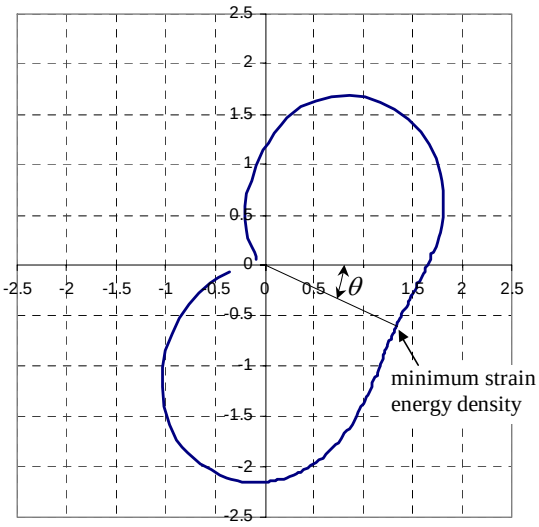

Figure 7: *Variation of strain energy density with respect to θ, for mixed mode loaded crack (β=60^0).*

The predicted crack propagation angle θ for various values of c_0, variable crack length a and angle β, are presented in the diagrams of Fig. 8. From these diagrams a complicated relationship of the crack propagation angle θ with respect to the parameters c_0, a and β is observed.

Although it is difficult to analyse the above dependencies, a general remark is that the effect of residual stress field on the predicted propagation angle θ is greater for smaller inclination angles β. The applicability of the minimum strain energy density criterion for cases of residual stresses could not been proven due to lack of experimental data and remains to be further examined.

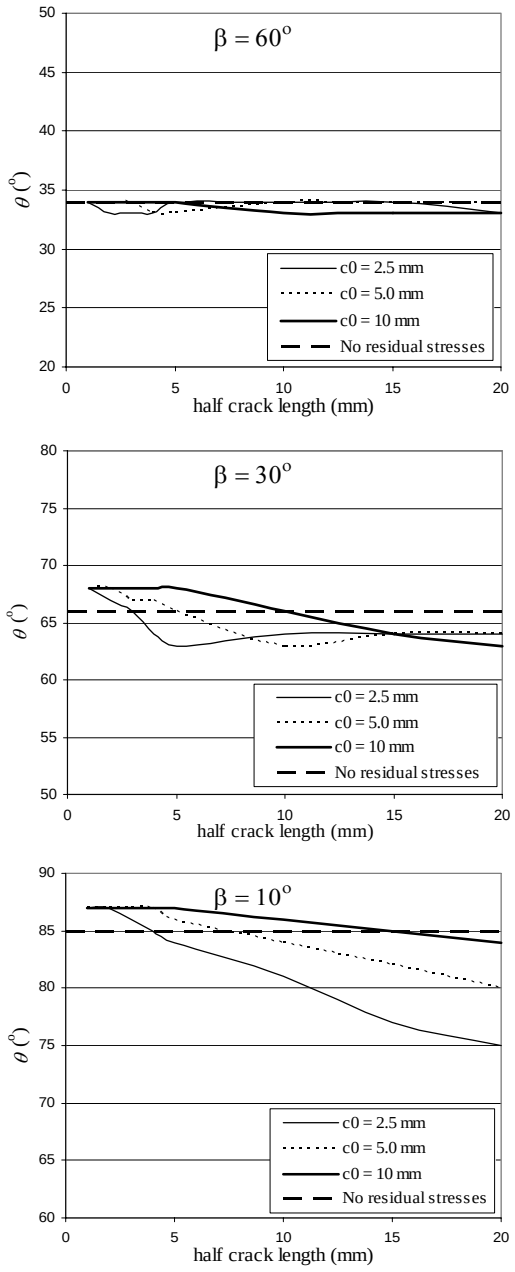

Figure 8: *Effect of crack length on the predicted crack propagation angle θ for various loading parameters, crack lengths and angles β.*

6. Conclusions

In the present work cracks under the influence of a two-dimensional residual stress field combined to remote loading are analyzed. A two-dimensional residual stress field described by simple functions typical for the residual stress distribution observed at welded structures is considered. The finite element method is utilized for the calculation of stress intensity factors and the variation of strain energy density around the crack. Calculated values of the strain energy density are used for the prediction of crack propagation angle, according to the minimum strain energy density criterion. Numerical results concerning SIFs are compared to existing analytical solutions for the specific case of a one-dimensional residual stress field, indicating an excellent agreement. The effect of the residual stress field parameter c_0, crack length a and crack inclination angle β on both the effective stress intensity factor and the crack propagation angle is studied. It has been observed that residual stresses have a major impact on SIF values, especially for small cracks. However the predicted crack propagation angle seems to be less sensitive to the existence of the residual stress field, in the studied cases.

References

[1] Yang, L. J., Xiao, Z. M., (1995), *J. Mat. Proc. Techn.*, **48**, pp. 589-601.

[2] Masubuchi, K. (1980), *Analysis of welded structures*, Pergamon Press, Oxford, UK.

[3] Tsirkas, S.A., Papanikos, P., Pericleous, K., Strusevich, N., Boitout, F., Bergheau, J. M., (2003), *Science and Technology of Welding and Joining*, **8**, pp.79-88.

[4] Tsirkas, S. A., Papanikos, P., Kermanidis, Th., (2003), *J. Mat. Proc. Tech.*, **134**, pp. 59-69.

[5] Dalle Donne, C., Biallas, G., Ghidini, T., Raimbeaux, G., (2000), In: *Second International Conference on Friction Stir Welding*, TWI, Abington Hall.

[6] Cho, S.-K., Yang, Y.-S., Son, K.-J. and Kim, J.-Y., (2004), *Finite Elem Anal Des*, **40**, pp. 1059–1070.

[7] Paris, P. and Erdogan, F., (1963), *Trans. ASME, J. Basic Eng.*, **85**, pp. 528.

[8] Sih, G.C., (1974), *Int. J. Fracture*, **10**, pp. 305-321.

[9] Tada, H. and Paris, P.C., (1982), *Int. J. Fracture*, **21**, pp. 279–284.

[10] Terada, H., (1976), *Eng. Fract. Mech.*, **8**, pp. 441-444.

[11] Terada, H., and T. Nakajima, (1985), *Int. J. Fracture*, **27**, pp. 83-90.

[12] Tada, H., Paris, P.C. and Irwin, G., (2000), *The Stress Analysis of Cracks Handbook*, ASTM, pp. 529-532.

[13] Sih, G.C., (1991), *Mechanics of Fracture Initiation and Propagation*, Kluwer Academic Publishers, Boston.

[14] Broek, D., (1986), *Elementary engineering fracture mechanics*, Martinus Nijhoff Publishers, Dordrecht, pp. 374.380.

Author index